Tailored near-infrared fluorescent carbon nanotube sensors for pathogen detection

DISSERTATION

for the award of the degree
"Doctor rerum naturalium"
of the Georg-August-Universität Göttingen

within the doctoral program
"IMPRS Physics of Biological and Complex Systems"
of the Georg-August University School of Science (GAUSS)

submitted by

Robert Nißler

from Jena, Germany

Göttingen, 2021

Thesis Advisory Committee & Members of the Examination Board

Prof. Dr. Sebastian Kruss (1st Referee)
Physical Chemistry II
Ruhr-University Bochum

Prof. Dr. Uwe Groß (2nd Referee)
Institute of Medical Microbiology
University Medical Center Göttingen

Prof. Dr. Marina Bennati
Institute for Organic and Biomolecular Chemistry
Georg-August University Göttingen

Further members of the Examination Board

Prof. Dr. Timo Betz, Third Institute of Physics, Georg-August University Göttingen

Prof. Dr. Frauke Alves, Institute of Diagnostic and Interventional Radiology, University Medical Center Göttingen

Dr. Tim Schäfer, Institute of Physical Chemistry, Georg-August University Göttingen

Date of oral examination: 06.10.2021

Table of Contents

1 Abstract

1.1 English

During the global COVID-19 pandemic, the needs and benefits of fast and specific analytical tools became apparent to everyone. In particular, advances in nanotechnology promise novel healthcare diagnostics, like the identification of bacterial pathogens. However, up to now, optical nanosensors for pathogen detection rarely exist, but could pave the way for fast, label-free *in situ* detection of infections in the future. One class of nanomaterials with extraordinary photophysical properties are semiconducting single-walled carbon nanotubes (SWCNTs) that can serve as building blocks for such optical biosensors. These tubular carbon allotropes exhibit a diameter-dependent band gap structure, described as 'chirality'. This leads to fluorescence emission (900-1700 nm) in the near-infrared (NIR), a spectral region most suitable for biosensing applications. To obtain functional and colloidally stable probes, the SWCNT's hydrophobic surface needs to be non-covalently modified with biomolecules. Such SWCNT-conjugates are able to translate changes in their local chemical environment into fluorescence signals, the basic principle of optical analyte detection by SWCNT-sensors. In this thesis, consecutive steps were undertaken to tailor the functional surface chemistry and optical properties of SWCNTs for detection of pathogens and pathogen-related interactions: 1) Initially, for a better understanding of the SWCNT's interface, a protocol to quantify adsorbed single-stranded (ss)DNA polymers was established. The calculated amount revealed several hundred DNA molecules on a single SWCNT, depending on oligonucleotide lengths and composition. This displayed the basis for further ratio-specific, bioorthogonal modifications of the nanoconjugates. 2) In addition to tailoring the surface chemistry, SWCNTs with defined emission properties for hyperspectral biosensing were isolated. One strategy made use of chirality specific SWCNT dispersions through polyfluorene polymers and further exchanged the organic interface to those needed for sensing in biological systems. The second approach generated purified samples by aqueous two-phase extraction (ATPE), and demonstrated after subsequent surface exchange a general concept for chemical sensing with chirality-pure SWCNTs. 3) Combination of these approaches facilitated the assembly of nanosensors able to detect bacterial virulence factors

like lipopolysaccharides (LPS) and siderophores or secreted enzymes like proteases or nucleases. Integrated into a functional hydrogel-system and combined in an array-structure, multiple of these sensors could be read out simultaneously by a camera-assisted setup. This enabled the remote detection and discrimination of typical infection-associated bacteria (e.g. *Escherichia coli*, *Staphylococcus aureus* or *Pseudomonas aeruginosa*), based on their chemical fingerprint. 4) Specific SWCNT sensors were developed to detect and visualize plant-pathogen interactions. In a rational approach, SWCNTs were designed to sense *in vivo* (*Arabidopsis thaliana*) reactive oxygen species (ROS, H_2O_2), important signaling molecules involved in plant stress response. Lastly, nanosensors for polyphenol detection were identified and used to visualize the spatiotemporal polyphenol secretion from plant roots (*Glycine max*), a chemical defense response after pathogen stimulus. The presented thesis introduced novel concepts to tailor the functional interface of SWCNTs for molecular recognition of important biomolecules and extends the spectral range to multiplexed approaches. These NIR-fluorescent sensors enabled detection of pathogens and pathogen interactions *in vitro* and *in vivo*, paving the way for improved healthcare- and agriculture-diagnostics.

1.2 Deutsch

Nutzen und Notwenigkeit schneller und spezifischer Analysemethoden wurden spätestens während der globalen COVID-19 Pandemie jedem deutlich. Vor allem Entwicklungen im Bereich der Nanotechnologie könnten zu bislang ungeahnten medizinischen Diagnostikmethoden führen. Bislang sind jedoch kaum optische Nanosensoren zur Pathogendetektion bekannt, könnten aber in Zukunft eine schnelle, markierungsfreie und ortsaufgelöste Identifikation bakterieller Infektionen ermöglichen. Eine Klasse an Nanomaterialien mit außergewöhnlichen photophysikalischen Eigenschaften, welche sich zum Aufbau solcher speziellen Biosensoren eignet, sind halbleitende, einwandige Kohlenstoff-Nanoröhren (SWCNTs). Diese röhrenförmigen Kohlenstoffallotrope besitzen eine Durchmesser-, genauer „Chiralitäts“-abhängige Bandlücke. Dies ermöglicht eine Fluoreszenzemission (900-1700 nm) im nah-Infrarot (NIR), ein spektraler Bereich, besonders geeignet für die Sensorik in biologischen Systemen. Bevor jedoch diese Nanopartikel in der Diagnostik eingesetzt werden können, muss deren hydrophobe Oberfläche nicht-kovalent modifiziert werden, was maßgeblich die spätere Funktionalität und kolloidale Stabilität beeinflusst. Diese funktionalisierten SWCNTs sind in der Lage Änderungen der lokalen chemischen Umgebung in Fluo-

reszenzsignale zu übersetzen, was das Grundprinzip dieser optischen Sensoren darstellt. Die vorliegende Arbeit beschäftigt sich mit der zielgerichteten Optimierung der Oberflächenchemie und optischen Eigenschaften der SWCNT-Sensoren, mit dem Ziel, Pathogene und Pathogeninteraktionen zu detektieren. Hierzu wurde 1) eine Methode entwickelt, um die Oberflächenmodifikation der SWNCTs im Detail zu verstehen, genauer, um die Menge adsorbierter einzelsträngiger DNA-Polymere zu quantifizieren. Die Resultate zeigten auf, dass auf einer Nanoröhre mehrere hundert DNA-Moleküle adsorbieren, abhängig von der Länge und Zusammensetzung der Oligonukleotide. Aufgrund dieser Quantifizierung konnten verhältnis-spezifische bioorthogonale Modifikationen der Nanokomplexe durchgeführt werden. 2) Zur Optimierung der Nanosensoren wurden einzelne SWCNT-Chiralitäten isoliert, welche definierte Emissionsspektren besitzen. Dazu wurde zuerst die Fähigkeit bestimmter Polyfluorenpolymere ausgenutzt, selektiv SWCNTs zu dispergieren, sodass diese nach Austausch der Oberflächenmodifikation in biologischen Systemen eingesetzt werden können. Ein weiterer Ansatz separierte SWCNTs mit Hilfe der wässrigen Zweiphasenextraktion und führte nach Austausch der Oberflächenchemie ein generelles Konzept zum chemischen Sensing mit aufgereinigten SWCNTs ein. 3) Die Kombination der zuvor genannten Konzepte ermöglichte die Entwicklung spezieller Nanoensoren, welche bakterielle Virulenzfaktoren wie Lipopolysaccharide (LPS), Siderophore oder sekretierte Enzyme (Protease, Nukleasen) detektieren. Mehrere dieser Sensoren wurden in einer funktionellen Hydrogelmatrix vereinigt, was ein zeitgleiches Auslesen mit Hilfe einer NIR-sensitiven Kamera ermöglichte. Mittels dieser Technik konnten typische bakterielle Infektionserreger (wie *Escherichia coli*, *Staphylococcus aureus* oder *Pseudomonas aeruginosa*) detektiert und ferner aufgrund ihres chemischen Fingerabdrucks unterschieden werden. 4) Zuletzt wurden Sensoren entwickelt, um Interaktionen von Pathogen mit Pflanzen zu visualisieren. Ein rationeller Ansatz ermöglichte die Detektion pflanzenstress-assoziierter Signalmoleküle wie reaktive Sauerstoffspezies (H_2O_2) *in vivo* in *Arabidopsis thaliana*. Darüber hinaus gelang die Detektion und Visualisierung von pflanzlichen Polyphenolen, welche als spezielle chemische Verteidigung von beispielsweise *Glycine max* gegen pilzliche Pathogene ausgeschüttet werden. In der vorliegenden Arbeit wurden verschiedene neue Konzepte zur spezifischen Erkennung von Biomolekülen mit SWCNTs vorgestellt und mit Hilfe aufgereinigter Nanosensoren eine hyperspektrale Detektion etabliert. Diese optimierten Sensoren ermöglichten die *in vitro* und *in vivo* Detektion von Pathogenen und deren Interaktionen, auf deren Basis in Zukunft eine verbesserte Analytik und Diagnostik im medizinischen und agrarwissenschaftlichen Bereich aufgebaut werden kann.

2 Introduction

2.1 Motivation

'*The first step in the solution of the problem — how to determine the nature of any given kind of matter follows from the knowledge of its properties, as these appeal to our senses.*' These are the first words in Wilhelm Ostwald's book 'The Scientific Foundations of Analytical Chemistry' published in 1894.[1] Even after more than 120 years, these general principles still hold true when it comes to solving issues in complex biological systems, as analytical investigations reveal the underlying principles needed to understand the system as a whole. Most recently, during the ongoing COVID-19 pandemic, the need and benefits of fast and specific analytical tools became visible to everyone. The detection and analysis of pathogen biomarkers indeed enabled the timely diagnostics and treatment of this disease.[2] However, other than spreading viral pathogens, mankind is facing different challenges in healthcare. This includes for instance increasing antibiotic resistance in bacterial infections or the development of novel tools for cancer identification and therapy. A lot of new concepts and methods were developed in the last decades giving dramatic rise of e.g DNA and RNA driven technologies, like CRISPR genome editing tools[3] or mRNA-based vaccines[4].

On the other hand, advances in nanoscience lead to innovative approaches in e.g. drug-delivery or chemical sensing applications, that could facilitate the next big step forward for improved healthcare diagnostics.[5] Materials that can be used for such purposes have at least one dimension in the nanometer regime, which primarily determines their physical, chemical and biological properties. One class of nanomaterials that will be the fundament of this thesis is represented by single-walled carbon nanotubes (SWCNTs).[6,7] These tubular carbon structures exhibit extraordinary photophysical properties like non-bleaching fluorescence emission in the near-infrared (NIR) and are recently discussed as optical nanosensors for a variety of applications.[8] Their emission in the NIR (900-1700 nm) is thereby most suitable for applications in biological systems right up to *in vivo* implementations. Light with such wavelengths can penetrate tissue more efficient and enable optical imaging tools, due to reduced photon scattering, tissue absorbance or low background autofluorescence.[9] In addition, the interface of SWCNTs can be modified with diverse biomolecules, giving

rise to colloidally stable probes that are known to react with altered emission to changes in their local chemical environment.[10] Such optical SWCNT-sensors are able to depict biological systems with great spatial, temporal and chemical resolution.[11]

Based on that, this thesis aims to develop specific SWCNT-based biosensors for the detection of pathogens and pathogen-related interaction. Those sensors could pave the way for fast and specific *in vivo* diagnostics, enabling optical, non-invasive readout of infections, e.g. through smart sensor implants. To facilitate such, yet unknown sensors, their surface chemistry needs to be specifically tailored in order to detect pathogen biomarkers like virulence factors. Multiple sensors could than provide substantial information about an ongoing infection, most desirably direct at the location it arises. Besides healthcare diagnostics, revealing the chemical processes in pathogen interactions is also essential to other areas like agricultural plant research.[12] Understanding and preventing crop-pathogen interactions holds the key for improved agriculture, as well as development and screening for resistant strains to improve food production. Hence, nanosensors for pathogen detection could improve fundamental studies in multiple disciplines, as well as provide diagnostic-analytical solutions beyond.

2.2 Structure

This interdisciplinary thesis will present several aspects in a cumulative form, ranging from functional sensor design to principles for hyperspectral SWCNT-sensing, including subsequent applications in pathogen detection and visualization of plant-pathogen interactions. Hence, the key results will be presented in a total of six manuscripts.

The general structure of the thesis starts with Chapter 3 (Scientific Background), were a theoretical introduction of SWCNTs (3.2) right up to their application as optical sensors (3.6) is presented. Chapter 4 (Aims and Objectives) outlines the conceptual improvements and aims on the way towards tailored SWCNT-based nanosensors. It is followed by the presentation of the above mentioned manuscripts in Chapter 5 (Results and Discussion), within four different Sections (5.1 - 5.4). Each manuscript contains a separate, short introduction, as well as a section discussing the novelty and impact of the presented findings, whereby their respective supplementary information are listed in the Appendix. Hereafter, an overall summary and perspective is given in Chapter 6, highlighting the most important insights and achievements of this thesis.

3 | Scientific Background

3.1 Single-walled Carbon Nanotubes (SWCNTs)

Nanostructured materials can be in general defined as particles in the nanometer (nm, 10^{-9} m) regime, having at least one dimension or their diameter in the range between 1 to 100 nm. They can be built from organic or inorganic materials, however, having in common that their size primarily defines their physical, chemical and biological properties.[13] Within carbon-based nanomaterials, single-walled carbon nanotubes are a class of highly functional nanoparticles, exhibiting unique structural and optoelectronic properties. In the following sections, the characteristic features of SWCNTs will be introduced before their possible application as optical biosensors is discussed.

3.2 Definition, Structure and Synthesis of SWCNTs

Carbon nanotubes (CNTs) are cylindrical, hollow carbon allotropes.[6] They can be basically imagined as rolled-up sheets of sp^2-hybridized graphene (Figure 3.1a). While multiple graphene layers will result into multi-walled carbon nanotubes (MWCNTs), graphene monolayers will, on the other side, form single-walled carbon nanotubes (SWCNTs). These seamless carbon cylinders can have a diameter of 0.4 to 5 nm and a length of several hundred nm, up to the µm scale or even larger in specific cases.[14–17] According to this enormous aspect ratio, CNTs can be seen as quasi-1D objects. By means of high resolution (HR) scanning probe techniques, like HR-STM (scanning tunneling microscopy), it is in fact possible to observe their cylindrical carbon honeycomb structure (Figure 3.1b).[18] The direction of the rolled-up graphene lattice will thereby determine the properties of the resulting SWCNTs, predominantly characterized by the '*chiral vector*' (C_h), or so called '*chirality*', denoted with the indices (n,m). Figure 3.1c illustrates the SWCNT classification[7], which can be expressed with the equation (3.1)

$$C_h = na_1 + ma_2 \tag{3.1}$$

where (n,m) is a pair of integers and a_1 and a_2 are the lattice unit vectors of the graphene sheet. As a result of the distinct SWCNT (n,m) assignment, it is possible to calculate the tube diameter (d_t) by:

$$d_t = C_h/\pi = a\sqrt{(m^2 + n^2 + nm)}/\pi \tag{3.2}$$

in which the lattice constant a = 0.246 nm. The constant a is derived from $\sqrt{3}d_{C-C}$, where d_{C-C} denotes the bond length between a pair of neighboring carbon atoms in the hexagonal graphitic lattice with ∼0.142 nm.[19] The chiral angle (Θ) can be furthermore calculated by:

$$\Theta = tan^{-1}\frac{\sqrt{3}m}{2n+m} \tag{3.3}$$

The overall tube structure (Figure 3.1d) can be further categorized into '*zig-zag*' if $m = 0$ ($\Theta = 0°$), '*armchair*' if $n = m$ ($\Theta = 30°$) and '*chiral*' if ($n \neq m \neq 0$).[7] Moreover, most of the electrical and optical properties of SWCNTs, which will be discussed in detail in Section 3.3, are determined by the chirality (n,m). A metallic (m-SWCNTs) character can be observed if $n - m = 0$, whereas semimetallic characteristics are present if $n - m$ is a multiple of 3. All other (n,m) combinations exhibit semiconducting (s-SWCNTs) behavior.[7,20] As seen in Figure 3.1c, a s-SWCNT can exist as two possible enantiomers, either as right-handed ($n - m > 0$) or as left-handed ($n - m < 0$) form.

In the early 1990s, CNTs were for the first time conclusively described by Sumio Iijima as a novel class of carbon allotropes.[6,21] Other previously known allotropes are for example sp^3-hybridized carbon atoms in diamonds, or sp^2-hybridized carbon in form of graphite or fullerenes. CNTs, however were first observed as a sort of secondary (side) product during arch discharge between two graphite electrodes, used for C_{60} fullerene production.[6,17] Under an inert atmosphere, a direct electric current arc discharge creates extremely high temperatures (4,000 °C), which leads to the sublimation of carbon from the anode. Small amounts of metal catalysts can then improve the condensation of CNTs on the cathode.[17,22] This displays already one method for SWCNT production, but multiple others have been described since then, whereas all lead to a specific distribution of generated SWCNTs in lengths and diameter.[19] Higher yields and purity can be obtained by a similar method, using laser ablation. Similarly to arc discharge, a graphitic source is consumed under high temperature (1,200 °C), but here carbon vaporization is mediated through a focused laser beam.[17,23] Moreover, defined SWCNT synthesis can be performed by chemical vapor deposition (CVD, Figure 3.1e).

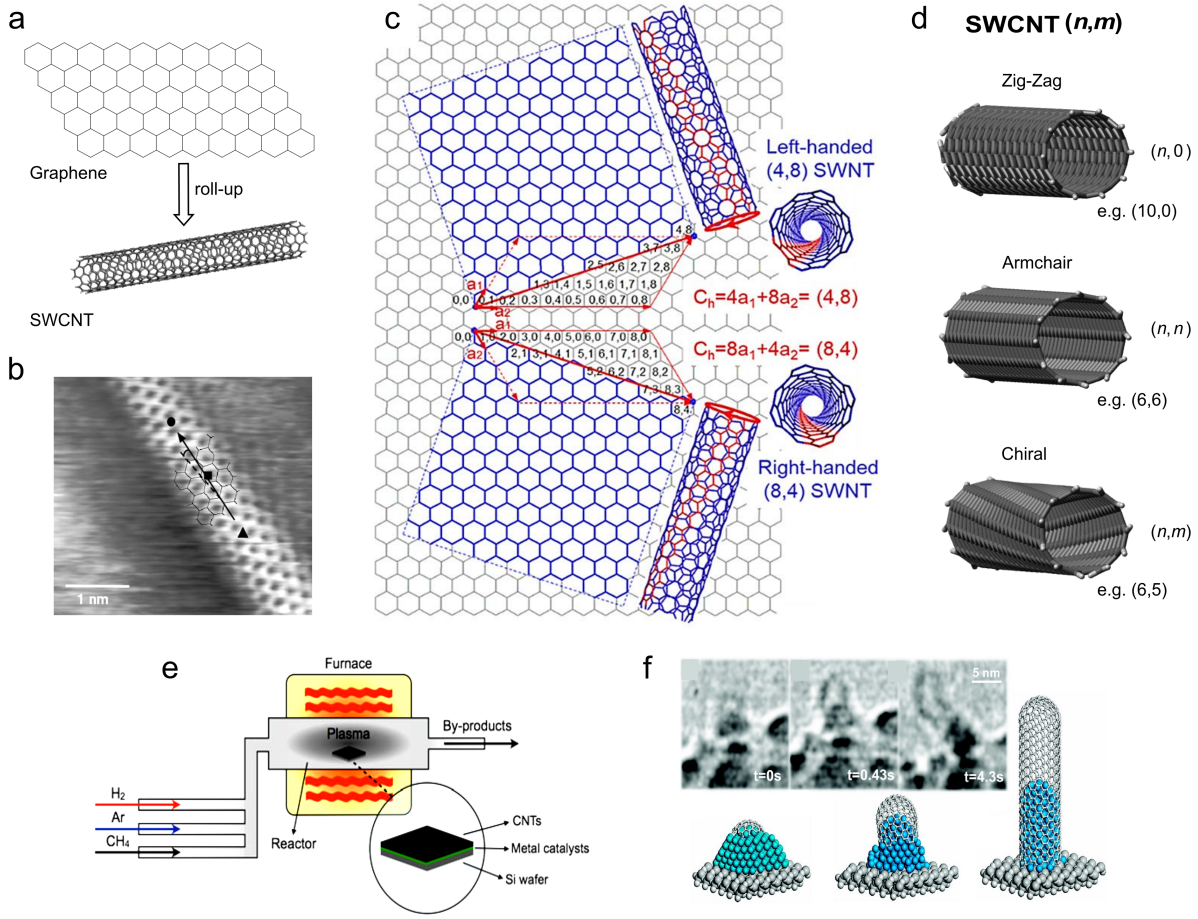

Figure 3.1.: **Structure and synthesis of single-walled carbon nanotubes (SWCNTs).** a) In the most simplified way, SWCNTs can be illustrated as a rolled-up sheet of sp^2-hybridized graphene. b) The SWCNT cylindrical carbon honeycomb structure can be visualized by high-resolution scanning tunneling microscopy (HR-STM). Reproduced with permission from[18]. c) SWCNT's exact chirality (n,m) depends on the direction the graphene lattice is (imaginary) rolled-up. (n,m) represents the integral multiple of the unit vectors a_1 and a_2 displayed in red, further described by equation (3.1). Reprinted (adapted) with permission from Yang *et al.*[16]. Copyright 2020 American Chemical Society. d) The general SWCNT structure can be subdivided into '*zig-zag*', '*armchair*' or '*chiral*', as shown by simulated SWCNTs of similar diameters ((10,0) = 0.78 nm; (6,6) = 0.81 nm; (6,5) = 0.75 nm). Only the chiral SWCNTs can furthermore exhibit left- and right-handed enantiomeric structures. e) SWCNT synthesis by chemical vapor deposition (CVD). In an inert atmosphere gaseous carbon is catalytically decomposed, which leads to carbon precipitation on catalyst nanoparticles. SWCNT chiral composition can be variated and tuned by using different carbon precursors (CH_4 or C_2H_2) or catalyst nanoparticles (varying compositions of Fe, Co and Ni). Reproduced with permission from[17]. f) High-resolution transmission electron microscopy (HR-TEM) image and schematic models of SWCNT formation during CVD. Here, *in situ* analysis reveals the time-resolved synthesis of Ni-catalyzed CNTs, as tubular structures grow from the bottom of the substrate. Reprinted (adapted) with permission from Hofmann *et al.*[24]. Copyright 2007 American Chemical Society.

During the CVD process, gaseous carbon precursors (e.g. CH_4 or C_2H_2) are catalytically decomposed in an inert atmosphere, followed by carbon precipitation on catalyst nanoparticles.[14,17] The resulting SWCNTs are strongly influenced by catalyst nanoparticle size and composition (e.g. Fe, Co, Ni) and can either grow from the bottom of the substrate ('root growth') like shown in Figure 3.1f, or during a 'tip growth', where the nanoparticle is detached and stays on top of the growing CNT.[24] Within the frame of CVD process, a great variety of synthetic protocols are described[16,25–27], right up to the generation of chirality-controlled SWCNTs.[15,28–30]

Since the commercially available SWCNT material used in this thesis was manufactured by two CVD synthesis routes, namely HiPco-(high-pressure carbon monoxide)- and CoMoCAT-(Cobalt-Molybdenum catalysis)-SWCNTs, these techniques will be shortly introduced. During HiPco synthesis, a high-pressure carbon monoxide stream (30 - 50 atm) is continuously mixed with $Fe(CO)_5$ or $Ni(CO)_4$ inside a furnace (900 – 1,100 °C).[17] The applied temperature and pressure lead to the disproportionation of carbon monoxide, which acts as a carbon feedstock, while the metal carbonyls decompose simultaneously.[16] Atomic carbon nucleates and elongates at the emerging catalytic particles, generating SWCNTs with an average diameter between 0.7 – 1.2 nm and length between ∼100 – 1000 nm.[17] In this large-scale process multiple m- and s-SWCNT chiralities are produced, however containing substantial amounts of amorphous carbon and catalyst residues. Using instead a mixture of cobalt and molybdenum as catalysts (CoMoCAT), carbon monoxide or acetylene is decomposed at temperatures between 500 - 700 °C.[15] The catalyst nanoparticles can be thereby anchored on e.g. a silica substrate, whereas the interaction between Mo and Co is believed to add an important contribution preventing nanoparticle aggregation at high temperatures.[15] The general control over catalyst composition, size, structure and temperature stability is important to facilitate chirality-controlled SWCNT growth.[14] As a result, CoMoCAT-SWCNTs contain a high content of s-SWCNTs with ∼50% (6,5)-SWCNTs.[31] These chirality-enriched SWCNTs, with an average tube diameter of 0.78 nm and a median length of 1000 nm, are so far the most defined commercially available CNT stock materials.

In summary:
i) SWCNTs can be imaged as rolled-up graphene sheets, whereby the so called chirality, expressed as tube indices (n,m), defines the nanomaterial's electronic properties. ii) Synthesis of SWCNTs by chemical vapor deposition (CVD) lead to a mixture of different chiralites.

3.3 Optoelectronic Properties of SWCNTs

The following section will introduce and discuss how SWCNT's electrical and optical features are linked to size and structure of the quasi 1D-nanomaterial. Since SWCNTs are tubular graphitic structures, their energy and band structure can be first compared with the energy landscape of graphene, on the basis of which the SWCNT band structure is derived.[20] This model of graphene zone folding conceptualizes the periodical boundary conditions of the two-dimensional energy dispersion of graphene.[32] Graphene itself is classified as semimetal, exhibiting a Fermi level at the six intersection points of the valence band and the conduction band. These are called K-points within the hexagonal lattice of the first Brillouin zone (Figure 3.2a).[7,20] SWCNTs cylindrical structure furthermore allows a quantization of the wavevector k around the tube circumference with

$$k \cdot C_h = 2\pi q \tag{3.4}$$

,where q is an integer, responsible for structure – property relationship in SWCNTs.[20,33] When mod(n – m, 3) = 0, the resulting wavevector is allowed to pass the K-points (i.e. Fermi level) of the graphene Brillouin zone, which characterizes SWCNTs as metallic (Figure 3.2a).[7,34] On the other side, if mod(n – m, 3) = 1 or 2, an allowed wavevector does not pass through the K-points. This condition defines a finite energy gap, giving rise to SWCNTs with semiconducting properties (Figure 3.2a).

The SWCNT system can now experience several resonant, optical transitions (absorption and photoluminescence) from the valence band to the conduction band, which are called S_{jj} for s-SWCNTs, M_{jj} for m-SWCNTs or E_{jj} for a general description (with j = 1,2,3,...). Hereby, the SWCNT diameter has an inverse relationship with the E_{jj}, as described in equation:

$$E_{jj} = \frac{2j\gamma_0 a_{C\text{-}C}}{d_t} \tag{3.5}$$

,where j is the index of transition, $a_{C\text{-}C}$ is the bond length between a pair of neighboring carbon atoms in the hexagonal graphitic lattice, γ_0 is the interaction energy between a pair of neighboring carbon atoms, and d_t the diameter of the SWCNT.[7] This diameter – transition energy dependency can be further visualized in the so-called Kataura-plot (Figure 3.2b). Differences between experimentally observed and calculated (*via* a tight binding model) values can be derived from strong electrostatic interactions in an excited

SWCNT.[35] Based on the quantum confinement effect along the transverse direction of a SWCNT, these nanostructures exhibit defined maxima in their electronic density of states (DOS)[34], so-called van Hove singularities in the energy band diagram.[19] Figure 3.2c visualizes this relationship, whereby the van Hove maxima in a band diagram are mainly dependent on SWCNT diameter and chiral angle.[19] Through absorption of a photon, an electron can be excited to the conductive band, creating a hole in the valence band. This electron-hole pair, called exciton, has a binding energy in the order of 300 – 500 meV (for s-SWCNTs), which allows an exciton stability at room temperature (300 K).[20] This excitonic nature of optical transitions in SWCNTs can have 16 possible states for each index *j*. However, most of them are determined as 'dark' states, hence not allowing a radiative emission after electron-hole recombination.[20] Photoluminescence (PL) emission dose therefore only occur from 'bright' states, and as previously outlined only in s-SWCNTs. For metallic ones, the density of states is zero at the Fermi level, so after absorption of a photon, the excited state can relax non-radiatively to the valence band.[19,20]

The process leading to NIR photoluminescence emission of s-SWCNTs can be described in three steps[19]:

1) The SWCNT absorbs a photon with the energy, e.g., matching the band gap of the E_{22} transition, defined as the energy difference between the second valence band v_2 and the second conduction band c_2. Besides this resonant excitation at the transition optimum, also non-resonant excitation is possible over a large spectral range. This process (green arrow in Figure 3.2c) generates an electron-hole pair (exciton).

2) The created excitation undergoes a fast, non-radiative relaxation to the lowest level in both valence and conduction bands.

3) The exciton travels along the length of the CNT through diffusion (∼90 nm)[20], until it recombines radiatively. The energy of the fluorescent photon corresponds to the band gap of the E_{11} transition minus the exciton energy (red arrow in Figure 3.2c), while the fluorescence lifetime ranges between 10 and 200 ps.[20] When the exciton encounters on its way a defect on the SWCNT sidewall or the end of the tube, it will recombine non-radiatively, resulting in fluorescence quenching.

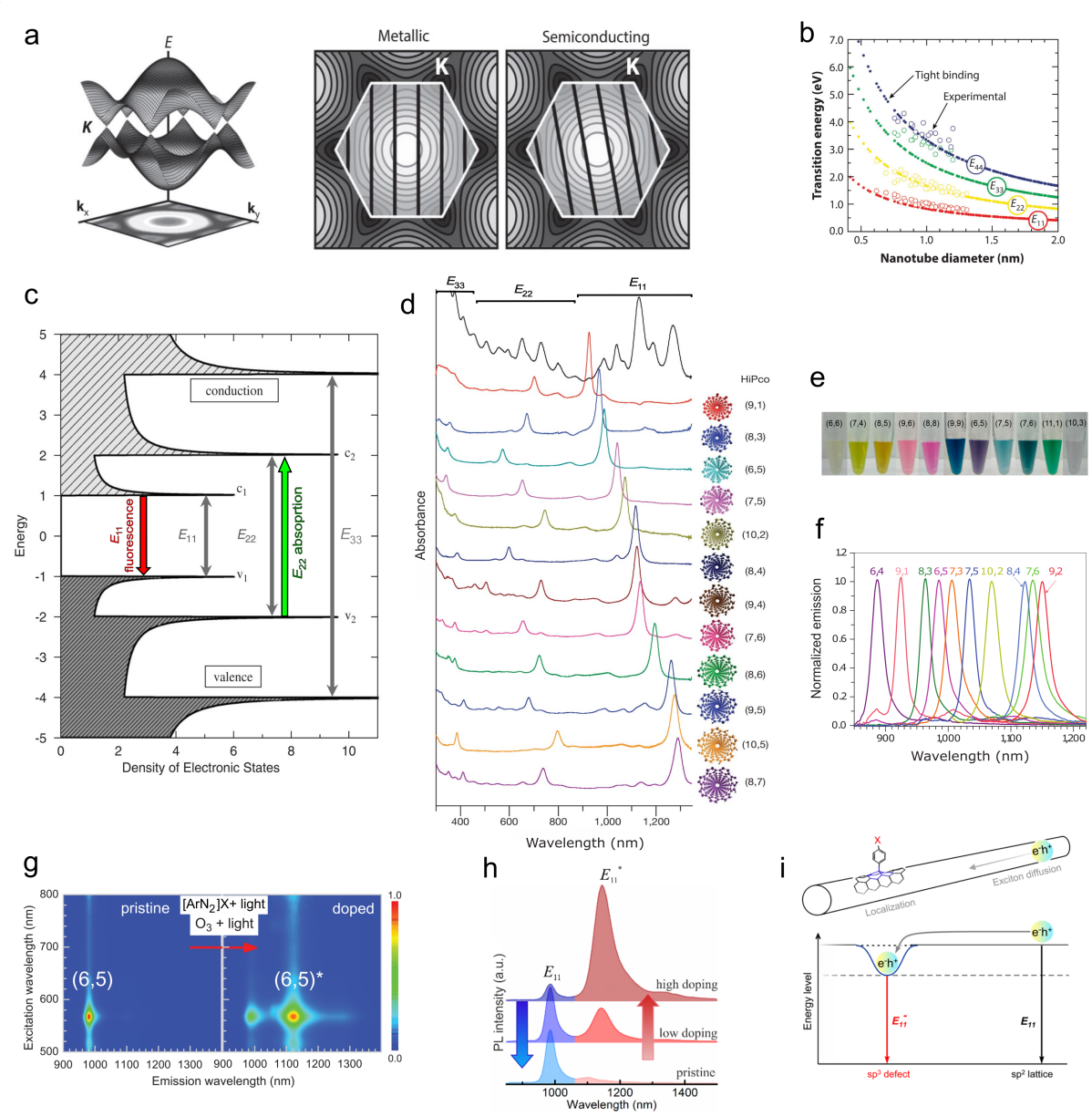

Figure 3.2.: **Optoelectronic properties of SWCNTs.**
a) 3D band structure of graphene Brillouin zone, combined with a 2D contour structure projection. E indicates energy, K is a point in reciprocal space, together with the x,y-axes in k-space. The allowed electric states of (m-/s-) SWCNTs are shown as black lines (right part of the figure), overlaid onto 2D projection of the graphene Brillouin zones. Reproduced with permission from[20]. b) Kataura-plot: Transition energies of SWCNTs are plotted versus nanotube diameter as experimental (empty circles) and calculated (solid circles) values. Reproduced with permission from[20]. c) Density of states (DOS) diagram for s-SWCNTs showing defined maxima, so-called van Hove singularities. The energy differences depend on the SWCNT chirality, indicating smaller band gaps for larger SWCNTs. Upon absorption of a photon (green arrow) with the energy of the E_{22} transition, an exciton is generated which can emit upon recombination a fluorescence photon with approximately the energy of the E_{11} transition (red arrow). Reproduced with permission from[34].

d) UV-Vis-NIR absorption spectra of SWCNTs with indicated E_{jj} transition regions. The first row (black spectra) shows a mixture of several HiPco-SWCNTs with multiple, overlying features. Spectral congestion is resolved in chirality-pure SWCNT samples, showing two main features as the absorption from the E_{22} and E_{11} transitions. Reproduced with permission from[36]. e) Fractions of chirality-pure SWCNTs have defined colors, rather than grayish-black solutions from unpurified SWCNT material. Reprinted (adapted) with permission from Ao *et al.*[37]. Copyright 2016 American Chemical Society. f) Fluorescence emission spectra of several chirality-pure SWCNTs. A clear dependency on SWCNT chirality and the emission wavelengths in the NIR region becomes visible, while larger chirality tubes show emission at lower energies (i.e. red-shifted wavelengths). Reproduced with permission from[38]. g) 2D excitation-emission photoluminescence map of (6,5)-SWCNTs before (labeled as pristine) and after oxygen-defect introduction (labeled as doped). This type of red-shifted emission peak (E_{11}^{*}) can also be obtained after reaction with diazonium salts. Reproduced with permission from[38]. h) Generation of sp^3 quantum defects and changes in photoluminescence depending on the doping level, whereby this covalent SWCNT modification can lead to an overall increase in photoluminescence quantum yield (PL QY). Reprinted (adapted) with permission from Sykes *et al.*[37,39]. Copyright 2019 American Chemical Society. i) Schematic representation of an exciton getting trapped by the quantum defect, which allows a radiative recombination from a previously forbidden state, leading to the red-shifted emission feature. Reprinted (adapted) with permission from Kim *et al.*[37,40]. Copyright 2016 American Chemical Society.

Since the binding energy depends on the SWCNT's diameter and chiral angle, the absorption and emission wavelength can be tailored using distinct SWCNT chiralities.[34] This can be seen in Figure 3.2d-f, where single chiralities show precise E_{11} and E_{22} transitions in the absorption spectra, as well as defined emission spectra. These spectra illustrate the enormous Stoke-shift of several hundreds of nanometers between absorption (at E_{22} in the Vis-region) and fluorescence emission (at E_{11} in the NIR region). Chirality-pure SWCNT samples even show a discrete color in solution as a result of non-overlapping absorption features.[41,42]

Moreover, the excitons in SWCNTs are extremely sensitive to the local environment, which strongly effects SWCNT's photophysics. All carbon atoms are located on the tube surface, hence the exciton can be easily influenced by the surrounding solvent and surfactant.[20] The photoluminescence quantum yield (QY), which is around 1%, not only strongly depends on the SWCNT environment, but is further influenced by SWCNT aggregation status and tube length.[20] Both aggregation and short tubes are generally believed to quench the PL, just as defects in the SWCNT sp^2 structure. However certain sp^3 defects, introduced by e.g. oxygen or diazonium compounds, can preserve the electronic

structure, and give rise to novel PL emission features (see Figure 3.2g).[43–45] Those defect emission states can occur in several varieties, depending on the conformational differences in the SWCNT carbon lattice.[46,47] The intensity and exact emission wavelength of the newly formed, red-shifted E_{11}^{*} emission peak (Figure 3.2h) furthermore depends on the amount of introduced defects, as well as on the nature of e.g. diazonium defects, carrying either electron withdrawing or electron donating groups.[39,48] The underlying hypothesis for defect-state emission is that the exciton gets trapped by the local defect, thus enabling the recombination from a previously forbidden dark state (Figure 3.2i).[43] This covalent SWCNT modification can in principle enhance the PL QY and make SWCNTs an interesting sources for single-photon generation.[49]

In summary:
i) The photophysical properties of SWCNTs are defined by excitons, i.e. strongly bound electron-hole pairs. ii) Only semiconducting SWCNTs have a band gap that allows photoluminescence emission in the near-infrared (NIR), while the emission wavelength depends on the SWCNT chirality. iii) Changes in the local dielectric environment strongly affects SWCNT photophysics, since all carbon atoms are located on the SWCNT surface. iv) Introduction of certain sp^3 defects into the SWCNT structure can generate red-shifted emission features.

3.4 SWCNT Surface Functionalization

In order to use SWCNTs as optical sensors, a second, equally important component has to be combined to the carbon nanostructures.[50–52] For a functional colloidal system, the surface of SWCNTs needs to be modified, in such a way to favor de-aggregation and dispersion of the inherently hydrophobic nanotube bundles, since pristine SWCNTs are practically insoluble.[53]. This form of solubilization and exfoliation of SWCNT bundles in an aqueous phase is required to later use colloidal SWCNT-probes in biological systems. Surface functionalization of SWCNTs can be generally categorized into covalent and non-covalent modifications.[51] Unfortunately most of the covalent approaches[17,54], like introduction of carboxyl groups into the carbon lattice by oxidative treatment, will quench the PL emission, making the SWCNTs unsuitable for subsequent sensor design. Only the sp^3 quantum defects, introduced in Section 3.3, can combine covalent attachment and optically emissive SWCNTs.[43] The most commonly used approach to generate fluorescent nano-constructs is therefore the non-covalent modification by electrostatic adsorption of amphiphilic molecules.[50,55] Again, only well dispersed s-SWCNTs emit NIR fluorescence, since bundled SWCNTs are quenched by energy transfer to neighboring tubes. To overcome the strong van der Waals attraction between CNT bundles, dispersion processes can be implemented using different forms of sonication, including bath or probe sonication, as well as high-speed shear force mixing.[56–58] Most typically, probe sonication generates high cavitational energy that debundles the SWCNTs, while ambient amphiphilic molecules adsorb onto the tube surface (Figure 3.3a). This surface modification, also described as the molecular '*corona*', helps to stabilize the colloidal particles in solution and prevents re-aggregation of the SWCNTs once the sonication process stops.[59] However, the resulting SWCNT solutions remain in a kinetically meta-stable state. Similar to other colloids, surfactants create electrostatic or steric repulsion forces between the SWCNTs, reducing the likelihood of tube-tube contacts, which overall slows down aggregation.[50,59] Those interactions of coating molecules and SWCNT surface are driven by favorable van der Waals forces, hydrophobic forces and π-π stacking.[51,60,61] Depending on the used dispersant, the colloidal interaction can generally be dynamic or static (Figure 3.3b).[50] This classification is further based on the stability of the SWCNT conjugates, when excess dispersant is removed from the surrounding environment. Dynamically dispersed SWCNTs will collapse and aggregate, while static dispersions remain colloidally stable (Figure 3.3c).[50,61]

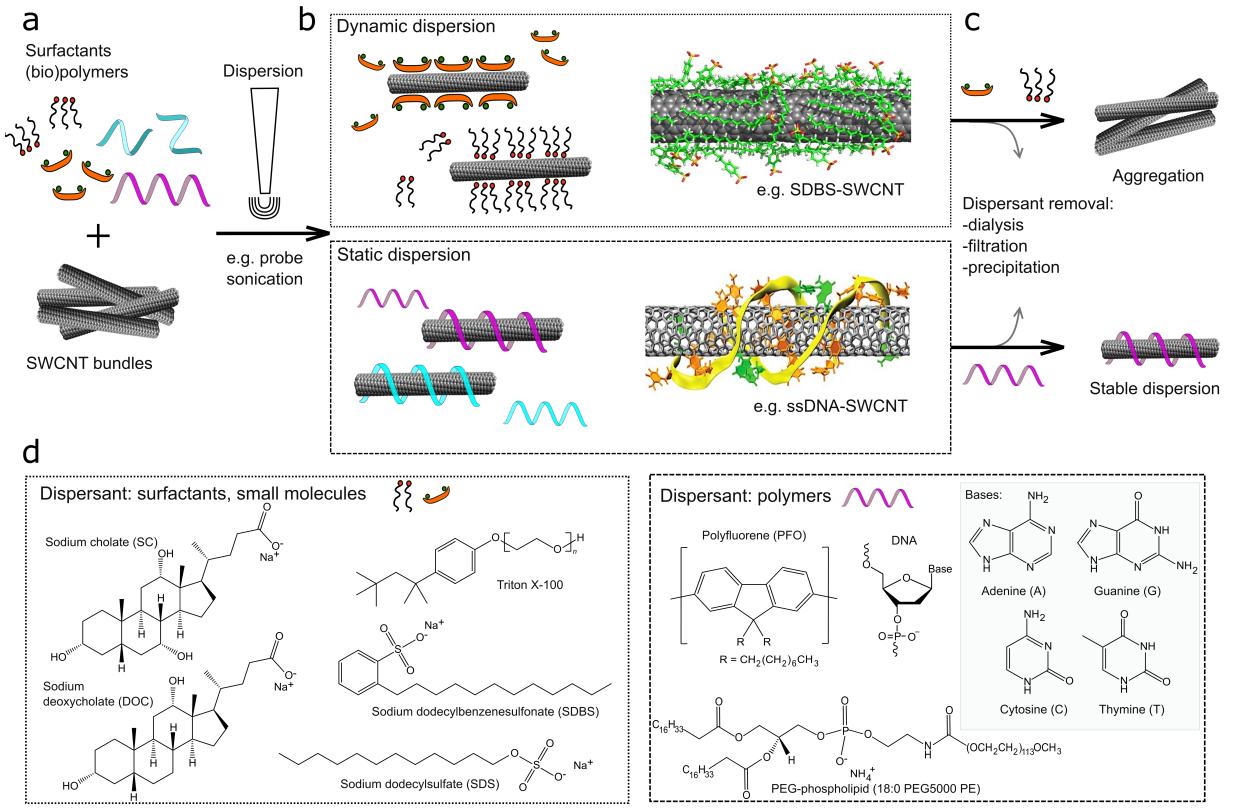

Figure 3.3.: **Surface functionalization of SWCNTs.**
a) As produced, pristine SWCNTs need to be dispersed to create colloidal probes. This dispersion and concomitant surface modification process is carried out in solution by e.g. sonification with amphiphilic surfactants or (bio)polymers. b) Depending on the used dispersant (specified in panel d), the colloidal system can be present as dynamic or static dispersion. Both systems contain, next to the modified SWCNTs, also free dispersant. Two exemplary molecular-dynamic (MD) simulations visualize the non-covalent surface modifications. Surfactant-(SDBS)-SWCNT is reproduced with permission from[62] and polymer-(ssDNA)-SWCNT is adapted with permission from[36]. c) When removing the free (excess) dispersant by dialysis, filtration or precipitation, dynamically dispersed SWCNTs collapse and aggregate, while static dispersions remain stable as colloidal SWCNT-system. d) Chemical structures of prominent dispersants. Surfactants such as sodium cholate (SC) or sodium dodecyl sulfate (SDS) form dynamic dispersions with dense structures. Polymers like desoxyribonucleic acid (DNA) or PEGylated phospholipids are important examples for static dispersants in aqueous systems, whereas polyfluorene(PFO)-polymers mediate a similar interaction in organic solvents. One of the most common biopolymer modification uses single-stranded (ss)DNA, whereby nucleotide length and composition (A,G,C,T) furthermore determine the exact structure and photophysical properties of the SWCNT conjugate.

For dynamic dispersions, the most typically employed surfactants are those that can form dense structures around the SWCNT, as visualized by the MD-simulation of sodium dodecylbenzenesulfonate (SDBS)-SWCNTs (Figure 3.3b). It is furthermore hypothesized that, depending on the surfactant, individual SWCNTs can be encapsulated by the hydrophobic interior of cylindrical micelles, while the hydrophilic part faces outwards.[50] Different structures and degrees of surface coverages can be obtained by using other anionic, cationic or non-ionic surfactants as shown in Figure 3.3d.[50,55] Static dispersions on the other hand are mediated by polymer adsorption onto the SWCNT surface.[50] The polymer type determines whether the nanostructure will be soluble in organic or aqueous systems. Polyfluorene (PFO)-conjugates for example are aromatic polymers suitable to disperse SWCNTs in organic solvents like toluene or tetrahydrofuran (Figure 3.3d).[61,63] Besides PEGylated co-polymers with e.g. phospholipids, stable nanocomplexes in aqueous media can be formed between SWCNTs and single-stranded (ss) desoxyribonucleic acid (DNA).[50] The aromatic rings of the purines (adenine (A) and guanine (G)) or pyrimidines (cytosine (C) and thymine (T)) bases interact by π-π stacking with the sp^2 hybridized carbon lattice, while the hydrophilic sugar-phosphate backbone is exposed to the aqueous surrounding.[53,64] The exact conformation of the resulting, highly soluble DNA-SWCNT complex varies significantly due to the nucleotide length and composition. Although helical self-assembly of ssDNA (Figure 3.3b) is widely discussed and assumed based on MD-simulations and atomic force microcopy (AFM) measurements, various loop, ring and distorted helical structures can be envisioned, including intra- and inter-base pair stackings.[50,64,65]

After examining how SWCNTs can be functionalized with a variety of surface-active molecules, it should be discussed how this process affects the nanotube photophysics. In general, surface chemistry and tube interface predominantly define the optical properties of the SWCNT conjugates. Individualized SWCNTs show in comparison with inferior dispersions improved resolution in absorbance and fluorescence spectra.[66–68] Based on the principles introduced in Section 3.3, according to which excitons in SWCNTs are highly sensitive to the surrounding environment, a solvatochromic model is discussed. This implies that the dielectric environment of SWCNTs is directly altered by exposure to surfactant and solvent molecules. An increase in dielectric constant will lead to a bathochromic (red)-shift in the optical transition energy, as well as to a loss of exciton oscillator strength.[20,69,70] Dispersions with low dielectric constant on the other hand will enhance the photoluminescence QY and lead to a hypsochromic (blue)-shift of the emission maxima.[69,70] Surfactants and polymers even further influence the system and affect optical transition energy and PL QY

of the SWCNT conjugates.[20] Strong bonds and dense surface modifications are believed to enhance the shielding of SWCNTs from quenching molecules like H_2O or O_2.[71] This is the most plausible explanation for the bathochromic shift, ssDNA modified SWCNTs exhibit compared to sodium cholate (SC)-modified ones.[20,50] The lower degree of surface coverage would thereby allow a greater accessibility of water molecules to the SWCNT surface, resulting in an increase of dielectric constant.[50]

In summary:
i) SWCNTs can be non-covalently modified by surfactants or polymers, which adsorb onto the tube sidewall *via* hydrophobic forces or π-π stacking. ii) Dynamic dispersions with surfactants will collapse when excess dispersant is removed, while polymer-based static dispersions remain colloidally stable. iii) Polymers like ssDNA form ordered structures on the nanotube surface, influencing the dielectric environment and thereby the photophysical properties of the nano-conjugates.

3.5 SWCNT Purification and Separation

On the way to defined SWCNT sensors, nanomaterial is required with uniform photophysical properties. However, since the commonly applied synthesis methods (Section 3.2) produce SWCNT material with multiple chiralities, further purification and separation is inevitable. Such further processing steps not only lead to chirality-pure SWCNTs, exhibiting defined optical emission spectra, but also remove quenching impurities like m-SWCNTs or catalyst residues at the same time. During the past decade, a variety of different methods were described for SWCNT sorting, enabling the separation by length, diameter or electronic structure.[14,16,25,72–75] To better understand how important it is to resolve spectral congestion, Figure 3.4a and 3.4b show examples of pristine and separated SWCNTs. In an unsorted HiPco-sample (Figure 3.4a) the absorbance features of a variety of different SWCNTs superimpose[38] and contain an inherent background from amorphous carbon and metallic SWCNTs.[76] Chirality-pure SWCNTs on the other hand show distinct E_{11} and E_{22} transition features, as seen for (6,4)-SWCNTs. This is also reflected in the corresponding photoluminescence spectra, shown in Figure 3.4b. Unpurified HiPco samples show multiple maxima in the 2D excitation-emission spectra, corresponding to the fluorescence emission of various resonant excited s-SWCNTs. Separated, mono-chiral (6,4)-SWCNTs on the other hand only exhibit one defined emission maximum. To achieve such kind of chirality enrichment and purity, different kinds of sorting methods can be applied. The SWCNTs separation process can either be mediated by a specific purification technique (e.g. chromatography), a specific polymer-dispersion or by a combination of both. The following part will introduce the most important examples of these methods, which were partly also applied in later parts of this thesis to obtain chirality-pure SWCNT sensors.

One of the earliest practices for SWCNT separation is based on chromatography methods, including size exclusion chromatography (SEC), ion exchange chromatography (IEC) or gel chromatography. Surfactant-coated SWCNTs are loaded onto polysaccharide gel (e.g. agarose, dextran or sephacryl beads), which can be encased in a classical chromatography column (Figure 3.4c). S-SWCNTs are strongly attracted by the gel beads, while m-SWCNTs are weakly retained.[77,78] This allows the separation by electronic structure as seen in Figure 3.4c, but can be further extended by gradual elution, using different surfactants, surfactant mixtures with pH modulations or temperature variations.[79,80] Since small diameter s-SWCNT exhibit the strongest interaction with the gel beads, they can be eluated as later fractions, comparable to the working principles of SEC.[77]

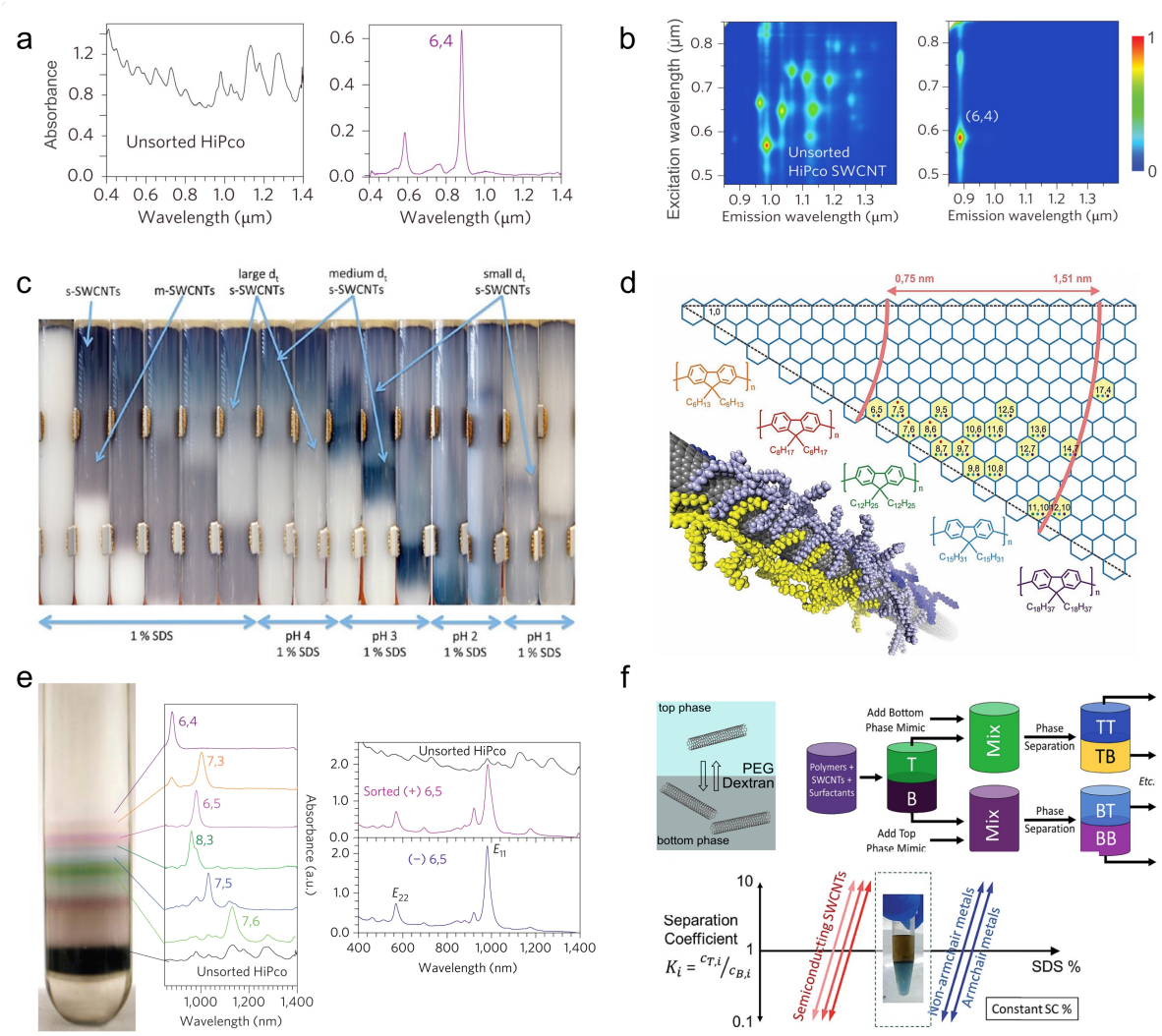

Figure 3.4.: **Separation, purification and sorting of SWCNTs.**
a) Exemplaric UV-Vis-NIR absorbance spectra of pristine (left) and chirality-separated (right) SWCNTs. E_{11} and E_{22} transition features of (6,4)-SWCNTs become clearly visible, being beforehand superimposed by other chiralities. Reproduced with permission from[38]. b) Normalized 2D excitation-emission spectra of NIR-fluorescent SWCNTs, again from unpurified (left) and separated (right) SWCNTs. Resonant excitation at the E_{22} transition leads to the maximum in E_{11} fluorescence emission. Again, separation resolves spectral congestion, leading to non-overlapping emission features. Reproduced with permission from[38]. c) Size-exclusion chromatography (SEC)-based purification of surfactant dispersed SWCNTs. Different affinities of m-/s-SWCNTs towards the sephacryl-material enable the separation of SWCNTs by electronic structure. Further gradual elution from the column by varying pH or surfactants allows fractionated collection of single chiralites. Reprinted (adapted) with permission from Flavel *et al.*[77]. Copyright 2013 American Chemical Society. d) Specific dispersions by polyfluorene(PFO)-polymers in organic solvents yield sorted nanotubes. The precise chemical structure of the PFO-variant selects for specific SWCNTs, depending on the electronic structure, chirality or handedness. Reproduced with permission from[63].

e) Separation of SWCNTs by density-gradient ultracentrifugation (DGU). Liquids of discrete densities are layered in a centrifugal tube, forming a vertical density profile. Dispersed SWCNTs migrate under strong centrifugal forces to regions matching their individual buoyant densities. Left part shows such DGU-sorted SWCNTs regions inside a centrifugal tube, with corresponding absorbance spectra of chirality-pure SWCNT fractions. Furthermore, separation of enantiomers is possible, as indicated by the absorbance spectra of (±)-(6,5)-SWCNTs. Reproduced with permission from[38]. f) Representation of the aqueous two-phase extraction (ATPE) technique. Combination of differently dense polymers (poly(ethylene glycol) (PEG) and dextran) can form two distinct phases in an aqueous solution, wherein surfactant- or ssDNA-dispersed SWCNT can be partitioned. Specific SWCNT chiralities show enhanced affinity towards the bottom or top phase and multiple iteration steps can yield chirality-pure SWCNTs fractions. Reproduced from[81] with permission from the Royal Society of Chemistry.

However, this diameter-dependent interaction can also lead to a chirality-specific occupation of the column material during the loading process, which allows so-called 'overloading' of multiple, sequential columns and later the column (chirality) specific elution.[82]

Specific interactions with (bio)polymers can furthermore yield superior stable SWCNT-conjugates. Hence, targeted extraction of certain SWCNT chiralities is possible, depending on the used polymer structures and solvent systems. In an aqueous system, this task can be achieved with specific ssDNA sequences, forming unique structures onto SWCNT's surface. This selective interplay between 'recognition' ssDNA sequence and tube diameter leads to unique nanostructures, which enables, in combination with further separation techniques like IEC, the recovery of chirality-pure SWCNT fractions.[36]

In organic solvents, solely dispersion with specific polyfluorene polymers is necessary to obtain particular SWCNT chiralities.[83–85] The exact PFO-derivate, as indicated in Figure 3.4d, will thereby select for the desired tubes.[63] This process uses straight-forward dispersion processes, which can be further extended to large-scale shear force mixing techniques[56], whereby after subsequent centrifugation, only the desired SWCNT type remains colloidally stable in the supernatant.[63,86] Hereby, the aromatic polymers likely form rigid-backbone like structures on the SWCNT interface, whose symmetry is solely optimal for specific tube diameters[83], electronic structures[87] or handedness[88]. This interaction is furthermore influenced by the solvent system and the SWCNT material composition itself.[89,90] For successive removal and re-utilization of the supramolecular PFO-polymers, different concepts were introduced in the last years, based on acid- or metal-ion induced cleavage and precipitation of the PFO-SWCNT nano-constructs.[87,91–93]

In general, these powerful dispersion methods can grant access to single chirality suspensions, however, other sorting methods even allow the separation of several chiralities in a single run. One example would be density gradient ultracentrifugation (DGU), a commonly used approach in biochemical separation science. First applied for SWCNT separation in 2005, it rapidly advanced to a straightforward, frequently used method, enabling sorting by length, diameter (chirality) or even handedness.[72,73,94–96] Hereby, liquids of discrete densities are layered in a centrifugal tube, forming a vertical density profile, following either a linear or non-linear gradient.[38,95] The simple working principal is based on the migration of SWCNTs under strong centrifugal forces to regions matching their individual buoyant densities.[75] Figure 3.4e shows such separated SWCNT-layers in a DGU centrifugal tube, visualizing the physical fractionation of the nanometer size objects.[38] As mentioned before, such chirality-pure SWCNT fractions exhibit a discrete color, as a result of non-overlapping absorption features.[41,42] However, the general differences in the buoyant densities arise from varieties in the SWCNT surfactant coating layer and its hydration structure, demonstrating that both depend on the chiral structure of the SWCNTs.[75] This separation method can therefore be tuned by using different surfactant mixtures, salt concentrations or counter-ion distributions, which makes optimization of all parameters challenging.[25,75,97] However, once the right settings are evaluated, chirality-specific and even enantiomer-specific separation can be performed (Figure 3.4e).[38]

In the recent years, another SWCNT separation method caught much attention, because of its easy, fast and straightforward purification results. During aqueous two-phase extraction (ATPE), surfactant- or ssDNA-dispersed SWCNTs are partitioned between aqueous solutions of differently dense polymers (Figure 3.4f).[98] Most commonly poly(ethylene glycol) (PEG, e.g. 6kDa) and dextran (e.g. 70 kDa) are used, which form two discrete phases at specific mass ratios.[81] Additional surfactants will distribute unevenly in both phases, according to a slight hydrophobic / hydrophilic character of the two polymer phases. This leads to the general observation, that SWCNTs modified by DOC or SC tend to accumulate in the dextran-rich bottom phase, while SDS covered SWCNTs are enriched the PEG-rich top phase.[75,81] As introduced before, the SWCNT electronic structure and chirality will determine the affinities and ratios of surfactants adsorbed to the sidewall. These differences in solvation energy will overall lead to a preferential affinity and hence to a directed and predictable partitioning of SWCNTs in the phases.[14,25,99] With increasing SDS concentrations, as shown exemplaric in Figure 3.4f, s-SWCNTs are separated from m-SWNCTs, whereas multiple replications of the ATPE process with virgin polymer phases

can generally yield chirality-pure fractions.[81] Hereby, the SWCNT partitioning and extraction can be tuned by either surfactant, pH or temperature variations, to obtain the desired chiralities.[100–102] Next to surfactant dispersed SWCNTs, also ssDNA-SWCNTs can be separated by ATPE. Again, particular DNA sequences form specifically ordered structures that mediate the preferential accumulation in one of the phases.[103,104] This interaction can be so unique, that extraction of single chiralites or even separation of SWCNT enantiomers is feasible.[37,105]

Overall, every SWCNT separation method has its benefits and disadvantages, depending on the desired application. Reproducibility, mass throughput, yield or purity are main factors, when it comes to the implementation of nanomaterial purification techniques, followed by practical aspects like equipment requirements, toxicity or costs of the used reagents.

In summary:
i) SWCNTs can be separated according to their electronical structure (m/s), length or diameter (chirality). ii) Sorting and purification can be realized by means of various techniques (e.g. gel chromatography, density gradient ultracentrifugation, aqueous two-phase extraction) or selective dispersions (e.g. polyfluorene polymers). iii) Chirality-pure SWCNT fractions are separated from quenching impurities and exhibit defined, non-overlapping absorbance and NIR photoluminescence features.

3.6 SWCNTs as Optical Biosensors

After introducing the unique optical properties of SWCNTs and elaborating how this nanomaterial can be dispersed and purified, the following section will explain their usage and application as optical nanosensors.

Biosensors, devices that can detect chemical (analytes) or physical quantities in a biological environment, in general consist of two functional parts, in further combination with a signal readout technique.[106] This includes a recognition element, capable of interacting with the specific target analyte, and a signal transduction component, able to translate a binding event into an output signal.[106] Transferring this definition to SWCNT-based biosensors, the surface modification represents the recognition element and the SWCNT itself plays the role of the signal transducer.[51,52,60,107] The basic, underlying concept was already outlined in Section 3.4, emphasizing that excitons in SWCNTs are highly sensitive to the surrounding environment and that changes in the local dielectric constant will directly affect the NIR fluorescence emission. Hence, to use SWCNTs as optical sensors, besides their utilization as electrochemical sensors[108,109], the interaction of analytes with the nanosensors must cause a concomitant changes in the local chemical or dielectric nanotube environment. Since biological systems require the application of colloidally stable, non-toxic surface modifications, most SWCNT-biosensor interfaces rely on adsorbed polymers. In order to now detect biomarkers and target analytes from complex biological systems, different forms of interactions can be envisioned (Figure 3.5 a,b). This includes direct adsorption of the analyte onto the SWCNT, analyte-induced changes of the biopolymer conformation or electron transfer between analyte and SWCNT.[50,51] Furthermore, doping and redox reactions with the polymer-SWCNT conjugate can occur, altering SWCNT exciton decay routes.[51] Such interactions and alterations can then be detected by e.g. NIR fluorescence spectroscopy, revealing spectral modulations in emission energy (wavelengths) and intensity (Figure 3.5c).

Figure 3.5 shows examples for biosensors responding with spectral shifts. At the same time, the underlying rationales for the binding and recognition events will be explained. Since the introduction of optical biosensing with SWCNTs in 2005 by Barone *et al.*[110], a variety of different sensing concepts were described, leading to major improvements in analyte detection sensitivity and selectivity. However, most of these concepts are based on signal transduction after modulation and perturbation of the biopolymers used for SWCNT surface modification.

These kind of molecular recognition events, whereby the analyte interacts (binds) with the polymer construct, can be generally subdivided into two forms. One is based on known recognition motives like antibodies, aptamers or lectins, which can be coupled to polymers or directly used for SWCNT modification.[51] Another one exploits the unique pathway that arise from specific polymers folding on top of the SWCNT surface. This newly shaped 3D structure of constrained bioheteropolymers can create a binding pocket at the SWCNT interface, which would otherwise not be accessible in solution.[10] Figure 3.5d shows this principle, called 'corona phase molecular recognition' (CoPhMoRe).[10] This artificial binding pocket can now recognize specific molecules for which conventional motives were earlier not existing. One example is shown in Figure 3.5d, leading to the fluorescence decrease of polymer-SWCNTs after addition of the vitamin riboflavin.[10] Later studies extended this concept to various small molecules or larger proteins.[111–113] This exemplary enabled the spatiotemporal detection of neurotransmitters secreted from living cells, as displayed in Figure 3.5e for the fluorescence increase of ssDNA-SWCNTs after neurotransmitter (dopamine) addition.[11] In addition to the specific DNA conformation at the tube interface, it was shown that the dihydroxy groups of the analyte play an important role for the molecular recognition. Supported by MD-simulations (Figure 3.5e), it was hypothesized that dopamine interacts with the phosphate groups of the DNA-backbone, pushing the polymer closer to the SWCNT surface, thus altering the dialectic landscape and furthermore shielding the system from quenching molecules.[11]

Changes in the emission energy (wavelength) can be observed for example, when SWCNT sensors are designed to detect genetic material like DNA or RNA. Heller and coworkers described a blue-shift of the nanosensor emission wavelength upon selective microRNA hybridization.[114] Moreover, Figure 3.5f visualizes an example of direct analyte adsorption onto the SWCNT sidewall. Specific lipid molecules like sphingomyelin or cholesterol showed great affinity to ssDNA-SWCNTs and caused upon interaction a several nanometer-wide blue-shift in emission wavelengths.[115] The proposed mechanism is based on hydrophobic adsorption onto the SWCNT surface, thus decreasing the dielectric constant by superior shielding of the SWCNT from surrounding water.[115] Lastly, Figure 3.5g shows ssDNA-SWCNT reacting with a strong red-shift to the addition of intercalating molecules, like the anticancer drug doxorubicin or DNA-staining agent ethidium bromide.[116] Most likely, the intercalating substances are bound to the DNA-SWCNT conjugate by π-π interactions, without replacing the DNA.[116]

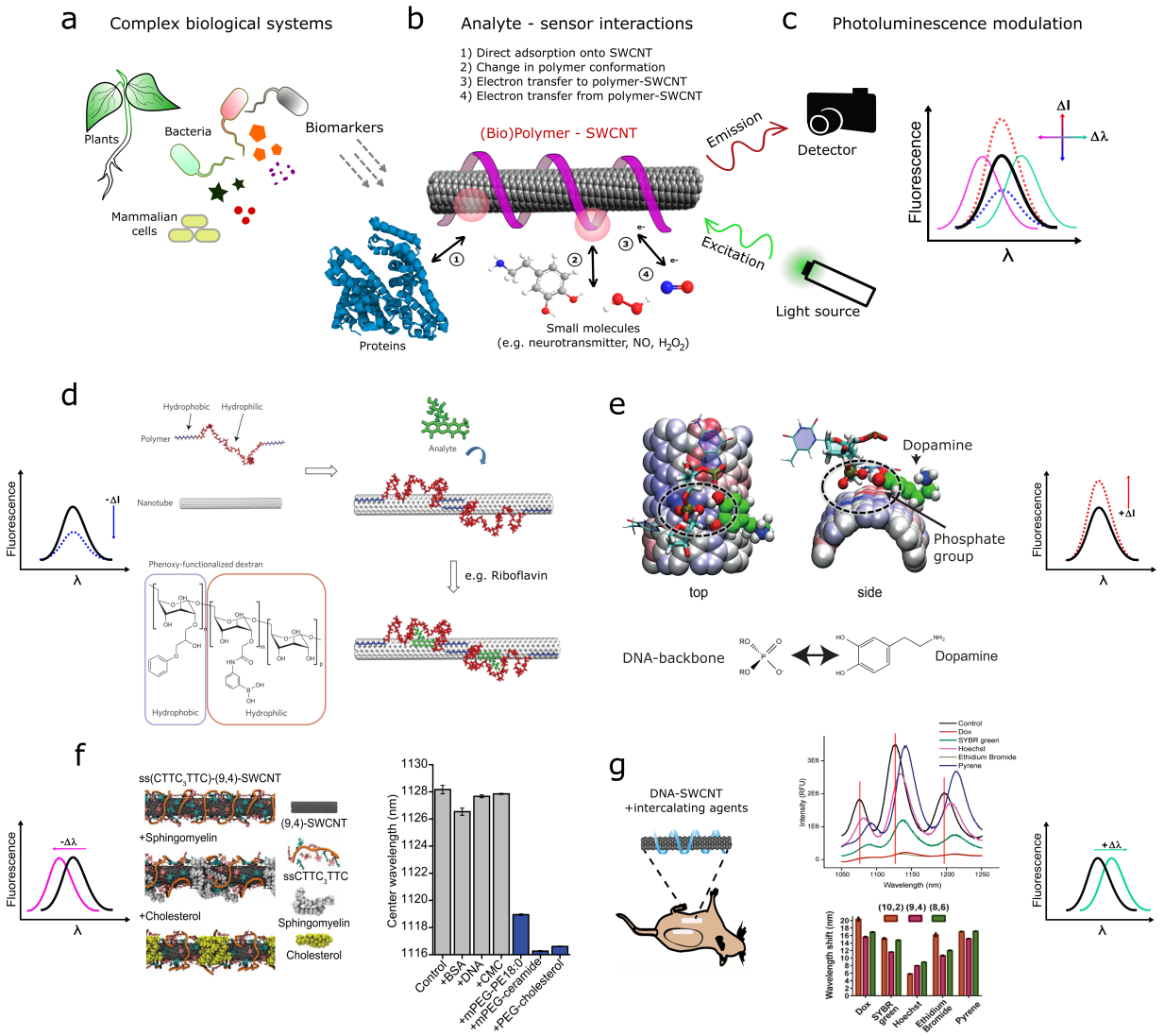

Figure 3.5.: **Optical biosensors based on SWCNTs.**
a) SWCNT-biosensors are able to detect biomarkers and analytes from various biological systems with great temporal, spatial and chemical resolution. b) Different principles of sensor – analyte interactions: a biopolymer-modified SWCNT can interact with different types of analytes (e.g. proteins or small molecules) by direct adsorption of the analyte onto the SWCNT, by changing the biopolymer conformation or by inducing an electron transfer (points 1-4).[50] The NIR emission will be altered if this analyte interaction (somehow) leads to a change in the local electric environment of the nanoconjugates. c) Photoluminescence modulation of the nanosensors can be detected by shifts in the emission intensity or energy (wavelength position). The following examples will illustrate each type of fluorescence modulation. d) Hypochromic shift (fluorescence decrease) of SWCNTs modified by amphiphilic polymers after addition of e.g. vitamins like riboflavin. The polymer forms a specific 3D structure when adsorbed onto the SWCNTs, mimicking a binding pocket, which summarizes the working principle of the so-called 'corona phase molecular recognition' (CoPhMoRe). Reproduced with permission from[10].

e) Hyperchromic shift (fluorescence increase) of ssDNA-SWCNTs interacting with small catecholamine neurotransmitters (e.g. dopamine). Hereby, the hypothesized principle relies on the hydroxy groups of dopamine interacting with the DNA phosphate groups and thus pushing the polymer closer to the SWCNT surface. Reproduced with permission from[11]. Copyright 2017 Academy of Sciences. f) Hypsochromic shift (blue-shift) of ssDNA-SWCNTs after exposure to specific lipids (e.g. cholesterol). Most likely, lipid molecules bind *via* hydrophobic interactions directly onto the SWCNT surface, thus decreasing the dielectric constant. From Galassi *et al.*[115]. Reprinted with permission from AAAS. g) Bathochromic shift (red-shift) of ssDNA-SWCNTs after addition of intercalating agents like doxorubicin. Such polycyclic, anti-tumor compounds are likely bound by π-π interactions to the DNA-SWCNT conjugate, without replacing the DNA. Reprinted (adapted) with permission from Harvey *et al.*[116]. Copyright 2019 American Chemical Society.

This example already indicates that, for some sensing events, more than one mechanism may be responsible for the fluorescence changes, since e.g. doxorubicin alters on one hand the DNA conformation, but on the other hand also tightly adsorbs on the nanotube structure. Such intermediate and mixed forms likely occur in a variety of analyte – sensor interactions, resulting in their sum into changes of the local nanotube environment. This could also hold true for the sensing of physicochemical parameters like changing pH values. Protons can directly interact with the SWCNT sidewall[117], but the 3D structure of e.g. DNA polymers can simultaneously be altered (e.g through pH-dependent protonation of the phosphate backbone).

Moreover, multiple different design strategies for optical SWCNT sensors were developed in the recent years to detect proteins[118], protein fragments[112], enzyme activity[119,120], genetic material[114], different neurotransmitters[121,122], sugars[123], steroids[124], lipids[115,125,126], volatiles[127], reactive oxygen species[128,129], nitric oxide[130] and multiple other analytes.[51,107] But next to the sensitive detection of the target, one has to emphasize that the selectivity of the sensor system might be limited to specific purposes and applications. In general, to obtain a functional SWCNT nanosensor, different kinds of (rational) design and test strategies can be applied. In the simplest version, possible sensor candidates (SWCNTs with variable polymer modifications) are screened against a library of target analytes.[10,111,113,131] 'Matches' in terms of prominent fluorescence changes are then classified as suitable sensor candidates. In order to improve this system and to find best matching SWCNT modifications, e.g. ssDNA sequences can be tuned in nucleotide composition and lengths,

using iterative cycles to advance structure – response relationships.[132] On the other hand, also known recognition motives can be immobilized on SWCNTs, as shortly mentioned above. Among them, we can mention peptide motives[133], antibodies[134] or smaller antibody fragments called nanobodies[135], which mediate for example the directed binding of SWCNT conjugates to cell compartments. Furthermore, specific analyte binding can also be achieved by applying aptamers[122,136,137], small ssDNA or RNA strands that form unique 3D structures and binding pockets through defined local base-pairings.[138,139] However, the development of novel design strategies to create sensitive and selective SWCNT sensors is still in the focus of ongoing research.

In addition to the ability of SWCNTs to translate changes in their chemical environment into optical signals, their emission in the NIR region of the electromagnetic spectrum makes them highly interesting for potential *in vivo* applications.[9,140] Imaging in the NIR, generally from 700 - 1700 nm can be further subdivided into the NIR-I (700 – 950 nm) and NIR-II (1000 – 1700 nm) windows.[141] With increasing emission wavelengths, a general reduction in photon scattering, tissue absorption and background autofluorescence occurs, which enables deeper potential tissue penetration of light ('biological transparency window').[9,141,142] This can facilitate for example *in vivo* imaging of vascular structures, organs or infection sites within entire animal bodies, in this way rising as promising tools for nanomedical applications.[5,19,142–145]

In summary:
i) SWCNT sensors are able to translate changes in their local chemical environment into optical signals, whereby their emission in the NIR 'biological transparency window' is most suitable for biosensing applications. ii) On the way towards functional sensors, diverse chemical design strategies can be applied, mediating analyte binding and optical detection through modulations in emission wavelength and intensity. iii) Optical SWCNT sensors can be used to detect target molecules in a variety of biological systems, from cell levels to whole organisms, with great temporal, spatial and chemical resolution.

4 | Aims and Objectives

SWCNT-based nanosensors show unique photophysical properties and promising applications for spatiotemporal analyte detection, as introduced in the previous chapters. So far, most of such sensors have used the principle of 'corona phase molecular recognition' (Section 3.6), whereby biopolymers are adsorbed to SWCNTs, leading to novel recognition units. However, creating those sensors by means of analyte screenings comes with the drawback of rather unpredictable sensing outcomes. Therefore, the aim for this thesis is to tailor the SWCNT interface in such a way that it becomes sensitive for pathogen biomarkers. This includes the tuning of nanotube's analyte specificity and emission features, in order to obtain functional nanosensors. To achieve this, several iterative implementations and improvements have to be realized:

1) The goal of the first Section 5.1 is to determine the amount of ssDNA adsorbed onto SWCNTs, mainly for two reasons: On one hand, it will be investigated, whether there is a correlation between the number of DNA molecules and the chemical sensing ability of the nano-conjugates. On the other hand, after understanding the quantity of accessible DNA on the SWCNT surface, the next step can be to perform a ratio-specific, bioorthogonal modification by linkage of established recognition motives. This presents a possible design strategy to obtain specific pathogen sensors.

2) A second goal is to generate SWCNTs for sensors that detect multiple targets simultaneously within a hyperspectral sensing approach. To achieve this goal, SWCNT probes need non-overlapping emission features so, upon combination, an unbiased readout can be performed. Two possible routes towards such single-chirality sensors will be examined in the Section 5.2, based on SWCNT separation methods introduced in Section 3.5.

3) Section 5.3 furthermore sets the focus on the development of specific sensors for bacterial biomarkers and pathogen detection as a whole. It will be evaluated, whether such SWCNT conjugates can be read out remotely, as a future tool for an optical, non-invasive medical diagnostics. Additionally, it will be investigated whether multiple of such tai-

lored sensors can facilitate the detection and differentiation of various infection-associated pathogens.

4) The last Section 5.4 aims to address the detection and visualization of interspecies pathogen interactions. Such interactions can be the result of stress responses of plants to pathogen attack. It will be studied whether SWCNT sensors can be tailored such a way to allow sensing of stress related signaling molecules as H_2O_2, or chemical compounds like polyphenols used for plant defense.

5 | Results and Discussion

5.1 Detailed Understanding of the SWCNT Surface Modification by ssDNA

One of the most commonly used (bio)polymers for SWCNT molecular assembly is single stranded (ss)DNA. Since its introduction by Zheng *et al.* in 2003 it became a straightforward method to solubilize the hydrophobic SWCNTs in an aqueous system, resulting in highly stable colloidal dispersions.[64,146] The DNA bases interact with the SWCNT surface by π-π stacking, while the phosphate backbone as the hydrophilic part of the quasi-amphiphilic polymer points towards the aqueous phase, mediating colloidal stability. In general, this type of surface modification leads to nano-conjugates with multiple beneficial properties: **1)** The DNA sequence and hence the polymer itself is easily variable in nucleotide composition and length, resulting in a huge variety of possible combinations. **2)** Unlike typical surfactants like SDS or DOC[61], ssDNA-SWCNTs are stable without excess polymer in the surrounding phase. **3)** Specific DNA sequences show extraordinary affinity towards particular SWCNT chiralities, enabling SWCNT purification and separation.[36,37,64] **4)** The ssDNA surface modification mediates signal transduction upon analyte interaction, the basis for molecular recognition and chemical sensing.[10] **5)** ssDNA-SWCNTs enable the incorporation of modified nucleotides (xenonucleotides[147] or locked nucleic acids[50]) and additional functional groups, such as linker motives (thiol, amin) or fluorophore labels.[135,148]

These properties underline the potential of ssDNA-SWCNTs and illustrate their advancing applications. However, not all physical properties of this colloidal system are well understood. One of the basic characteristics - how many polymer molecules adsorb on the SWCNT surface and how much lateral space requires one DNA molecule during this process – is controversially discussed in literature. Different methods, based on AFM or fluorescence spectroscopy, aimed to determine the occupied SWCNT segment, reporting values from ∼2 to ∼6 to 16-20 nm, as well as the overall quantity of surface adsorbed DNA.[148–150] But analyzing this dynamic system is challenging, since all approaches exhibit some limitations. AFM analysis of ssDNA-SWCNTs resulted in periodical height repe-

titions on the surface, which were assigned to helical wrapping of the DNA.[151] But this nanoscale depiction might differ from the DNA configuration in dispersion, exposed to a thermodynamically driven equilibrium of adsorption and desorption of the biopolymers. On the other hand, fluorescein-labeled DNA was adsorbed onto SWCNTs, which quenches the emission of the organic fluorophores. This process can later be reversed by surfactant addition, which replaces the DNA from the SWCNT surface.[148] Analyzing the resulting fluorescence increase of the free fluorescein-DNA was used to estimate the quantity of SWCNT surface modification. But next to the complex, non-linear quenching properties of fluorophore-DNA on SWCNTs, the fluorophore itself can adsorb onto the surface, possibly differing the overall configuration of the ssDNA-SWCNT system.

Therefore, a direct way to access the amount of surface-adsorbed DNA without using labeled DNA would be favorable. The aim of the following manuscript is to establish such an approach. Moreover, by using this technique, the influence of nucleotide length and composition on ssDNA-SWCNT's photophysical properties and chemical sensing abilities will be examined.

5.1.1 Quantification of the Number of Adsorbed DNA Molecules on Single-Walled Carbon Nanotubes

Manuscript I was published in the following journal:

Robert Nißler, Florian A. Mann, Parth Chaturvedi, Jan Horlebein, Daniel Meyer, Lela Vuković and Sebastian Kruss*

"Quantification of the Number of Adsorbed DNA Molecules on Single-Walled Carbon Nanotubes"

The Journal of Physical Chemistry C, **2019**, 123, 4837-4847

The article is available at: DOI: 10.1021/acs.jpcc.8b11058
* Corresponding author

Responsibility assignment: R.N. and S.K. designed and conceived the research, with input from F.A.M.. S.K. coordinated the project. J.H. and F.A.M. performed AFM experiments, P.C. and L.V. performed MD-simulations. All other experiments were performed by R.N.. Data analysis and manuscript writing was realized by R.N., with contributions of D.M., F.A.M and S.K..

THE JOURNAL OF PHYSICAL CHEMISTRY C

Article

Cite This: J. Phys. Chem. C 2019, 123, 4837−4847

pubs.acs.org/JPCC

Quantification of the Number of Adsorbed DNA Molecules on Single-Walled Carbon Nanotubes

Robert Nißler,[†] Florian A. Mann,[†] Parth Chaturvedi,[§] Jan Horlebein,[†] Daniel Meyer,[†] Lela Vuković,[§] and Sebastian Kruss*[,†,‡]

[†]Institute of Physical Chemistry, Göttingen University, Göttingen 37077, Germany

[‡]Center for Nanoscale Microscopy and Molecular Physiology of the Brain (CNMPB), Göttingen 37077, Germany

[§]Department of Chemistry and Biochemistry, University of Texas at El Paso, El Paso, Texas 79968, United States

Supporting Information

ABSTRACT: Single-walled carbon nanotubes (SWCNTs) have unique photophysical properties and promise many novel applications. Their functionalization is crucial, but the organic phase around SWCNTs is poorly understood. Noncovalent functionalization with single-stranded DNA (ssDNA) is one of the most used approaches to solubilize SWCNTs in water, and variation of ssDNA sequences leads to major advances in separation of SWCNT chiralities and SWCNT-based sensors. However, the exact number of adsorbed ssDNA molecules on ssDNA/SWCNT complexes and consequently the surface coverage are not precisely known. Here, we determine the number of adsorbed/bound ssDNA molecules per SWCNT for different ssDNA sequences. For this purpose, we directly quantify free and bound/adsorbed ssDNA and the concentration of SWCNTs using an approach based on filtration, absorption spectroscopy, and atomic force microscopy. We found that the number of adsorbed ssDNA molecules on 600 nm long (6,5)-SWCNTs varies between ~860 for $(GT)_5$ and ~130 for $(A)_{30}$. Interestingly, there are large differences in the average SWCNT segment lengths one ssDNA molecule occupies. It varies between sequences of the same length from ~2.1 nm $(T)_{30}$ and ~3.2 nm $(C)_{30}$ to ~4.6 nm $(A)_{30}$. The sequence $(GT)_{15}$ occupied an average SWCNT segment of ~2.3 nm. In contrast, for $(GT)_x$ repeats, we found a linear decrease of the number of adsorbed ssDNA molecules with sequence length x. We also correlated surface occupation with the ssDNA/SWCNT near-infrared (nIR) fluorescence responses to analytes such as dopamine, H_2O_2, riboflavin and pH changes. In most cases, the nIR fluorescence responses did not correlate with the number of adsorbed ssDNA molecules, indicating that the exact structure of the crowded corona around the SWCNT is crucial for photophysical changes. The occupied SWCNT segment length per ssDNA molecule is also an important parameter for molecular dynamics (MD) simulations. $(GT)_{15}$ ssDNA adsorbed and stacked on top of each, when using the determined parameters, in contrast to simulations with an excess SWCNT surface. This result highlights the importance of knowing the number of adsorbed ssDNA molecules per SWCNT. In summary, we present a versatile and direct assay to determine the amount of ssDNA molecules adsorbed on SWCNTs, report those numbers, and evaluate how they are related to photophysical properties.

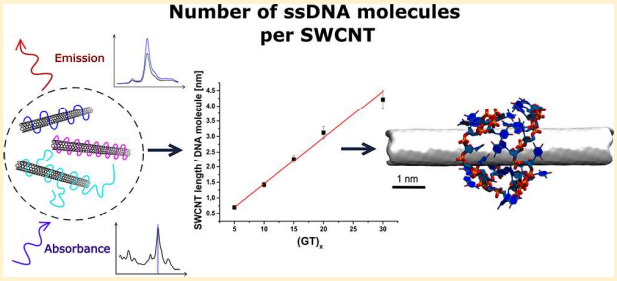

INTRODUCTION

Functional nanomaterials are often hybrid materials consisting of a solid core material and an organic interface that guarantees colloidal stability and functionality. Therefore, the properties of such hybrid materials are more complex than those of bulk materials. Single-walled carbon nanotubes (SWCNTs) are a highly interesting building block for functional nanomaterials such as biosensors, drug delivery agents, and optoelectronic devices.[1−4] Semiconducting SWCNTs fluoresce in the near-infrared (nIR), which is a useful property for optical applications such as imaging, biosensing, or optoelectronic applications.[1−3,5−7] However, SWCNTs are hydrophobic, and therefore, different concepts have been developed to ensure water solubility and colloidal stability.[8,9] One of the most common noncovalent functionalization approaches uses single-stranded DNA (ssDNA).[10] ssDNA functionalization has been extremely successful in separation of different chiralities of SWCNTs.[10,11] Therefore, the interface between ssDNA and SWCNTs is of special interest. One of the basic metrics of ssDNA/SWCNT conjugates is the number of ssDNA molecules per SWCNT, or in other words, the SWCNT segment length one ssDNA molecule occupies. Reported numbers vary, for example, for $(GT)_{16}$, from ~6 nm (adsorbed DNA train length) to 16−20 nm.[12,13] Additionally, the length

Received: November 14, 2018
Revised: January 18, 2019
Published: February 1, 2019

DOI: 10.1021/acs.jpcc.8b11058
J. Phys. Chem. C 2019, 123, 4837−4847

of one ssDNA pitch at the SWCNT surface has been reported to differ from ~2[14] to ~14 nm[15] up to 20 nm.[16,17]

ssDNA/SWCNT hybrid structures have also been a rich playground for molecular dynamics (MD) simulations.[18−21] One important question is why different ssDNA sequences adsorb with different affinities. Therefore, binding energies have been determined to understand better why there is an oligonucleotide sequence and SWCNT chirality dependence.[22] ssDNA sequences of different lengths and compositions also lead to different secondary structures.[23] It is even possible that ssDNA forms hairpin structures around SWCNTs.[24] So far, ssDNA functionalization has been used much more than other concepts because of the versatility and ease of changing the ssDNA sequence. Additionally, modified ssDNA sequences are available and xeno-nucleic acid functionalization is possible.[25] Other concepts that might be as powerful are chemically more difficult. Recently, it has been shown that certain peptides are able to form barrels that encapsulate SWCNTs and form stable conjugates.[26] This general encapsulation approach allows the modification of amino acids that are not important for the barrel structure. Other novel concepts include the combination of ssDNA and peptides, which would combine the best of both worlds.[21] Specifically, small peptide motifs for important cell surface receptors have been conjugated to ssDNA in different geometries to attain different binding affinities and have been used to label cell surface receptors in the nIR.[21] Besides peptides, novel defect-based covalent functionalization approaches have been reported that do not quench the nIR fluorescence.[27]

ssDNA functionalization does not only affect colloidal stability of SWCNTs but also their nIR fluorescence features.[28] Their functionalization may therefore affect absorption and fluorescence spectra. It was shown that ssDNA affinity for the SWCNT surface does not correlate with fluorescence changes for different sequences, which highlights that the organic corona created by ssDNA and its photophysical effect is complex.[29]

Owing to their nIR fluorescence, SWCNTs are versatile building blocks for optical sensors.[2] Molecular recognition is essential for sensing, and therefore, various (noncovalent) functionalization concepts have been used with different macromolecules. These conjugates have shown to be very successful for sensors including neurotransmitters such as dopamine, proteins, and small molecules.[30−35] Again, ssDNA functionalization has served as a key concept. The recognition and photophysical mechanism has been attributed on the one side to conformation changes that varies exciton decay pathways.[35] On the other side, the influence of redox chemistry has been discussed.[34,36−39] Interestingly, it was shown that for sensors of the important neurotransmitter dopamine, sequence and length affect sensitivity and also selectivity.[40] In this context, the ssDNA wrapping and the design of an organic corona have been discussed as a guide to create general recognition motifs.[17] The exact coverage, conformation, and dynamics of ssDNA on SWCNTs should play an important role, especially in light of recent simulations that show the importance of kinetics (rate constants) for sensing and imaging with such sensors.[41]

Even though ssDNA functionalization of SWCNTs is widely used, many fundamental aspects of the ssDNA phase around SWCNTs are still unclear. Most importantly, quantitative data regarding the adsorption of ssDNA are not fully available. Therefore, the simple question how many ssDNA molecules are bound to a single SWCNT has not been fully addressed.

The group of Hertel used a fluorescently labeled ssDNA and calculated the amount of ssDNA in the sample from fluorescence quenching on the SWCNT.[13] This approach is based on assumptions about how the fluorescence quantum yield of the fluorophore is reduced in the proximity of the SWCNT. Jena et al. explored the adsorption of ssDNA by displacement and surface saturation experiments.[29] However, the complex interplay between photophysics and surface coverage might affect such approaches. Therefore, a direct approach that does not rely on SWCNT fluorescence changes would be very powerful.

Here, we introduce a direct approach to determine the amount of bound ssDNA to SWCNTs, without using further assumptions. We determine the number of bound ssDNA molecules to SWCNTs for different sequences and also correlate it with nIR fluorescence changes in the presence of small molecules and different pH values.

MATERIALS AND METHODS

Chemicals. All used chemicals and oligonucleotides were purchased from Sigma-Aldrich (Taufkirchen, Germany) unless declared otherwise.

ssDNA/SWCNT Modification Procedure. Surface modification of SWCNTs was performed by mixing 125 μL of ssDNA oligonucleotide solution [2 mg/mL stock in phosphate-buffered saline (PBS)] and 125 μL of (6,5) chirality-enriched SWCNTs (Sigma-Aldrich, product no. 773735) (2 mg/mL stock in PBS). This mixture was tip-sonicated (36 W output power—10 min/30% Amplitude, Fisher Scientific model 120 Sonic Dismembrator) in an ice bath to stabilize the temperature during the dispersion process. Subsequently, centrifugation steps (2 × 30 min/4 °C/16 100*g*) removed large bundles and aggregates. The supernatant was used as a stock for experiments, and the two pellets of nondispersed SWCNTs were stored on ice. To measure the amount of free ssDNA in the supernatant, stepwise molecular weight cutoff filtration was performed. For this purpose, 450 μL of PBS was mixed together with 50 μL of ssDNA/SWCNT stock in Vivaspin 500 (100 000 Da molecular weight cutoff filter, Sartorius) and centrifuged 15 min/15 000*g* at room temperature (RT). The flow through was stored on ice for ssDNA quantification, and the ssDNA/SWCNT conjugates were washed with 500 μL 1× PBS by applying the same centrifugation conditions. This step was repeated up to five times. The pellets of nonsolubilized SWCNTs were suspended in 400 μL 1× PBS, transferred to the second molecular weight cutoff filter and centrifuged 15 min/15 000*g* at RT. The ssDNA absorbance in the flow through of each filtration step was determined using a Nanodrop 2000c UV−vis spectrometer (Thermo Scientific), by recording three technical replicates for each sample. To calculate the ssDNA concentration, the absorbance at 260 nm and the extinction coefficient of the oligonucleotide sequence (calculated by the base-pair model[42]) were used, while the cumulative amount equaled n_{free} (ssDNA).

UV−Vis−nIR Spectroscopy. ssDNA/SWCNT stock samples were diluted 1:100 in PBS, and absorption spectra were measured using a JASCO V-670 device from 450 to 1300 nm in 0.5 nm steps in a 10 mm path quartz cuvette. Maximum absorption values and full width at half-maximum of the (6,5)

DOI: 10.1021/acs.jpcc.8b11058
J. Phys. Chem. C 2019, 123, 4837−4847

chirality absorption peak were quantified with the spectrometer's Spectra Manager software.

AFM Analysis. For atomic force microscopy (AFM) measurements, 20 μL of a 0.5−2 nM ssDNA/SWCNT dispersion was incubated on freshly cleaved muscovite mica for 10 min. Subsequently, the mica surface was washed with MilliQ grade water and dried under nitrogen flow. AFM images were acquired in the tapping mode on an Asylum Research MFP-3D Infinity microscope with Olympus AC-160-TS cantilevers. The images were analyzed with Gwyddion. For all images, the background/tilt was removed using the second order polynomial fit. The surface plane was set to zero using three-point leveling, and horizontal scars were corrected. Lengths of ssDNA/SWCNTs were measured with the distance measurement tool, and statistical analysis was performed in OriginPro using descriptive statistics.

ssDNA/SWCNT Surface Coverage Calculation. After quantifying the free ssDNA, it is possible to calculate the amount of bound ssDNA as n_{bound} (ssDNA) = n_{total} (ssDNA) − n_{free} (ssDNA).

The amount of colloidally dispersed carbon of (6,5)-SWCNTs is determined according to Hertel and co-workers.[13] Hereby, the carbon atom concentration c_C in the suspension (mol·L^{-1}) was calculated from the OD of the S_{11} transition by

$$C_C = B\frac{\Delta_{\text{fwhm}}\text{OD}}{\text{fd}} \tag{1}$$

Here, $B = 5.1 \times 10^{-8}$ mol·L^{-1}·cm·nm^{-1} is a proportional factor, d corresponds to the thickness of the cuvette, f is the C-atom oscillator strength (0.01 for (6,5)-SWCNT),[13,43] Δ_{fwhm} is the full width half-maximum, and OD is the optical density at the S_{11} transmission of (6,5)-SWCNT obtained from the spectrometer software.

The total amount of dispersed carbon n_{carbon} can be obtained by multiplying c_C with the volume V (L). The following equation leads to the average (6,5)-SWCNT segment (nm), which is occupied by a single ssDNA molecule

$$\text{SWCNT segment/ssDNA molecule} = \frac{n_{\text{carbon}}}{n_{\text{bound}}(\text{ssDNA}) \cdot 88\ [\text{nm}^{-1}]} \tag{2}$$

A 1 nm (6,5)-SWCNT corresponds to 88 carbon atoms,[13] while the overall SWCNT absorption does not depend on the SWCNT lengths.[44] The absolute number of adsorbed ssDNA sequences on a (6,5)-SWCNT is calculated by considering the different lengths of the SWCNTs (weighted mean) and the formula

$$\text{ssDNA molecules/SWCNT} = \frac{\text{SWCNT length [nm]}}{\text{SWCNT segment/ssDNA molecule [nm]}} \tag{3}$$

Errors were calculated using an error progression analysis and included the following errors: error of ssDNA quantification, ssDNA recovery/unspecific binding, and error of the carbon concentration measurements.

nIR Fluorescence Spectroscopy. nIR fluorescence spectra were recorded with a Shamrock 193i spectrometer (Andor Technology Ltd., Belfast, Northern Ireland) connected to an IX53 microscope (Olympus, Tokyo, Japan). Excitation was performed with a 561 nm Cobolt Jive laser (Cobolt AB, Solna, Sweden). For measurements, 200 μL of 0.1 nM ssDNA/SWCNT solution was placed in a 96-well plate and measured in triplicates, using 10 s integration time, 500 μm slit width, and 300 mW excitation power. The nIR fluorescence response to analytes and different pH values were acquired in the following way: 20 μL of (1 μM dopamine-HCl solution in 1× PBS; 10 μM Riboflavin in 1× PBS; 1 mM H_2O_2 in 1× PBS; 0.01 M NaOH in H_2O; and 0.06 M HCl in H_2O) was added in triplicates to 180 μL of 0.1 nM ssDNA/SWCNTs in 1× PBS (pH = 7.3).

Zeta-Potential Measurements. Zeta-potential measurements were performed with a Zetasizer Nano S (Malvern Instruments) device and evaluated with Zetasizer software. For this purpose, the ssDNA/SWCNT stock was diluted 1:100 in PBS (pH 7.3) and measured directly.

MD Simulations. We used classical atomistic MD simulations to examine the structure of $(GT)_{15}$ ssDNA/(6,5)-SWCNT conjugates. We determined the likely structures of these conjugates and calculated the contact areas between ssDNA and SWCNTs. The simulated systems contained (6,5)-SWCNTs wrapped with $(GT)_{15}$. The initial configurations of all simulations were generated by using Material Studio (Accelrys Software Inc. Materials Studio, Release 4.5; Accelrys Software Inc.: San Diego, CA, 2007) and VMD software.[45] First, a helical structure of $(GT)_{15}$ ssDNA was constructed by using Material Studio. Then, a (6,5)-SWCNT was wrapped by the helical ssDNA by using VMD plugins. The systems were solvated and ionized by solvate and ionize VMD plugins, respectively;[45] the salt concentration of 150 mM NaCl was selected to mimic physiological conditions. The final systems contained approximately 29 725 atoms.

The CHARMM36 force-field parameters[46] and TIP3P water model were used to define interactions for all the simulated molecules.[47] MD simulations were performed with NAMD2.12.[48] Long-range electrostatics were evaluated by the particle-mesh Ewald method.[49] The evaluation of van der Waals and long-range Coulomb interactions was performed every 1 and 2 time steps, respectively; the time step was set to 2 fs. All the simulations were conducted in the *NpT* ensemble and with periodic boundary conditions applied. Temperature and pressure remained constant at 310 K and 1 bar, respectively; the Langevin constant was set to γ_{Lang} = 1.0 ps^{-1}. The first prepared system, containing the (6,5)-SWCNT wrapped by a helically arranged $(GT)_{15}$, was initially minimized for 10 000 steps. After minimization and warming the system, water and ions were equilibrated for 2 ns around the hybrid systems, which were restrained using harmonic forces with a spring constant of 1 kcal/(mol Å^2). Then, the system was equilibrated for 100 ns, while only SWCNT atoms were held restrained. The second system was simulated to examine the structure of a $(GT)_{15}$ molecule wrapping (6,5)-SWCNTs, while occupying an SWCNT fragment 2.24 nm in length, as determined by experiments. In the second set of simulations, the above system was simulated for additional 327 ns. In these simulations, all the heavy atoms of $(GT)_{15}$ were restrained to occupy a 2.24 nm long fragment of SWCNTs, by means of a square potential

$$V(z) = 0; \qquad z > -z_0 \text{ and } z < z_0 \tag{4}$$

$$V(z) = V_0; \qquad z < -z_0 \text{ and } z > z_0 \tag{5}$$

where V_0 was gradually increased from 0.01 kcal/mol per atom to 0.1 kcal/mol per atom. Overall, the second system was progressively simulated for 100 ns (V_0 = 0.01 kcal/mol, z_0 = 11

DOI: 10.1021/acs.jpcc.8b11058
J. Phys. Chem. C 2019, 123, 4837−4847

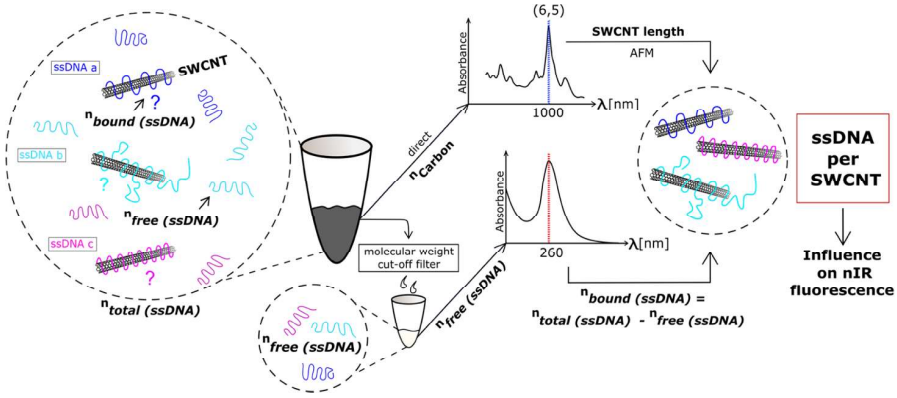

Figure 1. Assay to determine the number of adsorbed ssDNA molecules on carbon nanotubes. A typical ssDNA/SWCNT sample contains both bound/adsorbed and free ssDNA. The free ssDNA of an ssDNA/SWCNT sample is removed using a molecular weight cutoff filter and used to determine the number of free n_{free} (ssDNA) and consequently adsorbed/bound ssDNA n_{bound} (ssDNA). SWCNT absorption measurements in the nIR are performed to calculate the amount of dispersed carbon n_{Carbon}. These two numbers are used to determine the average (6,5)-SWCNT segment, which is occupied by a single ssDNA molecule (SWCNT segment/ssDNA molecule) for different ssDNA sequences. The resulting ssDNA/SWCNT numbers can be correlated with nIR fluorescence changes to better understand the interplay between the organic phase and photophysics, or they can be used as parameters for MD simulations.

nm), 100 ns (V_0 = 0.02 kcal/mol, z_0 = 11 nm), 100 ns (V_0 = 0.03 kcal/mol, z_0 = 11 nm), 100 ns (V_0 = 0.04 kcal/mol, z_0 = 11 nm), and 200 ns (V_0 = 0.1 kcal/mol, z_0 = 11.2 nm). To analyze the stacking of SWCNTs by $(GT)_{15}$ in two simulations above, the contact area between ssDNA and SWCNTs was calculated in time t, defined as

$$\frac{a_{DNA}(t) + a_{SWCNT}(t) - a_{DNA-SWCNT}(t)}{2} \quad (6)$$

where $a_{DNA}(t)$, $a_{SWCNT}(t)$, and $a_{DNA-SWCNT}(t)$ are the solvent-accessible surface areas of the ssDNA, SWCNTs, and the ssDNA/SWCNT conjugate, respectively, at time t. The analyses were performed during the last 50 ns of production runs. The contact area evaluation was performed by the SASA built-in VMD plugin,[45] where the van der Waals radius of 1.4 Å was assigned to atoms to identify the points on a sphere that are accessible to the solvent. The ssDNA/SWCNT contact areas reported in Figure 7c were calculated by averaging the data obtained by eq 6. Images of simulated systems were prepared with VMD.[45]

RESULTS

The number of adsorbed macromolecules on a nanomaterial is of fundamental importance to understand the organic corona and crucial for many applications. We developed a direct approach to quantify the number of ssDNA molecules on SWCNTs noncovalently functionalized with ssDNA. In a typical sample of ssDNA-suspended SWCNTs, a certain amount of ssDNA remains as free (not adsorbed) n_{free} (ssDNA) in solution (Figure 1). This excess ssDNA is not necessary for the colloidal stability of the SWCNTs in contrast to surfactants such as sodium dodecyl sulfate.[50] The overall amount of added ssDNA n_{total} (ssDNA) is known, and therefore, the amount of bound ssDNA is the difference between n_{total} (ssDNA) and n_{free} (ssDNA). SWCNTs have known extinction coefficients, and therefore, the concentration of the SWCNTs can also be determined via absorption spectroscopy.[13,43] However, as both ssDNA and SWCNTs absorb light, it is difficult to calculate the concentration from spectral regions in which both components absorb. Therefore, a sequential filtration process with molecular weight cutoff filters was applied to measure the free ssDNA excluded from SWCNTs. The absorption of the ssDNA at 260 nm was then used to quantify its concentration. In contrast to ssDNA, SWCNTs absorb in the nIR and thus the S_{11} absorption feature of the (6,5)-SWCNTs at ~990 nm was used to measure the carbon/SWCNT concentration, as shown by Hertel and co-workers.[13] The herein presented approach enables the quantification of ssDNA molecules per SWCNT and the evaluation of its influence on photophysical properties such as responses to small analytes, which is highly relevant for biosensing applications.

First, we verified that this approach is feasible and that effects such as unspecific adsorption to the filter or the reaction tubes do not bias quantification. Figure 2a shows a control experiment without any SWCNTs. ssDNA (three exemplary ssDNA sequences) is filtered through the cutoff filter. More than 95% of the total ssDNA was recovered after the first two washing steps, while most of the free ssDNA was washed through the molecular weight cutoff filter during the first filtration. The sum of all filtration cycles gives the overall amount of free ssDNA n_{free} (ssDNA), which equals in the absence of SWCNTs, the amount of the added ssDNA n_{total} (ssDNA). The error (<5.4%) due to unspecific adsorption of ssDNA to the surfaces was accounted in the error propagation. ssDNA/SWCNT samples were evaluated in the same way (Figure 2b). In the first filtration step, a reduced amount of free ssDNA was detected, which is in agreement with adsorption of ssDNA onto the SWCNT surfaces.

The cumulative amount of n_{free} (ssDNA) is then used to calculate the amount of n_{bound} (ssDNA). Interestingly, the amount of bound ssDNA depends on the sequence, which raises the question about the impact of the sequence on ssDNA surface coverage/occupation. Up to five washing steps were performed, but as practically, all the free ssDNA (~95%) was recovered after the second step, all the following quantifications are based on two washing cycles. To verify that there is no bias because of binding of ssDNA to the nondispersed SWCNTs, the pellet was extensively washed. Less than 10% of n_{total} (ssDNA) was detected and accounted for in the calculation for n_{free} (ssDNA) (washed pellet in Figure

DOI: 10.1021/acs.jpcc.8b11058
J. Phys. Chem. C 2019, 123, 4837−4847

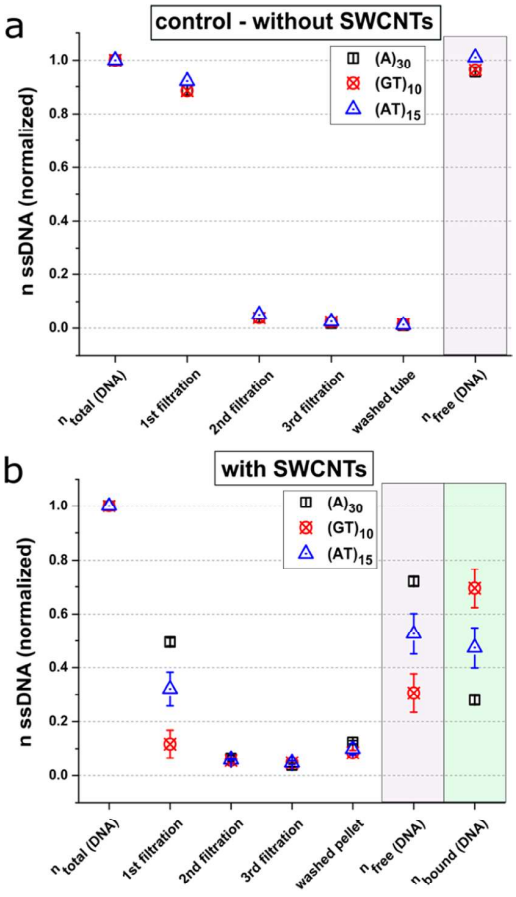

Figure 2. Accuracy of the ssDNA adsorption assay. (a) Control experiment that shows that the amount of free ssDNA in the absence of SWCNTs is not biased by the filtering process (three representative oligonucleotide sequences, n = 1). (b) Measured amount of ssDNA (three representative oligonucleotides) after different filtering/washing steps. Note that n_{free} (ssDNA) represents the sum of all filtration cycles, while the n_{bound} (ssDNA) is the difference of n_{total} (ssDNA) and n_{free} (ssDNA). The cumulative amount of free ssDNA in (a) is already close to the total amount after one filtration step. These results show that the assay can measure the amount of adsorbed/bound ssDNA and display the differences between ssDNA sequences. Data are normalized to n_{total} (ssDNA) of each ssDNA sequence. (n = 3. Errors are SEM).

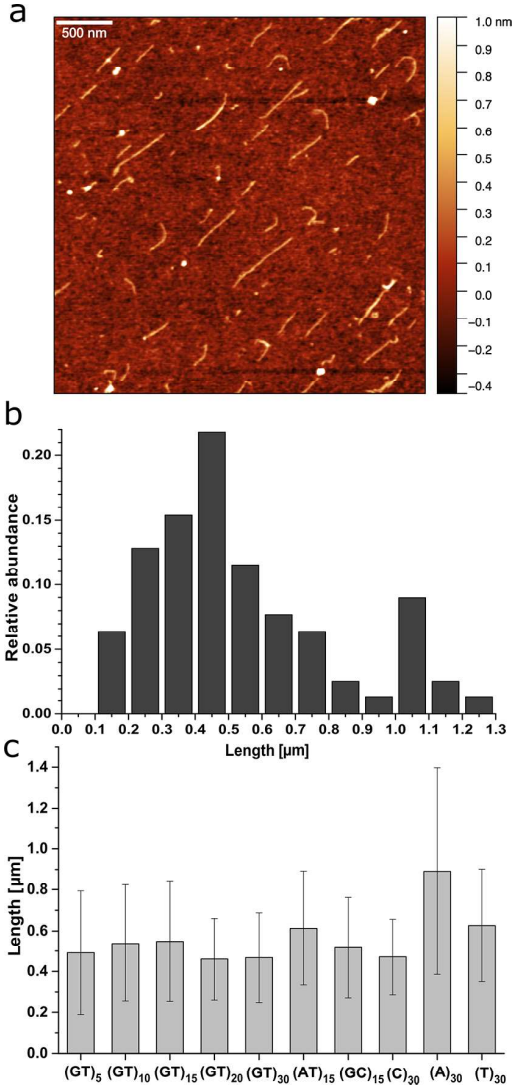

Figure 3. Length of ssDNA/SWCNTs for different ssDNA sequences. (a) Typical AFM image of $(GT)_{15}$/SWCNTs. (b) Exemplary length distribution histogram of $(GT)_{15}$/SWCNTs. (c) Mean length of ssDNA/SWCNT conjugates, n (total) = 736 or n > 44 for each sequence (detailed information in Supporting Information, Table S1). Error bars = standard deviation.

2b). In general, SWCNTs are known to get colloidally dispersed by ssDNA if there is a sufficient amount.[10,34] This result demonstrates that no significant quantities of ssDNA remain bound to undispersed SWCNTs, which would overestimate the number of adsorbed ssDNA molecules.

To correlate the amount of dispersed carbon (n_{Carbon}) obtained from UV–vis–nIR absorption spectroscopy to the SWCNT length distribution, AFM measurements were performed. For this purpose, the lengths of ssDNA/SWCNT conjugates were directly measured from AFM images similar to the one shown in Figure 3a for $(GT)_{15}$/SWCNTs and analyzed for their length distribution (Figure 3b). The average lengths (Figure 3c) of the conjugates were in a similar range (mean values from 461 to 626 nm) except for $(A)_{30}$ with 892 nm (see also Supporting Information, Table S2). The mean length of all 736 analyzed SWCNTs was 575 nm and therefore we considered around 600 nm as a typical length.

When n_{bound} (ssDNA) and n_{carbon} are known, it is possible to calculate the average (6,5)-SWCNT segment length for one adsorbed ssDNA molecule. As every ssDNA/SWCNT complex has different lengths, we normalized these numbers to a typical/medium SWCNT length of 600 nm. These results are summarized in Figure 4a (red columns). ssDNA sequences of different lengths have been used, and therefore, the number of adsorbed ssDNA nucleotides per 600 nm (6,5)-SWCNTs has been calculated (blue color in the same plot). Clear differences are observed by altering the sequence length of $(GT)_5$–$(GT)_{30}$, while the base composition is fixed. For ssDNA/SWCNTs with the same sequence length but different nucleotide compositions, values range from ~130 for $(A)_{30}$ to ~280 for $(T)_{30}$ ssDNA molecules per 600 nm SWCNT. The absolute numbers of ssDNA molecules per SWCNT (with weighted SWCNTs lengths) are shown in the Supporting Information, Figure S4a. The number of adsorbed nucleotides

DOI: 10.1021/acs.jpcc.8b11058
J. Phys. Chem. C 2019, 123, 4837–4847

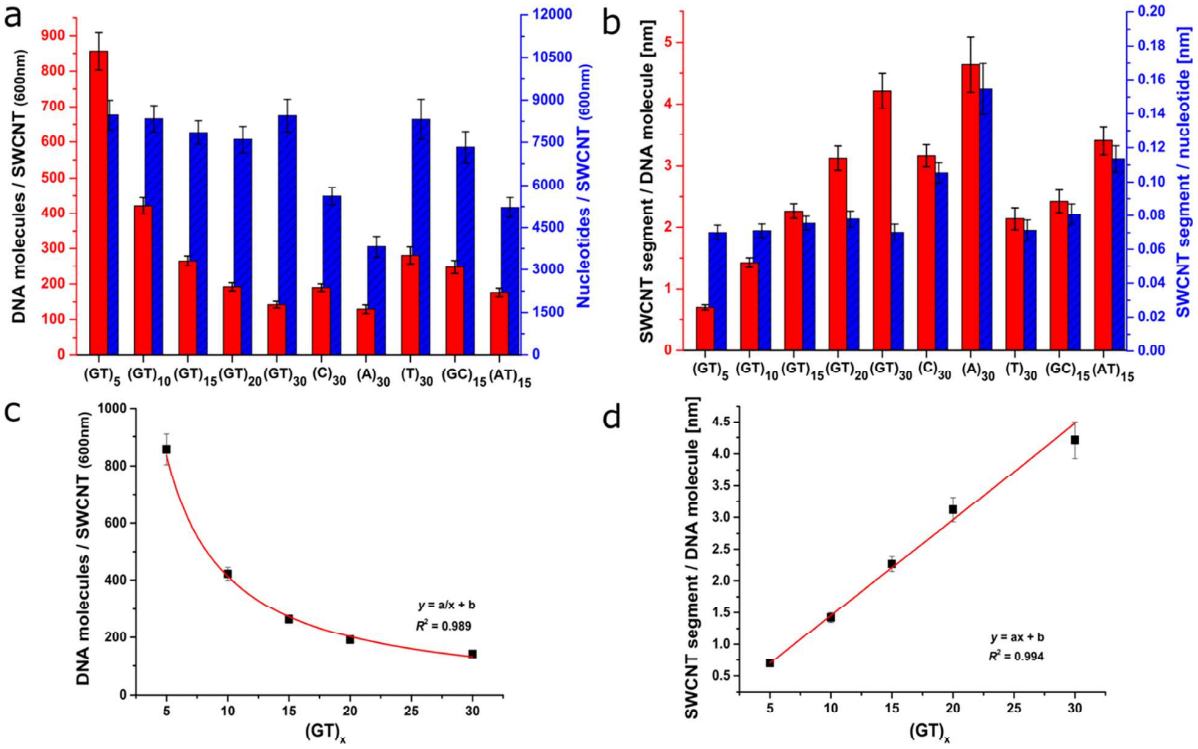

Figure 4. Number of adsorbed/bound ssDNA molecules on SWCNTs for different ssDNA sequences. (a) Adsorbed ssDNA molecules per (normalized) 600 nm (6,5)-SWCNT (left axis/red bars). The right axis/blue bars show the number of nucleotides per 600 nm (6,5)-SWCNT. (n = 3; error bars = SD). (b) Mean (6,5)-SWCNT segment length for one adsorbed ssDNA molecule in nm (left axis/red bars). The corresponding right axis/blue bars shows the (6,5)-SWCNT segment length for one adsorbed nucleotide. (n = 3; error bars = SD). (c) Correlation between the number of adsorbed molecules per (6,5)-SWCNT and the length of the $(GT)_x$ sequence. The red curve corresponds to the $y = (a/x) + b$ fit, with a = 4179.67 and b = −5.69 (R^2 = 0.989) (n = 3; error bars = SD). (d) Correlation between the (6,5)-SWCNT segment length for one adsorbed ssDNA molecule and the length of the $(GT)_x$ sequence. The correlation of the data can be described using a linear fit $y = ax + b$, with a = 0.1508 and b = −0.05 (R^2 = 0.994) (n = 3; error bars = SD).

for $(GT)_x$ sequences of different lengths is very similar [7689 $(GT)_{20}$–8566 $(GT)_5$]. In contrast, for sequences of different compositions, the numbers can vary by >100% [3880 $(A)_{30}$, 5693 $(C)_{30}$, and 8412 $(T)_{30}$]. The number of adsorbed $(GT)_x$ molecules on the SWCNT surface strongly depended on the sequence length, following the $y = (a/x) + b$ function (Figure 4c), without showing any cooperativity. Next to these total numbers of adsorbed ssDNA molecules on (6,5)-SWCNTs, it is of general interest to illustrate the resulting mean (6,5)-SWCNT segment length for one adsorbed ssDNA molecule and also the correlating values for one adsorbed nucleotide (Figure 4b). These segments for one adsorbed ssDNA molecules varied between the different 30 nucleotide-containing sequences from ∼2.1 nm for $(T)_{30}$ to ∼4.6 nm for $(A)_{30}$. The SWCNT segment for adsorbed $(GT)_x$ molecules depended strongly on the sequence length. In contrast, the segment for bound/adsorbed $(GT)_x$ nucleotides remained the same. Figure 4d evaluates furthermore the correlation between the length of the $(GT)_x$ sequence and the mean segment length of the SWCNT that is attributed to the coverage by the ssDNA, while the relation is best described by a linear fit (R = 0.994). A summary about the presented data is given in the Supporting Information, Table S1.

Small differences for the molecular absorption coefficient of ssDNA could occur by calculating with the nearest neighbor model instead of the base-composition model.[42] These could lead to small-sequence specific differences/uncertainties from −4.7% $(GT)_5$ to +12.5% $(A)_{30}$ ssDNA/SWCNT. The error from SWCNTs going through the filter can be neglected (see Supporting Information, Figure S5).

To study the influence of ssDNA/SWCNT numbers on nIR fluorescence properties, the ssDNA/SWCNT complexes were exposed to different analytes that are known to affect the fluorescence of SWCNTs. One example is the important neurotransmitter dopamine, which is known to increase the nIR fluorescence of ssDNA/SWCNTs.[30,34,35,40] Another example is riboflavin, which has been described to reduce their fluorescence.[30,34,40] The exact ssDNA sequences have been shown to affect the fluorescence changes.[40] It was also shown that the redox chemistry of analytes plays a role but cannot explain alone the observed fluorescence changes.[34] Therefore, we wanted to understand if the number of ssDNA molecules per SWCNT can explain these fluorescence changes.

The nIR fluorescence responses, exemplarily shown in Figure 5a,b, were evaluated and summarized in a heatmap (Figure 5c). Addition of dopamine generally leads to a fluorescence increase, while the nIR fluorescence is reduced in the presence of riboflavin. However, the magnitude of fluorescence changes differed significantly. In contrast, H_2O_2 did only slightly change the fluorescence and both increase and decrease were observed (−4% for $(GT)_{15}$/SWCNT to +9% for $(T)_{30}$/SWCNT). H_2O_2 has been reported to decrease the fluorescence of different functionalized SWCNTs.[51]

DOI: 10.1021/acs.jpcc.8b11058
J. Phys. Chem. C 2019, 123, 4837−4847

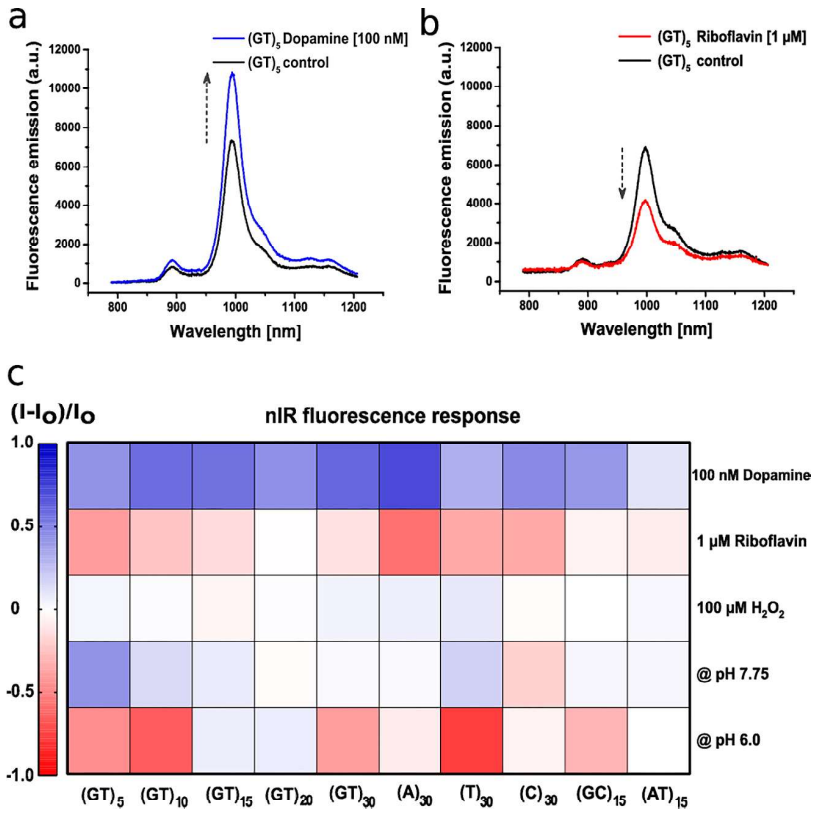

Figure 5. nIR fluorescence responses of ssDNA/SWCNT conjugates to different analytes. (a) Exemplary fluorescence change of the $(GT)_5$/(6,5)-SWCNT after addition of dopamine (100 nM). (b) Exemplary fluorescence decrease after the addition of riboflavin (1 μM) to the $(GT)_5$/(6,5)-SWCNT; gray arrows indicate the fluorescence change. (c) Overview heatmap that displays the fluorescence changes of different ssDNA/SWCNT conjugates after the addition of several relevant analytes or change of pH. Blue indicates a fluorescence increase and red indicates a fluorescence decrease (n = 3).

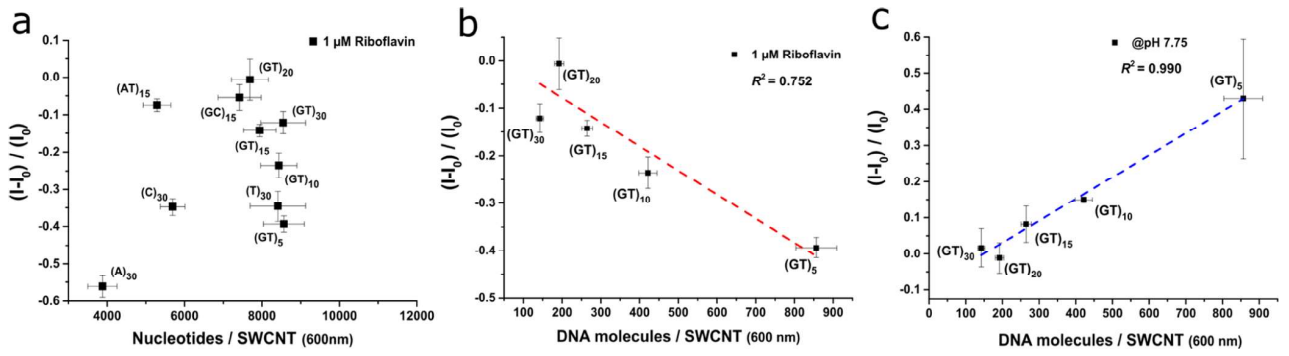

Figure 6. Correlation between fluorescence response and adsorbed ssDNA molecules. (a) nIR fluorescence response after riboflavin addition (1 μM) versus surface coverage (ssDNA nucleotides per 600 nm SWCNT) for different ssDNA sequences. (b) Length dependence for $(GT)_x$/SWCNT nIR fluorescence in response to riboflavin (1 μM). The red, dotted line represents a linear fit of the data (R^2 = 0.752). The shorter the sequence, the stronger the observed fluorescence decrease, even though the absolute number of nucleotides differs much less (see Figure 4). (c) $(GT)_x$ nIR fluorescence increases in response to basic conditions (pH 7.75, in comparison to pH 7.3) for different $(GT)_x$ sequences. Again, the shorter the sequence, the higher was the fluorescence response, which can be described by a linear fit (blue, dotted line; R^2 = 0.990). (n = 3; error bars = SEM).

Protons are also known to affect the fluorescence of SWCNTs.[38] Increasing the pH value from 7.3 in a PBS system to 7.75 resulted in a general increase in nIR fluorescence, with a maximum of +43% for $(GT)_5$/SWCNT, except for $(C)_{30}$/SWCNT, which showed a fluorescence decrease of −18%. Decreasing the pH value from 7.3 to 6.0 caused a general nIR fluorescence decrease with a maximum of −63% for $(GT)_{10}$/SWCNT and −75% for $(T)_{30}$/SWCNT, while $(GT)_{20}$/SWCNT and $(GT)_{15}$/SWCNT showed a fluorescence increase of +7%.

These fluorescence changes were correlated with the number of adsorbed ssDNA molecules/nucleotides to identify whether there is a pattern. A typical example is shown in Figure 6a for the fluorescence change after riboflavin addition. In this

DOI: 10.1021/acs.jpcc.8b11058
J. Phys. Chem. C 2019, 123, 4837−4847

case, no clear correlation could be observed similar to most other data sets. Only for $(GT)_x$/SWCNTs, the number of bound molecules per 600 nm SWCNT correlated with the fluorescence response after riboflavin addition (Figure 6b) or pH change (Figure 6c). In both plots, the nIR fluorescence change increased with the increasing number of absorbed ssDNA molecules, even if the number of absorbed nucleotides stayed similar (see Figures 4a and 6a). $(GT)_5$/SWCNT showed the strongest difference with −39% (Figure 6b) and +43% (Figure 6c), while $(GT)_{30}$/SWCNT and $(GT)_{20}$/SWCNT responded in a quite similar way. For dopamine, no clear correlation could be found (Supporting Information, Figure S2). This indicates that the exact conformation rather than the absolute number of bound or adsorbed molecules is crucial for the mechanism, which is in agreement with mechanistic insights reported for dopamine sensing.[35]

The absolute fluorescence intensity of (6,5)-ssDNA/SWCNTs did not correlate with the number of adsorbed nucleotides. Additionally, neither the peak position of the nIR absorbance/fluorescence maxima nor the fluorescence emission intensity of ssDNA/SWNCTs seems to depend on the amount of adsorbed ssDNA molecules/nucleotides (see Supporting Information, Figures S1c,d and S5b). This indicates that the distinct correlation between nIR absorbance/fluorescence maxima with the fluorescence emission intensity of ssDNA/SWNCTs and therefore the quantum yield depends mainly on the sequence composition of the ssDNA (Supporting Information, Figure S1a,b). There are also differences in the zeta potential of the ssDNA/SWCNT, but they did not correlate with the number of adsorbed ssDNA molecules (Supporting Information, Figure S3).

To determine the most likely conformations of ssDNA molecules on SWCNTs, we performed atomistic MD simulations of $(GT)_{15}$ molecules adsorbing on (6,5)-SWCNTs. $(GT)_{15}$ molecules were adsorbed and simulated on the SWCNT surface, either with restraints imposed, so that $(GT)_{15}$ molecule spans the experimentally determined segment length of SWCNTs, or without any restraints present. In both simulations, ssDNA molecules initially wrapped SWCNTs in helical conformations.[52−54] In a 100 ns simulation of the $(GT)_{15}$/SWCNT conjugate without any restraints present, ssDNA remained helically wrapped and the majority of the bases stacked on the SWCNT, as shown in Figure 7b. However, in a ∼500 ns simulation of the $(GT)_{15}$/SWCNT conjugate, where $(GT)_{15}$ was restrained to occupy a 2.24 nm long segment of SWCNTs, only a fraction of bases can stack on the SWCNT, while the rest of the bases stack on top of each other (Figure 7a). The analysis of the $(GT)_{15}$/SWCNT contact area, shown in Figure 7c, indicates that less than half of ssDNA bases stack directly on the SWCNT surface in the system as shown in Figure 7a. Furthermore, the thickness of the ssDNA corona around the SWCNT increased (see Supporting Information, Figure S7). This shows that the experimentally determined number of bound ssDNA molecules is important to understand the organic phase around SWCNTs and that this parameter affects MD simulations significantly.

DISCUSSION

ssDNA functionalization is one of the major approaches to modify SWCNTs and is used in various applications. Therefore, understanding the structure and dynamics of the organic phase created by the ssDNA around the SWCNTs is highly important for a broad range of applications including sensing, imaging, and separation. We present a direct and straightforward approach to quantify a basic property of ssDNA/SWCNT hybrids: the number of bound ssDNA molecules per SWCNT.

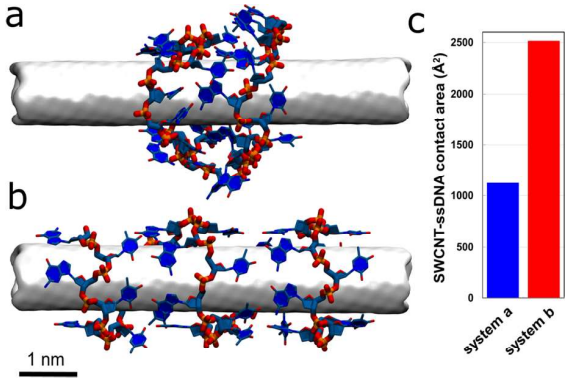

Figure 7. Molecular dynamics simulations of $(GT)_{15}$ ssDNA on a (6,5)-SWCNT with experimentally determined adsorption numbers as parameters. (a) Representative view of a $(GT)_{15}$−ssDNA molecule adsorbed on a (6,5)-SWCNT. ssDNA is restrained to stack on an SWCNT segment of the length determined in experiments. When $(GT)_{15}$ occupies the SWCNT segment as determined in experiments, only a fraction of bases stack on the SWCNT, while the rest of the bases stack on top of each other (less than half). (b) Representative view of a $(GT)_{15}$ molecule that fully adsorbs on a (6,5)-SWCNT. (c) Contact area between $(GT)_{15}$ and (6,5)-SWCNTs for systems shown in panels (a,b). In panels (a,b), the SWCNT is shown as a white surface, and ssDNA atoms are shown in subdued blue (C), red (O), orange (P), and blue (N) colors. Hydrogen atoms are not shown for clarity.

The approach uses the fact that after filtration, the free ssDNA concentration is measurable via UV−vis absorption spectroscopy and together with the starting concentration of ssDNA, one can derive the concentration of bound ssDNA. Additionally, the absorption of SWCNTs in the nIR can be used to calculate the concentration of dispersed carbon of (6,5)-SWCNTs. This calculation is based on a previously measured molar extinction coefficient and absorption cross section (1.7×10^{-17} cm^2 per C-atom).[13] Different absolute numbers for these coefficients have been reported (2.9×10^{-18}, 0.7×10^{-17} to $\sim 1 \times 10^{-17}$, and 2.54×10^{-17} cm^2 per C-atom).[10,43,55] Therefore, the absolute numbers reported in our work may vary in this range, but the relative values between different ssDNA sequences are not affected. SWCNTs of other chirality would have different absorption cross sections, which has to be taken into account when other chiralities are analyzed using our approach. In this work, we focused on (6,5)-SWCNTs. The adsorption of different DNA sequences to varying SWCNT chiralities can be very different as known from chirality separation experiments.[56] Therefore, the occupied SWCNT segment per DNA molecule might differ for other chiralities and depend on parameters such as adsorption energies.[22]

Our quantification assay for adsorbed ssDNA molecules on SWCNTs extends the already described (indirect) methods by a direct approach, with the possibility of using unlabeled ssDNA sequences. It reduces the uncertainties resulting from the interaction of fluorophores like fluorescein with the SWCNT surface by itself or the not completely known quenching properties of organic fluorophores in the immediate

DOI: 10.1021/acs.jpcc.8b11058
J. Phys. Chem. C 2019, 123, 4837−4847

proximity of SWCNTs.[30] The presented values in this study are expressed on the one side as the mean lateral SWCNT segment length per ssDNA molecule. On the other side, it is important to stress that our approach aims to determine the number of bound/adsorbed ssDNA molecules. The exact conformation and the actual area of ssDNA adsorption on the SWCNT surface are not directly accessible. Previously, it was shown that on SWCNTs, only a part of the ssDNA seems to be adsorbed and the Kuhn length is a relevant length scale for this process.[12] In that study, $(GT)_{16}$ ssDNA adsorbed on around 6 nm on the SWCNT surface with one bound part and a free second part of the molecule. Our results also suggest that the ssDNA is only partially adsorbed to the SWCNT surface and the number of bound ssDNA molecules is much higher than expected. Interestingly, increasing $(GT)_x$ sequence repeat length leads to a linear increase of occupied SWCNT segment length, suggesting that there is no cooperativity between single ssDNA molecules.

The contour length of the used ssDNA sequences with the same amount of nucleotides should be quite similar,[57,58] while it is known that the persistence length is influenced by the base composition. This property could affect the ssDNA/SWCNT surface coverage and adsorption, while also the rigidity and stiffness of ssDNA can vary depending on the sequence composition. Comparing poly(A) and poly(T) sequences, for example, reveals different persistence lengths [poly(T) < poly(A)], next to the different rigidity and stiffness [poly(T) < poly(A)].[59−62] ssDNA surface adsorption is known to be sensitive to the ionic strength of the surrounding phase.[63] Furthermore, it was reported that the stability and density of the helical ssDNA wrapping are increased in salt-containing media, compared to pure H_2O.[64] Our experiments were performed in biologically relevant buffers (PBS) but could be performed in other buffers or solvents as well.[30] Interestingly, it was recently shown that ions cause phase transition of ssDNA/SWCNTs and ssDNA composition determines stability of the nanohybrid.[63,65] Varying the ssDNA sequence next to the $(GT)_x$ sequence length was found to influence the ratios of nIR fluorescence quenching by oxygen.[66] This might be further explained by correlating the different amounts of adsorbed ssDNA sequences because $(GT)_{10}$—more ssDNA molecules—showed a higher response to oxygen quenching than $(GT)_{30}$.[66] Our data on fluorescence responses indicate that the pure number of adsorbed ssDNA molecules is in certain cases able to predict the fluorescence response. However, in most cases, no direct correlation was found, indicating that beyond the pure number, the exact conformation is governing photophysical properties. The reported numbers are very useful as parameters for MD simulations. In typical simulations, the ssDNA sees an excess of SWCNTs. If we add the experimentally determined ssDNA numbers per SWCNT as a parameter, MD simulations are strongly affected. Figure 7 clearly shows that the mean available space of ssDNA on an SWCNT should be considered as an important factor. Our results suggest that interactions between the ssDNA molecule itself play a more important role than previously thought. In the future, MD simulations could use our experimentally determined numbers as starting parameters.

CONCLUSIONS

In summary, we introduce a direct method to measure the number of bound ssDNA molecules on ssDNA/SWCNT complexes. We used it to quantify and report numbers for different ssDNA sequences, which are helpful to assess further surface modification and can serve as parameters for MD simulations. The mean (6,5)-SWCNT segment length that is attributed to one 30 nucleotide long ssDNA depends on the sequence and varies between ∼2.1 and ∼4.6 nm, showing that the nucleotide composition can change this value by more than 100%. These results highlight the complex interplay between the ssDNA composition/sequence and adsorption on SWCNTs.

ASSOCIATED CONTENT

Supporting Information

The Supporting Information is available free of charge on the ACS Publications website at DOI: 10.1021/acs.jpcc.8b11058.

Extended formula to calculate the ssDNA/SWCNTs, correlation of absorption and fluorescence properties with the ssDNA/SWCNT surface coverage, additional correlation to dopamine response, zeta-potential measurements of ssDNA/SWCNTs, number of adsorbed ssDNA molecules correlated to the SWCNT length distribution from AFM, UV−vis−nIR absorbance spectra before and after MWCO filtration, radial distance distribution of all ssDNA atoms, and summarized numbers of the presented data (PDF)

AUTHOR INFORMATION

Corresponding Author

*E-mail: skruss@uni-goettingen.de.

ORCID

Lela Vuković: 0000-0002-9053-5708

Sebastian Kruss: 0000-0003-0638-9822

Notes

The authors declare no competing financial interest.

ACKNOWLEDGMENTS

This project was supported by the state of Lower Saxony (life@nano) and the VW foundation. Part of this work was supported by the Cluster of Excellence and DFG Research Center Nanoscale Microscopy and Molecular Physiology of the Brain (CNMPB). We thank Andreas Janshoff and Claudia Steinem as well as their groups for fruitful discussions and support. We thank Ali A. Alizadehmojarad for helping with helical DNA model construction. The authors gratefully acknowledge computer time provided by the Texas Advanced Computing Center (TACC). This research is part of the Blue Waters sustained-petascale computing project, which is supported by the National Science Foundation (awards OCI-0725070 and ACI-1238993) and the state of Illinois.

REFERENCES

(1) He, X.; Htoon, H.; Doorn, S. K.; Pernice, W. H. P.; Pyatkov, F.; Krupke, R.; Jeantet, A.; Chassagneux, Y.; Voisin, C. Carbon Nanotubes as Emerging Quantum-Light Sources. *Nat. Mater.* **2018**, *17*, 663−670.

(2) Kruss, S.; Hilmer, A. J.; Zhang, J.; Reuel, N. F.; Mu, B.; Strano, M. S. Carbon Nanotubes as Optical Biomedical Sensors. *Adv. Drug Delivery Rev.* **2013**, *65*, 1933−1950.

(3) Hong, G.; Diao, S.; Antaris, A. L.; Dai, H. Carbon Nanomaterials for Biological Imaging and Nanomedicinal Therapy. *Chem. Rev.* **2015**, *115*, 10816−10906.

(4) Hirsch, A. Functionalization of Single-Walled Carbon Nanotubes. *Angew. Chem., Int. Ed. Engl.* **2002**, *41*, 1853−1859.

DOI: 10.1021/acs.jpcc.8b11058
J. Phys. Chem. C 2019, 123, 4837−4847

(5) Polo, E.; Kruss, S. Nanosensors for Neurotransmitters. *Anal. Bioanal. Chem.* **2015**, *408*, 2727−2741.
(6) Graf, A.; Held, M.; Zakharko, Y.; Tropf, L.; Gather, M. C.; Zaumseil, J. Electrical Pumping and Tuning of Exciton-Polaritons in Carbon Nanotube Microcavities. *Nat. Mater.* **2017**, *16*, 911−917.
(7) Giraldo, J. P.; Landry, M. P.; Faltermeier, S. M.; McNicholas, T. P.; Iverson, N. M.; Boghossian, A. A.; Reuel, N. F.; Hilmer, A. J.; Sen, F.; Brew, J. A.; et al. Plant Nanobionics Approach to Augment Photosynthesis and Biochemical Sensing Juan. *Nat. Mater.* **2014**, *13*, 400−408.
(8) Singh, P.; Campidelli, S.; Giordani, S.; Bonifazi, D.; Bianco, A.; Prato, M. Organic Functionalisation and Characterisation of Single-Walled Carbon Nanotubes. *Chem. Soc. Rev.* **2009**, *38*, 2214−2230.
(9) Vázquez, E.; Giacalone, F.; Prato, M. Non-Conventional Methods and Media for the Activation and Manipulation of Carbon Nanoforms. *Chem. Soc. Rev.* **2014**, *43*, 58−69.
(10) Zheng, M.; Jagota, A.; Semke, E. D.; Diner, B. A.; Mclean, R. S.; Lustig, S. R.; Richardson, R. E.; Tassi, N. G. DNA-Assisted Dispersion and Separation of Carbon Nanotubes. *Nat. Mater.* **2003**, *2*, 338−342.
(11) Zheng, M.; Jagota, A.; Strano, M. S.; Santos, A. P.; Barone, P.; Chou, S. G.; Diner, B. A.; Dresselhaus, M. S.; Mclean, R. S.; Onoa, G. B.; et al. Structure-Based Carbon Nanotube Sorting by Sequence-Dependent DNA Assembly. *Science* **2003**, *302*, 1545−1548.
(12) Brunecker, F. K.; Schöppler, F.; Hertel, T. Interaction of Polymers with Single-Wall Carbon Nanotubes. *J. Phys. Chem. C* **2016**, *120*, 10094−10103.
(13) Schöppler, F.; Mann, C.; Hain, T. C.; Neubauer, F. M.; Privitera, G.; Bonaccorso, F.; Chu, D.; Ferrari, A. C.; Hertel, T. Molar Extinction Coefficient of Single-Wall Carbon Nanotubes. *J. Phys. Chem. C* **2011**, *115*, 14682−14686.
(14) Cathcart, H.; Nicolosi, V.; Hughes, J. M.; Blau, W. J.; Kelly, J. M.; Quinn, S. J.; Coleman, J. N. Ordered DNA Wrapping Switches on Luminescence in Single-Walled Nanotube Dispersions. *J. Am. Chem. Soc.* **2008**, *130*, 12734−12744.
(15) Campbell, J. F.; Tessmer, I.; Thorp, H. H.; Erie, D. A. Atomic Force Microscopy Studies of DNA-Wrapped Carbon Nanotube Structure and Binding to Quantum Dots. *J. Am. Chem. Soc.* **2008**, *130*, 10648−10655.
(16) Jin, H.; Jeng, E. S.; Heller, D. A.; Jena, P. V.; Kirmse, R.; Langowski, j.; Strano, M. S. Divalent Ion and Thermally Induced DNA Conformational Polymorphism on Single-Walled Carbon Nanotubes. *Macromolecules* **2007**, *40*, 6731−6739.
(17) Bisker, G.; Ahn, J.; Kruss, S.; Ulissi, Z. W.; Salem, D. P.; Strano, M. S. A Mathematical Formulation and Solution of the CoPhMoRe Inverse Problem for Helically Wrapping Polymer Corona Phases on Cylindrical Substrates. *J. Phys. Chem. C* **2015**, *119*, 13876−13886.
(18) Landry, M. P.; Vuković, L.; Kruss, S.; Bisker, G.; Landry, A. M.; Islam, S.; Jain, R.; Schulten, K.; Strano, M. S. Comparative Dynamics and Sequence Dependence of DNA and RNA Binding to Single Walled Carbon Nanotubes. *J. Phys. Chem. C* **2015**, *119*, 10048−10058.
(19) Roxbury, D.; Mittal, J.; Jagota, A. Molecular-Basis of Single-Walled Carbon Nanotube Recognition by Single-Stranded DNA. *Nano Lett.* **2012**, *12*, 1464−1469.
(20) Zhao, X.; Johnson, J. K.; Pennsyl, V. Simulation of Adsorption of DNA on Carbon Nanotubes. *J. Am. Chem. Soc.* **2007**, *129*, 10438−10445.
(21) Polo, E.; Nitka, T. T.; Neubert, E.; Erpenbeck, L.; Vuković, L.; Kruss, S. Control of Integrin Affinity by Confining RGD Peptides on Fluorescent Carbon Nanotubes. *ACS Appl. Mater. Interfaces* **2018**, *10*, 17693−17703.
(22) Shankar, A.; Mittal, J.; Jagota, A. Binding between DNA and Carbon Nanotubes Strongly Depends upon Sequence and Chirality. *Langmuir* **2014**, *30*, 3176−3183.
(23) Roxbury, D.; Jagota, A.; Mittal, J. Structural Characteristics of Oligomeric DNA Strands Adsorbed onto Single-Walled Carbon Nanotubes. *J. Phys. Chem. B* **2012**, *117*, 132−140.
(24) Mu, K.; Malik, S.; Richert, C. Sequence-Specifically Addressable Hairpin DNA-Single-Walled Carbon Nanotube Complexes for Nanoconstruction. *ACS Nano* **2010**, *4*, 649−656.
(25) Gillen, A. J.; Kupis-Rozmysłowicz, J.; Gigli, C.; Schuergers, N.; Boghossian, A. A. Xeno Nucleic Acid Nanosensors for Enhanced Stability Against Ion- Induced Perturbations. *J. Phys. Chem. Lett.* **2018**, *9*, 4336−4343.
(26) Mann, F. A.; Horlebein, J.; Meyer, N. F.; Meyer, D.; Thomas, F.; Kruss, S. Carbon Nanotubes Encapsulated in Coiled-Coil Peptide Barrels. *Chem.—Eur. J.* **2018**, *24*, 12241−12245.
(27) Setaro, A.; Adeli, M.; Glaeske, M.; Przyrembel, D.; Bisswanger, T.; Gordeev, G.; Maschietto, F.; Faghani, A.; Paulus, B.; Weinelt, M.; et al. Preserving π-Conjugation in Covalently Functionalized Carbon Nanotubes for Optoelectronic Applications. *Nat. Commun.* **2017**, *8*, 14281.
(28) Connell, M. J. O.; Bachilo, S. M.; Huffman, C. B.; Rialon, K. L.; Boul, P. J.; Noon, W. H.; Kittrell, C.; Ma, J.; Hauge, R. H.; Smalley, R. E. Band Gap Fluorescence from Individual Single-Walled Carbon Nanotubes. *Science* **2002**, *297*, 593−597.
(29) Jena, P. V.; Safaee, M. M.; Heller, D. A.; Roxbury, D. DNA-Carbon Nanotube Complexation Affinity and Photoluminescence Modulation Are Independent. *ACS Appl. Mater. Interfaces* **2017**, *9*, 21397−21405.
(30) Kruss, S.; Landry, M. P.; Ende, E. V.; Lima, B. M. A.; Reuel, N. F.; Zhang, J.; Nelson, J.; Mu, B.; Hilmer, A.; Strano, M. Neurotransmitter Detection Using Corona Phase Molecular Recognition on Fluorescent Single-Walled Carbon Nanotube Sensors. *J. Am. Chem. Soc.* **2014**, *136*, 713−724.
(31) Reuel, N. F.; Grassbaugh, B.; Kruss, S.; Mundy, J. Z.; Opel, C.; Ogunniyi, A. O.; Egodage, K.; Wahl, R.; Helk, B.; Zhang, J.; et al. Emergent Properties of Nanosensor Affined Hypermannosylation, and IgG Affinity Distributions, Weakly Arrays: Applications for Monitoring Colony Selection for Biomanufacturing. *ACS Nano* **2013**, *7*, 7472−7482.
(32) Zhang, J.; Kruss, S.; Hilmer, A. J.; Shimizu, S.; Schmois, Z.; De La Cruz, F.; Barone, P. W.; Reuel, N. F.; Heller, D. A.; Strano, M. S. A Rapid , Direct , Quantitative , and Label-Free Detector of Cardiac Biomarker Troponin T Using Near-Infrared Fluorescent Single-Walled Carbon Nanotube Sensors. *Adv. Healthcare Mater.* **2013**, *3*, 412−423.
(33) Bisker, G.; Dong, J.; Park, H. D.; Iverson, N. M.; Ahn, J.; Nelson, J. T.; Landry, M. P.; Kruss, S.; Strano, M. S. Protein-Targeted Corona Phase Molecular Recognition. *Nat. Commun.* **2016**, *7*, 10241.
(34) Polo, E.; Kruss, S. Impact of Redox-Active Molecules on the Fluorescence of Polymer-Wrapped Carbon Nanotubes. *J. Phys. Chem. C* **2016**, *120*, 3061−3070.
(35) Kruss, S.; Salem, D. P.; Vuković, L.; Lima, B.; Ende, E. V..; Boyden, E. S.; Strano, M. S. High-Resolution Imaging of Cellular Dopamine Efflux Using a Fluorescent Nanosensor Array. *Proc. Natl. Acad. Sci. U.S.A.* **2017**, *114*, 1789−1794.
(36) Lee, A. J.; Wang, X.; Carlson, L. J.; Smyder, J. A.; Loesch, B.; Tu, X.; Zheng, M.; Krauss, T. D. Bright Fluorescence from Individual Single-Walled Carbon Nanotubes. *Nano Lett.* **2011**, *11*, 1636−1640.
(37) Ishibashi, Y.; Ito, M.; Homma, Y.; Umemura, K. Monitoring the Antioxidant Effects of Catechin Using Single-Walled Carbon Nanotubes: Comparative Analysis by near-Infrared Absorption and near-Infrared Photoluminescence. *Colloids Surf., B* **2018**, *161*, 139−146.
(38) Cognet, L.; Tsyboulski, D. A.; Rocha, J.-D. R.; Doyle, C. D.; Tour, J. M.; Weisman, R. B. Stepwise Quenching of Exciton Fluorescence in Carbon Nanotubes by Single-Molecule Reactions. *Science* **2007**, *316*, 1465−1468.
(39) Kurnosov, N. V.; Leontiev, V. S.; Karachevtsev, V. A. Probing the Influence of Amino Acids on Photoluminescence from Carbon Nanotubes Suspended with DNA. *J. Fluoresc.* **2016**, *26*, 1951−1958.
(40) Mann, F.; Herrmann, N.; Meyer, D.; Kruss, S. Tuning Selectivity of Fluorescent Carbon Nanotube-Based Neurotransmitter Sensors. *Sensors* **2017**, *17*, 1521.

DOI: 10.1021/acs.jpcc.8b11058
J. Phys. Chem. C 2019, 123, 4837−4847

(41) Meyer, D.; Hagemann, A.; Kruss, S. Kinetic Requirements for Spatiotemporal Chemical Imaging with Fluorescent Nanosensors. *ACS Nano* **2017**, *11*, 4017−4027.
(42) Tataurov, A. V.; You, Y.; Owczarzy, R. Predicting Ultraviolet Spectrum of Single Stranded and Double Stranded Deoxyribonucleic Acids. *Biophys. Chemisrty* **2008**, *133*, 66−70.
(43) Streit, J. K.; Bachilo, S. M.; Ghosh, S.; Lin, C.-W.; Weisman, R. B. Directly Measured Optical Absorption Cross Sections for Structure-Selected Single-Walled Carbon Nanotubes. *Nano Lett.* **2014**, *14*, 1530−1536.
(44) Naumov, A. V.; Tsyboulski, D. A.; Bachilo, S. M.; Weisman, R. B. Length-Dependent Optical Properties of Single-Walled Carbon Nanotube Samples. *Chem. Phys.* **2013**, *422*, 255−263.
(45) Humphrey, W.; Dalke, A.; Schulten, K. VMD : Visual Molecular Dynamics. *J. Mol. Graphics* **1996**, *14*, 33−38.
(46) Best, R. B.; Zhu, X.; Shim, J.; Lopes, P. E. M.; Mittal, J.; Feig, M.; MacKerell, A. D. Optimization of the Additive CHARMM All-Atom Protein Force Field Targeting Improved Sampling of the Backbone ϕ , ψ and Side-Chain χ 1 and χ 2 Dihedral Angles. *J. Chem. Theory Comput.* **2012**, *8*, 3257−3273.
(47) Vanommeslaeghe, K.; Hatcher, E.; Acharya, C.; Kundu, S.; Zhong, S.; Shim, J.; Darian, E.; Guvench, O.; Lopes, P.; Vorobyov, I.; et al. CHARMM General Force Field : A Force Field for Drug-Like Molecules Compatible with the CHARMM All-Atom Additive Biological Force Fields. *J. Comput. Chem.* **2009**, *31*, 671−690.
(48) Phillips, J. C.; Braun, R.; Wang, W.; Gumbart, J.; Tajkhorshid, E.; Villa, E.; Chipot, C.; Skeel, R. D.; Kalé, L.; Schulten, K. Scalable Molecular Dynamics with NAMD. *J. Comput. Chem.* **2005**, *26*, 1781−1802.
(49) Darden, T.; York, D.; Pedersen, L. Particle Mesh Ewald : An N · Log (N) Method for Ewald Sums in Large Systems Particle Mesh Ewald : An N -Log (N) Method for Ewald Sums in Large Systems. *J. Chem. Phys.* **1993**, *98*, 10089−10092.
(50) Fujigaya, T.; Nakashima, N. Non-Covalent Polymer Wrapping of Carbon Nanotubes and the Role of Wrapped Polymers as Functional Dispersants. *Sci. Technol. Adv. Mater.* **2015**, *16*, 024802.
(51) Jin, H.; Heller, D. A.; Kim, J.-H.; Strano, M. S. Stochastic Analysis of Stepwise Fluorescence Quenching Reactions on Single-Walled Carbon Nanotubes : Single Molecule Sensors. *Nano Lett.* **2008**, *8*, 4299−4304.
(52) Gigliotti, B.; Sakizzie, B.; Bethune, D. S.; Shelby, R. M.; Cha, J. N. Sequence-Independent Helical Wrapping of Single-Walled Carbon Nanotubes by Long Genomic DNA. *Nano Lett.* **2006**, *6*, 159−164.
(53) Johnson, R. R.; Johnson, A. T. C.; Klein, M. L. Probing the Structure of DNA − Carbon Nanotube Hybrids with Molecular Dynamics. *Nano Lett.* **2008**, *8*, 69−75.
(54) Johnson, R. R.; Kohlmeyer, A.; Johnson, A. T. C.; Klein, M. L. Free Energy Landscape of a DNA - Carbon Nanotube Hybrid Using Replica Exchange Molecular Dynamics. *Nano Lett.* **2009**, *9*, 537−541.
(55) Berciaud, S.; Cognet, L.; Lounis, B. Luminescence Decay and the Absorption Cross Section of Individual Single-Walled Carbon Nanotubes. *Phys. Rev. Lett.* **2008**, *101*, 077402.
(56) Tu, X.; Manohar, S.; Jagota, A.; Zheng, M. DNA Sequence Motifs for Structure-Specific Recognition and Separation of Carbon Nanotubes. *Nature* **2009**, *460*, 250−253.
(57) Murphy, M. C.; Rasnik, I.; Cheng, W.; Lohman, T. M.; Ha, T. Probing Single-Stranded DNA Conformational Flexibility Using Fluorescence Spectroscopy. *Biophys. J.* **2004**, *86*, 2530−2537.
(58) Mills, J. B.; Vacano, E.; Hagerman, P. J. Flexibility of Single-Stranded DNA : Use of Gapped Duplex Helices to Determine the Persistence Lengths of Poly (DT) and Poly (DA). *J. Mol. Biol.* **1999**, *285*, 245−257.
(59) Goddard, N. L.; Bonnet, G.; Krichevsky, O.; Libchaber, A. Sequence Dependent Rigidity of Single Stranded DNA. *Phys. Rev. Lett.* **2000**, *85*, 2400−2403.
(60) McIntosh, D. B.; Duggan, G.; Gouil, Q.; Saleh, O. A. Sequence-Dependent Elasticity and Electrostatics of Single-Stranded DNA : Signatures of Base-Stacking. *Biophys. J.* **2014**, *106*, 659−666.
(61) Mitchell, J. S.; Glowacki, J.; Grandchamp, A. E.; Manning, R. S.; Maddocks, J. H. Sequence-Dependent Persistence Lengths of DNA. *J. Chem. Theory Comput.* **2017**, *13*, 1539−1555.
(62) Rechendorff, K.; Witz, G.; Adamcik, J.; Dietler, G. Persistence Length and Scaling Properties of Single-Stranded DNA Adsorbed on Modified Graphite. *J. Chem. Phys.* **2009**, *131*, 095103−095103-6.
(63) Salem, D. P.; Gong, X.; Liu, A. T.; Koman, V. B.; Dong, J.; Strano, M. S. Ionic Strength-Mediated Phase Transitions of Surface-Adsorbed DNA on Single-Walled Carbon Nanotubes. *J. Am. Chem. Soc.* **2017**, *139*, 16791−16802.
(64) Li, Z.; Yu Song, A. L.; Xu, W.; Zhang, W. Direct Observation of the Wrapping/Unwrapping of SsDNA around/from SWCNT at Single-Molecule Level: Towards Tuning the Binding Mode and Strength. *Nanoscale* **2018**, *10*, 18586−18596.
(65) Albertorio, F.; Hughes, M. E.; Golovchenko, J. A.; Branton, D. Base Dependent DNA-Carbon Nanotube Interactions: Activation Enthalpies and Assembly-Disassembly Control. *Nanotechnology* **2009**, *20*, 395101.
(66) Zheng, Y.; Bachilo, S. M.; Weisman, R. B. Quenching of Single-Walled Carbon Nanotube Fluorescence by Dissolved Oxygen Reveals Selective Single-Stranded DNA Affinities. *J. Phys. Chem. Lett.* **2017**, *8*, 1952−1955.

DOI: 10.1021/acs.jpcc.8b11058
J. Phys. Chem. C 2019, 123, 4837−4847

5.1.2 Discussion

The presented manuscript introduces a novel method to determine the amount of ssDNA adsorbed on the SWCNT surface. The protocol itself is based on UV-Vis-NIR absorption spectroscopy, molecular weight cut-off filtration and AFM, and extends existing studies in this area by a direct method. Thus, it can quantify all kinds of DNA variations without the need of an external fluorophore modification. The quantification of free (excess) ssDNA after SWCNT modification was also performed by previous studies. Salem *et al.*[152] used such an approach to study the ionic strength-mediated phase transition of ssDNA-SWCNTs, while others aimed to examine ssDNA-SWCNT stability[153] or to control dialysis performance[154]. The functionality of the presented approach is therefore in agreement with previous literature. Since the SWCNT length distribution was also analyzed, the determined number of adsorbed DNA molecules can be converted into an average SWCNT segment length one ssDNA molecule occupies. This allows a comparison with previous studies, which used different methods to study this parameter as introduced before. In general, the determined number of adsorbed DNA molecules and hence the SWCNT length occupation suggest a denser surface modification as previously reported. As expected, the sequence length, but surprisingly also the sequence composition, had a major influence on the quantity of adsorbed DNA. Occupancy of the respective SWCNT segments by (GT) oligonucleotide repeats increased linearly with sequence lengths, suggesting a nearly constant surface coverage, in contrast to prior research.[125] This implies a partial adsorption of the DNA, like postulated by Brunecker *et al.*[150], but without a cooperativity between particular ssDNA molecules. However, the findings from **Manuscript I** can be seen as partly controversial to the commonly used solvatochromism model, which attributes the densest SWCNT surface coverage to the most hypsochrom absorbance wavelength.[155] The amount of adsorbed DNA nucleotides somehow does not correlate with the model-predicted absorption and photoluminescence features of the respective DNA-SWCNTs (Supplementary Information Manuscript I, 7.1, Figure S1). But since the overall amount of adsorbed DNA was probed and not the actual conformation, this observation and discrepancy needs to be studied further. Moreover, the correlation between ssDNA-SWCNT's chemical sensing ability and the number of adsorbed DNA molecules was found to be mostly independent. However, for some scenarios it was reported that shorter oligonucleotide sequence-SWCNTs (more adsorbed DNA molecules) showed an increased fluorescence response, similar to the presented fluorescence increase after pH modulation (Figure 6).[75,125,156] In general, this

implements a complex interplay for the chemical sensing mechanism, with the result that the exact structure of the crowded corona around the SWCNT is most likely crucial for analyte recognition and sensing.
In addition, the determined mean SWCNT segment length, which is occupied by one DNA molecule, can be used as an important parameter for molecular dynamic (MD) simulations. So far, such very precise but time consuming analyses are performed in such a way that ssDNA molecules can freely interact with the SWCNT surface, without facing further restrictions.[157,158] When now applying the calculated space a DNA molecule occupies, as presented in Figure 7 in **Manuscript I**, a dense and crowded DNA surface modification becomes visible. Next to a partwise helical wrapping onto the SWCNT surface, the DNA stacked on top of each other. This indicates that next to higher secondary structures[159], intra- and intermolecular DNA interactions and non-Watson-Crick hydrogen bonds might have a stronger influence than previously suggested. As a final point, the quantification of the surface adsorbed DNA on SWCNTs now allows its ratio-specific, bioorthogonal modification. As mentioned beforehand, DNA variations carrying functional groups for later coordination chemistry can be introduced in a straightforward way, resulting in ssDNA-SWCNTs with functional handles.[133] The reported method was used in later studies to assess the amount of surface adsorbed DNA-aptamers[160] and facilitate the ratio-specific linkage of nanobodies[135] or peptides[161] to amino-functionalized DNA-SWCNTs. Furthermore, the range of determined ssDNA molecules adsorbed on SWCNT surface was recently confirmed by a fluorescence spectroscopy-based approach.[162]
In summary, the presented **Manuscript I** adds a valuable contribution to the general understanding of SWCNT nano-conjugates, which will help to advance these nanosensors in the future.

5.2 Towards Chirality-pure SWCNT-Sensors

SWCNT-based biosensing evolved in the recent years to a powerful technique, able to resolve chemical information in great spatiotemporal manner, combined with the beneficial NIR-fluorescence properties. Those sensors can be used in various analytical settings and biological systems, ranging from *in vitro* analysis to cell studies[122], to *in vivo* whole animal[134] and plant systems[160,163]. During sensor development, specific design strategies can be applied to tailor sensitivity and selectivity, necessary to detect the desired analyte. However, in such biological systems a variety of complex processes occur at the same time, like co-release of neurotransmitters from neurons[164] or co-secretion of virulence factors from bacteria[165,166]. In order to depict the spatiotemporal distribution of a variety of analytes and consequently gain novel insights into those biological systems, multiple sensors are necessary that can be read out simultaneously and independently.

To achieve this goal, the particular SWCNT sensors require non-overlapping emission features, which means single SWCNT chiralities with defined emission wavelengths are specifically modified to act as NIR-sensors. However, all as-synthesized SWCNT materials used so far contain multiple chiralities, which leads to strong spectral congestion, thus inhibiting hyperspectral sensing. Therefore, SWCNT purification techniques are needed, in order to create sensors with optically defined emission features.

As discussed in Section 3.5, diverse methods for SWCNT purification were developed in the last decade, leading to variable purities of separated SWCNT chiralities. Thereby, all approaches have in common that resulting chirality-pure SWCNT fractions are prepared in solvents or surfactants unsuitable for universal application in biosensing. Those aspects of biocompatibility, colloidal stability in aqueous systems and functional surface chemistry to mediate target analyte binding were so far not part of the SWCNT purification approaches. Consequently, the upcoming challenge is to find a route that combines SWCNT purification with further surface modification of the obtained chirality-pure fractions, in order to receive tailored biosensors.

The following manuscripts approached this challenge, using different strategies for nanomaterial dispersion and concomitant surface exchange. In the **Manuscript II**, entitled "*Chirality enriched carbon nanotubes with tunable wrapping via corona phase exchange purification (CPEP)*" it will be evaluated, whether the straightforward purification approach

of chirality-specific SWCNT dispersion *via* polyfluorene-polymers could be used to obtain mono-chiral sensors.

Moreover, the aim of **Manuscript III** "*Sensing with Chirality-Pure Near-Infrared Fluorescent Carbon Nanotubes*" is the assembly of mono-chiral sensors after SWCNT separation by aqueous two-phase extraction (ATPE).

5.2.1 Chirality Enriched Carbon Nanotubes with Tunable Wrapping *via* Corona Phase Exchange Purification

Manuscript II was published in the following journal:

Robert Nißler, Florian A. Mann, Helen Preiß, Gabriele Selvaggio, Niklas Herrmann and Sebastian Kruss*

"Chirality enriched carbon nanotubes with tunable wrapping *via* corona phase exchange purification (CPEP)"

Nanoscale, **2019**, 11, 11159-11166

The article is available at: DOI: 10.1039/c9nr03258d
* Corresponding author

Responsibility assignment: R.N. and S.K. designed and conceived the research. S.K. coordinated the project. G.S. and F.A.M. helped with AFM experiments, H.P. developed Python-based scripts for absorption and photoluminescence spectroscopy analysis. N.H. synthesized diazonium compound and PEG-polymer. All other experiments were performed by R.N.. Data analysis and manuscript writing was realized by R.N., with input of S.K..

Nanoscale

PAPER

View Article Online
View Journal

Cite this: DOI: 10.1039/c9nr03258d

Chirality enriched carbon nanotubes with tunable wrapping *via* corona phase exchange purification (CPEP)†

Robert Nißler, Florian A. Mann, Helen Preiß, Gabriele Selvaggio, Niklas Herrmann and Sebastian Kruss *

Single-walled carbon nanotubes (SWCNTs) have unique photophysical properties and serve as building blocks for biosensors, functional materials and devices. For many applications it is crucial to use chirality-pure SWCNTs, which requires sophisticated processes. Purification procedures such as wrapping by certain polymers, phase separation, density gradient centrifugation or gel chromatography have been developed and yield distinct SWCNT species wrapped by a specific polymer or surfactant. However, many applications require a different organic functionalization (corona) around the SWCNTs instead of the one used for the purification process. Here, we present a novel efficient and straightforward process to gain chirality pure SWCNTs with tunable functionalization. Our approach uses polyfluorene (PFO) polymers to enrich certain chiralities but the polymer is removed again and finally exchanged to any desired organic phase. We demonstrate this concept by dispersing SWCNTs in poly[(9,9-dioctylfluorenyl-2,7-diyl)-*alt*-*co*-(6,6′-{2,2′-bipyridine})] (PFO-BPy), which is known to preferentially solubilize (6,5)-SWCNTs. Then PFO-BPy is removed and recycled, while letting the SWCNTs adsorb/agglomerate on sodium chloride (NaCl) crystals, which act as a toluene-stable but water-soluble filler material. In the last step these purified SWCNTs are redispersed in different polymers, surfactants and ssDNA. This corona phase exchange purification (CPEP) approach was also extended to other PFO variants to enrich and functionalize (7,5)-SWCNTs. CPEP purified and functionalized SWCNTs display monodisperse nIR spectra, which are important for fundamental studies and applications that rely on spectral changes. We show this advantage for SWCNT-based nIR fluorescent sensors for the neurotransmitter dopamine and red-shifted sp^3 defect peaks (E_{11}^*). In summary, CPEP makes use of PFO polymers for chirality enrichment but provides access to chirality enriched SWCNTs functionalized in any desired polymer, surfactant or biopolymer.

Received 16th April 2019,
Accepted 25th May 2019

DOI: 10.1039/c9nr03258d

rsc.li/nanoscale

Introduction

One of the great challenges in nanoscience is to obtain materials of well-defined structure and size.[1,2] Polydisperse nanomaterials can lead to wrong conclusions in fundamental studies on structure–function relationships but also affect performance in applications. Therefore, progress in synthesis and purification of nanomaterials is crucial to advance the whole nanotechnology field. An important class of nanomaterials are single walled carbon nanotubes (SWCNTs).[3,4] Semiconducting SWCNTs are fluorescent in the near infrared (nIR) region and the emission wavelength depends on their structure described by the chirality or chiral index (*n*,*m*).[5–9] The nIR fluorescence of SWCNTs has been used for example for imaging, biosensing or single-photon generation.[10–14] Even though the synthesis of specific SWCNT chiralities has seen progress over the past years typical SWCNT starting materials still contain multiple chiralities.[15–17] Therefore, purification and separation of SWCNTs remains a major area of research.

Different approaches have been developed that separate SWCNTs according to length, diameter and chirality.[18–22] The most used purification protocols are based on density gradient centrifugation,[23,24] phase separation,[25–27] gel chromatography[28–31] or ion exchange chromatography.[32] In most of these approaches surfactants such as sodium dodecyl sulfate (SDS) or sodium cholate (SC) are used to disperse SWCNTs in aqueous solution. Other methods rely on the favored interaction of specific macromolecules/polymers with a certain SWCNT chirality. A very powerful approach is based on certain ssDNA sequences that disperse specific chiralities.[33,34] In organic solvents polymers of the polyfluor-

Institute of Physical Chemistry, Göttingen University, Germany.
E-mail: skruss@uni-goettingen.de

†Electronic supplementary information (ESI) available. See DOI: 10.1039/c9nr03258d

ene (PFO) family such as poly[(9,9-dioctylfluorenyl-2,7-diyl)-*alt*-*co*-(6,6′-{2,2′-bipyridine})] (PFO-PBy) have been used to enrich for example (6,5)-SWCNTs.[35–38] Most of the purification methods yield chirality-enriched SWCNTs with fixed organic phase (corona) compositions, either in non-biocompatible surfactants/polymers or with fixed ssDNA sequences. Especially for biosensing applications water-dispersable SWCNTs are required and specific surface modifications are crucial to tailor molecular interactions.[11,14,39] It was shown that the sequence of ssDNA modified SWCNTs has a dramatic impact on colloidal properties and the nIR-fluorescence response/kinetics to analytes.[40–43] For example, $(GT)_{10}$ – ssDNA functionalized SWCNTs report secretion of the neurotransmitter dopamine and can even discriminate between different catecholamines.[44,45] Many other non-covalent functionalization concepts with DNA/peptide hybrids, xeno nucleic acids, peptide barrels, sugars, lipids and antibodies have been developed to tailor SWCNT properties.[46–52] Most of these approaches would profit from a general access to chirality enriched SWCNTs instead of the polydisperse SWCNT starting material that is typically used. Isolation procedures of distinct SWCNT chiralities and further corona phase modification to other ssDNA sequences, phospholipids or surfactants have only been reported in a few specific cases.[53–56] In principle it is therefore possible to remove surfactants from enriched SWCNTs, as shown for distinct PFO-SWCNTs,[57–61] but a general procedure is still missing. One challenge is to avoid strong aggregation of purified SWCNTs during the process, which could hamper redispersion.

Here, we report a general but straightforward route to chirality enriched SWCNTs with tunable wrapping. We make use of the high-selectivity of PFO polymers for certain chiralities, remove/recycle the PFO polymer and obtain a chirality enriched SWCNT material stabilized in a NaCl filler/scaffold to avoid strong aggregation. This material is then used for different non-covalent functionalization approaches and the advantages of monodisperse SWCNTs are shown for different applications.

Results and discussion

To get access to nearly chirality-pure SWCNTs with any desired non-covalent functionalization we developed a three-step approach.

It makes use of the high selectivity of polymers of the PFO family for certain SWCNT chiralities. Then the PFO-polymer is removed and recycled, while the purified SWCNTs can be further surface modified *via* standard tip sonication. This corona phase exchange purification (CPEP) approach makes the organic phase independent of the surfactant and polymer used for purification, which is crucial for most applications of SWCNTs.

The CPEP approach (see Fig. 1) is based on the high selectivity of PFO-BPy for (6,5)-SWCNTs. A CoMoCAT SWCNT sample is dispersed with PFO-BPy in toluene *via* shear force mixing and separated from larger bundles by centrifugation.[36] The highly enriched PFO-BPy-(6,5)-SWCNTs are precipitated with isopropyl alcohol (4 : 1, toluene : isopropyl alcohol), while the excess PFO-polymer stays in solution after centrifugation (Fig. 2a). Redispersion of the SWCNT pellet in toluene and repeated precipitation decreased the concentration of the free PFO-BPy to a minimum, which can be monitored by UV-Vis-nIR absorbance spectroscopy (Fig. 2a). The purified nanotubes were then transferred to a solvent-resistant filter loaded with NaCl crystals, which act as toluene-resistant, but later on water-soluble filler/scaffold (see ESI Fig. S1†). Washing with hot toluene removed the remaining PFO-BPy from the (6,5)-

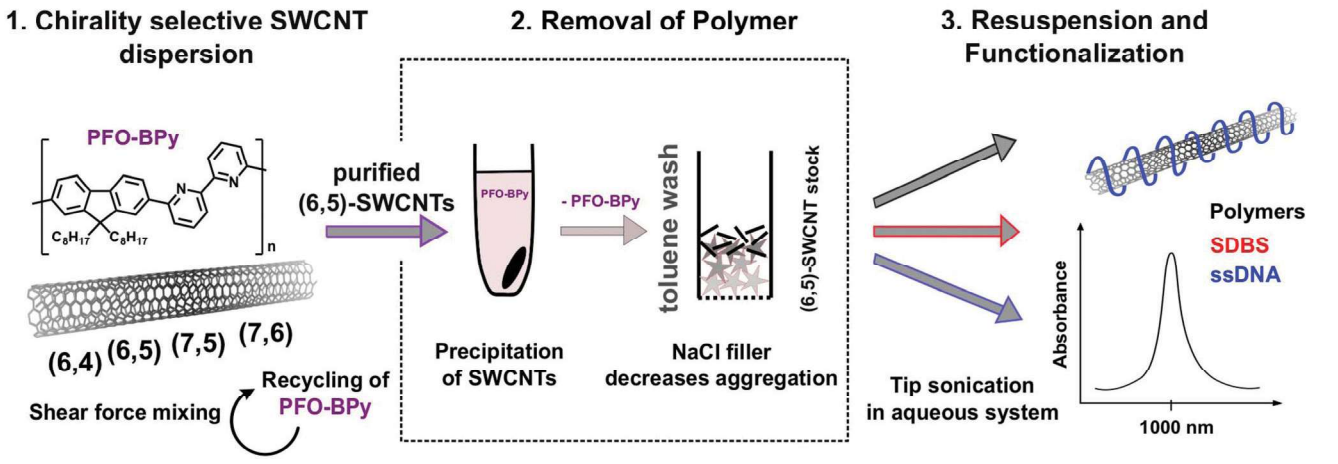

Fig. 1 Schematic of the corona phase exchange purification (CPEP) process. The process is based on selective dispersion of (6,5)-SWCNTs by PFO-BPy or certain SWCNT chiralities by other members of the PFO family in toluene. PFO-BPy is removed by adding isopropyl alcohol, which precipitates the SWCNTs, while the majority of PFO-BPy stays in solution and can be recycled. The (6,5)-SWCNT pellet is transferred to a solvent-resistant filter equipped with NaCl crystals, which act as water-soluble filler material during removal of remaining PFO-BPy residues. The (6,5)-SWCNT flakes are then available for any functionalization approach *e.g.* with ssDNA, SDBS or biopolymers.

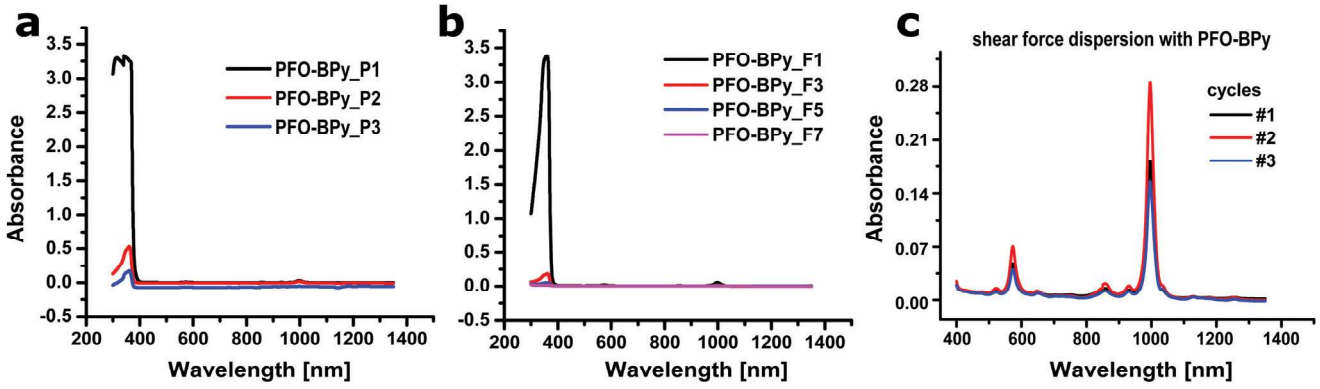

Fig. 2 Removal of PFO-polymer during the CPEP process. After large scale shear force mixing of (6,5)-SWCNTs with PFO-BPy in toluene the excess polymer is removed, which can be monitored by the PFO-BPy absorption peak at 300–400 nm. (a) Isopropyl alcohol addition decreases the colloidal stability of the SWCNTs and precipitates (P) them, while most of PFO-BPy stays in solution. Iteration of this progress decreases the concentration of the free PFO-BPy in the SWCNT sample (in toluene). (b) Stepwise filtration (F) process with 90 °C toluene removes the residue PFO-BPy of the SWCNT/NaCl pellet. (c) Dispersion of (6,5)-SWCNTs with recycled PFO-BPy shows that PFO-polymer can be reused.

SWCNTs (Fig. 2b), while SWCNTs adsorbed/agglomerated on and in between the filler. After drying and removing the NaCl, the purified (6,5)-SWCNT flakes were ready to be resuspended with any desired polymer. Addition of trifluoroacetic acid (TFA) to support PFO removal from SWCNTs decreased the nIR-fluorescence of redispersed (6,5)-SWCNTs and was therefore not used (see ESI Fig. S2†).

Combining the PFO-BPy supernatants furthermore enabled us to recycle and reuse the (expensive) PFO-BPy polymer for nanotube dispersion (see Fig. 2c).

The normalized absorption spectra of CPEP processed $(GT)_{10}$-(6,5)-SWCNTs, $(AT)_{15}$-(6,5)-SWCNTs and SDBS-(6,5)-SWCNTs are shown in Fig. 3a–c. The CPEP purified samples show as a major feature the S_{11} transition of the (6,5)-SWCNT but other chiralities have been substantially removed.

The S_{11} absorbance feature at around 890 nm (assigned to (6,4)-SWCNTs), 1040 nm (assigned to (7,5)-SWCNTs) and 1130 nm (mainly assigned to (7,6)/(8,4)-SWCNTs) are not any longer present in the highly enriched sample. Besides a reduced background in the S_{22} transition region, the phonon-sideband at around 850 nm becomes visible.

The SDBS sample shows a strong blue shift of the S_{11} and S_{22} transition, which could indicate a more effective debundling in the CPEP processed sample. Absorbance spectra were fitted (Fig. 3d–f) to quantify the ratio of SWCNT-chiralities. The S_{11} transitions showed that PFO-BPy dispersion yielded ~94% pure (6,5)-SWCNTs while resuspending in *e.g.* ssDNA did not change this enrichment significantly (87% for $(AT)_{15}$-(6,5) and 90% for $(GT)_{10}$-(6,5)-SWCNTs after CPEP), which is mainly attributed to differences in background and not the chirality composition itself. The yield of SWCNT dispersion could be further improved, by using a higher-power shear force mixer[36] instead of the customary homogenizer for shear force dispersion that was used here for CPEP.

We also evaluated the nanotube lengths after the CPEP of the two exemplaric ssDNA-SWCNTs and compared it with the one from the PFO-BPy-(6,5)-SWCNTs (see ESI Fig. S3†). The mean length from the PFO-BPy SWCNTs was ~1460 nm (SE 723 nm), which is slightly smaller than the length reported in literure.[36] Both ssDNA-(6,5)-SWCNT were in mean nearly half as long with 770 nm (SE 358 nm) for $(AT)_{15}$ and 757 nm (SE 347 nm) for $(GT)_{10}$. This results shows, that the resuspension of the purified (6,5)-SWCNTs obviously decreases the lateral mean size, while the absolute lengths is larger than the one, known from dispersing unpurified SWCNTs with ssDNA.[41]

The success of the purification procedure can be further visualized in SWCNT fluorescence spectra. Fig. 4a shows a 2D-fluorescence spectrum of ssDNA modified SWCNTs without further purification. It shows the emission of (6,5)-SWCNTs and other chiralities such as (6,4), (7,5) or (8,3). In contrast, the PFO-BPy modified SWCNTs (Fig. 4b) contain mainly (6,5)-SWCNTs as expected. The exchange to ssDNA and aqueous solution does not significantly (Fig. 4c and d) change the spectra. This result highlights how effective CPEP is to remove other chiralities and obtain monodisperse samples with a desired functionalization.

For biosensing application, it is of special interest whether CPEP processed and redispersed (6,5)-SWCNTs are still functional in terms of nIR-fluorescence responses to analytes. Fig. 5a shows a fluorescence spectrum of CPEP $(GT)_{10}$-(6,5)-SWCNTs and its increase after addition of dopamine [100 nM]. This type of functionalization is known to make SWCNTs responsive to the important neurotransmitter dopamine.[41,45] A single fluorescence peak of such sensors is essential for multiplexing approaches that use multiple SWCNT chiralities or other fluorophores. Therefore, monochiral samples could improve multiplexed sensing and imaging approaches for example to exploit differences in responsiveness by different chiralities.[50,62]

Another application that requires non-congested spectra is defect engineering.[13,63,64] These approaches lead new emission features and even to single-photon emitting SWCNTs and fun-

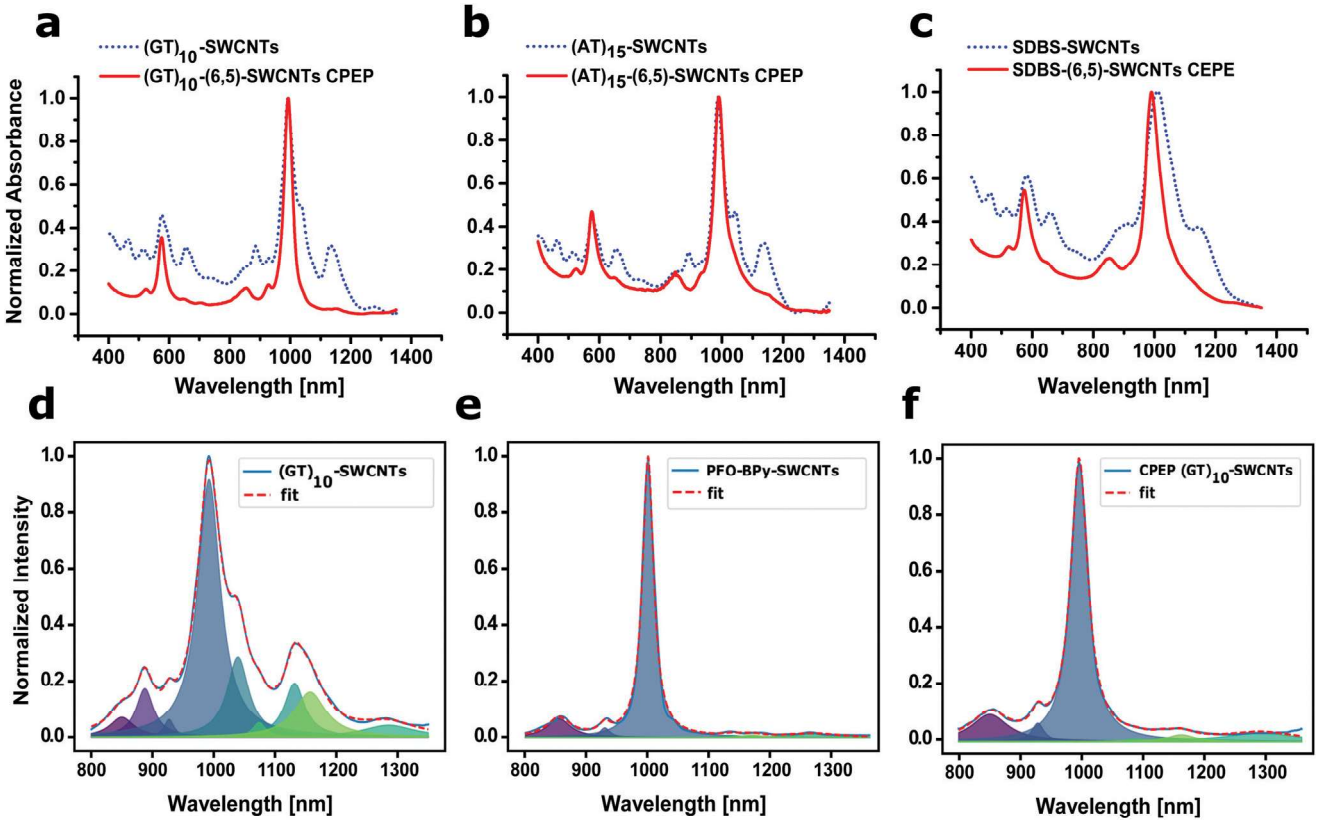

Fig. 3 Absorption spectra of corona phase exchange purified (6,5)-SWCNTs. Different functionalizations/coatings were used to resuspend the CPEP purified (6,5)-SWCNTs (red lines). Non-purified SWCNTs functionalized in the same way contain additional chiralities (blue dotted line). Two different ssDNA sequences (a) $(GT)_{10}$ and (b) $(AT)_{15}$ as well as (c) SDBS are shown as an example. The wavelengths of the absorption maxima are similar for ssDNA modified (6,5)-SWCNTs. CPEP purified SDBS SWCNTs showed a blue-shift, which indicates debundling compared to the non-purified sample. (d) Fitted absorption spectra of the raw SWCNT material, modified with $(GT)_{10}$-ssDNA. (e) Fitted absorption spectra of the raw SWCNT material, dispersed with PFO-BPy in toluene reveals a nearly monodisperse (6,5)-SWCNT sample. (f) Fitted absorption spectra of CPEP $(GT)_{10}$-SWCNTs displays again almost monodisperse (6,5)-SWCNTs.

damental insights into the mechanism rely on well-defined and unambiguous spectra. CPEP processed SWCNTs can be used to introduce defects as shown in Fig. 5b. The introduction of ($PhNO_2$) aryl sp^3-defects into the SWCNT surface causes a second, red-shifted fluorescence peak at ~1165 nm. Related studies with $PhNO_2$ defected SDBS-(6,5)-SWCNTs report E_{11}^* fluorescence maxima at ~1145 nm.[65]

Especially the tunable corona modification with different ssDNA sequences could help to improve SWCNT-based chemical sensing and imaging. Importantly, it expands the possibilities of non-covalent functionalization schemes to purified SWCNTs closer to covalent functionalization schemes.[66,67]

In addition to the modification of highly enriched (6,5)-SWCNTs with different ssDNA sequences and surfactants (see ESI Fig. S4†), it is possible to exchange the corona to biocompatible PEG-polymers (ESI Fig. S5†). Hereby, the purified SDBS- and PEG-(6,5)-SWCNTs showed a minor nIR-fluorescence peak at ~1120 nm, which cannot be monitored in the complimentary spectra from the raw nanotube material. Either other chiralities superimpose these features (see also ESI Fig. S6†), or they get enhanced due to the purification process. The spectral region of the minor peak could be assigned to oxygen induced defects to (6,5)-SWCNTs.[68]

Besides the specific dispersion of (6,5)-SWCNTs by PFO-BPy, other PFO-polymers are known to solubilize particular SWCNT chiralities.[35,69] Dispersing the crude SWCNT material with PFO in toluene, similar to the procedure using PFO-BPy, yielded highly enriched (7,5)-SWCNTs and a smaller fraction of (7,6)-SWCNTs (ESI Fig. S7†). Applying the CPEP, it was possible to remove PFO from the (7,5)-SWCNTs (see ESI Fig. S7a and b†) and further exchange the surface functionalization to different aqueous soluble surfactants or polymers (see ESI Fig. S8 and S9†). Therefore, the CPEP approach appears to be a general concept for PFO-polymer exchange, beyond the most used (6,5)-SWCNTs and PFO-BPy. Especially for SWCNT-based chemical imaging different specifically modified nanotube chiralities would be favorable to allow ratiometric sensing. By combining $(GT)_{10}$-(6,5)-SWCNTs and PEG-PL-(7,5)-SWCNTs (ESI Fig. S10†) it is in principle possible to create also a ratiometric dopamine sensor.

Besides the advantages of well-defined fluorescence features CPEP processed samples appear to be brighter compared

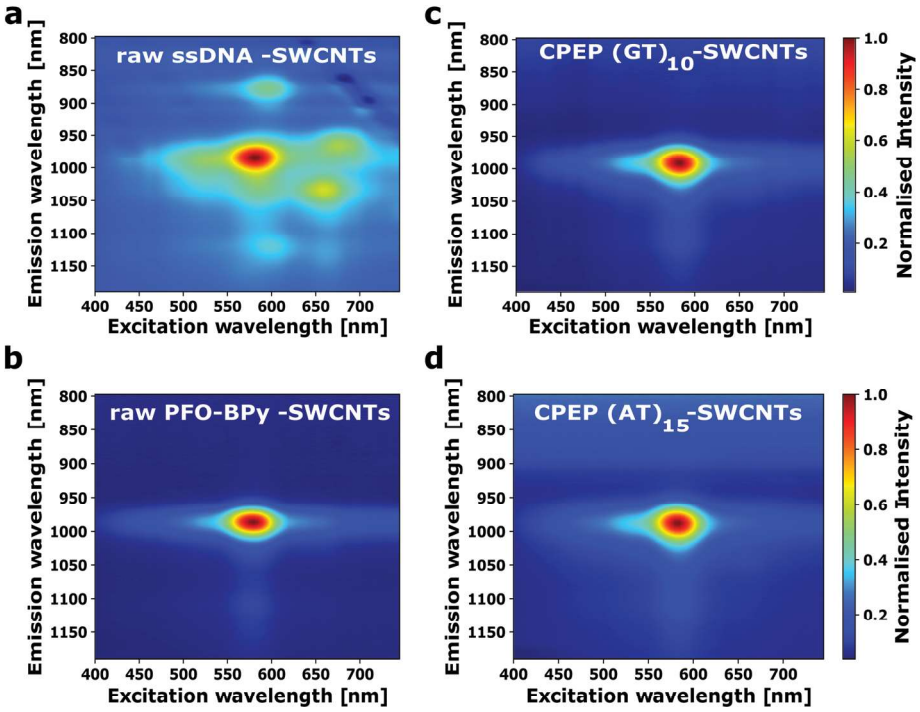

Fig. 4 2D excitation/emission spectra of CPEP-SWCNTs. (a) CoMoCAT SWCNT sample dispersed in $(GT)_{10}$-ssDNA. The major chirality is (6,5) but there are also (6,4), (7,5) and (8,3)-SWCNTs present. (b) PFO-BPy dispersed SWCNTs (in toluene) contain nearly exclusively (6,5)-SWCNTs. After removing PFO-BPy and resuspending the SWCNTs with ssDNA *via* the CPEP approach the same level of purity is achieved for (c) $(GT)_{10}$ or (d) $(AT)_{15}$-ssDNA functionalized SWCNTs in aqueous solution.

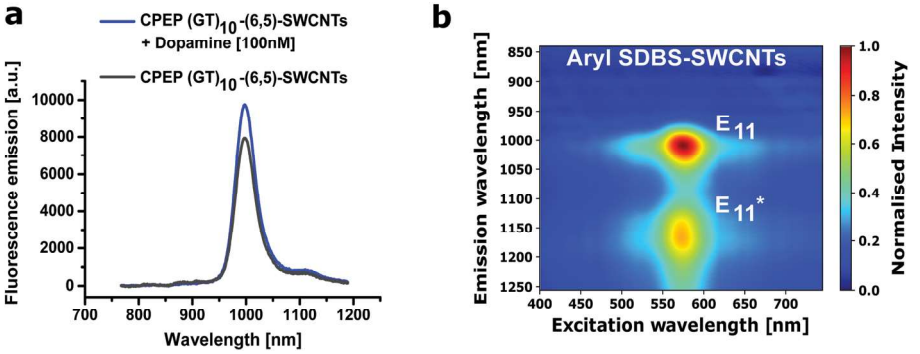

Fig. 5 Corona phase exchange purified SWCNTs for sensors and defect engineering. A major benefit of CPEP is the possibility to use any desired non-covalent surface modification, which is especially useful for sensors based on ssDNA-SWCNTs. (a) $(GT)_{10}$-(6,5)-SWCNTs increase their fluorescence in the presence of the neurotransmitter dopamine without interference from other chiralities. (b) Introducing sp^3 defects to SDBS-(6,5)-SWCNTs leads to a second well-defined red-shifted fluorescence peak that is not congested by other chiralities.

to similar non-purified samples with the same functionalization (ESI Fig. S11†). $(GT)_{10}$-(6,5)-SWCNTs display around 70% higher fluorescence intensities at the same concentration/absorption, which could be either explained by their increased length or the absence of quenching impurities.

The high monodispersity of CPEP processed SWCNTs is based on the specific dispersion of certain SWCNT chiralities by polyfluorene polymers.[37,38] This step relies also on the raw nanotube material and its ratio of semiconducting to metallic nanotubes and the containing chiralities.[70] Therefore, by choosing the appropriate SWCNT material and PFO-polymer for dispersion, CPEP can grant access to a brought range of enriched SWCNTs with desired surface modifications. This approach can be especially relevant for fundamental studies and applications of SWCNTs that require sophisticated surface chemistry beyond standard surfactants. Consequently, applications such as biosensors, imaging, drug delivery and defect engineering can profit from CPEP.

Conclusions

Chirality pure SWCNTs are necessary both for fundamental studies and biomedical applications. In this work we present a novel route to chirality enriched SWCNTs with tunable functionalization. It uses the selective dispersion of SWCNTs in PFO-polymers but removes/recycles them again and exchanges them to any non-covalent modification. These chirality enriched SWCNTs are functional and can be employed in applications for which the functionalization plays a crucial role and monodisperse spectra are essential such as single-emission fluorescence sensors and defect peak engineering.

Materials and methods

Purification protocol

Highly enriched (6,5)-SWCNTs were obtained based on the dispersion protocol from Graf *et al.*[36] 50 mg PFO-BPy (American Dye Source) were dissolved in 100 mL toluene by gently warming the solution. 25 mg chirality enriched (6,5)-SWCNTs (Sigma Aldrich, Product No. 773735) were added and placed for 20 h shear-force mixing (Homogenizer PT3100, Polytron) in a water bath, in order to keep the temperature during the surface modification process constantly at 20 °C. The following centrifugation step (15 min/20 500*g*/15 °C) yielded the highly enriched PFO-BPy-(6,5)-SWCNT stock solution. Two times 8 mL of the PFO-BPy-(6,5)-SWCNT solution were mixed with 2 ml isopropyl alcohol and centrifuged 15 + 5 min (20 500*g*/15 °C). This ratio of toluene to isopropyl alcohol led to a loss of the colloidal stability of the nanotubes, while the majority of the PFO-PBy stayed in solution. Lower ratios of isopropyl alcohol to toluene resulted in an incomplete precipitation of the SWCNTs, while a much higher ratio increased the amount of precipitated polymer. The (6,5)-SWCNT pellet was resuspended in 8 ml toluene and bath sonicated for 2 min. Afterwards, two more rounds of precipitation with isopropyl alcohol, centrifugation and resuspension were performed. The progress of PFO-BPy removal was followed by its UV-Vis absorption. The pellet was further transferred to a solvent resistant filter (2.2 NY, Ciro), which was equipped with 200 mg powdered NaCl crystals, which act as toluene-resistant but water-soluble filler/scaffold material. In the following washing step, the nanotube pellet was washed with 5 × 600 μl (90 °C) hot toluene, which removed the remaining PFO-BPy from the sample. The SWCNT loaded NaCl crystals were dried under vacuum and dialyzed for 24 h in a 1 kDa dialysis bag (Spectra/Por®) against ddH_2O. The resulting (6,5)-SWCNT flakes were transferred to a reaction tube, ready for further surface modification with a desired water-soluble surfactant. For ssDNA modification, 150 μl PBS and 125 μl (2 mg ml^{-1}) oligonucleotide solution were tip sonicated (30%, 45 min, Fisher ScientificTM Model 120 Sonic Dismembrator), followed by 10 min centrifugation at 10 000*g*. The same sonication conditions were used for SWCNT dispersion in 275 μl 0.2% SDBS aqueous solution. The residual PFO-BPy solution was evaporated and reused for SWCNT modification, while the undispersed SWCNT material was also recycled.[36] SWCNT dispersion with PFO was performed similarly using 1 mg ml^{-1} PFO in toluene.

UV-Vis-nIR absorption and nIR-fluorescence spectroscopy

UV-Vis-nIR absorbance spectra of the SWCNT conjugates were acquired with a JASCO V-670 device in a 10 mm path quartz cuvette. Fitting of absorption spectra was based on the approach by Pfohl *et al.*[71] In short, a background profile of the form $e^{-b\lambda}$ was fitted to the absorption spectra and subtracted. The normalized spectra were then fitted in Python to a function consisting in the sum of nine Lorentzians using a standard least squares fit, with the Trust Region Reflective algorithm.

1D and 2D nIR-fluorescence spectra were acquired with a Shamrock 193i spectrometer (Andor Technology Ltd, Belfast, Northern Ireland) connected to an IX53 microscope (Olympus, Tokyo, Japan). Excitation was performed with a Monochromator MSH150, equipped with a LSE341 light source (LOT-Quantum Design GmbH, Darmstadt, Germany). 200 μl of aqueous SWCNT conjugates were placed in a 96-well plate, while toluene-based samples were analyzed in a glass vial.

Conflicts of interest

There are no conflicts to declare.

Acknowledgements

This project was supported by the VW foundation. We thank Prof. Dr Andreas Janshoff and Prof. Dr Claudia Steinem as well as their groups for fruitful discussions and support.

Notes and references

1 A. Albanese, P. S. Tang and W. C. W. Chan, *Annu. Rev. Biomed. Eng.*, 2012, **14**, 1–16.
2 M. L. Personick and C. A. Mirkin, *J. Am. Chem. Soc.*, 2013, **135**, 18238–18247.
3 J. Li and G. P. Pandey, *Annu. Rev. Phys. Chem.*, 2015, **66**, 331–356.
4 V. Z. Zamolo, E. Vazquez and M. Prato, *Top. Curr. Chem.*, 2013, **286**, 1–72.
5 M. S. Arnold, J. L. Blackburn, J. J. Crochet, S. K. Doorn, J. G. Duque, A. Mohite and H. Telg, *Phys. Chem. Chem. Phys.*, 2013, **4**, 1166–1169.
6 A. R. Amori, Z. Hou and T. D. Krauss, *Annu. Rev. Phys. Chem.*, 2018, **69**, 81–100.
7 S. M. Bachilo, M. S. Strano, C. Kittrell, R. H. Hauge, R. E. Smalley and R. B. Weisman, *Science*, 2002, **298**, 2361–2367.

8 S. Nanot, E. H. Hároz, J. H. Kim, R. H. Hauge and J. Kono, *Adv. Mater.*, 2012, **24**, 4977–4994.
9 M. J. O. Connell, S. M. Bachilo, C. B. Huffman, K. L. Rialon, P. J. Boul and W. H. Noon, *Science*, 2002, **297**, 593–597.
10 G. Hong, S. Diao, A. L. Antaris and H. Dai, *Chem. Rev.*, 2015, **115**, 10816–10906.
11 S. Kruss, A. J. Hilmer, J. Zhang, N. F. Reuel, B. Mu and M. S. Strano, *Adv. Drug Delivery Rev.*, 2013, **65**, 1933–1950.
12 C. Farrera, F. Torres Andón and N. Feliu, *ACS Nano*, 2017, **11**, 10637–10643.
13 X. He, H. Htoon, S. K. Doorn, W. H. P. Pernice, F. Pyatkov, R. Krupke, A. Jeantet, Y. Chassagneux and C. Voisin, *Nat. Mater.*, 2018, **17**, 663–670.
14 E. Polo and S. Kruss, *Anal. Bioanal. Chem.*, 2016, **408**, 2727–2741.
15 J. Prasek, J. Drbohlavova, J. Chomoucka, J. Hubalek, O. Jasek, V. Adam and R. Kizek, *J. Mater. Chem.*, 2011, **21**, 15872–15884.
16 J.-Q. Wang, F. Ding, D. Luo, D. Zhang, X. Wang, J. Yang, X. Bai, F. Peng, Z. Xu, J. Wei, Y. Li, M. Li, R. Li, F. Yang, X. Li, Y. Li and Z. Xu, *Nature*, 2014, **510**, 522–524.
17 H. An, A. Kumamoto, H. Takezaki, S. Ohyama, Y. Qian, T. Inoue, Y. Ikuhara, S. Chiashi, R. Xiang and S. Maruyama, *Nanoscale*, 2016, **8**, 14523–14529.
18 A. S. R. Bati, L. Yu and M. Batmunkh, *Nanoscale*, 2018, **10**, 22087–22139.
19 D. Janas, *Mater. Chem. Front.*, 2017, **2**, 36–63.
20 M. C. Hersam, *Nat. Nanotechnol.*, 2008, **3**, 387–394.
21 J. Cui, D. Yang, X. Zeng, N. Zhou and H. Liu, *Nanotechnology*, 2017, **28**, 452001.
22 M. Zheng, *Top. Curr. Chem.*, 2017, **375**, 1–36.
23 M. S. Arnold, A. A. Green, J. F. Hulvat, S. I. Stupp and M. C. Hersam, *Nat. Nanotechnol.*, 2006, **1**, 60–65.
24 S. Ghosh, S. M. Bachilo and R. B. Weisman, *Nat. Nanotechnol.*, 2010, **5**, 443–450.
25 J. A. Fagan, C. Y. Khripin, C. A. Silvera Batista, J. R. Simpson, E. H. Hároz, A. R. Hight Walker and M. Zheng, *Adv. Mater.*, 2014, **26**, 2800–2804.
26 C. Y. Khripin, J. A. Fagan and M. Zheng, *J. Am. Chem. Soc.*, 2013, **135**, 6822–6825.
27 S. Reich, H. Li, O. Garrity, B. S. Flavel and G. Gordeev, *ACS Nano*, 2019, **13**, 2567–2578.
28 H. Liu, D. Nishide, T. Tanaka and H. Kataura, *Nat. Commun.*, 2011, **2**, 1–8.
29 H. Liu, T. Tanaka, Y. Urabe and H. Kataura, *Nano Lett.*, 2013, **13**, 1996–2003.
30 B. S. Flavel, M. M. Kappes, R. Krupke and F. Hennrich, *ACS Nano*, 2013, **7**, 3557–3564.
31 K. Tvrdy, R. M. Jain, R. Han, A. J. Hilmer, T. P. Mcnicholas and M. S. Strano, *ACS Nano*, 2013, **2**, 1779–1789.
32 X. Tu, S. Manohar, A. Jagota and M. Zheng, *Nature*, 2009, **460**, 250–253.
33 M. Zheng, A. Jagota, M. S. Strano, A. P. Santos, P. Barone, S. G. Chou, B. A. Diner, M. S. Dresselhaus, R. S. Mclean, G. B. Onoa, G. G. Samsonidze and E. D. Semke, *Science*, 2003, **302**, 1545–1549.
34 M. Zheng, A. Jagota, E. D. Semke, B. A. Diner, R. S. McLean, S. R. Lustig, R. E. Richardson and N. G. Tassi, *Nat. Mater.*, 2003, **2**, 338–342.
35 N. Ide and N. Yasuro, *Chem. Lett.*, 2011, 239–241.
36 A. Graf, Y. Zakharko, S. P. Schießl, C. Backes, M. Pfohl, B. S. Flavel and J. Zaumseil, *Carbon*, 2016, **105**, 593–599.
37 F. Hennrich, S. Lebedkin and M. M. Kappes, *J. Phys. Chem. C*, 2009, **113**, 14628–14632.
38 A. Nish, J. Y. Hwang, J. Doig and R. J. Nicholas, *Nat. Nanotechnol.*, 2007, **2**, 640–646.
39 J. Pan, F. Li and J. H. Choi, *J. Mater. Chem. B*, 2017, **5**, 6511–6522.
40 S. Kruss, M. P. Landry, E. Vander Ende, B. M. A. Lima, N. F. Reuel, J. Zhang, J. Nelson, B. Mu, A. Hilmer and M. Strano, *J. Am. Chem. Soc.*, 2014, **136**, 713–724.
41 R. Nißler, F. A. Mann, P. Chaturvedi, J. Horlebein, D. Meyer, L. Vukovic and S. Kruss, *J. Phys. Chem. C*, 2019, **123**, 4837–4847.
42 D. Meyer, A. Hagemann and S. Kruss, *ACS Nano*, 2017, **11**, 4017–4027.
43 G. Bisker, J. Ahn, S. Kruss, Z. W. Ulissi, D. P. Salem and M. S. Strano, *J. Phys. Chem. C*, 2015, **119**, 13876–13886.
44 S. Kruss, D. P. Salem, L. Vuković, B. Lima, E. Vander Ende, E. S. Boyden and M. S. Strano, *Proc. Natl. Acad. Sci. U. S. A.*, 2017, **114**, 1789–1794.
45 F. A. Mann, N. Herrmann, D. Meyer and S. Kruss, *Sensors*, 2017, **17**, 1521.
46 E. Polo, T. Nitka, E. Neubert, L. Erpenbeck, L. Vuković and S. Kruss, *ACS Appl. Mater. Interfaces*, 2018, **10**, 17693–17703.
47 A. J. Gillen, J. Kupis-rozmysłowicz, C. Gigli, N. Schuergers and A. A. Boghossian, *J. Phys. Chem. Lett.*, 2018, **9**, 4336–4343.
48 A. F. Mann, J. Horlebein, N. F. Meyer, F. Thomas and S. Kruss, *Chem. – Eur. J.*, 2018, **24**, 12241–12245.
49 N. E. Kallmyer, J. Musielewicz, J. Sutter and N. F. Reuel, *Anal. Chem.*, 2018, **90**, 5209–5216.
50 G. Bisker, J. Dong, H. D. Park, N. M. Iverson, J. Ahn, J. T. Nelson, M. P. Landry, S. Kruss and M. S. Strano, *Nat. Commun.*, 2016, **7**, 1–14.
51 R. M. Williams, C. Lee and D. A. Heller, *ACS Sens.*, 2018, **3**, 1838–1845.
52 F. A. Mann, Z. Lv, J. Grosshans, F. Opazo and S. Kruss, *Angew. Chem., Int. Ed.*, 2019, DOI: 10.1002/anie.201904167.
53 J. K. Streit, A. Fagan and M. Zheng, *Anal. Chem.*, 2017, **89**, 10496–10503.
54 J. P. Giraldo, M. P. Landry, S. Y. Kwak, R. M. Jain, M. H. Wong, N. M. Iverson, M. Ben-Naim and M. S. Strano, *Small*, 2015, **11**, 3973–3984.
55 K. Welsher, Z. Liu, S. P. Sherlock, J. T. Robinson, Z. Chen, D. Daranciang and H. Dai, *Nat. Nanotechnol.*, 2009, **4**, 773–780.
56 X. Wu, M. Kim, H. Kwon and Y. H. Wang, *Angew. Chem., Int. Ed.*, 2018, **57**, 648–653.
57 C. Kanimozhi, G. J. Brady, M. J. Shea, P. Huang, Y. Joo, M. S. Arnold and P. Gopalan, *ACS Appl. Mater. Interfaces*, 2017, **9**, 40734–40742.

58 Y. Joo, G. J. Brady, M. J. Shea, M. B. Oviedo, C. Kanimozhi, S. K. Schmitt, B. M. Wong, M. S. Arnold and P. Gopalan, *ACS Nano*, 2015, **9**, 10203–10213.
59 S. Liang, Y. Zhao and A. Adronov, *J. Am. Chem. Soc.*, 2014, **136**, 970–977.
60 T. Lei, X. Chen, G. Pitner, H. S. P. Wong and Z. Bao, *J. Am. Chem. Soc.*, 2016, **138**, 802–805.
61 I. Pochorovski, H. Wang, J. I. Feldblyum, X. Zhang, A. L. Antaris and Z. Bao, *J. Am. Chem. Soc.*, 2015, **137**, 4328–4331.
62 E. Polo and S. Kruss, *J. Phys. Chem. C*, 2016, **120**, 3061–3070.
63 H. Kwon, L. R. Powell, G. C. Schatz, B. Meany, N. Valley, Y. Piao and Y. Wang, *Nat. Chem.*, 2013, **5**, 840–845.
64 X. He, N. F. Hartmann, X. Ma, Y. Kim, R. Ihly, J. L. Blackburn, W. Gao, J. Kono, Y. Yomogida, A. Hirano, T. Tanaka, H. Kataura, H. Htoon and S. K. Doorn, *Nat. Photonics*, 2017, **11**, 577–582.
65 T. Shiraki, S. Uchimura, T. Shiraishi, H. Onitsuka and N. Nakashima, *Chem. Commun.*, 2017, **53**, 12544–12547.
66 M. Prato, K. Kostarelos and A. Bianco, *Acc. Chem. Res.*, 2008, **41**, 275–294.
67 D. Tasis, N. Tagmatarchis, A. Bianco and M. Prato, *Chem. Rev.*, 2006, **106**, 1105–1136.
68 S. Ghosh, S. M. Bachilo, R. A. Simonette, K. M. Beckingham and R. B. Weisman, *Science*, 2010, **330**, 1656–1659.
69 F. Jakubka, S. B. Grimm, Y. Zakharko, F. Gannott and J. Zaumseil, *ACS Nano*, 2014, 8477–8486.
70 S. Liang, H. Li, B. S. Flavel and A. Adronov, *Chem. – Eur. J.*, 2018, **24**, 9799–9806.
71 M. Pfohl, D. D. Tune, A. Graf, J. Zaumseil, R. Krupke and B. S. Flavel, *ACS Omega*, 2017, **2**, 1163–1171.

5.2.2 Discussion

The presented manuscript shows a successful route to obtain chirality-pure SWCNTs for potential biosensing applications, thought exchanging the surface chemistry from polyfluorenes to various other biopolymers.

PFO-SWCNTs were studied extensively beforehand, since specific polyfluorene conjugates are able to disperse distinct SWCNT chiralities.[63,83,86] This particular interaction can separate SWCNT chiralites from one another, which differ for instance by 0.1 nm in diameter, or thanks to their general band-gap structure (m-/s-SWCNTs).[89,90] The resulting PFO-SWCNTs exhibit a relatively high photoluminescent quantum yield[56] and can be colloidally stable, even without excess polymer e.g. after filtration[167].

Manuscript II now enabled the link between PFO-SWCNT purification and surfactant exchange, the essential step to use those colloidal nanoparticles in biological (aqueous) systems as NIR-labels or chemical sensors. In contrast to previous studies, it is the first comprehensive approach for further exchange the PFO-sorted SWCNT's organic surface modification and surrounding phase. Preceding studies used specifically designed PFO-polymers to trigger the release of dispersed SWCNTs. This was facilitated by acid-induced depolymerization[87,92,93,168], conformational switching[169] or selective chelation of the PFO-polymer[91]. These methods showed selective dispersion and further polymer removal and its potential recycling, but did not introduce additional re-dispersion of the separated SWCNTs. This critical step is especially challenging, since purified SWCNTs tend to agglomerate and stick to each other when the surface modification is removed. Those tube-tube interactions in the homogenous system are typically mediated through strong van der Waals forces.[170] Thereby, the van der Waals-London interaction depends on the nanotube diameter[171], while furthermore objects of same properties experience a strong attraction towards each other[58]. For purified SWCNTs, this effect can be so strong (e.g. in aligned films) that it leads to irreversibly bonding upon contact.[172] In **Manuscript II** this issue was tackled by precipitating the PFO-SWCNTs on a NaCl-filler (Supplementary Information Manuscript II, 7.2, Figure S1), stable during toluene-based polymer removal and dissolvable for later SWCNT redispersion in water, overall decreasing SWCNT agglomeration.

In general, the corona phase exchange purification (CPEP) approach seems very likely to be independent of the used polyfluorene polymer, since it was demonstrated with the commonly applied poly[(9,9-dioctylfluorenyl-2,7-diyl)-alt-co-(6,6'-2,2'-bipyridine)] and poly(9,9-dioctylfluorenyl-2,7-diyl) polymers. However, it cannot be ruled out that different

PFO-variants bind much stronger to the SWCNT surface, resulting in a nano-conjugate resistant towards the removal and exchange of the surface modification. Due to the possible usage of large-scale shear force mixing[56] and further polymer recycling, the presented approach could be considered as scientific framework for an industrial route to chirality-pure SWCNT material. Nevertheless, the (limited) amounts obtained at laboratory-scale were sufficient to assemble e.g. chirality-pure ssDNA-(6,5)-SWCNTs. Spectroscopic analysis of the chirality-pure DNA-SWCNTs suggested a functional biopolymer modification. This enabled the first proof-of-principle biosensing of neurotransmitters with chirality-pure SWCNTs, shown for the monochiral fluorescence emission increase after dopamine addition (Figure 5). As hypothesized, the CPEP approach can be used to obtain specifically tailored nanosensors, the basis for multispectral SWCNT sensing. Recently, defect engineering[49] and its combination with radical spin labels[173] were introduced to PFO-sorted SWCNTs. CPEP could present a useful route to transfer these systems into aqueous phases, thus enabling novel nanoconjugates for functional NIR-labeling and sensing.

5.2.3 Sensing with Chirality-Pure Near-Infrared Fluorescent Carbon Nanotubes

Manuscript III was published in the following journal:

Robert Nißler, Larissa Kurth, Han Li, Alexander Spreinat, Ilyas Kuhlemann, Benjamin S. Flavel and Sebastian Kruss*

"Sensing with Chirality-Pure Near-Infrared Fluorescent Carbon Nanotubes"

Analytical Chemistry, **2021**, 93, 6446-6455

The article is available at: DOI: 10.1021/acs.analchem.1c00168
* Corresponding author

Responsibility assignment: R.N. and S.K. designed and conceived the research. S.K. coordinated the project. L.K. and R.N. separated (6,5)-SWCNTs, performed surface exchange and chemical sensing experiments. A.S. and I.K. wrote Python-based analysis scripts for absorbance and sensing evaluation. H.L. and B.S.F. separated (7,5)-, (9,4)-, and (7,6)-SWCNTs and enantiomers of (6,5)-SWCNTs. R.N. performed all remaining experiments, analyzed the data and wrote the manuscript, with input from S.K..

analytical chemistry

pubs.acs.org/ac Article

Sensing with Chirality-Pure Near-Infrared Fluorescent Carbon Nanotubes

Robert Nißler, Larissa Kurth, Han Li, Alexander Spreinat, Ilyas Kuhlemann, Benjamin S. Flavel, and Sebastian Kruss*

Cite This: *Anal. Chem.* 2021, 93, 6446−6455 Read Online

ACCESS | Metrics & More | Article Recommendations | Supporting Information

ABSTRACT: Semiconducting single-wall carbon nanotubes (SWCNTs) fluoresce in the near-infrared (NIR) region, and the emission wavelength depends on their chirality (*n*,*m*). Interactions with the environment affect the fluorescence and can be tailored by functionalizing SWCNTs with biopolymers such as DNA, which is the basis for fluorescent biosensors. So far, such biosensors have been mainly assembled from mixtures of SWCNT chiralities with large spectral overlap, which affects sensitivity as well as selectivity and prevents multiplexed sensing. The main challenge to gain chirality-pure sensors has been to combine approaches to isolate specific SWCNTs and generic (bio)functionalization approaches. Here, we created chirality-pure SWCNT-based NIR biosensors for important analytes such as neurotransmitters and investigated the effect of SWCNT chirality/handedness as well as long-term stability and sensitivity. For this purpose, we used aqueous two-phase extraction (ATPE) to gain chirality-pure (6,5)-, (7,5)-, (9,4)-, and (7,6)-SWCNTs (emission at ~990, 1040, 1115, and 1130 nm, respectively). An exchange of the surfactant sodium deoxycholate (DOC) to specific single-stranded (ss)DNA sequences yielded monochiral sensors for small analytes (dopamine, riboflavin, ascorbic acid, pH). DOC residues impaired sensitivity, and therefore substantial removal was necessary. The assembled monochiral (6,5)-SWCNTs were up to 10 times brighter than their nonpurified counterparts, and the ssDNA sequence determined the absolute fluorescence intensity as well as colloidal (long-term) stability and selectivity for the analytes. $(GT)_{40}$-(6,5)-SWCNTs displayed the maximum fluorescence response to the neurotransmitter dopamine (+140%, $K_d = 1.9 \times 10^{-7}$ M) and a long-term stability of >14 days. The specific ssDNA sequences imparted selectivity to the analytes mostly independent of SWCNT chirality and handedness of (±) (6,5)-SWCNTs, which allowed a predictable design. Finally, multiple monochiral/single-color SWCNTs were combined to achieve ratiometric/multiplexed sensing of the important analytes dopamine, riboflavin, H_2O_2, and pH. In summary, we demonstrated the assembly, characteristics, and potential of monochiral (single-color) SWCNTs for NIR fluorescence sensing applications.

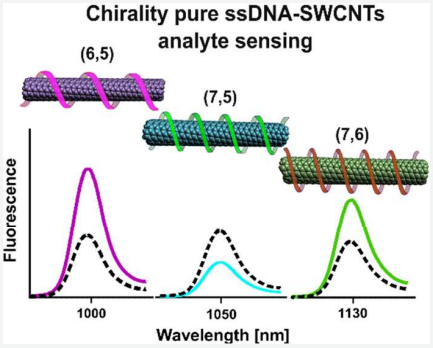

INTRODUCTION

Single-wall carbon nanotubes (SWCNTs) are 1D nanomaterials with unique photophysical properties.[1−4] Semiconducting SWCNTs show fluorescence in the near-infrared (NIR) region of the electromagnetic spectrum (optical tissue transparency window), which offers ultralow background and high tissue penetration.[5] The emission wavelength depends on their carbon lattice structure, described by the chiral index/chirality (*n*,*m*).[6] Because of these properties SWCNTs are versatile building blocks for NIR labels and sensors.[7−11] As nanosensors they are powerful tools to study biological processes with high spatial, temporal, and chemical resolution.[12−19] The most prominent examples are the detection of signaling molecules such as neurotransmitters,[12,20,21] reactive oxygen species (ROS),[13,14] and nitric oxide (NO).[17] Additional sensing concepts have been developed for genetic material,[15,22] lipids,[23] proteins,[24−26] and bacterial motifs.[27] Not only are such sensors able to report the presence of the molecule but also imaging of many of them allows one to get spatiotemporal chemical information.[28] Using this concept, for example, the release and secretion of the neurotransmitters dopamine and serotonin from cells could be resolved.[12,21] So far NIR fluorescent sensors based on SWCNTs have been assembled mainly from an as-synthesized SWCNT material, which contains multiple chiralities, catalyst residues, and impurities. However, for the simultaneous detection of different analytes, multiple sensors with unambiguous fluorescence emission and hence SWCNT chirality are required. The synthesis of chirality-enriched SWCNTs has improved over the last years, but commercially available SWCNT materials still contain multiple chiralites.[29,30] Therefore, separation and purification

Received: January 13, 2021
Accepted: March 29, 2021
Published: April 8, 2021

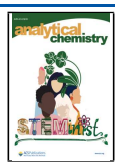

https://doi.org/10.1021/acs.analchem.1c00168
Anal. Chem. 2021, 93, 6446−6455

approaches are required to obtain samples with well-defined characteristics.[31,32] SWCNTs have been separated by density gradient centrifugation,[33,34] gel chromatography,[35−37] ion exchange chromatography,[38] and aqueous two-phase extraction (ATPE).[39−41] Furthermore, certain macromolecules such as single-stranded (ss)DNA sequences[42,43] or polyfluorenes (PFOs)[44] preferentially solubilize certain chiralities, which provides a route to monochiral samples. In the past years ATPE of SWCNTs has made tremendous progress in the isolation of various small and large SWCNT chiralities.[41,45−48] In this approach SWCNTs are dispersed in either a surfactant such as sodium deoxycholate (DOC) or chirality-specific ssDNA[49,50] sequences and separated between aqueous phases of two different polymers. This fast, reliable, and low-cost separation method appears to be an optimal starting point to obtain monochiral sensors. Unfortunately, chirality-pure SWCNTs extracted by these approaches are coated with the macromolecule or surfactant used for the purification process. The surfactant can be removed, but the purer a sample becomes, the more the hydrophobic SWCNTs tend to stick to each other and redispersion in other surfactants and biopolymers becomes difficult.[51]

In contrast, the chemical design of sensors requires functionalization with biomolecules that impart specificity to the SWCNT. Chemical approaches include noncovalent functionalization with DNA,[43] peptides,[52] peptide−DNA conjugates,[53] protein−DNA conjugates,[16,54] proteins,[26] and lipids.[24,55] Recently, also sp^3-quantum defects on SWCNTs have been modified covalently with biomolecules.[56] Overall, the surface chemistry is crucial for molecular recognition and signal transduction. Some of the best studied systems so far are DNA-functionalized SWCNTs that recognize small molecules. Certain sequences make the SWCNT sensitive to biomolecules: for example, to the neurotransmitter dopamine.[20,57] In this particular case, it was shown that interactions of the two hydroxy groups of dopamine with the DNA backbone cause conformational changes that lead to an increase in quantum yield.[12,58] In contrast, simple adsorption and redox chemistry could be ruled out.[58,59]

Consequently, the surface chemistry on SWCNTs is the most important part to tailor sensor properties, but this has not been explored in detail and combined with purified monochiral SWCNTs. The aforementioned difficulties have so far impaired the obvious next step to use monochiral SWCNTs as building blocks for NIR fluorescent sensors and labels.

Here, we isolate monochiral SWCNTs to assemble single-color fluorescent sensors and study the effect of chirality and surface functionalization on the fluorescent sensing of biomolecules. For this purpose, we combine ATPE with surface exchange methods to ssDNA sequences (including aptamers) and polymers. The presented strategy minimizes SWCNT aggregation during surface exchange and redispersion. We quantify and compare the photophysical properties, stabilities, and fluorescence responses of monochiral and multichiral sensors. Finally, we make use of the nonoverlapping emission spectra of monochiral SWCNTs and demonstrate ratiometric and multiplexed sensing.

MATERIALS AND METHODS

All materials, if not otherwise stated, were purchased from Sigma-Aldrich.

SWCNT Surface Modification. (6,5)-Chirality-enriched CoMoCat SWCNTs (Sigma-Aldrich, product no. 773735) were modified with varying single-stranded (ss)DNAs such as $(GT)_5$, $(GT)_{10}$, $(GT)_{20}$, $(GT)_{40}$, $(C)_{30}$, $(A)_{30}$, $(T)_{30}$, $(GC)_{15}$, $(GA)_{15}$, and $(AT)_{15}$ (oligonucleotide sequences purchased from Sigma-Aldrich) following a previously described protocol.[59] Thereby, 100 μL of ssDNA (2 mg/mL in H_2O) was mixed with 100 μL of 2×PBS and 100 μL of SWCNTs (2 mg/mL in PBS), tip-sonicated for 15 min @ 30% amplitude (36 W output power, Fisher Scientific Model 120 Sonic Dismembrator) and centrifuged 2× for 30 min @ 16100*g*. DOC-dispersed SWCNTs were obtained by tip-sonicating 4 mg of CoMoCat SWCNTs in 2 mL 1% DOC for 30 min @ 40% amplitude, followed by 2× 30 min centrifugation @ 16100*g*.

SWCNT Separation. The separation of (6,5)-SWCNTs was performed according to a previously reported aqueous two-phase extraction (ATPE) protocol from Li et al.[41] Briefly, in a three-step approach SWCNT chiralities were separated between two aqueous phases, containing dextran (MW 70000 Da, 4% *m*/*m*) and PEG (MW 6000 Da, 8% *m*/*m*) with varying pH values *via* HCl addition. The final B_3 (bottom) phase yielded monochiral (6,5)-SWCNTs, which were diluted with DOC to obtain a stable 1% DOC-SWCNT solution. Dialysis (300 kDa dialysis bag, Spectra/Por, Spectrum Laboratories Inc.) against 1% DOC removed the dextran polymer used for SWCNT separation. The separation of (7,5)- and (9,4)-SWCNTs followed a pH-modulated ATPE process similar to that described above. Instead of 0.05% DOC and 0.5% SDS for the normal process, 0.07% DOC and 0.5% SDS were used here to improve the resolution of (7,5)- as well as (9,4)-SWCNTs. (7,6)-SWCNTs were obtained by using a similar ATPE method but from a different CoMoCAT raw soot (CHASM, lot #SG76-L39). Briefly a three-stage ATPE process was used to sort single chirality (7,6). In stage 1, SDS concentrations were changed from 0.5% to 1.5% with a constant DOC concentration (0.04%) to get a (7,6)-enriched top fraction (T_4, with SDS ∼0.7%). Then a fresh bottom phase was added to T_4, and SDS concentrations were again changed from 0.6% to 1% with the same DOC of 0.04% to further purify this enriched (7,6) fraction. In the end, a metal semiseparation was performed to remove the metallic tubes at stage 3.

Enantiomerically pure (6,5)-SWCNTs were prepared by a similar diameter sorting on the basis of DOC/SDS.[39] First the concentrations of SDS 0.9% and DOC 0.04% were used in order to push all species larger than (6,5)-SWCNTs to the top phase and remove them. Then the SDS concentrations were increased very slowly and step by step to 1.3%. The next seven continuous fractions (T_1−T_7) were collected, and all of them were (6,5) enriched. After the next semiconducting-metallic separation, T_2 was found to be highly enantiomerically (−)-(6,5) enriched. Sodium cholate (SC) was then used to further separate highly enriched (+)-(6,5) from the fraction T_4. CD measurements were performed on an CD spectrometer (J-1500, JASCO) from 800 to 200 nm through a 1 mm path length cuvette in 1 nm steps (scanning speed 100 nm/min, bandwidth ∼2.2 nm).

Monochiral SWCNT Surface Exchange to ssDNA. Surface exchange of the SWCNTs toward ssDNA was achieved by applying the steps from Streit et al.[60] Purified (6,5)-SWCNTs in 1% DOC were diluted to an absorbance of 2.0 at the E_{11} transition (986 nm). The concentration of (7,5)-SWCNTS was 2.0 at 1032 nm, for (9,4)-SWNCTs 0.9 at 1112 nm, and for (7,6)-SWCNTs 1.6 at 1129 nm. A 150 μL portion of purified SWCNTs in 1% DOC was mixed with 25 μL of PEG (MW 6 kDa, 25% *m*/*v* in H_2O) and 30 μL of ssDNA (2.0

https://doi.org/10.1021/acs.analchem.1c00168
Anal. Chem. 2021, 93, 6446−6455

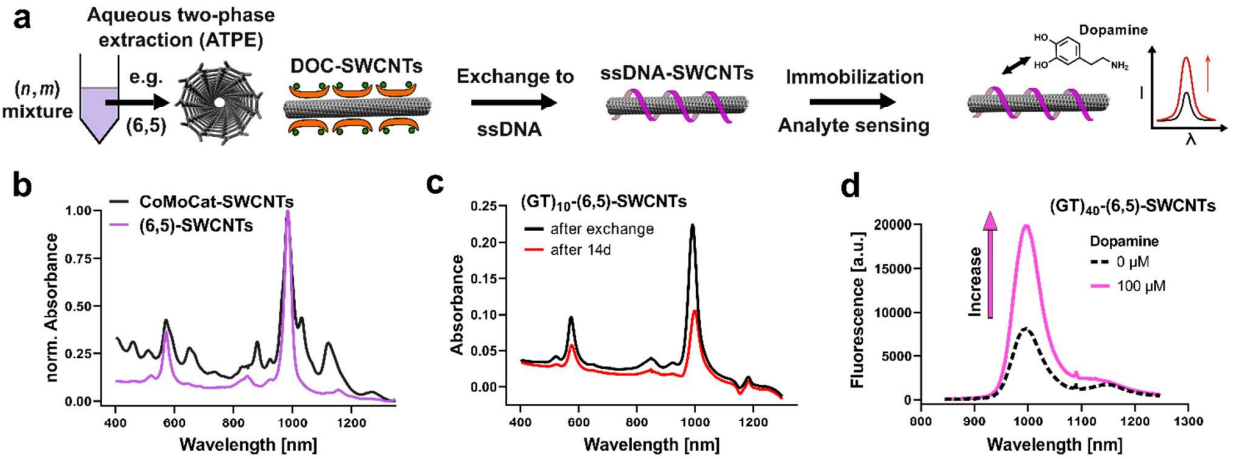

Figure 1. Assembly of chirality-pure near-infrared fluorescent carbon nanotube-based sensors. (a) Schematic of the workflow. Aqueous two-phase extraction (ATPE) yielding chirality pure SWCNTs (e.g., (6,5)-SWCNTs) from a parental mixture. Exchange of the organic corona from the surfactant sodium deoxycholate (DOC) to single-stranded (ss)DNA or other (bio)polymers leads to monochiral functionalized SWCNTs that serve as sensors for small molecules such as the neurotransmitter dopamine. (b) Exemplary normalized absorbance spectra of parental CoMoCat-SWCNTs and purified (6,5)-SWCNTs in 1% DOC. (c) Nine different ssDNA-(6,5)-SWCNTs were assessed. Here, exemplary absorbance spectra of $(GT)_{10}$-(6,5)-SWCNTs directly after surface exchange and after 14 days are shown. (d) ssDNA-SWCNTs immobilized on a glass surface and exposed to analytes that change their NIR fluorescence in a DNA sequence dependent way. Here, the exemplary monochiral fluorescence spectrum of a sensor for the neurotransmitter dopamine is shown.

mg/mL in H_2O). After one precipitation cycle, due to the stepwise addition of 270 μL of methanol and subsequent addition of 600 μL of isopropyl alcohol, the loose nanotube pellet was separated from the supernatant by short (1 s) centrifugation @ 16100*g*. The supernatant was further centrifuged for 2 min @ 16100*g*, and the obtained DNA pellet residue was redispersed in 300 μL of 1×PBS. This solution was used to redisperse the nanotube pellet by bath sonication or 10 s of tip sonication. Further centrifugation (5 min @ 16100*g*) yielded the monochiral nanosensors, which were characterized afterward by absorption spectroscopy. For stability measurements the ssDNA-(6,5)-SWCNTs were diluted to an absorbance at an E_{11} transition (~991 nm) of 0.2 and measured again after time intervals of 1, 3, 7, and 14 days. Surface exchange toward PEG-PL (18:0 PEG5000 PE, Avanti Lipids) was performed by following a modified protocol.[55] DOC-dispersed chirality-pure SWCNT fractions were concentrated and washed with sodium cholate (SC, 12 mg/mL in 1xPBS) using molecular cutoff spin filtration (Vivaspin 500, 100000 Da molecular weight cutoff, Sartorius). A 800 μL portion of these SC-SWCNTs was mixed with 2 mg of 18:0 PEG5000 PE dissolved in 200 μL of PBS and dialyzed 2 days against 1×PBS, using a 1 kDa cutoff dialysis tube. The final PEG-PL-SWCNTs were obtained after 20 min of centrifugation @ 16100*g*. For ratiometric H_2O_2 sensing, the hemin-binding aptamer (HeApta) 5′-AGTGTG-AAA-TAT-CTA-AAC-TAA-ATG-TGG-AGG-GTG-GGA-CGG-GAA-GAA-GTT-TAT-TTT-TCA-CAC-T-3′ was used,[13,61] with a concentration of 50 nM hemin.

NIR Spectroscopy. Absorption spectra were acquired with a JASCO V-670 device from 400 to 1350 nm in 0.2 nm steps in a 10 mm path length glass cuvette. 1D-NIR fluorescence spectra were measured with a Shamrock 193i spectrometer (Andor Technology Ltd., Belfast, Northern Ireland) connected to an IX53 Microscope (Olympus, Tokyo, Japan). Excitation was performed with a gem 561 laser (Laser Quantum, Stockport, UK). 2D excitation-emission spectra were collected with a Monochromator MSH150 instrument, equipped with a LSE341 light source (LOT-Quantum Design GmbH, Darmstadt, Germany) as the excitation source.

NIR fluorescence analyte response measurements were performed by letting 60 μL of a 0.2 nM ssDNA-SWCNT solution (molar nanotube concentration calculation based on previous literature[62−64]) adsorb overnight (12 h) on a glass bottom 96-well plate (#1 cover glass, 0.13−0.16 mm, Cellvis, P96-1-N), followed by washing with PBS and addition of 20 μL of the analyte to 180 μL of PBS (addition of 20 μL of 0.06 M HCl to obtain pH 6 as validated by a pH meter). NIR fluorescence spectra were acquired with 130 mW excitation @ 561 nm and 10 s integration time. D-Adrenaline was purchased from AKos GmbH (Lörrach, Germany). Dose−response measurements were fitted with a one-site specific binding fit (GraphPad Prism 8) using $Y = B_{max}X/(K_d + X)$ with X = concentration of the analyte, Y = specific binding; B_{max} = maximum binding, and K_d = dissociation constant.

Atomic Force Microscopy. AFM analysis was performed on an JPK NanoWizard (Bruker) instrument in tapping mode. SWCNT dispersions were drop-casted on a freshly cleaved muscovite mica surface, incubated for 15 min, and rinsed with deionized H_2O. A total number of 732 individualized SWCNTs were analyzed with Gwyddion (2.53), and the corresponding descriptive statistics were fitted with a Weibull distribution (Origin 9.1).

RESULTS AND DISCUSSION

To create nanosensors with narrow emission spectra, chirality-pure SWCNTs are necessary, and we used a scalable ATPE approach that yields large amounts of e.g. (6,5)-SWCNTs (Figure 1a,b and Figure S1 in the Supporting Information). Exchange and variation of the ssDNA surface modification enabled the synthesis of different nanosensors, which were evaluated regarding their optical properties, colloidal stability, and sensitivity in biosensing (Figure 1c,d).

https://doi.org/10.1021/acs.analchem.1c00168
Anal. Chem. 2021, 93, 6446−6455

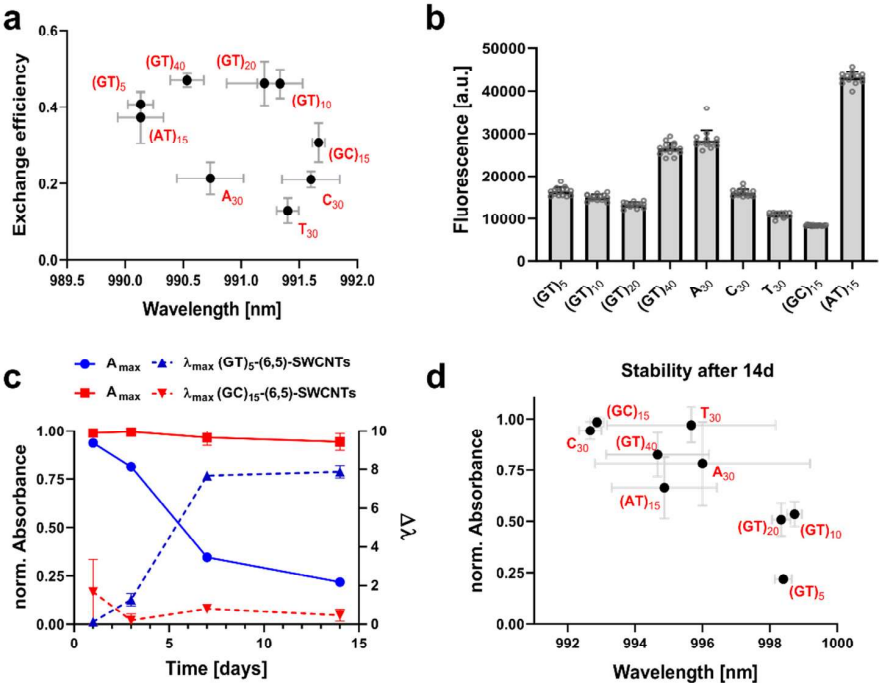

Figure 2. Surface exchange and colloidal stability of chirality-pure ssDNA-(6,5)-SWCNTs. (a) Exchange efficiency and E_{11} absorbance maxima of nine different ssDNA-(6,5)-SWCNTs for surfactant exchanges to ssDNA (n = 3, mean ± SEM). All monochiral nanosensors have very similar absorbance features (maxima and FWHM of E_{11} transmission). (b) Fluorescence intensities of 0.2 nM ssDNA-(6,5)-SWCNTs. $(AT)_{15}$-(6,5)-SWCNTs show the highest fluorescence emission (mean ± SD, n = 15, technical replicates from three independent exchange experiments). (c) Normalized E_{11} absorbance and wavelength shift evaluated after 1, 3, 7, and 14 days post (6,5)-SWCNT surface exchange to ssDNA for two exemplary sequences (normalized to the absorbance at t = 0). $(GT)_5$-(6,5)-SWCNTs show a decrease in absorbance and red shift, which indicate lower colloidal stability. In contrast, for example $(GC)_{15}$-(6,5)-SWCNTs remain stable over weeks (mean ± SEM, n = 3). (d) Colloidal stability for different ssDNA sequences as measured by the normalized E_{11} absorbance 14 days after surface exchange (normalized to the absorbance at t = 0) (mean ± SEM, n = 3).

Impact of ssDNA Sequence on Brightness and Stability. Variation of the ssDNA sequence leads to ssDNA/SWCNT conjugates that are sensitive to different biologically important molecules.[57,65] Therefore, we first evaluated the influence of the ssDNA sequence on the surface exchange process and optical properties. For this purpose, DOC-(6,5)-SWCNTs (Figure 1b) of the same concentration/absorbance (Figure S2 in the Supporting Information) were exchanged to different ssDNA sequences.

A typical ssDNA-(6,5)-SWCNT absorption spectrum is shown in Figure 1c, and an analysis of all E_{11} absorption features for the different ssDNA-(6,5)-SWCNTs after surface exchange is summarized in Figure 2a. All monochiral nanosensors displayed an absorbance maximum between 990.2 nm and 991.6 nm but large differences in absolute absorption. ssDNA sequences were able to redisperse 13% (T_{30}) to 47% ($(GT)_{40}$) of the parent surfactant stabilized (6,5)-SWCNTs in 1% DOC (shown as mean ± standard error of the mean (SEM)). This exchange efficiency was calculated by correlating the E_{11} absorption features (maximum absorption × FWHM) from the DOC and ssDNA solutions, similarly to the approach by Streit et al.[60] We assumed a similar absorption cross section for SWCNTs with different ssDNA functionalizations and diluted all ssDNA-(6,5)-SWCNTs accordingly to the same concentration (0.2 nM in PBS), but we observed strong differences in fluorescence (Figure 2b). The calculation of concentrations is based on the approach by Schöppler et al. (see Materials and Methods).[64] It accounts for spectral features of SWCNTs and assumes that the SCWNT length is not changed by surface exchange: e.g., to ssDNA. Atomic force microscopy (AFM) revealed a mean length of ∼1000 nm for purified ssDNA-(6,5)-SWCNTs and supported this assumption (Figure S3 in the Supporting Information). The fluorescence intensity for these concentration-calibrated samples showed distinct differences for different ssDNA sequences (Figure 2b). $(AT)_{15}$-SWCNTs showed both the strongest emission for chirality-pure and unpurified (CoMoCat)-SWCNTs (Figures S4 and S5 in the Supporting Information). In contrast, $(A)_{30}$-SWCNTs showed the lowest fluorescence intensity for nonpurified CoMoCat-SWCNTs but high fluorescence emission for chirality-pure (6,5)-SWCNTs. Distinct differences between chirality-pure ssDNA-(6,5)-SWCNTs were also observed in terms of colloidal stability. Monochiral ssDNA-SWCNTs showed a tendency to aggregation/precipitation after several days. This could be attributed to a higher purity without catalyst residues or amorphous carbon. Consequently, the stronger hydrophobic interactions between SWCNTs would cause more aggregation. Measurements over 14 days revealed a decrease in E_{11} absorbance, as well as a concomitant red shift for $(GT)_5$-(6,5)-SWCNTs. In contrast, for example $(GC)_{15}$-(6,5)-SWCNTs the spectra remained stable (Figure 2c and Figures S4 and S5 in the Supporting Information). Both a decrease in absorbance and red shift (broadening) are known parameters indicating SWCNT aggregation and hence loss of colloidal stability.[66]

https://doi.org/10.1021/acs.analchem.1c00168
Anal. Chem. 2021, 93, 6446−6455

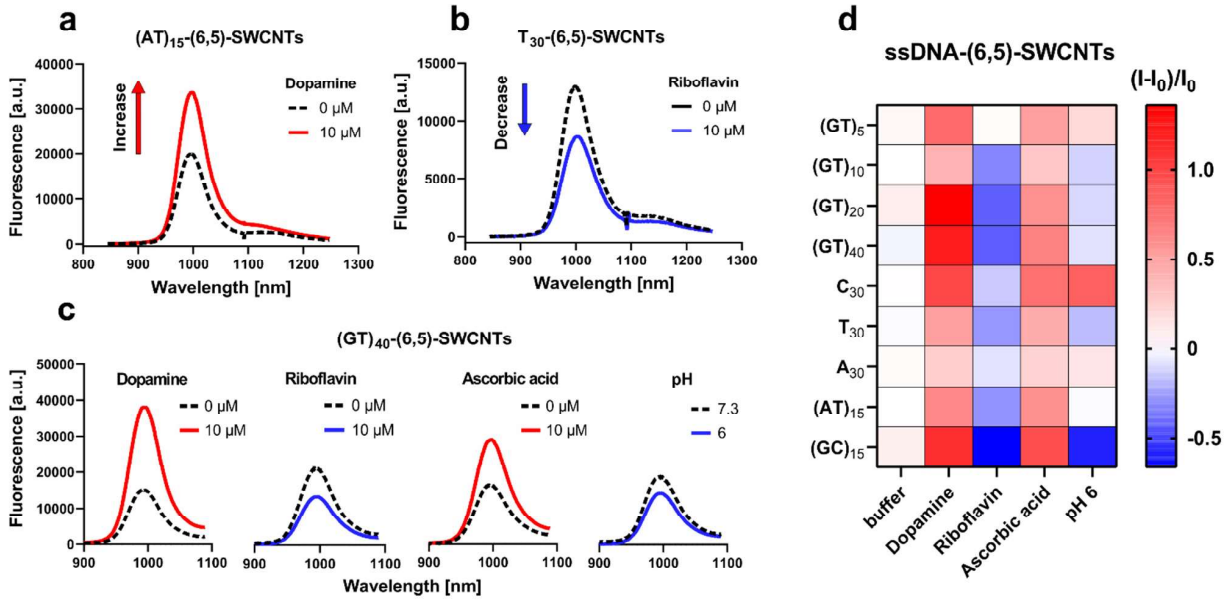

Figure 3. Sensitivity of monochiral ssDNA-(6,5)-SWCNT-based sensors. Exemplary NIR fluorescence spectra: (a) increase in $(AT)_{15}$-(6,5)-SWCNTs fluorescence in the presence of the neurotransmitter dopamine; (b) decrease in T_{30}-(6,5)-SWCNTs fluorescence in the presence of riboflavin; (c) fluorescence response of $(GT)_{40}$-(6,5)-SWCNTs for different analytes; (d) overview of the responses of different functionalized (6,5)-SWCNTs. Fluorescence increases are shown in shades of red and fluorescence decreases in shades of blue (mean, $n = 3$). The dopamine, riboflavin, and ascorbic acid concentrations are 10 μM.

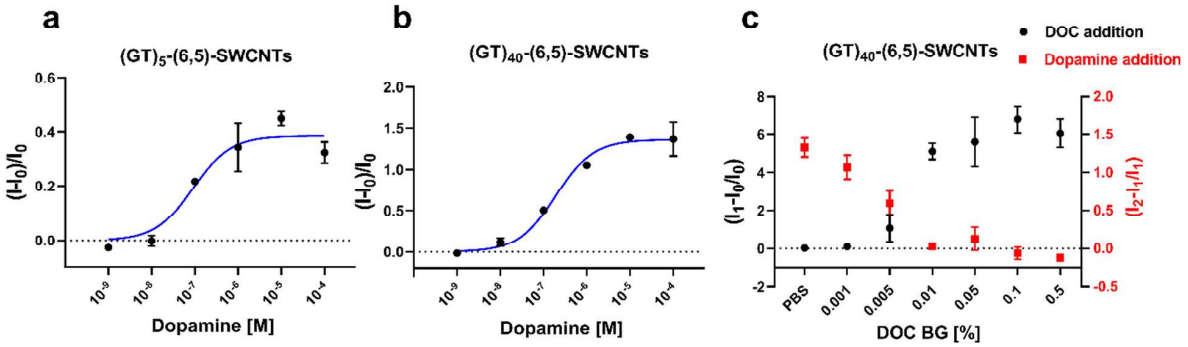

Figure 4. Sensitivity of $(GT)_x$-(6,5)-SWCNT dopamine sensors and effect of surfactant residues: (a) dose-dependent fluorescence response of $(GT)_5$-(6,5)-SWCNT showing a maximum increase of ~40% and K_d = of 9.2 × 10^{-8} M dopamine (mean ± SEM, $n = 3$; the blue curve indicates the fit); (b) $(GT)_{40}$-(6,5)-SWCNT response showing a maximum of ~140% fluorescence increase with K_d = 1.1 × 10^{-7} M dopamine (mean ± SEM, $n = 3$); (c) dopamine sensing (10 μM) with DOC background. The addition of ≥0.01% DOC (w/v) (black data points, I_1) to $(GT)_{40}$-(6,5)-SWCNTs abolishes fluorescent sensing (red data points, I_2) (mean ± SEM, $n = 3$).

C_{30}- and $(GC)_{15}$-(6,5)-SWCNTs were the most stable sequences (Figure 2d), whereas $(GT)_5$- to $(GT)_{20}$-(6,5)-SWCNTs lost >50% of the initial absorbance accompanied by a strong red shift (for more details see Figure S6 in the Supporting Information). In contrast, the longer $(GT)_{40}$ sequence showed a high colloidal stability. This result shows that the ssDNA sequence and length play a crucial role in the properties of monochiral conjugates.

Sensitivity of Monochiral Sensors. Chemical sensing with SWCNTs is a powerful tool to resolve biological processes in a spatiotemporal manner, even down to single-molecule interactions.[12,17,21,67] With distinct chirality-pure and hence multicolor sensors it is possible to study multiple analytes simultaneously. To mimic this scenario and rule out possible colloidal stability effects, chemical sensing of the monochiral ssDNA-SWCNTs was performed after physisorption onto a glass surface.[12] Analytes that are known to modulate the fluorescence intensity of nonpurified SWCNTs in solution were added (Figure 3a,b).[58,59] The fluorescence responses for $(GT)_{40}$-(6,5)-SWCNTs are highlighted in Figure 3c,d and show all sensor responses. Overall responses were similar for monochiral and multichiral ssDNA-(6,5)-SWCNTs, indicating that the sensing mechanism is preserved after SWCNT purification (Figure S7 in the Supporting Information). The magnitude of the fluorescence response depended on the ssDNA sequence, but no shifts in the emission peak positions were observed. In some cases, the response was stronger for nonpurified DNA-SWNCTs: e.g., after 10 μM dopamine addition +120% for $(GT)_{40}$-(6,5)-SWCNTs and +250% for parental $(GT)_{40}$-(CoMoCat)-SWCNTs. In some cases, such as T_{30}- and $(AT)_{15}$-(6,5)-SWCNTs (Figure 3a and Figure S7 in the Supporting Information) the sensor response

https://doi.org/10.1021/acs.analchem.1c00168
Anal. Chem. 2021, 93, 6446−6455

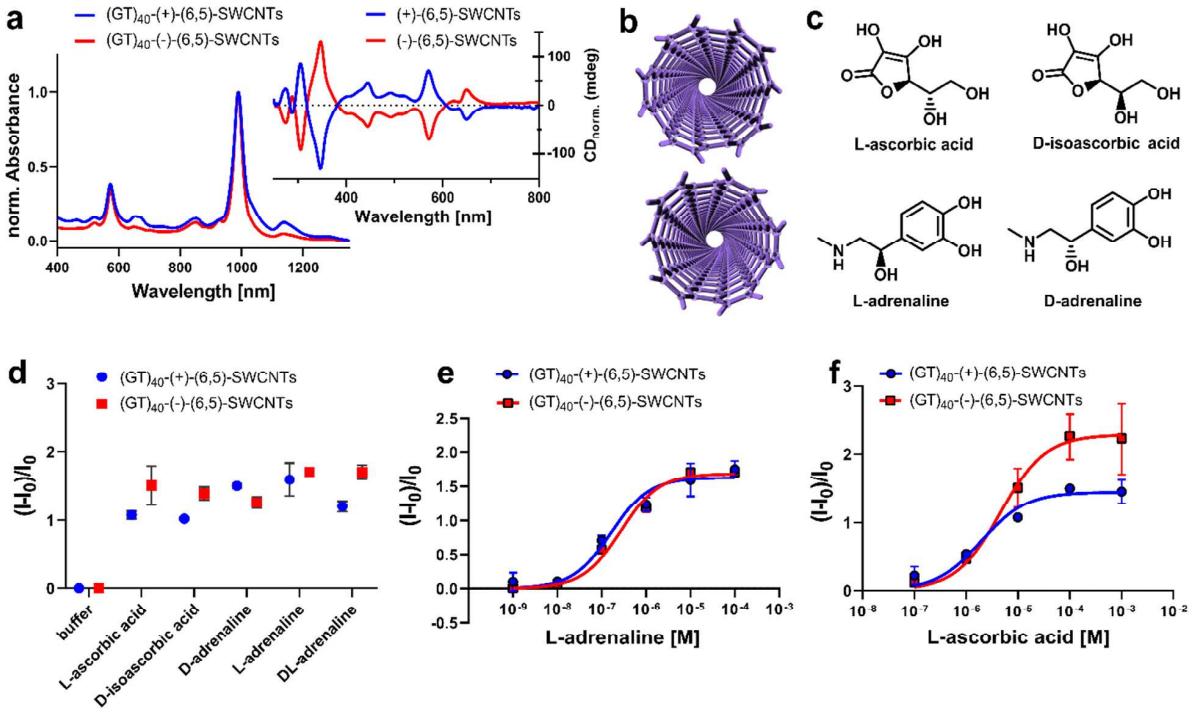

Figure 5. Sensing with (6,5)-SWCNT enantiomers: (a) normalized absorbance spectra of (6,5)-SWCNT enantiomers with $(GT)_{40}$-ssDNA surface modification (the inset shows the CD spectra of both (6,5)-SWCNT enantiomers; (b) illustration of helical chirality of both (−)- and (+)-(6,5)-SWCNTs; (c) tested chiral molecules; (d) fluorescence response of $(GT)_{40}$-(+)-(6,5)-SWCNTs and $(GT)_{40}$-(−)-(6,5)-SWCNTs to stereoisomers of ascorbic acid and adrenaline (mean ± SD, n = 3, analytes = 10 μM); dose−response curves of (e) L-adrenaline and (f) L-ascorbic acid using $(GT)_{40}$-(+)-(6,5)-SWCNTs and $(GT)_{40}$-(−)-(6,5)-SWCNTs (mean ± SD, n = 3; blue and red curves indicate fits).

was enhanced for monochiral sensors. Monochiral (6,5)-SWCNTs showed an up to 10× stronger fluorescence emission (Figure S8 in the Supporting Information). The lower (relative) sensor response in some cases can be explained by the smaller room for a (relative) quantum yield increase. In general the higher brightness of monochiral SWCNTs does not lower the absolute sensor responses; however, the actual DNA confirmation might differ between purified and nonpurified SWCNT sensors.[68]

The oligonucleotide length appears to play an important role in chemical sensing and therefore dose−response curves for monochiral $(GT)_x$-(6,5)-SWCNTs were collected (Figure 4a,b). The $(GT)_5$-(6,5)-SWCNT response increased by +40% and saturated at ∼1 μM dopamine with a dissociation constant K_d of 9.2 × 10^{-8} M. A much stronger increase in intensity was observed for $(GT)_{40}$-(6,5)-SWCNTs (+140%, saturation at ∼10 μM, K_d = 1.9 × 10^{-7} M). Furthermore, we evaluated how dopamine sensing is affected by DOC, which is a potential residue of the purification and surface exchange process.

Addition of DOC ≥0.01% (w/v) increased the fluorescence of $(GT)_{40}$-(6,5)-SWCNTs (e.g. +500% for 0.01% DOC), causing a spectral (∼7 nm) blue shift and diminishing the response to dopamine (Figure 4c). A similar trend was also observed when dopamine sensing was performed 1 h after addition of DOC or when $(GT)_5$-(6,5)-SWCNTs were used (Figure S9 in the Supporting Information). In turn, the red-shifted peak position and the fluorescence response of ssDNA-(6,5)-SWCNTs to dopamine indicates that the optimized exchange procedure leaves no or a negligible amount of DOC on the SWCNT surface. These DOC addition experiments show that it abolishes sensing and (nearly) complete surfactant removal is necessary for nonbiased sensing.

Effect of SWCNT Chirality and Handedness. By using ATPE, not only specific SWCNT chiralities but also SWCNT enantiomers can be isolated.[41,45,46] We aimed to find out if the handedness itself has an effect on sensing and calls for tailored functionalization. ssDNA-modified enantiomers of (6,5)-SWCNTs can react differently to oxidizing agents.[49] To test chiral interactions, stereoisomers of ascorbic acid and the catecholamine adrenaline were tested. We hypothesized that the response of sensors based on enantiomerically pure SWCNTs might differ for the enantiomers of an analyte such as adrenaline.

$(GT)_{40}$-ssDNA was used for surface modification, because of its high exchange efficiency, colloidal stability, and sensor response. The enantiomeric purity, based on the CD spectra (Figure 5a) was calculated for both enantiomer fractions to be ∼80% (see Figure S10 in the Supporting Information).[69,70] Further surface exchange to $(GT)_{40}$-ssDNA yielded defined enantiomerically pure ssDNA-SWCNT conjugates, used for sensing experiments (Figure 5b,c). No significant differences between the stereoisomers were found, while $(GT)_{40}$-(−)-(6,5)-SWCNTs reacted with a stronger response to ascorbic acid in comparison to $(GT)_{40}$-(+)-(6,5)-SWCNTs (Figure 5d). To rule out that fluorescence changes after analyte addition (10 μM final concentration) are biased by a possible saturation, we collected dose−response curves. The results (Figure 5e,f) indicate no difference in the response to stereoisomers of adrenaline but higher fluorescence responses for the (−)-(6,5) enantiomer towards stereoisomers of ascorbic acid (see also Figure S11 in the Supporting

https://doi.org/10.1021/acs.analchem.1c00168
Anal. Chem. 2021, 93, 6446−6455

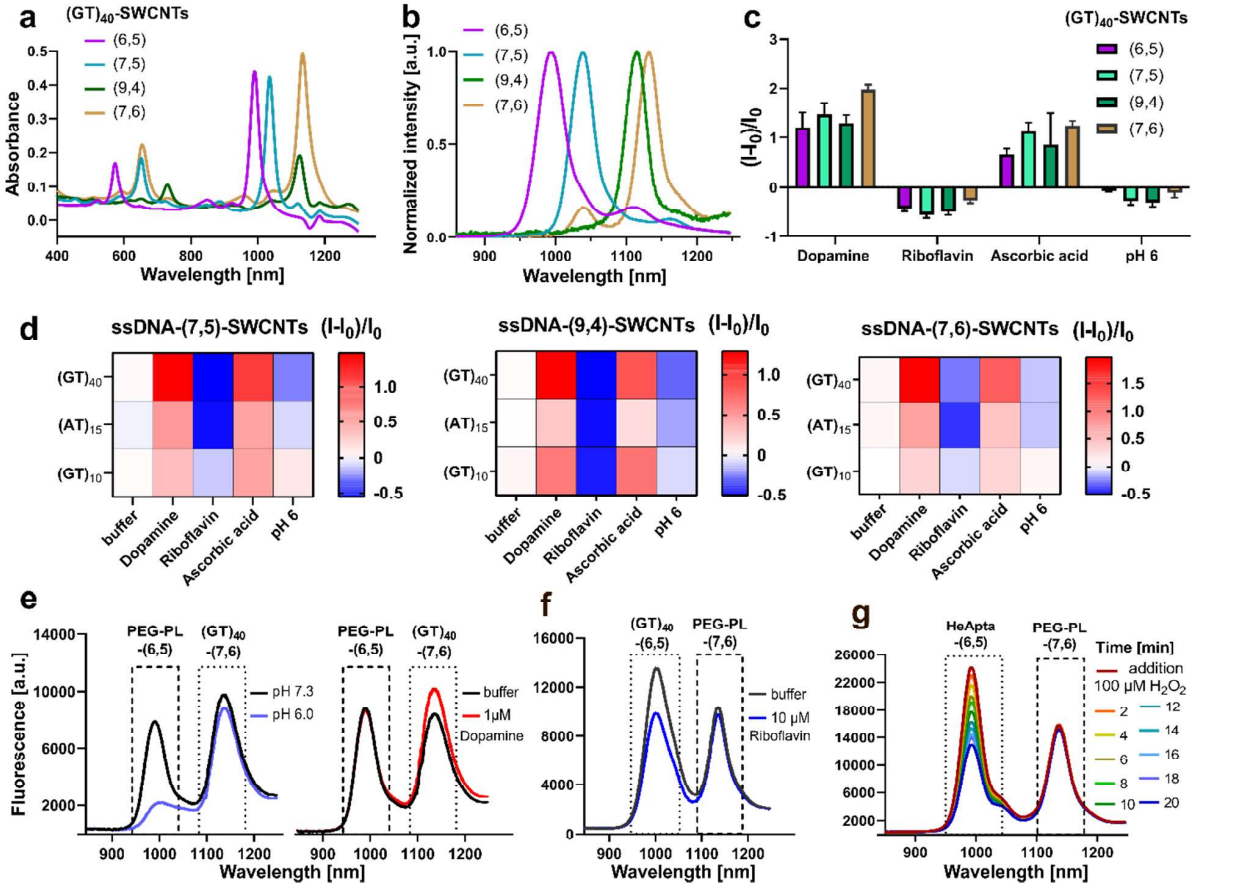

Figure 6. Multicolor and ratiometric sensing with monochiral SWCNTs: (a) absorbance spectra of different monochiral $(GT)_{40}$-SWCNTs; (b) normalized fluorescence spectra, excited at the E_{22} transition (570 nm for (6,5)-SWCNTs, 650 nm for (7,5)-SWCNTs, 730 nm for (9,4)-SWCNTs, 650 nm for (7,6)-SWCNTs); (c) similarity of the responses of monochiral $(GT)_{40}$-SWCNTs for different chiralities (mean ± SD, n = 3, c(analytes) = 10 μM); (d) fluorescence response of ssDNA-(7,5)-, ssDNA-(9,4)-, and ssDNA-(7,6)-SWCNT nanosensors to different analytes (mean, n = 3, analytes = 10 μM); (e) ratiometric sensing of pH change (blue) and dopamine (red) using PEG-PL-(6,5)-SWCNTs and $(GT)_{40}$-(7,6)-SWCNTs; (f) ratiometric riboflavin sensing with $(GT)_{40}$-(6,5)-SWCNT and PEG-PL-(7,6)-SWCNTs as a reference; (g) ratiometric H_2O_2 sensing with the hemin binding aptamer (HeApta)-(6,5)-SWCNTs and PEG-PL-(7,6)-SWCNTs as a reference.

Information). Therefore, we conclude that the sensing and recognition mechanism (for these sensors) is not significantly affected by the handedness of the SWCNT and the chirality of these analytes. This does not rule out that other sensing mechanisms differ. Most likely, the diffusion of the exciton is affected mainly by the interaction between the analyte and the SWCNT and the chirality/band gap energy plays a minor role in the fate of the exciton. As discussed already,[49] the conformation and 3D structure of the surface-adsorbed ssDNA could differ between the enantiomers[71] and might be the reason for the differences in sensing magnitudes.

Multicolor and Ratiometric Sensing. ATPE is not only feasible for (6,5)-SWCNTs but also other chiralities, which opens up the possibility for nanosensors with tunable emission wavelengths. To study the effect of the SWCNT chirality on sensing, we used ATPE-separated (7,5)-, (9,4)-, and (7,6)-SWCNTs (see Figure S12 in the Supporting Information) and exchanged the surface modification again to ssDNA. This exchange process could be performed in a way similar to that shown with (6,5)-SWCNTs, leading to monochiral $(GT)_{40}$-SWCNTs (Figure 6a). The distinct emission features of the used SWCNT chiralities (Figure 6b) highlight the potential for multicolor applications.

Detection of the analytes dopamine, pH, riboflavin, and ascorbic acid (Figure 6c) showed trends similar to those for monochiral (6,5)-SWCNTs (Figures 6d and 3c and Figure S13 in the Supporting Information). We did not find a strong effect of SWCNT chirality on the sensor responses as has been reported in a few cases for nonpurified SWCNT samples.[72] However, the results shown in Figure 6 are the first with monochiral SWCNTs for these analytes and with well-defined concentrations. In mixed samples chemical and photophysical interactions between SWCNTs of the same or different chirality might affect the fluorescence changes. From our results one can conclude that the SWCNT chirality plays a minor role in the sensitivity and mechanism of the sensors presented here. This finding does not rule out that there is a large effect of chirality for other sensor designs. However, it means that the same chemical design concepts can be applied to different chiralities, which is a big advantage. The combination of specifically modified monochiral sensors furthermore enabled ratiometric sensing (Figure 6e–g). On the basis of the variable nanosensor design (see Figures S14 and S15 in the Supporting Information) the (6,5)- and the (7,6)-SWCNTs can both be modified either with ssDNA (e.g., responsive to riboflavine or dopamine) or with poly(ethylene

https://doi.org/10.1021/acs.analchem.1c00168
Anal. Chem. 2021, 93, 6446−6455

glycol)-phospholipid (PEG-PL) as reference. Another ratiometric sensor detects H_2O_2 at micromolar concentrations (Figure 6g). Here, the SWCNT was modified with an aptamer that binds a protoporphyrin (hemin), which was shown to create an effective H_2O_2 sensor.[13] The choice of the reference signal is also flexible. For example, the "reference" SWCNT in ratiometric sensing can be either (6,5) or (7,6) (Figure 6e,f). Consequently, these chemical design concepts are universal and enable ratiometric sensors for multiple analytes.

DISCUSSION

Chemical sensors are powerful tools to detect biomolecules and shed light on biological processes. Fluorescent nanosensors are able to report local properties and provide the high spatial and temporal resolution that is needed to study for example cellular communication in networks of cells or even *in vivo*.[12,21,28] The biochemical complexity requires the detection of multiple analytes (multiplexing). Therefore, sensors/probes should have nonoverlapping fluorescence spectra. SWCNT-based NIR fluorescent nanosensors have shown great potential to detect a range of biomolecules from neurotransmitters, reactive oxygen species, proteins, lipids, and nucleic acids.[12,13,15,24] However, in most cases the samples contained multiple chiralities of SWCNTs, which leads to congested spectra and prevents multiplexing. Additionally, it is known that the SWCNT concentration affects sensor responses due to direct and photophysical chirality-dependent interactions.[20,72,73] These processes lead to a bias in sensitivity and hamper selectivity. In this work we used SWCNT purification to get close to monochiral sensors. Until now only a few studies[23,27,74] have been aimed at working with chirality pure sensors but a general concept of tunable chemical functionalization and emission wavelength was missing. This lack of progress can be explained by the experimental challenges to exchange the surface chemistry required for purification to the surface chemistry required for sensing. To obtain single SWCNT chiralities, different approaches have been developed and ATPE-based protocols recently showed great potential.[41,45,46] However, even when the surface exchange of PFO-sorted SWCNTs was recently established via CPEP[51] (corona phase exchange purification), most protocols stop when it comes to a modular surface chemistry beyond typical surfactants. We modified and optimized a DOC to ssDNA exchange process[60] and used the commercially available PEG (6 kDa) as the polymer.

For monochiral SWCNTs immobilized on a surface, we found the strongest dopamine responses for $(GT)_{40}$-SWCNTs. Most other studies in the literature used mixed-chirality SWCNT sensors in solution. In contrast, nonspecific interactions or aggregation is minimized on a surface. The evaluated K_d value for $(GT)_{40}$-(6,5)-SWCNTs of 190 nM outlines the potential for neurotransmitter imaging in fast biological prosesses.[28] Additionally, we studied to our knowledge for the first time enantiomerically pure ssDNA-SWCNTs for sensing. No significant difference was observed for the chiral catecholamine adrenaline, indicating that the analyte sensing and recognition mechanism is not affected by the stereochemical conformation of the small molecules. Our results also indicate that the handedness of the SWCNT does not change the sensing mechanism, at least for these catecholamine sensors. The current understanding is that the interaction between the catechol moiety and the phosphate backbone leads to conformational changes that affect exciton dynamics.[12] It is also known that the direct chemical environment can change the exciton diffusion substantially.[75] This indicates that changes in the surface chemistry affect exciton dynamics but do not necessarily depend on the stereochemistry. Consequently, the chiral part of the catecholamines plays a less important role. On the basis of these results one can conclude that mixed-enantiomer samples do not reduce sensor performance. However, it does not rule out that for other sensing mechanisms the handedness of the SWCNT itself plays a different role.

Sensing with (7,5)-, (9,4)-, and (7,6)-SWCNTs showed qualitatively results very similar to those for for ssDNA-(6,5)-SWCNTs: e.g. a 120−190% fluorescence increase for $(GT)_{40}$-SWCNTs after dopamine addition. It is known that the fluorescence response to analytes is influenced by the SWCNT sensor concentration, and therefore we performed these experiments with exactly the same SWCNT concentrations.[73] These experiments are the first ones outside of mixtures and report fluorescence changes in a well-defined system. They provide a much clearer picture of the effect of the heterogeneity of nanomaterials on their function. The developed approach to exchange the coating DOC of chirality-pure SWCNTs to a biopolymer is feasible for all kinds of chirality-pure samples (Figure 6). From these large-scale and stable stock solutions, various sensors can be created by methanol-based exchange,[60] which opens up the possibilities to all desirable combinations of SWCNT chiralities (emission features) and diverse surface modifications (sensing and recognition units). Technical and conceptual challenges have so far prevented the preparation of tunable monochiral sensors. In our work we show the potential and difficulties such as surfactant residues (Figure 3) in the preparation of monochiral SWCNT-based sensors. These results indicate that the surface chemistry creates the different sensing responses and enables a predictable design concept. Additionally, the nonoverlapping spectra allow a combination of multiple sensors in ratiometric and multiplexed approaches, which increases the selectivity and robustness in imaging. These advances will help to increase sensing performance for example when neurotransmitter release from cells is imaged.[12,21]

CONCLUSION

In summary, we systematically studied the properties of monochiral ssDNA-SWCNT NIR fluorescent sensors. We developed a robust surface functionalization exchange process and show how the ssDNA sequence and length affects the colloidal stability, photophysics, and sensing. These functional SWCNTs allowed us to gain insights into the effects of chirality, handedness, and residues from SWCNT separation on the sensitivity of sensors for multiple analytes. Consequently, NIR ratiometric sensors for the important analytes dopamine, riboflavin, and H_2O_2 or pH changes were demonstrated. These conceptual and mechanistic insights pave the way for tailored multicolor and ratiometric biosensing and imaging applications.

ASSOCIATED CONTENT

Supporting Information

The Supporting Information is available free of charge at https://pubs.acs.org/doi/10.1021/acs.analchem.1c00168.

https://doi.org/10.1021/acs.analchem.1c00168
Anal. Chem. 2021, 93, 6446−6455

Aqueous two-phase extraction (ATPE)-based isolation of (6,5)-SWCNTs, (6,5)-SWCNTs in 1% DOC, SWCNT length characterization by atomic force microscopy (AFM), baseline-corrected ssDNA-SWCNT absorbance spectra for colloidal stability evaluation, colloidal stability and spectral shifts of ssDNA-CoMoCat-SWCNTs, time-dependent colloidal stability of ssDNA-SWCNTs, chemical sensing with surface-immobilized multichiral ssDNA-(CoMoCat)-SWCNTs, comparison of the fluorescence intensity of monochiral and multichiral ssDNA-SWCNTs, dopamine sensing in the presence of surfactant (DOC) background, properties of (6,5)-SWCNT enantiomers, sensing with ssDNA-(6,5)-SWCNT enantiomers, separation of (7,5)-, (9,4)-, and (7,6)-SWCNTs, chemical sensing with single-chirality ssDNA-SWCNTs, nanosensor surface design for ratiometric sensing, and monochiral and ratiometric analyte sensing (PDF)

AUTHOR INFORMATION

Corresponding Author

Sebastian Kruss − *Institute of Physical Chemistry, Göttingen University, 37077 Göttingen, Germany; Physical Chemistry II, Bochum University, 44801 Bochum, Germany; Fraunhofer Institute for Microelectronic Circuits and Systems, 47057 Duisburg, Germany;* orcid.org/0000-0003-0638-9822; Email: sebastian.kruss@rub.de

Authors

Robert Nißler − *Institute of Physical Chemistry, Göttingen University, 37077 Göttingen, Germany; Physical Chemistry II, Bochum University, 44801 Bochum, Germany;* orcid.org/0000-0003-1282-2901

Larissa Kurth − *Institute of Physical Chemistry, Göttingen University, 37077 Göttingen, Germany*

Han Li − *Institute of Nanotechnology, Karlsruhe Institute of Technology (KIT), 76344 Eggenstein-Leopoldshafen, Germany*

Alexander Spreinat − *Institute of Physical Chemistry, Göttingen University, 37077 Göttingen, Germany*

Ilyas Kuhlemann − *Institute of Physical Chemistry, Göttingen University, 37077 Göttingen, Germany*

Benjamin S. Flavel − *Institute of Nanotechnology, Karlsruhe Institute of Technology (KIT), 76344 Eggenstein-Leopoldshafen, Germany;* orcid.org/0000-0002-8213-8673

Complete contact information is available at: https://pubs.acs.org/10.1021/acs.analchem.1c00168

Author Contributions

R.N. and S.K. designed and conceived the research. S.K. coordinated the project. L.K. and R.N. separated (6,5)-SWCNTs and performed and characterized surface exchange and chemical sensing experiments, R.N. performed AFM experiments, A.S. and I.K. wrote Python-based analysis scripts for absorbance and sensing evaluation. H.L. and B.S.F. separated (7,5)-, (9,4)-, and (7,6)-SWCNTs and enantiomers of (6,5)-SWCNTs. All authors contributed to the writing of the manuscript and analysis of data. All authors have given approval to the final version of the manuscript.

Notes

The authors declare no competing financial interest.

ACKNOWLEDGMENTS

This project was supported by the VW foundation. Funded by the Deutsche Forschungsgemeinschaft (DFG, German Research Foundation) under Germany's Excellence Strategy − EXC 2033 − 390677874 − RESOLV. We thank the DFG for funding within the Heisenberg program (B.S.F. and S.K.). We thank Gabriele Selvaggio for help with AFM measurements.

ABBREVIATIONS

SWCNT, single-wall carbon nanotubes; NIR, near-infrared; ATPE, aqueous two-phase extraction; DOC, sodium deoxycholate; ssDNA, single-stranded DNA; PEG-PL, poly(ethylene glycol)-phospholipid

REFERENCES

(1) Li, J.; Pandey, G. P. *Annu. Rev. Phys. Chem.* **2015**, *66* (1), 331−356.
(2) Zamolo, V. Z.; Vazquez, E.; Prato, M. *Top. Curr. Chem.* **2013**, *286*, 1−72.
(3) Nanot, S.; Hároz, E. H.; Kim, J. H.; Hauge, R. H.; Kono, J. O. *Adv. Mater.* **2012**, *24* (36), 4977−4994.
(4) Amori, A. R.; Hou, Z.; Krauss, T. D. *Annu. Rev. Phys. Chem.* **2018**, *69* (1), 81−100.
(5) O'Connell, M. J.; Bachilo, S. M.; Huffman, C. B.; Moore, V. C.; Strano, M. S.; Haroz, E. H.; Rialon, K. L.; et al. *Science* **2002**, *297* (5581), 593−596.
(6) Bachilo, S. M.; Strano, M. S.; Kittrell, C.; Hauge, R. H.; Smalley, R. E.; Weisman, R. B. *Science* **2002**, *298*, 2361−2367.
(7) Kruss, S.; Hilmer, A. J.; Zhang, J.; Reuel, N. F.; Mu, B.; Strano, M. S. *Adv. Drug Delivery Rev.* **2013**, *65* (15), 1933−1950.
(8) Hong, G.; Diao, S.; Antaris, A. L.; Dai, H. *Chem. Rev.* **2015**, *115* (19), 10816−10906.
(9) Farrera, C.; Torres Andón, F.; Feliu, N. C. *ACS Nano* **2017**, *11* (11), 10637−10643.
(10) Hendler-Neumark, A.; Bisker, G. *Sensors* **2019**, *19* (24), 5403.
(11) Dinarvand, M.; Elizarova, S.; Daniel, J.; Kruss, S. *ChemPlusChem* **2020**, *85* (7), 1465−1480.
(12) Kruss, S.; Salem, D. P.; Vuković, L.; Lima, B.; Vander Ende, E.; Boyden, E. S.; Strano, M. S. *Proc. Natl. Acad. Sci. U. S. A.* **2017**, *114* (8), 1789−1794.
(13) Wu, H.; Nißler, R.; Morris, V.; Herrmann, N.; Hu, P.; Jeon, S.; Kruss, S.; Giraldo, J. P. *Nano Lett.* **2020**, *20* (4), 2432−2442.
(14) Lew, T. T. S.; Koman, V. B.; Silmore, K. S.; Seo, J. S.; Gordiichuk, P.; Kwak, S.-Y.; Park, M.; et al. *Nat. Plants* **2020**, *6* (4), 404−415.
(15) Harvey, J. D.; Jena, P. V.; Baker, H. A.; Zerze, G. H.; Williams, R. M.; Galassi, T. V.; Roxbury, D.; Mittal, J.; Heller, D. A. *Nat. Biomed. Eng.* **2017**, *1* (4), 1−43.
(16) Williams, R. M.; Lee, C.; Galassi, T. V.; Harvey, J. D.; Leicher, R.; Sirenko, M.; Dorso, M. A.; Shah, J.; Olvera, N.; Dao, F. *Sci. Adv.* **2018**, *4* (4), eaaq1090.
(17) Kim, J. H.; Heller, D. A.; Jin, H.; Barone, P. W.; Song, C.; Zhang, J.; Trudel, L. J.; Wogan, G. N.; Tannenbaum, S. R.; Strano, M. S. *Nat. Chem.* **2009**, *1* (6), 473−481.
(18) Gravely, M.; Safaee, M. M.; Roxbury, D. *Nano Lett.* **2019**, *19* (9), 6203−6212.
(19) Beyene, A. G.; Delevich, K.; Del Bonis-O'Donnell, J. T.; Piekarski, D. J.; Lin, W. C.; Thomas, A. W.; et al. *Sci. Adv.* **2019**, *5* (7), eaaw3108.
(20) Kruss, S.; Landry, M. P.; Vander Ende, E.; Lima, B. M. A.; Reuel, N. F.; Zhang, J.; Nelson, J.; Mu, B.; Hilmer, A.; Strano, M. *J. Am. Chem. Soc.* **2014**, *136* (2), 713−724.
(21) Dinarvand, M.; Neubert, E.; Meyer, D.; Selvaggio, G.; Mann, F. A.; Erpenbeck, L.; Kruss, S. *Nano Lett.* **2019**, *19* (9), 6604−6611.
(22) Harvey, J. D.; Baker, H. A.; Ortiz, M. V.; Kentsis, A.; Heller, D. *ACS Sensors* **2019**, *4* (5), 1236−1244.

(23) Galassi, T. V.; Jena, P. V.; Shah, J.; Ao, G.; Molitor, E.; Bram, Y.; Frankel, A.; Park, J.; Jessurun, J.; Ory, D. S.; et al. *Sci. Transl. Med.* **2018**, *10* (461), eaar2680.
(24) Bisker, G.; Dong, J.; Park, H. D.; Iverson, N. M.; Ahn, J.; Nelson, J. T.; Landry, M. P.; Kruss, S.; Strano, M. S. *Nat. Commun.* **2016**, *7*, 1−14.
(25) Bisker, G.; Bakh, N. A.; Lee, M. A.; Ahn, J.; Park, M.; O'Connell, E. B.; Iverson, N. M.; Strano, M. S. *ACS Sensors* **2018**, *3* (2), 367−377.
(26) Zubkovs, V.; Schuergers, N.; Lambert, B.; Ahunbay, E.; Boghossian, A. A. *Small* **2017**, *13* (42), 1701654.
(27) Nißler, R.; Bader, O.; Dohmen, M.; Walter, S. G.; Noll, C.; Selvaggio, G.; Groß, U.; Kruss, S. *Nat. Commun.* **2020**, *11* (1), 1−12.
(28) Meyer, D.; Hagemann, A.; Kruss, S. *ACS Nano* **2017**, *11* (4), 4017−4027.
(29) Wang, J.-Q.; Ding, F.; Luo, D.; Zhang, D.; Wang, X.; Yang, J.; Bai, X.; Peng, F.; Xu, Z.; Wei, J.; et al. *Nature* **2014**, *510* (7506), 522−524.
(30) An, H.; Kumamoto, A.; Takezaki, H.; Ohyama, S.; Qian, Y.; Inoue, T.; Ikuhara, Y.; Chiashi, S.; Xiang, R.; Maruyama, S. *Nanoscale* **2016**, *8* (30), 14523−14529.
(31) Yang, F.; Wang, M.; Zhang, D.; Yang, J.; Zheng, M.; Li, Y. *Chem. Rev.* **2020**, *120* (5), 2693−2758.
(32) Zheng, M. *Top. Curr. Chem.* **2017**, *375* (1), 1−36.
(33) Arnold, M. S.; Green, A. A.; Hulvat, J. F.; Stupp, S. I.; Hersam, M. C. *Nat. Nanotechnol.* **2006**, *1* (1), 60−65.
(34) Ghosh, S.; Bachilo, S. M.; Weisman, R. B. *Nat. Nanotechnol.* **2010**, *5* (6), 443−450.
(35) Liu, H.; Nishide, D.; Tanaka, T.; Kataura, H. *Nat. Commun.* **2011**, *2*, 1−8.
(36) Flavel, B. S.; Kappes, M. M.; Krupke, R.; Hennrich, F. *ACS Nano* **2013**, *4*, 3557−3564.
(37) Tvrdy, K.; Jain, R. M.; Han, R.; Hilmer, A. J.; Mcnicholas, T. P.; Strano, M. S. *ACS Nano* **2013**, *7*, 1779−1789.
(38) Tu, X.; Manohar, S.; Jagota, A.; Zheng, M. *Nature* **2009**, *460* (7252), 250−253.
(39) Fagan, J. A.; Khripin, C. Y.; Silvera Batista, C. A.; Simpson, J. R.; Hároz, E. H.; Hight Walker, A. R.; Zheng, M. *Adv. Mater.* **2014**, *26* (18), 2800−2804.
(40) Khripin, C. Y.; Fagan, J. A.; Zheng, M. *J. Am. Chem. Soc.* **2013**, *135* (18), 6822−6825.
(41) Li, H.; Gordeev, G.; Garrity, O.; Reich, S.; Flavel, B. S. *ACS Nano* **2019**, *13*, 2567−2578.
(42) Zheng, M.; Jagota, A.; Strano, M. S.; Santos, A. P.; Barone, P.; Chou, S. G.; Diner, B. A.; Dresselhaus, M. S.; Mclean, R. S.; Onoa, G. B.; et al. *Science* **2003**, *302*, 1545−1549.
(43) Zheng, M.; Jagota, A.; Semke, E. D.; Diner, B. A.; McLean, R. S.; Lustig, S. R.; Richardson, R. E.; Tassi, N. G. *Nat. Mater.* **2003**, *2* (5), 338−342.
(44) Nish, A.; Hwang, J. Y.; Doig, J.; Nicholas, R. J. *Nat. Nanotechnol.* **2007**, *2* (10), 640−646.
(45) Fagan, J. A. *Nanoscale Adv.* **2019**, *1* (9), 3307−3324.
(46) Li, H.; Gordeev, G.; Garrity, O.; Peyyety, N. A.; Selvasundaram, P. B.; Dehm, S.; Krupke, R.; Cambré, S.; Wenseleers, W.; Reich, S.; et al. *ACS Nano* **2020**, *14* (1), 948−963.
(47) Wei, L.; Flavel, B. S.; Li, W.; Krupke, R.; Chen, Y. *Nanoscale* **2017**, *9* (32), 11640−11646.
(48) Sims, C. M.; Fagan, J. *Carbon* **2020**, *165*, 196−203.
(49) Ao, G.; Streit, J. K.; Fagan, J. A.; Zheng, M. *J. Am. Chem. Soc.* **2016**, *138* (51), 16677−16685.
(50) Lyu, M.; Meany, B.; Yang, J.; Li, Y.; Zheng, M. *J. Am. Chem. Soc.* **2019**, *141* (51), 20177−20186.
(51) Nißler, R.; Mann, F. A.; Preiß, H.; Selvaggio, G.; Herrmann, N.; Kruss, S. *Nanoscale* **2019**, *11* (23), 11159−11166.
(52) Mann, F. A.; Horlebein, J.; Meyer, N. F.; Meyer, D.; Thomas, F.; Kruss, S. *Chem. - Eur. J.* **2018**, *24*, 12241−12245.
(53) Polo, E.; Nitka, T.; Neubert, E.; Erpenbeck, L.; Vuković, L.; Kruss. *ACS Appl. Mater. Interfaces* **2018**, *10*, 17693−17703.
(54) Mann, F. A.; Lv, Z.; Grosshans, J.; Opazo, F.; Kruss, S. *Angew. Chem., Int. Ed.* **2019**, *58*, 11469−11473.
(55) Welsher, K.; Liu, Z.; Sherlock, S. P.; Robinson, J. T.; Chen, Z.; Daranciang, D.; Dai, H. *Nat. Nanotechnol.* **2009**, *4* (11), 773−780.
(56) Mann, F. A.; Herrmann, N.; Opazo, F.; Kruss, S. *Angew. Chem., Int. Ed.* **2020**, *59*, 11732−11738.
(57) Mann, F. A.; Herrmann, N.; Meyer, D.; Kruss, S. *Sensors* **2017**, *17*, 1521.
(58) Polo, E.; Kruss, S. *J. Phys. Chem. C* **2016**, *120* (5), 3061−3070.
(59) Nißler, R.; Mann, F. A.; Chaturvedi, P.; Horlebein, J.; Meyer, D.; Vukovic, L.; Kruss, S. *J. Phys. Chem. C* **2019**, *123*, 4837−4847.
(60) Streit, J. K.; Fagan, A.; Zheng, M. *Anal. Chem.* **2017**, *89*, 10496−10503.
(61) Pan, J.; Zhang, H.; Cha, T.-G.; Chen, H.; Choi, J. H. *Anal. Chem.* **2013**, *85* (17), 8391−8396.
(62) Streit, J. K.; Bachilo, S. M.; Ghosh, S.; Lin, C.; Weisman, R. B. *Nano Lett.* **2014**, *14*, 1530−1536.
(63) Sanchez, S. R.; Bachilo, S. M.; Kadria-Vili, Y.; Lin, C. W.; Weisman, R. B. *Nano Lett.* **2016**, *16* (11), 6903−6909.
(64) Schöppler, F.; Mann, C.; Hain, T. C.; Neubauer, F. M.; Privitera, G.; Bonaccorso, F.; Chu, D.; Ferrari, A. C.; Hertel, T. *J. Phys. Chem. C* **2011**, *115* (30), 14682−14686.
(65) Zhang, J.; Landry, M. P.; Barone, P. W.; Kim, J. H.; Lin, S.; Ulissi, Z. W.; Lin, D.; Mu, B.; Boghossian, A. A.; Hilmer, A. J.; et al. *Nat. Nanotechnol.* **2013**, *8* (12), 959−968.
(66) O'Connell, M.; Bachilo, S.; Huffman, C.; Moore, C.; et al. *Science* **2002**, *297*, 593−596.
(67) Meyer, D.; Telele, S.; Zelená, A.; Gillen, A. J.; Antonucci, A.; Neubert, E.; Nißler, R.; Boghossian, A. A.; et al. *Nanoscale* **2020**, *12*, 9104−9115.
(68) Yang, Y.; Sharma, A.; Noetinger, G.; Zheng, M.; Jagota, A. *J. Phys. Chem. C* **2020**, *124* (16), 9045−9055.
(69) Sato, N.; Tatsumi, Y.; Saito, R. *Phys. Rev. B* **2017**, *95* (15), 1−11.
(70) Wei, X.; Tanaka, T.; Hirakawa, T.; Yomogida, Y.; Kataura, H. *J. Am. Chem. Soc.* **2017**, *139* (45), 16068−16071.
(71) Zheng, Y.; Alizadehmojarad, A. A.; Bachilo, S. M.; Kolomeisky, A. B.; Weisman, R. B. *ACS Nano* **2020**, *14* (9), 12148−12158.
(72) Salem, D. P.; Landry, M. P.; Bisker, G.; Ahn, J.; Kruss, S.; Strano, M. S. *Carbon* **2016**, *97*, 147−153.
(73) Landry, M. P.; Vukovic, L.; Kruss, S.; Bisker, G.; Landry, A. M.; Islam, S.; Jain, R.; Schulten, K.; Strano, M. S. *J. Phys. Chem. C* **2015**, *119*, 10048−10058.
(74) Giraldo, J. P.; Landry, M. P.; Kwak, S. Y.; Jain, R. M.; Wong, M. H.; Iverson, N. M.; Ben-Naim, M.; Strano, M. S. *Small* **2015**, *11* (32), 3973−3984.
(75) Siitonen, A. J.; Tsyboulski, D. A.; Bachilo, S. M.; Weisman, R. *Nano Lett.* **2010**, *10* (5), 1595−1599.

https://doi.org/10.1021/acs.analchem.1c00168
Anal. Chem. 2021, 93, 6446−6455

5.2.4 Discussion

Manuscript III introduces a general and predictable design concept for chirality-pure SWCNT sensors, by using aqueous two-phase extraction (ATPE) and further solvent-based surface exchange. This, in its consequence, enables tailored NIR-fluorescent sensors, which are in principle freely selectable in emission wavelength (through the used SWCNT chirality) and analyte sensitivity (through the applied surface modification).

In general, multiple approaches are known (Section 3.5) to separate SWCNTs in aqueous systems.[16,57,75] ATPE was introduced in 2013 by Zheng *et al.*[98] and since then continuously improved and optimized to yield a variety of different SWCNT chiralities. This fast, inexpensive and straightforward purification technique does not require particular chromatography or ultracentrifugation equipment, thus allowing implementation in non-specialized labs. Within the ATPE, two general approaches are described: either using DNA-[103,105] or surfactant-[102,174] coated SWCNTs. But for the subsequent sensor modification, the exchange of DNA to variable biopolymers seemed to be more intricate than the established routes exchanging surfactant-SWCNTs. Therefore, ATPE yielding surfactant-stabilized SWCNTs emerged as suitable basis for chirality-pure SWCNT sensors with a flexible design concept. Especially the ATPE variation described by Li *et al.* in 2019 leads to a controllable separation process, since surfactant-dispersed SWCNT-partitioning was mediated through pH modulations.[101] This reversible process can be performed until the desired SWCNT composition is obtained. Previous approaches in contrast added surfactants to the ATPE system, making further corrections difficult. After obtaining chirality-pure (6,5)-SWCNTs, a method was required to exchange the surface modification to a system that is suited for biosensing applications. Multiple exchange protocols, including e.g. precipitation, molecular weight cut-off filtration or dialysis were tested, but failed to yield chirality-pure SWCNTs that could be used for biosensing. As already discussed for **Manuscript II**, the main difficulty was again to prevent aggregation of chirality-pure SWCNTs during surface replacement through enhanced van der Waal interactions. Only the methanol-supported surface exchange, following the steps introduced by Streit *et al.*, enabled a fast and sufficient way to coat the SWCNTs with various DNA polymers.[175] This combination of scalable SWCNT purification with fast surface exchange facilitated the assembly of various monochiral nano-conjugates and the possibility to study their colloidal, photophysical and sensing properties. **Manuscript III** can therefore be seen as the first conclusive report for chemical sensing with chirality-pure SWCNTs. Other studies like one

by Giraldo *et al.*[176] investigated in the direction of biosensing with purified SWCNTs, but next to an elaborate and low yield process, spectral congestion was not solved. Galassi *et al.*[115] performed lipid detection with purified DNA-(9,4)-SWCNTs obtained by *recognition*-DNA ATPE. However, surface modification was limited to the one used for SWCNT purification and does not allow a general modular design.

The data presented in **Manuscript III** furthermore does not suggests a clear trend or dependency of the SWCNT chirality for chemical sensing. However, previous studies with multichiral SWCNT probes observed a chirality-dependent effect.[177] Beyene *et al.*[156] reported enormous differences in fluorescence modulations upon analyte interaction analyzed by NIR-spectroscopy, but far less prominent during NIR-imaging.[121] Those sensing differences between the SWCNT chiralities could have multiple reasons, besides specific DNA configurations on the SWCNTs. For example it is known that the SWCNT concentration plays an important role during sensing, as well as the initial fluorescence quenching state of the DNA-SWCNTs.[156,178] These factors do vary in multichiral SWCNT samples, but can be highly controlled in monochiral systems. Since the diameter of the tested SWCNTs chiralities in **Manuscript III** were in a narrow range of 0.75 nm (6,5) to 0.91 nm (9,4), larger species would be required to evaluate if the postulated independency holds true. On the other hand, specific *recognition*-[36] or *resolving*[105]-DNA sequences could form more complex and stronger interactions with the SWCNTs, influencing the chemical sensing concept.[177,179]

When both approaches from **Manuscript II** and **Manuscript III** are compared, it can be summarized that both display successful routes towards chirality-pure SWCNT sensors. CPEP (**Manuscript II**) enables the assembly from PFO-sorted SWCNTs out of organic solvents. Its lower yield compared to the result of the workflow from **Manuscript III** makes SWCNT purification and exchange in aqueous systems the preferable technique to obtain tailored biosensors. Therefore, the approach from **Manuscript III** was further used in **Manuscript IV** and **Manuscript VI** to enable ratiometric and hyperspectral sensing. Moreover, Spreinat *et al.*[180] demonstrated recently chemical sensing with purified and further sp^3-defected ssDNA-SWCNTs by means of the in **Manuscript III** introduced principles. This highlights the possible advantages and applications of chirality-pure sensors in the future.

5.3 Tailored SWCNT-Sensors for Bacteria Detection

In the light of global healthcare problems like arising antibiotic resistant bacteria, novel diagnostic tools are needed for fast and specific pathogen detection, hence enabling optimal treatment. Conventionally used methods for identification of pathogenic bacteria made tremendous progress in the last decades.[181] Routine diagnostics in the hospital use bacterial cultivation combined with fast detection approaches like mass spectrometry (MS) to access bacteria's chemical composition or polymerase chain reaction (PCR) to decode their genetic material.[182,183] This allows determination of the respective pathogen within several hours to days.[181] However, the faster a diagnostic tool can be, the sooner a treatment can be delivered, which correlates e.g. in case of acute sepsis directly with the survival rate of the patients.[184] Moreover, novel approaches for *in situ* diagnostics could facilitate the readout and detection of pathogens at the location where they arise. Most desirably, an optical readout method could be performed through tissue, without the need of taking a sample (biopsy). This could ultimately lead to smart surfaces (e.g. on wound patches), implants in arthroplasty or stent modifications, that report a potential infection status in real time. As already introduced beforehand, nanosensors based on SWCNTs could be a valuable tool for such purposes, since they can report chemical information with great spatiotemporal resolution and their fluorescence emission in the NIR biological transparency window allows for optical tissue penetration. However, such approaches were not developed so far. The aim of the following **Manuscript IV**, entitled "*Remote near infrared identification of pathogens with multiplexed nanosensors*" is to introduce SWCNT sensors, specifically tailored to detect bacterial motives. Furthermore, it will be evaluated, whether such sensors can be used for remote (camera-assisted) stand-off detection. Moreover, it will be tested if SWCNT sensors are able to detect and discriminate different bacteria. Lastly, a hyperspectral bacteria sensing method should be developed, by combining tailored surface chemistry and purified SWCNTs.

5.3.1 Remote Near-Infrared Identification of Pathogens with Multiplexed Nanosensors

Manuscript IV was published in the following journal:

Robert Nißler, Oliver Bader, Maria Dohmen, Sebastian G. Walter, Christine Noll, Gabriele Selvaggio, Uwe Groß and Sebastian Kruss*

"Remote near infrared identification of pathogens with multiplexed nanosensors"

Nature Communications, **2020**, 11, 1, 1-12

The article is available at: DOI: 10.1038/s41467-020-19718-5
* Corresponding author

Responsibility assignment: R.N. and S.K. designed and conceived the research. S.K. coordinated the project. O.B., C.N., and U.G. collected the clinical bacteria isolates, characterized them, and helped with bacterial detection experiments. S.G.W. helped with human synovia collection and related sensing experiments. G.S. exfoliated EB-NS and performed SEM characterization. M.D. developed the simulation with input from S.K.. R.N. performed all other experiments, analyzed the data and wrote the manuscript, with input from S.K..

nature COMMUNICATIONS

ARTICLE

https://doi.org/10.1038/s41467-020-19718-5 OPEN

Remote near infrared identification of pathogens with multiplexed nanosensors

Robert Nißler[1,2], Oliver Bader[3], Maria Dohmen[1], Sebastian G. Walter[4], Christine Noll[3], Gabriele Selvaggio[1,2], Uwe Groß[3] & Sebastian Kruss[1,2,5]✉

Infectious diseases are worldwide a major cause of morbidity and mortality. Fast and specific detection of pathogens such as bacteria is needed to combat these diseases. Optimal methods would be non-invasive and without extensive sample-taking/processing. Here, we developed a set of near infrared (NIR) fluorescent nanosensors and used them for remote fingerprinting of clinically important bacteria. The nanosensors are based on single-walled carbon nanotubes (SWCNTs) that fluoresce in the NIR optical tissue transparency window, which offers ultra-low background and high tissue penetration. They are chemically tailored to detect released metabolites as well as specific virulence factors (lipopolysaccharides, siderophores, DNases, proteases) and integrated into functional hydrogel arrays with 9 different sensors. These hydrogels are exposed to clinical isolates of 6 important bacteria (*Staphylococcus aureus*, *Escherichia coli*,...) and remote (≥25 cm) NIR imaging allows to identify and distinguish bacteria. Sensors are also spectrally encoded (900 nm, 1000 nm, 1250 nm) to differentiate the two major pathogens *P. aeruginosa* as well as *S. aureus* and penetrate tissue (>5 mm). This type of multiplexing with NIR fluorescent nanosensors enables remote detection and differentiation of important pathogens and the potential for smart surfaces.

[1] Institute of Physical Chemistry, Göttingen University, Göttingen, Germany. [2] Physical Chemistry II, Bochum University, Bochum, Germany. [3] Institute of Medical Microbiology, University Medical Center Göttingen, Göttingen, Germany. [4] Department for Cardiothoracic Surgery and Intensive Care, University Hospital Cologne, Cologne, Germany. [5] Fraunhofer Institute for Microelectronic Circuits and Systems, Duisburg, Germany. ✉email: sebastian.kruss@rub.de

Microbial infections are one of the major causes of death in a global context. Often no or only limited diagnostic tools are available and treatment options are vanishing due to emerging antibiotic resistances[1,2]. One approach to counteract infections is their early detection and therefore there is a great need for fast and specific diagnostic tools. Additionally, tailored and personalized treatment pathways and antibiotic stewardship becomes increasingly important to reduce infection rates in hospitals and save lives and resources[3,4].

State-of-the art microbiological diagnosis[5] of bacteria relies on phenotyping characterization via cultivation on chromogenic media[6] in combination with DNA detection (PCR)[7] or mass spectrometry (MS) approaches[8]. Typical diagnosis times of these methods are on the order of several hours to several days[5]. Advancements in Raman spectroscopy and microfluidic lab-on-a-chip approaches aim to shorten time for diagnosis[9,10]. However, all these mentioned approaches require sampling, transport, purification, and/or cultivation. Therefore, not the analytical method itself limits time for diagnosis but rather multiple pre-analytical steps, which are necessary to receive, purify and process the sample. Label-free sensors could address this challenge by direct detection and identification of bacterial pathogens but need to be highly sensitive and selective to cover the diversity of potential pathogens and sample backgrounds[11–13].

Nanomaterials have been used to create highly sensitive biosensors[14,15]. For bacteria detection, different concepts including immobilization of antibodies against bacterial surface receptors and tailoring of electrostatic interactions have been employed[16]. However, remote optical detection with the desired selectivity and sensitivity remains a challenge. A versatile nanoscale building block for optical sensors are semiconducting single-walled carbon nanotubes (SWCNTs). They fluoresce without bleaching in the near infrared (NIR, 900–1700 nm) regime of the electromagnetic spectrum, thus offering tissue transparency due to decreased absorption and scattering, as well as ultra-low background fluorescence[17–19]. SWCNTs have been used as non-bleaching optical probes/sensors that are sensitive towards their chemical environment[20]. Such sensors were used to detect important small signaling molecules, nucleic acids, and proteins[21–24]. Furthermore, imaging many of them provides additional spatiotemporal information about biological processes[25–27]. The key challenge in sensor development is tailoring their selectivity and sensitivity. SWCNTs have therefore been non-covalently functionalized with, e.g., proteins[28,29], peptides[30,31], single stranded (ss)DNA[30,32] or lipids[33] to achieve this goal.

The sensor requirements for the detection of bacteria are very high because infections/contaminations are a highly complex biochemical process and for example biofilm-mediated infections on implants are difficult to detect because samples are not directly accessible[34,35]. Additionally, one sensor alone could not be selective enough and the concept of a chemical nose appears to be more promising[36]. Therefore, fast and contact-free local detection without extensive sample taking and processing could advance the field of personalized pathogen diagnostics.

Here, we developed a set of NIR fluorescent nanosensors to remotely/directly identify and fingerprint clinically important bacteria.

Results

NIR fluorescent nanosensors for various bacterial motifs. Bacteria are known to alter their chemical environment through the release of signaling molecules, enzymes, and metabolites[37]. Such molecules provide information about the nature of the bacterium. Especially virulence factors (e.g. exo- or endotoxins), signaling molecules (e.g. autoinducer or quorum sensing peptides), and matrix/biofilm materials can indicate the presence of specific bacteria[37–40]. However, a single molecular marker alone is unlikely to identify or at least narrow down bacterial species. Our approach is based on the idea that simultaneous detection of multiple analytes similar to an artificial nose increases sensitivity and selectivity of the analytical approach[36].

We therefore developed multiple NIR fluorescent nanosensors for different targets released by bacteria and incorporated them into biocompatible hydrogels (HG) onto which bacteria are plated (Fig. 1, step 1). Nine nanosensors were combined in a hydrogel array, which is remotely monitored by NIR stand-off detection (Fig. 1, step 2). This spatially encoded sensor pattern provides a NIR fingerprint of bacterial activity that is analyzed via multivariate data analysis (Fig. 1, step 3). In addition to spatial encoding, sensors could also be spectrally encoded (Fig. 1, step 4).

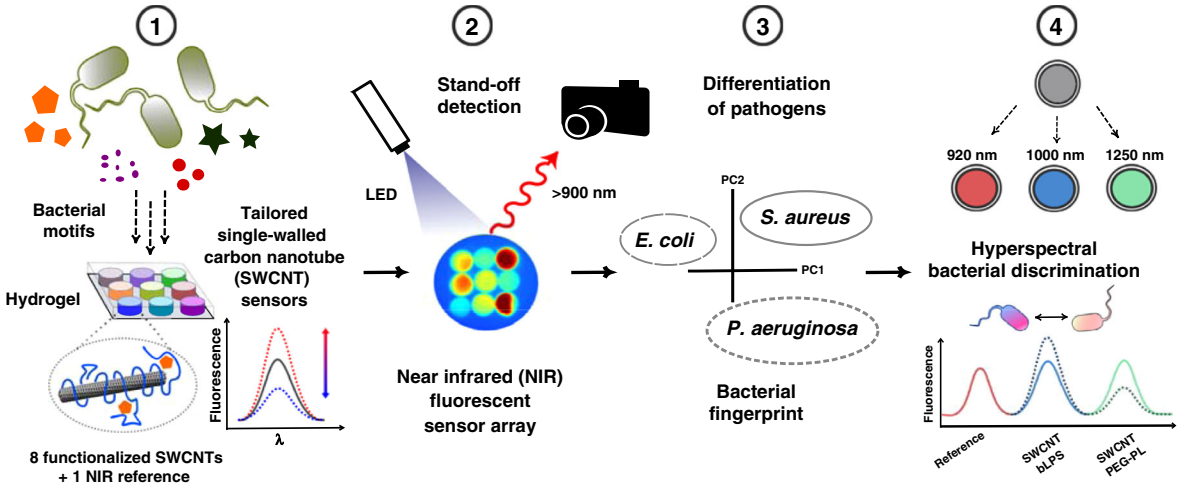

Fig. 1 Remote detection of pathogens. (1) Multiple nanosensors based on NIR fluorescent single-walled carbon nanotubes (SWCNTs) are synthesized in such a way that they change their fluorescence signal in response to bacterial metabolites and virulence factors (cell wall components, iron chelating molecules, secretory enzymatic activity). (2) Eight fluorescent nanosensors and one NIR fluorescent reference are incorporated into a polyethylene glycol hydrogel array that is remotely monitored in the NIR. (3) Bacteria growing on top of this hydrogel release molecules that change the (spatial) sensor array fingerprint, which allows us to differentiate important pathogens. (4) By using chirality-purified SWCNTs, multiple sensors can be spectrally encoded and used for hyperspectral differentiation of important bacteria such as *Staphylococcus aureus*.

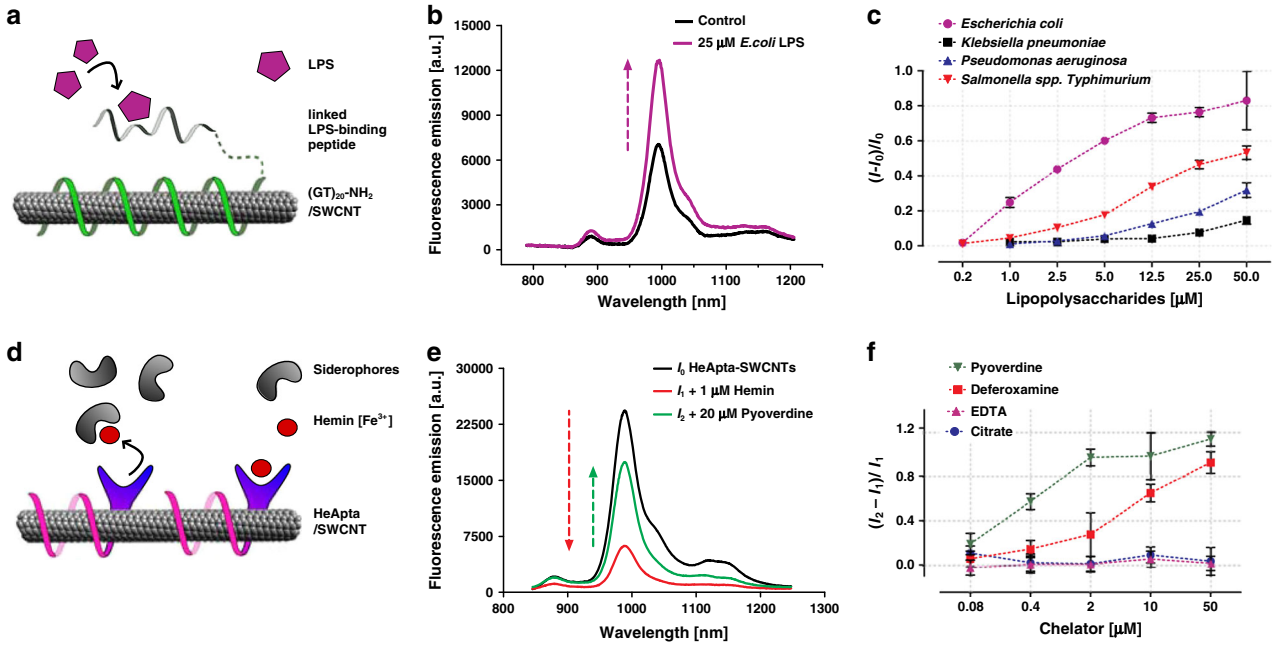

Fig. 2 NIR fluorescent nanosensors of virulence factors. a Design of an endotoxin sensor for bacterial lipopolysaccharides (LPS). NH_2-$(GT)_{20}$-ssDNA colloidally stabilizes the SWCNTs and was linked to a LPS-binding peptide via SMCC (succinimidyl 4-(N-maleimidomethyl) cyclohexane-1-carboxylate) chemistry. **b** NIR fluorescence increase of bindLPS-(bLPS)-SWCNTs after addition of 25 µM *E. coli* LPS. **c** Dose–response curve of bLPS sensors for LPS from *E. coli*, *K. pneumoniae*, *P. aeruginosa* and *Salmonella* spp. (n = 3 independent experiments, mean ± SD). **d** Design of the siderophore sensor. An aptamer (HeApta) binds hemin, which brings Fe^{3+} into the proximity of the SWCNT and quenches it. Siderophores can reverse this effect by removing iron (Fe^{3+}), which increases fluorescence again. **e** Exemplary spectra of HeApta-SWCNTs. Addition of hemin (I_0 to I_1) quenches their fluorescence and addition of siderophores (pyoverdine) increases it again (I_1 to I_2). **f** Calibration of chelating agents with different stability constants (K_f) for iron (Fe^{3+}), added to HeApta-SWCNTs with 1 µM hemin concentration. Pyoverdine ($K_f = 10^{32}$), deferoxamine ($K_f = 10^{30}$), EDTA ($K_f = 10^{25}$), hemin ($K_f = 10^{22}$), citrate ($K_f = 10^{12}$)[78,89–91] ($n = 3$ independent experiments, mean ± SD).

The mentioned sensor array consists of eight SWCNT-based NIR fluorescent sensors of which four were tailored for specific bacterial targets and the other four are generic lower-selectivity sensors. Additionally, one very stable NIR fluorophore ($CaCuSi_4O_{10}$, Egyptian Blue-nanosheets, EB-NS) served as reference. For the specific sensors, we used rational design strategies to detect bacterial compounds and virulence-related enzymatic activity. The rational of using a mixture of specific and non-specific sensors was to reduce/account for background sensor responses in the final analysis. Additionally, the chemical complexity of the secreted substances makes it difficult to predict the overall performance and increasing the number of sensors appeared beneficial.

First, we developed a sensor that detects lipopolysaccharides (LPS), an endotoxin, which is part of the cell wall of Gram-negative bacteria and is shed into the bacterial environment[37,41]. For this purpose, a LPS-binding peptide[42–44] was conjugated to ssDNA/SWCNTs[30,45] (Fig. 2a, Supplementary Fig. S1a). The DNA adsorbs onto the SWCNT and translates conformational changes by LPS binding to the peptide into fluorescence changes. After optimization of the conjugation parameters (Supplementary Fig. S1), a colloidally stable conjugate could be created (bLPS-SWCNT). The NIR fluorescence of bLPS-SWCNTs increased (Fig. 2b) after the addition of *E. coli* LPS (76% for 25 µM). This fluorescence increase was concentration dependent and saturated at > 10 µM LPS (Fig. 2c) with a K_d value of 1.87 µM (Supplementary Fig. S2). LPS from *Salmonella* spp., *P. aeruginosa* and *K. pneumoniae* showed similar but smaller fluorescence responses, indicating that the exact LPS structure[46] plays a role in fluorescence modulation. bLPS-SWCNTs also detect LPS when adsorbed onto a glass surface, which demonstrates that sensing is not based on aggregation or other colloidal effects in solution (Supplementary Fig. S2c).

Bacteria also release siderophores, which capture essential elements (e.g. iron or zinc) from their environment. These siderophores are important virulence factors and therefore targets for detecting bacterial pathogens[47,48]. Consequently, we designed a NIR sensor for siderophores (Fig. 2d) that is based on the idea that the removal of certain ions from the proximity of the SWCNT changes its fluorescence. Here, a hemin-binding ssDNA aptamer (HeApta) was adsorbed onto SWCNTs. Hemin addition quenched the SWCNT fluorescence, which can be attributed to the proximity of the iron (Fe^{3+}), complexed in the protoporphyrin IX (hemin), close to the SWCNT surface[24,49–51]. Stronger chelating agents such as the siderophore pyoverdine from *Pseudomonas fluorescens* (Fig. 2e, Supplementary Fig. S3) removed the iron and dequenched the NIR fluorescence. An optimal ratio of quenching by hemin and dequenching by pyoverdine addition was found at 1 µM hemin added to HeApta-SWCNTs ($A_{993nm} = 0.1$ for (6,5)-SWCNTs) (Supplementary Fig. S3b, c). This optimized siderophore sensor provides a concentration-dependent fluorescence increase for strong chelators ($K_f > 10^{30}$) such as pyoverdine ($K_d = 0.26$ µM) or deferoxamine ($K_d = 7.15$ µM) (Supplementary Fig. S3d). In contrast, weaker chelators such as ethylenediaminetetraacetic acid (ETDA) or citrate did not dequench hemin-HeApta-SWCNTs (Fig. 2f).

Integration in hydrogel sensor arrays. The rationally designed nanosensors for LPS and for siderophores are colloidally stable in solution. However, in complex media with many biomolecules, immobilized sensors should be even more resistant to unspecific effects such as aggregation or general degradation. This is especially relevant for sensors targeting enzymatic activity that rely on degradation of the organic functionalization around the SWCNT and would be prone to aggregation and precipitation in solution.

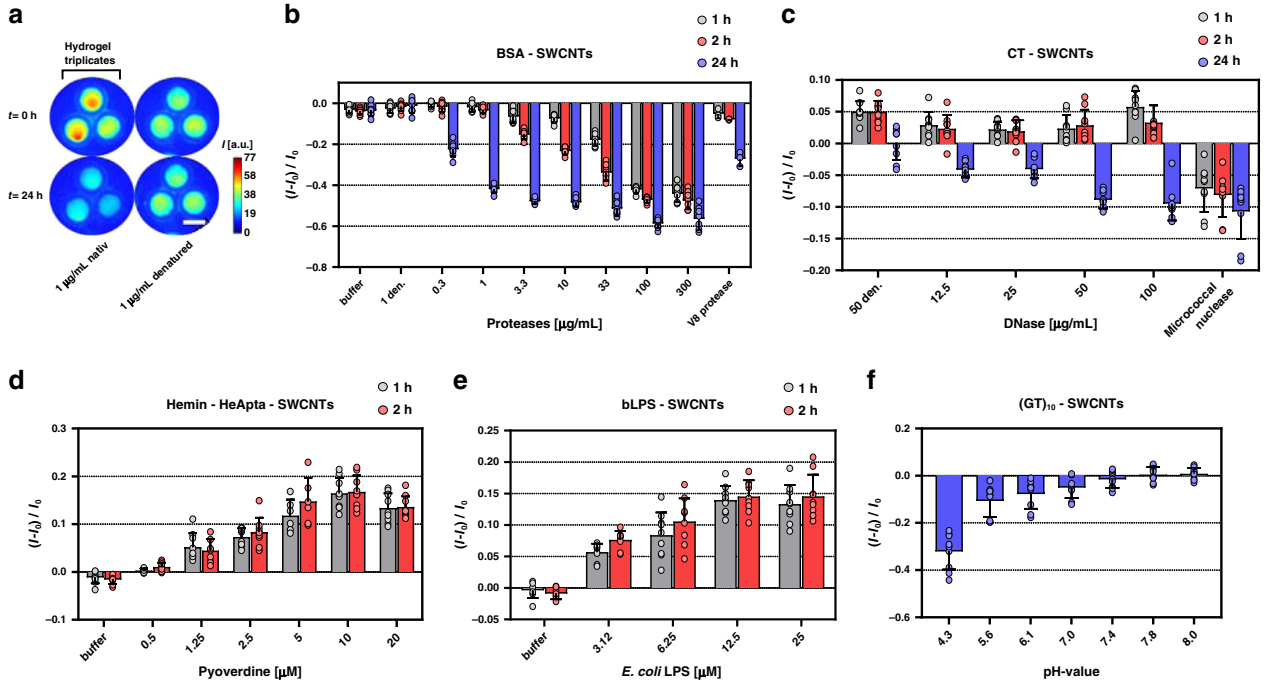

Fig. 3 NIR fluorescent sensor hydrogels. a NIR image of a polyethylene glycol hydrogel (PEG-HG) with embedded/copolymerized nanosensors in three identical regions (discs). Images were acquired remotely (distance 25 cm) with an InGaAs camera (see Fig. 4a for a picture of the setup). Here, only sensors reporting protease activity (see panel b) are depicted, but the concept applies to all sensors (scale bar = 0.5 cm). Note that the different NIR intensities of the discs are due to slight differences in illumination/imaging (distance/angle between sample and camera). **b** Protein (bovine serum albumin, BSA) functionalized SWCNTs, incorporated into a porous PEG-HG, decrease their fluorescence in response to protease from *Streptomyces griseus* ($n = 3$ independent experiments with three technical replicates each, mean ± SD) and V8 protease from *Staphylococcus aureus* (Endoproteinase Glu-C, 13.5 U/mL ~ 18 µg/mL) ($n = 3$ independent experiments, mean ± SD). **c** Long, genomic DNA molecules (denatured calf thymus (CT)-DNA) on SWCNTs serve as substrate for nucleases. Incorporated into a porous HG, fluorescence decreases in response to native DNases I or *S. aureus* nucleases (11 UN/mL ~ 55 µg/mL) ($n = 3$ independent experiments with three technical replicates each, mean ± SD). **d, e** Tailored nanosensors (see Fig. 2) are still functional when incorporated into a hydrogel ($n = 3$ independent experiments with three technical replicates each, mean ± SD). **f** $(GT)_{10}$-SWCNTs (as one of the generic DNA/SWCNT sensors) in a HG shows a pH-dependent fluorescence response (evaluated after 24 h) ($n = 3$ independent experiments with three technical replicates each, mean ± SD).

Therefore, we incorporated these sensors into porous HGs based on biocompatible poly(ethylene glycol)diacrylate hydrogels (PEG-HGs). HGs of low (type-I) and high porosity (type-II) (Supplementary Fig. S4, Table ST1, ST2) were created by using PEG-DA (700 g/mol), in combination with different concentrations of higher molecular weight PEG[52]. The rationale was that (type-II) gels would allow large enzymes to diffuse into the gel and reach the nanosensors. In contrast, for small molecules such as siderophores type-I gels are used to let relevant analytes pass through but prevent at the same time unspecific effects. As a first target, extracellular proteases were chosen[53–55]. For this purpose, SWCNTs were modified with bovine serum albumin (BSA), serving as an enzymatic substrate, and incorporated into porous (type-II) HGs. When the sensor gels were incubated with a serine protease from *Streptomyces griseus* (Fig. 3a), fluorescence decreased by more than 40% within 24 h in the presence of 1 µg/mL native protease compared to the negative control (thermally denatured protease). Additionally, fluorescence spectroscopy of the HGs revealed that the emission of (6,5)-SWCNTs shifted by 5–7 nm into the red (Supplementary Fig. S4) suggesting decomposition of the BSA surface coating. The fluorescence signal decreased faster for higher protease concentrations, resulting in an $EC_{50} = 0.4$ µg/mL for 24 h (Fig. 3b, Supplementary Fig S5). Another relevant protease from *S. aureus* (V8) showed the same response (Fig. 3b). Following the same principle, a sensor for nuclease activity was designed, which is an important virulence factors of *S. aureus*[56]. Micrococcal nuclease from *S. aureus* is known to degrade single-stranded calf thymus (CT) DNA[57] and therefore we used CT-ssDNA to functionalize and disperse SWCNTs (Supplementary Fig. S6). CT-SWCNTs were then incorporated in (type-II) HG and were able to report both DNase I and *S. aureus* nuclease activity (Fig. 3c). DNase I addition (12.5–50 µg/mL) increased fluorescence on short time scales (1 h) but furthermore reduced fluorescence for longer time scales (−10% for 100 µg/mL after 24 h). Addition of thermally denatured DNase I (50 µg/mL) did not decrease fluorescence, indicating that only active enzymes affect CT-SWCNTs fluorescence significantly. Micrococcal nuclease on the other hand directly decreased the fluorescence of CT-SWCNTs within 1 h. Therefore, it seems likely that target site specificity of different nucleases will cause different sensor responses and kinetics[58], a potential basis for the development of more specific sensors in the future.

All sensors including the colloidally stable ones (Fig. 2) were integrated into HGs to create a functional sensor material for NIR stand-off detection (HG sensor spot diameter = 5 mm, HG array: 15×15×0.8 mm). Sensors that did not require immobilization into a HG in the first place such as HeApta-SWCNTs sensors were integrated into type-I-HGs to exclude unspecific protein adsorption effects, but allow smaller molecules such as siderophores to reach the SWCNTs. This procedure had to be optimized to obtain highly fluorescent HGs (Supplementary Fig. S7). Similar to the solution experiments, HeApta-SWCNT HGs increased in response to pyoverdine (~1200 Da) (Fig. 3d), saturating at ~10 µM.

No further fluorescence change was observed for timepoints >1 h (Supplementary Fig. S8a, b) indicating a diffusion limited response within the first few minutes. Similarly, bLPS-SWCNTs were integrated in macroporous type-II-HG, to enhance diffusion of the ~10 kDa large target analyte LPS[59]. HG fluorescence increased upon *E. coli* LPS addition and saturated at a concentration of 12.5 µM within 20–40 min (Supplementary Fig. S8c).

The four sensors described above were each developed in a rational way to target specific bacterial moieties. Furthermore, pH changes due to metabolic activity of bacteria could be another marker and ssDNA-SWCNTs are known to respond to the proton concentration[60]. Consequently, we incorporated $(GT)_{10}$ -SWCNTs into type-I-HG and the NIR fluorescence of the resulting sensor HGs decreased with pH (Fig. 3f, Supplementary Fig. S8d) by more than 30% at pH 4.3. Such sensor HG reports therefore pH changes or could serve as reference for other sensors that are affected by metabolic acidification.

It is known that small changes in the chemical functionalization (e.g. DNA sequence) of SWCNTs change their selectivity to different small molecules[61]. Therefore, three other sensor hydrogels based on $(C)_{30}$- and $(GC)_{15}$-ssDNA as well as PEG-phospholipid (PEG-PL)-functionalized SWCNTs were created to further increase the multiplexing level. These sensors did not target specific analytes but are known to react to potential changes in pH[60], oxygen concentration[62] or to increasing protein concentrations[23] (see Supplementary Table ST3). Therefore, we hypothesized that characteristic fluorescence changes even if not directly related to one target molecule could increase the discrimination power of the sensor array and decrease the impact of background signals. Last, we added a reference hydrogel with incorporated nanosheets of the calcium copper silicate Egyptian Blue (EB-NS, $CaCuSi_4O_{10}$) as a highly stable reference NIR fluorophore at the lower end of the NIR emission capabilities of SWCNTs (emission at $\lambda \approx 920$ nm)[63]. All 9 sensor hydrogels were then assembled into a stable 3 × 3 HG array, suitable for further integration into microbiological agar (Supplementary Figs. S9–S11 and Table ST3). To avoid contamination, the hydrogels were disinfected by UV light before experiments.

Remote NIR imaging of bacteria. These hydrogels (embedded in agar) were used as local sensors for bacteria and were remotely imaged (stand-off detection) in a simple optical setup that is portable and could be transported into the labs with higher biosafety that were necessary to work with pathogens from patients. It consists of a NIR sensitive InGaAs camera, a LED white-light source with 700 nm short pass filter, an objective lens and optical filters for NIR light (>900 nm). To test the sensors ability to distinguish different bacterial species, each sensor array (Fig. 4b, c) was challenged with bacterial suspensions (in the same medium) to mimic exposure to bacteria, metabolic activity and biofilm formation (100 µL 0.5 McFarland standards) of six different pathogens (*S. aureus, S. epidermidis, S. pyogenes, E. faecalis, E. coli*, and *P. aeruginosa*). These pathogens (reference strains and clinical isolates from patients) are amongst the most prominent bacteria causing post-surgery infections in artificial joint implants, for which remote optical detection could be a promising tool[64,65]. During bacterial metabolic activity and growth, the NIR fluorescence of the sensor array was imaged remotely (25 cm) in a direct and non-destructive way. Exemplary NIR images during incubation with *S. aureus* indicated significant fluorescence changes over time (Fig. 4d). The corresponding sensor responses (ΔI_{SR}) were normalized to the EB-NS reference fluorophore, and differences increased over time as expected (Fig. 4e). These sensor patterns served as fingerprints (see data for all tested bacteria in Supplementary Fig. S12) and showed prominent differences between different pathogens (final 72 h timepoint: Fig. 4f, g). Generally, the presence of bacteria altered the pattern of the sensor array towards either increased (*S. aureus*, *S. epidermidis*, or *P. aeruginosa*) or decreased fluorescence (*E. faecalis* or *S. pyogenes*). Next to the interspecies differences, isolates from the same bacteria species varied in response e.g. *P. aeruginosa* and *E. coli* (Supplementary Fig. S12, S13). However, the presentation of the data in Fig. 4g is not optimal to highlight and distinguish different bacterial species. Consequently, a multivariate statistical analysis (principal component analysis, PCA) was performed (Fig. 4h), which revealed a time-dependent separation of clusters (0.68 bivariate ellipse confidence interval) corresponding to different bacterial species. Bacterial growth and metabolic activity did not strongly change the sensor array response within the first 12 h, possibly limited by release and diffusion of the target molecules into the sensor gel. Within 24 h *P. aeruginosa* and *S. aureus* / *S. epidermidis* clusters separated from the control. After 36 h, additionally *P. aeruginosa*, *S. aureus*, *S. epidermidis*, and *E. coli* clusters separated. Only *E. faecalis* and *S. pyogenes* could not be distinguished, even after 72 h. For different strains from one pathogen sub-clustering was observed, highlighting that the sensor array can not only distinguish pathogens species, but possibly even different strains from various clinical sources of the same species (Supplementary Fig. 13).

To test the medical relevance and potential, clinical isolates (n > 20) from *S. aureus* and *S. epidermidis* were analyzed. Both species are responsible for over 50% of all clinical joint infections[64]. The isolates were chosen to get a broad distribution of differences based on genotyping to cover a diverse population (Supplementary Table ST5). The sensor response from all isolates after 72 h incubation is shown in Fig. 4i. Both bacterial species caused similar response patterns that differed in mean intensity, with a certain variation in between the isolates (Supplement Fig. S14). PCA revealed that the two different bacteria populations can be distinguished (Fig. 4j). Both populations separated into two clusters with a small overlap, indicating that the majority of the tested isolates yield a similar sensor response and only a few isolates skewed the separation (extended dataset in Supplementary Fig. S15). Furthermore, when using the spectral fingerprints from all 43 clinical isolates as a trainings dataset for linear discriminant analysis (LDA), the analyzed *S. aureus* and *S. epidermidis* fingerprints from Fig. 4g could be classified and assigned with a ~80% likelihood (Supplementary Fig. S15c). As seen from these experiments, the magnitude of the sensor response depends on incubation time. However, this is not the real time-resolution of the sensor but rather reflects diffusion in the HG and metabolic rates of the different isolates. To evaluate the timescale on which the sensor array responds (see also Fig. S8), bacterial culture supernatants were added to the sensor array and monitored. For *P. aeruginosa* (Fig. 4k) and *S. aureus* (Supplementary Fig. S16) the sensor array responded between 15 and 45 min after addition with a specific pattern. The results shown in Fig. 4 raise the question if additional sensors could further increase the analytical performance of the sensor gel. To get a quantitative estimate we developed a stochastic simulation that predicts how the discrimination power scales with the number of sensors (Fig. 4l). It is based on the assumption that one can develop additional sensors in the experimental range found by us including non-responsive sensors, noise and typical sensor responses (see "Materials and Methods" for details and Supplementary Fig. S17). The results indicate that the analytical performance of the 9-sensor array could be further increased by more sensors but the gain would decrease for 15 sensors or more. For point-of care diagnostics, the overall size of an array and the number of sensors are competing features and this simulation provides a quantitative way for optimization.

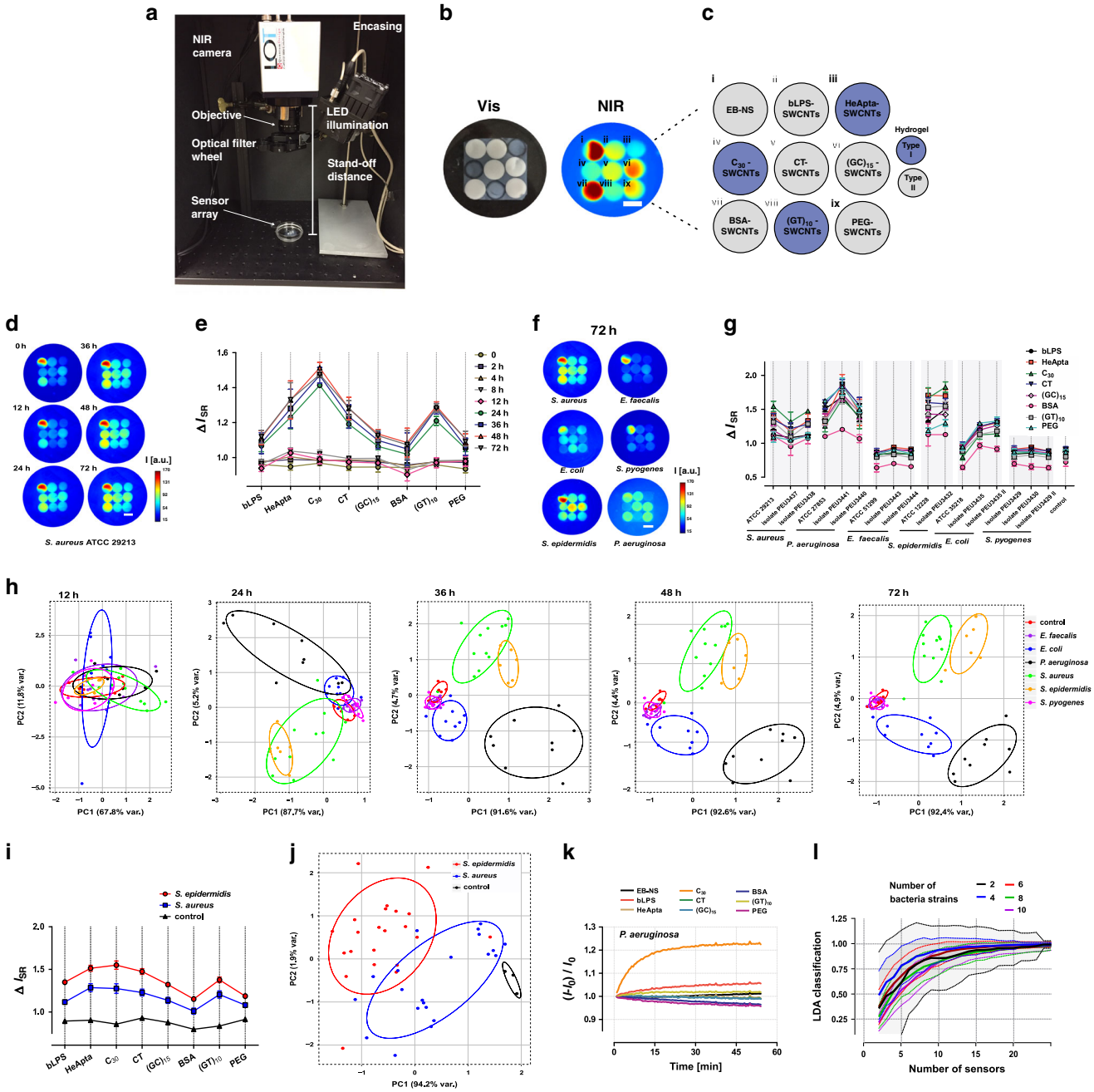

Fig. 4 Remote NIR identification of bacteria. a A simple NIR stand-off setup enables remote (25 cm) imaging of the NIR fluorescent sensors embedded in a hydrogel (HG) array. **b** Photograph (in the visible spectrum) of the HG nanosensor array and its corresponding NIR fluorescence image (scale bar 0.5 cm). **c** Arrangement and functionality of the 9 sensors in the HG array. **d** Remote NIR fluorescence image of a sensor array incorporated in a microbiological agar plate, inoculated with *S. aureus*. During bacterial growth the sensor pattern changes (scale bar 0.5 cm). **e** Corresponding sensor response normalized to the EB-NS signal during *S. aureus* growth, from 0 to 72 h (n = 3 independent experiments, mean ± SD). **f** Representative fluorescence response fingerprint of six pathogens, monitored after 72 h. **g** Fluorescence SWCNT array fingerprint of all bacteria and strains, evaluated after 72 h. (ΔI_{SR}—sensor response: $I_{S1}/I_{R1}/I_{SO}/I_{RO}$; I_S—intensity sensor, I_R—intensity reference (EB-NS)) ($n = 3$ independent experiments, mean ± SD). **h** PCA (principal component analysis) of the fluorescence fingerprint of all analyzed strains, plotted for different timepoints (12–72 h). Each point represents one bacterial sample including clinical isolates from different patients. Control = medium only. **i** Mean sensor array fingerprint from diverse clinical isolates of each *S. aureus* ($n = 21$ biologically independent samples) and *S. epidermidis* ($n = 22$ biologically independent samples) 72 h after incubation. (error = SE). **j** Corresponding PCA for the array fingerprint after 72 h growth of the clinical isolates of *S. aureus* and *S. epidermidis*. **k** Time resolved fluorescence change of the nanosensor array after addition of liquid culture supernatant from *P. aeruginosa*. (24 h incubation in LB-medium, I—intensity sensor at $t = x$; I_0—intensity sensor at $t = 0$) (mean of $n = 3$ independent experiments). **l** Stochastic simulation that predicts how bacteria discrimination improves with number of sensors. The simulation is based on experimental responses and selectivities as range for novel sensors and uses PCA as well as mean linear discrimination analysis (LDA) to distinguish bacteria. Mean values are plotted and the dashed lines/transparent area represent the SD from 25 independent simulations. Ellipses in (**h**, **j**) indicate the 0.68 bivariate confidence interval.

Overall, this multiplexing sensor array was able to detect the presence of bacteria and differentiate a majority on the species level, based on their metabolic fingerprint. Even closely related important pathogens isolated from diverse human infections (*S. aureus* and *S. epidermidis)* could be distinguished.

To evaluate the sensor array performance in the context of smart surface applications such as in implants, host-induced background responses were tested using human synovial fluid (Supplementary Fig. S18). The overall sensor response was not affected when synovia from in total 26 healthy and infected patients were compared, which indicates no interfering immune response background that could bias fingerprinting (Supplementary Fig. S18, Table ST4). Furthermore, bacterial targets like proteases or metabolism induced pH changes could be sensed in the presence of the synovia, while even sensing of methicillin-resistant *S. aureus* (MRSA) was possible in the synovial milieu (Supplementary Fig. S19). We concluded that the sensor array could respond towards a local, biofilm-based infection, while background signals in synovia would not lead to a false-positive readout.

Hyperspectral NIR detection of bacteria. In the array presented above, the different sensors are spatially encoded, which is useful for point-of-care in vitro bacteria diagnostics. However, for smart materials or in vivo applications spectrally encoded sensors would be beneficial. They would enable ratiometric detection and hence decrease problems due to inhomogeneous illumination, spatial resolution, etc. To achieve spectral multiplexing, SWCNTs are needed that do not overlap in their fluorescence emission (i.e. different SWCNT chiralities). Even though a lot of progress was made in the last decade in SWCNT purification[66–69], it is still an ongoing area of research and sensing with purified SWCNT has only been shown in a few cases[70,71].

To evaluate spectral multiplexing, three different sensors from the 9-sensor array were used to distinguish *S. aureus* and *P. aeruginosa*. Indeed, bacterial differentiation was still possible even with a reduced number of sensors (Supplementary Fig. S20 and Fig. S21) that differed most for different pathogens. bLPS- and PEG-SWCNTs showed distinct responses for *S. aureus* and *P. aeruginosa* (Fig. 4g) and were therefore chosen for spectral multiplexing. EB-NS (~920 nm emission) served again as NIR reference fluorophore. SWCNT chiralities were separated by aqueous two-phase extraction (ATPE), yielding monodisperse CoMoCAT (6,5)-SWCNTs (980 nm emission) and larger-diameter HiPco-SWCNTs chiralities (emission > 1110 nm) (detailed information in Supplementary Fig. S22 and S23). By surface exchange of the purified nanotubes, bLPS-(6,5)-SWCNTs and PEG(5 kDa)-PL-(9,4),(8,6),(9,5)-SWCNTs (Supplementary Fig. S22 and S23) could be created. These two different SWCNT sensors and EB-NS were incorporated together into a HG. Consequently, each sensor could be read out at a different wavelength by switching the emission filter (Fig. 5a) in the stand-off setup (Supplementary Fig. S24). This functional sensor HG (Supplementary Fig. S25) was integrated in microbiological agar and inoculated with *S. aureus* and *P. aeruginosa* (one reference strain and two clinical isolates), as described before. Clear differences were observed between the two species and also for isolates of *P. aeruginosa* (Fig. 5b). Similar to the spatially encoded sensor arrays, PCA revealed clusters that were fully separated after 72 h (Fig. 5c). The results indicate that the major spread within one bacterial cluster is due to the biological difference between the tested strains.

For a future smart implant application and in situ diagnostics, one major advantage of the NIR is tissue penetration. Consequently, we tested how deep we can probe such sensors especially because this would be a requirement for medical applications (e.g. sensors in artificial (knee) joint implants or venous catheters). Fluorescence decreased with thickness of a tissue phantom (chicken) (Fig. 5d, Supplementary Fig. S25) but at moderate excitation intensities (25 s, 0.176 W mm^{-2}) signals from below 7 mm thick tissue were detected (Fig. 5e). By using higher excitation energies and advanced imaging approaches such as pulsed laser illumination or fluorescence lifetime imaging, this level of tissue penetration could be further increased and enable in vivo applications especially in tissue close to the body surface. For deep-tissue applications in humans one could also make use of light-guides or miniaturized endoscopes. Additionally, due to the structure-dependent fluorescence emission wavelength of SWCNTs, one could envision up to around 15 spectrally different SWCNT sensors in the NIR range[72].

Discussion

Bacterial infections require timely treatment and local/fast detection is one of the great challenges in biomedicine. Here, we developed multiple NIR fluorescent sensors to remotely fingerprint important pathogens. The SWCNT-based sensors were engineered to detect bacteria via their secreted metabolites. This approach is different from concepts that detect genetic information (PCR) or the chemical composition of the bacteria itself (MS, Raman spectroscopy). The nanosensors detect major bacterial virulence factors (LPS, siderophores), as well as enzyme activity (DNases and proteases) and generic metabolic activity and are embedded in hydrogels that are remotely imaged in the NIR. The SWCNT's NIR fluorescence makes these nanosensors an ideal tool for non-invasive, fast and local identification of bacterial infections and contaminations. Spatial encoding of nine different sensors allowed to fingerprint pathogens such as *E. coli*, *S. aureus* or *P. aeruginosa* after 24–72 h on the species level. The fingerprints of 43 additional clinical isolates of *S. aureus* and *S. epidermidis* showed that even closely related bacterial species could be distinguished. The analysis of the sensor array pattern could be further improved by using more sophisticated machine learning algorithms[36,73]. Especially if the number of sensors is further increased such concepts would further improve and accelerate precise classification and identification of bacterial contaminations. In contrast to previous approaches, the developed sensors detect secreted bacterial motifs and are not only labels[74]. Multiplexing with non-SWCNT nanosensors has been used before to distinguish non-pathogenic from pathogenic biofilms[75]. However, the advantages of sensors that fluoresce in the NIR enable effective remote imaging in relevant distances (25 cm) or under tissue without the typical background fluorescence found in the visible of the electromagnetic spectrum. Additionally, a major advantage of these sensors is that their sensitivity/selectivity can be easily modified by changing the surface chemistry e.g. by using different DNA sequences. Consequently, upscaling the number of sensors is only limited by practical aspects such as the lateral size of the sensor array. The standoff imaging of the bacteria sensors presented in this work is not limited to smart surfaces in point-of-care tools, hospitals or implants but could be expanded to detect also bacterial infections (in plants) that reduce yields in agriculture[24,74,76].

The modular chemical design of the SWCNT functionalization is useful to create more sensors and increase the multiplexing level and thus sensor performance. In this context, the advent of covalent functionalization of SWCNTs with biomolecules without impairment of NIR fluorescence will open up additional possibilities[77]. For point-of-care diagnostics the current time resolution should be further increased. It is mainly limited by the diffusion of the analytes through the agar layer and the sensor

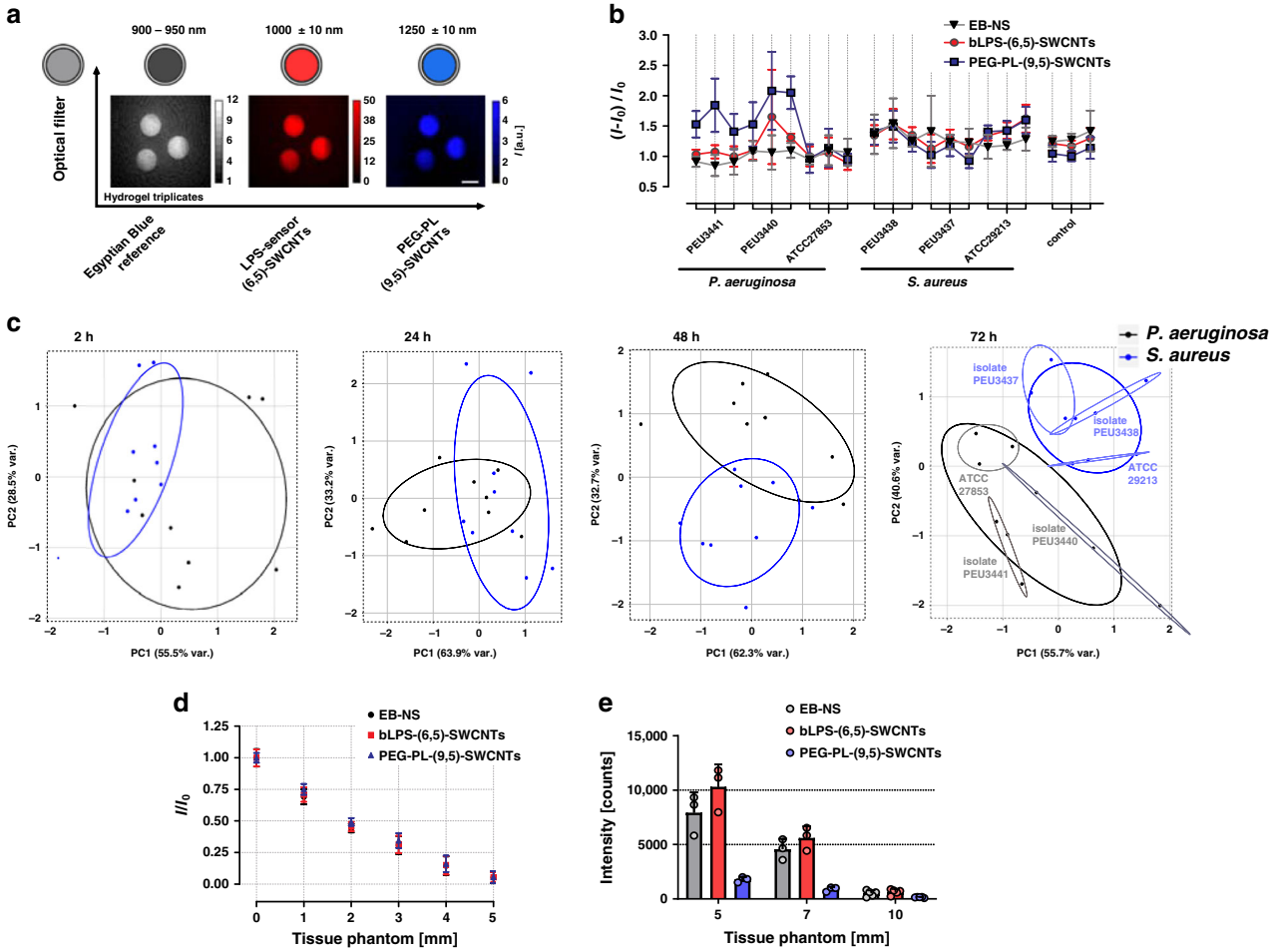

Fig. 5 Hyperspectral remote detection of bacteria. a Multi-color sensor HGs are created by incorporating EB-NS as reference NIR-fluorophore and two chirality-purified SWCNT sensors (LPS-binding-peptide-$(GT)_{20}$@(6,5)-SWCNTs and PEG(5 kDa)-PL@(9,5)-SWCNTS), which enables spectral multiplexing. NIR fluorescence images were captured with optical filters, resulting in three emission/color channels (EB-NS 900–950 nm, bLPS 1000 nm and PEG 1250 nm). Note that heterogeneity in fluorescence of the three technical replicates is caused by inhomogeneous illumination intensity and not relevant for quantification because of normalization to the EB-NS reference (scale bar 0.5 cm). **b** Fluorescence change of the hyperspectral sensors after 72 h of incubation with *P. aeruginosa* and *S. aureus* show distinct responses for one reference strain and two clinical isolates ($n = 3$ independent experiments, mean ± SD). **c** PCA of the spectrally encoded sensors for different timepoints. Each point represents one biological replicate of the indicated strain. Ellipses indicate the 0.68 bivariate confidence interval. **d** Tissue penetration through chicken phantom (561 nm excitation, 130 mW, 6 s integration time, $n = 3$ sensor spots, mean ± SD). Intensity decreases with tissue thickness. **e** If the integration time is increased (25 s, 190 mW excitation power) spectrally encoded bacterial sensors can be read out through 7 mm of tissue phantom ($n = 3$ independent experiments, mean ± SD).

hydrogel. Gel thickness as well as lateral sizes of sensor spots can be further miniaturized to increase time resolution and sensitivity. Such advances could facilitate fast in vitro testing without the need for large laboratory equipment and enable e.g. blood-culture based sepsis diagnostics. In contrast to the array, hyperspectral imaging will be limited to a smaller number of sensors. However, ratiometric imaging and detection as shown for the two major pathogens *S. aureus* and *P. aeruginosa* promises remote detection and is required for potential in vivo applications such as smart implants that would especially profit from NIR light. In the long-term, these developments could facilitate in situ diagnostics of infections in non-accessible locations such as on implants.

In summary, we developed NIR fluorescent nanosensors to remotely fingerprint bacteria. The combination of multiple sensors with different selectivities allowed us to distinguish clinically relevant bacteria based on their metabolic fingerprint. Multiplexing was achieved by spatial or spectral encoding, which highlights the opportunities for remote pathogen detection. In the future, NIR remote detection of bacteria could enable faster diagnostics and tailored antibiotic treatment, which would ultimately result in better clinical outcomes and lower mortality rates.

Methods

Materials. All materials, if not otherwise stated, were purchased from Sigma Aldrich.

SWCNT surface modification. (6,5)-chirality enriched CoMoCAT SWCNTs (Sigma Aldrich) were used and modified with different macromolecules. Functionalization with ssDNA such as $(GT)_{10}$, C_{30} and $(GC)_{15}$ (oligonucleotide sequences purchased by Sigma Aldrich) followed a previously described protocol[60]. In short, 100 µL ssDNA (2 mg/mL in PBS) were mixed with 100 µL PBS and 100 µL SWCNTs (2 mg/mL in PBS), tip sonicated for 15 min @ 30% amplitude (36 W output power, Fisher Scientific model 120 Sonic Dismembrator) and centrifuged 2 × 30 min @ 16,100 × *g*. If stated, the excess ssDNA was removed by molecular weight cut-off filtration (100 kDa, Sartorius). Supplementary Table 2 provides an overview about the conditions used for SWCNT modification. For the HeApt-SWCNTs the hemin-binding aptamer 5′- AGT GTG AAA TAT CTA AAC TAA ATG TGG AGG GTG GGA CGG GAA GAA GTT TAT TTT TCA CAC T-3′ was used.[49,50] To modify the SWCNT surface with a long, genomic ssDNA, 3 mg/mL calf-thymus (CT) DNA was beforehand denatured for 30 min @ 100 °C. Phospholipid-PEG-SWCNTs were synthesized by performing dialysis of sodium cholate suspended SWCNTs.[33] For this purpose, SWCNTs were tip-sonicated in

500 µL (10 mg/mL in PBS) sodium cholate. After centrifugation, 200 µL supernatant was mixed with 800 µL sodium cholate (10 mg/mL) containing 2 mg 18:0 PEG5000 PE (1,2-distearoyl-sn-glycero-3-phosphoethanolamine-N-[methoxy(polyethylene glycol)-5000], Avanti Lipids). The mixture was transferred to a 1 kDa dialysis bag (Spectra/Por®, Spectrum Laboratories Inc.) and dialyzed for several days against 1xPBS. Centrifugation 30 min @ 16100x g yielded the colloidal dispersed PEG-PL-SWCNTs.

Exfoliated Egyptian Blue nanosheets (EB-NS) were obtained by following a modified version of the previously reported protocol from Selvaggio et al.[63]. EB powder (Kremer Pigmente GmbH & Co. KG.) was milled by means of a planetary ball mill (PB, Pulverisette 7 Premium Line, Fritsch, Germany) equipped with 20 mL agate beakers and 5 mm agate balls, in deionized H_2O at 900 r.p.m. for 2 h. 100 mg of the dried supernatant were dispersed in 2 mL H_2O and tip sonicated for 2 h at 30 W amplitude, yielding EB-NS.

Synthesis of LPS-binding-(bLPS)-SWCNTs. A 13 amino acid long (KKNYSS-SISSIHC) peptide, which was reported to bind lipopolysaccharides (LPS)[42,44], was conjugated to a ssDNA-SWCNT. The LPS-binding peptide was synthesized via solid phase synthesis, precipitated with diethyl ether analyzed by high resolution mass spectrometry. 100 µL (2 mg/mL in 1 x PBS) $(GT)_{20}$-C_6-NH_2 ssDNA was mixed with 26.8 µL (6 mM in acetonitrile) SMCC (succinimidyl 4-(N-mal-eimidomethyl)cyclohexane-1-carboxylate) (molar ratio of ~ 1:10) and 125 µL 1x PBS (pH 7.4) and left for 1 h reaction at room temperature. Unreacted SMCC was excluded with a 7 kDa desalting column (Zebra^{TM} Spin Desalting Columns, Thermo Scientific). The SMCC coupled ssDNA was directly used for SWCNT surface modification, by adding 75 µL SWCNTs (2 mg/mL in PBS) and sonicating the mixture for 20 min at 25% amplitude, followed by 2 × 30 min centrifugation at 16,100 × *g*. The non-absorbed ssDNA was removed by sequential molecular cut-off filtration, while concomitant quantifying the bound DNA, following a previously described method by Nißler et al.[60]. The DNA-SWCNT filter-pellet was redispersed in 250 µL PBS by 30 s tip sonication (25% amplitude), followed by 10 min centrifugation (15,000 × *g*). According to the determined amount of bound SMCC-ssDNA on the SWCNTs, freshly reduced LPS-binding peptides was added with a molar ratio of 1:1 to a SMCC-$(GT)_{20}$-SWCNT solution with 0.8 absorbance at 993 nm and left overnight (12 h) for reaction at room temperature, while continuously shaking. Reduction of the LPS-binding peptide was carried out in PBS, by using an ~1:10 excess of TCEP (Tris(2-carboxyethyl)phosphine hydrochloride). The final LPS-sensor (bLPS-SWCNT) was obtained after 20 min centrifugation (16,100 × *g*).

PEG-DA-Hydrogels. Poly(ethylene glycol) diacrylate (PEG-DA) ($M_n = 700$) was polymerized with 2-hydroxy-4′-(2-hydroxyethoxy)−2-methylpropiophenone (photoinitiator) to create a stable scaffold for the SWCNT nanosensors. To vary the diffusion of the hydrogel (HG), two types of HG-formulas were used (see Supplementary Table ST1 and ST3). Type-I-HG were prepared by mixing 100 mg/mL PEG-DA with 0.5 mg/mL 2-Hydroxy-4′-(2-hydroxyethoxy)−2-methylpropiophenone in 1x PBS. The photoinitiator was dissolved in H_2O (12 mg/mL) while shaking at 60 °C for 15 min. Macroporous PEG-DA-HGs were obtained by following a previously described approach[52]. 100 mg/mL PEG (6 kDa) was added to the hydrogel solution, creating a type-II-HG via polymerization induced phase separation.

After evacuating and purging the liquid HG-solution with N_2, the surface-modified SWCNTs were added, characterized via UV-Vis-NIR absorption spectroscopy and directly polymerized in a 1 mL syringe, using an UV-chamber (Belichtungsgerät 1, 4 × 8 W, isel). The SWCNTs-PEG-DA-HG cylinder where dialyzed in 1× PBS for several days to exclude unreacted educts. A typical formulation to yield 5 ml SWCNTs-PEG-DA-HG is given in Supplementary Table ST1.

Pyoverdine extraction. *Pseudomonas fluorescens* ATCC 13525 (Supplementary Fig. S3) was cultivated in iron-deficient succinate medium for 4 d at 25 °C/200 rmp[78]. Cultures were centrifuged and sterile-filtrated, before performing solid phase extraction of pyoverdines[79,80]. The supernatant was adjusted to pH 6 with NaOH and passed through (~100 g) Amberlite XAD-4. The resin was washed with 500 mL H_2O, and the pyoverdine fraction eluated with 300 ml 80% MeOH: H_2O. MeOH was removed from the mixture by evaporation, followed by a liquid-liquid extraction (3 × 50 mL) with $CHCl_3$. Lyophilization yielded the crude extract, which was resuspended in 20 mL of H_2O and applied to an (10 g / 70 mL) washed and pre-conditioned C_{18}ec SPE column (Macherey-Nagel GmbH). After a washing step with 50 mL H_2O, pyoverdines were fractionally eluated with 10% MeOH in H_2O and lyophilized.

NIR spectroscopy. Absorption spectroscopy was performed with a JASCO V-670 device from 400 to 1350 nm in 0.2 nm steps in a 10 mm path cuvette. The NIR fluorescence spectra were acquired with a Shamrock 193i spectrometer (Andor Solis Software (version 4.29.30012.0), Andor Technology Ltd., Belfast, Northern Ireland) connected to a IX53 Microscope (Olympus, Tokyo, Japan). Excitation was performed with a gem 561 laser (Laser Quantum, Stockport, UK), Cobolt Jive laser (Cobolt AB, Solna, Sweden) and Monochromator MSH150, equipped with a LSE341 light source (LOT-Quantum Design GmbH, Darmstadt, Germany). NIR fluorescence analyte response measurements were performed, unless otherwise stated, by addition of 20 µL analyte to 180 µL 0.2 nM SWCNT solution in PBS. Data analysis was performed with GaphPad Prism 8.3 and OriginPro 9.1.

SWCNT separation. Separation of (6,5)-SWCNTs was performed according to a previously reported aqueous two-phase extraction (ATPE) protocol from Li et al.[81]. Briefly, in a three step approach SWCNT chiralities were separated between two aqueous phases, containing dextran (MW 70000 Da, 4% (by mass)) and PEG (MW 6000 Da, 8% (by mass)) with varying pH-values due to HCl addition. The final B3 (bottom)-phase yielded near monochiral (6,5)-SWCNTs, which were diluted with DOC to obtain a stable 1% DOC-SWCNT solution. Further dialysis with a 300 kDa dialysis bag against 1% DOC removed the dextran polymer, used for SWCNT separation. Surface exchange of the (6,5)-SWCNT towards LPS-binding peptide conjugated $(GT)_{20}$ ssDNA was achieved by applying the steps from Streit et al.[82]. Here, 150 µL of purified (6,5)-SWCNTs in 1% DOC (~2 absorption at 986 nm) were used with 25 µL of PEG (MW 6 kDa, 25% (*m*/*V*)) and 30 µL of conjugated DNA (2.5 mg/mL in H_2O). After one precipitation cycle, the nanotube pellet was directly redispersed in 200 µL 1xPBS and characterized by absorption spectroscopy.

HiPco-SWCNTs (Nano Integris, HiPco Raw SWCNTs, 2 mg/mL) were dispersed in 1% DOC for 20 min at 30% amplitude and centrifuged 2 × 30 min at 16,100×*g*. Using the ATPE protocol[81], large SWCNT diameters were separated from the raw SWCNT mixture. Using a 40 mL formulation with differing SDS concentration (0.375%), for the first separation 43 µL HCl (0.5 M) was added, mixed and centrifuged. Subsequently the T1 (top)-phase was transferred to the B1-mimic and mixed with 8 µL NaOH (0.5 M). Again, the top-phase (T2) was transferred to a fresh B1-mimic and mixed with 20 µL NaOH, which yielded after centrifugation the desired B3-phase with a fraction of large SWCNT chiralities (mainly (9,4), (8,6), and (9,5)-SWCNTs). Dialysis with a 300 kDa dialysis bag against 1% DOC removed the dextran polymer. For further surface exchange to PEG-phospholipids[33] (18:0 PEG5000 PE), the large-chirality SWCNT sample was concentrated in a 100 kDa molecular weight cut-off filter, washed and redispersed in 800 µL sodium cholate (12 mg/mL in PBS). 2.5 mg 18:0 PEG5000 PE was dissolved in 200 µL PBS and mixed with the large-chirality SWCNT fraction, flowed by dialysis against 1 × PBS, using a 1 kDa cut-off bag.

NIR stand-off imaging of sensor gels. NIR stand-off detection was performed with a custom made, portable setup, using a XEVA (Xenics, Leuven Belgium) NIR optimized InGaAs camera (Kowa objective, $f = 25$ mm/F1.4) and a white-light source (UHPLCC-01, UHP-LED-white, Prizmatix) equipped with a 700 nm short pass filter (FESH0700, ThorLabs) for excitation. Optical filters (FEL0900, FEL0950, FB1000-10, FB1250-10 ThorLabs) in a manual filter wheel (CFW6/M, ThorLabs) were mounted in front of the camera, which was equipped with an additional 900 nm long pass filter (FEL0900, ThorLabs). Stand-off distance for NIR fluorescence detection for the hydrogel-array experiments (1 s integration time, light intensity 54 mW cm^{-2}) was 25 cm and 10 cm for the hyperspectral imaging (5 s integration time, light intensity 18 W cm^{-2}). Light intensity was measured at 570 nm with a power meter (PM16-121, ThorLabs).

For evaluation of the sensor responses sensor gels were placed inside a 12-well plate and incubated with the appropriate buffer. Unless otherwise stated 1 × PBS pH 7.4 was used. DNase I (PanReac AppliChem, 5160.7 U/mg) and microbial nuclease (*S. aureus*, N5386 Sigma Aldrich) was tested in 10 mM Tris-HCl pH 7.5 (2.5 mM $MgCl_2$, 0.1 mM $CaCl_2$), Proteases (*S. griseus*, P5147 Sigma Aldrich) and Endoproteinase (Glu-C from *S. aureus* V8, P2922 Sigma Aldrich) was tested in 50 mM Tris-HCl pH 7.5. Thermal inactivation and denaturation of enzymes were performed by heating the desired solution up to 95 °C for 20 min under continuous shaking.

Assembly of the SWCNT-hydrogel array. 1.5 cm long hydrogel cylinders of all nine different nanosensors were placed in a cubic (1.5 cm) glass reaction chamber, sealed with parafilm and filled with 1 ml type-I-HG. UV-curing (Belichtungsgerät 1, 4 × 8 W, isel) was performed 8 min for each top and down side. The resulting HG block was sliced into 0.8 mm thin layers, using a specifically designed alumina cutting chamber and razor blades (Supplement Fig. S9). All nanosensor arrays were stored in 1 × PBS to remove non-reacted monomers. HG array sterilization was performed by multiple exchange of sterile buffer and UV-sterilization. Then, the hydrogel arrays in sterile PBS were placed under a sterile hood (TELSTAR AA-30/70) and were illuminated from the top (UV sterile hood, DRI SHIM 30T8/GL) and the bottom (UV-Kontaktlampe Chroma41, 254 nm, Vetter GmbH) with UV light with 2× buffer exchange for 20 min.

For sensor array response analysis during bacterial growth, the sterile hydrogel arrays were fixed with a small amount (~150 µL) 1.5% agarose to the bottom of sterile Petri dishes and overlaid with ~2 mm microbiological agar (total of 5 ml LB-agar with 5% FCS (fetal calf serum, FCS premium, bio west) and 2.5 mg/L Amphotericin B (Biodrom GmbH)), followed by a further UV-sterilization step. HG arrays cast in microbiological agar were stored at 4 °C until usage.

Image analysis. NIR images were acquired with Xeneth Software 2.7 (Xenics, Leuven Belgium) and converted in ImageJ (1.51k) into 8-bit data format. The intensities of the HG nanosensors were evaluated with a circular region of interest,

matching the size of the individual HG spot. The mean intensity value of each spot was measured at different timepoints (I) and referenced to its start intensity (I_0) as $(I-I_0)/I_0$. For HG array experiments, the mean intensity of each nanosensor spot was referenced to the EB-NS intensity, and further comparison of this ratio between different timepoints lead to the sensor response ΔI_{SR}:

$$\Delta I_{SR} = \frac{I_{S1}}{I_{R1}} / \frac{I_{S0}}{I_{R0}}. \quad (1)$$

Here, I_S is the intensity of a specific sensor and I_R the intensity of the EB-NS reference at timepoint ($t = 1$) compared to the start ($t = 0$). Sensor spots for hyperspectral imaging, were background corrected using an equal size area close to the sensor spots. Principle component analysis (PCA) was performed in R (version 3.6.1) using the package ggbiplot (version 0.55).

Bacterial strains. Reference isolates were purchased from the Leibniz Institute DSMZ-German Collection of Microorganisms and Cell Cultures GmbH. Clinical isolates were taken from routine diagnostics of the University Medical Center Göttingen. If available, isolates stemmed from native joint infection, implant loosening, or peri-prosthetic joint infection or related clinical samples. Supplementary Table ST5 summarized the bacteria strains used for pathogen differentiation experiments. Briefly, one reference strain for each species (except *S. pyogenes*) plus one or two fresh clinical isolates were used (*Staphylococcus aureus* ($n = 3$), *Pseudomonas aeruginosa* ($n = 3$), *Enterococcus faecalis* ($n = 3$), *Staphylococcus epidermidis* ($n = 2$), *Escherichia coli* ($n = 3$), and *Streptococcus pyogenes* ($n = 3$)). The strain set, for *S. epidermidis* and *S. aureus* differentiation, was composed of >20 isolates for each species (distinct from strain set I, listed in Supplementary Table ST6). *S. epidermidis* and *S.aureus* isolates were MLST-typed[83,84] specifically for this purpose and the data uploaded to pubmlst.org. When available, *S. aureus* spa-typing/MLST data was taken from previous routine diagnostic procedures. The strain set for hyperspectral bacteria differentiation (three biological and three technical replicates, $n = 3$) was composed of *S. aureus* ATCC 29213, isolate PEU3438, isolate PEU3437 and *P. aeruginosa* ATCC 27853, isolate PEU3441, and isolate PEU3440.

Bacterial detection procedure. Bacterial collection strains (Supplementary Table ST5 and ST6) were thawed and passaged twice overnight on Columbia blood-agar (Oxoid). Single colonies were picked and diluted with sterile 0.7% NaCl to 0.5 McFarland turbidity. Microbiological agar (LB-agar with 5% FCS and 2.5 mg/L Amphotericin B, plate diameter 5.4 cm) embedded with a single HG array were inoculated with 100 µL bacterial suspension, evenly plated, and incubated at 37 °C. In defined time intervals (1, 2, 4, 8, 12, 24, 36, 48, 72 h), the nanosensor NIR fluorescence was measured using the portable stand-off detection system with 1 s integration time. For each strain, three stated biological replicates within three technical replicates each were tested.

Liquid cultures of *S. aureus* ATCC 29213 and *P. aeruginosa* isolate PEU3440 were obtained by inoculating 25 ml LB-media with a single colony from a fresh overnight-culture (Columbia blood-agar). After 24 h incubation at 37 °C and constant shaking, (OD_{600} *S. aureus* 2.94; OD_{600} *P. aeruginosa* 0.86) 2 × 20 min centrifugation and further sterile filtration (0.45 µm) yielded a cell-free supernatant. For each condition, a sensor array was conditioned by 1 h incubation in sterile LB-medium in a 5.4 cm sterile petri dish, the medium then replaced by 5 ml culture supernatant, and NIR fluorescence images acquired in 30 s intervals.

Human joint fluids (synovia). Synovial liquid samples from human knee joints were collected after written consent was obtained from all patients (ethic proposal number 311/18, approved by medical faculty's ethic committee, University of Bonn). Samples were taken intraoperatively during surgery due to native joint infection, implant loosening, or peri-prosthetic joint infection as part of standard diagnostics for microbiologic and pathologic analysis. A small portion from each sample was kept for scientific analysis and samples were shock-frosted and stored at −80 °C.

350 µL human synovia was directly applied to the sensor arrays, which were incubated 1 h beforehand in 0.9% NaCl solution. 13 independent samples from high-grade infections, five independent samples of low-grade infections and 8 samples from patients without diagnosed infections were analyzed (infection classification based on the clinical report). pH of the synovia was tested by adding 20 µL to a pH-indicator paper (Dip in, pH 0–14, VWR). Sensing of bacterial targets with varying synovia background was performed by using three independent samples for non- and high-grade infections and analyzing the sensor response towards pH 4.5 and protease activity (from *S. griseus*, 100 µg/mL).

Stochastic simulation of sensor responses for bacteria differentiation and classification. For a number of bacteria species n_B a response pattern for the n_S sensors is randomly generated in a given range of responses modeled after values from the measurements. In this simulation up to n_B = 10 bacteria and n_S = 25 sensors were initiated. The response of the sensor set is either a uniformly positive or negative response (sensor responses = 0.7–1.7). A given number of sensors per set produce the same response pattern as they do for another bacterium, therefore are set to the same random value. According to the measurement data, approximately 40% of the sensors had an indistinguishable response compared the dataset of another bacterium. The response of the rest of the sensors was randomly chosen within the known experimental range for the different bacteria. To the response matrix a random noise is applied r times to account for experiment repetition. The noise observed in the data was up to 10%. For the principal component analysis (PCA), the number of sensors is equal to the number of principal components (PC), therefore the experiment was virtually repeated 25 times. When considering a rising number of PC, the response matrix is generated in its entirety and a rising number of senor entries are used in the calculation to model the development of additional sensors. The number of features in a PCA must be equal or exceed the number of PC, therefore r is equal to n_S to generate a doubled dataset for training and testing the PCA. The PCA as implemented in scikit-learn[85] is solved with a full singular value decomposition (SVD) and a logistic regression with a bilinear solver and is used to predict the bacteria species of the test dataset. The percentage of correctly assigned test cases can be calculated with a confusion matrix which has correct assignments as its diagonal elements. Used Python packages: matplotlib[86] (version 3.0.3), NumPy[87] (version 1.16.2), scikit-learn[85] (version 0.20.3), Pandas (version 0.24.2).[88]

Reporting summary. Further information on research design is available in the Nature Research Reporting Summary linked to this article.

Data availability

The main data supporting the results of this study are available within the paper and its Supplementary Information. The related source data files are available under https://doi.org/10.5281/zenodo.4072999. Data on bacterial strains were made accessible online (https://pubmlst.org/bigsdb?db=pubmlst_sepidermidis_isolates&page=query; https://pubmlst.org/bigsdb?db=pubmlst_saureus_isolates&page=query) as indicated in the manuscript. Information on the bacterial strain identification is available in Supplementary Table 6.

Code availability

The Python code for stochastic sensor simulation is described in the manuscript and is available on https://gitlab.gwdg.de/m.dohmen/bacteria-sensing.git.

Received: 3 August 2020; Accepted: 16 October 2020;
Published online: 25 November 2020

References

1. Willyard, C. Drug-resistant bacteria ranked. *Nature* **543**, 15 (2017).
2. Prestinaci, F., Pezzotti, P. & Pantosti, A. Antimicrobial resistance: a global multifaceted phenomenon. *Pathog. Glob. Health* **109**, 309–318 (2015).
3. Cecconi, M., Evans, L., Levy, M. & Rhodes, A. Sepsis and septic shock. *Lancet* **392**, 75–87 (2018).
4. Shohat, N. et al. Hip and knee section, what is the definition of a periprosthetic joint infection (PJI) of the knee and the hip? Can the same criteria be used for both joints?: Proceedings of international consensus on orthopedic infections. *J. Arthroplast.* **34**, 325–327 (2019).
5. Váradi, L. et al. Methods for the detection and identification of pathogenic bacteria: past, present, and future. *Chem. Soc. Rev.* **46**, 4818–4832 (2017).
6. Orenga, S., James, A. L., Manafi, M., Perry, J. D. & Pincus, D. H. Enzymatic substrates in microbiology. *J. Microbiol. Methods* **79**, 139–155 (2009).
7. Bertelli, C. & Greub, G. Rapid bacterial genome sequencing: methods and applications in clinical microbiology. *Clin. Microbiol. Infect.* **19**, 803–813 (2013).
8. Carbonnelle, E. et al. MALDI-TOF mass spectrometry tools for bacterial identification in clinical microbiology laboratory. *Clin. Biochem.* **44**, 104–109 (2011).
9. Ho, C. S. et al. Rapid identification of pathogenic bacteria using Raman spectroscopy and deep learning. *Nat. Commun.* **10**, 1–8 (2019).
10. Bocklitz, T. W., Guo, S., Ryabchykov, O., Vogler, N. & Popp, J. Raman based molecular imaging and analytics: a magic bullet for biomedical applications!? *Anal. Chem.* **88**, 133–151 (2016).
11. Kaittanis, C., Santra, S. & Perez, J. M. Emerging nanotechnology-based strategies for the identification of microbial pathogenesis. *Adv. Drug Deliv. Rev.* **62**, 408–423 (2010).
12. Gupta, A., Das, R., Yesilbag Tonga, G., Mizuhara, T. & Rotello, V. M. Charge-switchable nanozymes for bioorthogonal imaging of biofilm-associated infections. *ACS Nano* **12**, 89–94 (2017).
13. Ngernpimai, S. et al. Rapid identification of biofilms using a robust multichannel polymer sensor array. *ACS Appl. Mater. Interfaces* **11**, 11202–11208 (2019).
14. Howes, P. D., Chandrawati, R. & Stevens, M. M. Colloidal nanoparticles as advanced biological sensors. *Science* **346**, 1247390 (2014).

15. De La Rica, R. & Stevens, M. M. Plasmonic ELISA for the ultrasensitive detection of disease biomarkers with the naked eye. *Nat. Nanotechnol.* **7**, 821–824 (2012).
16. Chen, J., Andler, S. M., Goddard, J. M., Nugen, S. R. & Rotello, V. M. Integrating recognition elements with nanomaterials for bacteria sensing. *Chem. Soc. Rev.* **46**, 1272–1283 (2017).
17. O'Connell, M. J. et al. Band gap fluorescence from individual single-walled carbon nanotubes. *Science* **297**, 593–596 (2002).
18. Hong, G., Diao, S., Antaris, A. L. & Dai, H. Carbon nanomaterials for biological imaging and nanomedicinal therapy. *Chem. Rev.* **115**, 10816–10906 (2015).
19. Hong, G., Antaris, A. L. & Dai, H. Near-infrared fluorophores for biomedical imaging. *Nat. Biomed. Eng.* **1**, 0010 (2017).
20. Kruss, S. et al. Carbon nanotubes as optical biomedical sensors. *Adv. Drug Deliv. Rev.* **65**, 1933–1950 (2013).
21. Kim, J. H. et al. The rational design of nitric oxide selectivity in single-walled carbon nanotube near-infrared fluorescence sensors for biological detection. *Nat. Chem.* **1**, 473–481 (2009).
22. Harvey, J. D. et al. A carbon nanotube reporter of microRNA hybridization events in vivo. *Nat. Biomed. Eng.* **1**, 1–43 (2017).
23. Bisker, G. et al. Protein-targeted corona phase molecular recognition. *Nat. Commun.* **7**, 1–14 (2016).
24. Wu, H. et al. Monitoring plant health with near-infrared fluorescent H_2O_2 Nanosensors. *Nano Lett.* **20**, 2432–2442 (2020).
25. Kruss, S. et al. High-resolution imaging of cellular dopamine efflux using a fluorescent nanosensor array. *Proc. Natl Acad. Sci.* **114**, 1789–1794 (2017).
26. Dinarvand, M. et al. Near-infrared imaging of serotonin release from cells with fluorescent nanosensors. *Nano Lett.* **19**, 6604–6611 (2019).
27. Landry, M. P. et al. Single-molecule detection of protein efflux from microorganisms using fluorescent single-walled carbon nanotube sensor arrays. *Nat. Nanotechnol.* **12**, 368–377 (2017).
28. Antonucci, A., Kupis-Rozmysłowicz, J. & Boghossian, A. A. Noncovalent protein and peptide functionalization of single-walled carbon nanotubes for biodelivery and optical sensing applications. *ACS Appl. Mater. Interfaces* **9**, 11321–11331 (2017).
29. Reuel, N. F. et al. Emergent properties of nanosensor arrays: applications for monitoring igg affinity distributions, weakly affined hypermannosylation, and colony selection for biomanufacturing. *ACS Nano* **7**, 7472–7482 (2013).
30. Polo, E. et al. Control of integrin affinity by confining RGD peptides on fluorescent carbon nanotubes. *ACS Appl. Mater. Interfaces* **10**, 17693–17703 (2018).
31. Mann, A. F., Horlebein, J., Meyer, N. F., Thomas, F. & Kruss, S. Carbon nanotubes encapsulated in coiled-coil peptide barrels. *Chem. - A Eur. J.* **24**, 12241–12245 (2018).
32. Zheng, M. et al. DNA-assisted dispersion and separation of carbon nanotubes. *Nat. Mater.* **2**, 338–342 (2003).
33. Welsher, K. et al. A route to brightly fluorescent carbon nanotubes for near-infrared imaging in mice. *Nat. Nanotechnol.* **4**, 773–780 (2009).
34. Stacy, A., McNally, L., Darch, S. E., Brown, S. P. & Whiteley, M. The biogeography of polymicrobial infection. *Nat. Rev. Microbiol.* **14**, 93–105 (2016).
35. Arciola, C. R., Campoccia, D. & Montanaro, L. Implant infections: adhesion, biofilm formation and immune evasion. *Nat. Rev. Microbiol.* **16**, 397–409 (2018).
36. Geng, Y., Peveler, W. J. & Rotello, V. M. Array-based "chemical nose" sensing in diagnostics and drug discovery. *Angew. Chem. - Int. Ed.* **58**, 5190–5200 (2019).
37. Ramachandran, G. Gram-positive and gram-negative bacterial toxins in sepsis: a brief review. *Virulence* **5**, 213–218 (2014).
38. Whiteley, M., Diggle, S. P. & Greenberg, E. P. Progress in and promise of bacterial quorum sensing research. *Nature* **551**, 313–320 (2017).
39. Flemming, H. C. & Wingender, J. The biofilm matrix. *Nat. Rev. Microbiol.* **8**, 623–633 (2010).
40. Flemming, H. C. et al. Biofilms: an emergent form of bacterial life. *Nat. Rev. Microbiol.* **14**, 563–575 (2016).
41. Maldonado, R. F., Sá-Correia, I. & Valvano, M. A. Lipopolysaccharide modification in gram-negative bacteria during chronic infection. *FEMS Microbiol. Rev.* **40**, 480–493 (2016).
42. Lim, S. K., Chen, P., Lee, F. L., Moochhala, S. & Liedberg, B. Peptide-assembled graphene oxide as a fluorescent turn-on sensor for lipopolysaccharide (Endotoxin) detection. *Anal. Chem.* **87**, 9408–9412 (2015).
43. Zhang, J. et al. Biosensors and Bioelectronics Lipopolysaccharides detection on a grating-coupled surface plasmon resonance smartphone biosensor. *Biosens. Bioelectron.* **99**, 312–317 (2018).
44. Matsumoto, M. et al. Lipopolysaccaride-binding peptides obtained by phage display method. *J. Microbiol. Methods* **82**, 54–58 (2010).
45. Mann, F. A., Lv, Z., Grosshans, J., Opazo, F. & Kruss, S. Nanobody conjugated nanotubes for targeted near-infrared in vivo imaging and sensing. *Angew. Chem. Int. Ed.* **58**, 1469–11473 (2019).
46. Erridge, C., Bennett-Guerrero, E. & Poxton, I. R. Structure and function of lipopolysaccharides. *Microbes Infect.* **4**, 837–851 (2002).
47. Holden, V. I. & Bachman, M. A. Diverging roles of bacterial siderophores during infection. *Metallomics* **7**, 986–995 (2015).
48. Wilson, B. R., Bogdan, A. R., Miyazawa, M., Hashimoto, K. & Tsuji, Y. Siderophores in iron metabolism: from mechanism to therapy potential. *Trends Mol. Med.* **22**, 1077–1090 (2016).
49. Pan, J. et al. Multiplexed optical detection of plasma porphyrins using DNA aptamer-functionalized carbon nanotubes. *Anal. Chem.* **85**, 8391–8396 (2013).
50. Atsumi, H. & Belcher, A. M. DNA origami and G-quadruplex hybrid complexes induce size control of single-walled carbon nanotubes via biological activation. *ACS Nano* **12**, 7986–7995 (2018).
51. Meyer, D. et al. Transport and programmed release of nanoscale cargo from cells by using NETosis. *Nanoscale* **12**, 9104–9115 (2020).
52. Lee, A. G., Arena, C. P., Beebe, D. J. & Palecek, S. P. Development of macroporous poly(ethylene glycol) hydrogel arrays within microfluidic channels. *Biomacromolecules* **11**, 3316–3324 (2010).
53. Miyoshi, S. Extracellular proteolytic enzymes produced by human pathogenic vibrio species. *Front. Microbiol.* **4**, 1–8 (2013).
54. Frees, D., Brøndsted, L. & Ingmer, H. in *Regulated Proteolysis in Microorganisms* (ed. Dougan, D. A.) 161–192 (Springer Netherlands, 2013). https://doi.org/10.1007/978-94-007-5940-4_7.
55. Kolar, S. L. et al. Extracellular proteases are key mediators of Staphylococcus aureus virulence via the global modulation of virulence-determinant stability. *Microbiologyopen* **2**, 18–34 (2013).
56. Hernandez, F. J. et al. Noninvasive imaging of Staphylococcus aureus infections with a nuclease-activated probe. *Nat. Med.* **20**, 301–306 (2014).
57. von Hippel, P. H. & Felsenfeld, G. Micrococcal nuclease as a probe of DNA conformation. *Biochemistry* **3**, 27–39 (1964).
58. Yang, W. Nucleases: diversity of structure, function and mechanism. *Q. Rev. Biophys.* **44**, 1–93 (2011).
59. Steimle, A., Autenrieth, I. B. & Frick, J. S. Structure and function: Lipid A modifications in commensals and pathogens. *Int. J. Med. Microbiol.* **306**, 290–301 (2016).
60. Nißler, R. et al. Quantification of the number of adsorbed DNA molecules on single-walled carbon nanotubes. *J. Phys. Chem. C.* **123**, 4837–4847 (2019).
61. Mann, F. A., Herrmann, N., Meyer, D. & Kruss, S. Tuning selectivity of fluorescent carbon nanotube-based neurotransmitter sensors. *Sensors* **17**, 1521 (2017).
62. Zheng, Y., Bachilo, S. M. & Weisman, R. B. Quenching of single-walled carbon nanotube fluorescence by dissolved oxygen reveals selective single-stranded DNA affinities. *J. Phys. Chem. Lett.* **8**, 1952–1955 (2017).
63. Selvaggio, G. et al. Exfoliated near infrared fluorescent silicate nanosheets for (bio)photonics. *Nat. Commun.* **11**, 1–11 (2020).
64. Zimmerli, W. & Moser, C. Pathogenesis and treatment concepts of orthopaedic biofilm infections. *FEMS Immunol. Med. Microbiol.* **65**, 158–168 (2012).
65. Sandiford, N. A. et al. Prolonged suppressive antibiotic therapy is successful in the management of prosthetic joint infection. *Eur. J. Orthop. Surg. Traumatol.* **30**, 313–321 (2020).
66. Tu, X., Manohar, S., Jagota, A. & Zheng, M. DNA sequence motifs for structure-specific recognition and separation of carbon nanotubes. *Nature* **460**, 250–253 (2009).
67. Liu, H., Nishide, D., Tanaka, T. & Kataura, H. Large-scale single-chirality separation of single-wall carbon nanotubes by simple gel chromatography. *Nat. Commun.* **2**, 1–8 (2011).
68. Ghosh, S., Bachilo, S. M. & Weisman, R. B. Advanced sorting of single-walled carbon nanotubes by nonlinear density-gradient ultracentrifugation. *Nat. Nanotechnol.* **5**, 443–450 (2010).
69. Khripin, C. Y., Fagan, J. A. & Zheng, M. Spontaneous partition of carbon nanotubes in polymer-modified aqueous phases. *J. Am. Chem. Soc.* **135**, 6822–6825 (2013).
70. Nißler, R. et al. Chirality enriched carbon nanotubes with tunable wrapping via corona phase exchange purification (CPEP). *Nanoscale* **11**, 11159–11166 (2019).
71. Giraldo, J. P. et al. A ratiometric sensor using single chirality near-infrared fluorescent carbon nanotubes: application to in vivo monitoring. *Small* **11**, 3973–3984 (2015).
72. Roxbury, D. et al. Hyperspectral microscopy of near-infrared fluorescence enables 17-chirality carbon nanotube imaging. *Sci. Rep.* **5**, 1–6 (2015).
73. Li, Z., Askim, J. R. & Suslick, K. S. The optoelectronic nose: colorimetric and fluorometric sensor arrays. *Chem. Rev.* **119**, 231–292 (2019).
74. Bardhan, N. M., Ghosh, D. & Belcher, A. M. Carbon nanotubes as in vivo bacterial probes. *Nat. Commun.* **5**, 1–11 (2014).

75. Li, X. et al. Rapid identification of bacterial biofilms and biofilm wound models using a multichannel nanosensor. *ACS Nano* **8**, 12014–12019 (2014).
76. Wong, M. H. et al. Nitroaromatic detection and infrared communication from wild-type plants using plant nanobionics. *Nat. Mater.* **16**, 264–272 (2017).
77. Mann, F., Herrmann, N., Opazo, F. & Kruss, S. Quantum defects as a toolbox for covalent carbon nanotube functionalization with peptides and proteins. *Angew. Chem. Int. Ed.* https://doi.org/10.1002/anie.202003825 (2020).
78. Meyer, J. M. & Abdallah, M. A. The fluorescent pigment of Pseudomonas fluorescens: biosynthesis, purification and physicochemical properties. *J. Gen. Microbiol.* **107**, 319–328 (1978).
79. Meyer, J. M., Stintzi, A. & Poole, K. The ferripyoverdine receptor FpvA of pseudomonas aeruginosa PAO1 recognizes the ferripyoverdines of P. aeruginosa PAO1 and P. fluorescens ATCC 13525. *FEMS Microbiol. Lett.* **170**, 145–150 (1999).
80. Trapet, P. et al. The Pseudomonas fluorescens siderophore pyoverdine weakens Arabidopsis thaliana defense in favor of growth in iron-deficient conditions. *Plant Physiol.* **171**, 675–693 (2016).
81. Li, H., Gordeev, G., Garrity, O., Reich, S. & Flavel, B. S. Separation of small-diameter single-walled carbon nanotubes in one to three steps with aqueous two-phase extraction. *ACS Nano* **13**, 2567–2578 (2019).
82. Streit, J. K., Fagan, A. & Zheng, M. A low energy route to DNA-wrapped carbon nanotubes via replacement of bile salt surfactants. *Anal. Chem.* **89**, 10496–10503 (2017).
83. Thomas, J. C. et al. Improved multilocus sequence typing scheme for Staphylococcus epidermidis. *J. Clin. Microbiol.* **45**, 616–619 (2007).
84. Enright, M. C., Day, N. P. J., Davies, C. E., Peacock, S. J. & Spratt, B. G. Multilocus sequence typing for characterization of methicillin-resistant and methicillin-susceptible clones of Staphylococcus aureus. *J. Clin. Microbiol* **38**, 1008–1015 (2000).
85. Pedregosa, F. et al. Scikit-learn. *J. Machine Learn. Res.* **12**, 2825–2830 (2011).
86. Hunter, J. D. MATPLOTLIB: A 2D GRAPHICS ENVIRONMENT. *Comput. Sci. Eng.* **9**, 90–95 (2007).
87. Van Der Walt, S., Colbert, S. C. & Varoquaux, G. The NumPy array: a structure for efficient numerical computation. *Comput. Sci. Eng.* **13**, 22–30 (2011).
88. Reback, J. et al. pandas-dev/pandas: Pandas 1.0.5, https://doi.org/10.5281/ZENODO.3898987 (2020).
89. Hider, R. C. & Kong, X. Chemistry and biology of siderophores. *Nat. Prod. Rep.* **27**, 637–657 (2010).
90. Witter, A. E., Hutchins, D. A., Butler, A. & Luther, G. W. Determination of conditional stability constants and kinetic constants for strong model Fe-binding ligands in seawater. *Mar. Chem.* **69**, 1–17 (2000).
91. Field, T. B., McCourt, J. L. & McBryde, W. A. E. Composition and stability of iron and copper citrate complexes in aqueous solution. *Can. J. Chem.* **52**, 3119–3124 (1974).

Acknowledgements

This project was supported by the VW foundation. We furthermore acknowledge support by the German Research Foundation within the Cluster of Excellence RESOLV EXC2033 and the Heisenberg program (S.K.). We thank Prof. Dr. Andreas Janshoff and Prof. Dr. Claudia Steinem and their groups for fruitful discussions and support. We thank Hans-Joachim Heymel for the construction of the hydrogel cutting chamber, Dr. Elena Polo for peptide synthesis, Agnieszka Goretzki, Yvonne Laukat, and Nina Gerkens for help with bacteria cultivation and *MLST* typing, Dr. Thomas Randau, Dr. Sascha Gravius, and Dr. Frank A. Schildberg for intraoperative synovia collection, Seren Hamsici for help with initial LPS sensor development, Larissa Kurth for SWCNT purification and Dr. Ingo Mey for help during SEM measurements.

Author contributions

R.N. and S.K. designed and conceived the research S.K. coordinated the project. O.B., C.N., and U.G. collected the clinical bacteria isolates, characterized them, and helped with bacterial detection experiments. S.G.W. helped with human synovia collection and related sensing experiments. G.S. exfoliated EB-NS and performed SEM characterization. M.D. developed the simulation with input from S.K. All other experiments were performed by R.N. All authors contributed to the writing of the manuscript and analysis of data.

Funding

Open Access funding enabled and organized by Projekt DEAL.

Competing interests

The authors declare no competing interests.

Additional information

Supplementary information is available for this paper at https://doi.org/10.1038/s41467-020-19718-5.

Correspondence and requests for materials should be addressed to S.K.

Peer review information *Nature Communications* thanks Anand Jagota, Lucio Montanaro and the other, anonymous, reviewer(s) for their contribution to the peer review of this work. Peer reviewer reports are available.

Reprints and permission information is available at http://www.nature.com/reprints

Publisher's note Springer Nature remains neutral with regard to jurisdictional claims in published maps and institutional affiliations.

5.3.2 Discussion

Manuscript IV reports successful rational design of SWCNT sensors detecting bacterial targets and motives. It is the first study developing such sensors for specific virulence factors and showing their application in NIR-fluorescence spectroscopy and stand-off imaging. Thereby, different approaches for non-covalent SWCNT modifications were applied, ranging from commonly used SWCNT-decoration concepts with biomacromolecules to novel nanoconjugates. For the development of the lipopolysaccharide (LPS)-sensor, a small peptide with a specific amino acid sequence[185] was coupled to SWCNTs dispersed by amine-functionalized ssDNA. Hereby, **Manuscript I** outlines the basis for such ratio-specific linkage by quantifying the amount of ssDNA and thereby potential linker positions on the SWCNT. This step was essential to obtain functional and colloidally stable SWCNT sensors, since nanotubes aggregated when using high ratios of reduced peptide to SMCC-DNA-SWCNTs (Supplementary Information Manuscript IV, 7.4, Figure S1). This underlines that detailed understanding of the SWCNT surface is crucial for further bioorthogonal modifications. Detecting siderophores as important bacterial virulence factors was frequently demonstrated[186,187], as well as in combination with molecular imaging applications, like positron emission tomography (PET)[188]. However, detection with SWCNT-based sensors was not reported before. Cheung *et al.*[189] used deferoxamine-modified SWCNTs for the selective capturing of iron, whereas the approach in **Manuscript IV** for siderophore detection works the other way around. Inspired by organic fluorophores that are quenched upon iron-chelation and dequenched by a competing (stronger) siderophore[190], SWCNT sensors were designed to follow the same principle. Hereby, Pan *et al.* reported that SWCNTs modified with a specific hemin-binding aptamer[191] are quenched by the analyte interaction, likely due to a charge transfer resulting from the close proximity of the iron to the SWCNT surface.[137] Experiments from **Manuscript IV** now showed that the subsequent addition of strong siderophores like pyoverdine or deferoxamine (Figure 2) can reverse this quenching effect, which leads to an intense, concentration-dependent fluorescence increase. This principle could be extended to other iron-chelating motives used for SWCNT modification, resulting in various sensors with different affinities and iron-binding constants. On the other hand, bacterial iron capturing from protoporphyrin structures can also be enzymatically driven[192], hence monitoring the enzyme activity *in vivo* could be a another application for these HeApta-SWCNTs.

Fluorescent SWCNT-sensors detecting enzymatic activity were first introduced by Kallmyer *et al.*[119], while Wu *et al.*[193] showed that restriction enzymes can still recognize their substrates when those are partially adsorbed onto a SWCNT. The rational design approach for the detection of bacterial enzyme activity was based on the idea of presenting the substrate for the target enzyme on the SWCNT surface and following the nanosensor emission during enzyme performance. However, the expected change in fluorescence due to the alteration and degradation of the SWCNT organic corona (here enzyme substrate), could be prone to unspecific adsorption or stability effects in solution. Therefore, it is more favorable to incorporate these SWCNT-sensors into a functional hydrogel scaffold, stabilizing the SWCNTs and allowing dialysis of the unbound surface modification as well as further influx of the target enzymes. The sensors obtained in this study are the first ones reporting DNase or nuclease activity and the most sensitive ones for remotely detecting protease activity, down to a concentration of 10 pM serin-proteases from *S. griseus* (Figure 3). For the sake of completeness, it should be mentioned that at the same time, a paper-based SWCNT sensor for protease activity was independently reported.[120]

Manuscript IV further introduces NIR stand-off detection for bacterial targets. However, this remote, camera-assisted detection method was previously used for analyzing SWCNTs in divers settings, e.g. in plants[160,163,194] or hydrogels (implants)[124,195]. Kowaza *et al.*[196] furthermore showed SWCNT detection *via* endoscopic tips and a fiber optic, which could also be adapted for the developed bacteria sensors. The concept of a chemical 'nose' – SWCNTs with different selectivities combined in multiplex array structure – was presented in **Manuscript IV** for sensors incorporated into a hydrogel matrix. Beforehand, SWCNT sensor arrays were spotted onto glass cover slides[197] and solely used for microscopic readout.

For the first time, **Manuscript IV** introduces ratiometric imaging and sensing with 2D-nanosheets of a stable NIR-emitting silicate, called Egyptian Blue[198]. This reference material allows to correct for potential variances in illumination and sample position during the bacteria sensing experiments. Thus, enabling a reliable readout of the pathogen-fingerprint through the microbiological culture.

For the transfer of the bacteria sensing approach from spatially located, multiplexed sensors towards spectrally resolved sensors, SWCNT probes with a minimal overlap in NIR-emission are needed. **Manuscript III** enabled the purification and modification of SWCNT material towards this application, resulting in the first hyperspectral detection and differentiation of bacterial pathogens (Figure 4). Overall, rational design strategies for the detection of bacterial targets with SWCNT sensors were introduced. Beforehand, Bard-

han *et al.* modified SWCNTs with M13 bacteriophages which then accumulated *in vivo* at the site of infection.[143] This SWCNT application as NIR optical labels for bacterial infections is quite different to the presented sensing approach in **Manuscript IV**, but furthermore highlights SWCNT's beneficial NIR optical tissue penetration capabilities. A nanosensor array could be used in the future for fast *in vitro* diagnostics, like pathogen detection in liquid blood-cultures. Until now, these methods automatically detect pH changes or increasing CO_2 concentrations in a culture flask, due to metabolic activity of the contained pathogen.[199,200] SWCNT sensor arrays could remotely report whether a bacterial infection is present, but also provide a pathogen fingerprint. This could strongly improve this diagnostic tool and allow a preliminary classification and identification of the pathogen, hence optimizing treatment pathways and antibiotic stewardship. Beyond possible application as *in vitro* diagnostic tools, **Manuscript IV** also presents the scientific framework for potential smart implants. In the future, such sensors could be implemented onto stents, wound patches or endoscopic tips, able to sense the presence of bacteria specific markers. Furthermore, the development of smart arthroplasty implants for knee or hip replacement could enable a novel infection monitoring tool. Those sensors could be in principle read out through the skin and they could report whether an acute symptom is biased on mechanical dislocation or due to an infection of the implant. Hereby, even the detection and discrimination between *S. aureus* and *S. epidermidis* (see Figure 4) was possible. Both are responsible for over 50% of all infections in artificial knee joints, but conventional diagnostic methods are biased by the biopsy procedure itself. Since *S. epidermidis* is a constituent part of the skin microbiome, its detection after biopsy could always be falsified by contamination during the sampling process.

Such advanced SWCNT sensor applications require more research in the future including *in vivo* models. In addition, follow-up studies could aim to fractionate bacterial cultures and evaluate in an activity guided assay which metabolites contribute to the overall sensor response. Also, the influence of multiple present bacteria could be investigated and how co-cultures would affect the array-based chemical fingerprint. However, the first general scientific framework for SWCNT-sensor-based bacteria detection is introduced in **Manuscript IV**.

5.4 SWCNT-Sensors to Monitor Plant-Pathogen Interactions

Detection and analysis of pathogens and their related interactions is a key challenge not only in the healthcare sector. Especially in agriculture, it is of fundamental interest to understand how pathogens like bacteria or fungi interact with crop plants. To gain detailed insights into such plant-pathogen interactions[201], as well as from the infection strategies of pathogens or from recognition, response and defense reactions of plants, novel analytical tools are required. Advances in nanotechnology could help to develop such tools and facilitate smart sensors able to report health and potential infection status of plants.[12,202] Because crop yield can be reduced through pathogen-related stress, detecting, understanding and preventing these events could lead to more resistant strains.[203,204] These possible improvements in agricultural production could help to meet the demand of increasing food production, needed for a rising global population.[205] On the other side, specific sensors that visualize spatiotemporal distribution of desired analytes (from the plant or from the pathogen), could improve fundamental research. In the last years, few SWCNT-based sensor approaches for such purposes were established, including detection of cellular H_2O_2, pollutants like nitroaromates or heavy metals such as arsenic.[176,194,206] The following two chapters will introduce specifically tailored SWCNT sensors that enable the detection and further visualization of plant metabolites involved in plant-pathogen response.

In the **Manuscript V**, entitled "*Monitoring Plant Health with Near-Infrared Fluorescent H_2O_2 Nanosensors*" it will be evaluated if SWCNT can be tuned with a rational design strategy to sense physiological concentrations of hydrogen peroxide (H_2O_2). H_2O_2 and other reactive oxygen species (ROS) are important signaling molecules that communicate stress in plants and can be furthermore directly involved in plant defense (e.g. in the hypersensitive response[207,208]). A sensor that could remotely detect these processes, independently of the used plant species, could significantly improve knowledge about the involved dynamic processes.

In addition, it will be examined in **Manuscript VI** "*Detection and imaging of the plant pathogen response by near infrared fluorescent polyphenol sensors*" if SWCNT-sensors are capable to detect an important class of plant metabolites, called polyphenols. These compounds are widely distributed within the plant kingdom and show a great variety in chemical structures, modifications and ecological roles. Moreover, they can be directly involved

in plant defense against herbivores or pathogens, which makes them an interesting target to be detected and visualized by SWCNT-sensors.

5.4.1 Monitoring Plant Health with Near-Infrared Fluorescent H_2O_2 Nanosensors

Manuscript V was published in the following journal:

Honghong Wu[+],Robert Nißler[+], Victoria Morris, Niklas Herrmann, Peiguang Hu, Su-Ji Jeon, Sebastian Kruss[*] and Juan Pablo Giraldo[*]

"Monitoring Plant Health with Near-Infrared Fluorescent H_2O_2 Nanosensors"

Nano Letters, **2020**, 20, 4, 2432-2442

The article is available at: DOI: 10.1021/acs.nanolett.9b05159

[+]These authors contributed equally to this paper.
[*] Corresponding authors

Responsibility assignment: J.P.G., S.K., H.W., and R.N. conceived and designed the study. H.W., R.N., N.H., P.H., V.M., and S.J. conducted the experiments. H.W., J.P.G, S.K., R.N., P.H., and S.J. analyzed the data. R.N. developed and characterized the H_2O_2 sensor. All authors contributed to writing the paper.

NANO LETTERS

pubs.acs.org/NanoLett Letter

Monitoring Plant Health with Near-Infrared Fluorescent H_2O_2 Nanosensors

Honghong Wu,[‖] Robert Nißler,[‖] Victoria Morris, Niklas Herrmann, Peiguang Hu, Su-Ji Jeon, Sebastian Kruss,* and Juan Pablo Giraldo*

Cite This: *Nano Lett.* 2020, 20, 2432−2442 Read Online

ACCESS | Metrics & More | Article Recommendations | Supporting Information

ABSTRACT: Near-infrared (nIR) fluorescent single-walled carbon nanotubes (SWCNTs) were designed and interfaced with leaves of *Arabidopsis thaliana* plants to report hydrogen peroxide (H_2O_2), a key signaling molecule associated with the onset of plant stress. The sensor nIR fluorescence response (>900 nm) is quenched by H_2O_2 with selectivity against other stress-associated signaling molecules and within the plant physiological range (10−100 H_2O_2 μM). *In vivo* remote nIR imaging of H_2O_2 sensors enabled optical monitoring of plant health in response to stresses including UV-B light (−11%), high light (−6%), and a pathogen-related peptide (flg22) (−10%), but not mechanical leaf wounding (<3%). The sensor's high biocompatibility was reflected on similar leaf cell death (<5%) and photosynthetic rates to controls without SWCNT. These optical nanosensors report early signs of stress and will improve our understanding of plant stress communication, provide novel tools for precision agriculture, and optimize the use of agrochemicals in the environment.

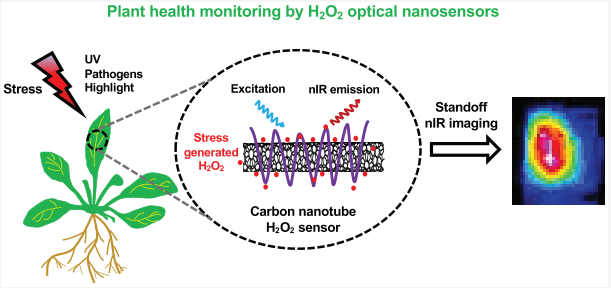

KEYWORDS: *Sensors, carbon nanotubes, plant stress, reactive oxygen species, agriculture, environmental nanotechnology*

Increased growth in the human population will require more than doubling food production[1]. This effort is impaired by a rapidly changing climate, exacerbating the frequency and intensity of environmental stresses and pathogen infections that negatively impact crop health and yield.[2−11] Precision agriculture aims to monitor crops for early detection of stress using sensors and autonomous and manned vehicles. However, these remote sensing instruments measure external environmental conditions or plant traits that often reveal stress after crops have begun to experience associated detrimental effects, including photosynthesis and chlorophyll content decline, and alone have limited potential of identifying the type of stress.[12,13] Plant phenotyping efforts identify traits that increase crop tolerance to environmental stress and disease and rely on plant structural, performance, or physiological parameters, but there are fewer tools available for monitoring plant's internal chemical signals associated with stress.[14−16]

Nanotechnology-based sensors are emerging tools for early detection of plant stress by enabling real-time monitoring of plant health via electronic devices.[17] Optical nanosensors have been demonstrated to report plant signaling molecules that communicate and trigger plant stress responses through epifluorescence microscopy of H_2O_2 and nitric oxide (NO) in leaf sections and remote detection of glucose in algae and whole plants.[18−20] Accumulation of reactive oxygen species (ROS) such as H_2O_2 is a hallmark of plant responses to stress.[21,22] Generation and accumulation of plant H_2O_2 have been reported in plants under most stresses including light stress, heat, salinity, wounding, and pathogen infection.[15,23,24] However, there are currently no H_2O_2 nanotechnology-based sensors able to respond to H_2O_2 in the plant physiological range from 10 to 100 μM.[17] Previous studies have demonstrated that single-walled carbon nanotubes (SWCNTs) are promising tools for biosensing applications.[25,26] Semiconducting SWCNTs display a chirality-dependent fluorescence in the near-infrared (nIR).[27] Different chemical functionalization approaches with nucleic acids, peptides, lipids, and proteins have been applied to tailor SWCNT surface chemistry.[28−31] These functionalized SWCNTs are highly sensitive to important molecules such as neurotransmitters (dopamine, serotonin), proteins, and nucleic acids.[32−36] It has been also known that nIR fluorescent SWCNTs coated with single-stranded DNA (deoxyribonucleic acid) ($ss(GT)_{15}$) report exogenously applied H_2O_2 from leaf sections at a concentration of 100 μM.[19] These studies were performed using custom-made nIR fluorescence microscopes under laboratory conditions. Similar sensors have also been

Received: December 15, 2019
Revised: February 14, 2020
Published: February 25, 2020

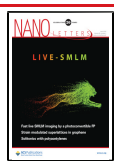

https://dx.doi.org/10.1021/acs.nanolett.9b05159
Nano Lett. 2020, 20, 2432−2442

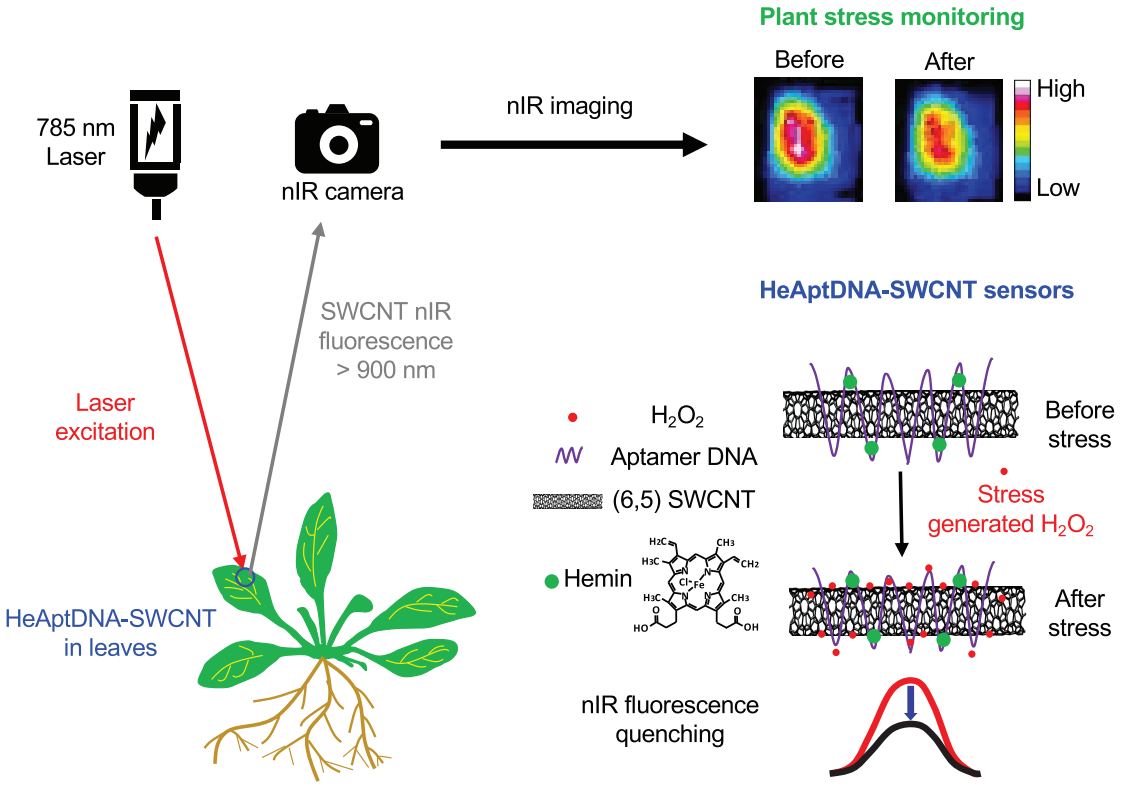

Figure 1. *In vivo* monitoring of plant health by SWCNT sensors for H_2O_2. SWCNTs functionalized with a DNA aptamer that binds to hemin (HeAptDNA-SWCNT) quench their nIR fluorescence upon interaction with H_2O_2 generated by the onset of plant stress. The spatial and temporal changes in nIR fluorescence intensity in leaves embedded with HeAptDNA-SWCNT sensors are remotely recorded by a nIR camera to assess plant health status.

shown to detect H_2O_2 molecules released from mammalian cells in real-time.[37,38] Optical nanosensors that signal the onset and type of stress to agricultural and phenotyping nIR imaging devices could indicate where and when improvement on plant growing conditions is needed, provide new monitoring tools for environmental stress and disease, and allow rapid screening of key plant chemical traits promoting stress tolerance. Because H_2O_2 is an excellent indicator for plant stress levels, the ability to monitor whole-leaf signaling molecule levels in mature plants could be very valuable for large-scale phenotyping purposes.[14,15]

Currently, we lack the ability to use noncontact electronic devices for remote monitoring of signaling molecules (e.g., H_2O_2) in wild-type plant species that remain difficult to genetically transform. Existing approaches to monitor plant H_2O_2 are based on genetically encoded sensors expressed in transgenic lines of plant model systems[39] that are not easily translatable to crops. Recently, fluorescent dyes for ROS detection were shown to report these signaling molecules to phenotyping devices such as Lumina S5 enclosed imaging systems under environmental and pathogen stresses.[15] Although it is an exciting application, fluorescent dyes photobleach and lack the signal-to-noise ratios to be detected by hyperspectral imaging cameras or portable devices, like smartphones, for applications in growth chambers, greenhouses, or the field. By contrast, SWCNT-based sensors do not photobleach and provide a temporal resolution adequate to detect plant stress responses and associated signaling molecules (H_2O_2) in both short- and long-term, from milliseconds to months.[17] These nanosensors have been reported to detect single molecules *in vitro*,[37] and their spatial resolution is only limited by the Abbe-limit, which allows localization of biomolecule generation sites at subcellular resolution.[40] SWCNTs are reversible sensors with long lifetimes that fluoresce in a region of the nIR spectrum where living tissues are relatively transparent.[41] We have previously used these water-soluble, nontoxic synthetic sensors in model and nontraditional plant systems[18,42] and demonstrated the crucial capability to monitor H_2O_2 in real-time in leaf sections of *Arabidopsis* plants.[19] However, the existing sensing approaches do not provide the necessary sensitivity that would enable remote H_2O_2 detection from living whole plants.[37,38]

Herein, we developed a H_2O_2 sensor based on SWCNTs functionalized with a DNA aptamer that binds to hemin (HeAptDNA-SWCNT) and allows remote monitoring of plant health and detection of both environment- and pathogen-related stresses. For accomplishing this goal we: (1) performed *in vitro* optimization of HeAptDNA-SWCNT detection of H_2O_2 within the plant physiological range (10−100 μM); (2) characterized the *in vivo* response of nanosensors to H_2O_2 in plant leaves; (3) assessed the biocompatibility of the nanosensors in plants; and (4) tested their performance in remote monitoring of plant stresses including UV-B, high light, wounding, and pathogen-related peptide (flg22). The newly developed HeAptDNA-SWCNT nIR sensors report H_2O_2 *in vivo* with a sensitivity and selectivity that enables the detection

https://dx.doi.org/10.1021/acs.nanolett.9b05159
Nano Lett. 2020, 20, 2432−2442

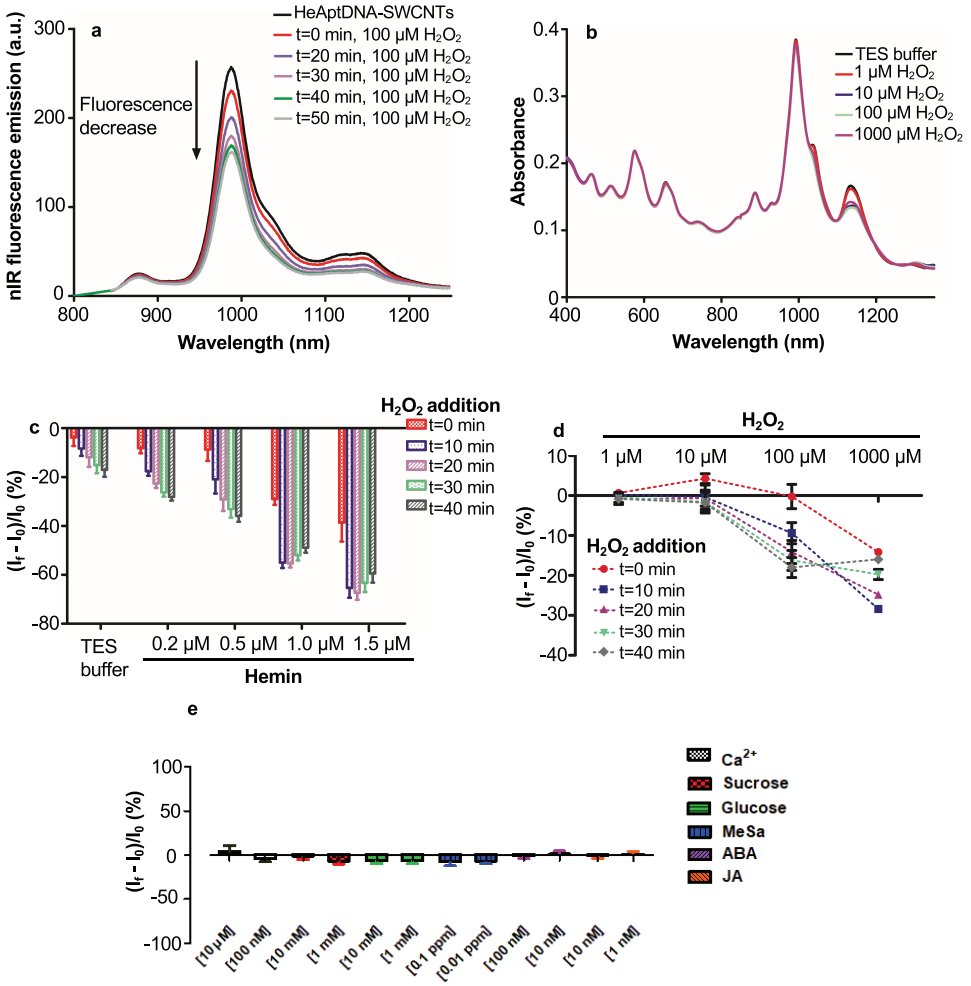

Figure 2. *In vitro* characterization of nIR HeAptDNA-SWCNT fluorescence response to H_2O_2. (a) nIR fluorescence emission of HeAptDNA-SWCNT sensors strongly decreases within 40 min after addition of H_2O_2 (100 μM). (b) Absorption spectra of HeAptDNA-SWCNTs (2 nM) with hemin (0.5 μM) 24 h after H_2O_2 addition of varying concentrations [1−1000 μM] indicate high colloidal stability. (c) Quantification of the optimal hemin concentration in HeAptDNA-SWCNTs (2 nM) to maximize the fluorescence response of sensors to 100 μM H_2O_2. (d) Fluorescence response of HeAptDNA-SWCNT to different H_2O_2 concentrations at the optimal hemin concentration of 0.5 μM. (e) Sensor nIR-fluorescence responses were below 10% $(I_f - I_0)/I_0$ for stress-associated plant ions, sugars, and hormones (Ca^{2+}, sucrose, glucose, methyl salicylate, abscisic acid, jasmonate); mean + SD (n = 3).

of the onset of plant stress using nIR imaging devices that are already utilized for precision agriculture applications.

Results and Discussion. *In Vitro HeAptDNA-SWCNT Sensor Response to H_2O_2.* To design a highly sensitive nIR reporter of H_2O_2 for monitoring plant health, we used SWCNTs as backbone and noncovalently functionalized it with an aptamer sequence (5′- AGTGTGAA ATATCTAAAC-TAAATGTGGAGGGTGGGACGGGAAGAAGTT-TATTTTTCACACT-3′) that binds to porphyrins[43,44] (Figure 1). This approach enabled the specific binding of hemin, a protoporphyrin IX complex that binds ferric iron (Fe^{3+}), which is known to undergo a Fenton-like reaction with H_2O_2 producing hydroxyl radicals.[38,45−47] SWCNTs have been reported to quench their nIR fluorescence in response to ROS.[38] However, previously published ss$(GT)_{15}$ coated SWCNTs sensors[19] could not achieve the desired sensitivity within the plant physiological range of <100 μM. Therefore, we tested hemin coated HeAptDNA-SWCNT in which H_2O_2 reacts to hydroxyl radicals, resulting in SWCNT fluorescence quenching. The HeAptDNA-SWCNTs exhibited a strong fluorescence quenching up to 50 min after H_2O_2 addition (Figure 2a). The characteristic SWCNT absorbance peaks were preserved for most chiralities in the presence of H_2O_2 at a range of concentrations from 1 to 1000 μM, indicating high long-term colloidal stability (Figure 2b). However, in the presence of H_2O_2, the absorbance of larger SWCNT chiralities, for example, (12,1), (8,4), (9,4), (8,4), (10,3), or (8,6)-SWCNTs decreased (Figures 2b and S1). Therefore, (6,5)-chirality enriched SWCNTs were used as a building block for sensing in biological experiments. The absorption spectra of these HeAptDNA-SWCNT show the presence of minor fractions of (6,4), (8,3), (7,5), (8,4), and (9,4) SWCNTs. Similarly, the two-dimensional (2D) excitation−emission spectra of HeAptDNA-SWCNTs indicate the most prominent nIR emission from the (6,5) chirality, followed by (7,5), (8,3), and (6,4)-SWCNT chiralities with lower nIR intensity (Figure S2). The number of bound aptamer-DNA was determined to be approximately 1 per 2.5 nm of SWCNT length (around 240

https://dx.doi.org/10.1021/acs.nanolett.9b05159
Nano Lett. 2020, 20, 2432−2442

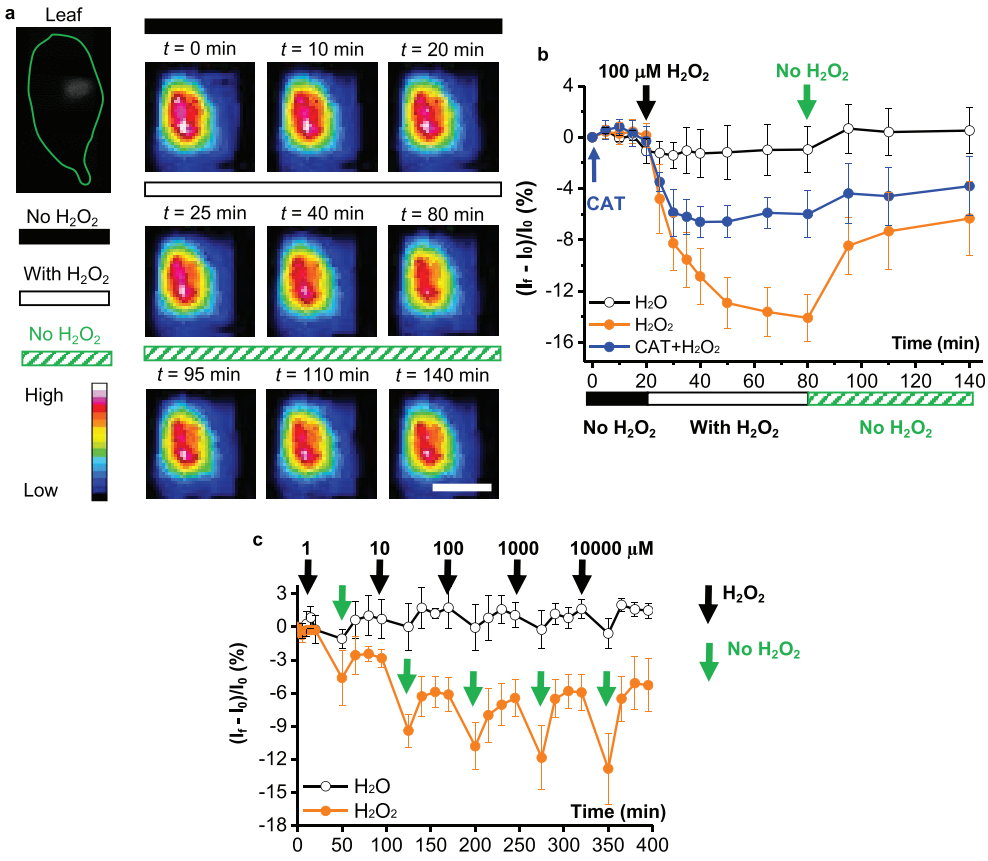

Figure 3. *In vivo* sensing of H_2O_2 by HeAptDNA-SWCNT in plant leaves. (a) nIR fluorescence images of HeAptDNA-SWCNT sensors embedded within *Arabidopsis* leaves and (b) corresponding nIR intensity changes in response to 100 μM H_2O_2 added topically on the leaf surface. Sensor fluorescence emission quenches upon exposure to H_2O_2, followed by partial recovery and stabilization of the fluorescence signal under the absence of H_2O_2. A H_2O_2 scavenging treatment of adding catalase (1500 U/mL) during the initial 20 min of nIR imaging resulted in decreased sensor fluorescence response to H_2O_2; mean ± SE (n = 4–6). (c) Sensitivity and reversibility of HeAptDNA-SWCNT sensors assessed by measuring the nIR fluorescence intensity changes after successive exposure to H_2O_2 at different concentrations from 1 to 10,000 μM; mean ± SE (n = 4); scale bar, 0.5 cm.

aptamers for a 600 nm long SWCNT) following a previously published method.[48]

The functionalization of SWCNTs with hemin leads to quenching of the sensor's nIR fluorescence in a concentration-dependent manner (Figure S3), and H_2O_2 further quenches the sensor fluorescence (Figure 2a). However, hemin also increases the relative H_2O_2 response (Figure 2c). Therefore, we evaluated the optimal ratio of hemin to aptamer DNA coated SWCNTs to improve the H_2O_2 sensing ability without compromising the photoluminescence readout of nanosensors for nIR remote detection. These *in vitro* experiments indicated that a ratio of 0.5 μM hemin to 2 nM HeAptDNA-SWCNTs is optimal for H_2O_2 sensing (Figure S3c,d). The corresponding sensor calibration curve (Figure 2c) shows sensitivity in the μM range and saturation around 100 μM in a time-dependent fashion (Figure 2d). The H_2O_2 sensing mechanism could be direct quenching of SWCNT fluorescence by H_2O_2 adsorption on the carbon nanotube surface as reported for certain functionalized SWCNTs.[49] However, without hemin functionalization, we observed no enhanced nIR fluorescence change. Therefore, it is more likely that hemin catalyzes a Fenton-like reaction of H_2O_2 to reactive hydroxyl radicals that quench SWCNT fluorescence in a similar fashion to the reaction with protons.[50] To evaluate the impact of other stress-related plant metabolites on HeAptDNA-SWCNT sensing ability, selectivity tests were performed against Ca^{2+}, sugar (sucrose and glucose), and plant hormone levels (methyl salicylate, abscisic acid, and jasmonate) (Figure 2e). Ca^{2+}, glucose, and sucrose regulate physiological and developmental responses to plant stress across diverse plant taxa.[23,51,52] Plant hormones such as abscisic acid are early signals of water stress,[53] jasmonate coordinates stress responses to salinity, freezing, drought, and wounding,[54] and methyl salicylate is involved in plant pathogen defense.[55] These stress-associated plant signaling molecules did not substantially affect the nIR fluorescence response of the HeAptDNA-SWCNTs. Additionally, the H_2O_2 sensing ability of HeAptDNA-SWCNTs in the presence of these stress-associated molecules was not impaired (Figure S4), highlighting their selectivity and capability for *in vivo* applications.

In Vivo Sensing of H_2O_2 by HeAptDNA-SWCNT Embedded in Plant Leaves. The SWCNT fluorescence in the nIR region falls into the tissue transparency window and low leaf autofluorescence range, making SWCNT-based sensors ideal for *in vivo* applications in plants. The nanosensors were embedded in leaves of *Arabidopsis* plants by a facile method of leaf lamina infusion using a needleless syringe, as performed previously in other plants.[18,19,42] Leaves were exposed to H_2O_2

https://dx.doi.org/10.1021/acs.nanolett.9b05159
Nano Lett. 2020, 20, 2432–2442

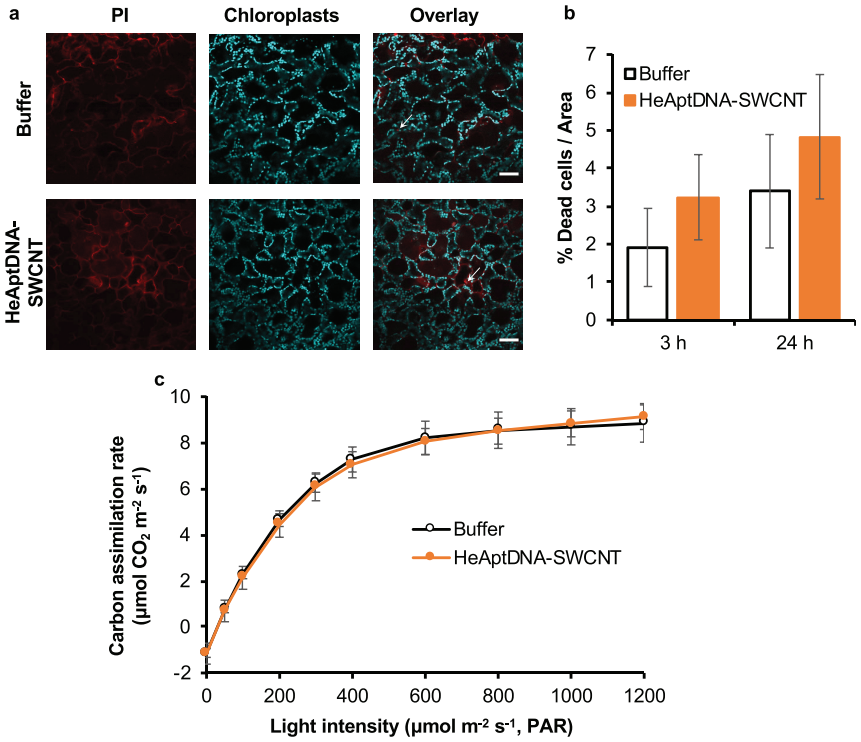

Figure 4. Biocompatibility of HeAptDNA-SWCNT sensors in plants. (a) Confocal microscopy images of *Arabidopsis* leaf mesophyll cells exposed to PI, a fluorescent dye that stains dead cells. Scale bar, 50 μm. (b) No significant differences in percentage of dead cells per area were observed between plants interfaced with HeAptDNA-SWCNT sensors and those treated with buffer (control) ($P < 0.05$, Student's t test); mean ± SE (n = 5). (c) Plant photosynthesis measured as leaf carbon assimilation rates at varied PAR levels was not impacted by HeAptDNA-SWCNT sensors compared to controls (buffer) ($P < 0.05$, Student's t test); mean ± SE (n = 6).

by direct application on the leaf surface, whereas plants treated with water instead of H_2O_2 were used as controls. Sensor fluorescence intensity changes in response to the leaf H_2O_2 exposure was monitored via its nIR fluorescence emission (Figure 3). The nIR imaging was performed using a remote nIR camera (Xeva-1.7-320 TE3) coupled to a 900 nm long-pass filter that allowed the detection of only nIR wavelengths from fluorescent SWCNTs, while deflecting the laser excitation (785 nm) and plant autofluorescence in the red and far-red range of the spectrum. A maximum emission intensity change (−14%) of HeAptDNA-SWCNT sensor was observed in *Arabidopsis* plants exposed to 100 μM H_2O_2 for 60 min (Figure 3a,b). After the removal of H_2O_2, the nIR emission intensity of HeAptDNA-SWCNT sensors was partially recovered (up to −6%), demonstrating that the sensor is reversible. The addition of a well-known H_2O_2 enzymatic scavenger (catalase, 1500 U/mL) to leaves before treatment with H_2O_2 resulted in a significant reduction of the sensor nIR fluorescence response to H_2O_2. Together, these results indicate that the sensor fluorescence quenching occurs in response to H_2O_2 in plants.

To investigate the sensitivity of HeAptDNA-SWCNT to H_2O_2 *in vivo*, we tested the sensor nIR fluorescence response in plant leaves to 1, 10, 100, 1000, and 10,000 μM H_2O_2 (Figure 3c, Video S1). The range of H_2O_2 concentrations from 1 to 100 μM is within the reported physiological range in plants.[17] The nIR emission intensity of HeAptDNA-SWCNT sensors was significantly reduced in response to 10 μM H_2O_2 down to −9.4% with further intensity decreases to −12.9% upon exposure to higher H_2O_2 concentrations. To our knowledge, this is the optical SWCNT sensor having the highest sensitivity to H_2O_2 (10 μM) *in vivo*, with an order of magnitude higher sensitivity than previous SWCNT sensor approaches using $(GT)_{15}$-SWCNTs.[19] After removal of H_2O_2 exposure at different concentrations, we observed the partial recovery of nIR emission intensity of HeAptDNA-SWCNT sensors, indicating their reversibility *in vivo* (Figure 3c). The HeAptDNA-SWCNT sensors in control leaves exposed to ddH_2O exhibited nonsignificant ($P > 0.05$) changes in nIR emission intensity (Figure 3c). These results demonstrate that HeAptDNA-SWCNTs are reversible sensors that report physiological levels of H_2O_2 in plants via nIR fluorescence signals to electronic devices.

The HeAptDNA-SWCNT sensors are also biocompatible within plants (Figure 4). We assessed the impact of embedded sensors in leaves by a cell viability assay using propidium iodide (PI), a fluorescent dye that stains dead plant cells.[56] Confocal images of leaf mesophyll cells stained with PI indicated no significant differences in the percentage of dead cells per leaf area for HeAptDNA-SWCNT sensor treated plants (4.8 ± 1.6%) compared with buffer control counterparts (3.2 ± 1.1%) (Figure 4a,b). Similarly, plant photosynthetic performance was not affected by HeAptDNA-SWCNT sensors (Figures 4c and S4). Both HeAptDNA-SWCNT and control plants showed similar leaf CO_2 assimilation rates over a wide range of light intensities (Figure 4c) and CO_2 concentrations (Figure S5). Thus, the high biocompatibility of these H_2O_2 optical nanosensors indicates minimal impact on plant health status.

https://dx.doi.org/10.1021/acs.nanolett.9b05159
Nano Lett. 2020, 20, 2432−2442

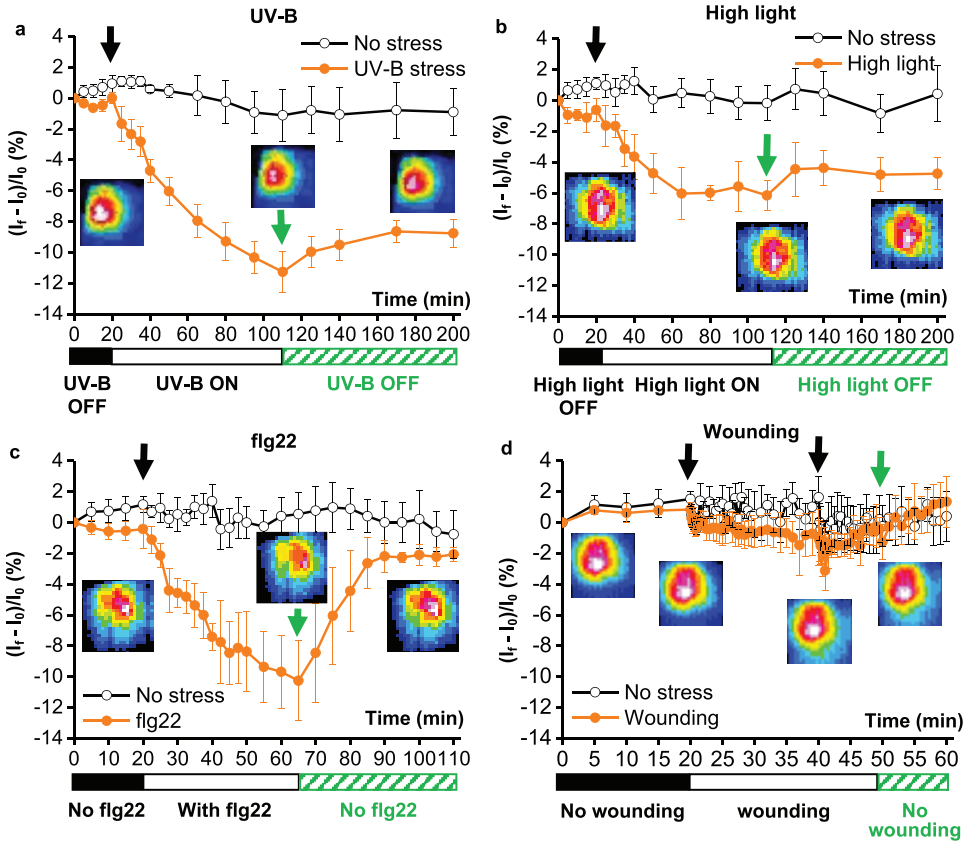

Figure 5. *In vivo* optical monitoring of plant health by H_2O_2 nanosensors. The nIR fluorescence intensity changes of HeAptDNA-SWCNT sensors in leaves (color map insets) report the onset of environmental stresses including UV-B, high light, and pathogen-associated peptide stress (flg22), but not leaf wounding. The sensor nIR fluorescence intensity decreases under (a) UV-B and (b) high light with a minor recovery of the initial fluorescence signal after the stress is removed. In contrast, (c) HeAptDNA-SWCNT nIR fluorescence quenching is followed by a strong recovery of emission intensity upon exposure and subsequent removal of flg22 peptide. (d) Leaf mechanical wounding did not impact sensor nIR fluorescence emission; mean ± SE (n = 4).

In Vivo Optical Monitoring of Plant Health under Stress. We observed a significant decrease in HeAptDNA-SWCNT nIR emission intensity from plants under UV-B (−11%), high light (−6%), and pathogen-related flg22 peptide (−10%) stresses relative to nonstress controls ($p < 0.05$) (Figure 5a–c). Rapid systemic ROS accumulation has been reported in plants in response to light stress, infection with bacterial pathogens, and mechanical wounding.[15] The flg22 peptide is used as a model for research on microbial pathogen induced response.[57] This peptide has a sequence derived from the flagellin N-terminus of the bacteria *Pseudomonas spp.* that is known to elicit immune responses in plants.[57] Leaf wounding by insects is also a common stress related to herbivore attack that negatively impacts plant growth.[58] However, mechanical wounding on leaves did not result in changes of the nIR emission intensity of HeAptDNA-SWCNT sensors ($p > 0.05$) (Figure 5d). The UV-B, high light, and flg22 treatments induced a decrease in nIR emission intensity of H_2O_2 sensors in plants within 60–120 min of stress exposure. The sensor fluorescence recovery after removal of the stress treatment varied from a strong change of −10% to −2% for flg22 and smaller changes of −11 to −9% for UV-B and −6% to −5% for high light, indicating different kinetics of the stress response to stress, especially for the microbial pathogen-related stress (flg22). Control plants under no stress conditions exhibited minor changes in sensor nIR emission intensity from 1.4 to −0.9% (Figure 5). Using a quantitative biochemical assay for H_2O_2, we measured a significant accumulation of leaf H_2O_2 concentration associated with the exposure of plants to UV-B, high light, and flg22 ($p < 0.05$), but not for leaf wounding compared to nonstress controls (Figure S6). The increase in leaf H_2O_2 levels from 30 to 60 μM relative to controls was within the sensor sensitivity (>10 μM H_2O_2). Together, these results demonstrate that HeAptDNA-SWCNT are able to monitor plant health in real-time by sensing H_2O_2 and report the onset of environmental stresses including UV-B, high light, and microbial pathogens.

Determining both the onset and type of plant stress would likely improve by multiplexing plant chemical signal sensing. Using chirality enriched SWCNTs, multiple spectrally encoded sensors could be imaged simultaneously[19,59] to allow other signaling molecules associated with plant health to be monitored in parallel. For example, this can be accomplished by interfacing plants with (6,5) and (7,6) enriched chirality SWCNT sensors having distinct fluorescence emission peaks in the nIR that can be recorded by hyperspectral imaging devices. For adequate performance in the field, the sensor durability is expected to span a growing season. SWCNT sensor lifetime has been reported in mammalian systems under laboratory conditions to be at least six months,[41] but needs to

https://dx.doi.org/10.1021/acs.nanolett.9b05159
Nano Lett. 2020, 20, 2432–2442

be assessed in plants under field conditions. The required spatial resolution of plants with nanosensors from sentinel individuals to groups of plants will depend on applications in plant phenotyping, urban or industrial agriculture, and microenvironment variations. Nanosensors with high sensitivity and selectivity, multiplexing and long lasting nonphotobleaching capabilities, and optical communication capabilities with existent nIR agricultural equipment are an emerging toolkit for chemical phenotyping and monitoring crop plant health.

Conclusions. Long-term sustainability of crop productivity will rely on precision agriculture, the use of data-driven technology in crop management, and improved plant phenotyping tools.[14,60,61] Plant nanobiotechnology promises transformative solutions to improve global agricultural security,[62−64] including the prospect of plant nanosensors able to communicate crop health status before stress symptoms manifest.[17] The HeAptDNA-SWCNT are selective sensors for H_2O_2, a fundamental plant signaling molecule associated with stress, and respond within the H_2O_2 plant physiological range (10−100 μM). The temporal dynamics of the nIR fluorescence quenching in response to plant stresses *in vivo* occurred in distinct time frames reaching a peak in intensity decrease at 60 min for pathogen-related stress (flg22) and 120 min for environmental stresses (UV-B and high light). Sensor reversibility *in vivo* was high after exposure to microbial pathogen-related stress (flg22) but not to environmental stresses (UV-B and high light). These differences in temporal patterns of fluorescence signal quenching and recovery opens opportunities for interpreting stress patterns and fingerprinting type and level of stress. It is known from other signaling processes in living systems that the spatiotemporal patterns of stress response might contain underlying information to pinpoint cell health status.[40] To analyze these complex spatiotemporal patterns, simulations and analysis require considering both sensor and stress kinetics.[65]

One advantage of SWCNT sensors is that they can be delivered through the leaf lamina on selected leaves or individuals using a needleless syringe, a simple, controlled, and practical nanoparticle foliar delivery method.[19,42] SWCNT can become kinetically trapped within plant cell and organelle lipid bilayers.[18,66,67] Thus, we expect that SWCNT translocation outside of leaves through the vascular tissue would be limited. Size and surface coating modifications can be tailored to localize nanoparticles in plant subcellular compartments,[67] which could allow more efficient delivery into specific leaf cells and organelles (e.g., stomatal guard cells, chloroplasts, and extracellular space). SWCNTs have also been functionalized with nanobodies as recognition units to bind to specific locations in organisms.[68] Such an approach combined with the H_2O_2 sensing demonstrated in this study could enable localization of nanosensors to specific compartments in plants. Overall, our results indicate that SWCNT-based nIR fluorescent nanosensors for H_2O_2 are able to report plant stress status remotely to macroscopic imaging devices. This nanobiotechnology-based approach provides a powerful sensing tool that can be translated to crop plant species for a more sustainable nano-enabled agriculture.

Methods. *Plant Growth.* *Arabidopsis thaliana* (Columbia 0) plants 4−5 weeks old were used in this study. Seeds were sown in standard soil mix (Sunshine, LC1 mix) filled pots (2 × 2 in., 32 inserts). One week after seed germination, only one seedling was kept in each pot. Plants were grown in an Adaptis 1000 growth chamber (Conviron). The growth chamber settings were set at 200 μmol m^{-2} s^{-1} photosynthetic active radiation (PAR), 24 ± 1 °C and 21 ± 1 °C at day and night times, respectively, 70% relative humidity, and 14h/10 h day/night regime. Plants were hand watered with deionized water twice per week.

Synthesis of Hemin Complexed Aptamer DNA-SWNCT (HeAptDNA-SWCNT). Hemin complexed HeAptDNA-SWCNT were synthesized by mixing 125 μL, 1 mg/mL (6,5) chirality enriched SWCNTs (Sigma-Aldrich, product no. 773735, in 10 mM *N*-[Tris(hydroxymethyl)methyl]-2-aminoethanesulfonic acid (TES), pH 7.0) with 125 μL, 2 mg/mL ssDNA (5′-AGTGTGAAATATCTAAACTAAATGTGGAGGGTGGGACGGGAAGAAGTTTATTTTTCACACT-3′, in 10 mM TES, pH 7.0) in a 1.5 mL eppendorf tube. After pipetting for 5 times, the mixture was tip sonicated (15 min, 30% Amplitude, Fisher Scientific Model 120 Sonic Dismembrator) in an ice bath. The sonicated mixture was then centrifuged for 60 min, 16,000*g*, at ambient temperature (two times). The supernatant was then transferred to a Vivaspin 500 MWCO (molecular weight cut off) filter (100,000 Da cutoff) and mixed with 500 μL of TES buffer, followed by centrifugation at 15,000*g* to remove excess ssDNA (3 times washing). Centrifugation cycles of 6−10 min allowed the mixture to be concentrated to 25 μL in the filter. After the washing steps, the purified samples were redispersed via tip sonication for 30 s (30% Amplitude, Fisher Scientific Model 120 Sonic Dismembrator). The sonicated mixture was centrifuged twice for 90 min at 16,000*g* and ambient temperature. The supernatant was collected in a new 1.5 mL eppendorf tube, and the concentration of this sample was determined by measuring the absorbance at 991 nm with a Cary 500 UV−vis/nIR spectrophotometer. The absorbance was used to calculate the SWCNT molar concentration by following a previously published protocol.[48] The concentrations used for *in vivo* experiments were 8 μM hemin and 16 nM aptamer DNA-SWCNTs. The synthesized hemin complexed aptamer DNA-SWCNT was stored at ambient temperature until further use.

In Vitro Characterization of HeAptDNA-SWCNT Sensor. UV-vis-nIR absorption spectroscopy was performed with a JASCO V-670 device acquiring a spectral range from 400 to 1350 nm in 0.2 nm steps. Fitting of absorbance spectra was performed as reported previously,[59] based on an approach from Pfohl et al.[69] The nIR fluorescence spectra were recorded with a Shamrock 193i spectrometer (Andor Technology Ltd., Belfast, Northern Ireland) connected to an IX53 microscope (Olympus, Tokyo, Japan). Excitation was performed with a gem 561 laser (Laser Quantum, Stockport, UK). 2D excitation−emission spectra were recorded with an monochromatic light source (MSH150; LSE341 light source, LOT-Quantum Design GmbH, Darmstadt, Germany). HiPco-SWCNTs (NanoIntegris HiPco Raw SWCNTs) were coated with HeAptDNA to determine the optimal SWCNT chirality for hemin complexation. For analyte-dependent nIR fluorescence response measurements, 180 μL of 2 nM HeAptDNA-SWCNT was placed in a 96-well plate and mixed with 20 μL of analyte at the desired concentration. The response of HeAptDNA-SWCNT to different H_2O_2 concentrations within 0.2−1.5 μM hemin concentration range was recorded from 0 to 40 min to analyze the sensors kinetic fluorescence response. Selectivity analysis of sensors was performed against plant molecules associated stress within

https://dx.doi.org/10.1021/acs.nanolett.9b05159
Nano Lett. 2020, 20, 2432−2442

the reported plant physiological range[17] by recording *in vitro* responses to nIR fluorescence intensity of the HeAptDNA-(6,5)-SWCNT spectra.

Nanosensor Delivery into Plant Leaves. A detailed protocol for leaf lamina infiltration of nanoparticles is given in Wu et al.[70] Briefly, selected leaf regions were slowly infiltrated with ∼20 μL HeAptDNA-SWCNT (16 nM HeAptDNA-SWCNT, 8 μM hemin, in TES buffer) solution through the leaf abaxial (lower) side by gently pressing the tip of the syringe (1 mL NORM-JECT) against the leaf lamina. Kimwipes (Kimtech Science) were used to remove the excess nanoparticle solution on the leaf surface. The plants interfaced with the nanosensors were kept on the bench under room light (10−15 μmol m^{-2} s^{-1}) and ambient temperature at least 3 h for acclimation and incubation.

In Vivo Remote Imaging of HeAptDNA-SWCNT nIR Fluorescence Emission. A flat intact leaf of *Arabidopsis* plants (Col-0, 4−5 weeks old) grown in pots (2 × 2 in.) was infused with HeAptDNA-SWCNT. After incubation and adaption for at least 3 h on the lab bench, the pot and soil were carefully removed, while avoiding damage to the roots. The roots and remaining bounded soil were wrapped with cling wraps. Then the plant was laid down on a lab bench, and the flat leaf interfaced with HeAptDNA-SWCNT was immobilized on top of a laser safety screen (TPS5, THORLABS, USA) by using black tape without damaging the leaf. For nIR imaging of H_2O_2 nanosensors in leaves, a 785 nm laser (IBeam Smart, TOPTICA Photonics, Germany) and Xenics nIR camera (XEVA-CL-1.7-320, Xenics, Belgium) were used. The nIR laser was expanded by a plano-concave lens (N-BK7, Ø1/2″, THORLABS, USA) to a larger area on the plant leaf. The laser output was set at 250 mW. The Xenics nIR camera frame rate (up to 100 fps) was set to 2 fps. The camera was cooled below −40 °C. The distance between the nIR camera and the leaf was set to 70 cm, and the angle between the leaf surface and the line pointing from the camera to the leaf was about 75°.

To assess the *in vivo* sensing of H_2O_2 by HeAptDNA-SWCNT sensors, a 100 μL solution of different concentrations of H_2O_2 (30%, Thermo Fisher) was added on the adaxial (upper) leaf surface and removed during the nIR imaging for each time point. To facilitate diffusion of the H_2O_2 solution into the leaf, small holes were made on the leaf region infiltrated with HeAptDNA-SWCNT using the tip of fine forceps (Excelta 5SASE, Thermo Fisher), followed by 3 h acclimation to minimize impact of physical damage. During nIR imaging of nanosensors, plants were kept under room light conditions to prevent stomatal fully closure. For assessing the sensor nIR intensity changes in response to 100 μM H_2O_2, background images were recorded (0−20 min), then 100 μM H_2O_2 was added topically to the adaxial leaf surface (20−80 min), followed by removal of H_2O_2 (80−140 min). In addition, a H_2O_2 scavenging treatment was performed by adding 100 μL of catalase (1500 U/mL) on the adaxial side of the leaf surface. Images of nIR background were recorded (0−20 min) before removing catalase and adding 100 μM H_2O_2(20−80 min), followed by removal of H_2O_2 (80−140 min). The catalase or H_2O_2 solutions were removed before recording nIR images and re-added afterward. For assessing the sensitivity and reversibility of the sensors, the leaf nIR background was recorded (0−20 min), followed by applications of H_2O_2 at concentrations of 1 (20−50 min), 10 (95−125 min), 100 (170−200 min), 1000 (245−275 min), and 10,000 (320−350 min) μM H_2O_2, and removal of the applied H_2O_2 (50−95 min, 125−170 min, 200−245 min, and 350−395 min).

Plant stress treatments for UV-B, high light, flg22, and leaf wounding proceeded as follows: UV-B stress was induced in plants using a 365 nm UV lamp (3UV-38 UV lamp, UVP, LLC). High-light stress was generated by exposing leaves to ∼1800 μmol m^{-2} s^{-1} of photosynthetic active radiation using a blue and red LED (light-emitting diode) (GFS 3000 gas analyzer, Walz, Germany). Images of nIR background (0−20 min) were recorded before turning UV or LED light stress on (20−110 min), followed by light stress off (110−200 min). Microbial pathogen stress was simulated using a 10 μM flg22 peptide (Genscript, dissolved in molecular grade water). Flg22 is a highly conserved 22 amino acid peptide from a bacterial flagellin which is well-known to induce microbial pathogen defense response in plants.[57] A 100 μL flg22 peptide solution (10 μM) was added on the adaxial (top) side of the leaf and removed during each measuring time point. The diffusion of the solution into the leaf was increased by minor holes made on the HeAptDNA-SWCNT region by using the tip of fine forceps and allowing 3 h acclimation after making minor holes to minimize the side effects due to the physical damage. During imaging, plants were kept under room light conditions to prevent stomatal closure. Images of nIR background (0−20 min) were recorded before exposing leaves to flg22 (20−65 min), followed by removal of flg22 (65−110 min). Plant wounding stress was induced by a dissecting needle (diameter, 1 mm) and successive punctures on the adaxial side of the leaf lamina approximately 2 cm away from the location of the sensors. Images of nIR background were recorded (0−20 min), followed by a first wounding event (20 min), then multiple wounding events (40−50 min), and no wounding afterward (50−60 min).

nIR Image Analysis. Snapshots of nIR images of nanosensors embedded in leaves collected by the nIR camera were analyzed with ImageJ. For plotting the HeAptDNA-SWCNT nIR intensity changes in plants under stress, the images from each biological replicate were converted into stacks. A leaf region with the HeAptDNA-SWCNT was selected for analysis of average nIR fluorescence intensity over time. SWCNT nIR intensity images were plotted by converting them from RGB (red, green, blue) mode to 32-bit format with ImageJ. Then, a 16-color LUT format was applied to highlight the differences of HeAptDNA-SWCNT intensity.

Leaf H_2O_2 Content. A quantitative peroxide assay kit (Pierce, Thermo Scientific, USA) was used to measure the concentration of H_2O_2 in leaves as reported previously with modifications.[71] Plants were exposed to UV-B light (365 nm, 90 min), high light (1800 μmol m^{-2} s^{-1} of photosynthetic active radiation, 90 min), flg22 peptide (10 μM, 60 min), leaf wounding as described above, and no stress (controls). Leaf disks were harvested after plant stress and control treatments using a 12 mm cork borer, weighed immediately in a microbalance (ML802E, Mettler Toledo), and frozen into liquid nitrogen (in less than 1 min). Samples were then grinded in 0.5 mL of DI (deionized) water using a prechilled mortar and pestle. Ground samples in DI water were transferred to a microtube (0.5 mL) and centrifuged at 13,000 rpm for 1 min. Then, 50 μL of supernatant was added to 500 μL of quantitative peroxide assay working reagent (0.25 mM ammonium ferrous sulfate, 100 mM sorbitol, 125 μM xylenol in 25 mM H_2SO_4). The absorbance of the diluted solution was measured in a UV−vis spectrophotometer (UV-

https://dx.doi.org/10.1021/acs.nanolett.9b05159
Nano Lett. 2020, 20, 2432−2442

2600, Shimadzu) after reaction at ambient temperature for 30 min to determine H_2O_2 concentration.

Biocompatibility Assays of HeAptDNA-SWCNT Sensors. Cell viability staining of the hemin complexed HeAptDNA-SWCNT infiltrated *Arabidopsis* (Col-0) leaves was performed using PI (PI, 0.1 mM, plant cell viability assay kit, PA0100, Sigma-Aldrich) as described in our previous work.[20] Briefly, *Arabidopsis* leaves were infiltrated with buffer control (10 mM TES, pH 7.0) and hemin complexed HeAptDNA-SWCNT (in 10 mM TES, pH 7.0). Then, at 3 h and 24 h, leaf discs were stained with PI for 30 min. The stained samples were then mounted on microscopy slides for confocal microscopy (Leica SP5) imaging as described in our previous publication.[70] Confocal imaging detection range was set at 590−640 nm for PI and 700−800 nm for chloroplasts under laser excitation of 488 nm.

Plant Photosynthesis. Photosynthesis (A) measurements were performed in plants infiltrated with buffer (controls) or HeAptDNA-SWCNT sensors as we have described previously.[72] Briefly, a portable Gas-Exchange and Fluorescence System (GFS-3000, WALZ, Effeltrich, Germany) was programmed to expose leaves to a progressive stepwise decrease in PAR (A−light curve) and CO_2(A−Ci curve). Measurements were conducted in a leaf gas exchange chamber at a temperature of 23 °C and 50% relative humidity. Photosynthetic response curves were built with 10 PAR levels from 0 to 1200 (0, 50, 100, 200, 300, 400, 600, 800, 1000, and 1200) μmol m^{-2} s^{-1} and eight CO_2 ambient levels from 50 to 800 (50, 100, 150, 250, 300, 500,600, and 800) ppm. Measurements of photosynthesis response to CO_2 were conducted before measurements of light curves at saturating light (1200 μmol m^{-2} s^{-1}). Infiltrated leaves with buffer and HeAptDNA-SWCNT sensors were allowed to acclimate at room temperature for 24 h before photosynthesis measurements.

Statistical analysis. All data from *in vivo* experiments were analyzed using SPSS 23.0. Comparisons were performed by independent samples *t*-test (two tailed) or one-way ANOVA based on Duncan's multiple range test (two tailed). *, **, and *** represent $P < 0.05$, $P < 0.01$, and $P < 0.001$, respectively. Different lowercase letters mean significance at $P < 0.05$.

■ ASSOCIATED CONTENT

Supporting Information

The Supporting Information is available free of charge at https://pubs.acs.org/doi/10.1021/acs.nanolett.9b05159.

Supplementary figures for *in vitro* characterization of H_2O_2 nanosensors, photosynthesis in plants interfaced with nanosensors, and leaf H_2O_2 content of plants under stress (PDF)

Video S1: Sensor nIR fluorescence response to H_2O_2 in Arabidopsis plant leaves. *In vivo* exposure and removal of H_2O_2 in leaves with embedded HeAptDNA-SWCNT results in quenching and partial recovery of the sensor nIR intensity (AVI)

■ AUTHOR INFORMATION

Corresponding Authors

Juan Pablo Giraldo − *Department of Botany and Plant Sciences, University of California, Riverside, California 92521, United States;* orcid.org/0000-0002-8400-8944; Email: juanpablo.giraldo@ucr.edu

Sebastian Kruss − *Institute of Physical Chemistry, Georg August University, Göttingen, 37077 Göttingen, Germany;* orcid.org/0000-0003-0638-9822; Email: skruss@uni-goettingen.de

Authors

Honghong Wu − *Department of Botany and Plant Sciences, University of California, Riverside, California 92521, United States; College of Plant Science and Technology, Huazhong Agricultural University, Wuhan 430070, China*

Robert Nißler − *Institute of Physical Chemistry, Georg August University, Göttingen, 37077 Göttingen, Germany*

Victoria Morris − *Department of Botany and Plant Sciences, University of California, Riverside, California 92521, United States*

Niklas Herrmann − *Institute of Physical Chemistry, Georg August University, Göttingen, 37077 Göttingen, Germany*

Peiguang Hu − *Department of Botany and Plant Sciences, University of California, Riverside, California 92521, United States;* orcid.org/0000-0002-9526-6295

Su-Ji Jeon − *Department of Botany and Plant Sciences, University of California, Riverside, California 92521, United States;* orcid.org/0000-0002-5917-8837

Complete contact information is available at: https://pubs.acs.org/10.1021/acs.nanolett.9b05159

Author Contributions

‖These authors contributed equally to this paper. J.P.G., S.K., H.W., and R.N. conceived and designed the study. H.W., R.N., N.H., P.H., V.M., and S.J. conducted the experiments. H.W., J.P.G, S.K., R.N., P.H., and S.J. analyzed the data. All authors contributed to writing the paper.

Notes

The authors declare no competing financial interest.

■ ACKNOWLEDGMENTS

We thank Mr. James Eckhardt for assistance with the development of the *in vivo* remote detection system for nIR nanosensors in plants. This work was supported by the National Science Foundation under grant no. 1817363 to J.P.G. and a grant by the Volkswagen Foundation to S.K.

■ REFERENCES

(1) Croppenstedt, A.; Cattaneo, A. et al. *Leveraging Food Systems for Inclusive Rural Transformation: The State of Food and Agriculture 2017*; Food and Agriculture Organization of the United Nations: Rome, Italy, 2017

(2) Piao, S.; Ciais, P.; Huang, Y.; Shen, Z.; Peng, S.; Li, J.; Zhou, L.; Liu, H.; Ma, Y.; Ding, Y.; et al. The Impacts of Climate Change on Water Resources and Agriculture in China. *Nature* **2010**, *467* (7311), 43−51.

(3) Chakraborty, S.; Newton, A. C. Climate Change, Plant Diseases and Food Security: An Overview: Climate Change and Food Security. *Plant Pathol.* **2011**, *60* (1), 2−14.

(4) Fisher, M. C.; Henk, D. A.; Briggs, C. J.; Brownstein, J. S.; Madoff, L. C.; McCraw, S. L.; Gurr, S. J. Emerging Fungal Threats to Animal, Plant and Ecosystem Health. *Nature* **2012**, *484* (7393), 186−194.

(5) Williamson, C. E.; Zepp, R. G.; Lucas, R. M.; Madronich, S.; Austin, A. T.; Ballaré, C. L.; Norval, M.; Sulzberger, B.; Bais, A. F.; McKenzie, R. L.; et al. Solar Ultraviolet Radiation in a Changing Climate. *Nat. Clim. Change* **2014**, *4* (6), 434−441.

(6) van Ittersum, M. K.; van Bussel, L. G. J.; Wolf, J.; Grassini, P.; van Wart, J.; Guilpart, N.; Claessens, L.; de Groot, H.; Wiebe, K.;

Mason-D'Croz, D.; et al. Can Sub-Saharan Africa Feed Itself? *Proc. Natl. Acad. Sci. U. S. A.* **2016**, *113* (52), 14964−14969.
(7) Paini, D. R.; Sheppard, A. W.; Cook, D. C.; De Barro, P. J.; Worner, S. P.; Thomas, M. B. Global Threat to Agriculture from Invasive Species. *Proc. Natl. Acad. Sci. U. S. A.* **2016**, *113* (27), 7575−7579.
(8) Dosio, A.; Mentaschi, L.; Fischer, E. M.; Wyser, K. Extreme Heat Waves under 1.5 Degrees C and 2 Degrees C Global Warming. *Environ. Res. Lett.* **2018**, *13* (5), 054006.
(9) Ummenhofer, C. C.; Meehl, G. A. Extreme Weather and Climate Events with Ecological Relevance: A Review. *Philos. Trans. R. Soc., B* **2017**, *372* (1723), 20160135.
(10) Pathak, T. B.; Maskey, M. L.; Dahlberg, J. A.; Kearns, F.; Bali, K. M.; Zaccaria, D. Climate Change Trends and Impacts on California Agriculture: A Detailed Review. *Agronomy* **2018**, *8* (3), 25.
(11) Velásquez, A. C.; Castroverde, C. D. M.; He, S. Y. Plant-Pathogen Warfare under Changing Climate Conditions. *Curr. Biol.* **2018**, *28* (10), R619−R634.
(12) Mahlein, A.-K. Plant Disease Detection by Imaging Sensors - Parallels and Specific Demands for Precision Agriculture and Plant Phenotyping. *Plant Dis.* **2016**, *100* (2), 241−251.
(13) Zarco-Tejada, P. J.; Camino, C.; Beck, P. S. A.; Calderon, R.; Hornero, A.; Hernández-Clemente, R.; Kattenborn, T.; Montes-Borrego, M.; Susca, L.; Morelli, M.; et al. Previsual Symptoms of Xylella Fastidiosa Infection Revealed in Spectral Plant-Trait Alterations. *Nat. Plants* **2018**, *4* (7), 432−439.
(14) Dhondt, S.; Wuyts, N.; Inzé, D. Cell to Whole-Plant Phenotyping: The Best Is yet to Come. *Trends Plant Sci.* **2013**, *18* (8), 428−439.
(15) Fichman, Y.; Miller, G.; Mittler, R. Whole-Plant Live Imaging of Reactive Oxygen Species. *Mol. Plant* **2019**, *12* (9), 1203−1210.
(16) Li, L.; Zhang, Q.; Huang, D. A Review of Imaging Techniques for Plant Phenotyping. *Sensors* **2014**, *14* (11), 20078−20111.
(17) Giraldo, J. P.; Wu, H.; Newkirk, G. M.; Kruss, S. Nanobiotechnology Approaches for Engineering Smart Plant Sensors. *Nat. Nanotechnol.* **2019**, *14* (6), 541.
(18) Giraldo, J. P.; Landry, M. P.; Faltermeier, S. M.; McNicholas, T. P.; Iverson, N. M.; Boghossian, A. A.; Reuel, N. F.; Hilmer, A. J.; Sen, F.; Brew, J. A.; et al. Plant Nanobionics Approach to Augment Photosynthesis and Biochemical Sensing. *Nat. Mater.* **2014**, *13* (4), 400−408.
(19) Giraldo, J. P.; Landry, M. P.; Kwak, S.-Y.; Jain, R. M.; Wong, M. H.; Iverson, N. M.; Ben-Naim, M.; Strano, M. S. A Ratiometric Sensor Using Single Chirality Near-Infrared Fluorescent Carbon Nanotubes: Application to In Vivo Monitoring. *Small* **2015**, *11* (32), 3973−3984.
(20) Li, J.; Wu, H.; Santana, I.; Fahlgren, M.; Giraldo, J. P. Standoff Optical Glucose Sensing in Photosynthetic Organisms by a Quantum Dot Fluorescent Probe. *ACS Appl. Mater. Interfaces* **2018**, *10* (34), 28279−28289.
(21) Bose, J.; Rodrigo-Moreno, A.; Shabala, S. ROS Homeostasis in Halophytes in the Context of Salinity Stress Tolerance. *J. Exp. Bot.* **2014**, *65* (5), 1241−1257.
(22) Choudhury, F. K.; Rivero, R. M.; Blumwald, E.; Mittler, R. Reactive Oxygen Species, Abiotic Stress and Stress Combination. *Plant J.* **2017**, *90*, 856−867.
(23) Zhu, J.-K. Abiotic Stress Signaling and Responses in Plants. *Cell* **2016**, *167* (2), 313−324.
(24) Torres, M. A.; Jones, J. D. G.; Dangl, J. L. Reactive Oxygen Species Signaling in Response to Pathogens. *Plant Physiol.* **2006**, *141* (2), 373−378.
(25) Kruss, S.; Hilmer, A. J.; Zhang, J.; Reuel, N. F.; Mu, B.; Strano, M. S. Carbon Nanotubes as Optical Biomedical Sensors. *Adv. Drug Delivery Rev.* **2013**, *65*, 1933−1950.
(26) Hong, G.; Diao, S.; Antaris, A. L.; Dai, H. Carbon Nanomaterials for Biological Imaging and Nanomedicinal Therapy. *Chem. Rev.* **2015**, *115* (19), 10816−10906.
(27) O'Connell, M. J.; Bachilo, S. M.; Huffman, C. B.; Moore, V. C.; Strano, M. S.; Haroz, E. H.; Rialon, K. L.; Boul, P. J.; Noon, W. H.; Kittrell, C.; et al. Band Gap Fluorescence from Individual Single-Walled Carbon Nanotubes. *Science* **2002**, *297* (5581), 593−596.
(28) Zheng, M.; Jagota, A.; Semke, E. D.; Diner, B. A.; McLean, R. S.; Lustig, S. R.; Richardson, R. E.; Tassi, N. G. DNA-Assisted Dispersion and Separation of Carbon Nanotubes. *Nat. Mater.* **2003**, *2* (5), 338−342.
(29) Welsher, K.; Liu, Z.; Sherlock, S. P.; Robinson, J. T.; Chen, Z.; Daranciang, D.; Dai, H. A Route to Brightly Fluorescent Carbon Nanotubes for near-Infrared Imaging in Mice. *Nat. Nanotechnol.* **2009**, *4* (11), 773−780.
(30) Zubkovs, V.; Schuergers, N.; Lambert, B.; Ahunbay, E.; Boghossian, A. A. Mediatorless, Reversible Optical Nanosensor Enabled through Enzymatic Pocket Doping. *Small* **2017**, *13* (42), 1701654.
(31) Polo, E.; Nitka, T. T.; Neubert, E.; Erpenbeck, L.; Vuković, L.; Kruss, S. Control of Integrin Affinity by Confining RGD Peptides on Fluorescent Carbon Nanotubes. *ACS Appl. Mater. Interfaces* **2018**, *10*, 17693−17703.
(32) Kruss, S.; Landry, M. P.; Vander Ende, E.; Lima, B. M. A.; Reuel, N. F.; Zhang, J.; Nelson, J.; Mu, B.; Hilmer, A.; Strano, M. Neurotransmitter Detection Using Corona Phase Molecular Recognition on Fluorescent Single-Walled Carbon Nanotube Sensors. *J. Am. Chem. Soc.* **2014**, *136* (2), 713−724.
(33) Mann, F. A.; Herrmann, N.; Meyer, D.; Kruss, S. Tuning Selectivity of Fluorescent Carbon Nanotube-Based Neurotransmitter Sensors. *Sensors* **2017**, *17* (7), 1521.
(34) Dinarvand, M.; Neubert, E.; Meyer, D.; Selvaggio, G.; Mann, F. A.; Erpenbeck, L.; Kruss, S. Near-Infrared Imaging of Serotonin Release from Cells with Fluorescent Nanosensors. *Nano Lett.* **2019**, *19* (9), 6604−6611.
(35) Bisker, G.; Dong, J.; Park, H. D.; Iverson, N. M.; Ahn, J.; Nelson, J. T.; Landry, M. P.; Kruss, S.; Strano, M. S. Protein-Targeted Corona Phase Molecular Recognition. *Nat. Commun.* **2016**, *7*, 10241.
(36) Harvey, J. D.; Jena, P. V.; Baker, H. A.; Zerze, G. H.; Williams, R. M.; Galassi, T. V.; Roxbury, D.; Mittal, J.; Heller, D. A. A Carbon Nanotube Reporter of microRNA Hybridization Events in Vivo. *Nature Biomedical Engineering* **2017**, *1*, 0041 DOI: 10.1038/s41551-017-0041.
(37) Jin, H.; Heller, D. A.; Kalbacova, M.; Kim, J.-H.; Zhang, J.; Boghossian, A. A.; Maheshri, N.; Strano, M. S. Detection of Single-Molecule H2O2 Signalling from Epidermal Growth Factor Receptor Using Fluorescent Single-Walled Carbon Nanotubes. *Nat. Nanotechnol.* **2010**, *5*, 302.
(38) Heller, D. A.; Jin, H.; Martinez, B. M.; Patel, D.; Miller, B. M.; Yeung, T. K.; Jena, P. V.; Höbartner, C.; Ha, T.; Silverman, S. K.; et al. Multimodal Optical Sensing and Analyte Specificity Using Single-Walled Carbon Nanotubes. *Nat. Nanotechnol.* **2009**, *4* (2), 114−120.
(39) Exposito-Rodriguez, M.; Laissue, P. P.; Yvon-Durocher, G.; Smirnoff, N.; Mullineaux, P. M. Photosynthesis-Dependent H 2 O 2 Transfer from Chloroplasts to Nuclei Provides a High-Light Signalling Mechanism. *Nat. Commun.* **2017**, *8* (1), 49.
(40) Kruss, S.; Salem, D. P.; Vuković, L.; Lima, B.; Vander Ende, E.; Boyden, E. S.; Strano, M. S. High-Resolution Imaging of Cellular Dopamine Efflux Using a Fluorescent Nanosensor Array. *Proc. Natl. Acad. Sci. U. S. A.* **2017**, *114* (8), 1789−1794.
(41) Iverson, N. M.; Barone, P. W.; Shandell, M.; Trudel, L. J.; Sen, S.; Sen, F.; Ivanov, V.; Atolia, E.; Farias, E.; McNicholas, T. P.; et al. In Vivo Biosensing via Tissue-Localizable near-Infrared-Fluorescent Single-Walled Carbon Nanotubes. *Nat. Nanotechnol.* **2013**, *8* (11), 873−880.
(42) Wong, M. H.; Giraldo, J. P.; Kwak, S.-Y.; Koman, V. B.; Sinclair, R.; Lew, T. T. S.; Bisker, G.; Liu, P.; Strano, M. S. Nitroaromatic Detection and Infrared Communication from Wild-Type Plants Using Plant Nanobionics. *Nat. Mater.* **2017**, *16*, 264.
(43) Pan, J.; Zhang, H.; Cha, T.-G.; Chen, H.; Choi, J. H. Multiplexed Optical Detection of Plasma Porphyrins Using DNA Aptamer-Functionalized Carbon Nanotubes. *Anal. Chem.* **2013**, *85*, 8391−8396.

https://dx.doi.org/10.1021/acs.nanolett.9b05159
Nano Lett. 2020, 20, 2432−2442

(44) Atsumi, H.; Belcher, A. M. DNA Origami and G-Quadruplex Hybrid Complexes Induce Size Control of Single-Walled Carbon Nanotubes via Biological Activation. *ACS Nano* **2018**, *12*, 7986−7995.
(45) Ensing, B.; Buda, F.; Baerends, E. J. Fenton-like Chemistry in Water: Oxidation Catalysis by Fe(III) and H2O2. *J. Phys. Chem. A* **2003**, *107*, 5722−5731.
(46) Enami, S.; Sakamoto, Y.; Colussi, A. J. Fenton Chemistry at Aqueous Interfaces. *Proc. Natl. Acad. Sci. U. S. A.* **2014**, *111* (2), 623−628.
(47) Traylor, T. G.; Xu, F. Mechanisms of Reactions of iron(III) Porphyrins with Hydrogen Peroxide and Hydroperoxides: Solvent and Solvent Isotope Effects. *J. Am. Chem. Soc.* **1990**, *112* (1), 178−186.
(48) Nißler, R.; Mann, F. A.; Chaturvedi, P.; Horlebein, J.; Meyer, D.; Vuković, L.; Kruss, S. Quantification of the Number of Adsorbed DNA Molecules on Single-Walled Carbon Nanotubes. *J. Phys. Chem. C* **2019**, *123*, 4837−4847.
(49) Crochet, J. J.; Duque, J. G.; Werner, J. H.; Doorn, S. K. Photoluminescence Imaging of Electronic-Impurity-Induced Exciton Quenching in Single-Walled Carbon Nanotubes. *Nat. Nanotechnol.* **2012**, *7* (2), 126−132.
(50) Cognet, L.; Tsyboulski, D. A.; Rocha, J.-D. R.; Doyle, C. D.; Tour, J. M.; Weisman, R. B. Stepwise Quenching of Exciton Fluorescence in Carbon Nanotubes by Single-Molecule Reactions. *Science* **2007**, *316* (5830), 1465−1468.
(51) Rolland, F.; Baena-Gonzalez, E.; Sheen, J. Sugar Sensing and Signaling in Plants: Conserved and Novel Mechanisms. *Annu. Rev. Plant Biol.* **2006**, *57*, 675−709.
(52) Tognetti, J. A.; Pontis, H. G.; Martínez-Noël, G. M. A. Sucrose Signaling in Plants: A World yet to Be Explored. *Plant Signaling Behav.* **2013**, *8* (3), No. e23316.
(53) Yoshida, T.; Mogami, J.; Yamaguchi-Shinozaki, K. ABA-Dependent and ABA-Independent Signaling in Response to Osmotic Stress in Plants. *Curr. Opin. Plant Biol.* **2014**, *21*, 133−139.
(54) Howe, G. A.; Major, I. T.; Koo, A. J. Modularity in Jasmonate Signaling for Multistress Resilience. *Annu. Rev. Plant Biol.* **2018**, *69*, 387−415.
(55) Lin, Y.; Qasim, M.; Hussain, M.; Akutse, K. S.; Avery, P. B.; Dash, C. K.; Wang, L. The Herbivore-Induced Plant Volatiles Methyl Salicylate and Menthol Positively affect Growth and Pathogenicity of Entomopathogenic Fungi. *Sci. Rep.* **2017**, *7*, 40494.
(56) Rounds, C. M.; Lubeck, E.; Hepler, P. K.; Winship, L. J. Propidium Iodide Competes with Ca2 to Label Pectin in Pollen Tubes and Arabidopsis Root Hairs. *Plant Physiol.* **2011**, *157*, 175−187.
(57) Albert, M. Peptides as Triggers of Plant Defence. *J. Exp. Bot.* **2013**, *64* (17), 5269−5279.
(58) Mitchell, C.; Brennan, R. M.; Graham, J.; Karley, A. J. Plant Defense against Herbivorous Pests: Exploiting Resistance and Tolerance Traits for Sustainable Crop Protection. *Front. Plant Sci.* **2016**, *7*, 1132.
(59) Nißler, R.; Mann, F. A.; Preiß, H.; Selvaggio, G.; Herrmann, N.; Kruss, S. Chirality Enriched Carbon Nanotubes with Tunable Wrapping via Corona Phase Exchange Purification (CPEP). *Nanoscale* **2019**, *11* (23), 11159−11166.
(60) Zhang, C.; Kovacs, J. M. The Application of Small Unmanned Aerial Systems for Precision Agriculture: A Review. *Precis. Agric.* **2012**, *13* (6), 693−712.
(61) Atzberger, C. Advances in Remote Sensing of Agriculture: Context Description, Existing Operational Monitoring Systems and Major Information Needs. *Remote Sensing* **2013**, *5* (2), 949−981.
(62) Lowry, G. V.; Avellan, A.; Gilbertson, L. M. Opportunities and Challenges for Nanotechnology in the Agri-Tech Revolution. *Nat. Nanotechnol.* **2019**, *14* (6), 517−522.
(63) Kah, M.; Tufenkji, N.; White, J. C. Nano-Enabled Strategies to Enhance Crop Nutrition and Protection. *Nat. Nanotechnol.* **2019**, *14* (6), 532−540.
(64) White, J. C.; Gardea-Torresdey, J. Achieving Food Security through the Very Small. *Nat. Nanotechnol.* **2018**, *13* (8), 627−629.
(65) Meyer, D.; Hagemann, A.; Kruss, S. Kinetic Requirements for Spatiotemporal Chemical Imaging with Fluorescent Nanosensors. *ACS Nano* **2017**, *11*, 4017−4027.
(66) Wong, M. H.; Misra, R.; Giraldo, J. P.; Kwak, S. Y.; Son, Y.; Landry, M. P.; Swan, J.; Blankschtein, D.; Strano, M. S. Lipid Exchange Envelope Penetration (LEEP) of Nanoparticles for Plant Engineering: A Universal Localization Mechanism. *Nano Lett.* **2016**, *16*, 1161−1172.
(67) Lew, T. T. S.; Wong, M. H.; Kwak, S.-Y.; Sinclair, R.; Koman, V. B.; Strano, M. S. Rational Design Principles for the Transport and Subcellular Distribution of Nanomaterials into Plant Protoplasts. *Small* **2018**, *14*, No. 1802086.
(68) Mann, F. A.; Lv, Z.; Großhans, J.; Opazo, F.; Kruss, S. Nanobody-Conjugated Nanotubes for Targeted Near-Infrared In Vivo Imaging and Sensing. *Angew. Chem., Int. Ed.* **2019**, *58* (33), 11469−11473.
(69) Pfohl, M.; Tune, D. D.; Graf, A.; Zaumseil, J.; Krupke, R.; Flavel, B. S. Fitting Single-Walled Carbon Nanotube Optical Spectra. *ACS Omega* **2017**, *2* (3), 1163−1171.
(70) Wu, H.; Tito, N.; Giraldo, J. P. Anionic Cerium Oxide Nanoparticles Protect Plant Photosynthesis from Abiotic Stress by Scavenging Reactive Oxygen Species. *ACS Nano* **2017**, *11* (11), 11283−11297.
(71) Cheeseman, J. M. Hydrogen Peroxide Concentrations in Leaves under Natural Conditions. *J. Exp. Bot.* **2006**, *57* (10), 2435−2444.
(72) Wu, H.; Shabala, L.; Shabala, S.; Giraldo, J. P. Hydroxyl Radical Scavenging by Cerium Oxide Nanoparticles Improves Arabidopsis Salinity Tolerance by Enhancing Leaf Mesophyll Potassium Retention. *Environ. Sci.: Nano* **2018**, *5*, 1567−1583.

https://dx.doi.org/10.1021/acs.nanolett.9b05159
Nano Lett. 2020, 20, 2432−2442

5.4.2 Discussion

A functional approach for SWCNT sensors design that enables the remote detection and sensing of H_2O_2 inside leaf tissue is presented. Considering that the sensor development and characterization was contributed to **Manuscript V**, this part will be mainly discussed in the following section, together with implementations for plant biology research. Since the first introduction of SWCNT sensing[110] in 2005 and the characterization of SWCNT-based H_2O_2 sensors by Jin[209] and Heller[128] in 2008, this nanosensor approach was continuously modified and improved. Jin el al.[210] reported in 2010 the detection of H_2O_2 on a single molecule level during chemical imaging of epithelial cells, followed in 2011 by the expansion of the approach for human umbilical vein endothelial cells[129]. A ratiometric sensor was further presented by Giraldo *et al.*[176] in 2015 using chirality-enhanced SWCNT material. The sensing principle from all previous studies was described as direct quenching of SWCNT fluorescence by H_2O_2 adsorption on the carbon nanotube surface.[211] This concept was furthermore used in 2020 for a study released in *Nature Plants*[163], shortly after the publication of **Manuscript V**, showing likewise remote detection of H_2O_2 in leaves. But, in order to make the analyte-nanosensor interaction more specific, an iron motive close to the SWCNT surface was introduced (Figure 1), that could undergo a Fenton-like reaction[212,213], generating ROS, like hydroxyl radicals. Nanoscale presentation of the iron motive was achieved by modifying the SWCNT surface with the hemin-binding aptamer[137,214] (HeApta), as explained in **Manuscript IV**. The observed hemin-catalyzed[215] process (Figure 2) likely generated hydroxyl radicals that quench SWCNT fluorescence in a similar fashion to the reaction with protons.[117]

This sensor design improved the sensitivity of the resulting nanosensors towards µM analyte concentration, resulting in the most sensitive SWCNT-based approach up to now for (remote) H_2O_2 detection. Recently, a study by Safaee *et al.*[216] reported DNA-SWNCTs that were encapsulated into micro-fibrous textiles, thus also enabling a sensitive remote readout of ROS for a wearable diagnostics platform. Most likely, the developed HeApta-SWCNTs could be used for this propose as well.

Most interestingly, the obtained sensors were able to perform remote H_2O_2 detection in plant tissue, when mimicking a pathogen attack with the bacterial peptide flg22 from *Pseudomonas* spp. (Figure 5).[217] Recently established genetically-encoded H_2O_2 sensors show a remarkable selectivity and sensitivity, enabling detailed visualization of ROS in model plants.[218,219] The SWCNT-based sensors could now extend the sensor repertoire

researchers could choose from, depending on the aim of the study and target plants. Mainly two beneficial properties could be of interest: as the sensors fluoresce in the NIR, which is beyond the leaf (chlorophyll) autofluorescence range, the background interference is very low compared to sensors emitting in the visible part of the electromagnetic spectrum. Thus, SWCNT-based sensors offer an enhanced signal-to-noise ratio, desired for sensitive biosensing applications.[9,220] Secondly, the SWCNT-sensors could be introduced (infiltrated) into a variety of different plants[163], even wild-type plants, which bypasses the need for complex genetic modifications. This is especially important when studying non-model organism, where protocols for genetic manipulations rarely exists.

Furthermore, the HeApta-SWCNT sensor was used in a study by Meyer *et al.*[221] to sense H_2O_2 during immune response of white blood cells, so called neutrophils, undergoing neutrophil extracellular trap formation (NETosis)[222]. This shows that the sensing concept can be extended to other biological systems besides plants. In combination with chirality-pure SWCNTs it was further possible to create a ratiometric sensor (Figure 6, **Manuscript III**) with non-overlapping emission features, which could improve *in vivo* sensing in the future.

5.4.3 Detection and Imaging of the Plant Pathogen Response by Near-Infrared Fluorescent Polyphenol Sensors

Manuscript IV was published in the following journal:

Robert Nißler, Andrea T. Müller, Frederike Dohrman, Larissa Kurth, Han Li, Eric G. Cosio, Benjamin S. Flavel, Juan Pablo Giraldo, Axel Mithöfer and Sebastian Kruss*

"Detection and imaging of the plant pathogen response by near infrared fluorescent polyphenol sensors"

Angewandte Chemie International Edition, **2021**
The article is available at: DOI: 10.1002/anie.202108373
* Corresponding author

Responsibility assignment: R.N. and S.K. designed and conceived the research with input from J.P.G. and A.M.. S.K. coordinated the project. R.N., F.D. and L.K. performed chemical sensing experiments and separated (6,5)-SWCNTs. A.T.M., E.G.C. and A.M. performed plant cultivation, extraction and related analysis experiments. H.L. and B.S.F. performed (7,6)-SWCNT separation. R.N. performed all remaining experiments, analyzed the data and wrote the manuscript, with input from S.K..

RESEARCH ARTICLE

Detection and imaging of the plant pathogen response by near infrared fluorescent polyphenol sensors

Robert Nißler,[a,b] Andrea T. Müller,[c] Frederike Dohrman,[b] Larissa Kurth,[b] Han Li,[d] Eric G. Cosio,[e] Benjamin S. Flavel,[d] Juan Pablo Giraldo,[f] Axel Mithöfer[c] and Sebastian Kruss*[a,b,g]

[a] R. Nißler, Prof. Dr. S. Kruss
Physical Chemistry II
Bochum University
Universitätsstraße 150, 44801 Bochum, Germany
E-mail: sebastian.kruss@rub.de
[b] R. Nißler, F. Dohrman, L. Kurth, Prof. Dr. S. Kruss
Institute of Physical Chemistry
Georg-August Universität Göttingen
Tammannstraße 6, 37077 Göttingen, Germany
[c] A.T. Müller, PD Dr. A. Mithöfer
Research Group Plant Defense Physiology
Max Planck Institute for Chemical Ecology
Hans-Knöll-Straße 8, 07745 Jena, Germany
[d] Dr. H. Li, Dr. B. S. Flavel
Institute of Nanotechnology
Karlsruhe Institute of Technology (KIT)
76344 Eggenstein- Leopoldshafen, Germany
[e] Prof. Dr. E. Cosio
Institute for Nature Earth and Energy (INTE-PUCP)
Pontifical Catholic University of Peru
Av. Universitaria 1801, San Miguel 15088, Lima, Peru
[f] Prof. J. P. Giraldo
Department of Botany and Plant Sciences
University of California
Riverside, CA 92507, USA
[g] Prof. Dr. S. Kruss
Fraunhofer Institute for Microelectronic Circuits and Systems
Finkenstraße 61, 47057 Duisburg, Germany

Supporting information for this article is given via a link at the end of the document.

Abstract: Plants use secondary metabolites such as polyphenols for chemical defense against pathogens and herbivores. Despite their importance in plant pathogen interactions and tolerance to diseases, it remains challenging to detect polyphenols in complex plant tissues. Here, we create molecular sensors for plant polyphenol imaging that are based on near-infrared (NIR) fluorescent single wall carbon nanotubes (SWCNTs). We identified polyethylene glycol-phospholipids that render (6,5)-SWCNTs sensitive (K_d = 90 nM) to plant polyphenols (tannins, flavonoids, …), which red-shift (up to 20 nm) and quench their emission (~1000 nm). These sensors report changes in total polyphenol level after herbivore or pathogen challenge in crop plant systems (Soybean *Glycine max*) and leaf tissue extracts (*Tococa spp).* We furthermore demonstrate remote chemical imaging of pathogen-induced polyphenol release from roots of soybean seedlings over the time course of 24h. This approach allows *in situ* visualization and understanding of the chemical plant defense in real time and paves the way for plant phenotyping for optimized polyphenol secretion.

Introduction

Smart agricultural solutions are required to optimize production practices and crop yields to enable a sustainable food supply for a rising global population. The rapid growth in human population will require a 60% increase or more in food production by 2050 relative to 2005−2007 levels.[1] In contrast, pathogen-induced stresses significantly reduce crop health and yield.[2,3] One solution is precision agriculture that aims for early detection of crop disease using vehicle remote imaging or sensing[4] and crop phenotyping aims to breed plants with improved tolerance to pathogen stress. Tools for quantifying plants' internal chemical signals associated with stress in real-time are needed to boost these agriculture and phenotyping efforts.[5,6]

Recent advances in chemistry and nanotechnology can contribute to improve crop production *via* novel sensor approaches allowing for remote analysis and optimization of plant traits.[7,8] Semiconducting single wall carbon nanotubes (SWCNTs) are a powerful building block for these plant sensors because of their distinct photophysical properties.[9–11] Particularly, they fluoresce in the near infrared (NIR) region of the electromagnetic spectrum, which corresponds to the optical tissue transparency window due to decreased scattering and ultra-low background.[12] The discrete emission wavelength ranges from around 850 to 2400 nm and depends on their carbon lattice (bandgap) structure, determined by the chirality (*n,m*).[13] SWCNTs are not prone to photobleaching and can be used as optical labels and sensors, which are sensitive to their chemical environment.[14–16] SWCNT-based sensors have been used as powerful imaging tools to analyze biological processes with high spatiotemporal resolution.[17–19] This technique was applied to detect genetic material[20], proteins[21,22], lipids[23], bacterial motives[24] or small signaling molecules such as neurotransmitters[19,25], reactive oxygen species (ROS)[26–28] or nitric oxide (NO)[29]. More recently, their utilization as non-

genetically encoded sensors enabled the visualization of ROS patterns[27,30,31], auxins[32] or heavy metal uptake[33] in plants.[34] To tailor the SWCNT-sensor properties, different chemical design strategies for surface functionalization have been developed. Most commonly, biopolymers such as single stranded (ss)DNA are adsorbed on the SWCNT surface, which mediates colloidal stability in aqueous solution and molecular recognition of the analyte.[35–38] Other design and sensing concepts rely on non-covalent functionalization with aptamers[17,39], phospholipids[40], peptides[41,42], proteins[43], or peptide-DNA hybrids[44,45]. Recently, also covalent modification of fluorescent SWCNTs with (bio)molecules has been reported.[46,47]

Detecting dynamic physiological processes in plants, such as defense responses to pathogen attack, could improve our understanding of plant pathogen interactions and help breed plants with increased biotic stress tolerance. Polyphenols, ubiquitous in the plant kingdom, are a prominent class of plant secondary metabolites involved in the constitutive and also inducible defense against pathogens and herbivores.[48,49] They can be generally found in all plant tissues and organs and comprise a great variety of chemical structures with diverse ecological roles.[50] One distinct aspect of polyphenol-related plant defense is chemical secretion into the rhizosphere (root exudates), which modulates plant interactions within the soil ecosystem.[51] These exudates/secretions are able to repel, inhibit, or even kill pathogenic microorganisms[51]. Hence, increased production improves natural plant defense and is a goal of plant breeding.[52] However, *in situ* detection and visualization of these biological processes remain a challenge because most analytical approaches cannot non-invasively access *in vivo* systems.[53–55] Here, we created a NIR-fluorescent sensor/probe for plant polyphenol detection and imaging. It responds to polyphenols *in vitro* and enables *in vivo/in situ* chemical imaging of polyphenols released from plant roots challenged with pathogen-related stress.

Results and Discussion

Plant polyphenols are natural products with diverse chemical structures. Therefore, we tested how polyphenols (Figure 1b) from different subgroups (e.g. tannins, flavonoids, phenolic acids) modulate the NIR fluorescence of SWCNT-based molecular sensors. To assess the impact of surface chemistry (Figure 1) we used ssDNA with variable nucleotide composition (A,T,G,C) and polyethylene glycol (PEG)-phospholipid macromolecules for molecular assembly. Our rationale was, that some of them have been known to interact with compounds that possess multiple hydroxy groups such as tannins.[56] In general, the modified SWCNTs either increased or decreased their fluorescence in response to the target molecules, as shown for C_{30}- and PEG(5kDa)-PL-SWCNTs (Figure 1c-e). For different SWCNT conjugates we observed changes in fluorescence (Figure 1f) after addition of polyphenols in the physiologically relevant concentration range[50,57,58]. To exclude pH or ionic strengths related sensing effects[59], all experiments were performed in buffer. There is a general tendency of fluorescence increase for ssDNA-SWCNTs and a decrease for PEG-PL-SWCNTs (see also Supplementary Figure S1). All tested compounds with two or more hydroxy residues on the phenol structure led to a significant fluorescence change, while salicylic acid did not alter the emission features of the tested SWCNTs. This finding was further supported by the lacking response of a trimethylated version of gallic acid (GaA) (Supplementary Figure S1).

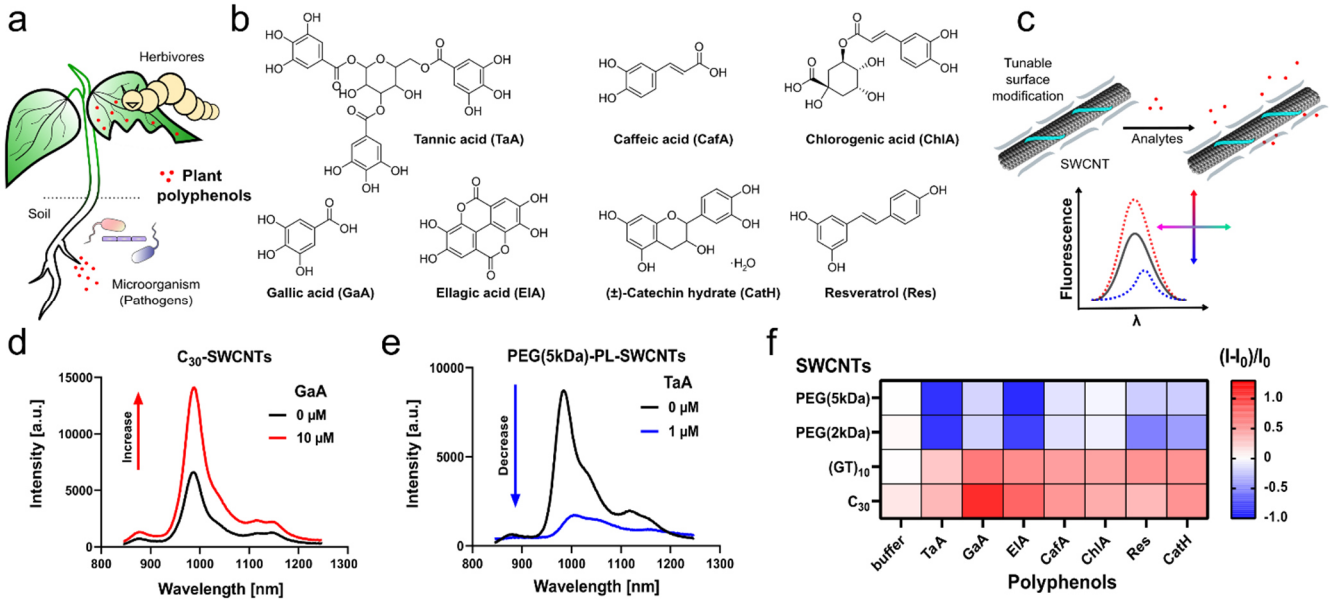

Figure 1. NIR fluorescent nanosensors for plant polyphenols. a) Plant polyphenols are released from leaves and roots in response to pathogens or herbivores and play an important role in chemical plant defense**. b)** Selected plant polyphenols investigated in this study. The compounds represent the subclasses of tannins, flavonoids and phenolic acids (see Supplementary Figure S1 for complete list). **c)** Non-covalently modified SWCNTs with different kind of biopolymers can change their fluorescence in response to polyphenols and serve as sensors, by modulating emission intensity and energy (wavelength). **d)** NIR fluorescence spectra of single stranded (ss)DNA and (**e**) PEG-phospholipid (PL) modified SWCNTs as examples for SWCNTs that change their fluorescence in response to polyphenols. **f)** Fluorescence change ($I-I_0/I_0$) of selected sensors in response to plant polyphenols (mean, n = 3). Shades of blue indicate fluorescence decrease and shades of red fluorescence increase (polyphenol concentration = 10 µM; TaA = 1 µM)

Next to the evaluated intensity changes, also shifts in the emission wavelengths occurred. This phenomenon is most prominently observed for tannic acid (TaA) (Figure 2, a-c), resulting in ~3 nm shifts for ssDNA- and ~20 nm shifts for PEG-PL-SWCNTs. Only TaA caused a large emission wavelengths shift, whereas GaA changed ssDNA-SWCNTs intensity more strongly (up to > 100 %). These results suggests that the three-dimensional structure of TaA affects sensing, an observation likely true also for other structurally large polyphenols. To better understand the interaction between tannins and the sensors, concentration-dependent measurements were performed for different ssDNA-SWCNTs. Interestingly, the fluorescence intensity increased in the nM regime, whereas it decreased for most sequences in the µM to mM range (Supplementary Figure S2). A uniform result was observed for PEG-PL-SWCNTs (Figure 2a, d). Unlike for most ssDNA-SWCNTs, the intensity decrease was clearly concentration dependent (K_d = 9.1 x10^{-8} M) and saturated in the lower µM range (-80 % intensity change and ~ 20 nm emission wavelength shift). GaA (1 mM) in contrast led to a much smaller sensor response of ≤ -36 % and ≤ 3 nm shift. In addition to the change in emission of PEG-PL-SWCNTs also E_{11} absorption maximum was redshifted by ~10 nm (Supplementary Figure S2). Overall, such interplay indicates a sensing mechanism based on a change in fluorescence quantum yield, without dominant aggregation effects. It furthermore suggests a strong interaction between sensor and analyte that goes beyond polyphenols acting as antioxidants[60,61] and might include changes in solvation that affects exciton diffusion. Hence, PEG-PL-SWCNTs showed the most promising response to plant polyphenols.

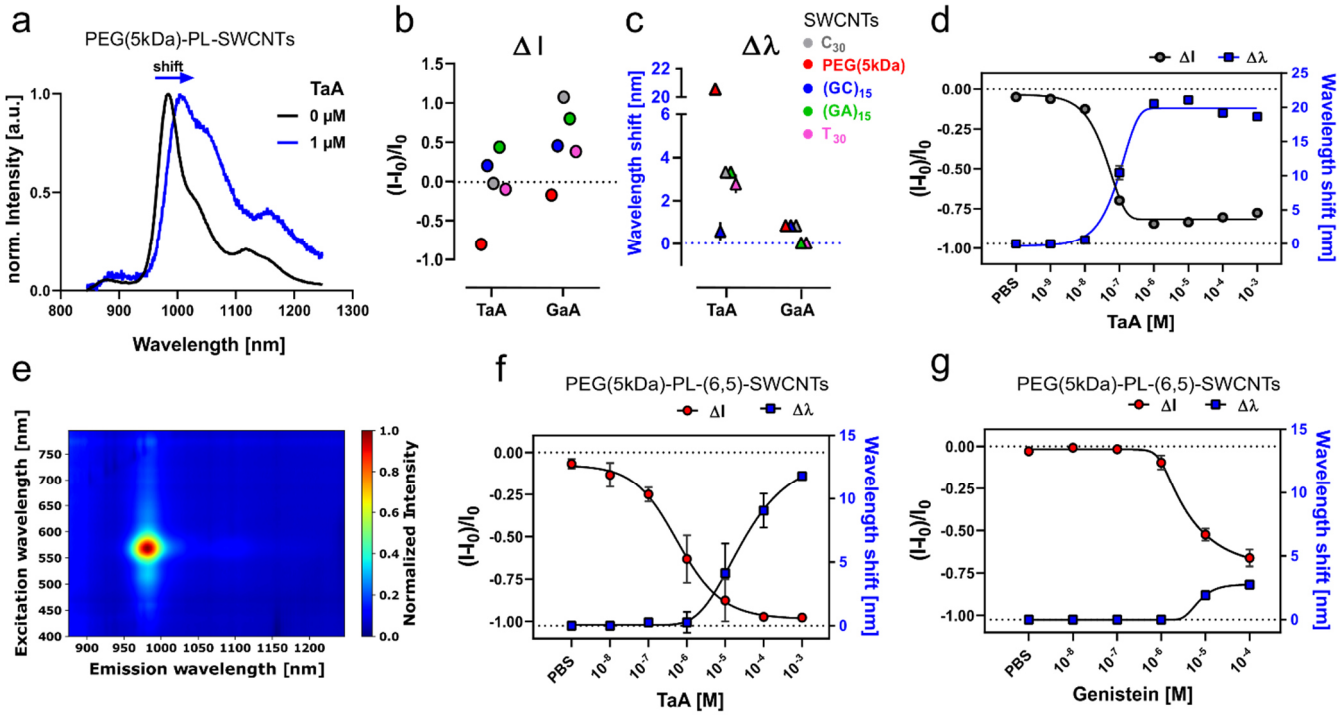

Figure 2. NIR detection of tannins *in vitro*. a) Normalized NIR fluorescence spectra of PEG-PL-SWCNTs without (black) and in presence (blue) of tannic acid (TaA). The emission wavelength shifts in addition to a change in fluorescence intensity. b) Comparison of intensity and in c) wavelength shifts of functionalized SWCNTs interacting with TaA and its subunits gallic acid (GaA) (10 µM; mean ± SD, n = 3). Similar trends are visible for intensity changes, while emission wavelengths are not shifted in presence of GaA. It suggests that the 3D structure of TaA and less the gallic acid subunits are crucial. d) NIR fluorescence shifts of PEG-PL-SWCNTs in response to TaA. Intensity (black fit) decreases and wavelength shift (blue fit) increases in a concentration dependent manner (mean ± SD, n = 3). e) 2D-exitation emission photoluminescence spectra of chirality-pure (6,5)-SWCNTs. f) Monochiral sensor response of PEG-PL-(6,5)-SWCNTs to TaA and g) to genistein addition. Intensity changes are indicated in red; wavelength shifts in blue (line = fit, mean ± SD, n = 3).

Next, we evaluated if sensing with monochiral SWCNTs of a well-defined emission wavelength (color) is possible. Non-overlapping emission spectra are required for multiplexed sensing and hyperspectral imaging approaches. To obtain monochiral (6,5)-SWCNTs, aqueous two-phase separation (ATPE) was performed, followed by surface exchange to PEG-PL (Figure 2e, Supplementary Figure S3). Monochiral sensors responded in a similar fashion (K_d = 4.3 x10^{-6} M) (Figure 2f). Similar sensor responses were observed for the iso-flavonoid called genistein (Figure 2g). It has been described that mainly surface modification imparts sensitivity and selectivity and not chirality.[62] However, experiments with multi-chirality (HiPco) PEG-PL-SWCNTs showed distinct differences pointing to a polyphenol profile and chirality dependent response (Supplementary Figure S4).

To test these sensors in more complex environments we used plant tissue extract and culture medium. For this purpose, methanol extracts from *Tococa spp*. leaf tissue (Figure 3a) and liquid media from soybean (*Glycine max*) suspension cell cultures (Figure 3b) were tested. Neotropical *Tococa spp*. is known for its high polyphenol content (i.e. ellagitannins) (Supplementary Figure S5) and serves as model system for polyphenol releasing plants. The sensors showed a strong fluorescence decrease (Figure 3c) along with a large emission shift in a low µg/mL range. This response correlates with the response of pure polyphenols (Figure 1 and Figure 2). The total phenol content was additionally

quantified with an established colorimetric assay (Folin–Ciocalteu reagent[63]). The sensor responses (K_d = 1.5 µM for purified polyphenols, Supplementary Figure S5) correlated with total phenol content (expressed as gallic acid equivalents). When correlating all tested *Tococa* leaf methanol-extracts, an overall curve fitting with a K_d of ~140 µM was obtained (Figure 3d). These results indicate that the sensors are able to probe the species-specific phenol content as relative increases even within a complex background (Supplementary Figure S6). Additionally, extracts of plants stressed by insect herbivory, caused a significant difference in sensor response (Figure 3e), which correlated with an increased total phenolic content (Figure 3d). The results are in agreement with classical HPLC-MS polyphenol detection (Supplementary Figure S7) and demonstrate that these NIR fluorescent sensors identify polyphenols even with a chlorophyll or sugar background (methanol extraction). Plant extracts from the field (Peruvian rainforest in the Tambopata National Reserve) showed a similar response as HPLC-MS based detection (Supplementary Figure S7). Therefore, these nanosensors are a valuable tool for rapid and high throughput screening, requiring very small volume (few µL) of plant extracts. These hallmarks are desired for testing of plant analytes that are difficult to extract in large volumes e.g. phloem sap or with low concentration of analytes e.g. xylem sap. The second plant system were soybean-based (*Glycine max*) suspension cells (Figure 3b, Supplementary Figure S8). They are known to release polyphenols, in particular pterocarpans, into the medium during aging or due to pathogen stress.[64,65] We directly added the cell-free supernatant of the culture to the nanosensors, without further purification. Mature cells showed a stronger sensor response, which means that they produced more polyphenols (Figure 3f, 3g, Supplementary Figure S9).

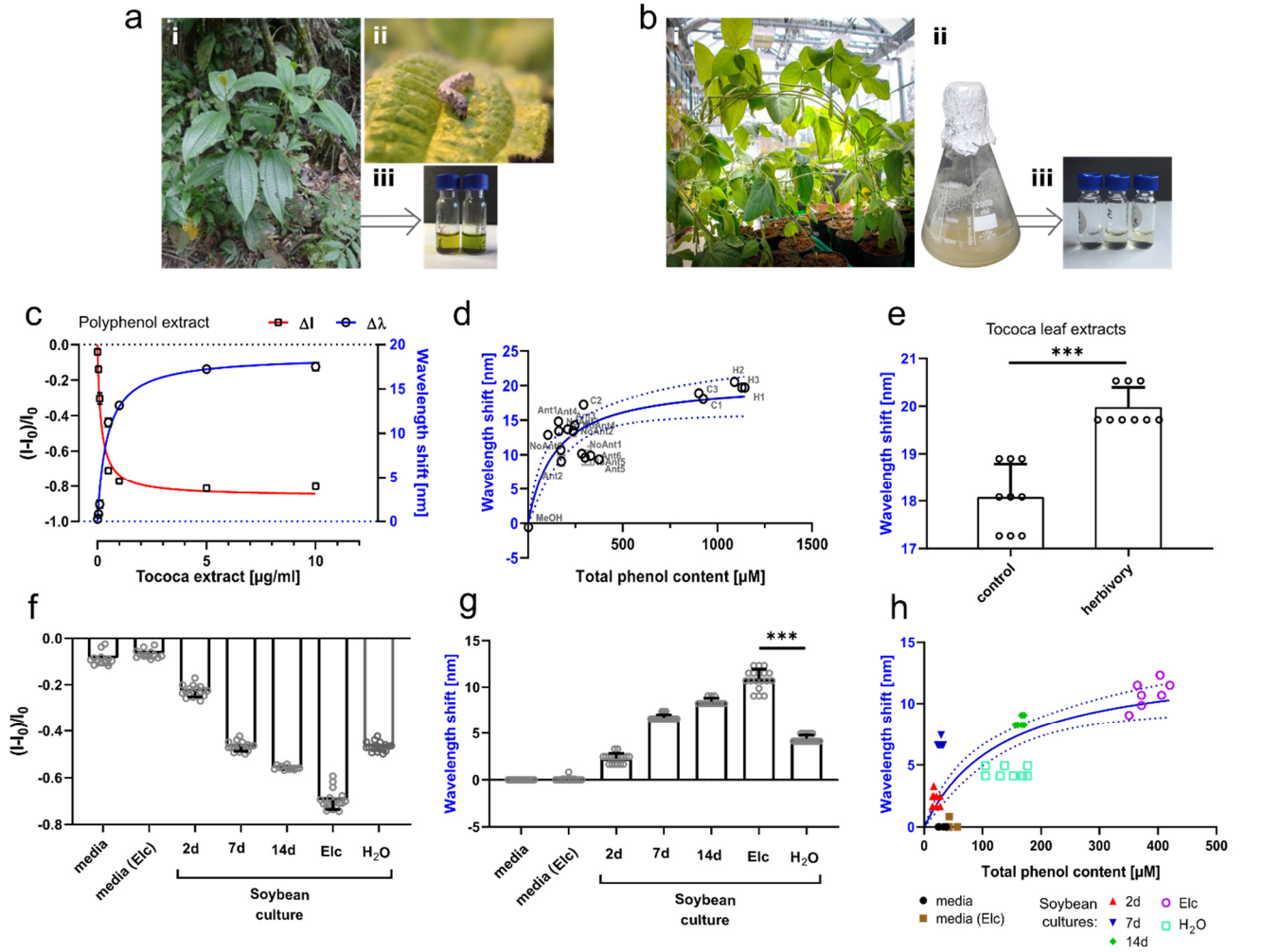

Figure 3. Polyphenol detection in plant extracts. ***a)*** *Tococa spp. plants. i – wild plants found in the Peruvian rain forest. ii – the herbivore Spodoptera littoralis on a Tococa leaf. iii – crude MeOH leaf extracts used for sensor testing.* ***b)*** *Soybean (Glycine max) plants. i – an adult G. max plant grown in the greenhouse. ii – G. max suspension cell culture. iii – cell culture supernatant used for nanosensor testing.* ***c)*** *Nanosensor (PEG-PL-SWCNTs) response against purified polyphenol extract from Tococa spp., containing all extractable leaf polyphenols with a predominantly high ellagitannin content. The NIR fluorescence decreases and simultaneously the emission wavelength shifts (mean ± SD, n = 3, colored line = hyperbolic fit).* ***d)*** *Correlation of emission wavelength shift and the total phenol content from multiple Tococa leaf MeOH-extracts (measured using the Folin–Ciocalteu reagent, which is an established colometric assay). The dynamic range of sensor is in the µM range (K_d = 142 µM, expressed as gallic acid equivalents) (mean ± SD, N =1, n = 3, tested as 2 µL non-diluted MeOH extracts, blue line = hyperbolic fit; C = control, H = herbivory, Ant = plants with ant symbionts).* ***e)*** *Tococa leaf extracts from plants challenged with herbivores (S. littoralis) give a significantly different nanosensor response compared to non-treated plants (mean ± SD, N =3, n = 3, unpaired t-test).* ***f)*** *Soybean (Glycine max) cell culture samples decrease fluorescence and shift emission wavelengths* ***(g)*** *of nanosensors, which allows detection of age- and pathogen-induced (Elc, elicitor) changes in polyphenol*

*levels (mean ± SD, N = 6, n = 3,***P<0.001; one-way ANOVA).* ***h)*** *Correlation of emission wavelength shift with total phenol content (quantified by Folin–Ciocalteu reagent) shows a hyperbolic trend with a K_d of 140 µM (N = 6, n = 2, blue line = hyperbolic fit).*

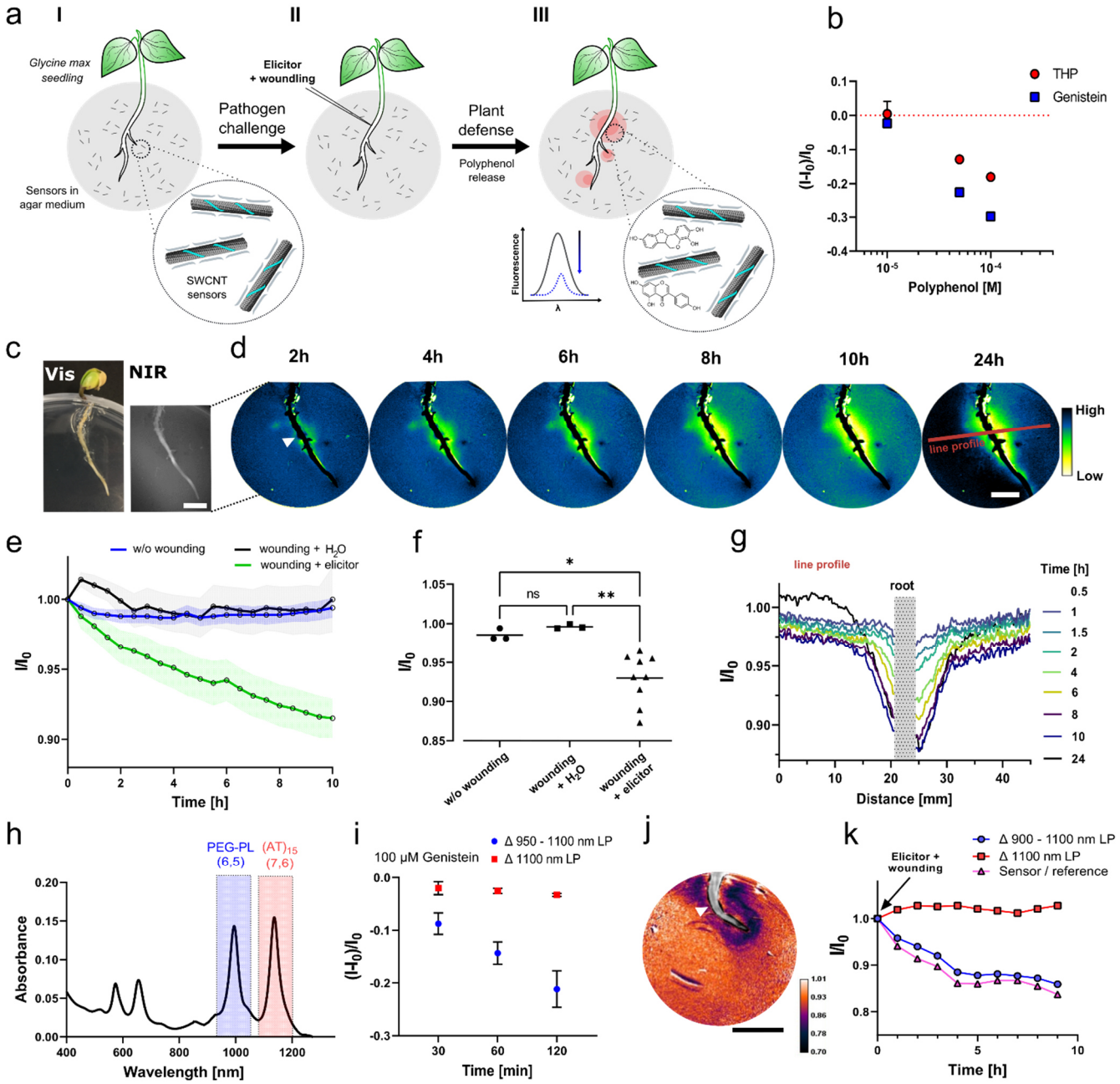

Figure 4. Real-time imaging of pathogen induced polyphenol release from roots. a) Chemical imaging concept with SWCNT-based fluorescent sensors incorporated in culture medium agar. Soybean seedling (G. max) grow through the agar. The plant is challenged with a pathogen elicitor and the response (polyphenol secretion) is monitored by NIR fluorescent stand-off imaging (> 20 cm). b) Genistein and trihydroxypterocarpan (THP) as prominent components of the soybean (G. max) polyphenol profile quench the fluorescence of PEG-PL-SWCNTs in agar (mean ± SD, n = 3). c) Visible and NIR image of the soybean seedling (scale bar =1 cm). d) The NIR fluorescence of the sensors (I/I_0) in the plant environment (rhizosphere) decreases over time close to the challenged root position (root tissue is overlayed with black; white triangle = position for elicitor induction; red line = line profile position, scale bar = 1 cm). e) Sensor image (500-pixel, ~170 mm²) reports polyphenol release to a fungal elicitor. In contrast, the sensor does not respond in the absence of stimulus (w/o wounding) or to wounding + H_2O (mean, error bars = SD, n = 1). f) Sensor intensity changes 10 h after stimulus. Mean pixel intensities of 500-pixel areas close to the challenged root position (mean, control and H_2O N = 3; elicitor N = 9, *P<0.033; **P<0.002; ns = not significant; one-way ANOVA). g) Spatiotemporal profile of the plant defense via polyphenol release (line profile for 5-pixel width section shown in Figure 4d). h) Absorbance spectra of monochiral (6,5)-PEG-PL as polyphenol sensor and $(AT)_{15}$-(7,6)-SWCNTs (reference) in agar. i) NIR stand-off imaging of monochiral sensors and their response. The fluorescence of PEG-PL-(6,5)-SWCNTs (950 nm long pass (LP) filter image - 1100 nm LP filter image) decreases in response to genistein (100 µM). In contrast, $(AT)_{15}$-7,6-SWCNTs (1100 LP filter) are not strongly affected and serve as a reference. j) Ratiometric image of challenged soybean seedling (t = 9h post induction, ratio Δ (900 LP – 1100 LP) / (1100 LP), white triangle = position for elicitor induction, scale bar = 1 cm). k) Ratiometric imaging of polyphenol release over time (sensor = PEG-PL-(6,5)-SWCNTs: 900 – 1100 nm; reference = (AT)15-(7,6)-SWCNTs: >1100 nm) (mean, N = 1) measured as mean pixel intensity (500-pixel, ~170 mm²) over time.

These soybean cultures were also stimulated with a pathogen-derived elicitor, a branched ß-glucan cell wall component of the Oomycete fungus *Phytophthora sojae*, which induces a defense-related response that triggers secretion of polyphenols.[66–68] This elicitor (Elc) caused a significant sensor response (intensity changes and emission wavelength shift) (Figure 3 f,g). Both the control (H_2O) and the stimulated cultures were 7 days old, hence containing next to the elicitor-induced polyphenols, pterocarpan derivates, also aging-related ones like genistein. HPLC-MS analysis further confirmed the increase in polyphenols after elicitor stimulus (see Supplementary Figure S8 and S10). Furthermore, soybean defensive polyphenols /genistein and trihydroxypterocarpan (THP) modulate the NIR fluorescence in a concentration dependent manner (Supplementary Figure S11). Together these results show that our sensor can report polyphenol release from plants or cells *in vitro.*

The sensor response to total phenol content of soybean cells (Figure 3h) is hyperbolic (K_d ~140 µM) and is not biased by cell medium or elicitor (Figure 3g,h). Even though there are differences in sensitivity toward different polyphenols, the presented PEG-PL-SWCNT is therefore a total polyphenol content sensor. A major advantage of a fluorescent sensor/probe is that it can be used for imaging and provide additional spatiotemporal information compared to standard analytical methods (e.g. HPLC / GC -MS, colorimetric assays, biosensors)[53–55,63]

To image plant polyphenol secretion over time (Figure 4a) we embedded the sensors in agar and let soybean seedlings grow on top. First, we had to optimize the conditions for embedding PEG-PL-SWCNTs into agar as agar and salt concentration seemed to play an important role for photoluminescence and sensing (Supplementary Figure S12). The representative polyphenols genistein and THP were used to evaluate the sensing performance (Figure 4b) and showed up to 30 % fluorescence decrease (100 µM) within 30 min. On the other hand, potential interfering substances from the root, such as sugars or H_2O_2 did not alter the fluorescence emission (Supplementary Figure S13). The plant defense by polyphenols was then imaged remotely in real-time by a NIR stand-off imaging[24] system (Supplementary Figure S13). For this purpose, soybean seedlings were plated onto the optimized sensor agar (Figure 4c) and the embryonic root was imaged for 24 h with elicitor stimulus or its respective control (Supplementary Video S1 and S2). The NIR (Figure 4d) image decreased close to the wound, indicating polyphenol secretions close to the elicitor-induced root area, as hypothesized before[64]. These results confirm studies with pathogen (*P. sojae)* infected soybean seedlings[69,70], performed by laborious and tissue destructive methods involving antibodies in combination with cryotome-prepared root tissue sections. Polyphenol secretion and diffusion increase in the first 4-8 hours and remain stable over the 24-hour experimental timeframe (see also Supplementary Figure S14). When wounding the embryotic root and applying H_2O instead of the elicitor, no enhanced nanosensor response was detected (Figure 4e), which confirms that both mechanical wounding and a chemical elicitor is necessary similar to a pathogen attack[69]. The difference in polyphenol secretion between individual plants (Figure 4f) could be used to identify plant cultivars with improved pathogen response. The largest sensor fluorescence modulation occurred in close proximity to the embryotic root (see Figure 4g) indicating higher changes of polyphenol content in this region of the rhizosphere. To further improve imaging we also implemented ratiometric sensing in which one sensor reports the analyte of interest at one wavelength and another sensor serves as reference at a different wavelength that is not affected by the analyte.[30] For such an approach chirality pure SWCNTs are necessary.[62] We prepared chirality-pure (6,5)-SWCNTs with PEG-PL to act as polyphenol-responsive sensor, while monochiral (7,6)-SWCNTs coated with $(AT)_{15}$-ssDNA served as reference that does not react to polyphenols (Figure 4h, Supplementary Figure S1, S15). Inside agar, they allowed ratiometric imaging using appropriate emission filters (PEG-PL-(6,5)-SWCNTs: 900 – 1100 nm and $(AT)_{15}$-(7,6)-SWCNTs: >1100 nm). This approach enabled ratiometric detection of the important soybean polyphenol genistein (Figure 4i) and also ratiometric imaging of the elicitor-induced secretion of root polyphenols (Figure 4j and 4k, Supplementary Video S3). The concept could be expanded to multiplexing to study the co-secretion of multiple plant-defense molecules (exudates) and improve our understanding of spatiotemporal chemical processes in the complex rhizosphere[71]. Additionally, this ratiometric approach is less prone to variations in the position of the light source and camera and therefore guarantees a more robust imaging concept with better signal/noise ratio.

Conclusions

We have synthesized molecular sensors based on SWCNTs for NIR imaging of polyphenols. They allow to observe the response of plants to pathogens *via* release of polyphenols with high spatiotemporal resolution in the beneficial NIR tissue transparency window. The sensors probe the polyphenol content in complex biological systems such as the plant rhizosphere. This tool can be used to better understand plant chemical defense mechanisms as well as plant chemical communication and accelerate phenotyping and identification of crop plants that are more tolerant to pathogens.[72–74] We showcased the potential for a main crop plant species (soybean) and in plant extracts or tissue culture media without further purification. Sensor responses showed a strong correlation with classical analytical methods like colorimetric assays or HPLC-MS quantification but had the major advantage of *in situ* detection without further sample taking or handling. Additionally, the spatiotemporal resolution provided novel insights into the time scale and spatial dimensions of polyphenol secretion. Such rapid optical detection could be used for high-throughput screenings tools that require minimal plant sample volumes down to the µL scale or to remotely visualize pathogen-induced plant defense and stress. In summary, this technique paves the way for precision agriculture and demonstrates the versatility of tailored nanoscale sensors for chemical imaging.

Acknowledgements

This project was supported by the VW foundation. Funded by the Deutsche Forschungsgemeinschaft (DFG, German Research Foundation) under Germany´s Excellence Strategy – EXC 2033 – 390677874 – RESOLV. We thank the DFG for funding within the Heisenberg program (S.K. & B.S.F.); the DAAD (German Academic Exchange Service) for scholarship funding (A.T.M.) and Dr. Michael Reichelt for support with the chemical analyses.

Keywords: Biosensors, carbon nanotubes, imaging, near infrared fluorescence, plant polyphenols

[1] N. Alexandratos, J. Bruinsma, "WORLD AGRICULTURE TOWARDS 2030/2050: The 2012 Revision. Food and Agriculture Organization ofthe United Nations: Rome, Italy," can be found under http://www.fao.org/3/ap106e/ap106e.pdf, **2012**.

[2] M. C. Fisher, D. A. Henk, C. J. Briggs, J. S. Brownstein, L. C. Madoff, S. L. McCraw, S. J. Gurr, *Nature* **2012**, *484*, 186–194.

[3] S. Chakraborty, A. C. Newton, *Plant Pathol.* **2011**, *60*, 2–14.

[4] P. J. Zarco-Tejada, C. Camino, P. S. A. Beck, R. Calderon, A. Hornero, R. Hernández-Clemente, T. Kattenborn, M. Montes-Borrego, L. Susca, M. Morelli, V. Gonzalez-Dugo, P. R. J. North, B. B. Landa, D. Boscia, M. Saponari, J. A. Navas-Cortes, *Nat. Plants* **2018**, *4*, 432–439.

[5] S. Dhondt, N. Wuyts, D. Inzé, *Trends Plant Sci.* **2013**, *18*, 428–439.

[6] Y. Fichman, G. Miller, R. Mittler, *Mol. Plant* **2019**, *12*, 1203–1210.

[7] J. P. Giraldo, H. Wu, G. M. Newkirk, S. Kruss, *Nat. Nanotechnol.* **2019**, *14*, 541–553.

[8] J. P. Giraldo, M. P. Landry, S. M. Faltermeier, T. P. Mcnicholas, N. M. Iverson, A. A. Boghossian, N. F. Reuel, A. J. Hilmer, F. Sen, J. A. Brew, M. S. Strano, *Nat. Mater.* **2014**, *13*, 400–408.

[9] J. Li, G. P. Pandey, *Annu. Rev. Phys. Chem.* **2015**, *66*, 331–356.

[10] V. Z. Zamolo, E. Vazquez, M. Prato, *Top. Curr. Chem.* **2013**, *286*, 1–72.

[11] S. Nanot, E. H. Hároz, J. H. Kim, R. H. Hauge, J. Kono, *Adv. Mater.* **2012**, *24*, 4977–4994.

[12] M. J. O. Connell, S. M. Bachilo, C. B. Huffman, K. L. Rialon, P. J. Boul, W. H. Noon, M. J. O'Connell, S. M. Bachilo, C. B. Huffman, V. C. Moore, M. S. Strano, E. H. Haroz, K. L. Rialon, P. J. Boul, W. H. Noon, C. Kittrell, J. Ma, R. H. Hauge, R. B. Weisman, R. E. Smalley, *Science (80-.).* **2002**, *297*, 593–597.

[13] S. M. Bachilo, M. S. Strano, C. Kittrell, R. H. Hauge, R. E. Smalley, R. B. Weisman, M. J. Zaworotko, S. Kitagawa, M. Kondo, K. Seki, E. Nishibori, M. Sakata, K. Fujimoto, S. Noro, H. Tanaka, M. Miyahara, K. E. Gubbins, J. O. Hirschfelder, C. F. Curtiss, R. B. Bird, C. Ueda, K. Sugiyama, M. Date, K. Bier, H. Jodl, R. Marx, A. Zamma, N. Setoyama, Y. Hanzawa, *Science (80-.).* **2002**, *298*, 2361–2366.

[14] S. Kruss, A. J. Hilmer, J. Zhang, N. F. Reuel, B. Mu, M. S. Strano, *Adv. Drug Deliv. Rev.* **2013**, *65*, 1933–1950.

[15] G. Hong, S. Diao, A. L. Antaris, H. Dai, *Chem. Rev.* **2015**, *115*, 10816–10906.

[16] C. Farrera, F. Torres Andón, N. Feliu, *ACS Nano* **2017**, *11*, 10637–10643.

[17] M. Dinarvand, E. Neubert, D. Meyer, G. Selvaggio, F. A. Mann, L. Erpenbeck, S. Kruss, *Nano Lett.* **2019**, *19*, 6604–6611.

[18] M. Dinarvand, S. Elizarova, J. Daniel, S. Kruss, *Chempluschem* **2020**, 1465–1480.

[19] S. Kruss, D. P. Salem, L. Vuković, B. Lima, E. Vander Ende, E. S. Boyden, M. S. Strano, *Proc. Natl. Acad. Sci.* **2017**, *114*, 1789–1794.

[20] J. D. Harvey, P. V. Jena, H. A. Baker, G. H. Zerze, R. M. Williams, T. V. Galassi, D. Roxbury, J. Mittal, D. A. Heller, *Nat. Biomed. Eng.* **2017**, *1*, 1–11.

[21] G. Bisker, J. Dong, H. D. Park, N. M. Iverson, J. Ahn, J. T. Nelson, M. P. Landry, S. Kruss, M. S. Strano, *Nat. Commun.* **2016**, *7*, 1–14.

[22] A. Hendler-Neumark, G. Bisker, *Sensors (Switzerland)* **2019**, *19*, 1–16.

[23] T. V. Galassi, P. V. Jena, J. Shah, G. Ao, E. Molitor, Y. Bram, A. Frankel, J. Park, J. Jessurun, D. S. Ory, A. Haimovitz-Friedman, D. Roxbury, J. Mittal, M. Zheng, R. E. Schwartz, D. A. Heller, *Sci. Transl. Med.* **2018**, *10*, 1–11.

[24] R. Nißler, O. Bader, M. Dohmen, S. G. Walter, C. Noll, G. Selvaggio, U. Groß, S. Kruss, *Nat. Commun.* **2020**, *11*, 1–12.

[25] S. Kruss, M. P. Landry, E. Vander Ende, B. M. A. Lima, N. F. Reuel, J. Zhang, J. Nelson, B. Mu, A. Hilmer, M. Strano, *J. Am. Chem. Soc.* **2014**, *136*, 713–724.

[26] D. A. Heller, H. Jin, B. M. Martinez, D. Patel, B. M. Miller, T. K. Yeung, P. V. Jena, C. Höbartner, T. Ha, S. K. Silverman, M. S. Strano, *Nat. Nanotechnol.* **2009**, *4*, 114–120.

[27] H. Wu, R. Nißler, V. Morris, N. Herrmann, P. Hu, S. Jeon, S. Kruss, J. P. Giraldo, *Nano Lett.* **2020**, *20*, 2432–2442.

[28] M. M. Safaee, M. Gravely, D. Roxbury, *Adv. Funct. Mater.* **2021**, *2006254*, 1–14.

[29] J. H. Kim, D. A. Heller, H. Jin, P. W. Barone, C. Song, J. Zhang, L. J. Trudel, G. N. Wogan, S. R. Tannenbaum, M. S. Strano, *Nat. Chem.* **2009**, *1*, 473–481.

[30] J. P. Giraldo, M. P. Landry, S. Y. Kwak, R. M. Jain, M. H. Wong, N. M. Iverson, M. Ben-Naim, M. S. Strano, *Small* **2015**, *11*, 3973–3984.

[31] T. T. S. Lew, V. B. Koman, K. S. Silmore, J. S. Seo, P. Gordiichuk, S.-Y. Y. Kwak, M. Park, M. C.-Y. Y. Ang, D. T. Khong, M. A. Lee, M. B. Chan-Park, N.-H. H. Chua, M. S. Strano, *Nat. Plants* **2020**, *6*, 404–415.

[32] M. C.-Y. Ang, N. Dhar, D. T. Khong, T. T. S. Lew, M. Park, S. Sarangapani, J. Cui, A. Dehadrai, G. P. Singh, M. B. Chan-Park, R. Sarojam, M. Strano, *ACS Sensors* **2021**, *6*, 3032–3046.

[33] T. T. S. Lew, M. Park, J. Cui, M. S. Strano, *Adv. Mater.* **2021**, *33*, 1–11.

[34] E. Voke, R. L. Pinals, N. S. Goh, M. P. Landry, *ACS Sensors* **2021**, *6*, 2802–2814.

[35] M. Zheng, A. Jagota, E. D. Semke, B. A. Diner, R. S. McLean, S. R. Lustig, R. E. Richardson, N. G. Tassi, *Nat. Mater.* **2003**, *2*, 338–342.

[36] J. Zhang, M. P. Landry, P. W. Barone, J. H. Kim, S. Lin, Z. W. Ulissi, D. Lin, B. Mu, A. A. Boghossian, A. J. Hilmer, A. Rwei, A. C. Hinckley, S. Kruss, M. A. Shandell, N. Nair, S. Blake, F. Şen, S. Şen, R. G. Croy, D. Li, K. Yum, J. H. Ahn, H. Jin, D. A. Heller, J. M. Essigmann, D. Blankschtein, M. S. Strano, *Nat. Nanotechnol.* **2013**, *8*, 959–968.

[37] R. Nißler, F. A. Mann, P. Chaturvedi, J. Horlebein, D. Meyer, L. Vukovic, S. Kruss, *J. Phys. Chem. C* **2019**, *123*, 4837–4847.

[38] A. Spreinat, M. M. Dohmen, N. Herrmann, L. F. Klepzig, R. Nißler, S. Weber, F. A. Mann, J. Lauth, S. Kruss, *J. Phys. Chem. C* **2021**, *125*, 18341–18351.

[39] M. P. Landry, H. Ando, A. Y. Chen, J. Cao, V. I. Kottadiel, L. Chio, D. Yang, J. Dong, T. K. Lu, M. S. Strano, *Nat. Nanotechnol.* **2017**, *12*, 368–377.

[40] K. Welsher, Z. Liu, S. P. Sherlock, J. T. Robinson, Z. Chen, D. Daranciang, H. Dai, *Nat. Nanotechnol.* **2009**, *4*, 773–780.

[41] V. Shumeiko, Y. Paltiel, G. Bisker, Z. Hayouka, O. Shoseyov, *Biosens. Bioelectron.* **2021**, *172*, 112763.

[42] A. F. Mann, J. Horlebein, N. F. Meyer, F. Thomas, S. Kruss, *Chem. - A Eur. J.* **2018**, *24*, 12241–12245.

[43] A. Antonucci, J. Kupis-Rozmysłowicz, A. A. Boghossian, *ACS Appl. Mater. Interfaces* **2017**, *9*, 11321–11331.

[44] E. Polo, T. Nitka, E. Neubert, L. Erpenbeck, L. Vuković, Kruss, *ACS Appl. Mater. Interfaces* **2018**, *10*, 17693−17703.

[45] F. A. Mann, Z. Lv, J. Grosshans, F. Opazo, S. Kruss, *Angew. Chemie Int. Ed.* **2019**, *58*, 1469–11473.

[46] A. Setaro, M. Adeli, M. Glaeske, D. Przyrembel, T. Bisswanger, G. Gordeev, F. Maschietto, A. Faghani, B. Paulus, M. Weinelt, R. Arenal, R. Haag, S. Reich, *Nat. Commun.* **2017**, *8*, 1–7.

[47] F. A. Mann, N. Herrmann, F. Opazo, S. Kruss, *Angew. Chemie - Int. Ed.* **2020**, 2–9.

[48] S. Singh, I. Kaur, R. Kariyat, *Int. J. Mol. Sci.* **2021**, *22*, 1–19.

[49] R. V. Barbehenn, C. Peter Constabel, *Phytochemistry*

2011, *72*, 1551–1565.
[50] J. Salminen, M. Karonen, *Funct. Ecol.* **2011**, *25*, 325–338.
[51] U. Baetz, E. Martinoia, *Trends Plant Sci.* **2014**, *19*, 90–98.
[52] A. Lanoue, V. Burlat, U. Schurr, U. S. R. Röse, *Plant Signal. Behav.* **2010**, *5*, 1037–1038.
[53] A. Khoddami, M. A. Wilkes, T. H. Roberts, *Molecules* **2013**, *18*, 2328–2375.
[54] F. Della Pelle, D. Compagnone, *Sensors (Switzerland)* **2018**, *18*, 1–32.
[55] M. David, M. Florescu, C. Bala, *Biosensors* **2020**, *10*, 1–19.
[56] J. Zhou, Z. Lin, Y. Ju, M. A. Rahim, J. J. Richardson, F. Caruso, *Acc. Chem. Res.* **2020**, *53*, 1269–1278.
[57] C. P. Constabel, K. Yoshida, V. Walker, in *Recent Adv. Polyphen. Res.*, **2014**.
[58] S. Cesco, T. Mimmo, G. Tonon, N. Tomasi, R. Pinton, R. Terzano, G. Neumann, L. Weisskopf, G. Renella, L. Landi, P. Nannipieri, *Biol. Fertil. Soils* **2012**, *48*, 123–149.
[59] D. P. Salem, X. Gong, A. T. Liu, V. B. Koman, J. Dong, M. S. Strano, *J. Am. Chem. Soc.* **2017**, *139*, 16791–16802.
[60] K. Umemura, Y. Ishibashi, M. Ito, Y. Homma, *ACS Omega* **2019**, *4*, 7750–7758.
[61] Y. Yamazaki, K. Umemura, *J. Near Infrared Spectrosc.* **2020**, 1–3.
[62] R. Nißler, L. Kurth, H. Li, A. Spreinat, I. Kuhlemann, B. S. Flavel, S. Kruss, *Anal. Chem.* **2021**, *93*, 6446–6455.
[63] E. A. Ainsworth, K. M. Gillespie, *Nat. Protoc.* **2007**, *2*, 875–877.
[64] A. Mithöfer, A. A. Bhagwat, M. Feger, J. Ebel, *Planta* **1996**, *199*, 270–275.
[65] J. Fliegmann, G. Schüler, W. Boland, J. Ebel, A. Mithöfer, *Biol. Chem.* **2003**, *384*, 437–446.
[66] A. R. Ayers, J. Ebel, F. Finelli, N. Berger, P. Albersheim4, *Plant Physiol* **1976**, *57*, 751–759.
[67] J. K. Sharp, P. Albersheim, P. Ossowski, A. Pilotti, P. Garegg, B. Lindberg, *J. Biol. Chem.* **1984**, *259*, 11341–11345.
[68] J. Ebel, H. Grisebach, *Trends Biochem. Sci.* **1988**, *3*.
[69] M. G. Hahn, A. Bonhoff, H. Grisebach, *Plant Physiol.* **1985**, *77*, 591–601.
[70] P. Moesta, H. Grisebach, *Nature* **1980**, *286*, 710–711.
[71] L. J. Shaw, P. Morris, J. E. Hooker, *Environ. Microbiol.* **2006**, *8*, 1867–1880.
[72] A. Sugiyama, *J. Adv. Res.* **2019**, *19*, 67–73.
[73] S. Hassan, U. Mathesius, *J. Exp. Bot.* **2012**, *63*, 3429–3444.
[74] A. Sugiyama, K. Yazaki, *Plant Biotechnol.* **2014**, *31*, 431–443.

Table of Contents

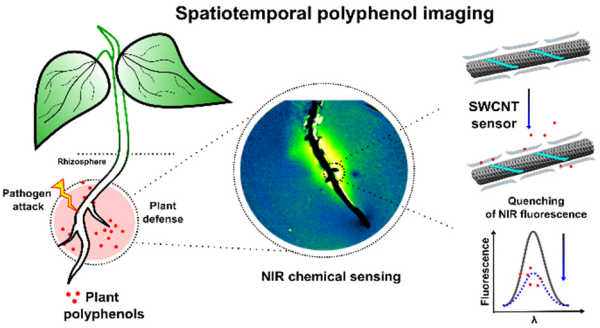

Molecular sensors for plant polyphenol imaging based on near-infrared (NIR) fluorescent single wall carbon nanotubes (SWCNTs) are presented. These sensors probe the polyphenol content in complex biological systems such as the plant rhizosphere. In summary, this approach enables real-time spatiotemporal visualization of plant defense via polyphenols release.

Institute and/or researcher Twitter usernames: @KrussLab

5.4.4 Discussion

A NIR-fluorescent sensor for the detection of plant polyphenols is described in **Manuscript VI**. It probes the total phenol content in complex biological samples, based on shifts in the sensor emission intensity and wavelength. With the help of camera-assisted NIR stand-off imaging, polyphenol release from soybean seedings into the rhizosphere was visualized, as part of pathogen-induced plant defense. To obtain a tuned polyphenol sensor, a semi-rational screening was performed. Polyphenols are known for their relatively high pKa-value in the physiological range, thus acting as multiple hydrogen bond donors.[223] For that reason, e.g. tannins can interact with proteins, DNA or poly(ethylen glycols) (PEG), causing precipitation of the respective biomacromolecules.[224] Therefore, it was hypothesized that these interactions can also lead to signal transduction upon analyte binding during SWCNT chemical sensing. To evaluate this assumption, SWCNTs were modified with such biomacromolecules, here ssDNA oligonucleotides and PEG-phospholipids (PL) and used for the polyphenol screening presented in Figure 1 (Supplementary Information Manuscript IV, 7.6, Figure S1).

Manuscript VI thereby shows for the first time a comprehensive study about the fluorescence modulation from surface-functionalized SWCNTs after interaction with different (plant) polyphenols. Beforehand, polyphenols were discussed by Umemura and coworkers as antioxidant compounds, countering oxidation-dependent changes in SWCNT absorbance and photoluminescence.[225–227]

The PEG-PL-SWCNTs, which were identified as most optimal polyphenol sensors, were however used in previous studies as nanosensor modifications, known for their high biostability, not prone to unspecific interactions.[145,228] Nevertheless, some PEG-PL-SWCNTs showed in presence of certain proteins and protein fragments a reduction in photoluminescence emission.[111,112] However, without the significant shift in emission wavelength when interacting with polyphenols (Figure 2). Established polyphenol detection methods like colorimetric assays or HPLC-MS show great sensitivity and incomparable selectivity, especially true for mass-spectrometry-based approaches.[229] However, these methods and even new types of biosensors or nanoparticle-based sensors for polyphenol detection, need extraction of target analytes and therefore can not resolve *in vivo* processes.[230,231] The introduced SWCNT sensors can now visualize for the first time the release of polyphenolic compounds optically in the NIR, as shown for pathogen-induced secretion from soybean seedings (Figure 4). In the future, this optical tool could be used for fundamental studies[232],

whereas polyphenols are involved in rhizosphere chemical communication between plants and microorganisms or between (neighboring) plants.[233] The spatiotemporal detection of this specialized communication could lead to better understanding of those systems and perhaps resolve dynamic pattern like waves, otherwise not detectable with other methods. In addition, by using chirality-pure SWCNTs, it was possible to even create a ratiometric polyphenol sensing and imaging approach which could improve the robustness of the system in the future.

On the other hand, the large-scale visualization of polyphenol release could lead to crop-screening approaches, identifying cultivars and isolates with enhanced polyphenol secretion capability and therefore increased pathogen defense properties.[234,235] Such a potential technique could be used in agricultural research for time-resolved analyte tracking in a greenhouse environment, where e.g. novel soybean hybrids are cultivated either in liquid or on agar media.

Moreover, the *in vitro* polyphenol detection with SWCNTs could hold great promise with regards to a high-throughput screening assay for plant-derived samples, just requiring very small sample volumes in the µL range. This could be especially interesting for analysis of the phloem, the vascular structure in plant tissue responsible for transport of photosynthesis products like sugars. The commonly used, elaborate sampling process[236] only allows to recover sample volumes in the µL range[237], insufficient for most classical analytical tools. However, SWCNT sensors could enable analysis of phloem metabolite levels, also beyond polyphenols, when using different kinds of tailored and multiplexed sensors. In summary, the presented polyphenol sensing tool is the first one based on NIR-fluorescent SWCNTs. The sensitive spectroscopic detection exploits shifts in nanosensor's emission intensity and wavelengths after analyte interaction. This concept was further extended towards NIR fluorescence imaging, which enabled *in situ* visualization of chemical plant defense.

6 | Conclusion and Outlook

Global challenges in healthcare, agriculture or environmental science require fast, specific and cost-effective analytical tools, in order to detect, understand and tackle existing and upcoming issues. One possible solution is based on smart sensors that enable label-free detection of infectious diseases or antibiotic-resistant pathogens in healthcare. However, to design such sensors, different kind of requirements regarding selectivity, sensitivity, stability or readout possibilities have to be considered. Especially nanosensor tools based on SWCNTs, which are known for their unique optoelectronic features, showed promising application as chemo- and biosensors. But how can these SWCNT-sensors be further optimized and tailored to detect specific targets? And on the other hand, how can the photoluminescence properties of the sensor building blocks be modified in order to obtain hyperspectral probes? These central questions were addressed in the presented thesis, focusing on tailored NIR-fluorescent SWCNT-sensors for the detection of bacteria and plant-pathogen interactions. Within the thesis, multiple areas and aspects are discussed, ranging from surface modification chemistry, to nanoparticle separation up to hydrogel assembly and remote optical analyte visualization. This chapter will summarize the introduced sensing approaches and achievements and will outline how the presented findings can improve chemical sensing right up to diagnostics in the future. The following figure illustrates and recapitulates the discussed themes and manuscripts.

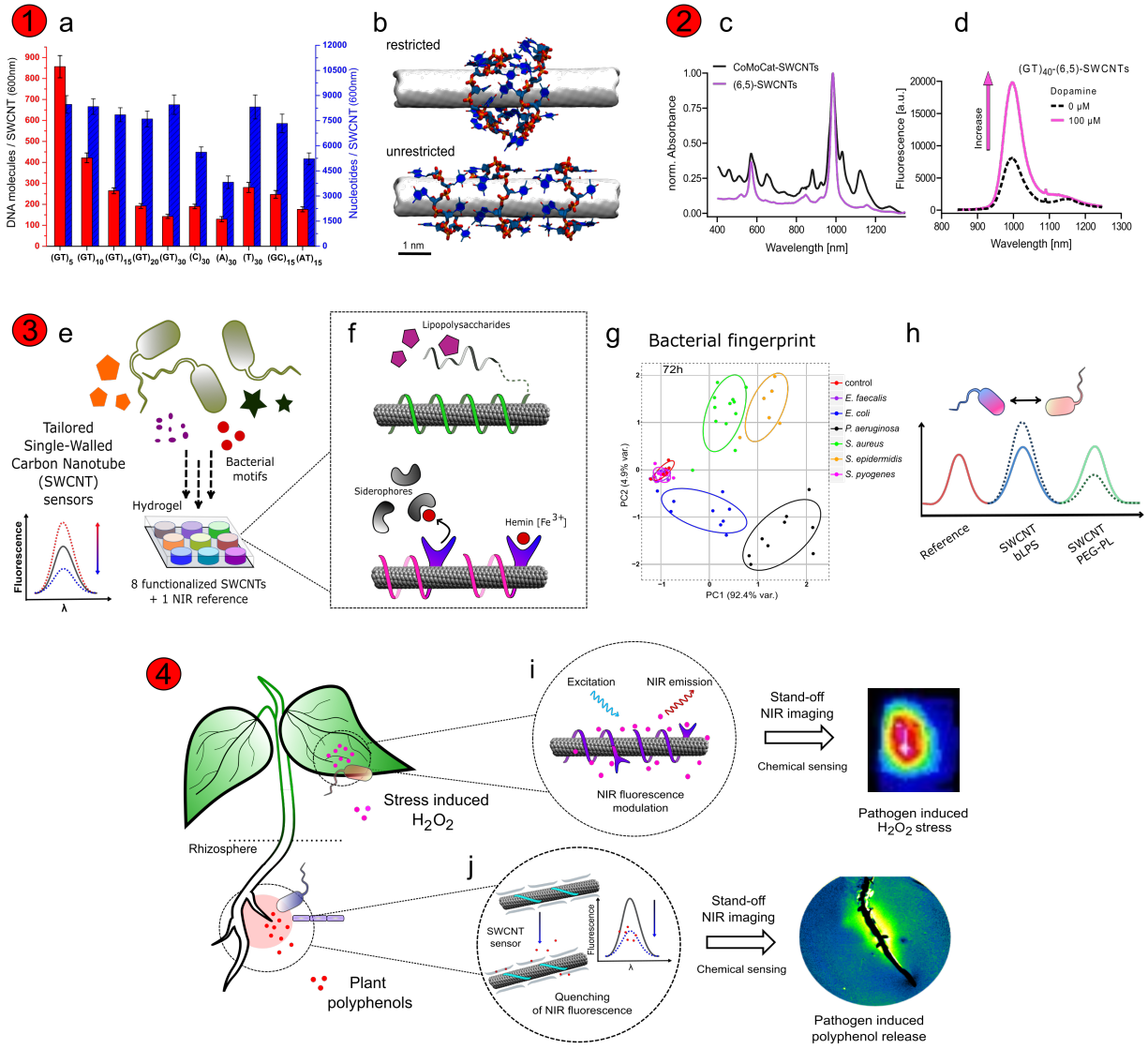

Figure 6.1.: **Overview of the covered themes and SWCNT-sensor approaches.** The presented chapters (red numbers) and manuscripts are sorted in the order of their apperance in the thesis: **1)** To gain a more detailed understanding of the SWCNT surface modification, an approach was established to quantify the amount of ssDNA adsorbed on the SWCNTs (a, **Manuscript I**). The results indicate a dense DNA corona, as visualized by MD-simulations (b, restricted panel), and furthermore allow for ratio-specific linkages and bioorthogonal modifications of the ssDNA-SWCNTs. **2)** In order to obtain SWCNT-sensors with non-overlapping emission features, different nanomaterial purification approaches were combined with non-covalent surface functionalization techniques (c). This allowed the assembly of chirality-pure SWCNT-sensors either from polyfluorene (PFO) sorted SWCNTs (**Manuscript II**) or from SWCNTs purified by aqueous two-phase extraction (ATPE, **Manuscript III**). These results display the basis for chemical sensing with chirality-pure SWCNTs (d) and moreover for combined hyperspectral approaches.

3) Different rational sensors for bacterial targets (e.g. LPS, siderophores) were introduced in **Manuscript IV** and assembled into a hydrogel array (e,f). Their readout by camera-assisted NIR stand-off detection allowed remote differentiation of bacterial pathogens, based on their chemical fingerprints (g). In addition, purified and specifically modified SWCNTs enabled hyperspectral bacteria sensing (h). **4)** Design of SWCNT sensors that are able to visualize the interaction of pathogens with plants. A tailored nanosensor for the detection of H_2O_2 (i, **Manuscript V**) could be introduced into leaf tissue and reported plant stress response after mimicking a bacterial attack, by means of NIR stand-off detection. **Manuscript VI** furthermore described sensitive polyphenol nanosensors (j) and how they can be used to visualize polyphenol secretion from root tissue, as a chemical defense response upon pathogen challenge.

6.1 Tailored SWCNT-Sensors

SWCNTs can be used as label-free sensors that are able to depict biological processes with great spatial, temporal and chemical resolution. In order to tune these NIR-fluorescent sensors, both functional components, the receptor (surface modification) and transducer (SWCNT), were tailored. Those optimized constructs are then able to report specific analytes while exhibiting superior optical properties.

6.1.1 Insights to ssDNA-SWCNT Surface Modification

In general, it is important to understand the interplay between surface adsorbed biopolymers with SWCNTs in great detail, since the surface modification is the molecular recognition element and responsible for analyte interaction and binding event transduction. **Manuscript I** introduced a direct approach to quantify the amount of ssDNA adsorbed on the SWCNT surface, since it is one of the most used non-covalent surface functionalization concepts for SWCNT biosensing and purification. The protocol itself was based on UV-Vis-NIR absorption spectroscopy, molecular weight cut-off filtration and AFM, and it can in principle quantify all kinds of DNA variations without the need of an additional fluorophore label. It furthermore allowed to correlate the number of adsorbed DNA molecules (Figure 6.1a) with the chemical sensing ability of ssDNA-SWCNTs. As it was found to be mostly independent, a more complex interplay for the chemical sensing mechanism seems likely. This suggests that the exact structure and composition of the crowded corona around the SWCNT is probably crucial for photophysical changes upon analyte interac-

tion. **Manuscript I** furthermore paves the way for MD-simulations (Figre 6.1b) that take the overall number of adsorbed DNA molecules into account. Most importantly in the direction of tailored nanosensors, by quantifying the amount of adsorbed DNA, a subsequent ratio-specific modification of the DNA *via* linker chemistry can be performed. This allows to bring known recognition and binding motives into proximity of the SWCNT. Thus, potentially enabling and enhancing signal transduction after analyte interaction, which displays the basis for functional and selective fluorescent probes.

6.1.2 Towards Chirality-pure SWCNT-Sensors

Next to the optimization of the surface functionality, it is desirable to generate nanosensors with defined optical properties. This could reduce unspecific interactions e.g. with other (metallic) SWCNTs in a mixture and minimize spectra congestion, so different sensors with non-overlapping emission features can be united for a hyperspectral sensing approach. The challenge thereby is to combine nanomaterial purification approaches with further non-covalent surface functionalization techniques. This is essential, since the obtained chirality-pure SWCNT fractions are present after purification in solvents or surfactants unsuitable for universal application in biosensing. **Manuscript II** enabled this link between PFO-purified SWCNTs and surfactant exchange, which is essential to use those colloidal nanoparticles in biological (aqueous) systems as NIR-labels or chemical sensors. It can be seen as the first comprehensive approach, facilitating the removal, recycling and surface exchange of PFO-sorted SWCNTs. Thereby, the polymer replacement itself seems to be most likely independent of the used polyfluorene type, providing access to various SWCNT chiralities in the future. In addition, **Manuscript III** described the assembly of chirality-pure SWCNT-sensors, based on nanotube sorting *via* aqueous two-phase extraction (ATPE). This straightforward purification technique allows the isolation of desired chiralities (Figure 6.1c) by multiple-step partitioning of dispersed SWCNTs between aqueous phases of immiscible polymers. The subsequent variation of SWCNT surface modification was facilitated by a methanol-supported surface exchange process. This enabled the assembly of various chirality-pure nanoconjugates and the possibility to study their colloidal, photophysical and sensing properties. Most importantly, monochiral ssDNA-SWCNTs were found to be functional for chemical sensing (Figure 6.1d). Hereby, the ssDNA sequence determined the nanosensors absolute fluorescence intensity, colloidal (long-term) stability and selectivity against analytes. This sensing concept was demonstrated with several

chirality-pure SWCNTs, as well with enantiomer-pure (±) (6,5)-SWCNTs. In summary, it can be postulated, that SWCNT chirality and handedness have an insignificant influence on chemical sensing, compared to the structure and properties of the surface functionalization. This, in its consequence, enables tailored NIR-fluorescent sensors, which are in principle freely selectable in emission wavelength (through the used SWCNT chirality) and analyte sensitivity (through the applied surface modification). However, **Manuscript II** and **Manuscript III** display both successful routes towards chirality-pure SWCNT sensors. The assembly from ATPE-sorted SWCNTs (**Manuscript III**) has a higher yield compared to the recovery rate of **Manuscript II**, which makes SWCNT purification and exchange in aqueous systems the preferable approach on the way to tailored biosensors. Overall, the presented methods and obtained insights towards chemical sensing with chirality-pure SWCNTs will pave the way for hyperspectral detection approaches in the future.

6.1.3 Tailored SWCNT-Sensors for Bacteria Detection

After developing possibilities to perform ratio-specific modifications on DNA-SWCNTs by evaluating the amount of surface adsorbed polymers and accessing chirality-pure nanosensors, these approaches can be used to create tailored SWCNT-sensors for the detection of bacterial motives (Figure 6.1e,f). **Manuscript IV** introduced rational design strategies to sense virulence factors, specific markers for bacterial infections. These novel sensors were able to detect low µM concentrations of lipopolysaccharides (LPS), important endotoxins from gram-negative bacteria, as well as siderophores, small iron chelating secondary metabolites (Figure 6.1f). In addition, sensors that report enzyme activity of proteases and nucleases were developed and integrated into functional hydrogel systems. A set of several rationally designed sensors for the bacterial motives were combined with further generic SWCNT conjugates that are known to recognize changing physiochemical parameters like pH or O_2 levels. This was the first reported assembly of hydrogel-based SWCNT sensor assays, which included moreover a NIR-fluorescent reference material called Egyptian Blue. Growth and metabolic activity of bacterial pathogens changed the chemical environment of the sensor-array, which led to specific NIR-fluorescent fingerprints. For the first time, such an implemented SWCNT- 'chemical nose' could remotely detect and differentiate multiple pathogens (Figure 6.1g). These findings were used to translate the locally separated sensors into a hyperspectral sensing approach, using purified SWCNT fractions. These sensors, that combine tuned surface chemistry and defined photoluminescence emis-

sion, were able to differentiate in a proof-of-principle experiment the important pathogens *P. aeruginosa* and *S. aureus* (Figure 6.1h). In summary, this type of multiplexing with NIR-fluorescent nanosensors demonstrated for the first time the remote detection and differentiation of infection-associated pathogens. In the future, these smart sensors could be used for improved *in vitro* diagnostics, e.g. for remote readout of pathogen fingerprints from blood cultures, or ultimately for smart implants and *in situ* detection of infections through wound patches or tissue. The presented concepts could be furthermore extended towards the detection of pathogen antibiotic resistance, as a possible strategy to improve antibiotic stewardship in the future.

6.1.4 SWCNT-Sensors Detecting Plant-Pathogen Interactions

Next to the nanosensor development for novel diagnostic tools, specific sensing approaches are also needed in agricultural science, in order to understand and possibly even prevent pathogen interactions with crop plants. The last part of the thesis introduced sensors that respond to plant metabolites, which are associated with plant stress and chemical defense responses after pathogen attack. This included a tailored sensor for a universal stress signal in plants, more precise an optical tool that can visualize H_2O_2 secretion. The related concept was presented in **Manuscript V**. It enabled the remote detection and sensing of H_2O_2 inside leaf tissue, since H_2O_2 and other reactive oxygen species (ROS) are important signaling molecules, which can also be directly involved in plant defense. In order to tailor the sensors for sensitive H_2O_2 detection, the SWCNTs were modified with a specific DNA-aptamer, that is able to bring an iron-binding molecule in close proximity to the nanotube surface. This was found to maximize the concentration dependent fluorescence quenching of the SWCNT-sensors, likely due to an iron mediated Fenton-like reaction. These nano-constructs were able to respond to physiological concentrations of H_2O_2 during strong light or pathogen stimulus, while showing high biocompatibility and no reduction in plant photosynthetic rates. Generally speaking, this approach enabled for the first time the visualization of pathogen-induced stress in plants with NIR-fluorescent nanosensors. In the future, this sensor tool could be introduced in a variety of different plants, most importantly in wild-type plants, bypassing the need for genetic modifications. In perspective, such nanosensors could improve our understanding of plant stress communication and could provide novel tools for precision agriculture. Moreover, plants

developed a variety of strategies to respond to and defend against pathogen attacks. One special case of plant defense is thereby the secretion of polyphenols from the root system. These secondary metabolites are in general widely distributed in the plant kingdom and show great variety in chemical structures and ecological roles, including antimicrobial activity. **Manuscript VI** screened for SWCNT-sensors that are sensitive to polyphenols and found PEG-PL-SWCNTs as most suitable for this purpose. Upon analyte interaction, the sensors showed a shift in emission intensity and wavelength, probing the total phenol content in complex biological samples. Furthermore, this NIR-fluorescent sensor tool was able to detect significant differences in polyphenol levels from soybean cell cultures, when challenged with a fungal elicitor. This concept was further extended to a polyphenol imaging approach, able to visualize the secretion of polyphenols from soybean seedlings after mimicking a fungal pathogen attack. In the future, this optical probe could be used in fundamental studies to visualize polyphenols that are involved in rhizosphere chemical communication between plants and microorganisms or also among plants. On the other hand, the macroscopic and hyperspectral visualization of polyphenol release could hold great promise to large-scale crop-screening approaches. Thus, identification of cultivars and isolates with increased polyphenol secretion potential could become possible, improving the plant pathogen resistance.

6.2 Nanosensors for Pathogen Detection

To summarize the presented thesis, multiple fundamental approaches to tailor SWCNT's surface chemistry and photoluminescence properties were presented, with the aim to design specific pathogen sensors. Such nanosensors were used to detect various bacterial motives, enabling in its consequence the array-based optical differentiation of infection-associated pathogens. This could majorly improve existing techniques, making blood-culture analysis faster and more specific, or enable *in situ* diagnostics, which were not available before. In perspective, these optical probes have the potential to solve existing biomedical challenges by *in vivo* biomarker visualization. Furthermore, this chemical sensing strategy was extended to visualize plant-pathogen interactions, by depicting underlying plant stress and defense responses. These sensor approaches can help to automatize crop breeding processes, hence creating resistant and high-yielding cultivars to secure global food production. Overall, the introduced conceptual advances will improve the field of chemical

sensing with NIR-fluorescent SWCNTs in the future and will facilitate novel diagnostic tools, both in healthcare and agriculture.

7 | Appendix

7.1 Supplementary Information Manuscript I

Quantification of the Number of Adsorbed DNA Molecules on Single-Walled Carbon Nanotubes

Robert Nißler[1], Florian A. Mann[1], Parth Chaturvedi[3], Jan Horlebein[1], Daniel Meyer[1], Lela Vuković[3] and Sebastian Kruss[1,2*]

[1]Institute of Physical Chemistry, Göttingen University, Göttingen 37077, Germany
[2]Center for Nanoscale Microscopy and Molecular Physiology of the Brain (CNMPB), Göttingen 37077, Germany
[3]Department of Chemistry and Biochemistry, University of Texas at El Paso, El Paso, TX 79968

[*] Corresponding author

The Journal of Physical Chemistry C, **2019**, 123, 4837-4847
DOI: 10.1021/acs.jpcc.8b11058

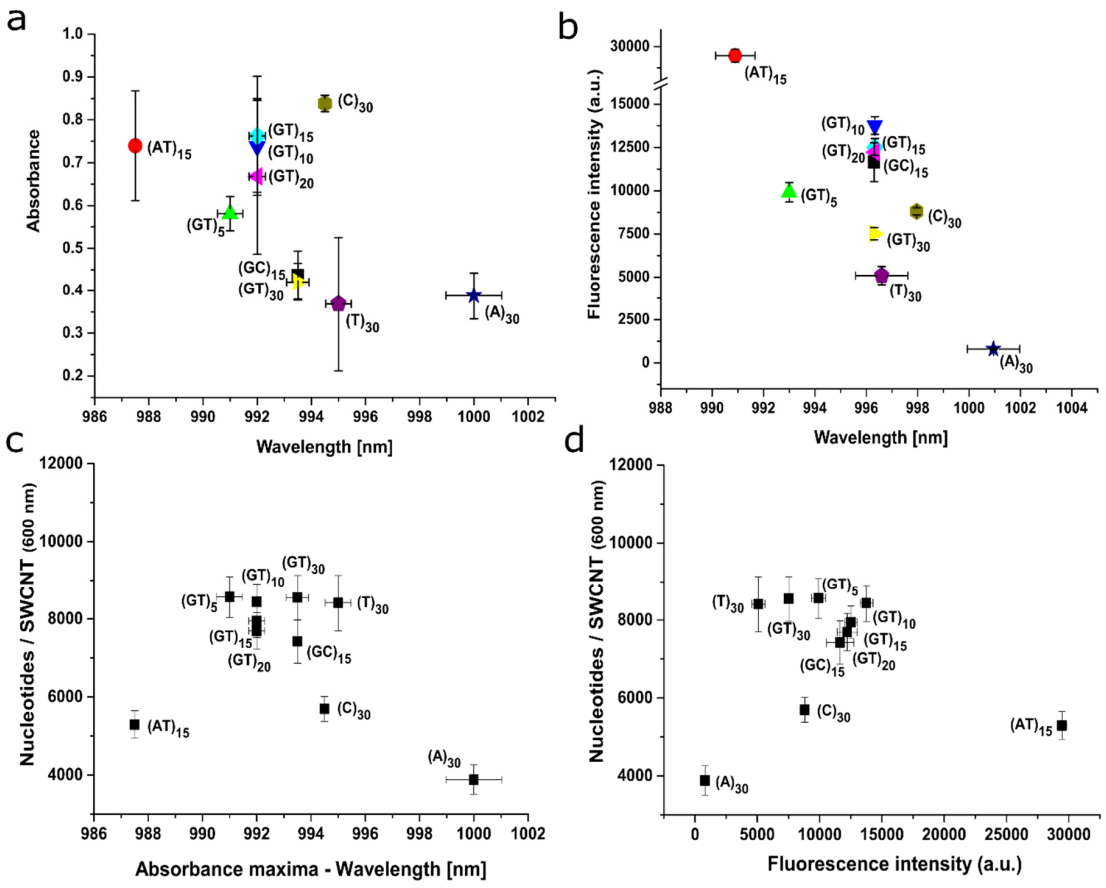

Figure S1: Absorption and emission spectra of ssDNA/SWCNT hybrids vary with oligonucleotide sequence.

a) Absorption maxima of (6, 5) ssDNA/SWCNT of 1:100 diluted stock samples (n = 3, errors are SEM). b) Fluorescence intensity and position of (6, 5) peak maxima of 0.1 nM ssDNA/SWCNT (n=3 with SEM). In a) and b) colors/symbols are used for different ssDNA sequences. c) Bound DNA nucleotides per SWCNT (normalized to 600 nm length) vs. nIR-absorption of ssDNA/SWCNTs. d) Bound DNA nucleotides per SWCNT vs. the fluorescence emission intensity of 0.1 nM ssDNA/SWCNT (n = 3 with SEM). There is no obvious correlation between the number of bound ssDNA molecules and nIR absorbance or fluorescence features, which indicates that the ssDNA/SWCNT photoluminescence mainly depends on the nucleotide composition/conformation, rather than only on the number of bound/adsorbed ssDNA molecules.

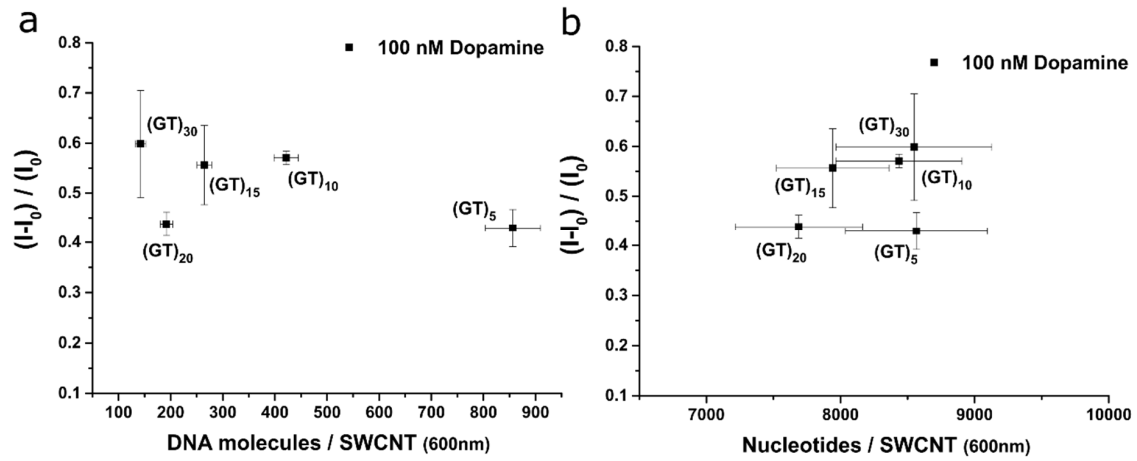

Figure S2: $(GT)_x$/SWCNT nIR-fluorescence response to dopamine.

a) Fluorescence response vs. numbers of nucleotides per SWCNT. b) Fluorescence response to dopamine vs. number of DNA molecules / SWCNT (n = 3, errors are SEM). There is no obvious correlation between the number of adsorbed $(GT)_x$ molecules and the nIR-fluorescence response after dopamine addition.

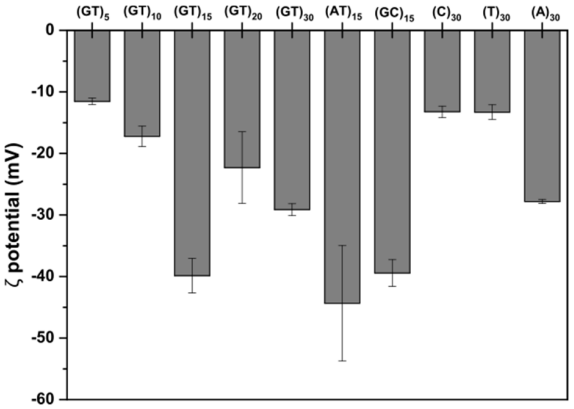

Figure S3: Zeta-potential of the different ssDNA/SWCNT conjugates.

(n = 3, errors are SEM)

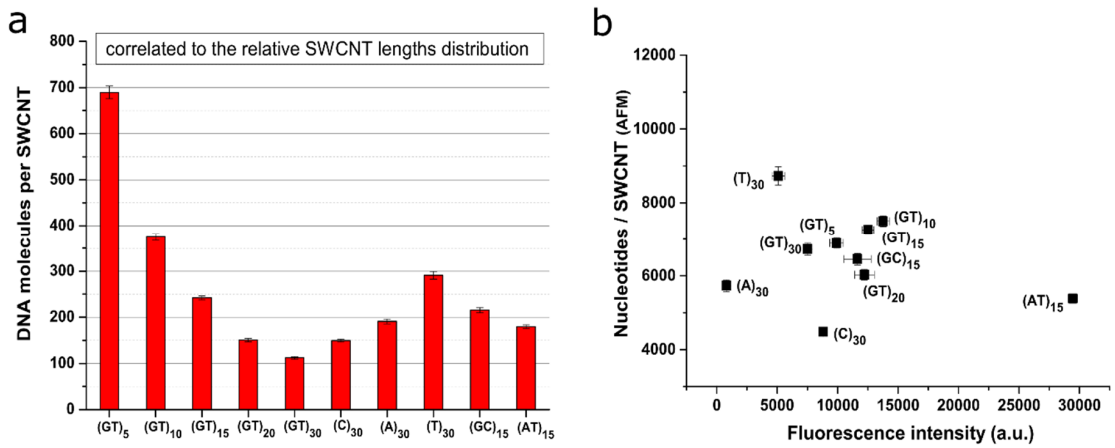

Figure S4: Adsorbed ssDNA molecules per SWCNT.

a) DNA molecules per SWCNT using the actual AFM lengths (n = 3, errors are SD). b) Number of adsorbed nucleotides per SWCNT vs. the fluorescence intensity of a 0.1 nM ssDNA/SWCNT solution.

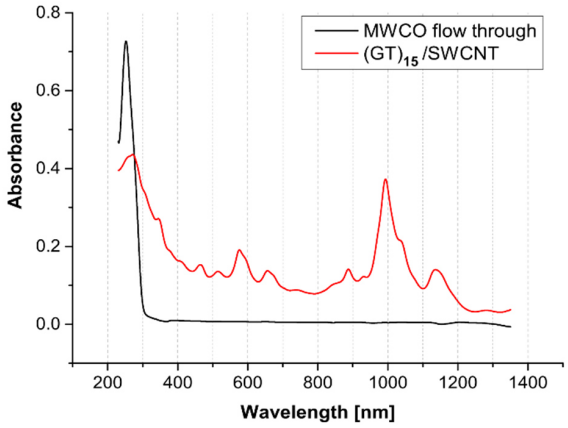

Figure S5: UV-Vis-nIR Absorbance spectra before and after filtration.

Red spectrum represents a 1:100 dilution of the prepared stock solution of $(GT)_{15}$/SWCNT. The black spectrum shows the absence of SWCNTs after the molecular weight cut-off filtration process (1st filtration; 1:10 diluted stock solution). The free DNA gives a discreet absorbance feature at ~ 260 nm.

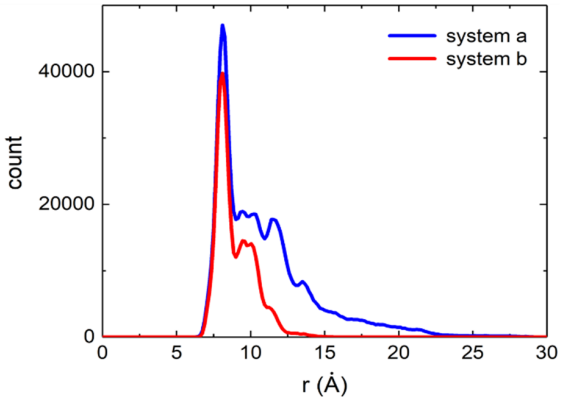

Figure S6: Radial distance distribution of all ssDNA atoms from the central (6,5)-SWCNT axis for systems in panels a and b of Figure 7.

The distributions were obtained for all ssDNA atoms over 200 ns (system a) and 100 ns (system b) (see Figure 7). The thickness of the ssDNA corona for the system in panel a is uneven and ~ 13.5 Å, while the thickness of the DNA corona for the system in panel b is more even and ~ 6 Å.

Table S1: Lengths of the ssDNA/SWCNT conjugates measured by AFM

	n	length [µm]	SD [µm]
$(GT)_{20}$	89	0.461	0.200
$(GT)_{15}$	78	0.550	0.295
$(C)_{30}$	111	0.471	0.185
$(GT)_{10}$	60	0.540	0.284
$(AT)_{15}$	66	0.613	0.279
$(GT)_{5}$	55	0.491	0.302
$(A)_{30}$	44	0.892	0.506
$(T)_{30}$	62	0.626	0.275
$(GC)_{15}$	71	0.517	0.245
$(GT)_{30}$	100	0.468	0.220

Table S2: Number of bound ssDNA molecules of ssDNA/SWCNT hybrids (values normalized to 600 nm long (6,5)-SWCNTs).

	ssDNA molecules / SWCNT	SD	ssDNA nucleotides / SWCNT	SD	Mean SWCNT segment for one ssDNA molecule [nm]	SD [nm]
$(GT)_5$	857	53	8566	530	0.70	0.04
$(GT)_{10}$	422	23	8435	470	1.42	0.08
$(GT)_{15}$	265	14	7942	420	2.27	0.12
$(GT)_{20}$	192	12	7689	474	3.12	0.19
$(GT)_{30}$	142	10	8548	581	4.21	0.29
$(C)_{30}$	190	11	5693	318	3.16	0.18
$(A)_{30}$	129	13	3880	377	4.64	0.45
$(T)_{30}$	280	24	8412	718	2.14	0.18
$(GC)_{15}$	247	19	7420	559	2.43	0.18
$(AT)_{15}$	176	12	5290	355	3.40	0.23

Extended explanation of the occupation calculation

Extended formula to calculate the average (6,5)-SWCNT segment, which is occupied by a single ssDNA molecule (SWCNT segment / ssDNA molecule):

$$c_{SWCNT} = \frac{c_c}{L_{SWCNT}\ [\mathrm{nm}] \cdot 88\ [\mathrm{nm}^{-1}]}$$

$$\text{ssDNA/SWCNT} = \frac{n_{bound}\ (ssDNA)}{n_{SWCNT}}$$

$$\text{ssDNA/SWCNT} = \frac{\frac{n_{bound}\ (ssDNA)}{c_c \cdot V}}{\frac{}{L_{CNT} \cdot 88\ [\mathrm{nm}^{-1}]}} = \frac{n_{bound}\ (ssDNA) \cdot L_{SWCNT} \cdot 88\ [\mathrm{nm}^{-1}]}{c_c \cdot V}$$

$$\text{SWCNT segment / ssDNA molecule} = \frac{\cancel{L_{SWCNT}}}{\frac{n_{bound}\ (ssDNA) \cdot \cancel{L_{SWCNT}} \cdot 88\ [\mathrm{nm}^{-1}]}{c_c \cdot V}} = \frac{c_c \cdot V}{n_{bound}\ (ssDNA) \cdot 88\ [\mathrm{nm}^{-1}]}$$

$$= \frac{n_{carbon}}{n_{bound}\ (ssDNA) \cdot 88\ [\mathrm{nm}^{-1}]}$$

c_{SWCNT}	concentration of dispersed SWCNTs
c_c	concentration of dispersed carbon
ssDNA/SWCNT	number of adsorbed ssDNA molecules per SWCNT
n_{SWCNT}	amount of dispersed SWCNTs
n_{bound} (*ssDNA*)	amount of adsorbed ssDNA
L_{SWCNT}	mean length $SWCNT_{AFM}$
V	Volume

7.2 Supplementary Information Manuscript II

Chirality enriched carbon nanotubes with tunable wrapping via corona phase exchange purification (CPEP)

Robert Nißler[1], Florian A. Mann[1], Helen Preiß[1], Gabriele Selvaggio[1], Niklas Herrmann[1] and Sebastian Kruss[1*]

[1]Institute of Physical Chemistry, Göttingen University, Göttingen 37077, Germany

[*] Corresponding author

Nanoscale, **2019**, 11, 11159-11166
DOI: 10.1039/c9nr03258d

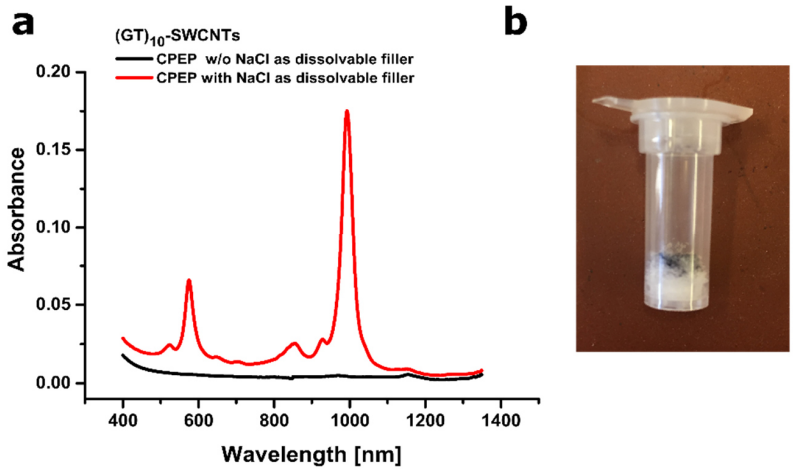

Figure S1: Effect of using NaCl as filler material during PFO-polymer removal.

Remaining PFO-BPy was removed by a stepwise filtration process with hot toluene (see Figure 1). Without NaCl SWCNTs agglomerated with themselves and the filter material and the nanotube pellet could not be dispersed with ssDNA in a tip sonication step (black line in a). By using NaCl as toluene-resistant but water-soluble filler SWCNTs adsorbed/agglomerated mainly on the filler material (photograph in b). After dissolving the NaCl the SWCNT could be redispersed (red line in a).

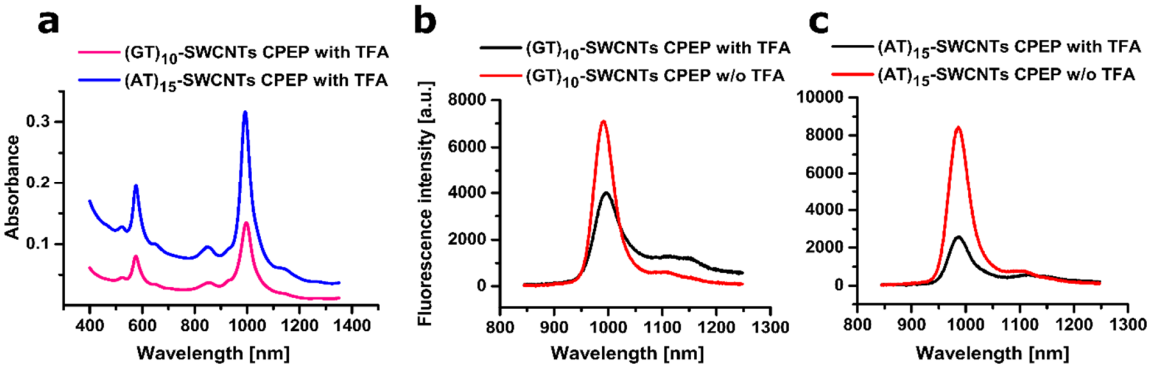

Figure S2: Effect of trifluoroacetic acid (TFA) during CPEP.

To support the separation of the purified SWCNT material and the PFO-BPy, 1 µl TFA was added to the mixture of toluene and iso-propyl alcohol (10 ml). Redispersion with ssDNA was not to affected (a) but the nIR-fluorescence emission decreased compared to a protocol without TFA (b,c - compared to samples from Figure 3 and Figure 4). Therefore, we did not use TFA in the CPEP protocol and relied solely on precipitation of SWCNTs by iso-propyl alcohol addition and centrifugation.

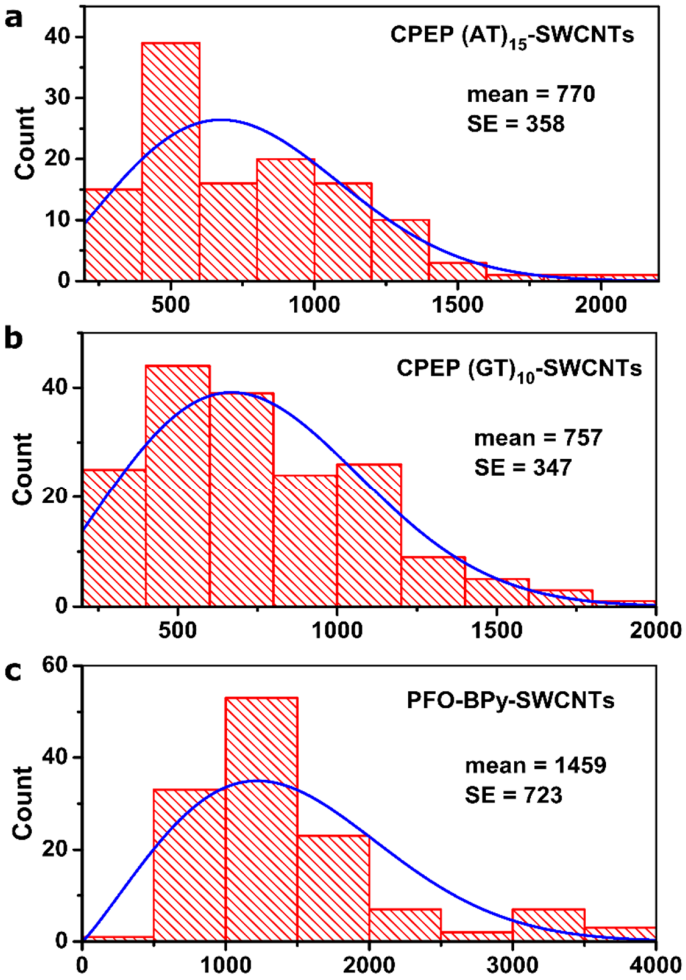

Figure S3. SWCNT length analysis *via* atomic force microscopy (AFM).

The lengths of total 427 SWCNTs were evaluated in Gwyddion and fitted with an asymmetric probability density function (Weibull distribution; OriginPro 9.1). AFM measurements in intermittent contact mode were performed on an Asylum Research MFP-3D Infinity microscope with Olympus AC-160-TS cantilevers. Freshly cleaved muscovite mica substrates were incubated for 12 h at 4 °C with 20 µl ssDNA-(6,5)-SWCNTs and subsequently rinsed carefully with ddH_2O. PFO-BPy wrapped SWCNTs were spin coated on a silica wafer and washed with 20 µl toluene. n(CPEP $(AT)_{15}$-SWCNTs) = 122; n(CPEP $(GT)_{10}$-SWCNTs) = 176; n(PFOBPy-SWCNTs) = 129

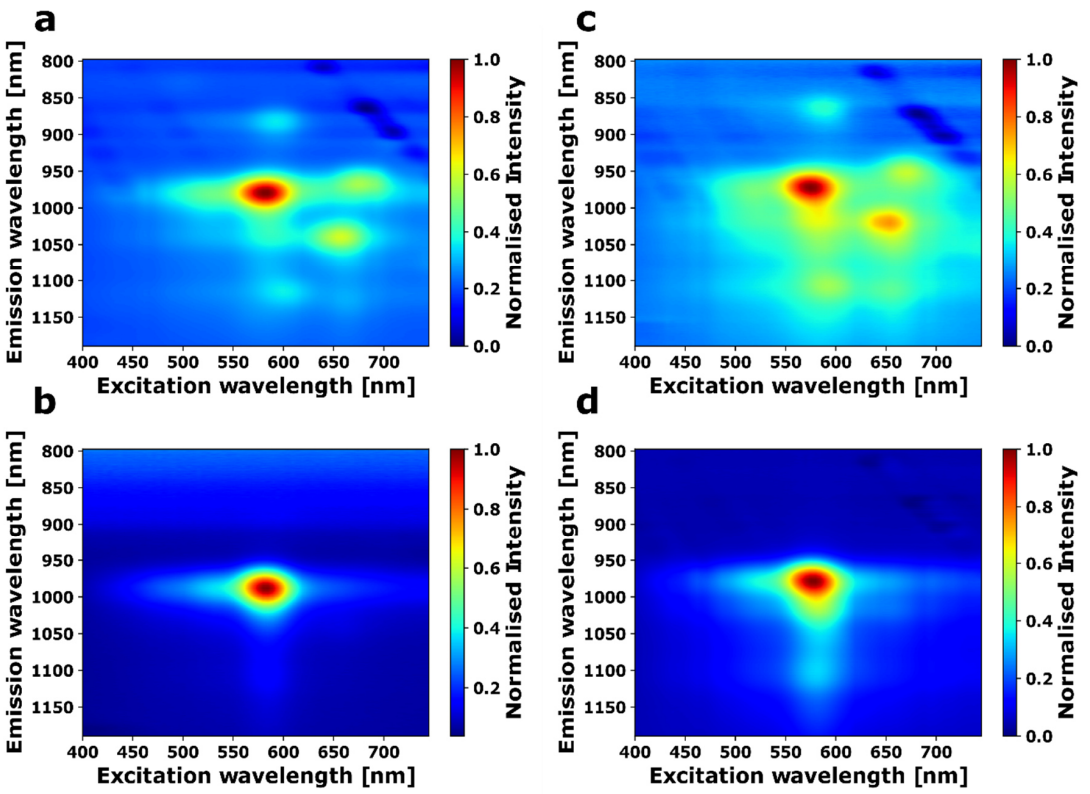

Figure S4. 2D-nIR-fluorescence spectra of CPEP enriched (6,5)-SWCNTs versus their unpurified counterparts.

a) 2D spectra of $(AT)_{15}$-SWCNTs using the SWCNT starting material. b) 2D spectra of CPEP $(AT)_{15}$-(6,5)-SWCNTs (same as Figure 4) c) 2D spectra of SWCNTs starting material dispersed in SDBS. d) 2D spectra of CPEP SDBS-(6,5)-SWCNTs shows an enhanced fluorescence feature at ~1120 nm in the fluorescence spectra but no additional feature in the absorption spectra. This peak could be attributed to SWCNTs with oxygen defects.[1]

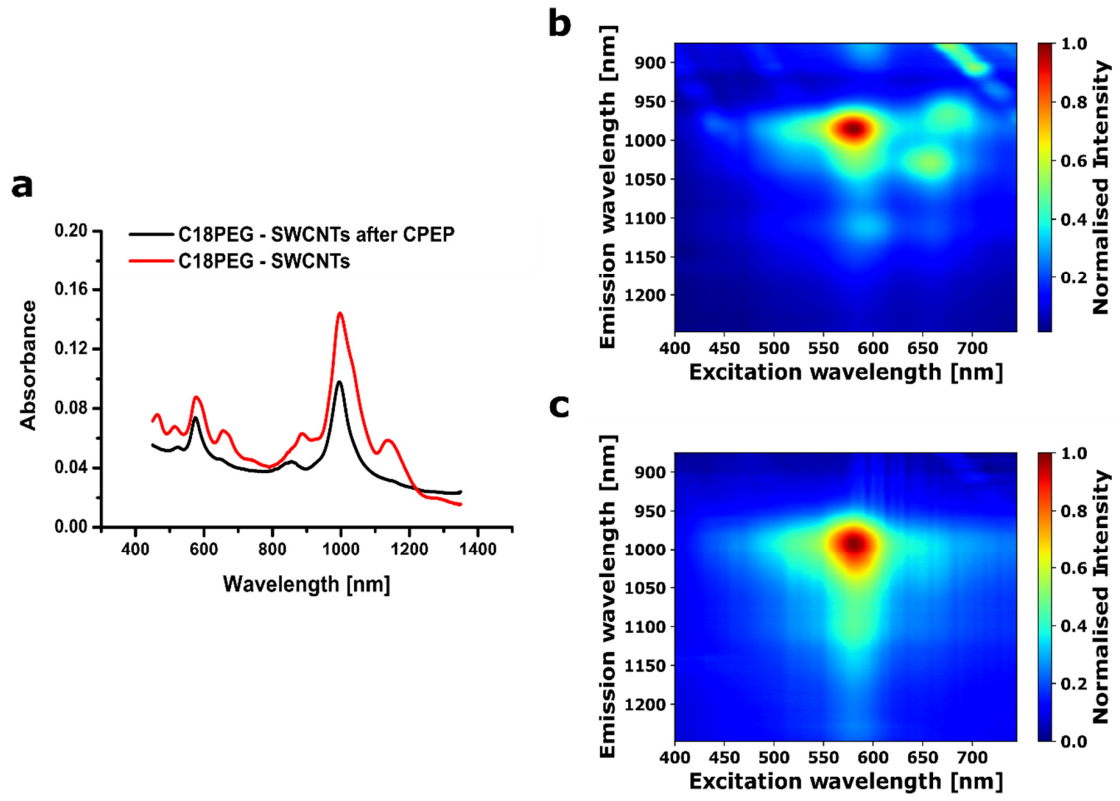

Figure S5. CPEP of (6,5)-SWCNTs with PEG-functionalization.

a) Vis-nIR absorption spectra of CPEP and non-purified PMAC18PEG-SWCNTs. b) 2D-fluorescence spectrum of the crude PMAC18PEG-SWCNTs. c) 2D-fluorescence spectra of the crude PMAC18PEG-(6,5)-SWCNTs.

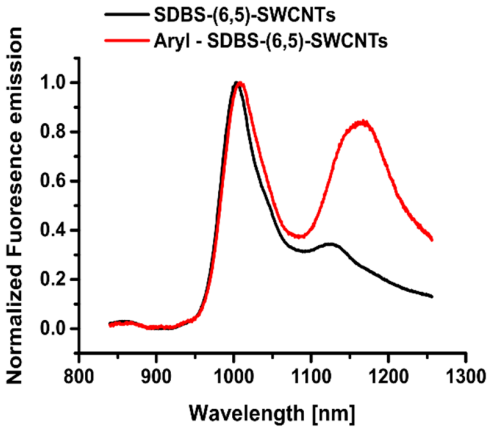

Figure S6. Fluorescence emission spectra of CPEP processed SDBS-(6,5)-SWCNTs.

The black line represents the normalized fluorescence emission spectrum before defect reaction vs. the red line, which was acquired after defect reaction (excited at 570 nm). Compared to the SDBS-(6,5)-SWCNTs, the CPEP purified ssDNA functionalized SWCNTs (see Figure 4c-d) do not show an emission shoulder (black line; ~1120 nm) that could be attributed to oxygen defects[1].

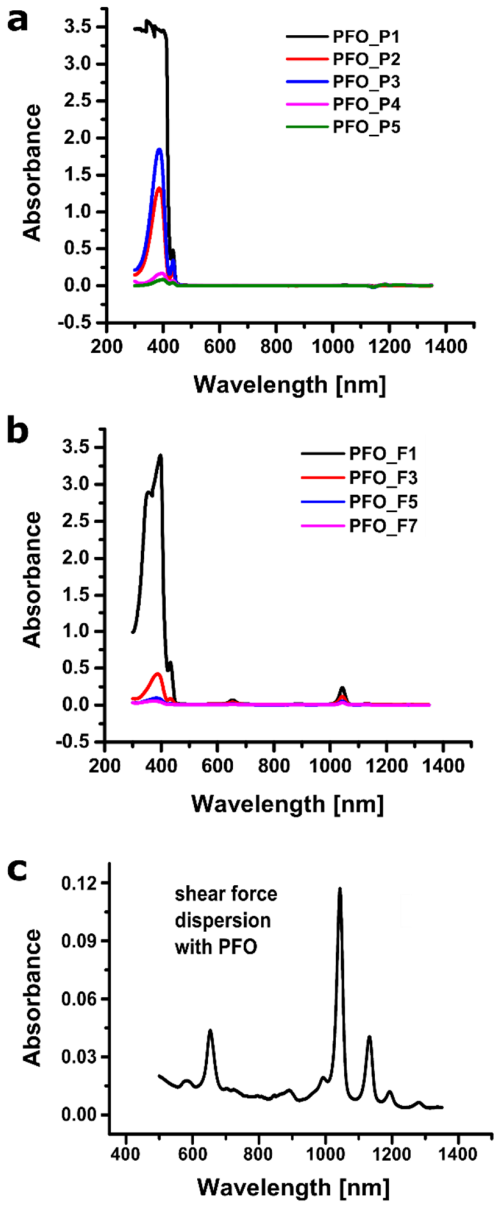

Figure S7. Removal of PFO-polymer during the CPEP process.

UV-Vis-nIR absorption spectra monitor the polymer concentration in toluene to follow the stepwise removal. a) Decreasing PFO concentration due to the precipitation (P) steps with isopropyl alcohol. The majority of PFO stays in solution, while the (7,5)-SWCNTs precipitated during centrifugation. b) Stepwise filtration (F) process with 90 °C toluene removes the residue PFO from the SWCNT-pellet, which is loaded on NaCl crystals. A minor (7,5)-SWCNT fraction is solubilized and therefore removed. The general procedure of PFO-polymer removal for PFO-BPy and PFO were similar besides two additional precipitation steps during PFO-removal. c) UV-Vis-nIR absorption spectra after large scale shear force mixing. PFO mainly disperses (7,5)-SWCNTs and a minor fraction of (7,6)-SWCNTs.

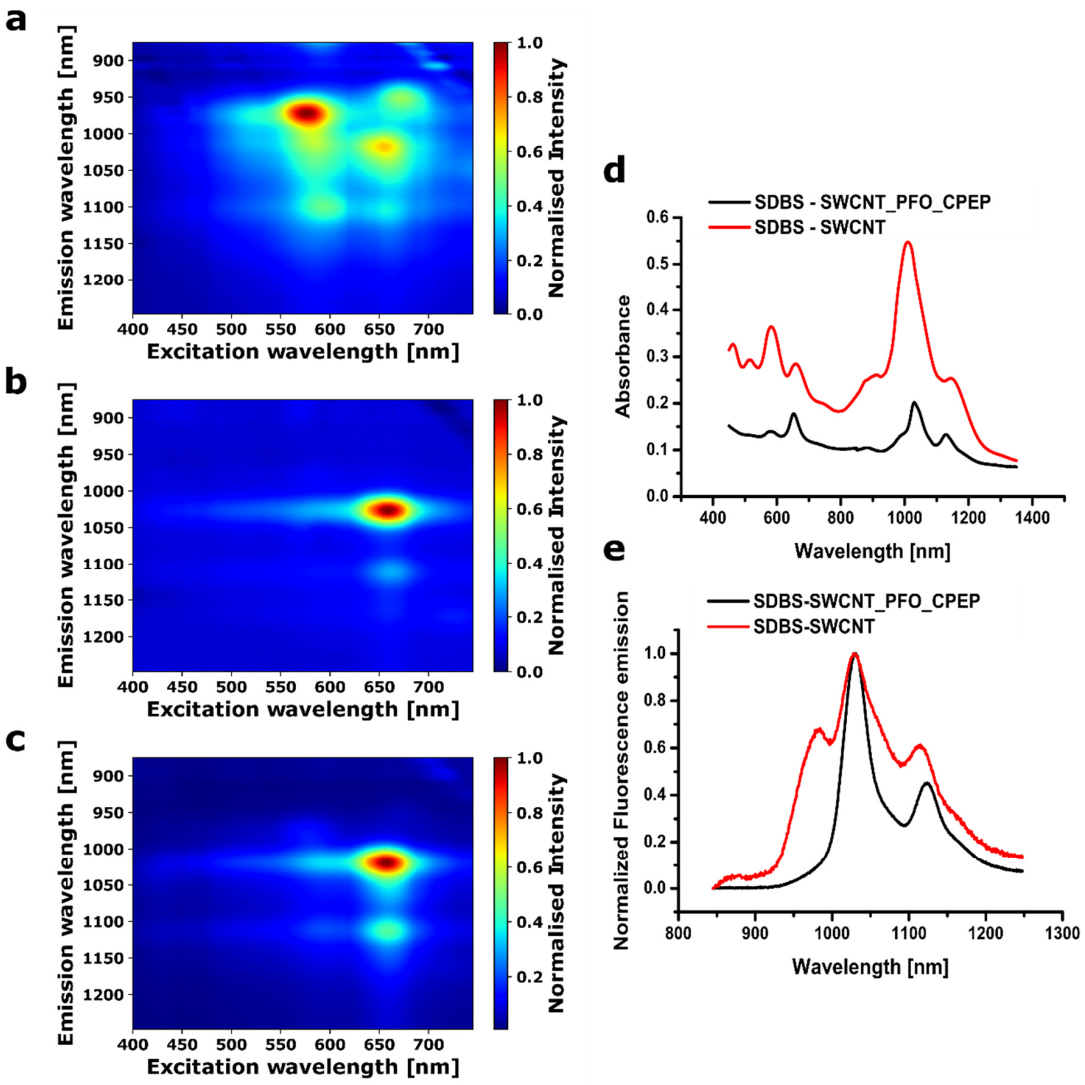

Figure S8. CPEP with PFO to enrich (7,5)-SWCNTs.

a) 2D-fluorescece spectra of the raw SWCNT starting material, dispersed with SDBS. b) 2D-fluorescence spectra of the raw SWCNT starting material, dispersed with PFO in toluene. Mainly (7,5)-SWCNTs and a minor fraction of (7,6)-SWCNTs are solubilized. c) 2D-fluorescecne spectra of enriched SWCNTs after CPEP dispersed in SDBS. d) Vis-nIR absorption spectra of SDBS dispersed SWCNTs, before and after CPEP. e) Fluorescence spectrum of SDBS dispersed SWCNTs before and after CPEP reveals the drastic removal of (6,5)-SWCNTs (excited at 630 nm).

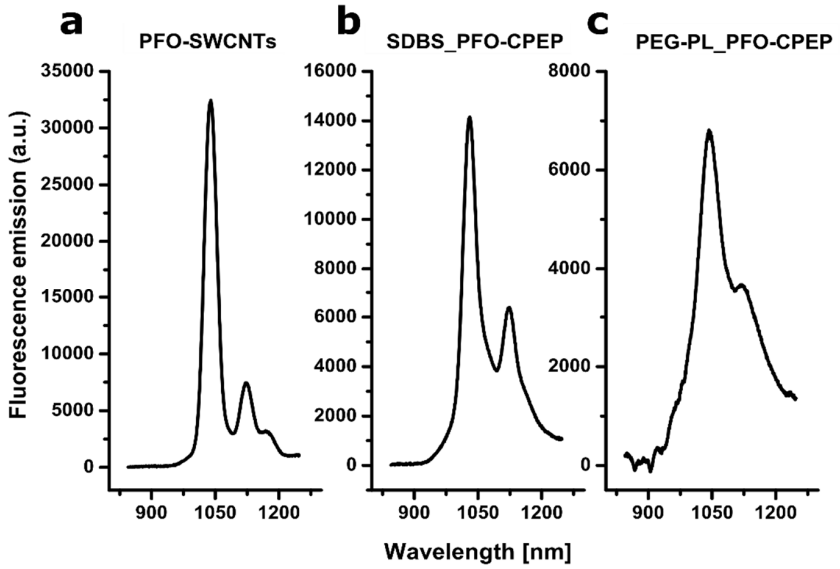

Figure S9. nIR-fluorescence spectra of CPEP enriched (7,5)-SWCNTS.

a) SWCNT stock dispersed by PFO in toluene. b) SWCNTs dispersed in SDBS after CPEP process with PFO. c) SWCNTs dispersed in PEG-Phospho-lipid (MW 5 kDa) after CPEP process with PFO.

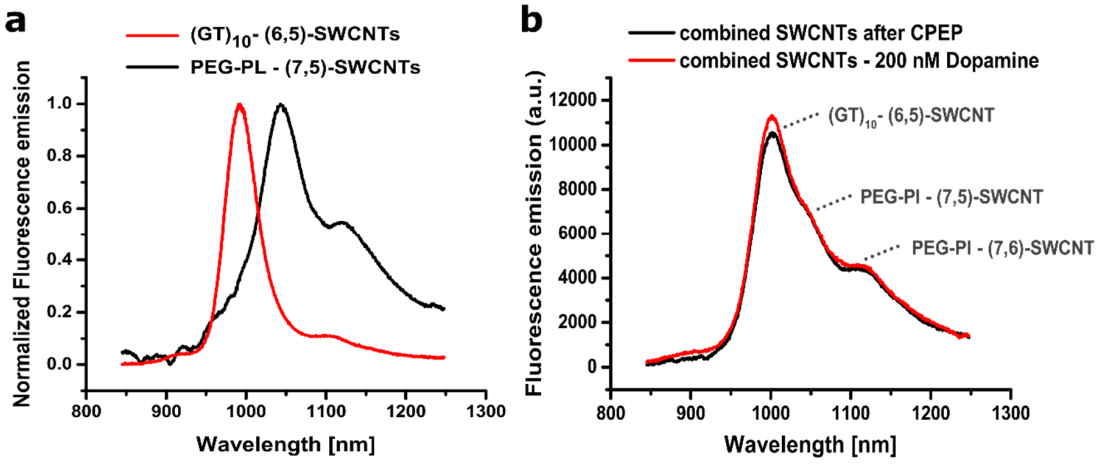

Figure S10. CPEP enriched SWCNTs for ratiometric sensing.

a) Normalized nIR-fluorescence spectra of $(GT)_{10}$-(6,5)-SWCNTs and PEG-PL-(7,5)-SWCNTs. The highly enriched (6,5)-SWCNT sample does not contain (7,5) or (7,6)-SWCNTs after the CPEP process from PFO-BPy, and the same applies *vice versa* for the SWCNTs from CPEP after PFO dispersion. b) A combination of a dopamine sensitive $(GT)_{10}$-SWCNTs and a non-sensitive PEG-PL-SWCNT act as a ratiometric sensor for dopamine detection.

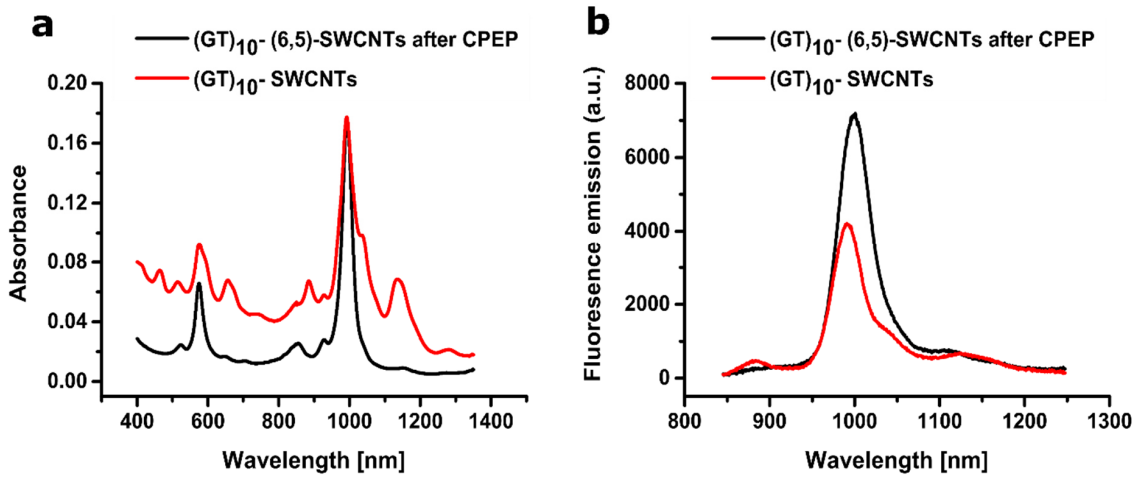

Figure S11. Comparison of absorption and fluorescence emission spectra of CPEP purified and non-purified $(GT)_{10}$-SWCNTs.

a) Absorption spectra, diluted to the same absorption of the (6,5)-SWCNT peak. b) nIR-fluorescence spectra of the same samples reveal a stronger fluorescence emission by CPEP purified $(GT)_{10}$-SWCNTs.

Synthesis of 4-nitrobenzenediazonium tetrafluoroborate

A recently published protocol was used[2]**.** Chemicals were received from Sigma-Aldrich, unless declared elsewhere. NMR spectra were recorded on a Bruker Avance III HD 300 MHz device. ^{1}H and ^{13}C spectra were internally calibrated to the residual proton solvent or carbon solvent peaks, respectively.

In a snap-cap vial, 4-nitroaniline (104 mg, 0.753 µmol, 1.0 eq.) is dissolved in ethanol (500 mL) and tetrafluoroboric acid (Alfa Aesar) (50% aq., 190 mL, 1.49 µmol, 2.0 eq). The mixture is cooled to 0 °C and *tert.*-butylnitrite (200 mL, 1.68 mmol, 2.3 eq.) is added dropwise *via* syringe. The mixture is stirred for 30 min at 0 °C and for 1 h at room temperature. The product is precipitated with diethyl ether (1 mL), centrifuged (2 min at 16100 *g*) and the supernatant is discarded. The crude product is washed with diethyl ether (3x 1 mL) and dried at room temperature under reduced pressure for 30 min. The compound is isolated as a brownish solid which can be stored at -20 °C for several weeks.

^{1}H NMR (300 MHz, CD_3CN) δ 8.76 (d, J = 9.2 Hz, 2H), 8.62 (d, *J* = 9.2 Hz, 2H).

^{11}B NMR (96 MHz, CD_3CN) δ -1.15.

^{19}F NMR (282 MHz, CD_3CN) δ -151.14, -151.19. (two signals due to the two NMR-active boron isotopomers)

^{13}C NMR (75 MHz, CD_3CN) δ 155.18, 135.33, 127.51, 121.43.

The NMR data is in accordance with literature.[3]

HR-MS (negative mode): calculated: 150.0298 (C4H4N3O2); found: 150.0295

Defect introduction to (6,5)-SWCNTs

In a 96-well plate, 90 µL of a 2 nM (6,5)-SWNT dispersion in 0.2 % SDBS was mixed with 10 µL of a 20 µM aqueous solution of 4-nitrobenzenediazonium tetrafluoroborate (DzNO2). The solution is irradiated (λ= 561 nm) for 10 min using a monochromator (MSH150) connected to a LSE341 light source (LOT-Quantum Design GmbH, Darmstadt, Germany). Spectra are taken every 10 s.

Synthesis of PMAC18PEG

This synthesis was recently published[4]. Methoxypolyethylene glycol amine (5000 Da, 214 mg) and Poly(maleic anhydride-*alt*-1-octadecene) (15 mg) are dissolved in methylene chloride (3 mL). Triethylamine (300 mL) is added and the solution is stirred at room temperature for 3 h. Volatile compounds are removed in a stream of argon and the crude product is dissolved in water (7.5 mL). The mixture is purified *via* dialysis (14 kDa MWCO dialysis tube, Sartorius) against water and lyophilized to yield a colourless solid.

Dispersion of PMAC18PEG -SWCNTs.

A recently published protocol was used and adapted[5]. A mixture of (6,5)-SWCNTs and PMAC18PEG (2 mg/mL in ddH_2O, 300 µL) was sonicated (30 min / 30 % Amplitude Fisher, Scientific™ Model 120) and larger aggregates were removed by centrifugation (10 min /10.000 *g*).

^{1}H NMR (500 MHz, $CDCl_3$) δ 3.7-3.6 (m, CH_2 of mPEG), 1.13-1.12 (m, CH_2 of C_{18} chains), 0.85 (m, CH_3 of $PMHC_{18}$)

The NMR data is in accordance with literature.[5]

References

(1) Ghosh, S.; Bachilo, S. M.; Simonette, R. A.; Beckingham, K. M.; Weisman, R. B. Oxygen Doping Modifies Near-Infrared Band Gaps in Fluorescent Single-Walled Carbon Nanotubes. *Science.* **2010**, *330* (6011), 1656–1659.

(2) Zhang, K.; Xu, X.; Qing, F. Copper-Promoted Ritter-Type Trifluoroethoxylation of (Hetero) - Arenediazonium Tetrafluoroborates : A Method for the Preparation of Trifluoroethyl Imidates. *European J. Org. Chem.* **2016**, 5088–5090.

(3) Bonin, H.; Delbrayelle, D.; Demonchaux, P.; Gras, E. Base Free Aryl Coupling of Diazonium Compounds and Boronic Esters : Self-Activation Allowing an Overall Highly Practical Process W. *Chem. Commun.* **2010**, No. entry 6, 2677–2679.

(4) Yang, K.; Feng, L.; Hong, H.; Cai, W.; Liu, Z. Preparation and Functionalization of Graphene Nanocomposites for Biomedical Applications. *Nat. Protoc.* **2013**, *8* (12), 2392–2403.

(5) Liu, X.; Tao, H.; Yang, K.; Zhang, S.; Lee, S.; Liu, Z. Biomaterials Optimization of Surface Chemistry on Single-Walled Carbon Nanotubes for in Vivo Photothermal Ablation of Tumors. *Biomaterials* **2011**, *32* (1), 144–151.

7.3 Supplementary Information Manuscript III

Sensing with Chirality-Pure Near-Infrared Fluorescent Carbon Nanotubes

Robert Nißler[1,2], Larissa Kurth[1], Han Li[3], Alexander Spreinat[1], Ilyas Kuhlemann[1], Benjamin S. Flavel[3] and Sebastian Kruss[1,2,4*]

[1]Institute of Physical Chemistry, Göttingen University, Göttingen 37077, Germany
[2]Physical Chemistry II, Bochum University, 44801 Bochum, Germany
[3]Institute of Nanotechnology, Karlsruhe Institute of Technology (KIT), 76344 Eggenstein-Leopoldshafen, Germany
[4]Fraunhofer Institute for Microelectronic Circuits and Systems, 47057 Duisburg, Germany

[*] Corresponding author

Analytical Chemistry, **2021**, 93, 6446-6455
DOI: 10.1021/acs.analchem.1c00168

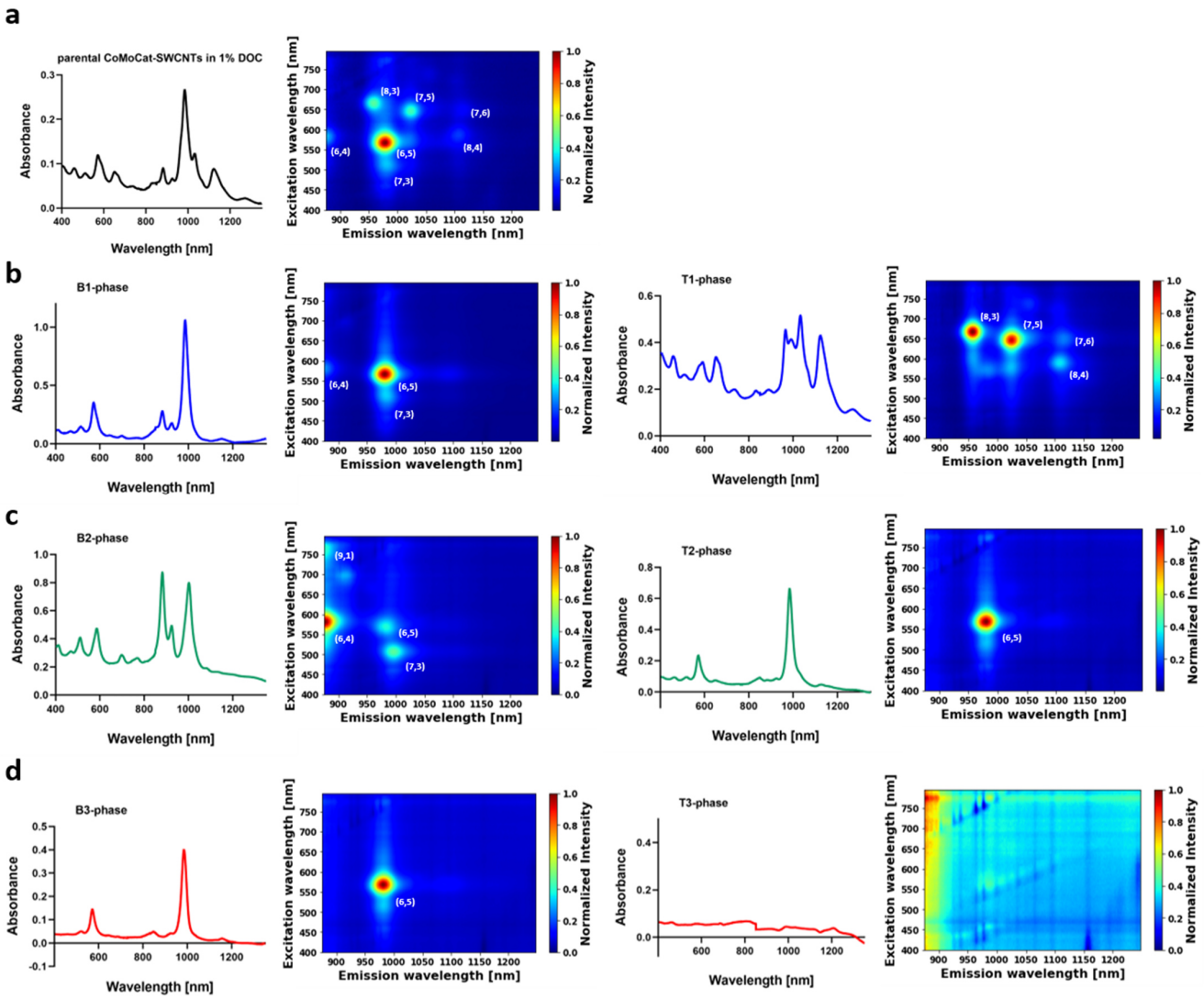

Figure S1: Aqueous two-phase extraction (ATPE)-based isolation of (6,5)-SWCNTs.

Isolation of (6,5)-SWCNTs is based on the procedure described by Li et al.[1] The plots depict the extraction of specific SWCNT chiralities by pH variation during separation between two aqueous phases. Absorbance spectra and 2D excitation/emission spectra with indicated SWCNT chiralities are shown for the three separation steps. a) Parental CoMoCat-SWCNTs dispersed in 1% sodium deoxycholate (DOC). b) Top and bottom phase for the first separation cycle shows exclusion of larger diameter chiralities than (6,5)-SWCNTs from the bottom phase. c) Top and bottom phase for the second cycle shows elimination of smaller chiralities than (6,5)-SWCNTs from the top phase. d) The third bottom phase yields almost monochiral (6,5)-SWCNTs.

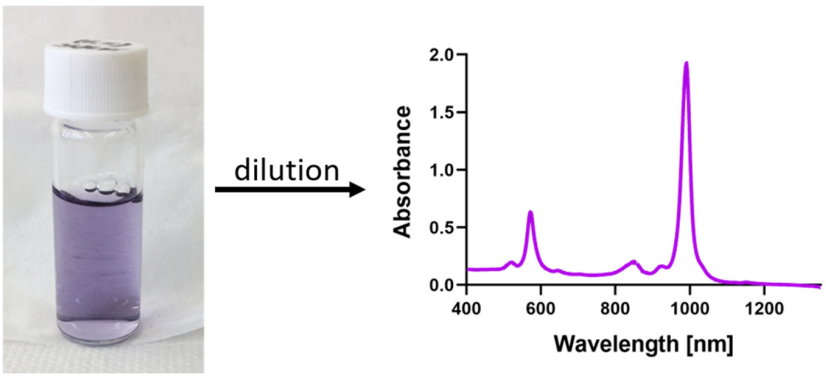

Figure S2: (6,5)-SWCNTs in 1% DOC.

Isolated (6,5)-SWCNTs were dialyzed against 1% DOC to exclude surfactant residues and dextran polymer, needed during the separation process. The photograph of the (6,5)-SWCNTs shows an intense purple color indicative of a high concentration and purity. For surface exchange experiments to single stranded (ss)DNA, the (6,5)-SWCNTs stock solution was diluted to an absorbance of 2 at the E_{11} transition near 985 nm (10 mm cuvette).

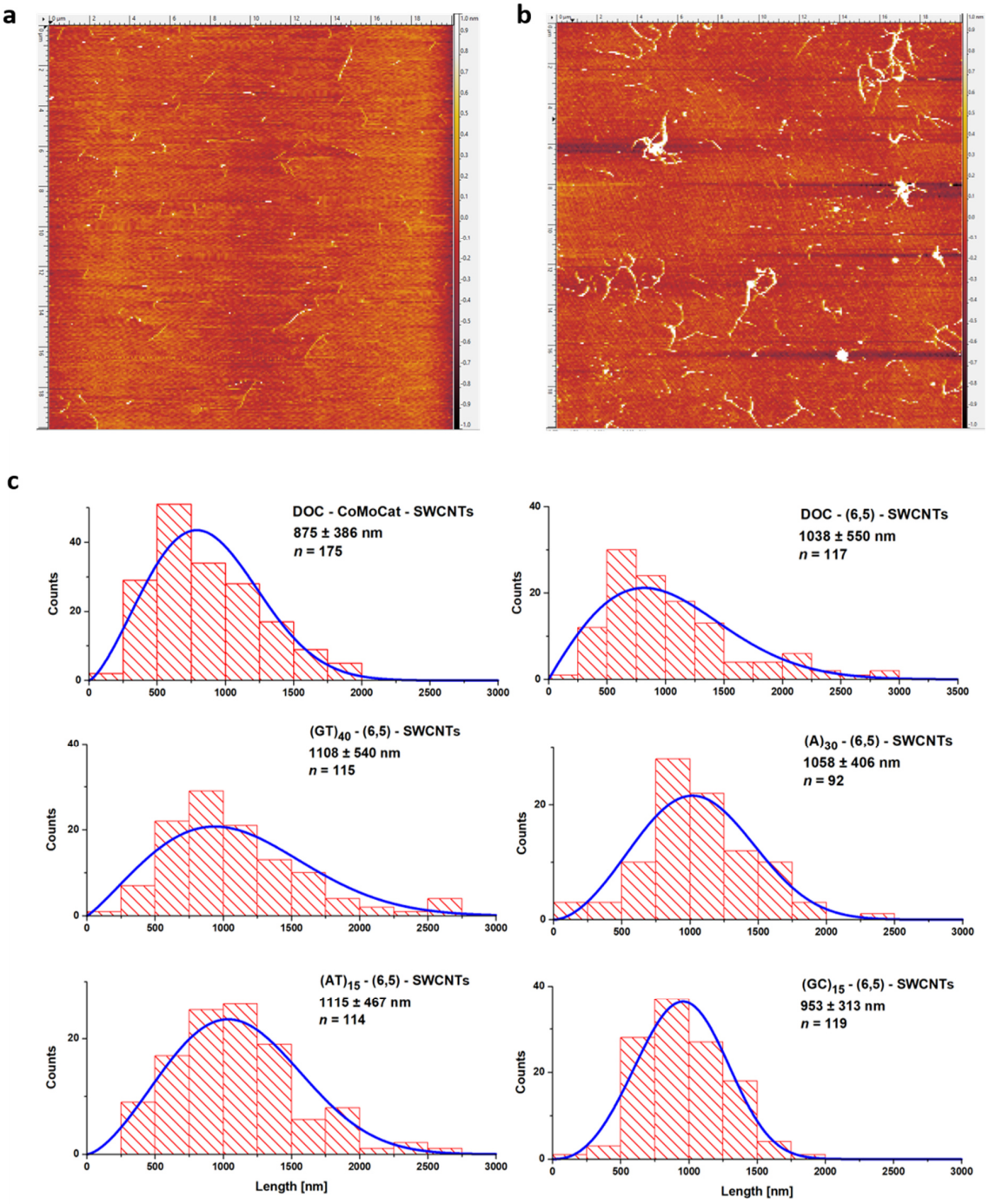

Figure S3: SWCNT lengths characterization by atomic force microscopy (AFM).

a) Typical AFM image (tapping mode) of CoMoCat-SWCNTs dispersed in DOC with a mean lengths of ~ 900 nm. b) Representative AFM image of purified (6,5)-SWCTNTs after surface exchange to ssDNA, here $(GC)_{15}$-ssDNA, showing more bundling after physisorption on the mica surface. c) Length evaluation of in total 732 SWCNTs reveal the mean length of purified (6,5)-ssDNA SWCNTs of around 1000 nm. They are therefore considerably longer than the tip-sonicated raw CoMoCat-ssDNA-SWCNTs, evaluated in our previous study.[2] Histograms in 250 nm intervals with a asymmetric probability density function (Weibull distribution, blue line) (mean ± SEM).

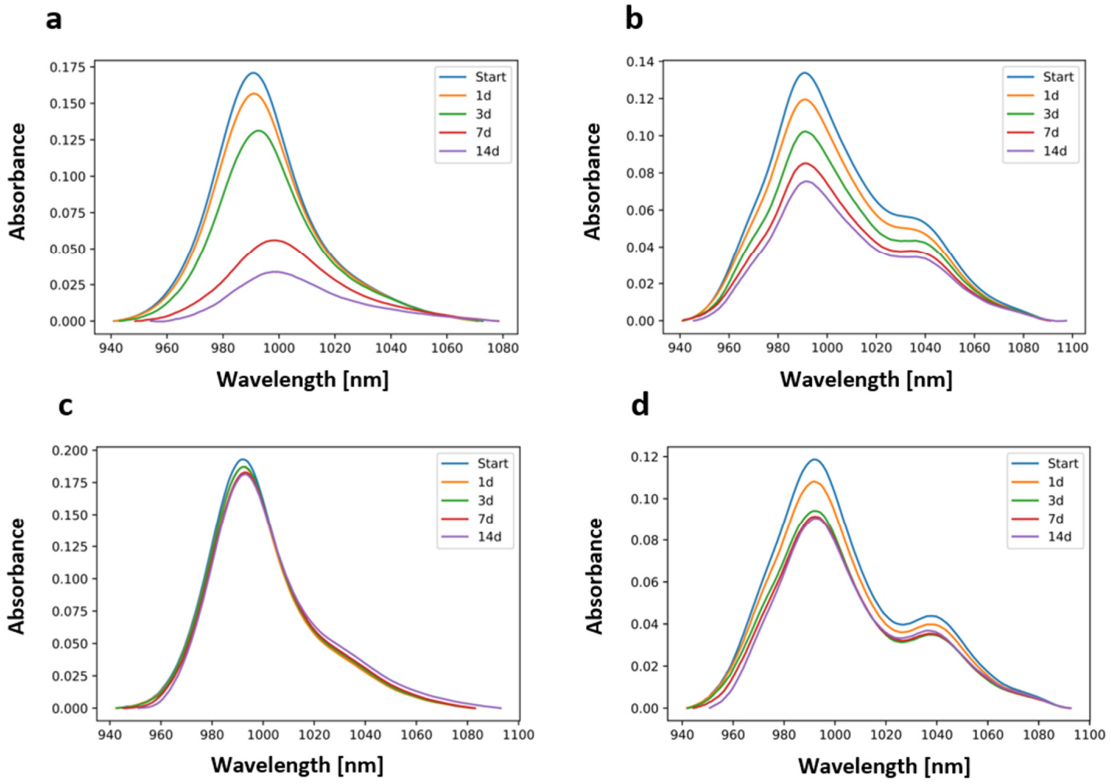

Figure S4: ssDNA-SWCNT absorbance spectra to evaluate colloidal stability.

Absorbance spectra of ssDNA-SWCNTs measured over 14 days. Spectra were background corrected and the (6,5)-SWCNT E_{11} transition region magnified. a) $(GT)_5$-(6,5)-SWCNTs. b) $(GT)_5$-(CoMoCat)-SWCNTs. c) $(GC)_{15}$-(6,5)-SWCNTs. d) $(GC)_{15}$-(CoMoCat)-SWCNTs.

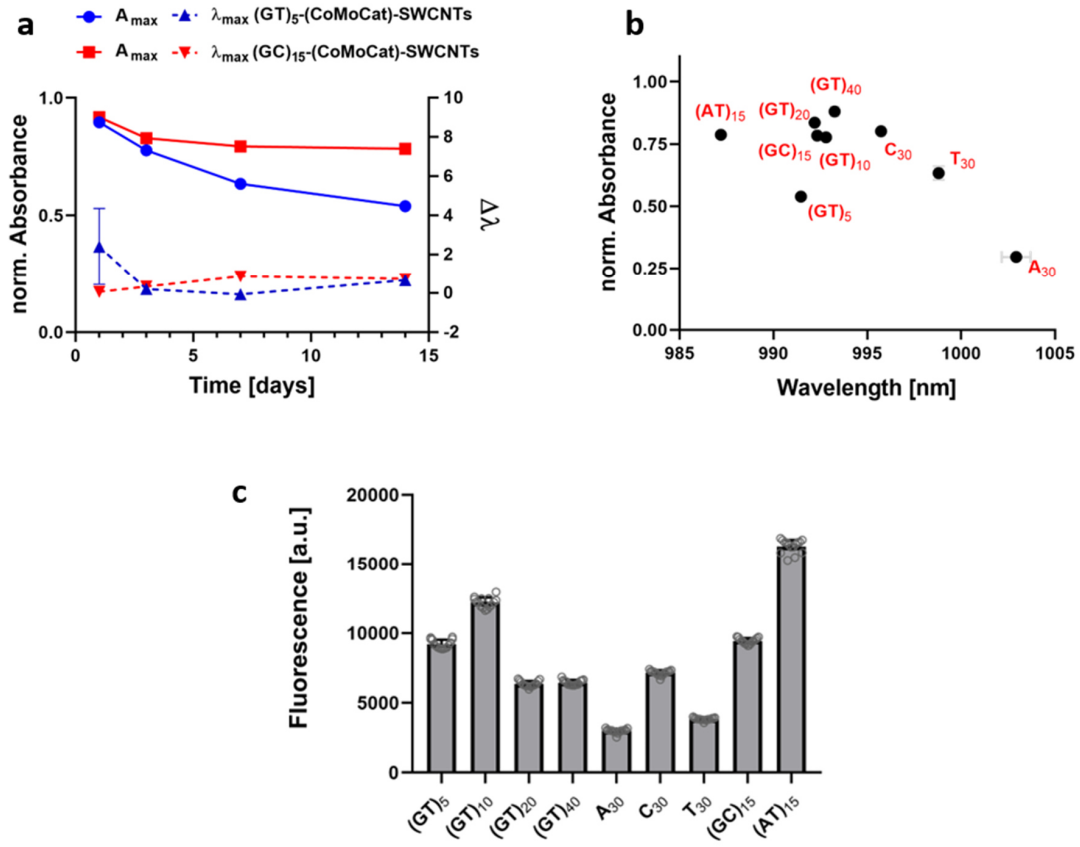

Figure S5: Colloidal stability and spectral shifts of ssDNA-CoMoCat-SWCNTs.

a) Evaluation of the two non-purified ssDNA-SWCNTs as counterparts of the monochiral nanoconjugates shown in Figure 2. Absorbances decrease ($(GT)_5$>$(GC)_{15}$), but no significant wavelength shift of the absorbance maxima occur (n = 3, mean ± SEM). b) Influence of ssDNA sequence on colloidal stability. Normalized (maximum) E_{11} absorbance evaluated after 14 days (mean ± SE, n = 3). c) Fluorescence emission of 0.2 nM ssDNA-CoMoCat-SWCNTs (mean ± SD, n = 15 (technical replicates)).

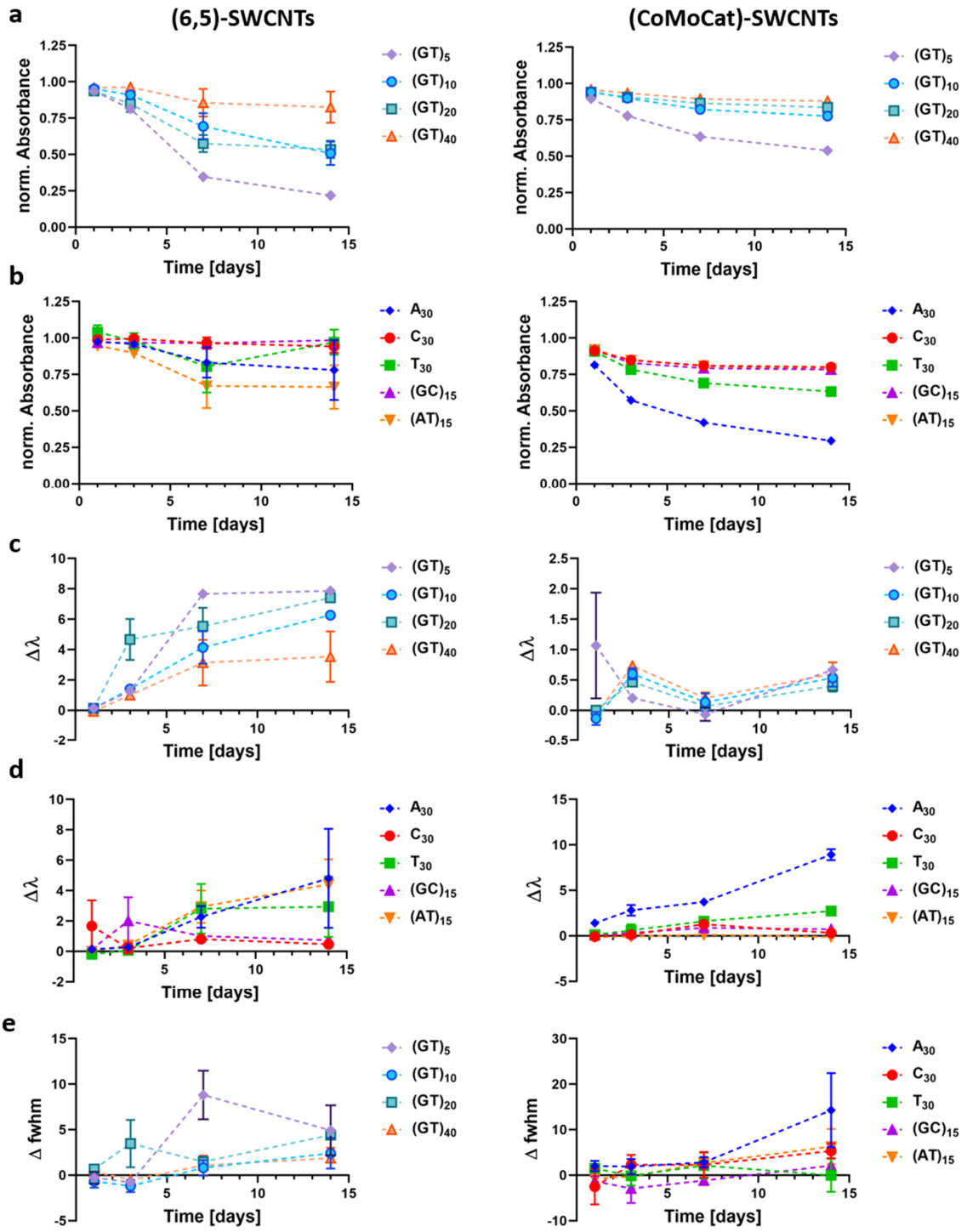

Figure S6: Time dependent colloidal stability of ssDNA-SWCNTs.

Comparison between monochiral ssDNA-(6,5)-SWCNTs (left panel) and non-purified ssDNA-CoMoCat-SWCNTs (right penal) (n = 3, mean ± SEM). a) Normalized absorbance from $(GT)_x$-SWNCTs and in b) for other ssDNA sequences. c) Wavelength shift ($\Delta\lambda$) of $(GT)_x$-SWNCTs over 14 days and in d) for the other ssDNA-SWCNTs. e) Change of the full-width-half-maximum (fwhm) of monochiral ssDNA-(6,5)-SWCNTs over time.

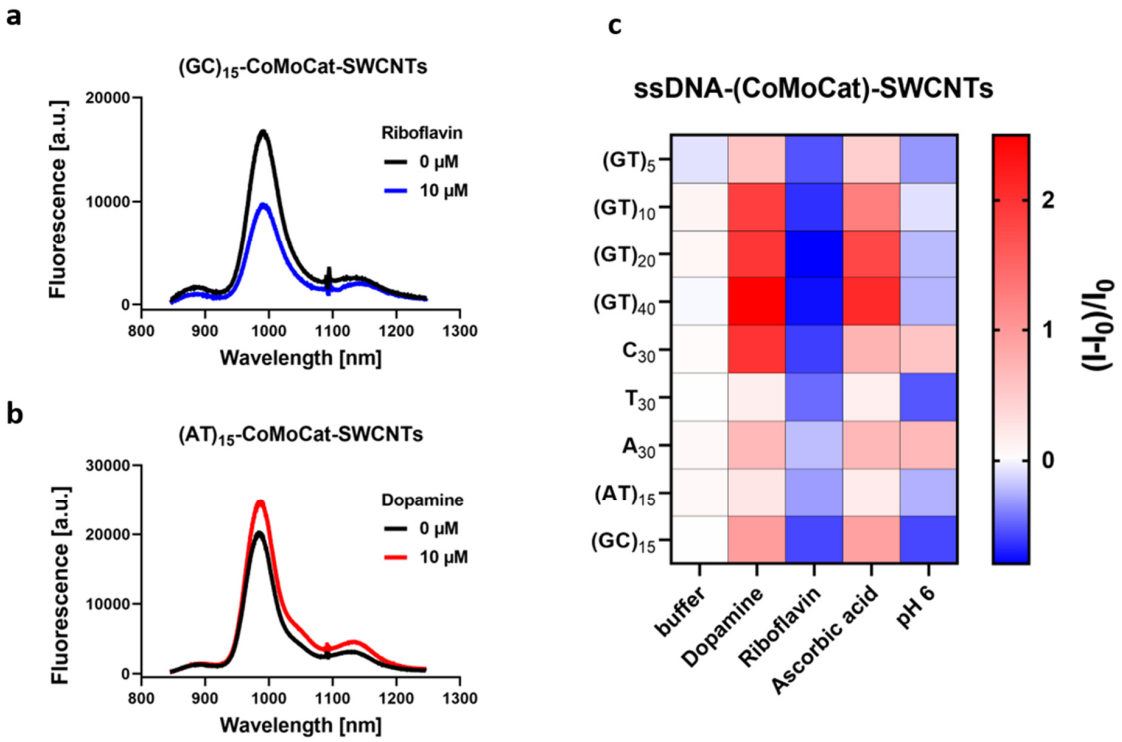

Figure S7: Chemical sensing with surface immobilized multichiral ssDNA-(CoMoCat)-SWCNTs.

a) Exemplaric fluorescence spectrum of $(GC)_{15}$-(CoMoCat)-SWCNTs shows a decrease (blue line) after riboflavin addition. b) Exemplaric fluorescence spectrum of $(AT)_{15}$-(CoMoCat)-SWCNTs shows a small fluorescence increase after dopamine addition. c) Summary of NIR-fluorescence responses of various ssDNA-SWCNT-conjugates to important analytes. Fluorescence increases are presented in shades of red and fluorescence decreases in shades of blue (mean values, n = 3, analyte concentration = 10 µM, buffer = 1xPBS).

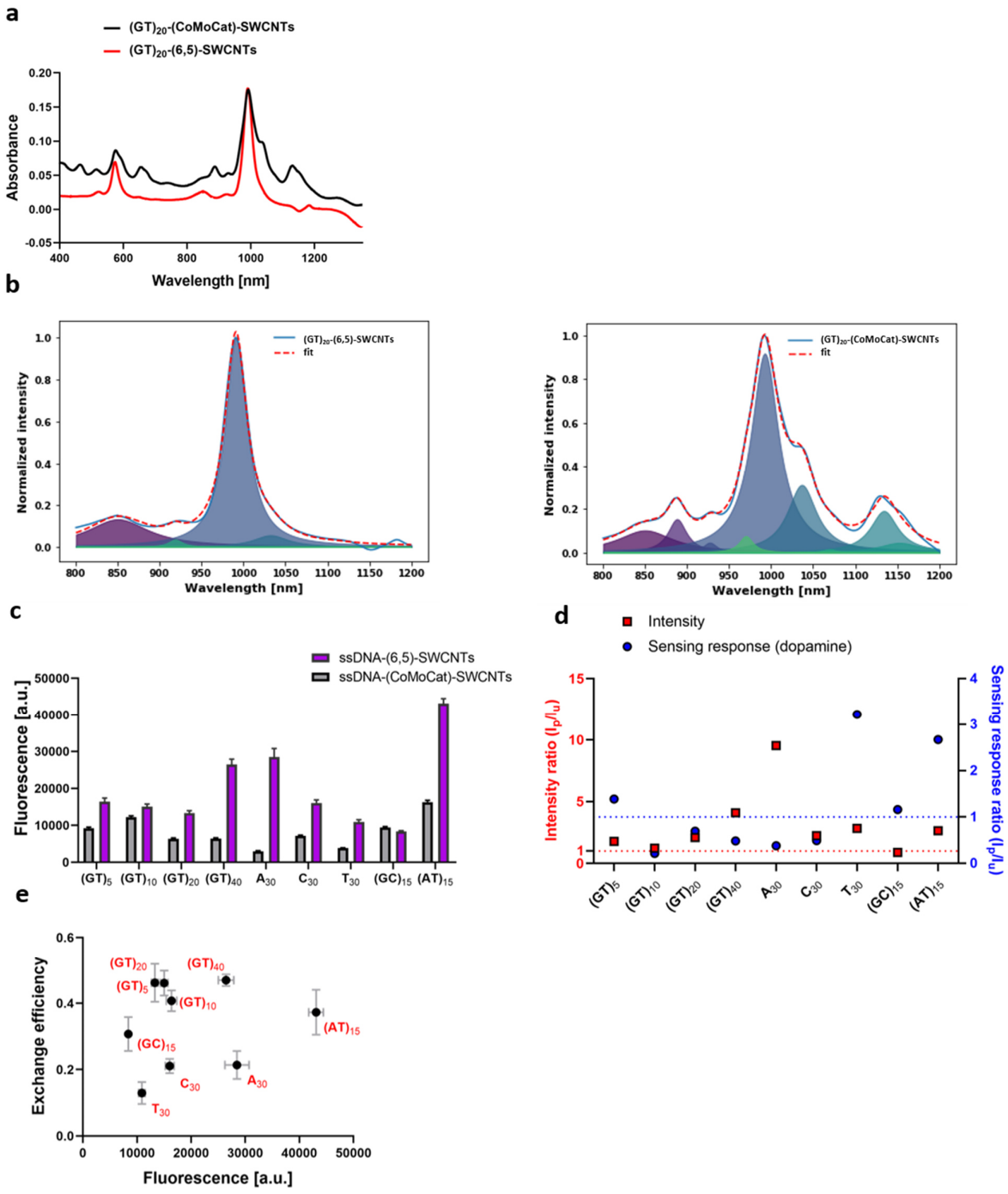

Figure S8: Comparison of the fluorescence intensity of monochiral and multichiral ssDNA-SWCNTs.

a) Absorbance spectra of $(GT)_{20}$-(6,5)-SWCNTs and $(GT)_{20}$-(CoMoCat)-SWCNTs with an equal NIR absorbance at ~990 nm. b) Fitted absorbance spectra of both samples show the absence of overlapping features and spectral congestion in monochiral samples around the E_{11} transition. c) NIR fluorescence emission of 0.2 nM ssDNA-SWCNT solutions (based on the extinction at the (6,5) E_{11} emission maximum. Purified ssDNA-SWCNTs have a stronger fluorescence emission, compared to non-purified ssDNA-CoMoCat-SWCNTs. (n = 15, error = SD). d) Comparison of emission intensity and relative sensor response to 10 µM dopamine reveals no clear trend. (n = 3, I_p – Intensity purified sensor, I_u – Intensity unpurified sensors). e) No correlation was observed, when comparing the exchange efficiency and the resulting fluorescence emission (brightness) of the monochiral ssDNA-(6,5) -SWCNTs.

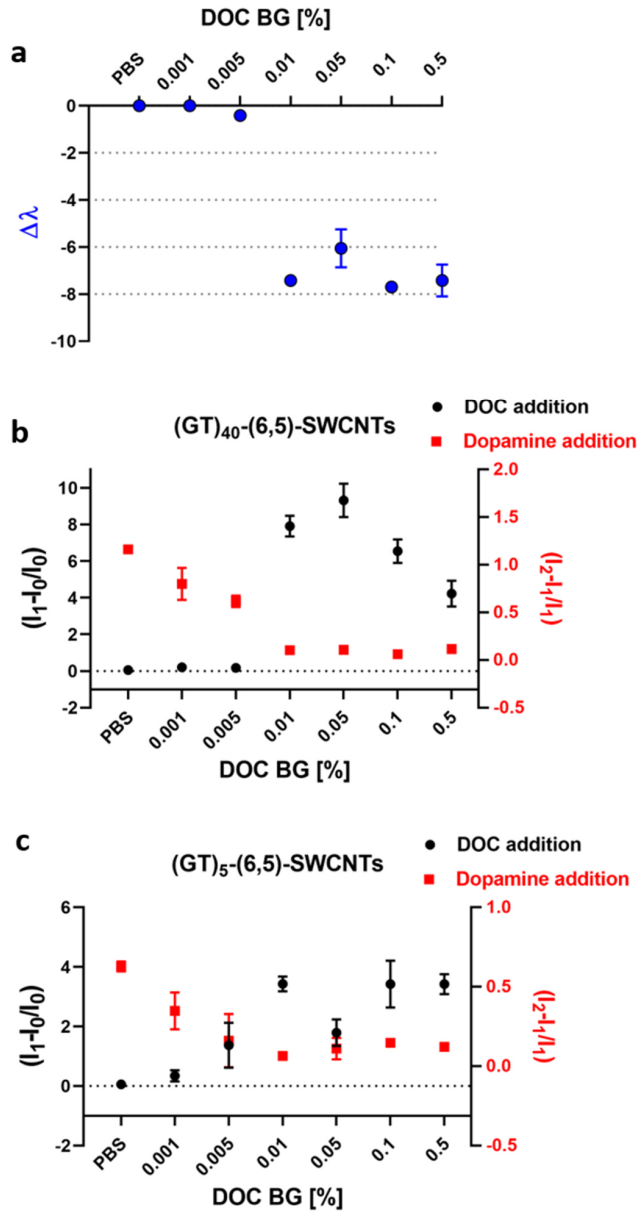

Figure S9: Dopamine sensing in the presence of surfactant (DOC) background.

a) Wavelength shift ($\Delta\lambda$) of immobilized $(GT)_{40}$-(6,5)-SWCNTs after addition of DOC (n = 3, mean ± SEM). b) Fluorescence change (I_0- fluorescence intensity at start, I_1 – fluorescence intensity after DOC addition, I_2 – fluorescence intensity after dopamine addition) was evaluated one hour after DOC addition and subsequently tested for further dopamine sensing. The results from Figure 4c, directly obtained after surfactant addition show the same trend, as the ones presented here, after one hour of incubation (n = 3, mean ± SEM). c) Similar fluorescence changes for $(GT)_5$-(6,5)-SWCNTs evaluated one hour after DOC addition. (n = 3, mean ± SEM).

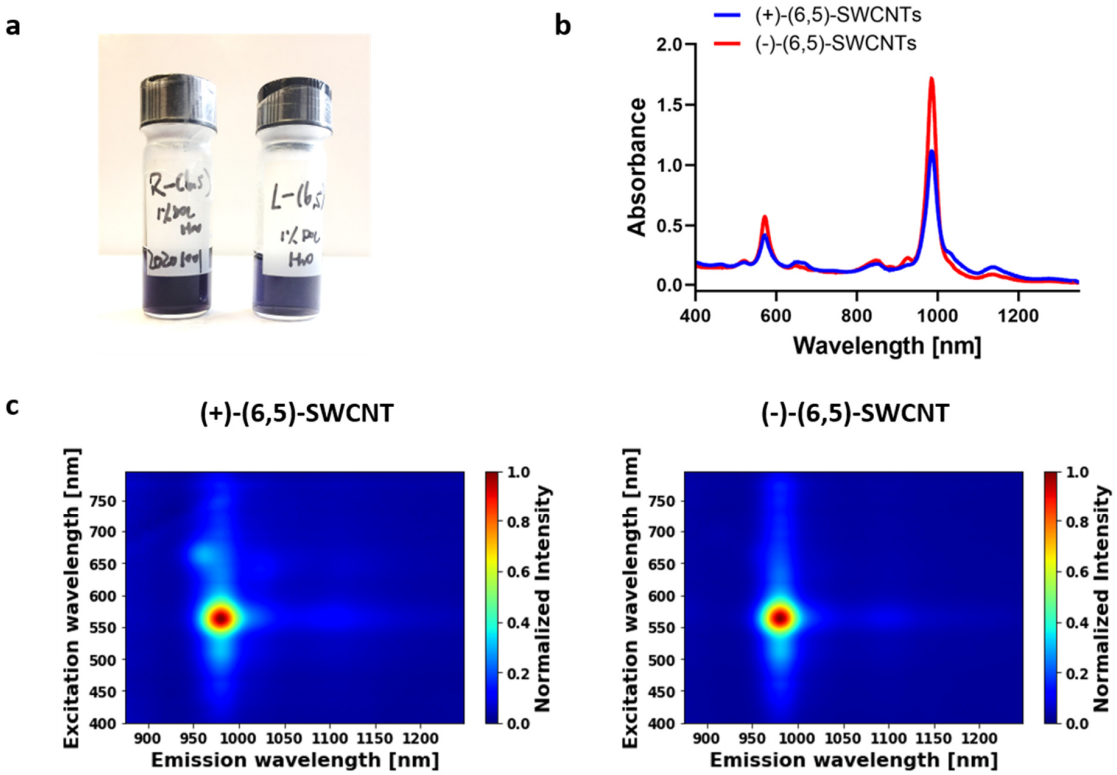

Figure S10: Properties of (6,5)-SWCNT enantiomers.

a) Photograph of both enantiomer pure fractions obtained by ATPE (dark purple color indicates a high concentration and therefore yield of the ATPE enantiomer separation; R-enantiomer = (-)-(6,5)-SWCNT, L-enantiomer = (+)-(6,5)-SWCNT). Enantiomer purity is determined by using the equation from Wei et al.[3]: EP (+(6,5)) = 50 + 0.421* CDnorm and EP (-(6,5)) = 50 - 0.421* CDnorm. b) Absorbance spectra of (+)- and (-)-(6,5)-SWCNTs in 1% DOC don't show a shift at the E_{11} transition (measured in 10 mm cuvette; (+)-(6,5)-SWCNTs diluted 1:4 and (+)-(6,5)-SWCNTs diluted 1:10). c) 2D excitation-emission fluorescence spectra of both enantiomers.

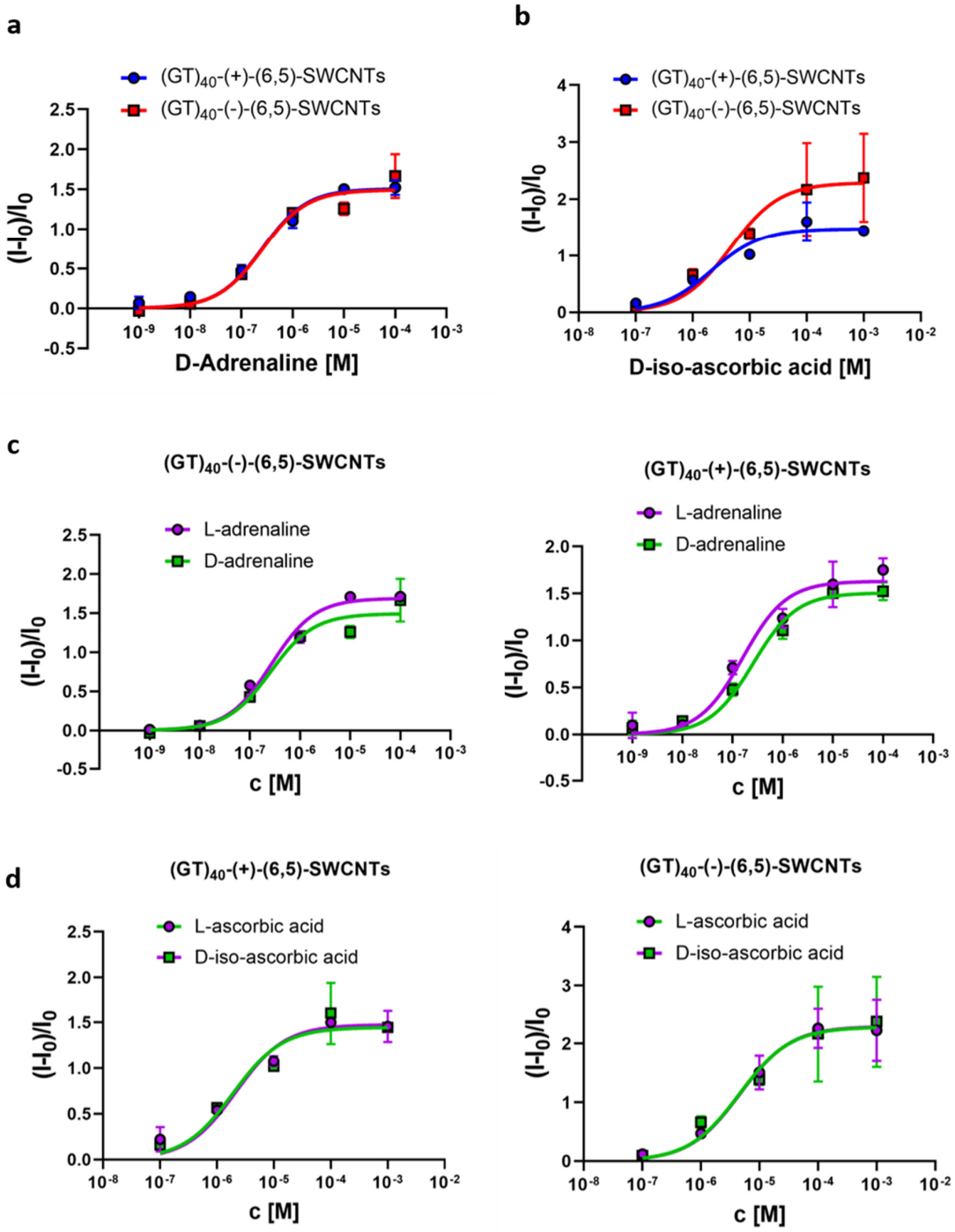

Figure S11: Sensing with ssDNA-(6,5)-SWCNT enantiomers.

a) Sensing of D-adrenalin stereoisomers with $(GT)_{40}$-(+)-(6,5)-SWCNTs and $(GT)_{40}$-(-)-(6,5)-SWCNTs. b) Sensing of D-iso-ascorbic acid with both $(GT)_{40}$ functionalized (6,5)-enantiomers. c) and d) Dose-Response curves to compare the sensing responses of the different analyte stereoisomers. The similar trends for both analytes indicate that this particular stereochemical conformation does not affect the sensing mechanism (mean ± SD, n = 3)

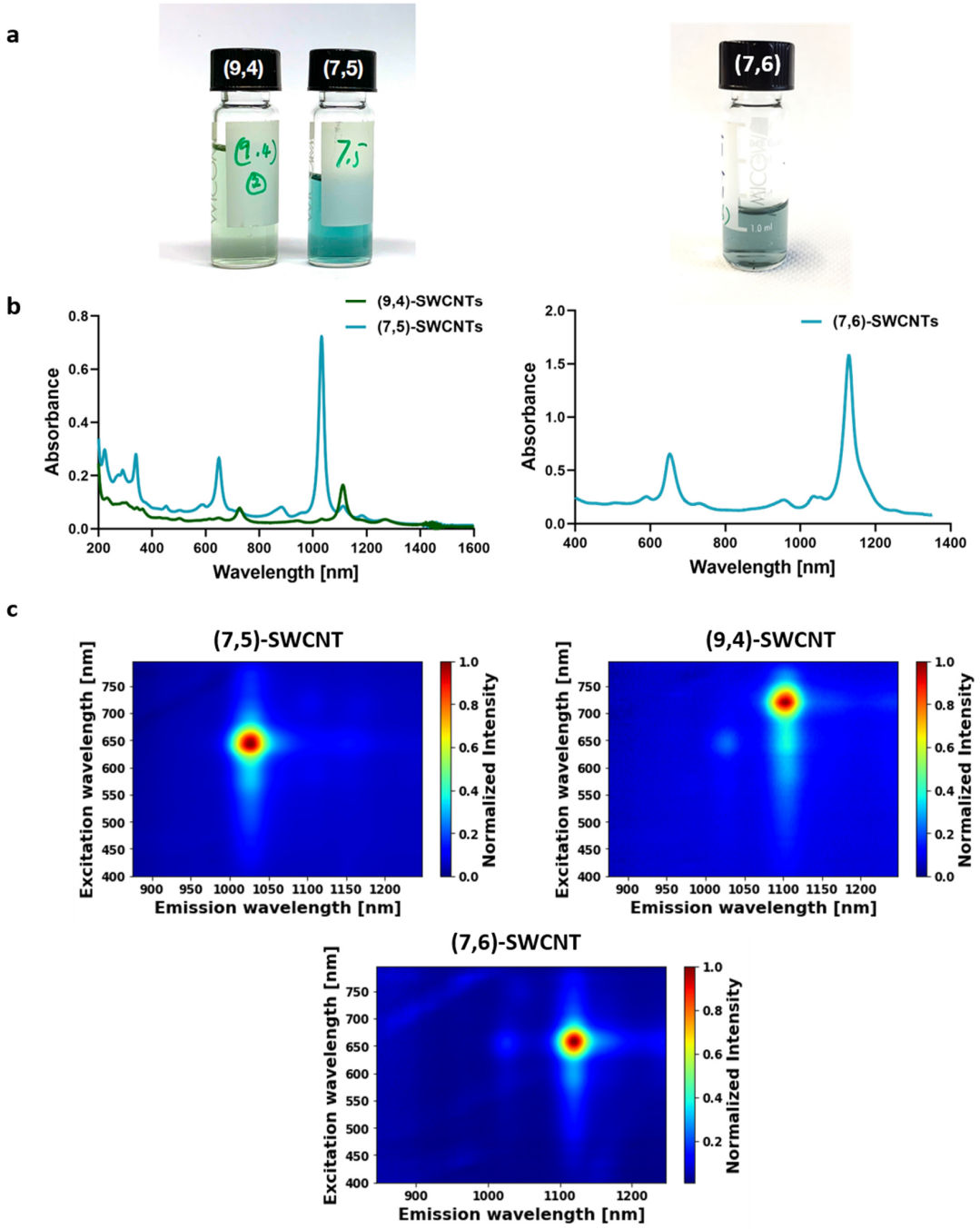

Figure S12: Separation of (7,5)-, (9,4)- and (7,6)-SWCNTs.

a) Photograph of SWCNT fractions with isolated chiralities. b) Absorbance spectra of (9,4)- and (7,5)-SWCNTs in 1% DOC from the shown stock solutions (left spectra, measured in 2 mm cuvette) and (7,6)-SWCNTs in 1% DOC (right spectra, measured as 1:1 dilution in a 10 mm cuvette). c) 2D excitation-emission fluorescence spectra of the SWCNT fractions indicate monochiral stock samples.

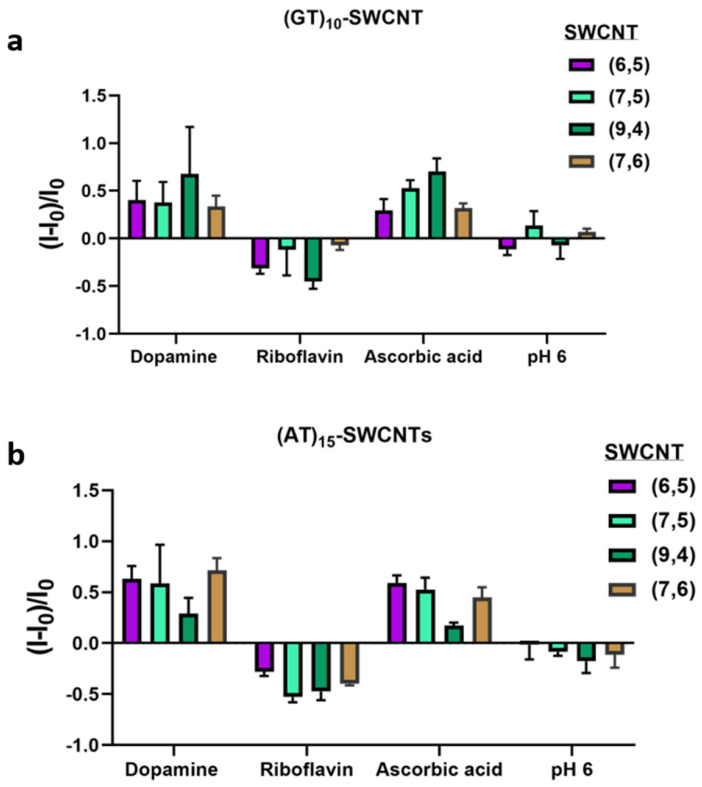

Figure S13: Chemical sensing with single chirality ssDNA-SWCNTs.

a) $(GT)_{10}$-SWCNT sensor responses of three different SWCNT chiralities (n = 3, mean ± SD). b) Sensor response of monochiral $(AT)_{15}$-SWCNTs (n = 3, mean ± SD). The responses show a similar trend for different chiralities, which indicates that such sensors can be assembled independent of the chirality (analyte concentration = 10 µM).

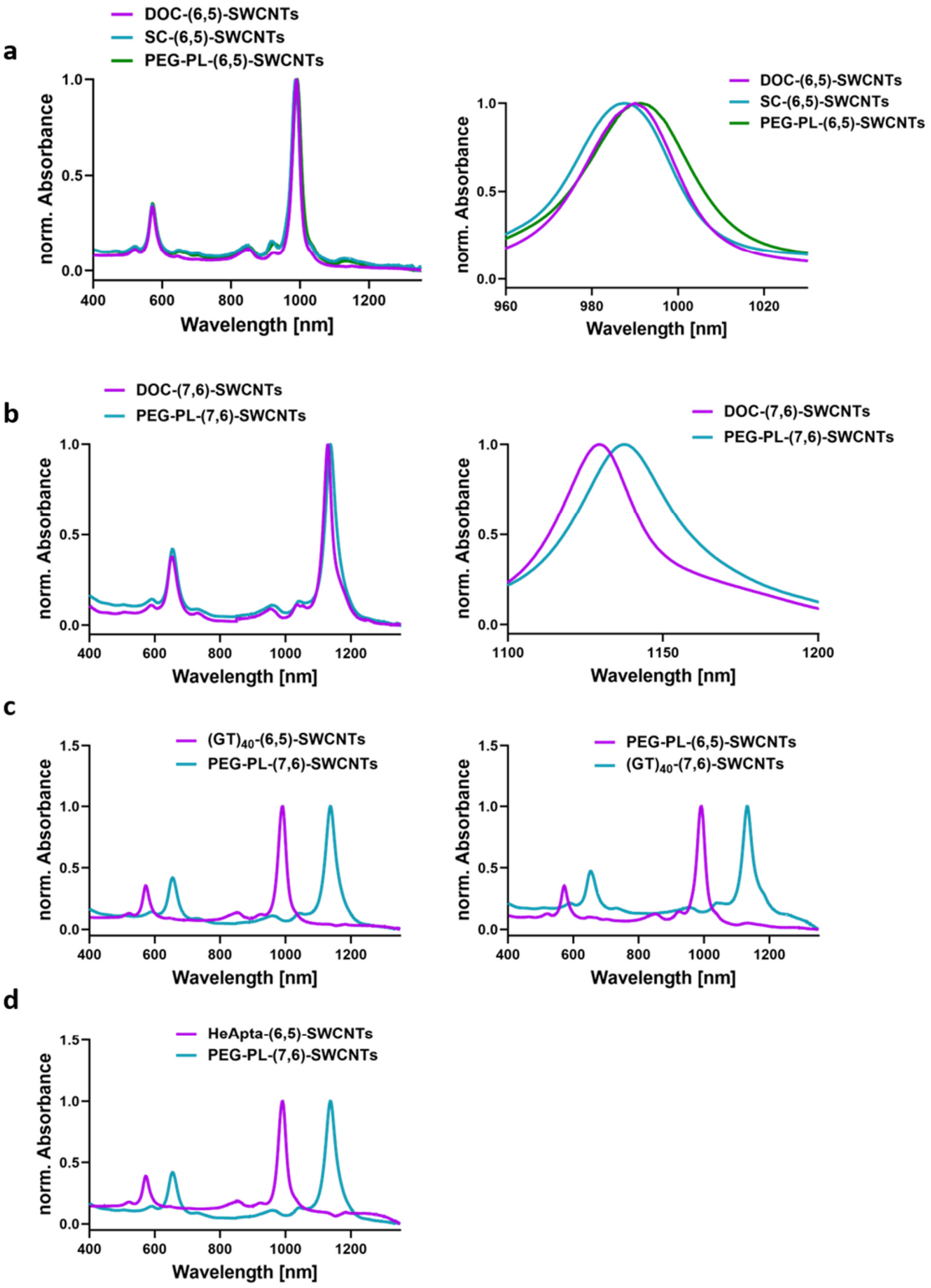

Figure S14: Nanosensor surface design for ratiometric sensing.

a) (6,5)-SWCNTs exchange of surfaces (DOC, SC) to poly(ethylene glycol)-phospholipid (PEG-PL). Right spectra show the magnified E11 transition and indicates a slight absorbance maxima redshift. b) Surface exchange of (7,6)-SWCNTs towards PEG-PL modification. Again, the magnification on the right shows a ~8 nm redshift in the absorbance maxima. c) Normalized absorbance spectra for both variants of nanosensor combination: (6,5)- and (7,6)-SWCNTs with ether $(GT)_{40}$-ssDNA or PEG-PL surface modification. d) Normalized absorbance spectra of hemin binding aptamer (HeApta) (6,5)-SWCNTs as H_2O_2-sensor and PEG-PL-(7,6)-SWCNTs as reference.

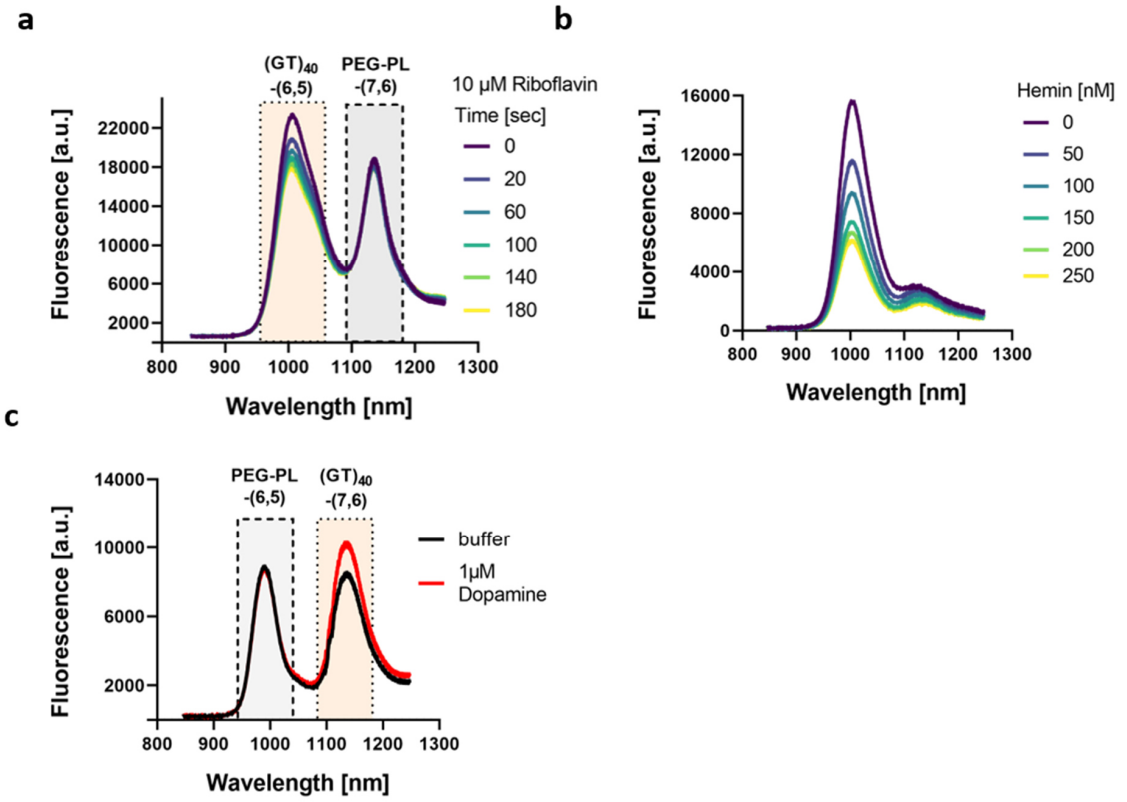

Figure S15: Monochiral and ratiometric analyte sensing.

a) Time-dependent fluorescence response of $(GT)_{40}$-(6,5)-SWCNTs and PEG-PL-(7,6)-SWCNTs to 10 µM riboflavin. b) Monochiral HeApta-(6,5)-SWCNTs responding to various concentrations of hemin with a strong fluorescence decrease, similar to the previously described multichiral systems[4]. This shows that the aptamer configuration on monochiral SWCNTs is capable to bind their target molecule (here the protoporphyrin hemin). c) Ratiometric sensing of 1 µM dopamine with changed functionalities / SWCNT buildings blocks: $(GT)_{40}$-(7,6)-SWCNTs reacting with a fluorescence increase to dopamine addition, while PEG-PL-(6,5)-SWCNTs were unaffected.

References

(1) Li, H.; Gordeev, G.; Garrity, O.; Reich, S.; Flavel, B. S. Separation of Small-Diameter Single-Walled Carbon Nanotubes in One to Three Steps with Aqueous Two-Phase Extraction. *ACS Nano* **2019**, *13*, 2567–2578.

(2) Nißler, R.; Mann, F. A.; Chaturvedi, P.; Horlebein, J.; Meyer, D.; Vukovic, L.; Kruss, S. Quantification of the Number of Adsorbed DNA Molecules on Single-Walled Carbon Nanotubes. *J. Phys. Chem. C* **2019**, *123*, 4837–4847.

(3) Wei, X.; Tanaka, T.; Hirakawa, T.; Yomogida, Y.; Kataura, H. Determination of Enantiomeric Purity of Single-Wall Carbon Nanotubes Using Flavin Mononucleotide. *J. Am. Chem. Soc.* **2017**, *139* (45), 16068–16071.

(4) Wu, H.; Nißler, R.; Morris, V.; Herrmann, N.; Hu, P.; Jeon, S.; Kruss, S.; Giraldo, J. P. Monitoring Plant Health with Near-Infrared Fluorescent H2O2 Nanosensors. *Nano Lett.* **2020**, *20* (4), 2432–2442.

7.4 Supplementary Information Manuscript IV

Remote near infrared identification of pathogens with multiplexed nanosensors

Robert Nißler[1,2], Oliver Bader[3], Maria Dohmen[1], Sebastian G. Walter[4], Christine Noll[3], Gabriele Selvaggio[1,2], Uwe Groß[3] and Sebastian Kruss[1,2,5*]

[1]Institute of Physical Chemistry, Göttingen University, Göttingen 37077, Germany
[2]Physical Chemistry II, Bochum University, 44801 Bochum, Germany
[3]Institute of Medical Microbiology, University Medical Center Göttingen, Göttingen, Germany
[4]Department for Cardiothoracic Surgery and Intensive Care, University Hospital Cologne, Cologne, Germany
[5]Fraunhofer Institute for Microelectronic Circuits and Systems, 47057 Duisburg, Germany

[*] Corresponding author

Nature Communications, **2020**, 11, 1, 1-12
DOI: 10.1038/s41467-020-19718-5

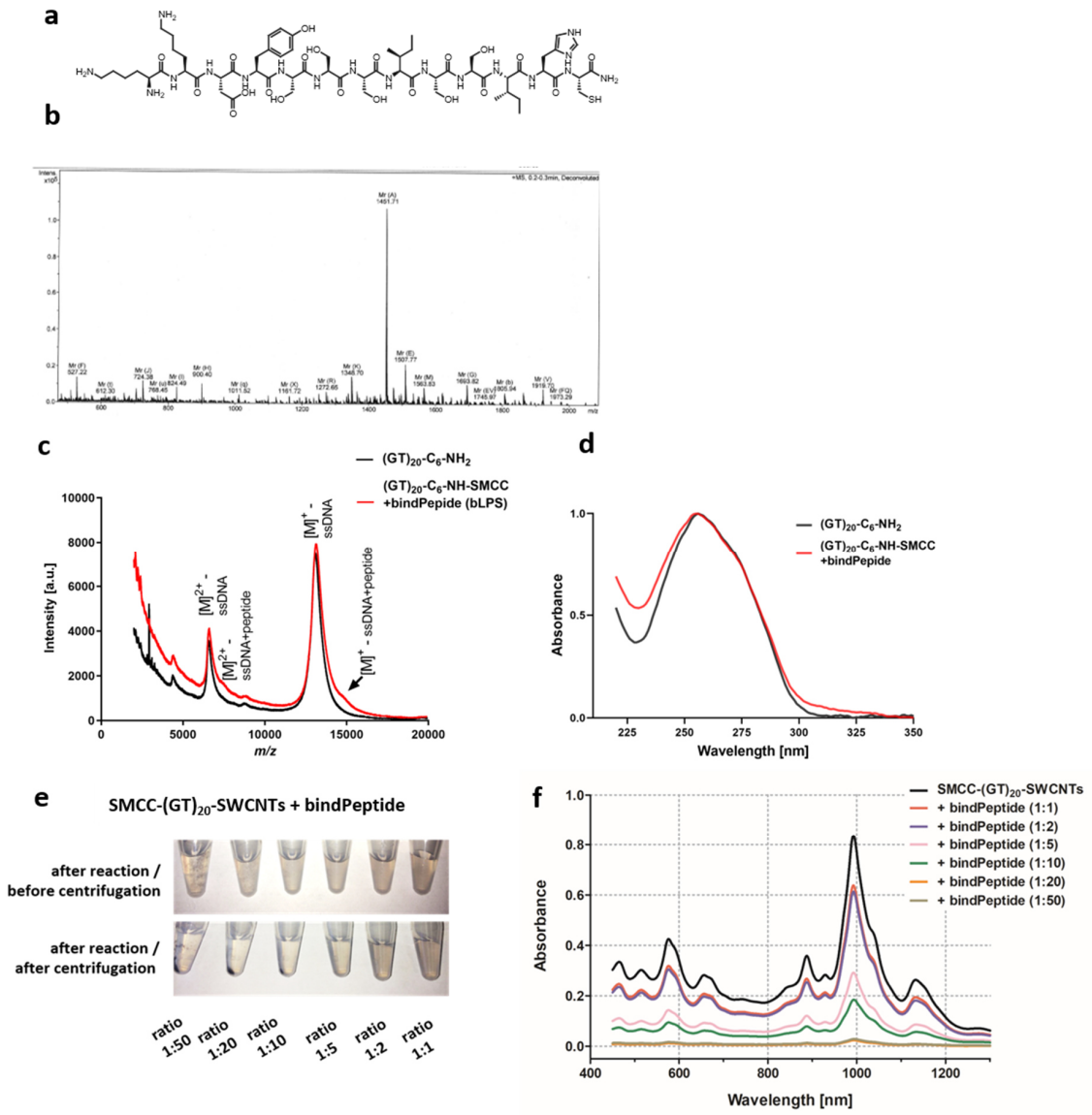

Figure S1: Lipopolysaccharide (LPS) sensor development.

a) Chemical formula and b) mass spectroscopy (MS) analysis of the synthesized LPS-binding peptide (detected: 1451.71 Da, expected 1452.64 Da). MS was acquired in positive mode, using direct injection and electron spray ionization with an microOTOF (Bruker Daltonics) device. c) Matrix-assisted Laser Desorption/Ionization (MALDI)-MS spectra of the single stranded (ss)DNA before and after conjugation with the (linked) LPS-binding peptide, acquired with Autoflex Speed (MALDI-TOF, Bruker Daltonics) in positive mode with 3-hydroxypicolinic acid matrix. The mean spectra from each 10 different spots on the MALDI target plate, show a ~1550 Da shifted [M]+ peak, which corresponds well with the additional mass from the peptide linked to SMCC (~1700 Da). This indicates a successful coupling of the LPS-binding peptide to ssDNA, which is in combination with a SWCNT the building block of the bLPS-sensor. The peak ratios should not be quantitatively interpreted as ionization and detection were optimized for ssDNA ($(GT)_6$-$(GT)_{30}$). d) Normalized UV absorbance spectra (Nanodrop 2000c, Thermo Scientific) show a shift towards peptide absorbance features at ~230 nm after peptide conjugation. e) Screening for optimal conjugation conditions regarding the SMCC-linked-$(GT)_{20}$-SWCNTs and the LPS-binding peptide. Different ratios of SMCC-DNA-SWCNTs to peptide were used, showing that for ratios above 1:5, the nanoconjugates form visible aggregates after overnight reaction and are no longer colloidally stable. f) Corresponding absorbance spectra for different reaction conditions show that for 1:1 and 1:2 ratios E_{11} absorbance of (6,5)-SWCNTs (at 992.2 nm) only slightly decreases. No wavelength shift was observed even for higher ratios. Based on these results, a ratio of 1:1 to 1:2 was used as final conjugation parameters.

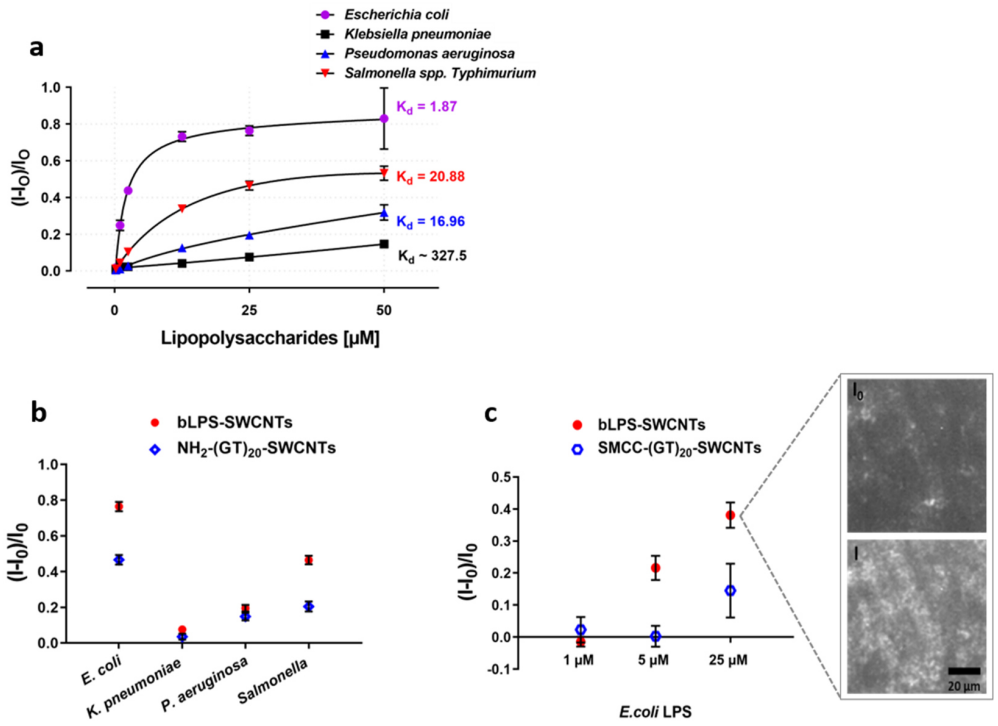

Figure S2: LPS sensor characterization.

a) Calibration curve of bLPS-SWCNT for LPS from different bacteria. *Escherichia coli* LPS showed the strongest response and the lowest K_d = 1.87 µM (Binding fit, nonlinear curve fit (GraphPad Prism 8), data from Fig. 2c) (n = 3 independent experiments, mean ± SD). b) Fluorescence response to 25 µM LPS for NH_2-$(GT)_{20}$-SWCNTs (blue) and bLPS-SWCNTs (red). The results show a non-specific smaller response of ssDNA-SWCNT to LPS probably due to sugar moieties in LPS (n = 3 independent experiments, mean ± SD). c) Fluorescence response of nanosensors immobilized on a glass surface. bLPS-SWCNTs (red) increase their fluorescence in response to 5 – 25 µM *E. coli* LPS, which is significantly higher than the unspecific response for sensors without the LPS-binding peptide (blue) (n = 3 independent experiments, mean ± SD). Therefore, the conjugation of the LPS-binding unit enhances sensing of the bacterial target.

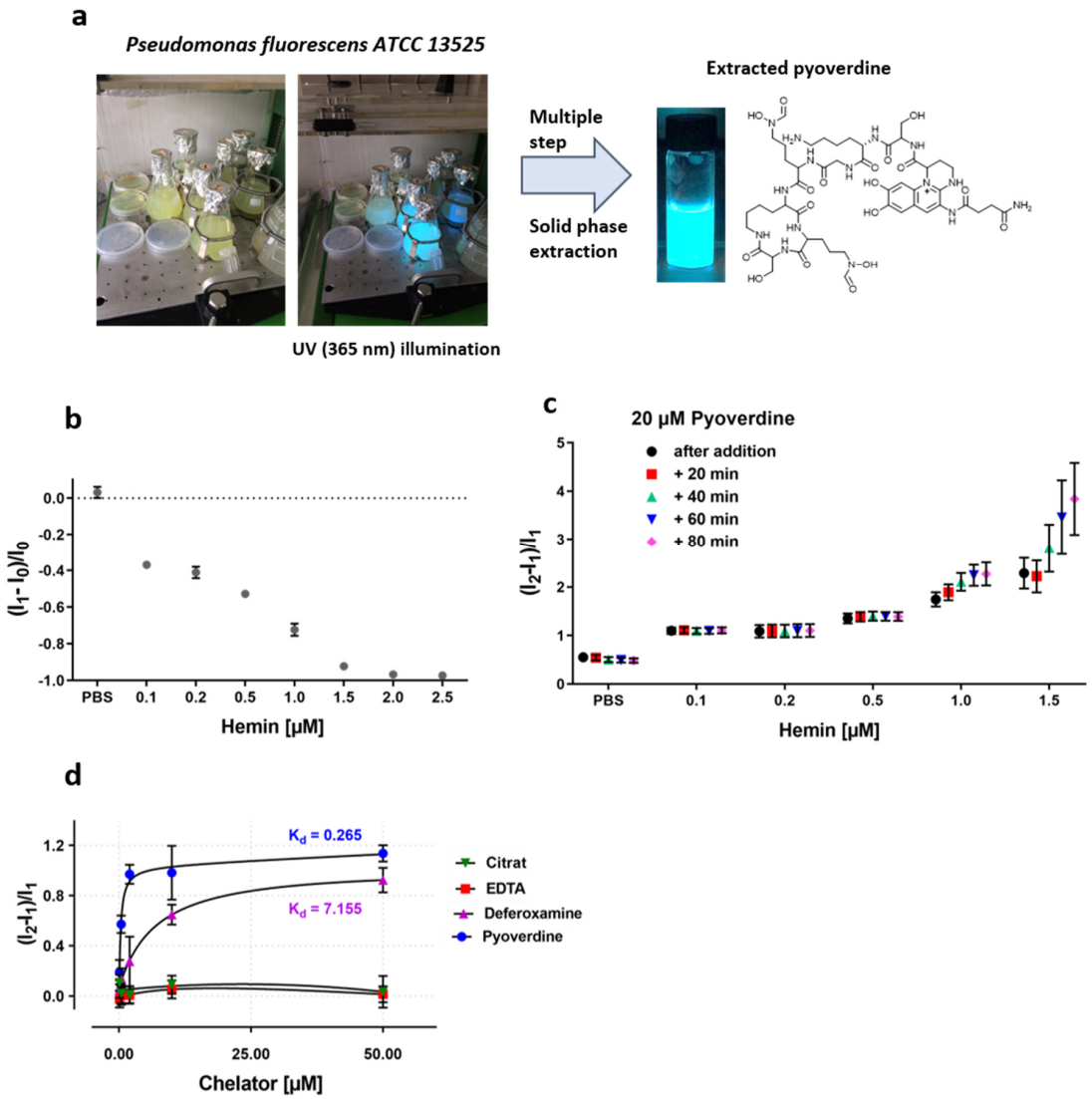

Figure S3: Siderophore sensing with hemin-aptamer-(HeApta)-SWCNTs.

a) Illustration of the pyoverdine extraction from *Pseudomonas fluorescens* ATCC 13525: Photographs of bacterial cultures with UV illumination show blue fluorescence of pyoverdines. A cascade of solid phase extraction (SPE) with fractionated elution from a C18ec resin isolates pyoverdines. b) Addition of hemin to HeApta-SWCNTs quenches the fluorescence emission (I_1) in a concentration dependent manner. 2 µM and more lead to complete quenching (n = 3 independent experiments, mean ± SD). c) Addition of 20 µM pyoverdine leads to a fluorescence increase (I_2), which correlates with the previous quenching (n = 3 independent experiments, mean ± SD). This indicates that dequenching of HeApta-SWCNTs (with hemin) in response to pyoverdine can be attributed to countering iron chelation. For further experiments, a hemin concentration of 1 µM was used for HeAtpa-SWCNTs (0.1 absorption at 993 nm) quenching, as it shows the highest relative fluorescence increase, without leading to non-fluorescent or non-stable sensors. Previous studies from Wu and Nißler *et al.* [1] showed furthermore that (6,5)-chirality enriched SWCNTs are most suitable and stable for HeApta modification and hemin addition. d) Calibration curve of Hemin-HeApta-SWCNT for different chelating agents. The isolated pyoverdines showed the lowest K_d = 0.26 µM (Binding fit, nonlinear curve fit (GraphPad Prism 8), data from Fig. 2f, (n = 3 independent experiments, mean ± SD).

Table ST1: Conditions for incorporation of SWCNTs into hydrogels (HG).

Formula	Type-I	Type-II	Concentration
PEG-DA (M_n = 700)	500 mg	500 mg	10 % (*m/V*)
PEG (6 kDa) (240 mg/ml in PBS)	-	2082 µL	10 % (*m/V*)
1xPBS	4296.6 µL	2215 µL	
UV-starter (2-Hydroxy-4′-(2-hydroxyethoxy)-2-methylpropiophenone, 12 mg/ml in H_2O)	208 µL	208 µL	0.5 mg/mL
SWCNT-dispersion in PBS	50 µL	50 µL	~ 0.3 absorption (6,5)-SWNCTs at ~ 990 nm

PBS and SWCNT-dispersion volumes were adjusted to obtain the desired nanosensor concentration. Egyptian blue - nanosheets (EB-NS) stock solution was diluted of 1:40 for the HG incorporation (125 µL EB-NS in water for 5 mL type-II HG).

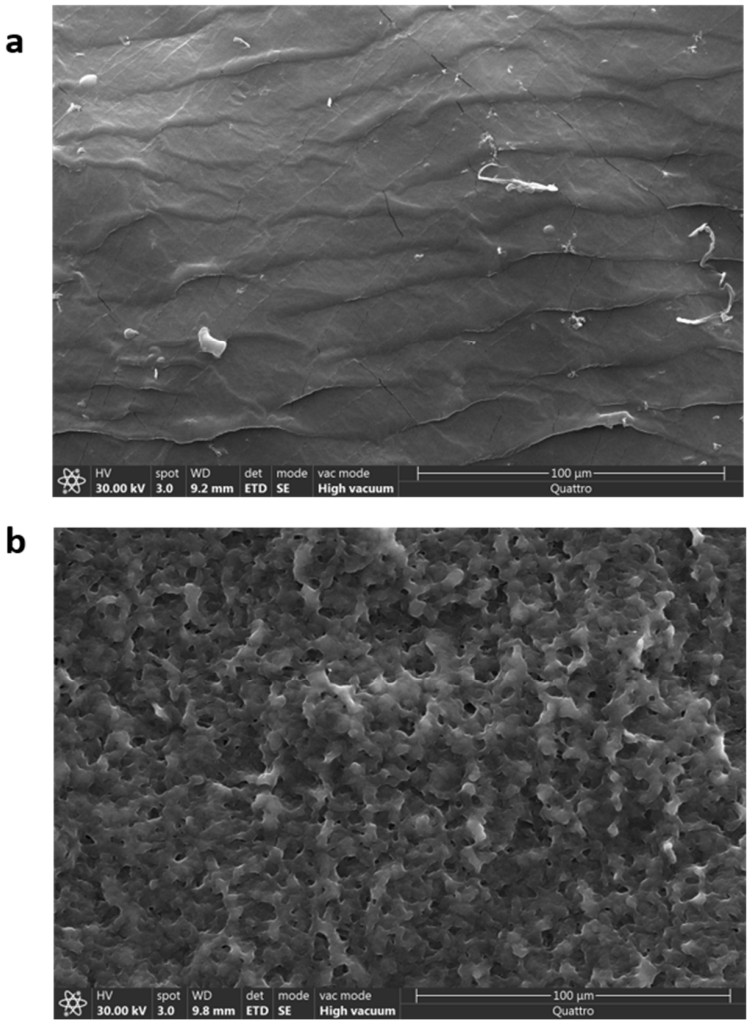

Figure S4: Scanning electron microscopy (SEM) of the sensor hydrogels.

a) Exemplary image of the type-I HG shows a uniform surface, while the porous type-II HG in b) displays a sponge-like structure. SEM was acquired with a LEO SUPRA 35 microscope (Zeiss) with an Inlens detector at 30 kV (secondary electrons). Hydrogel arrays were dialyzed in ddH_2O and lyophilized before gold sputtering (~4 nm layer). Experiments were repeated at least five times independently with similar results.

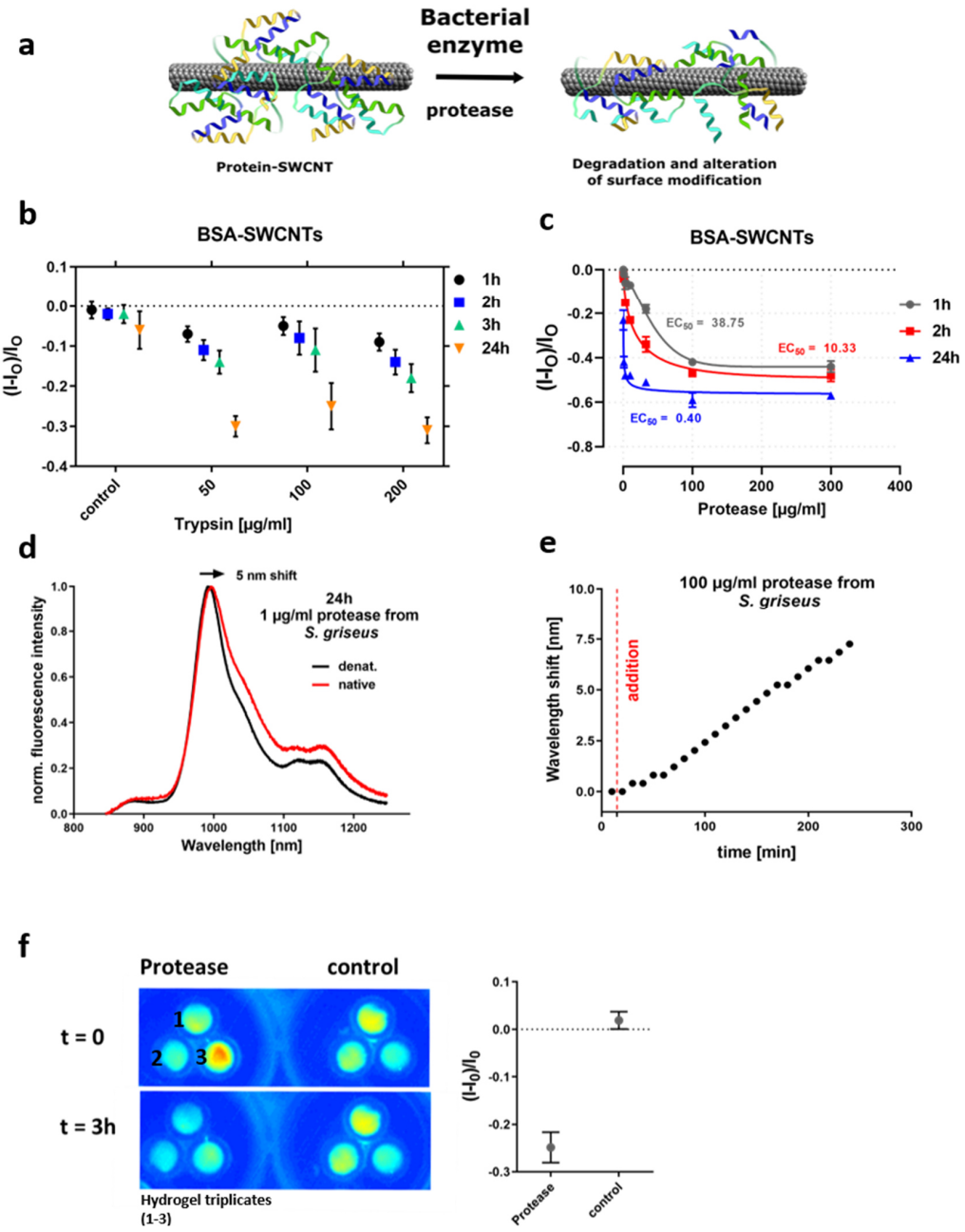

Figure S5: Extended characterization of BSA-SWCNTs as protease sensors.

a) Schematic of the protease sensing approach. The SWCNT surface is modified with a substrate (here the protein bovine serum albumin, BSA) for (bacterial) proteases, with the result that enzymes degrades and alters the organic phase around the SWCNTs, causing a fluorescence change of the nanosensor. b) BSA-SWCNTs in HG respond to trypsin (2.5% solution, 59427C, Sigma Aldrich) with a strong fluorescence decrease (control = 100 µg/mL thermally denatured trypsin in sodium dodecyl sulfate (SDS), n = 9 technical replicates in 3 independent experiments, mean ± SD). c) Calibration curves of BSA-SWCNTs in response to protease activity and corresponding EC_{50} (effective concentration) values (Dose-Response, nonlinear (asymmetric) curve fit (GraphPad Prism 8), data from Fig. 3b, (n = 9 technical replicates in 3 independent experiments, mean ± SD)). d) Fluorescence spectra of BSA-SWCNTs in HG after 24 h of incubation with 1 µg/mL protease from *Streptomyces griseus* show a 5 nm bathochromic shift for the native (active) enzyme (mean spectra of n = 3 independent experiments, see Figure 3 a,b). e) BSA-SWCNTs in HG after 3 h of incubation at room temperature with 100 µg/mL *Streptomyces griseus* protease: evaluation of the peak maxima from the (6,5)-SWCNTs emission around 1000 nm during enzyme performance. Dashed read line indicates the addition of protease. Within 3 h a peak shift of 7.5 nm was observed (n = 1). f) NIR stand-off images of the same experiment show a fluorescence decrease of ~25% (n = 3 independent experiments, mean ± SD) (control = PBS).

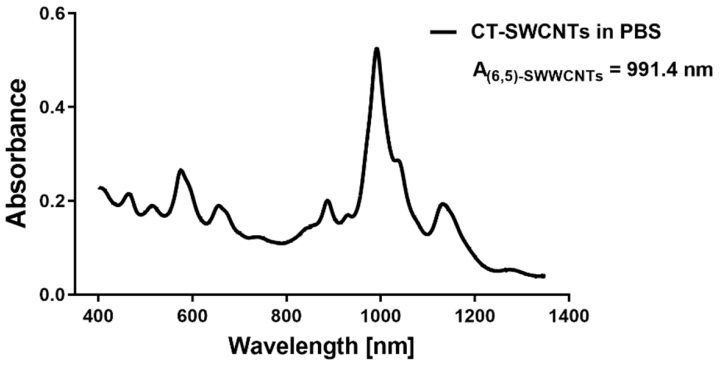

Figure S6: Absorbance spectra of CT-SWCNTs (nuclease sensor).

Calf thymus (CT)-SWCNTs 1:25 diluted in PBS. The E_{11} peak of the (6,5)-SWCNTs at 991.4 nm indicate well dispersed SWCNTs in denatured, long genomic CT-DNA.

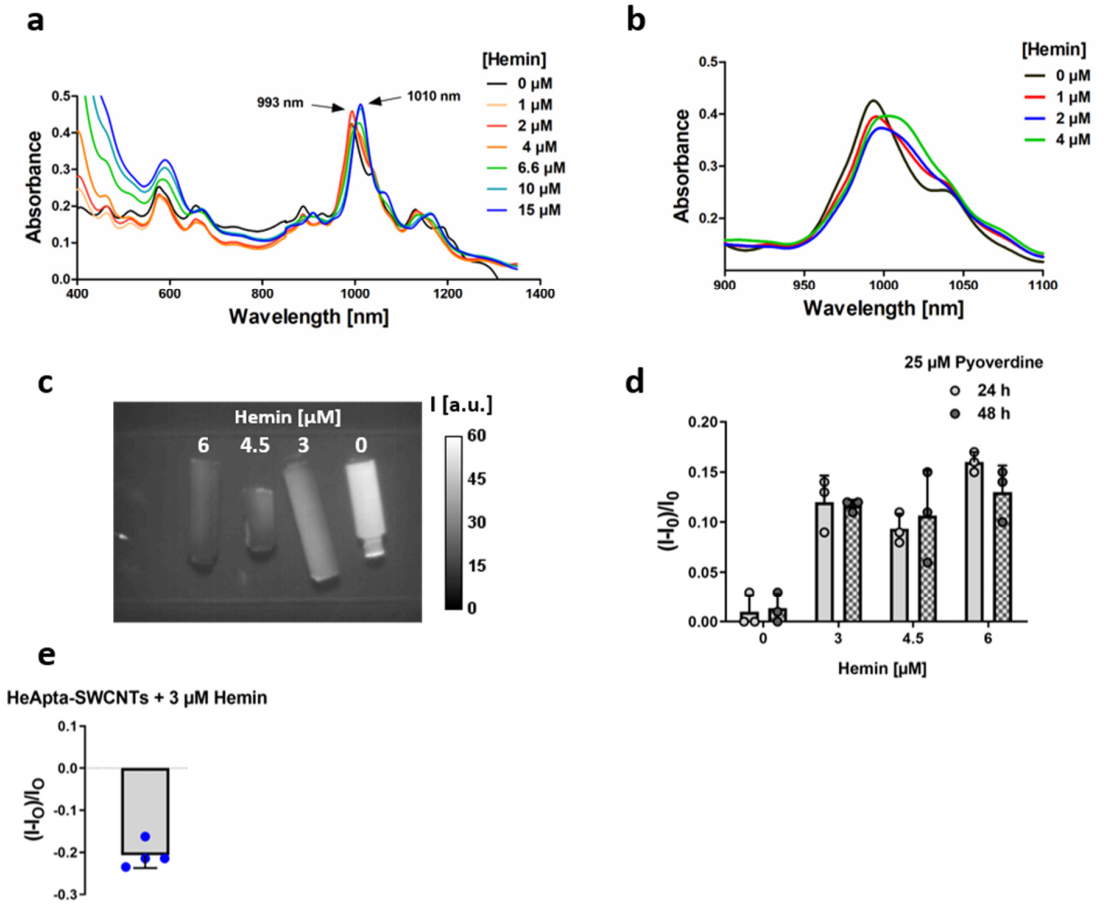

Figure S7: Integration of HeApta-SWCNTs in hydrogel.

a) Absorbance spectra of HeApta-SWCNTs in non-polymerized type-I HG. The addition of hemin redshifts the spectrum and results in visible aggregates that increase with hemin concentration (= loss of colloidal stability). b) Even for a hemin concentration ≤ 4 µM, redshift and broadening of the E_{11} transition of the HeApta-SWCNTs in the HG takes place and sensing of pyoverdine fails. Therefore, hemin addition before hydrogel polymerization was excluded. c) HeApta-SWCNTs in polymerized HG incubated with different hemin concentrations, to screen for optimal quenching and siderophore induced dequenching conditions. NIR stand-off image of HG-sensor cylinders show decreasing fluorescence intensities with increasing hemin concentration. The pyoverdine (25 µM) response in (d) is similar for all used hemin concentrations beforehand (n = 3 independent experiments, mean ± SD). Therefore, incubation in 3 µM hemin for 12 h, followed by HG dialysis in PBS for 2 days was used for all further HeApta-SWCNTs HG experiments. e) Fluorescence decrease of the HeApta-SWCNTs after incubation with the optimized hemin concentration (3 µM) (n = 4 independent experiments, mean ± SD).

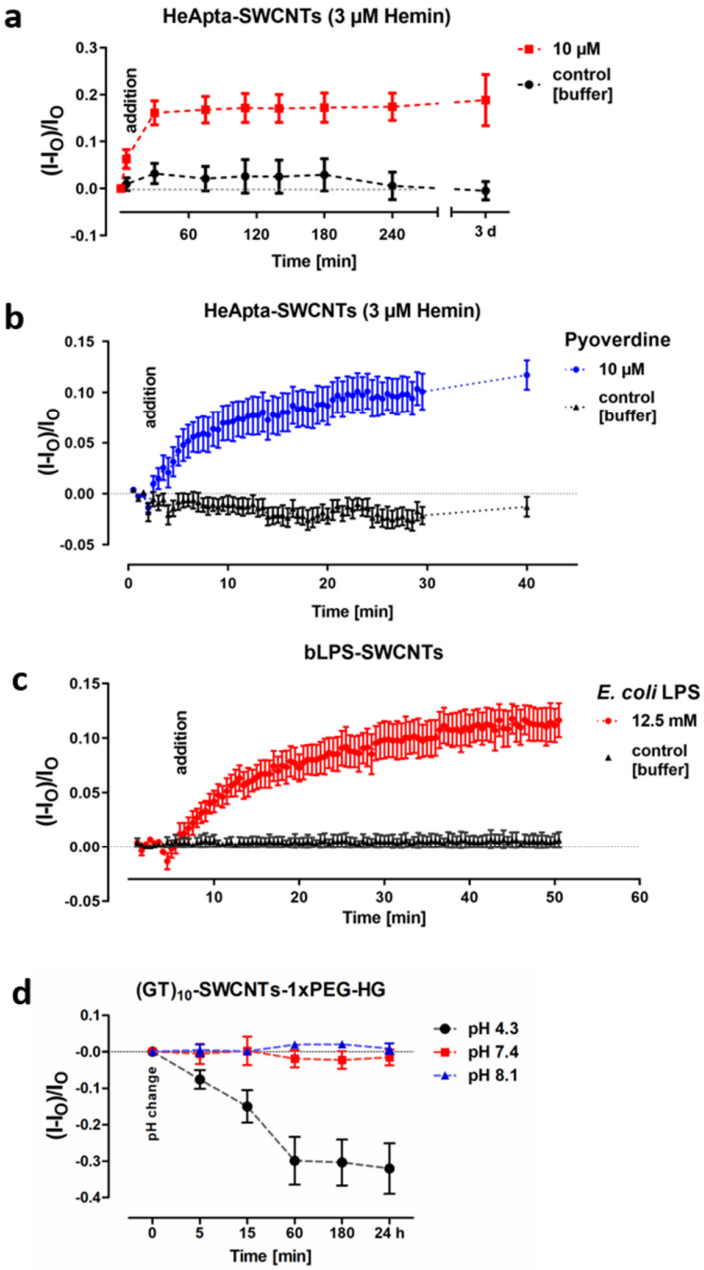

Figure S8: Time resolved fluorescence response of the sensor HGs to analytes.

a) The fluorescence readout of HG HeApta-SWCNTs (3 µM hemin) was evaluated *via* NIR stand-off detection. Addition of 10 µM pyoverdine (n = 3 independent experiments, mean ± SD) quickly increases the fluorescence and the response is not changing significantly for up to 3 days. b) A similar experiment with better time resolution shows that most of the response occurs in the first 10 min (n = 3 independent experiments, mean ± SD). c) Fluorescence response of bLPS-SWCNTs (n = 3 independent experiments, mean ± SD) to 12.5 µM *E. coli* LPS shows that most of the change happens in the first 20 min. d) Lowering the pH from 7.4 to pH 4.3, decreases the fluorescence of $(GT)_{10}$-SWCNTs HGs within 60 min by about -30%. pH increases to 8.1 do not significantly increase fluorescence compared to the control with pH 7.4 (n = 9 technical replicates in 3 independent experiments, mean ± SD).

Table ST2: Conditions for SWCNT surface modification

Nano-conjugate	Volume macromolecule	Volume PBS	Volume SWCNTs (2 mg/ml)	Tip sonication	Centrifugation	Removal of excess polymer
$(GT)_{10}$, C_{30} and $(GA)_{15}$ -SWCNTs	100 µL (2 mg/mL ssDNA in PBS)	100 µL	100 µL	15 min @ 36 W output power	2x 30 min @ 16100x *g*	Dialysis in HG
BSA-SWCNTs	100 µL (5 mg/mL BSA in PBS)	150 µL	50 µL	15 min @ 30 W output power	2x 20 min @ 16100x *g*	Dialysis in HG
HeApta-SWCNTs	100 µL (2 mg/mL aptamer in PBS)	100 µL	100 µL	15 min @ 36 W output power	2x 30 min @ 16100x *g*	Spin filtration
bLPS-SWCNTs	See protocol		75 µL	20 min @ 30 W output power	2x 30 min @ 16100x *g*	Spin filtration
CT-SWCNTs	100 µL (3 mg/mL ssDNA in PBS)	300 µL	50 µL	20 min @ 36 W output power	2x 30 min @ 16100x *g*	Dialysis in HG
PEG-PL-SWCNTs	See protocol		100 µL	20 min @ 36 W output power	2x 30 min @ 16100x *g*	Dialysis in HG

Dialysis in HG stands for the incubation (dialysis) of nanosensor HGs in PBS, removing non-reacted HG monomers, as well as excess polymers from SWCNT surface modification.

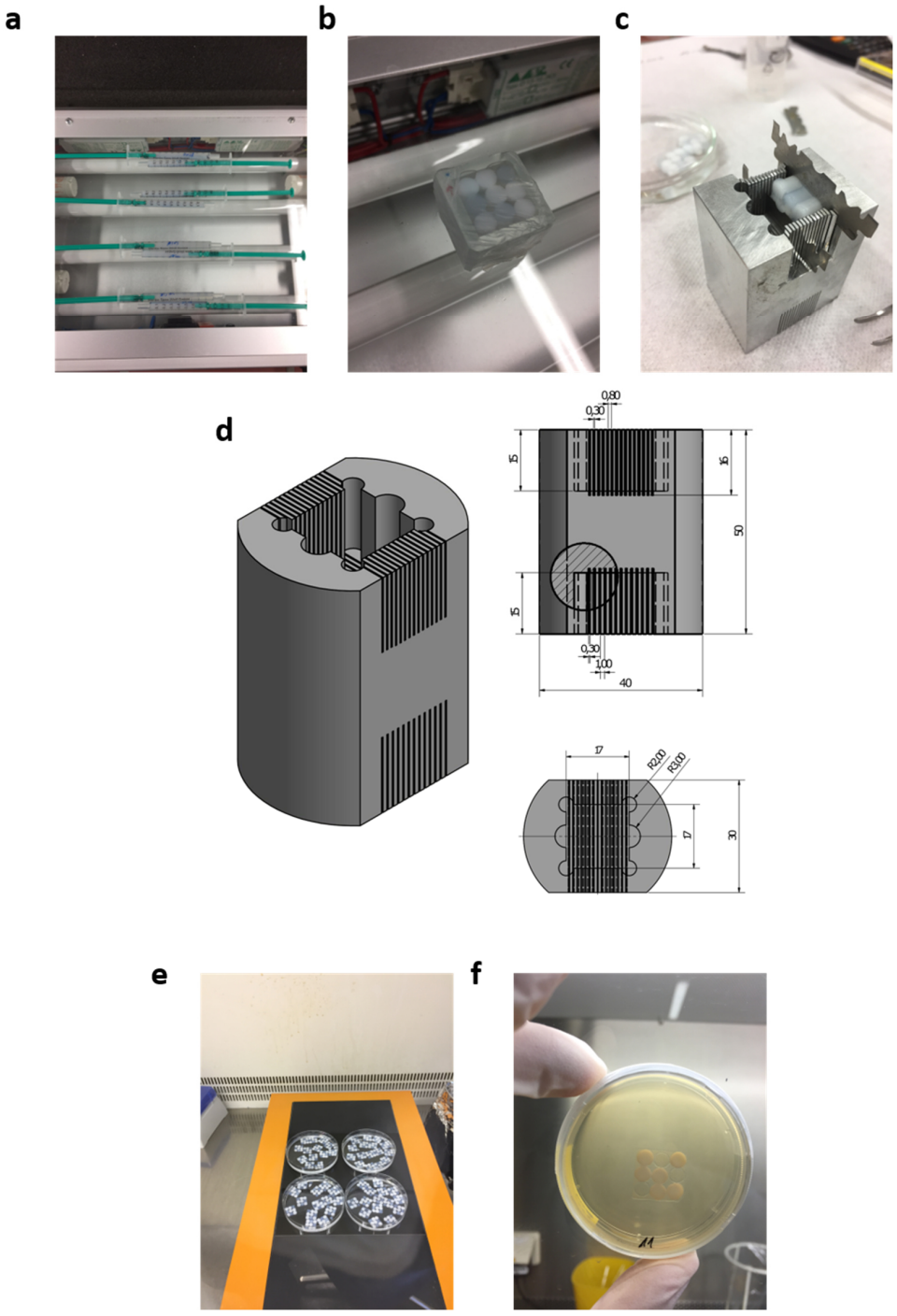

Figure S9: Engineering of the nanosensors hydrogel array.

a) Photograph of the hydrogel with nanosensors polymerized in a 1 ml syringe, which creates a uniform cylinder and excludes oxygen during the polymerization reaction. b) Assembly of different hydrogel sensor cylinders in a glass cube (1.5x 1.5x 1.5 cm, open at the two lateral planes). The cube is sealed with parafilm on one side, hydrogel cylinders are placed inside and the space in between filled with liquid type-I-HG (with 15% PEG-DA (*m/V*)). After complete sealing, the HG block is polymerized *via* UV illumination. c) Hydrogel array slices are generated by using a custom-made cutting chamber with razor blades. This way, uniform 0.8 mm thick slices of sensor array hydrogels are created. d) Detailed information on the alumina HG cutting chamber. e) UV sterilization of the HG array slides guarantees contamination free conditions for microbiological experiments. f) Sterilized HG array embedded in microbial agar.

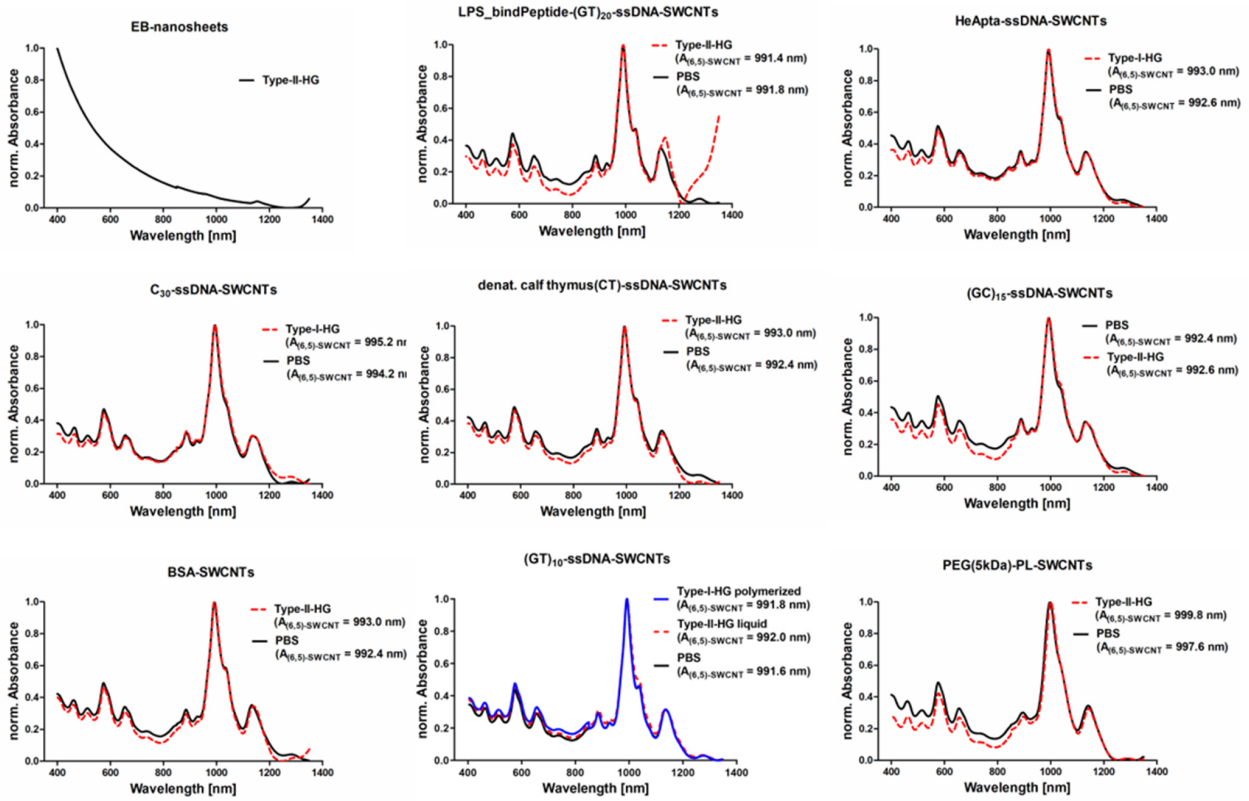

Figure S10: Absorbance spectra of the sensor array components in solution and in hydrogel.

Normalized absorbance spectra of the nanosensors of the sensor array, before and after incorporation in the HG. No major shifts were noticed, indicating colloidal nanosensor stability even in the hydrogel environment.

Table ST3: Overview nanosensor array

Acronym	Hydrogel	Nano-conjugate	Main target	Reference
EB-NS	Type-II	Egyptian blue nanosheets	nIR reference	[2]
bLPS	Type-II	$(GT)_{20}$-ssDNA-linker-LPS-binding peptide	Lipopolysaccharides (LPS)	This study
HeApta	Type-I	Hemin-aptamer-SWCNTs (+hemin)	Iron chelating siderophores	This study
C_{30}	Type-I	C_{30}-ssDNA-SWCNTs	Unspecific, pH	[3]
CT	Type-II	Genomic, denatured calf thymus (CT) ssDNA-SWCNTs	Nucleases	This study
$(GC)_{15}$	Type-II	$(GC)_{15}$-ssDNA-SWCNTs	Unspecific, pH	[3]
BSA	Type-II	Protein modified BSA-SWCNTs	Protease	This study
$(GT)_{10}$	Type-I	$(GT)_{10}$-ssDNA-SWCNTs	pH, O_2 concentration	[3,4]
PEG	Type-II	Phospholipid (18:0 PEG5000PE) DSPE-PEG(5000) -SWCNTs	Proteins	[5,6]

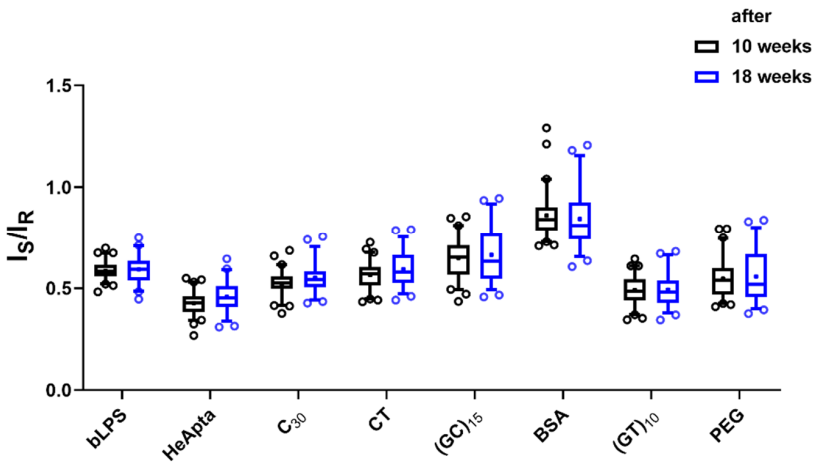

Figure S11: Stability of the nanosensor hydrogel array.

The intensity ratios for HG embedded nanosensors are shown as Box-plots (5 - 95% percentile). The fluorescence intensities of the sensor spots (I_S) are shown relative to the fluorescence intensity of the NIR reference material (EB-NS) (I_R). The ratios of in total 60 arrays (n = 60 independent experiments), evaluated after 10 weeks of nanosensor-HG manufacturing and storage in PBS, are shown in black and do not differ significantly from the ratios of in total 55 arrays (n = 55 independent experiments) shown in blue, assembled 2 months later from the same nanosensor HGs (25-75 percentile box with median as bar and mean as square, 5-95 percentile whiskers, individual datapoints outside the 5-95 percentile as dots). This result indicates a high stability of the nanosensors in the HG matrix over several months, as degradation or loss of colloidal stability would change the fluorescence emission of the nanosensors relative to the reference. No significant differences between HG type or SWCNT surface modification (ssDNA, proteins or PEG-phospholipid) was observed.

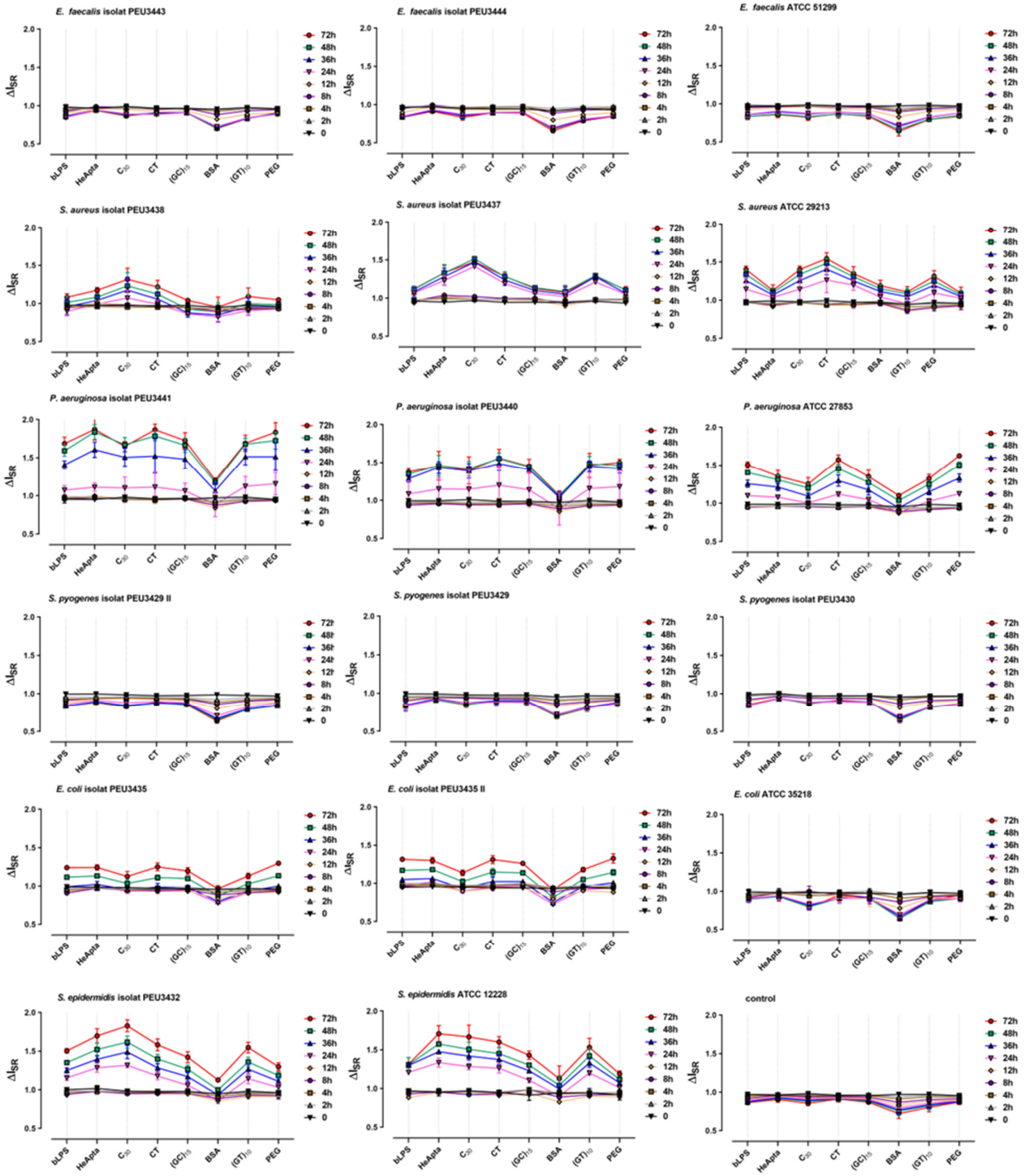

Figure S12: Bacterial sensor array fingerprints.

Corresponding to Fig. 4d-h, time resolved bacterial fingerprints are presented for different bacteria. The different sensor arrays responses indicate major differences between some of the tested pathogens (n = 9 technical replicates in 3 independent experiments, mean ± SD).

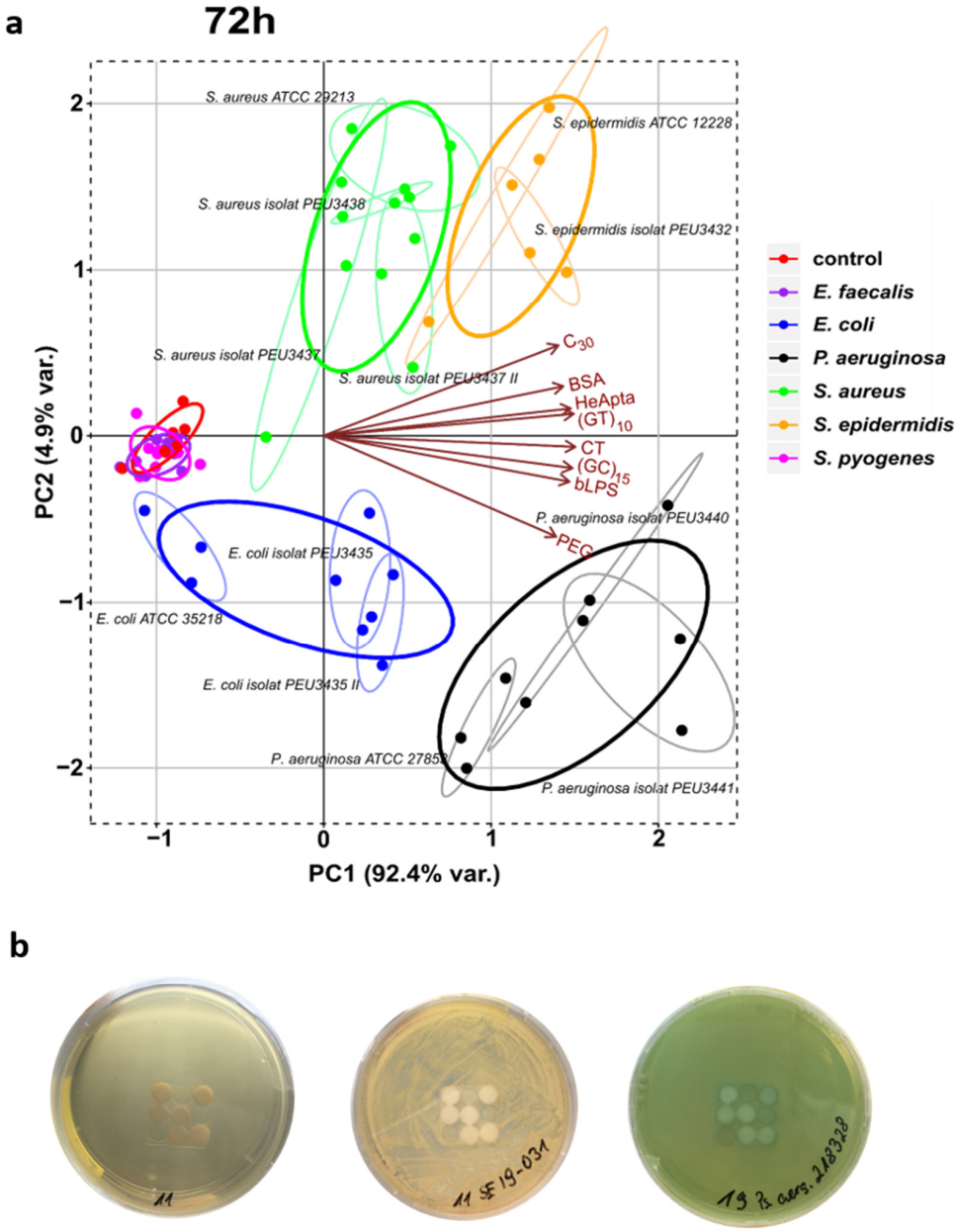

Figure S13: Principal component analysis (PCA) based differentiation of bacteria with indicated strains.

a) Sensor array fingerprints lead to the PCA differentiation clusters shown in Fig. 4h, but the different isolates of the same species were not shown, for reasons of clarity and comprehensibility. Here, a more detailed representation for the timepoint 72 h after incubation is presented. Next to the different species, also strain/isolates sub-clusters, as well as the variables (as vectors) for the different sensor responses are indicated. The spread of the datapoints within the cluster of one bacterium is therefore mainly attributed to the epigenetically different strains and not due to a large spread within the sub strains (n = 3 technical replicates). b) Photographs of the sensor arrays incorporated in agar: on the left side, before bacterial inoculation (equal to control without bacterial growth), in the middle of *S. epidermidis* and on the right of *P. aeruginosa (isolate PEU3440= specimen 218328)* after 72 h.

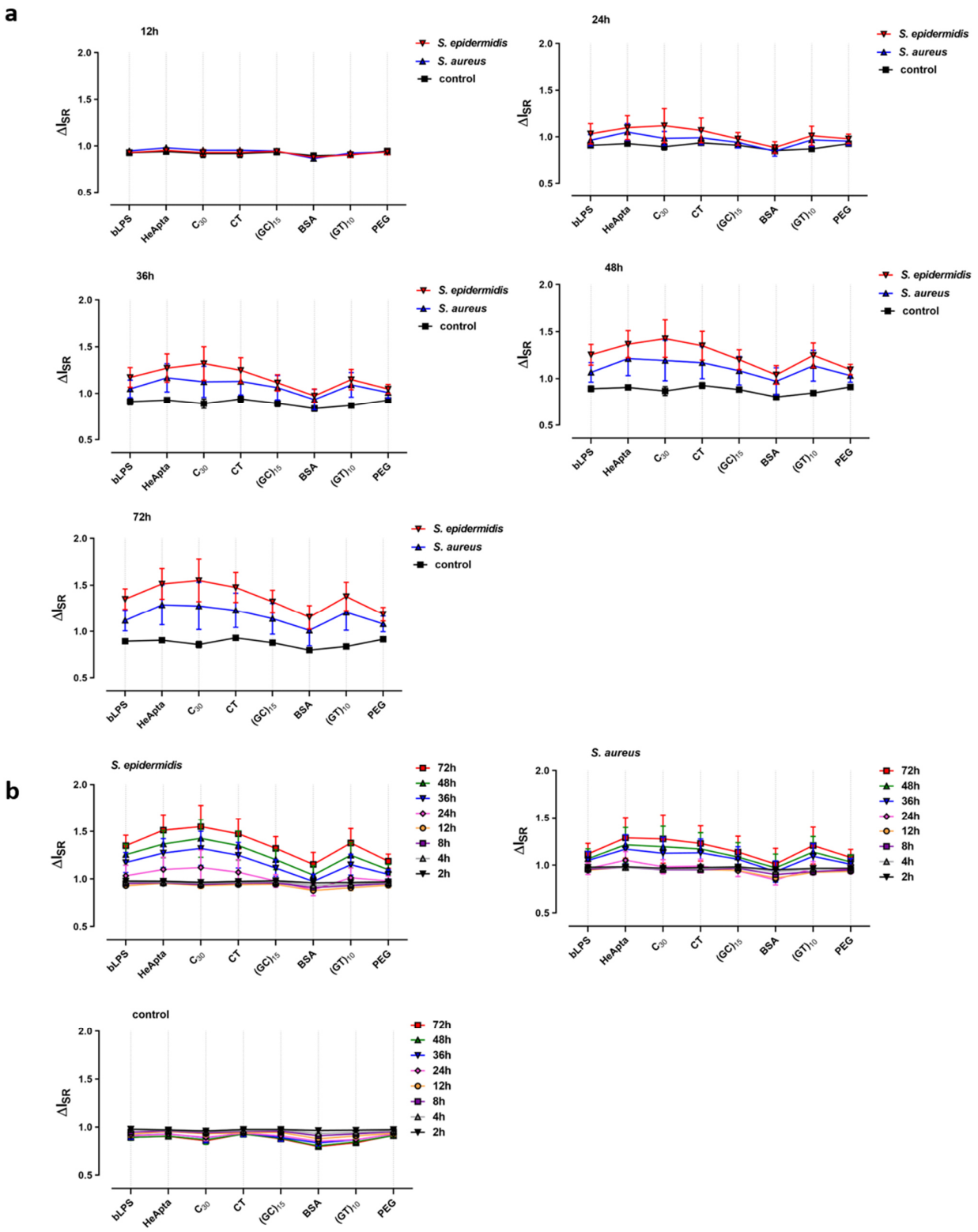

Figure S14: Bacterial fingerprints from *S. aureus* and *S. epidermidis*.

Corresponding to Figure 4i, time resolved bacterial fingerprints are presented. a) Comparison between the mean sensor readout from clinical isolates from *S. aureus* (n = 21 biologically independent samples) and *S epidermidis* (n = 22 biologically independent samples) at different timepoints after inoculation (control n = 3 independent experiments) (mean ± SD). b) Overview about the sensor fingerprint evolution during the experiment. Note that the 'error' reflects the spread within the clinical isolates and not a technical error (same samples as presented in a).

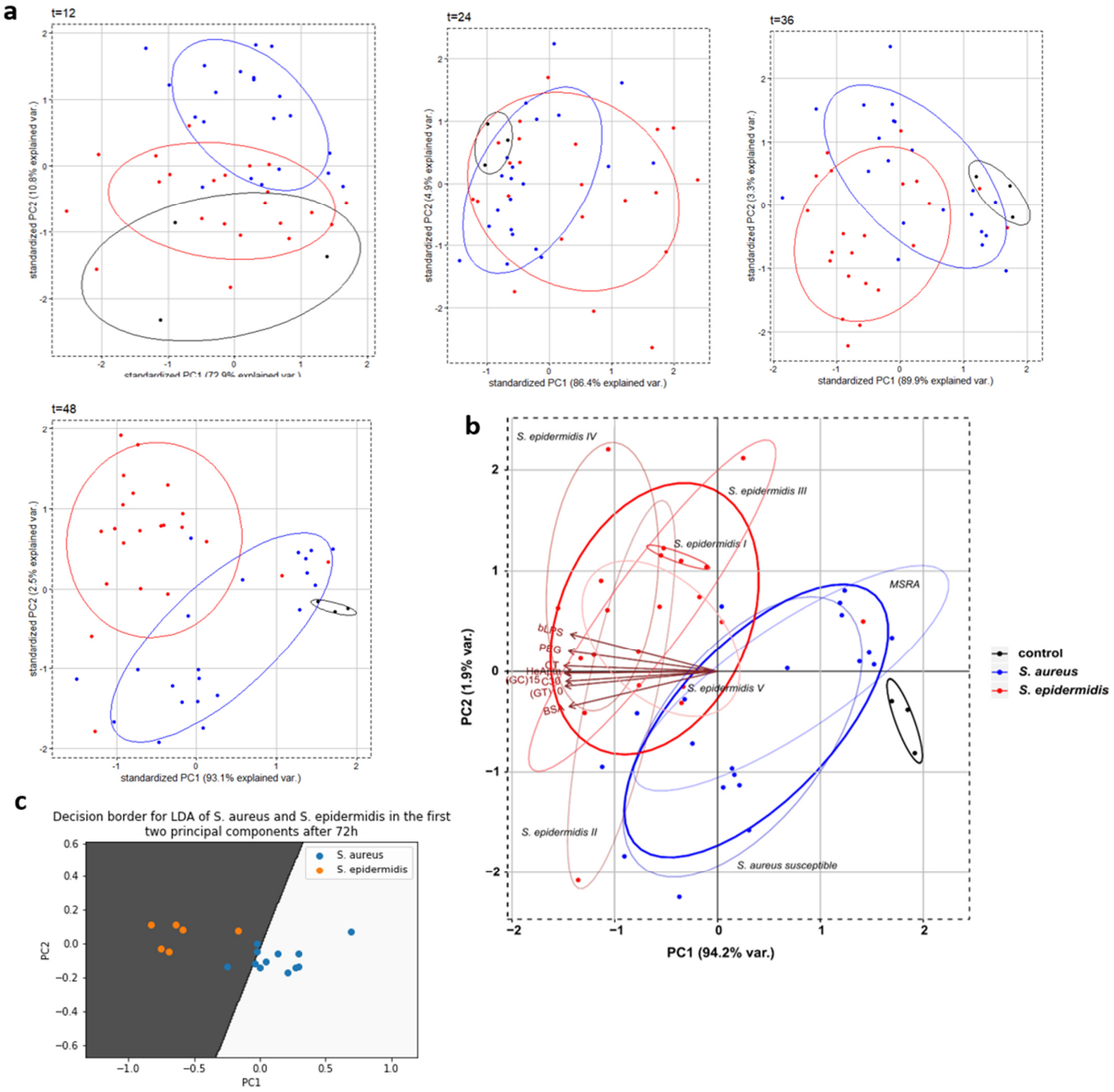

Figure S15: PCA for sensor fingerprint of *S. aureus* and *S. epidermidis*.

a) PCA of the array fingerprints of clinical isolates of *S. aureus* and *S epidermidis* (43 independent clinical isolates) at different timepoints. The two clusters separate after 48 -72 h. b) Sub-clusters of isolates are indicated for *S. epidermidis*, and *S. aureus* including antibiotic susceptibility, as well as the variables (as vectors) for the different sensor responses, 72 h after incubation. c) Linear discriminant analysis for the classification of *S. aureus* and *S. epidermidis* from Figure S12 by training data set based on the 43 clinical isolates shown above. The result indicates, that independent isolates can be distinguished, classified and assigned to its bacterial group with a > 80 % likelihood.

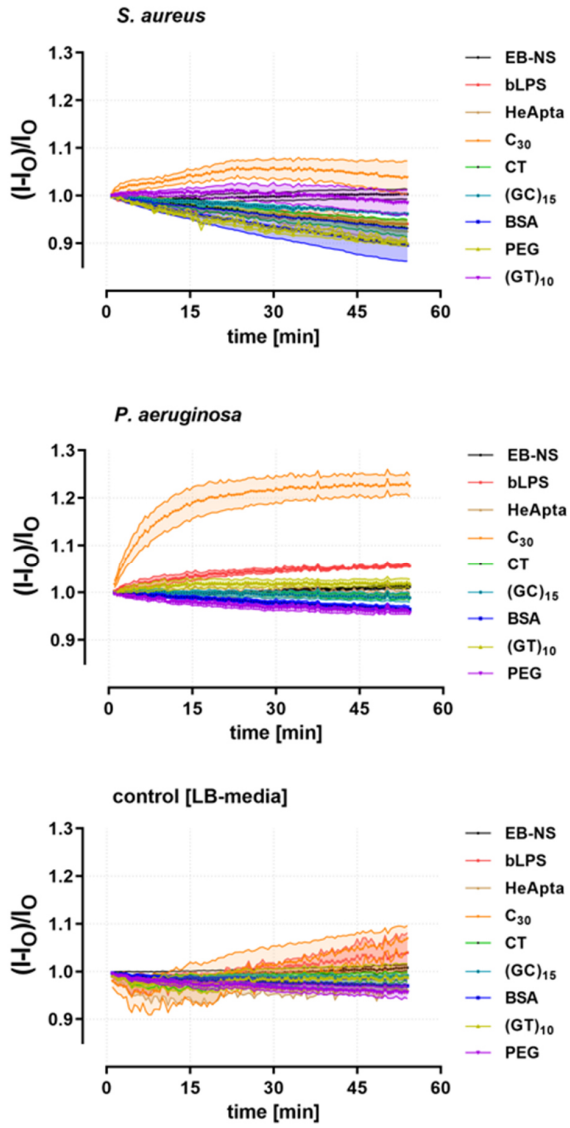

Figure S16: Response kinetics of sensor array.

Time resolved mean fluorescence change, with SD (pale boundaries), of the nanosensors in the hydrogel array after addition of liquid culture supernatant from *S. aureus*, *P. aeruginosa* and LB-media as control. (24 h incubation in LB-medium, I- intensity sensor at timepoint t, I_0- intensity sensor at t = 0) (n = 3 independent experiments, mean ± SD). Note: For reasons of clarity, the mean time resolved changes are shown in Fig. 4k. Comparison with LB-media response shows a clear difference of the sensor array response.

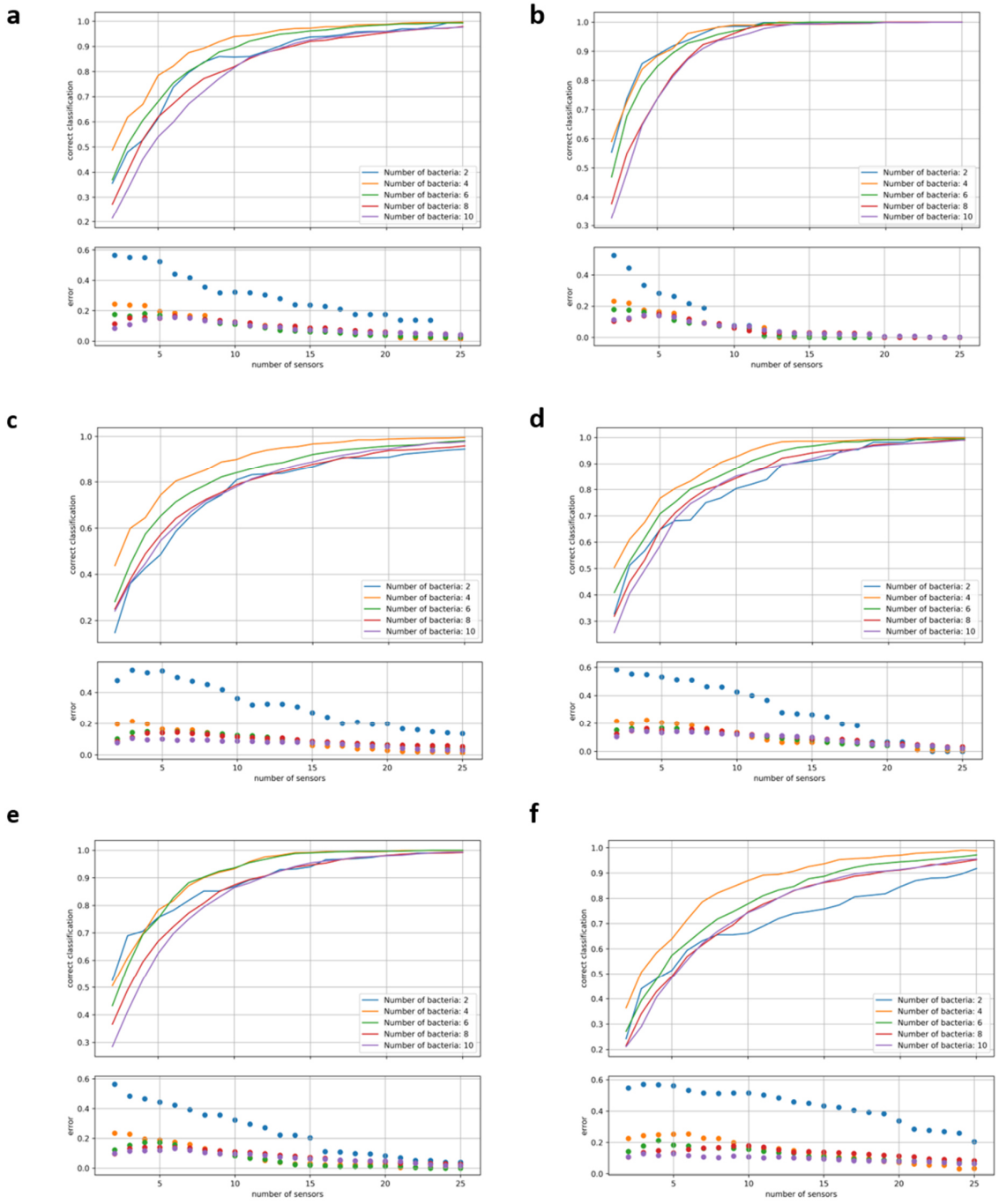

Figure S17: Sensor array response simulation.

a) Simulation with the parameters, extracted from the original HG sensor experiments (noise = 10 %, indistinguishable sensor responses = 40 %, sensor responses = 0.7 – 1.7) (note = same data as Figure 5f, shown here again for reasons of comparability). b) Increasing the sensor response to 0.5 – 2 would strongly enhance the bacterial differentiation, while other parameters stay fixed (noise = 10 %, indistinguishable sensor responses = 40 %, sensor responses = 0.5 – 2). c) noise = 5 %. d) noise = 15 %. Changing the noise level dos not significantly change the simulation output (indistinguishable sensor responses = 40 %, sensor responses = 0.7 – 1.7). e) Simulation with less indistinguishable sensor responses lead to a decreased number of necessary sensors for bacteria differentiation (noise = 10 %, indistinguishable sensor responses = 20 %, sensor responses = 0.7 – 1.7). f) Simulation with more indistinguishable sensor responses lead to an increased number of necessary sensors for bacteria differentiation (noise = 10 %, indistinguishable sensor responses = 60 %, sensor responses = 0.7 – 1.7). The results show that both, more specific sensor responses and an increased number of sensors improves bacteria differentiation and identification (e.g. for more pathogen species or further evaluation on the subspecies level).

M4-S20

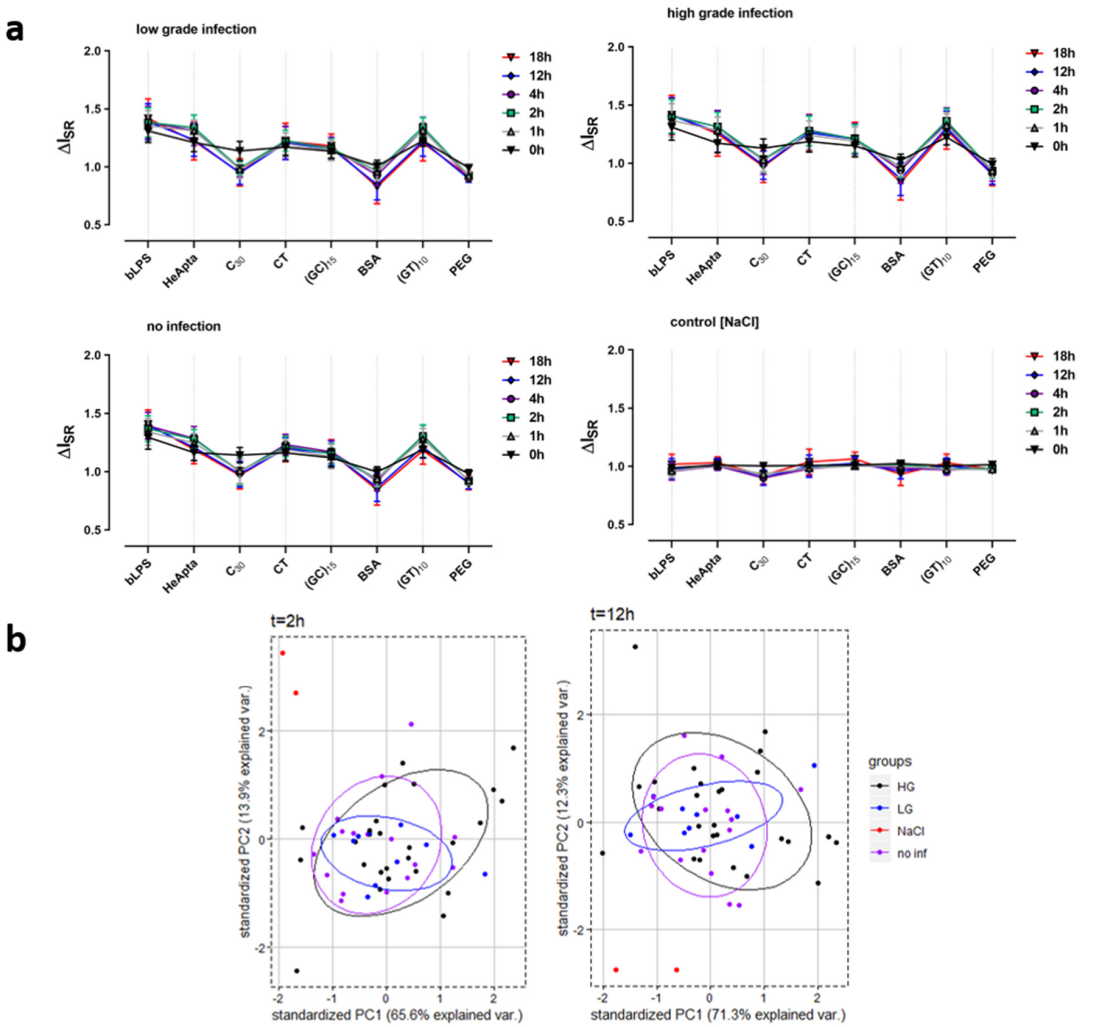

Figure S18: Human joint fluid (synovia) influence on sensor response.

Sensor array responses to human joint fluids from different patients (n = 26 biologically independent samples). Fluid from non-infected patients and low/high-grade infections were applied to the sensor array to evaluate the impact of different immune responses and synovia compositions. a) Sensor array fingerprints for synovia fluid samples for different timepoints show uniform pattern, indicating that synovia from diverse human background does not unspecifically bias the sensor array response (mean ± SD, for n see table ST4). b) Corresponding PCs do not show differences for various synovia types and samples from diverse patient backgrounds. These results indicate robustness of the sensor array performance towards a future smart implant application.

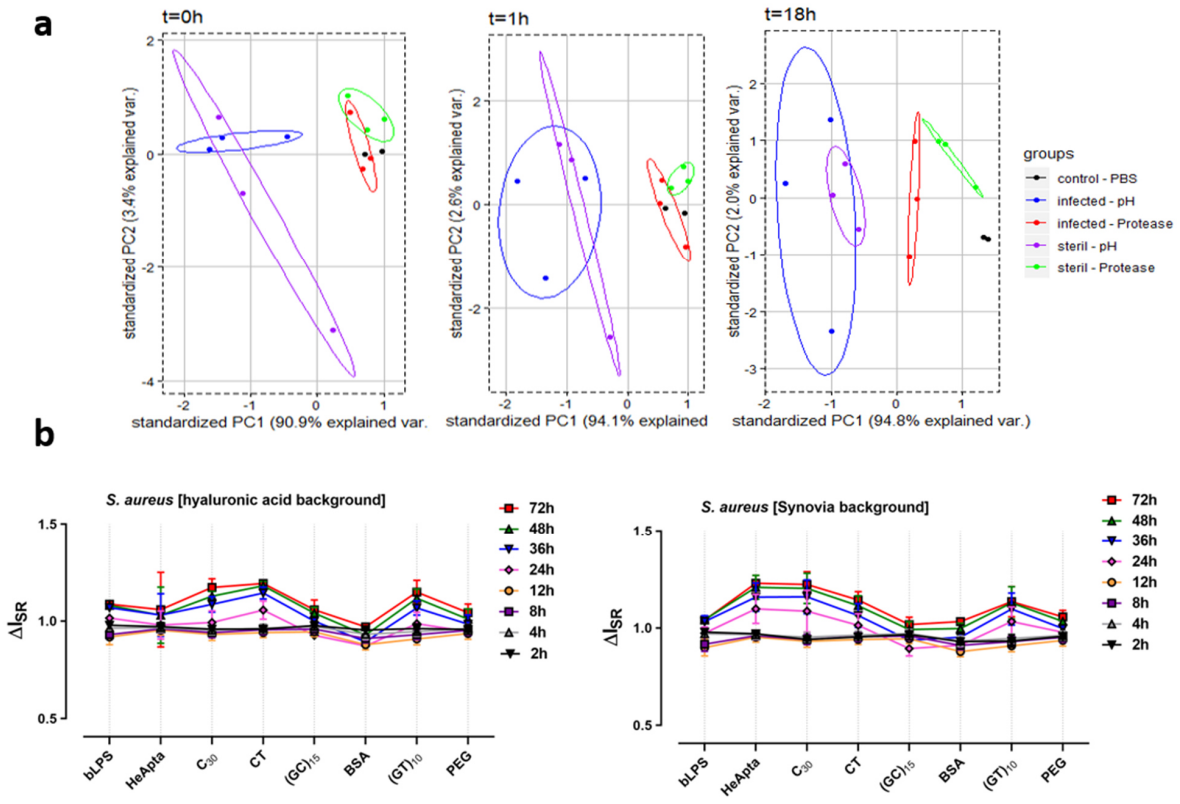

Figure S19: Sensor array performance in synovia background.

a) Sensing of pH changes and protease activity in human knee fluid background. Sensor arrays show a direct response to change of pH to 4.5. Protease activity requires longer to be detected. Differences between infected and non-infected knee-fluid are apparent, probably due to different amounts of proteins present *via* prevalent immune response. b) Sensing of methicillin resistant *S. aureus* (MRSA) during bacterial growth, in a microbiological agar after incubation / with background of hyaluronic acid (main component of the synovia) and the synovia itself from non-infected patients (n = 3 independent experiments, mean ± SD). The array is able to sense bacterial targets and bacterial growth, even in complex matrixes such as synovia. Therefore, only direct biofilm infections on a potential smart implant surface would be sensed by the nanosensor array.

Table ST4: Human joint fluids.

Number	Infection state	Pathogen	pH synovia
1	HG	Coagulase negative Staphylococci	7.5
2	HG	*Staphylococcus epidermidis*	7.5
3	HG	*Staphylococcus epidermidis*	7.5
4	HG	*Candida albicans*	7.5
5	HG	*Staphylococcus lugudensis*	7.0
6	HG	*Streptococcus agalactiae*	8.0
7	HG	Not detected	8.0
8	HG	*Staphylococcus aureus*	7.0
9	HG	Not detected	8.0
10	HG	Lactobacillus	7.0
11	HG	*Escherichia coli*	8.0
12	HG	*Staphylococcus aureus*	6.5
13	LG	Not detected	7.0
14	LG	Not detected	8.0
15	LG	Not detected	7.0
16	LG	Not detected	7.5
17	LG	Not detected	7.0
18	Sterile	Sterile	7.5
19	Sterile	Sterile	7.5
20	Sterile	Sterile	7.5
21	Sterile	Sterile	7.5
22	Sterile	Sterile	7.0
23	Sterile	Sterile	7.0
24	Sterile	Sterile	7.0
25	Sterile	Sterile	7.0
26	HG	Propiobacterium	7.5

HG- high grade, LG- low grade infection

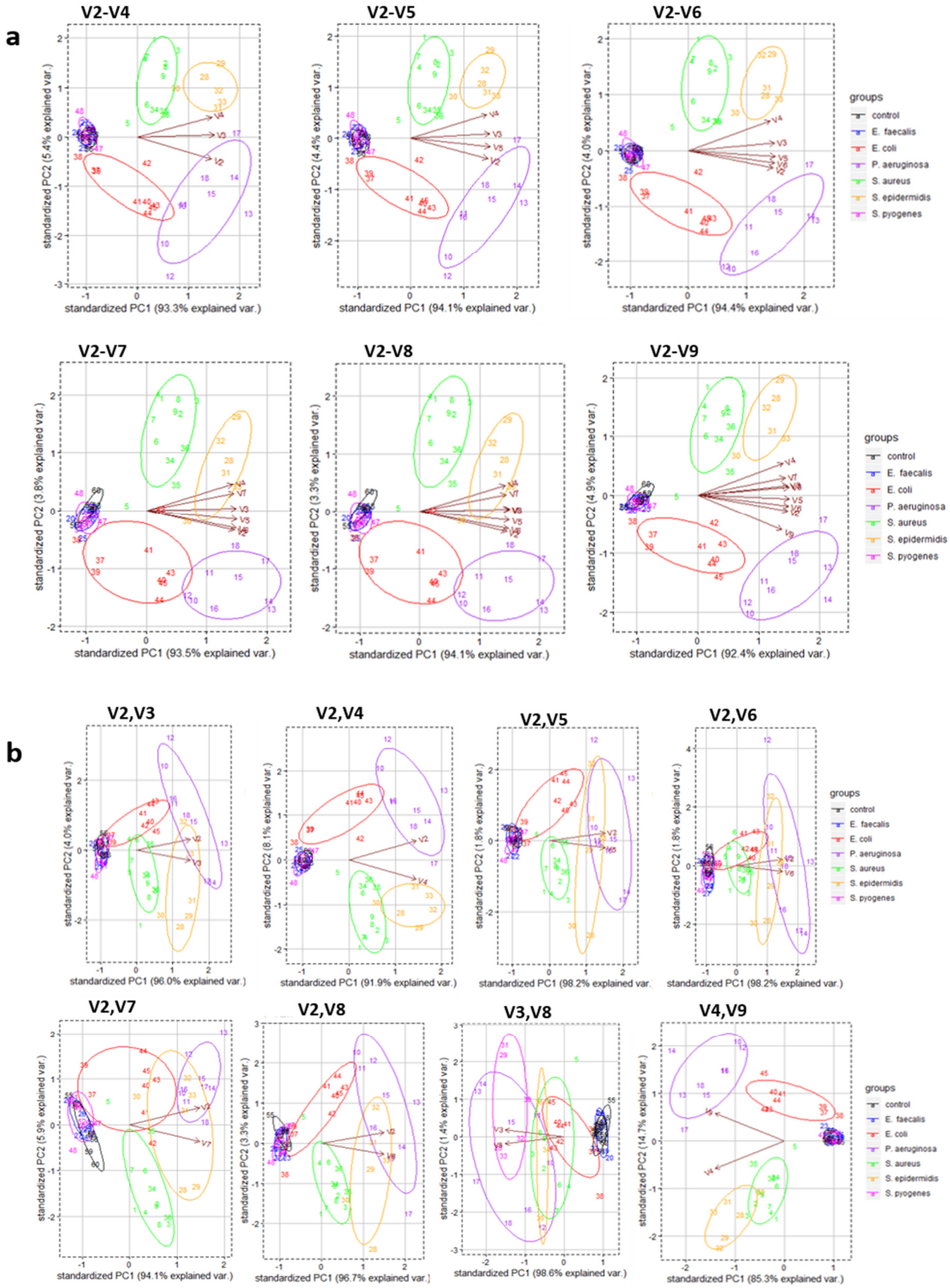

Figure S20: PCA based pathogen differentiation with reduced number of sensors.

All graphs are based on the sensor fingerprint after 72 h (Fig. 4h). Numbers indicate single biological samples. Vectors display the influence of the variables (V) as different sensors responses; V2: bLPS-SWCNTs, V3: HeApta-SWCNTs, V4: C_{30}-SWCNTs, V5: CT-SWCNTs, V6: $(GC)_{15}$-SWCNTs, V7: BSA-SWCNTs, V8: $(GT)_{10}$-SWCNTs and V9: PEG-SWCNTs; all related to EB-NS. a) Comparison of using different sensor responses for the PCA from V2 to V9 shows the principle bacteria differentiation is even possible with 3 sensors (V2-V4). b) Different combinations for V2 and another sensor response. Herby, the combination with V4 (C30) and V9 (PEG) showed a promising differentiation of the bacteria, while using the response of two sensors. The best separation was found for V4 with V9. V3 and V8 is exemplarily shown for all sensor combinations, which does not lead to cluster separation.

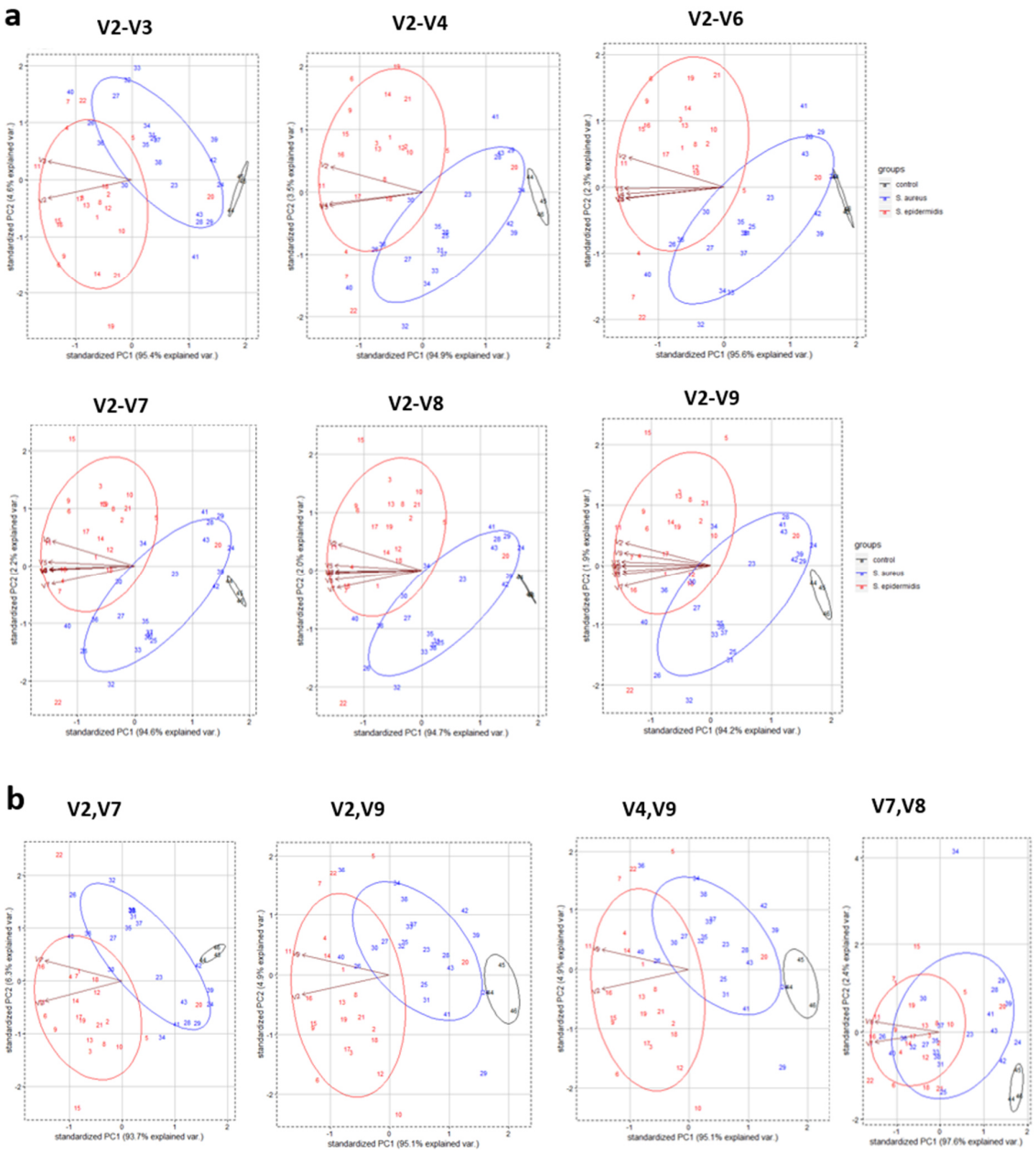

Figure S21: PCA differentiation of *S. aureus* and *S. epidermidis* with reduced number of sensors.

All graphs are based on the sensor fingerprint after 72 h (Fig. 4j). Numbers indicate single biological samples. Vectors display the influence of the variables (V) as different sensors responses; V2: bLPS-SWCNTs, V3: HeApta-SWCNTs, V4: C_{30}-SWCNTs, V5: CT-SWCNTs, V6: $(GC)_{15}$-SWCNTs, V7: BSA-SWCNTs, V8: $(GT)_{10}$-SWCNTs and V9: PEG-SWCNTs; all related to EB-NS. a) Comparison of using different sensor responses for PCA from V2 to V9 shows that differentiation of both strains is possible with two to three sensors (V2-V4). b) Different combinations of two sensor responses indicating for V2 and V7 or V2 and V9 a strong separation, while V4 and V9 or V7 and V8 generating a large overlap of the two bacteria, within the 43 tested isolates.

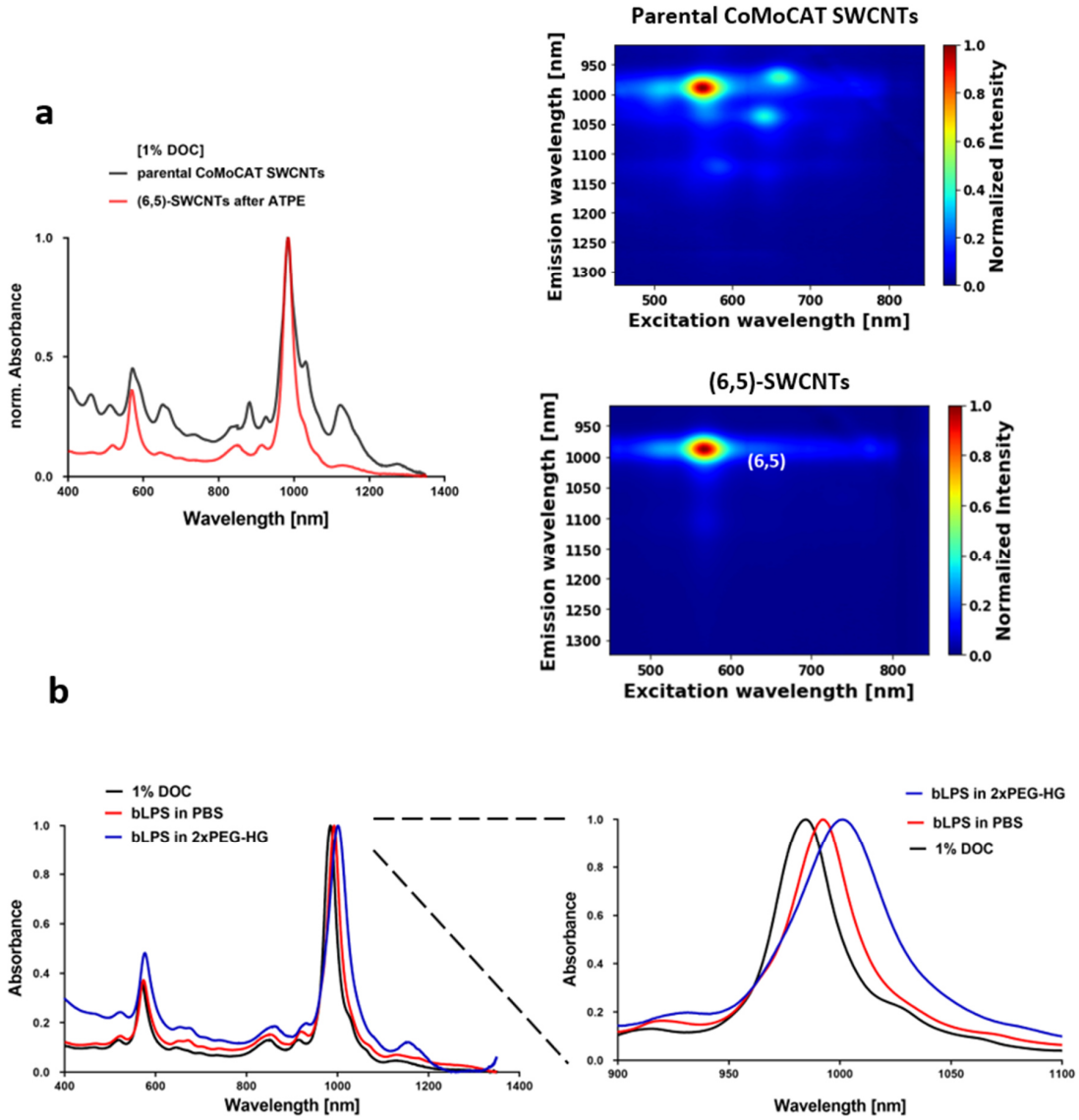

Figure S22: (6,5)-SWCNT purification and surface exchange for LPS sensing.

a) Absorbance spectra of (6,5)-SWCNTs and its parental CoMoCAT SWCNTs. Aqueous two-phase separation (ATPE) yields quasi monochiral (6,5)-SWCNT by following the protocol from Li *et al.*[7]. 2D excitation emission fluorescence spectra of the purified (6,5)-SWCNTs show the clear absence of other fluorescent SWCNT chiralities, compared to their parental SWCNT solution. b) These purified (6,5)-SWCNTs in 1% DOC were exchanged[8] to the LPS-bind-peptide-$(GT)_{20}$ (bLPS), which causes an absorbance shift from 985 nm to 992 nm. Incorporation into type-II-HG redshifts the absorption peak to 1001 nm.

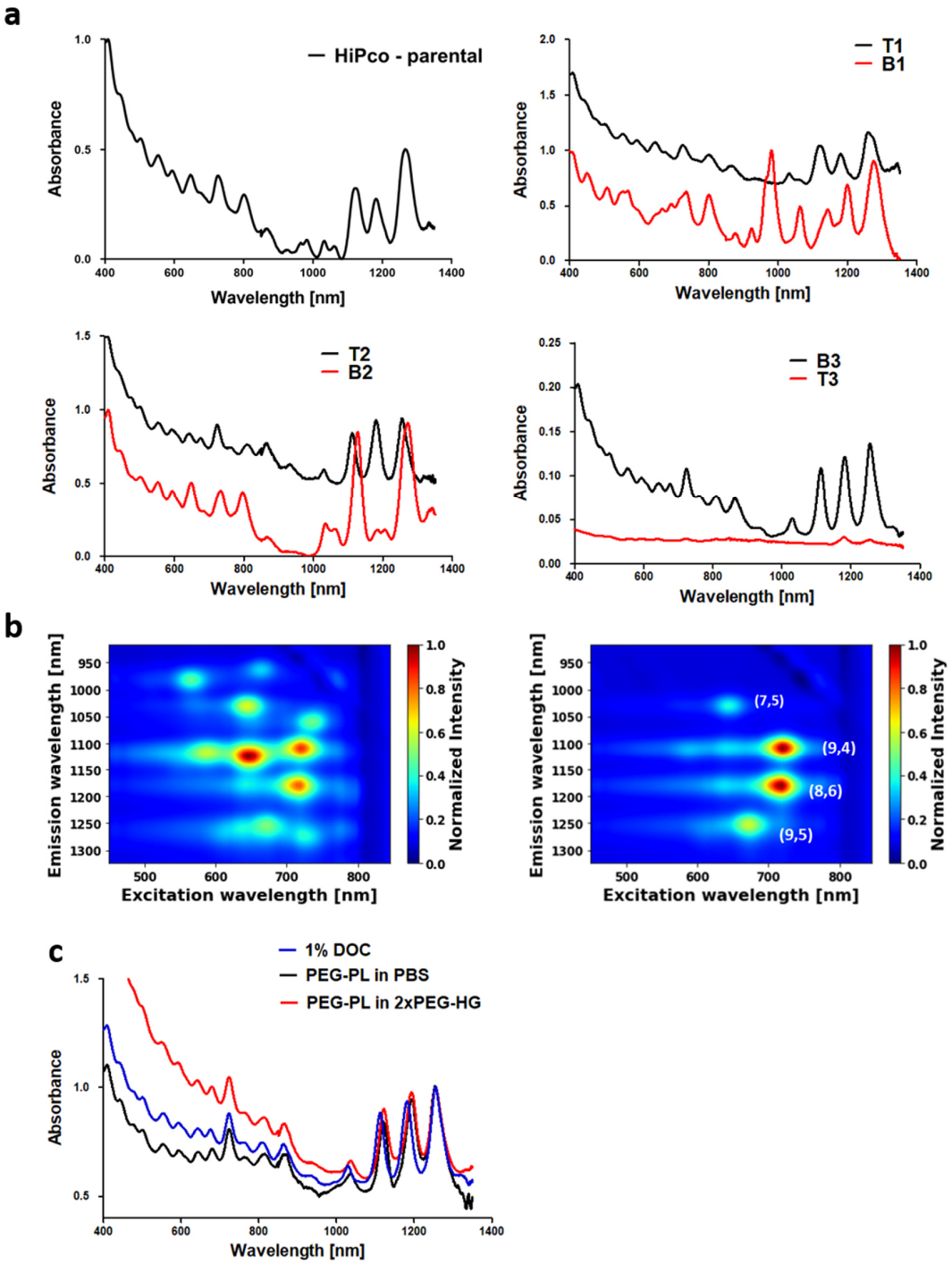

Figure S23: ATPE purification from HiPco-SWCNTs and surface exchange to PEG-PL surface modification.

a) UV-Vis-NIR absorbance spectra for the several ATPE steps. The goal was to obtain a SWCNT sample, which lacks the small diameter fluorescent SWCNTs to avoid overlap with (6,5)-SWCNTs. Most importantly, in the first separation step, the bottom phase (B1) gets enriched with SWCNTs, absorbing below 1100 nm. In the second step, another fraction of undesired, smaller diameters gets excluded, while in the third step, the purified SWCNTs are transferred and therefore concentrated to the bottom (B3) phase. b) The 2D excitation emission fluorescence spectra show three major, large SWCNT chiralities (9,4), (8,6) and (9,5), next to a smaller fraction of (7,5)-SWCNTs, compared to the parental solution, which contains multiple, also smaller diameter SWCNTs. c) Surface exchange from 1% DOC to DSPE-PEG(5000) (PEG-PL) leads to a shift in absorbance for all SWCNT chiralities, except (9,5)-SWCNTs. This separation provides access to large-diameter SWCNTs with a fluorescence emission >1100 nm.

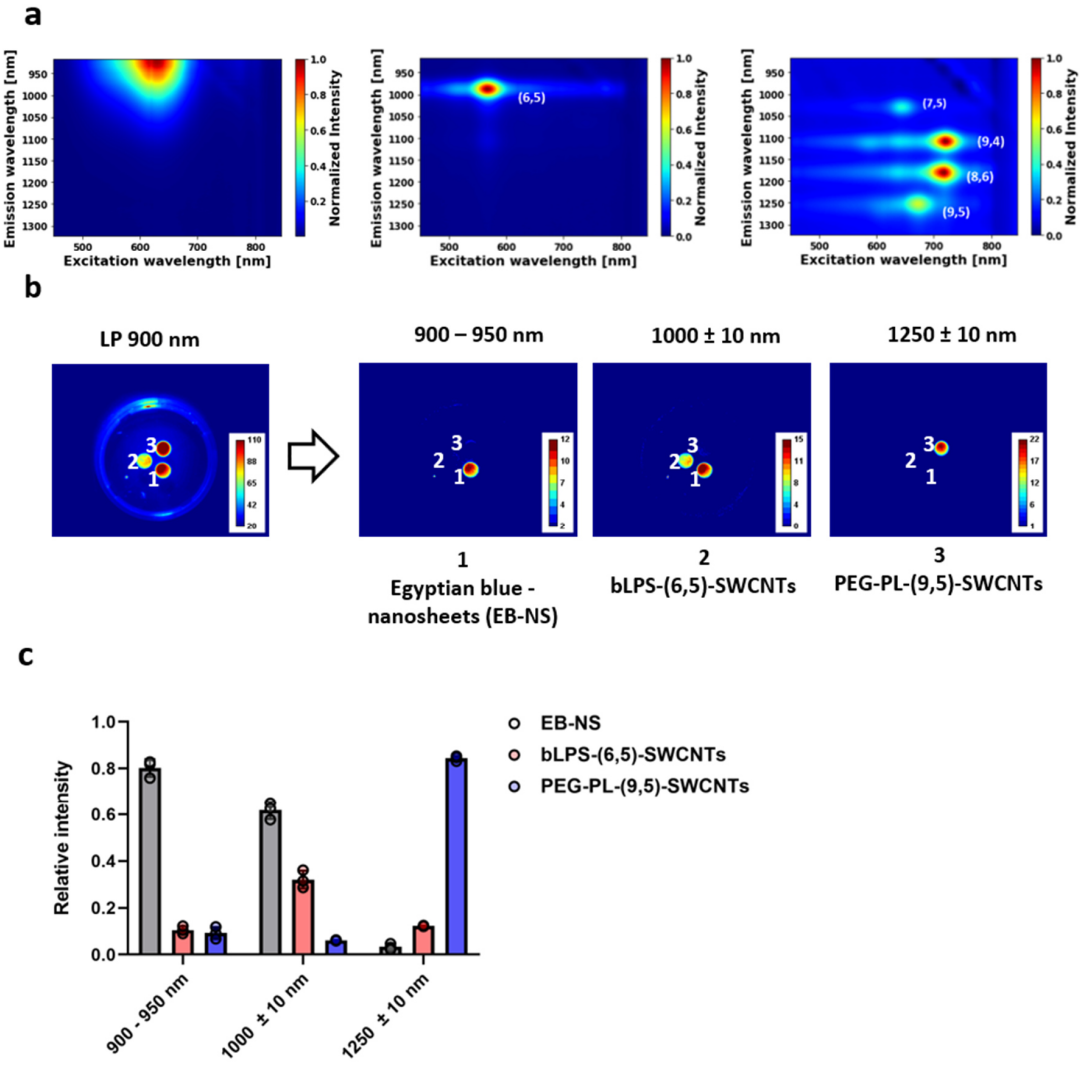

Figure S24: Characterization of sensors for hyperspectral sensing.

a) 2D spectra of the used NIR fluorophores: EB-NS, (6,5)-SWCNTs and large diameter HiPco-SWCNTs. b) NIR fluorescence stand-off image of three different HG sensors (left- 900 nm LP filter). Different used filters allow differentiation of the spectral encoded sensors, each one in a single type-II HG. c) Evaluated spectral overlap for the different HG sensors, separated by the used emission filters. EB-NS and PEG-PL-SWCNTs show a very small overlap, while the bLPS-(6,5)-SWCNTs sensor signal contains a (constant) EB-NS background (n = 3 independent experiments, mean ± SD).

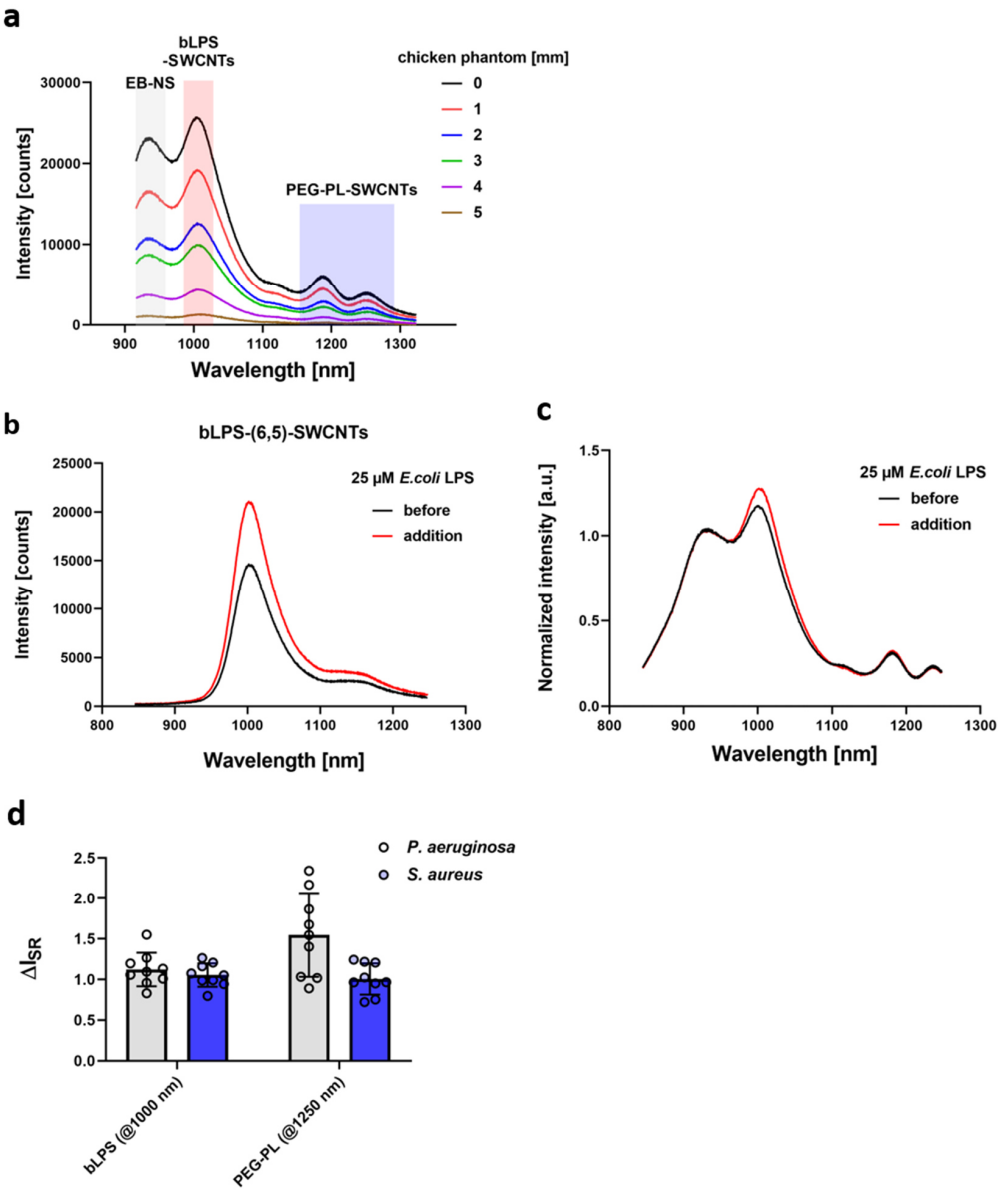

Figure S25: Hyperspectral sensing.

a) Decrease of fluorescence emission for increasing chicken phantom tissue thickness. b) Monochiral bLPS-(6,5)-SWCNT sensor reaction response to LPS addition with a fluorescence increase, which is less prominent if compared to the one from non-purified bLPS-sensors in Fig. 2. c) LPS addition to hyperspectrally encoded sensor HG leads to a small increase. d) Sensor response of the hyperspectral encoded sensors, referenced to EB-NS (900-950 nm) intensity, after 72 h of incubation with *P. aeruginosa* and *S. aureus* (n = 9 independent experiments with 3 biologically independent samples, mean ± SD) (see Fig. 5c).

Table ST5: Bacteria strains I.

Species	Designation	Gender	Age	Year	Source material
S. aureus	ATCC 29213	-	-	-	-
S. aureus	PEU3437	male	66	2019	other
S. aureus	PEU3438	male	7 mts	2019	nasal swab
Ps. aeruginosa	ATCC 27853	-	-	-	-
Ps. aeruginosa	PEU3441	male	69	2019	urine
Ps. aeruginosa	PEU3440	female	46	2019	skin swab
Ent. faecalis	ATCC 51299	-	-	-	-
Ent. faecalis	PEU3443	male	24	2019	urine
Ent. faecalis	PEU3444	female	72	2019	wound swab
S. epidermidis	ATCC 12228	-	-	-	-
S. epidermidis	PEU3432	n.r.	n.r.	2019	n.r.
E. coli	ATCC 35218	-	-	-	-
E. coli	PEU3435	n.r.	n.r.	2019	n.r.
Str. pyogenes	PEU3430	male	3	2019	skin swab (ear)
Str. pyogenes	PEU3429	n.r.	n.r.	2019	n.r.

n.r. – not recorded

Table ST6: Bacteria strains II.

Species	Strain designation*	Gender	Age	Year	Source material	Subtype	Oxa
S. epidermidis	SE19_007	male	67	2019	central venous catheter tip	ST 820	S
S. epidermidis	SE19_008	female	92	2019	blood	ST 35	R
S. epidermidis	SE19_012	male	80	2019	blood	ST 2	R
S. epidermidis	SE19_014	female	55	2019	blood	ST 297	S
S. epidermidis	SE19_016	female	39	2019	tissue (spine)	ST 23	R
S. epidermidis	SE19_018	male	3	2019	cerebrospinal fluid	ST 495	S
S. epidermidis	SE19_021	male	59	2019	central venous catheter tip	ST 966	R
S. epidermidis	SE19_023	male	47	2019	surgery (tibia)	ST 2	R
S. epidermidis	SE19_025	female	81	2019	joint punctate (hip)	ST 19	S
S. epidermidis	SE19_026	male	51	2019	punctate (inguinal region)	ST 967	S
S. epidermidis	SE19_031	female	51	2019	abscess (neck)	ST 218	S
S. epidermidis	SE19_037	male	27	2019	tissue (clavicle)	ST 968	S
S. epidermidis	SE19_039	male	79	2019	tissue (ankle joint)	ST 2	R
S. epidermidis	SE19_040	female	84	2019	tissue (elbow joint)	ST 5	R
S. epidermidis	SE19_043	male	63	2019	tissue (knee)	ST 17	S
S. epidermidis	SE19_046	female	89	2019	joint punctate (knee)	ST 969	S
S. epidermidis	SE19_058	male	73	2019	punctate (lower leg)	ST 19	S
S. epidermidis	SE19_067	male	56	2019	tissue (clavicle)	ST 19	S
S. epidermidis	SE19_073	female	88	2019	implant (upper leg)	ST 970	S
S. epidermidis	SE19_088	male	83	2019	tissue (hip)	ST 87	R
S. epidermidis	SE19_097	female	68	2019	hip prosthesis (sonication)	ST 2	R
S. epidermidis	SE19_099	male	67	2019	cerebrospinal fluid	ST 595	S
S. aureus	MRSA1297	male	n.r.	2005	swab (nose)	ST 8	R
S. aureus	MRSA1337	male	n.r.	2005	urine catheter tip	ST 6327	R
S. aureus	MRSA1796	male	54	2009	blood	ST 398	R
S. aureus	MRSA2115	female	60	2010	blood	ST 5	R
S. aureus	MRSA2418	male	73	2012	blood	ST225	R
S. aureus	MRSA2516	male	73	2012	blood	ST 225	R
S. aureus	PEU3489	male	61	2020	wound swab (lower leg)	ST 30	S
S. aureus	PEU3490	male	71	2020	wound swab (hand)	ST 22	S
S. aureus	PEU3491	female	87	2020	blood (hip infection)	ST 15	S
S. aureus	PEU3492	female	78	2020	wound swab (forearm)	ST 1	S
S. aureus	PEU3493	male	60	2020	intraoperative swab (lower leg)	ST 8	S
S. aureus	PEU3494	female	52	2020	intraoperative swab (abscess leg)	ST 8	S
S. aureus	PEU3495	female	55	2020	intraoperative swab (foot)	ST 737	S
S. aureus	PEU3496	female	79	2020	blood	ST6328	S
S. aureus	PEU3497	female	97	2020	wound swab	ST 34	S
S. aureus	PEU3498	male	50	2020	tissue (lower leg)	ST 30	S
S. aureus	PEU3499	female	53	2020	tissue (finger)	ST 15	S
S. aureus	PEU3500	male	14	2020	skin swab (leg)	ST 1	S
S. aureus	PEU3501	male	59	2020	blood	ST 9	S
S. aureus	PEU3502	female	88	2020	wound swab (finger)	ST 30	S
S. aureus	PEU3503	male	4mts	2020	other (leg)	ST 188	S

n.r. – not recorded

* Uploaded to the database pubmlst.org and accessible via the hyperlink or by searching for the strain name/designation in this column

References:

1. Wu, H. *et al.* Monitoring Plant Health with Near-Infrared Fluorescent H_2O_2 Nanosensors. *Nano Lett.* **20**, 2432–2442 (2020).
2. Selvaggio, G. *et al.* Exfoliated near infrared fluorescent silicate nanosheets for (bio)photonics. *Nat. Commun.* **11**, 1–11 (2020).
3. Nißler, R. *et al.* Quantification of the Number of Adsorbed DNA Molecules on Single-Walled Carbon Nanotubes. *J. Phys. Chem. C* **123**, 4837–4847 (2019).
4. Zheng, Y., Bachilo, S. M. & Weisman, R. B. Quenching of Single-Walled Carbon Nanotube Fluorescence by Dissolved Oxygen Reveals Selective Single-Stranded DNA Affinities. *J. Phys. Chem. Lett.* **8**, 1952–1955 (2017).
5. Bisker, G. *et al.* Protein-targeted corona phase molecular recognition. *Nat. Commun.* **7**, 1–14 (2016).
6. Bisker, G. *et al.* Insulin Detection Using a Corona Phase Molecular Recognition Site on Single-Walled Carbon Nanotubes. *ACS Sensors* **3**, 367–377 (2018).
7. Reich, S., Li, H., Garrity, O., Flavel, B. S. & Gordeev, G. Separation of Small-Diameter Single-Walled Carbon Nanotubes in One to Three Steps with Aqueous Two-Phase Extraction. *ACS Nano* **13**, 2567–2578 (2019).
8. Streit, J. K., Fagan, A. & Zheng, M. A Low Energy Route to DNA-Wrapped Carbon Nanotubes via Replacement of Bile Salt Surfactants. *Anal. Chem.* **89**, 10496–10503 (2017).

7.5 Supplementary Information Manuscript V

Monitoring Plant Health with Near-Infrared Fluorescent H_2O_2 Nanosensors

Honghong Wu[1,2+], Robert Nißler[3+], Victoria Morris[1], Niklas Herrmann[3], Peiguang Hu[1], Su-Ji Jeon[1], Sebastian Kruss[3*] and Juan Pablo Giraldo[1*]

[1]Department of Botany and Plant Sciences, University of California, Riverside, California 92521, United States
[2]College of Plant Science and Technology, Huazhong Agricultural University, Wuhan 430070, China
[3]Institute of Physical Chemistry, Göttingen University, Göttingen 37077, Germany

[+]These authors contributed equally to this paper.
[*] Corresponding author

Nano Letters, **2020**, 20, 4, 2432-2442
DOI: 10.1021/acs.nanolett.9b05159

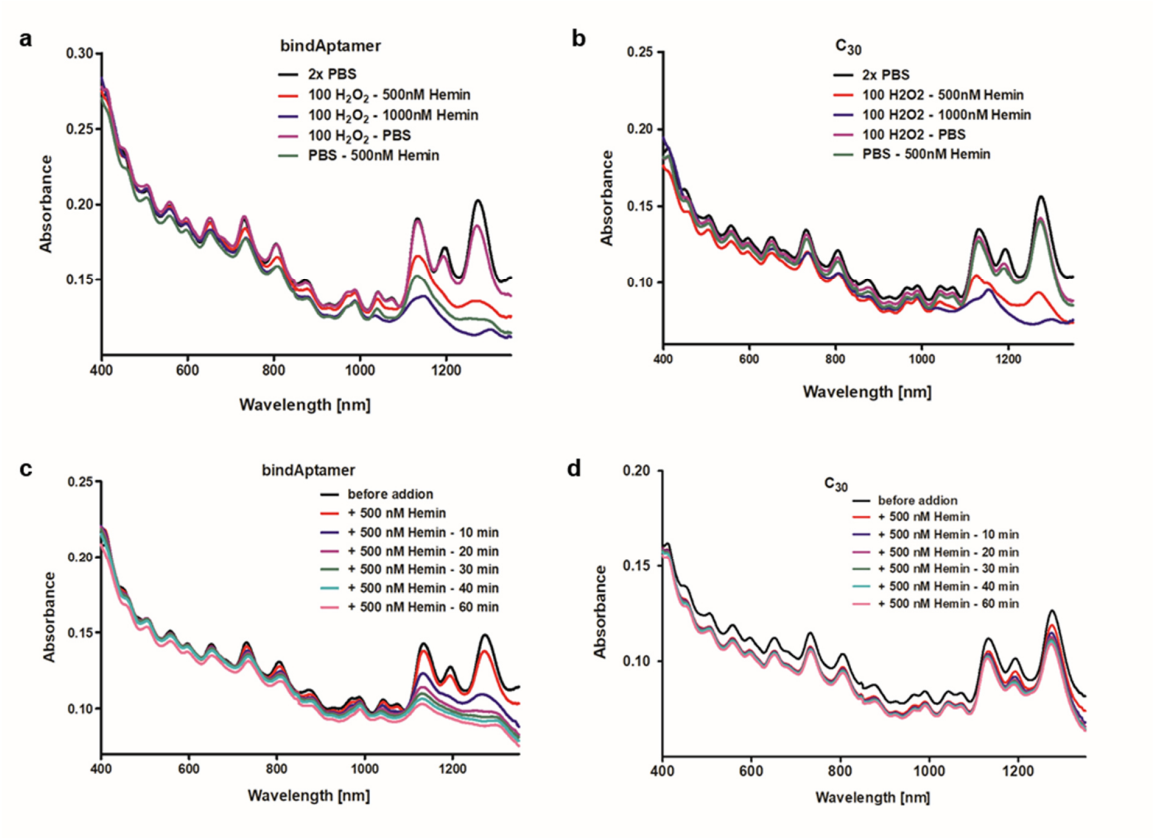

Figure S1: Absorbance spectra of larger diameter (HiPco) SWCNTs in the presence of hemin and H_2O_2.

a) HeAptDNA-HiPco-SWCNTs after 24 h incubation with varying hemin concentrations and 100 µM H_2O_2. The decrease of absorbance features of larger SWCNT chiralites is more prominent when using HiPco (Nano Integris HiPco Raw SWCNTs) samples. b) Complementary experiment with C_{30}–HiPco-SWCNTs shows a similar effect on larger chiralities upon exposure to H_2O_2 and hemin, but not after solely hemin addition. c) Absorbance spectra of HeAptDNA-HiPco-SWCNTs after addition of 500 nM Hemin. A strong reduction during the first 10 min is detectable and increases during the timeframe of the experiment. This shows that the binding of hemin to larger SWCNT chiralites affects their photophysics and stability, which makes them less suitable for H_2O_2 sensing. d) C_{30}–HiPco-SWCNTs having no binding affinity to hemin show no reduction of absorbance features.

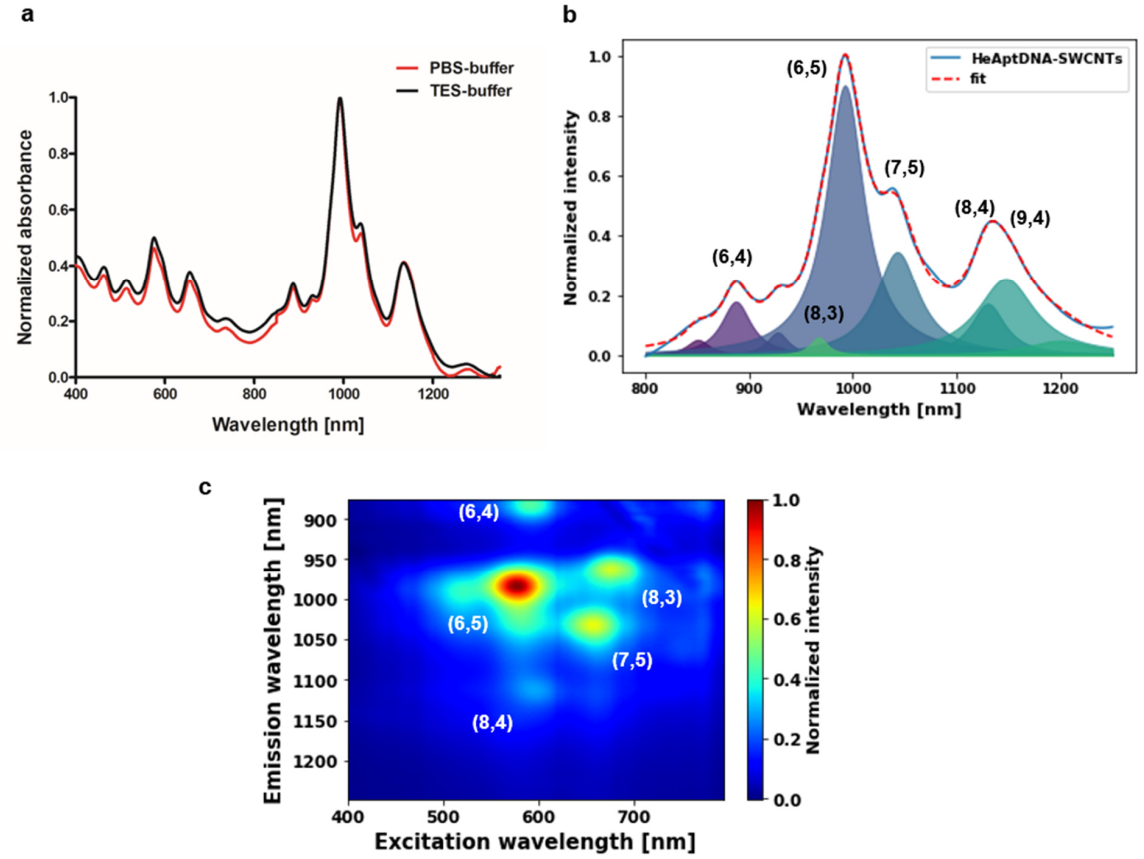

Figure S2: Optical characterization of HeAptDNA-SWCNT.

a) The distinct absorption features of (6,5)-enriched SWCNTs indicate well-dispersed SWCNTs with a maximum peak at 992.4 nm for (6,5)-SWCNTs, both in PBS and TES buffer. b) Fitted absorption of E_{11} transitions of the HeAptDNA-SWCNTs show minor chirality fractions of (6,4), (8,3), (7,5), (8,4), and (9,4) SWCNTs. c) 2D excitation-emission spectra of HeAptDNA-SWCNTs indicate the most prominent nIR emission from the (6,5) chirality, followed by (7,5), (8,3), and (6,4)-SWCNT chiralities with lower nIR intensity.

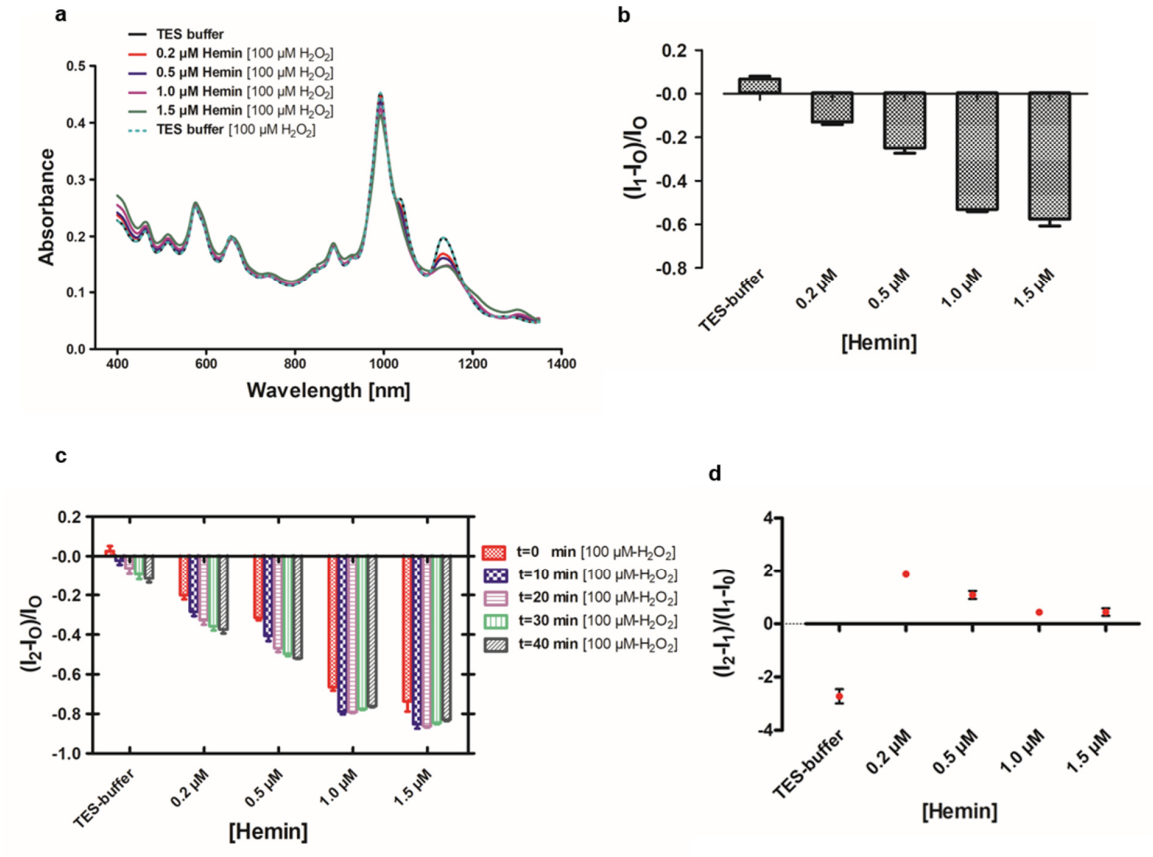

Figure S3: Advanced *in vitro* characterization of HeAptDNA-SWCNT based H_2O_2 sensors.

a) Absorbance spectra of HeAptDNA-SWCNTs having different hemin concentrations in response to 100 µM H_2O_2. The absorbance of some larger SWCNT chiralites (> 1100 nm) slightly decreases in the presence of hemin and H_2O_2 while (6,5)-SWNCTs features are preserved, indicating high stability. b) Fluorescence response of 2 nM HeAptDNA-(6,5)-SWCNTs to different hemin concentrations (n=3, error = SD). A higher hemin concentration leads to a stronger SWCNT fluorescence reduction which can hamper *in vivo* imaging in plant tissue due to low fluorescence signal. c) Fluorescence response of 2 nM HeAptDNA-SWCNTs with different hemin concentrations to 100 µM H_2O_2. The $(I_2\text{-}Io)/Io$ is a relative value comparing the initial fluorescence emission (Io) with quenching events due to both hemin and H_2O_2 addition (I_2) (n=3, error = SD). d) Ratio between the hemin (I_1) and H_2O_2 (I_2) quenching events $(I_2\text{-}I_1)/(I_1\text{-}I_0)$ reveals that concentrations between 0.2 and 0.5 µM hemin are best suitable for H_2O_2 sensing (n=3, error = SD).

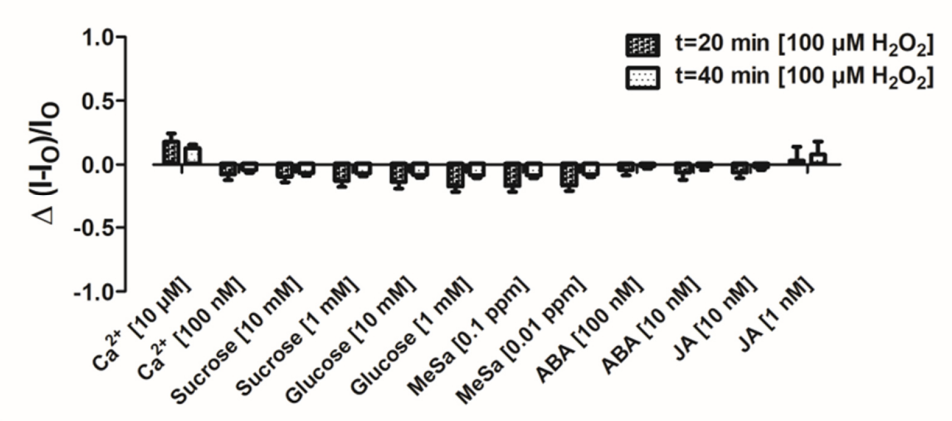

Figure S4: Assessment of the influence of plant stress induced metabolites on H_2O_2 sensing performance of HeAptDNA-SWCNT.

The $\Delta (I-I_0)/I_0$ describes the difference in nIR emission intensity response to H_2O_2 between HeAptDNA-SWCNTs (2 nM) in TES-buffer and in the presence of plant metabolites associated with stress (Ca^{2+}, sucrose, glucose, MeSa - Methyl salicylate, ABA - Abscisic acid, JA - Jasmonic acid). A positive $\Delta (I-I_0)/I_0$ can be interpreted as a reduction in sensor fluorescence response whereas a negative $\Delta (I-I_0)/I_0$ indicates a stronger fluorescence response to H_2O_2 sensing. The effect of plant metabolites during H_2O_2 sensing is less prominent after 40 min (n=3; error = SD).

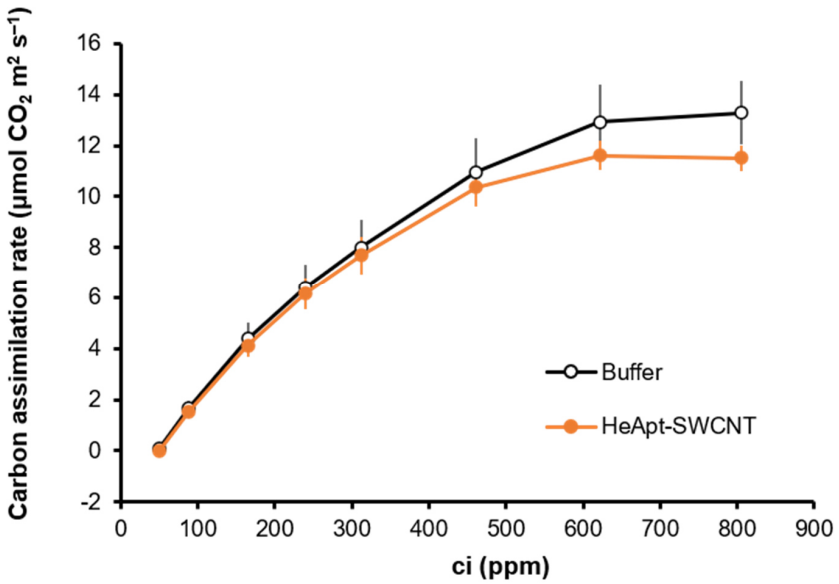

Figure S5: No impact of HeAptDNA-SWCNT sensors on plant photosynthesis.

Carbon assimilation rates under varied internal CO_2 concentrations (ci) in leaves infused with buffer (control) or HeAptDNA-SWCNT. No statistical differences in carbon assimilation rates were observed between controls and nanosensor treated plants at each CO_2 level ($p < 0.05$, Student's t-test). Mean ± SE (n = 6).

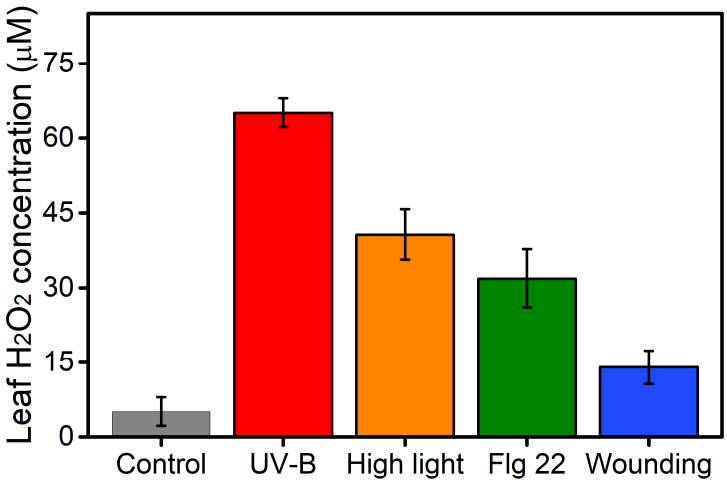

Figure S6 | Leaf H_2O_2 content in leaves of plants under stress.

Determination of H_2O_2 concentration in leaves by a quantitative peroxide assay from plants exposed to UV-B light (365 nm, 90 min), high light (1800 µmol m^{-2} s^{-1} of photosynthetic active radiation, 90 min), flg 22 peptide (10 µM, 60 min), leaf wounding, and no stress (controls). Significant differences in leaf H_2O_2 content were observed between control leaves and UV-B light, high light, and flg 22 but not compared to leaf wounding ($p < 0.05$, Student's t-test). Mean ± SE (n = 3).

7.6 Supplementary Information Manuscript VI

Detection and imaging of the plant pathogen response by near infrared fluorescent polyphenol sensors

Robert Nißler[1,2], Andrea T. Müller[3], Frederike Dohrman[2], Larissa Kurth[2], Han Li[4], Eric G. Cosio[5], Benjamin S. Flavel[4], Juan Pablo Giraldo[6], Axel Mithöfer[3] and Sebastian Kruss[1,2,7*]

[1]Physical Chemistry II, Bochum University, 44801 Bochum, Germany
[2]Institute of Physical Chemistry, Göttingen University, Göttingen 37077, Germany
[3]Research Group Plant Defense Physiology, Max Planck Institute for Chemical Ecology, 07745 Jena, Germany
[4]Institute of Nanotechnology, Karlsruhe Institute of Technology (KIT), 76344 Eggenstein-Leopoldshafen, Germany
[5]Institute for Nature Earth and Energy (INTE-PUCP), Pontifical Catholic University of Peru, San Miguel 15088, Lima, Peru
[6]Department of Botany and Plant Sciences, University of California, Riverside, California 92521, United States
[7]Fraunhofer Institute for Microelectronic Circuits and Systems, 47057 Duisburg, Germany

[*] Corresponding author

Angewandte Chemie International Edition, **2021**
DOI: 10.1002/anie.202108373

Experimental Procedures

All materials, if not otherwise stated, were purchased from Sigma Aldrich.

SWCNT surface modification

(6,5)-chirality enriched CoMoCat SWCNTs (Sigma-Aldrich, product no. 773735) were modified with varying single-stranded (ss)DNA sequences such as $(GT)_{10}$, $(CT)_{15}$, $(GA)_{15}$, $(GC)_{15}$, $(AT)_{15}$, $(A)_{30}$, $(T)_{30}$ and $(C)_{30}$ (oligonucleotide sequences purchased by Sigma Aldrich) following a previously described protocol.[1] In short, 100 µL ssDNA (2 mg/mL in H_2O) were mixed with 100 µL 2xPBS and 100 µL SWCNTs (2 mg/mL in PBS), tip-sonicated for 15 min @ 30% amplitude (36 W output power, Fisher Scientific model 120 Sonic Dismembrator) and centrifuged 2x 30 min @ 16100x g.
Phospholipid-PEG-SWCNTs were assembled by performing dialysis of sodium cholate suspended SWCNTs.[2] Here, 2 mg SWCNTs (CoMoCat (Sigma-Aldrich, product no. 773735) or HiPco (NanoIntegris HiPco Raw SWCNTs)) were tip-sonicated in 750 µL sodium cholate (10 mg/mL in PBS). After centrifugation (2x 30 min @ 16100x g), 200 µL supernatant was mixed with 800 µL sodium cholate (12 mg/mL) containing 2 mg 18:0 PEG5000 PE (1,2-distearoyl-sn-glycero-3-phosphoethanolamine-N-[methoxy(polyethylene glycol)-5000]) or 2 mg DSPE-PEG(2000) Amine (1,2-distearoyl-sn-glycero-3-phosphoethanolamine-N-[amino(polyethylene glycol)-2000]), Avanti Lipids). The mixture was transferred to a 1 kDa dialysis bag (Spectra/Por®, Spectrum Laboratories Inc.) and dialyzed for several days (>5 d) against 1xPBS. The colloidally stable PEG-PL-SWCNTs sensors were obtained after centrifugation for 30 min @ 16100x *g*.

NIR spectroscopy

Absorption spectra were acquired with a JASCO V-670 device from 400 to 1350 nm in 0.2 nm steps in a 10 mm path glass-cuvette. 1D-NIR fluorescence spectra were measured with a Shamrock 193i spectrometer (Andor Technology Ltd., Belfast, Northern Ireland) connected to a IX73 Microscope (Olympus, Tokyo, Japan). Excitation was performed with a gem 561 laser (Laser Quantum, Stockport, UK) or a 785 nm laser (iBeam smart WS CW Laser). 2D excitation emission spectra were collected in the same setup as above with a Monochromator MSH150, equipped with a LSE341 light source (LOT-Quantum Design GmbH, Darmstadt, Germany) as excitation source.
NIR fluorescence analyte response measurements were performed, by using 180 µL of a 0.2 nM ssDNA-SWCNT solution (calculation of molar nanotube concentration based on an approach by Schöppler et al.[3]) or 180 µL of a 0.1 absorbance (measured at E_{11} transition, ~ 995 nm) PEG-PL-SWCNT solution. NIR fluorescence spectra were acquired at 150 mW excitation (561 nm) and 3 s integration time and 200 mW (785 nm) and 10 s integration time. Dose-response measurements were fitted with a one site – specific binding fit or with a hyperbolic fit (GraphPad Prism 9) using $Y = B_{max} * X / (K_d + X)$ with X = concentration of the analyte; Y = specific binding; B_{max} = Maximum binding and K_d = dissociation constant.

SWCNT separation

Separation of (6,5)-SWCNTs was performed according to a previously reported aqueous two-phase extraction (ATPE) protocol from Li *et al*.[4] Briefly, in a three step approach SWCNT chiralities were separated between two aqueous phases, containing dextran (MW 70000 Da, 4% m/m) and PEG (MW 6000 Da, 8% m/m) through varying pH-values *via* HCl addition. The final B3 (bottom)-phase yielded monochiral (6,5)-SWCNTs, which were dialyzed against a 1% (w/v) DOC solution. After further surfactant exchange to sodium cholate, a similar dialysis approach for PEG-PL was performed as described before.[2,5] Separation of (7,6)-SWCNTs and their surface modification to ssDNA was performed following a recently published protocol.[5]

NIR stand-off imaging

NIR stand-off detection was performed with a custom made, portable set-up[6], using a XEVA (Xenics, Leuven Belgium) NIR InGaAs camera (Kowa objective, f = 25 mm/F1.4) with a 900 nm long pass filter (FEL0900, ThorLabs) and a white light source (UHPLCC-01, UHP-LED-white, Prizmatix) equipped with a 700 nm short pass filter (FESH0700, ThorLabs) for excitation. Stand-off distance for NIR fluorescence detection for the seedling-agar experiments (3 s integration time, light intensity 48 $mWcm^{-2}$) was 20 cm. Light intensity was measured at 570 nm with a power meter (PM16-121, ThorLabs). Hyperspectral imaging was performed with additional 950 nm (FEL0950, ThorLabs) and 1100 nm (FEL1100, ThorLabs) long pass filters and 5 s integration time.

Plant material and classical polyphenol detection
Plants and Insects

Tococa guianensis plants were raised from cuttings in a glasshouse (day, 23-25°C; night, 16-18°C; 60-70% rel. humidity; 16 h/8 h light/dark cycle). Once the plants were big enough, they were potted into a 400 mL pot filled with a mixture of 1/4 Klasmann potting substrate (Klasmann-Deilmann, Geeste, Germany), 1/4 Latvian white peat, 1/4 pine bark (7-15 mm), 1/8 sand and 1/8 Legan (5-7 mm) and inoculated with BioMyc™ Vital Mykorrhiza **(**BioMyc, Brandenburg/Havel, Germany). Experiments were performed with one-year-old Tococa plants.
Field studies on *Tococa quadrialata* were conducted in the Tambopata Reserve [12° 50’ 10’’ S, 69° 17’ 34 ‘’ W] close to the Explorer`s Inn lodge in the lowland Amazon basin in Peru at an elevation a.s.l. 210 m. The average annual rainfall is 2335 mm with a dry season

from June until October. The maximum monthly temperature is around 30° C whereas the monthly minimum is around 19 °C. The subpopulation of *Tococa quadrialata* used for this study was found alongside a small path. All these myrmecophytic plants were colonized by ants of the genus *Azteca spec.* (subfamily Dolichoderinae). The experiment was performed and leaves were sampled when the plants were on average 56 cm tall and had 14 leaves.

Spodoptera littoralis larvae used for the greenhouse herbivore experiment were hatched from eggs and reared on an agar-based optimal diet at 23°C–25°C with 8 h light/16 h dark cycles.[7] Third instar *S. littoralis* larvae were chosen for the herbivory experiment and starved 24 h prior to plant feeding. For the field experiments, *Spodoptera* larvae of third to fifth instar were collected from a local area.

Herbivore treatment

One leaf of the second pair of fully expanded leaves was enclosed with a perforated PET bag. Two *Spodoptera* larvae were released on the bagged leaves and allowed to feed for 24 h, whereas the control leaves were enclosed with an empty bag for 24 h. At the end of the experiment, these leaves were excised and photographed to determine the leaf damage, domatia were removed and the leaves flash-frozen in liquid nitrogen. The field samples were lyophilized for the transport to Germany and subsequent chemical analyses.

Cell culture of *Glycine max*

Soybean (*Glycine max* L. cv. Harosoy 63) cell suspension cultures were cultivated according to Fliegmann et al.[8] Briefly, cells were kept in the dark at 26 °C under shaking conditions (110 rpm) and were subcultured in fresh medium every 7 days. To document the accumulation of phenolic compounds with age, subcultures were harvested after 2, 7 and 14 days. More specifically, the cultures were filtrated utilizing Whatman® Grad 1 filter paper (GE Healthcare, Chicago, IL, USA) and the filtrates were used for further analyses.

For the induction of isoflavonoid production, soybean cell suspension cultures were sub-cultured after 5 days in fresh medium (6 g fresh mass per 40 ml medium) and after another 2 days of growth, 1 mL of suspension culture was carefully transferred to each well of a 24 well plate **(**CELLSTAR® 662102, Greiner Bio-One, Kremsmünster, Austria). 10 µL of 50 mg/mL raw elicitor isolated from the cell walls of the phytopathogenic oomycete *Phytophthora sojae* in ddH_2O was added to half of the wells. Wells to which 10 µL of pure ddH_2O were added served as control treatment. The plate was kept in the dark at room temperature under constant shaking conditions (100 rpm) for 4 days. The suspensions were then carefully transferred to 1.5 mL Eppendorf tubes (Eppendorf, Hamburg, Germany), cells spinned down (5000 rpm, 4 °C, 20 min) and the supernatant transferred to a new vial for subsequent chemical analysis. As a negative control, six 1 mL samples of the starting culture were transferred to 1.5 mL Eppendorf tubes instead of the well plate and harvested immediately. 20 µL of the cell suspension supernatant was directly added to the nanosensors for polyphenol detection.

Extraction of ellagitannins and anthocyanins from *Tococa*

1 g freeze-dried, finely ground powder of *Tococa* leaves was extracted five times with 10 mL of acetone/water (7/3, v/v) containing 0.1 % (m/v) ascorbic acid to obtain the crude extract. Acetone was evaporated below 40 °C with a rotary evaporator and the remaining water phase was subjected to SPE using a CHROMABOND® HR-X column (6 mL, 500 mg; Macherey-Nagel, Düren, Germany). After the equilibration of the column with methanol and water, the extract was applied to the column and different fractions were subsequently eluted with water, increasing concentrations of acetone/water (1/1, 3/1, *v*/*v*) and acetone. Fraction volume was 6 mL per eluent, whereas three fractions per one eluent were collected. Whenever it was possible to obtain smaller fractions of similar chemical compounds based on visual hints, fractions smaller than 6 mL were collected. Fractions were analyzed by a diode array detector (DAD) system after separation by Agilent 1100 HPLC (Agilent Technologies, Santa Clara, CA, USA) using a Luna® Phenyl-Hexyl 100 Å (4.6 × 150 mm, 5 µm, Phenomenex, Aschaffenburg, Germany) column. The binary mobile phase consisted of acetonitrile (A) and 0.5 % trifluoroacetic acid in water (B) at the flow rate of 1 mL min^{-1}. The elution profile was: 0 – 18 min, 5 – 41 % A in B; 18 – 18.1 min, 41 – 100 % A in B; 18.1 – 21 min 100 % A in B; 21 – 21.1 min 100 – 5 % A in B; 22 – 26 min 5 % A. Absorbance was detected at 254 nm, 270 nm, 280 nm and 520 nm. 1 mL of the fraction of interest was dried under nitrogen stream to yield 38 mg of a red glittering solid residue enriched in ellagitannins and anthocyanins. This fraction was dissolved in MeOH and diluted to the desired concentration. 2 µL of this solution was added to the nanosensor solution for polyphenol sensing.

Further polyphenolic compounds

Anthocyanidins used for nanosensor screening were extracted from dried hibiscus (purchased in a local store), following a described protocol.[9] Trihydroxypterocarpan (THP) were extracted from soybean according to previous literature.[10,11]

Targeted analysis of herbivore treated leaves

40 mg of freeze-dried ground leaf powder or 100 mg of frozen fresh leaf powder ground in liquid nitrogen were extracted with 1 mL of methanol (MeOH) containing 10 ng/mL trifluoromethyl-cinnamic acid as an internal standard. The homogenate was mixed for 30 min and centrifuged at 16000 rcf for 10 min. The supernatant was used for subsequent analysis. Compound separation and targeted analysis was achieved by LC-MS/MS as described in Lackus et al.[12], using multiple reaction monitoring to monitor analyte parent ion → product ion formation for detection of the phenolic compounds (Catechin: *m*/*z* 289→109; DP: -30 V CE: -32 V; Apigenin: *m*/*z* 269→117, DP: -30 V, CE: -44 V; TMCA (internal standard): *m*/*z* 215 → 171 DP: - 30 V, CE: -18 V).

Chromatograms were analyzed using the software Analyst 1.6.3 (Applied Biosystems) with automated peak integration. The internal standard was used to normalize the peak areas. 2 µL of these MeOH extracts were added to the nanosensor solution for polyphenol sensing.

High-resolution mass spectrometry of *Tococa* and soybean samples

The methanolic extracts and interesting fractions of *Tococa* and the aqueous supernatants of the soybean cell cultures were furthermore subjected to high-resolution mass spectrometry in order to obtain the accurate masses of the compounds. Samples were analyzed with a Dionex Ultimate 3000 RS Pump system (Agilent) coupled to a timsTOF mass spectrometer with a turbospray ion source (Bruker Daltonics, Bremen, Germany). Separation was achieved as described by Lackus et al.[12] The mass spectrometer was successively operated in negative and positive ionization mode scanning a mass range from *m*/*z* 50 to 1,500 with the capillary voltage set at 4,500 V (positive mode) or 3500 V (negative mode), respectively. Nitrogen served as drying gas (8 L/min, 280°C) and nebulizer gas (2.8 bar). As internal calibrators, sodium formate adducts were used. Compass Hystar 3.2 (Bruker) was used for data acquisition and MetaboScape (Bruker) for data processing, sum formula calculation, structure prediction and preliminary statistical analysis. Additionally, SciFinder (https://scifinder.cas.org) was used for structure prediction and compound identification. Peak integration of extracted ion chromatograms corresponding to known soybean compounds was achieved with Compass Quant Analysis (Bruker).

Total phenol content quantification

An established protocol[13] enables the colorimetric quantification of the total phenol content. In short, 100 µL sample were mixed with 200 µL Folin–Ciocalteu reagent (10 %; *v*/*v*) and 800 µL Na_2CO_3 (700 mM) and left for reaction (1.5 h at RT). Reaction tubes were shortly centrifuged (2 min @ 16.100x *g*) and subsequently the absorbance of the solution was measured at 765 nm with a JASCO V-670 device. Soybean cultures were directly used, while *Tococa* extracts were diluted accordingly, to not exceed the linear range of the calibration.

Incorporation of *G. max* seedlings into NIR fluorescent agar

PEG-PL-SWCNTs sensors were incorporated into 5 mL 0.4 % agarose culture medium (containing Murashige & Skoog (MS) media) and casted into a sterile petri dish (Ø 8.5 cm), yielding a final SWCNT absorbance of 0.3 at the E_{11} transition at ~995 nm. Further UV sterilization was performed for 15 min (UV-Kontaktlampe Chroma41, 254 nm, Vetter GmbH) before placing 3-days old seedlings of *Glycine max* L. cv. Maraquise or cv. Edamame Green Shell onto the sensor-agar. The root of the seedling was covered with 10 mL 0.8 % agarose MS medium. Polyphenol sensing experiments were performed after >12 h post seedling incorporation.

Polyphenol visualization

Seedlings were challenged with 50 µL (10 mg/mL) raw-elicitor of *Phytophthora sojae*, or as a control 50 µL ddH_2O, after wounding the root tissue with a 0.4 mm cannula. Automated image recoding was performed for every 30 min over 10 h and subsequently after 24 h, using 3 s integration time. Excitation was synchronized in the same way, whereby only for NIR fluorescence acquisition the illumination system was turned on for 2 min.

Image analysis

NIR images were acquired with Xeneth Software 2.7 (Xenics, Leuven Belgium) and converted in ImageJ (1.51k) into 8-bit data format. Differential NIR fluorescent images (I/I_0) were obtained by dividing the time series of the recorded images (I) by the first image (I_0), while using a masked root tissue region. The intensity changes in the 32-bit images were then further analyzed with a 5-pixel with line profile or using a 500-pixel large area, close to the challenged root position.
Hyperspectral images were analyzed by subtracting the corresponding 1100 nm long pass filter images from the ones acquired with a 900 or 950 nm long pass filter, to obtain the fluorescence intensities of the (6,5)-SWCNTs which emit at ~ 1000 nm. Fluorescence emission of (7,6)-SWCNTs were detected with a > 1100 nm long pass filter.

Results and Discussion

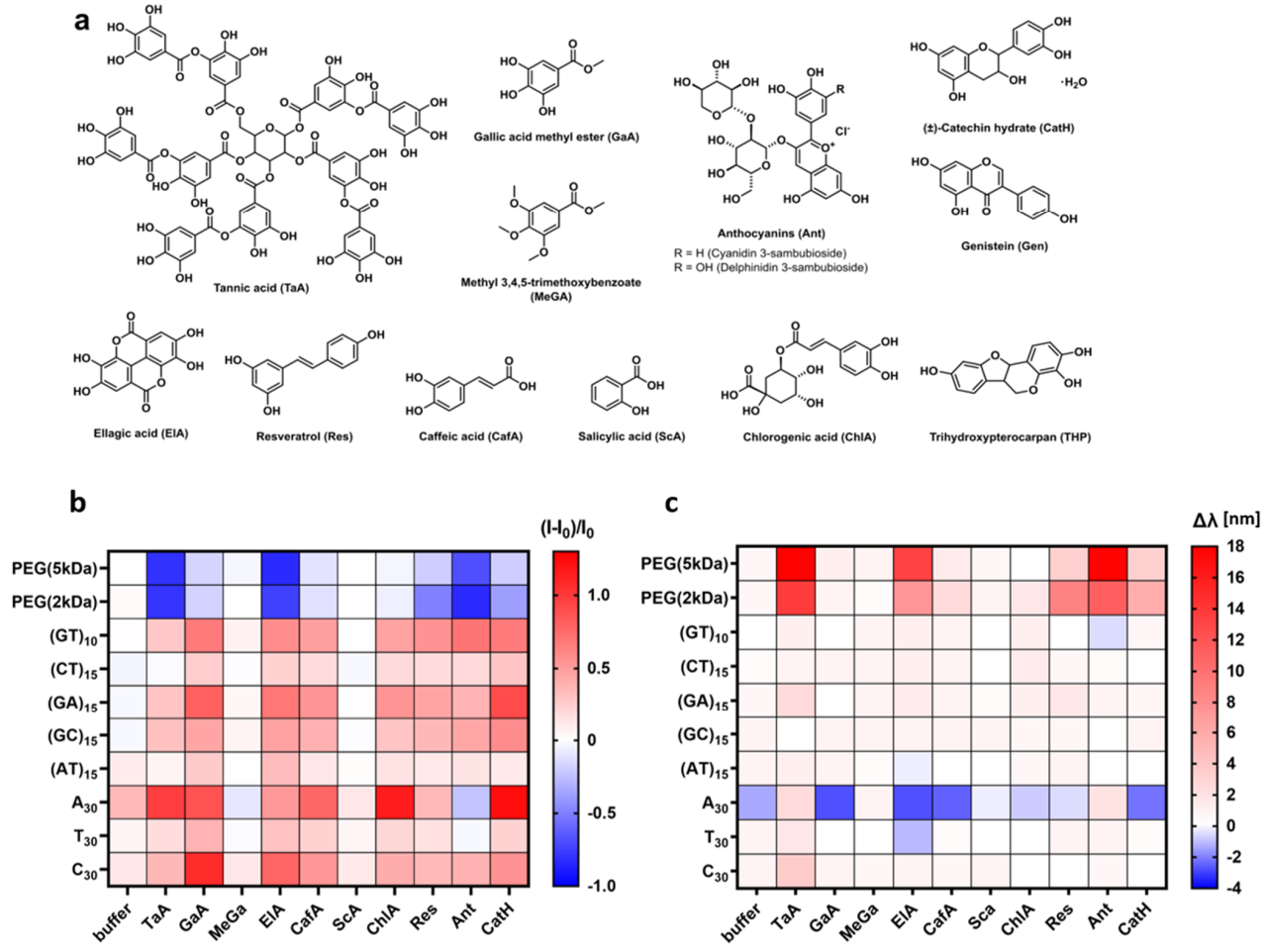

Figure S1: Sensor screening for plant polyphenol detection.

a) Chemical structures of the used polyphenolic compounds. b) Fluorescence changes ($I-I_0/I_0$) of all SWCNT-based sensors with different surface modifications, in response to different plant polyphenols summarized in a heatmap (mean, n = 3). Shades of blue indicate fluorescence decrease and shades of red fluorescence increase, within the indicated range. c) Emission wavelength changes ($\Delta\lambda$) of all SWCNT sensors after polyphenol addition. Shades of blue indicate hypsochromic shift and shades of red bathochromic shift, within the indicated range (polyphenol concentration = 10 µM; TaA = 1 µM).
ssDNA-SWCNTs responded with a general pattern of fluorescence increase, however, showing distinct differences in sensing magnitudes. PEG-PL-SWCNTs on the other side responded with a fluorescence decrease. Note: It is known, that A-rich ssDNA-SWCNTs exhibit decreased colloidal stability over time[5], which affects aggregation/quenching state, biassing the total emission intensity and sensors response. Moreover, a variety of molecules can modulate their photoluminescence, which makes this particular ssDNA modification less suitable for further sensor design. For the sake of completeness, we showed these screening results, but furthermore excluded A_{30}-SWCNTs for final polyphenol sensor development. To exclude pH or ionic strengths related sensing effects[14], all experiments were performed under buffered conditions. $(AT)_{15}$-ssDNA surface modification seem less sensitive to the tested polyphenolic compounds, which would make them a suitable reference material for multichiral sensing.

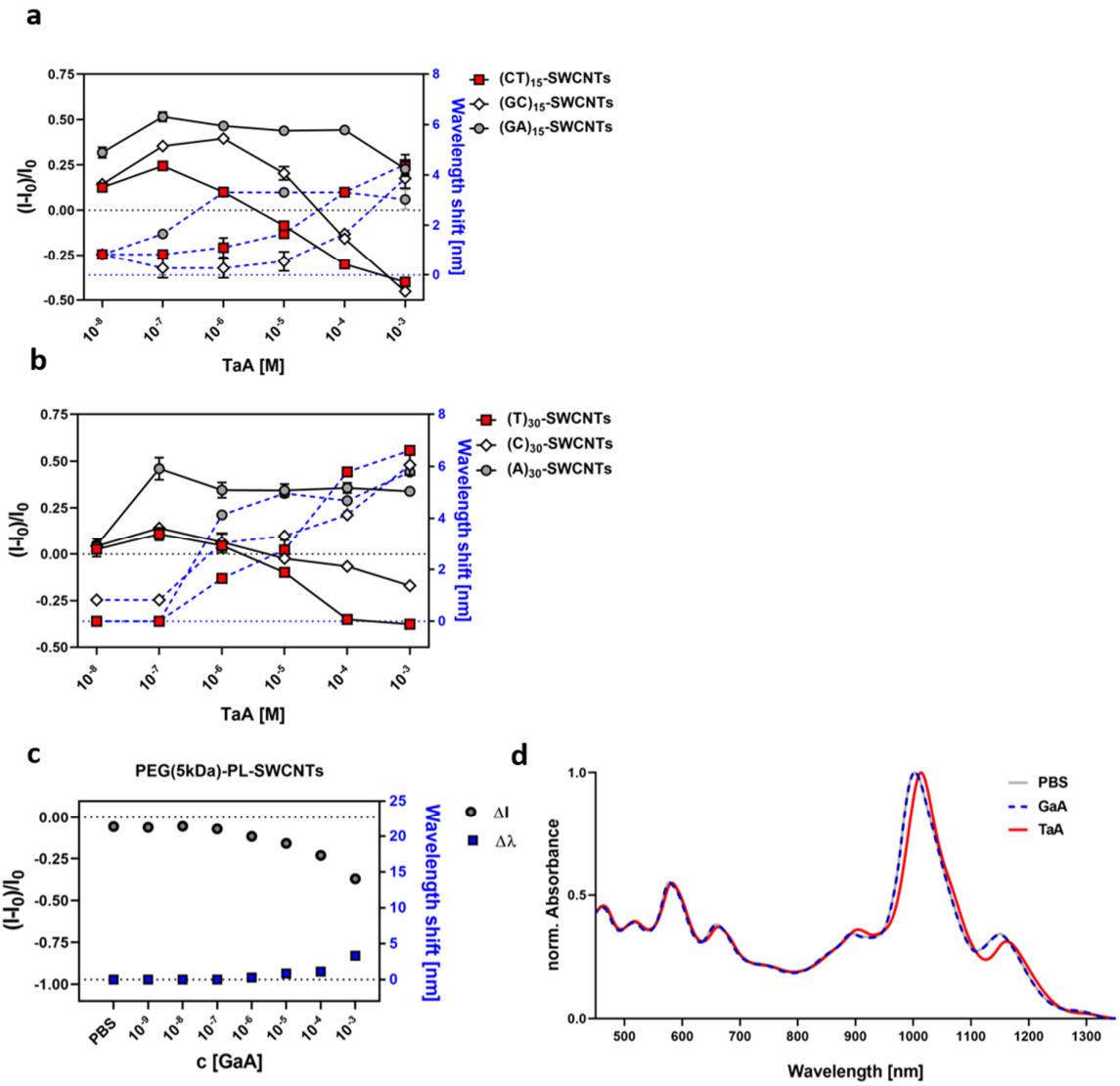

Figure S2: Sensing of tannic acid (TaA).

a) and b) Concentration dependent NIR fluorescence shifts of multiple ssDNA-SWCNTs in response to tannic acid. Intensity (black line) increases in the nM range, while higher concentrations lead to decreased fluorescence emissions, whereas wavelengths shift (dotted blue line) increases with TaA concentration (mean ± SD, n = 3). This observation could be the result of two different principles of interaction. The increase could be similar to the one known for dihydroxy group containing catecholamines[3] (like dopamine), so polyphenols could push the DNA-phosphate backbone closer to the SWCNT surface. At higher concentrations, polyphenol could lead to colloidal instability of the polymer-SWCNT complex, as known for PEG or protein precipitations[4], resulting in the fluorescence decrease. Since the fluorescence modulation from ssDNA-SWCNTs (e.g. $(CT)_{15}$- and $(GA)_{15}$-SWCNTs) were observed with quite different magnitudes, these types of interface modifications were excluded as further polyphenol-sensitive probes. c) GaA addition only slightly alternates the emission of PEG-PL-SWCNTs (mean ± SD, n = 3), indicating that the three-dimensional architecture of structurally large polyphenols contributes significantly to the sensing mechanism. d) TaA interaction with PEG(5kDa)-PL-SWCNTs causes a ~10 nm bathochromic shift in E_{11} absorbance maximum, while GaA does not cause a spectral shift (TaA, GaA = 10 µM). The absorption at the excitation wavelength (E_{22} transition), however, just showed a minor shift. Therefore, the observed shifts at the E_{11} transition could correlate partly with the detected energy differences in fluorescence emission. However, we assume, that interaction of PEG-PL-SWCNTs with certain polyphenols will increase the local dialectic constant around the SWCNTs, thus causing the red-shifted emission features.

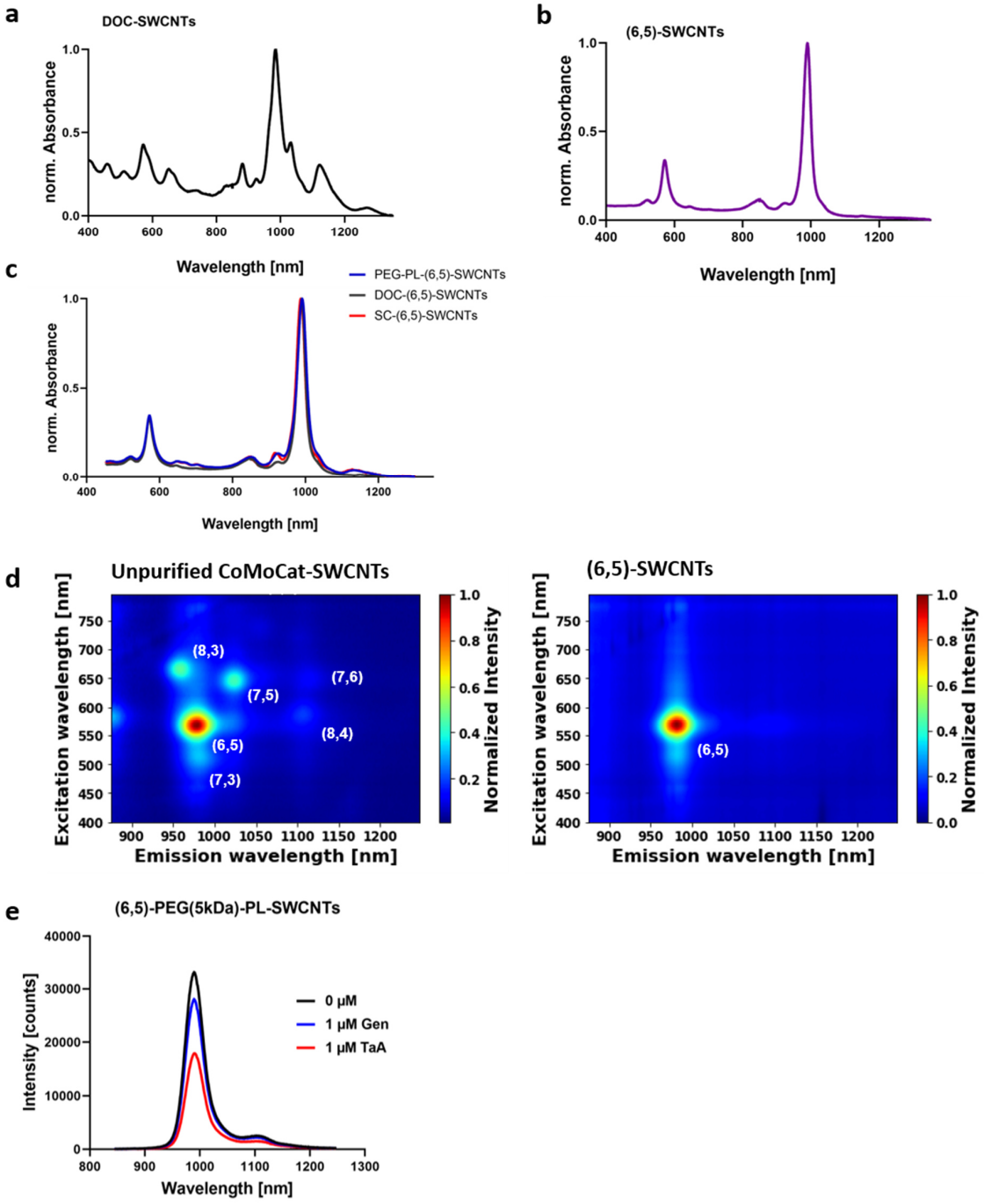

Figure S3: SWCNT purification to obtain monochiral PEG-PL-(6,5)-SWCNT sensors.

a) Normalized absorbance spectra of unpurified CoMoCat-SWCNTs dispersed in 1% DOC. b) Normalized absorbance spectra of purified (6,5)-SWCNTs, obtained by multiple step aqueous two-phase extraction (ATPE), following an approach described by Li et al.[4] c) Normalized absorbance spectra of (6,5)-SWCNTs, exchanging the surface modification from sodium deoxycholate (DOC) to sodium cholate (SC) and to a biocompatible polyethylenglycol-phospholipid (PEG-PL). d) Corresponding 2D photoluminescence spectra of the non-purified and the purified (6,5)-SWCNTs. e) Exemplaric fluorescence spectra of monochiral PEG(5kDa)-PL-(6,5)-SWCNTs before and after addition of tannic acid and genistein, showing a strong fluorescence decrease.

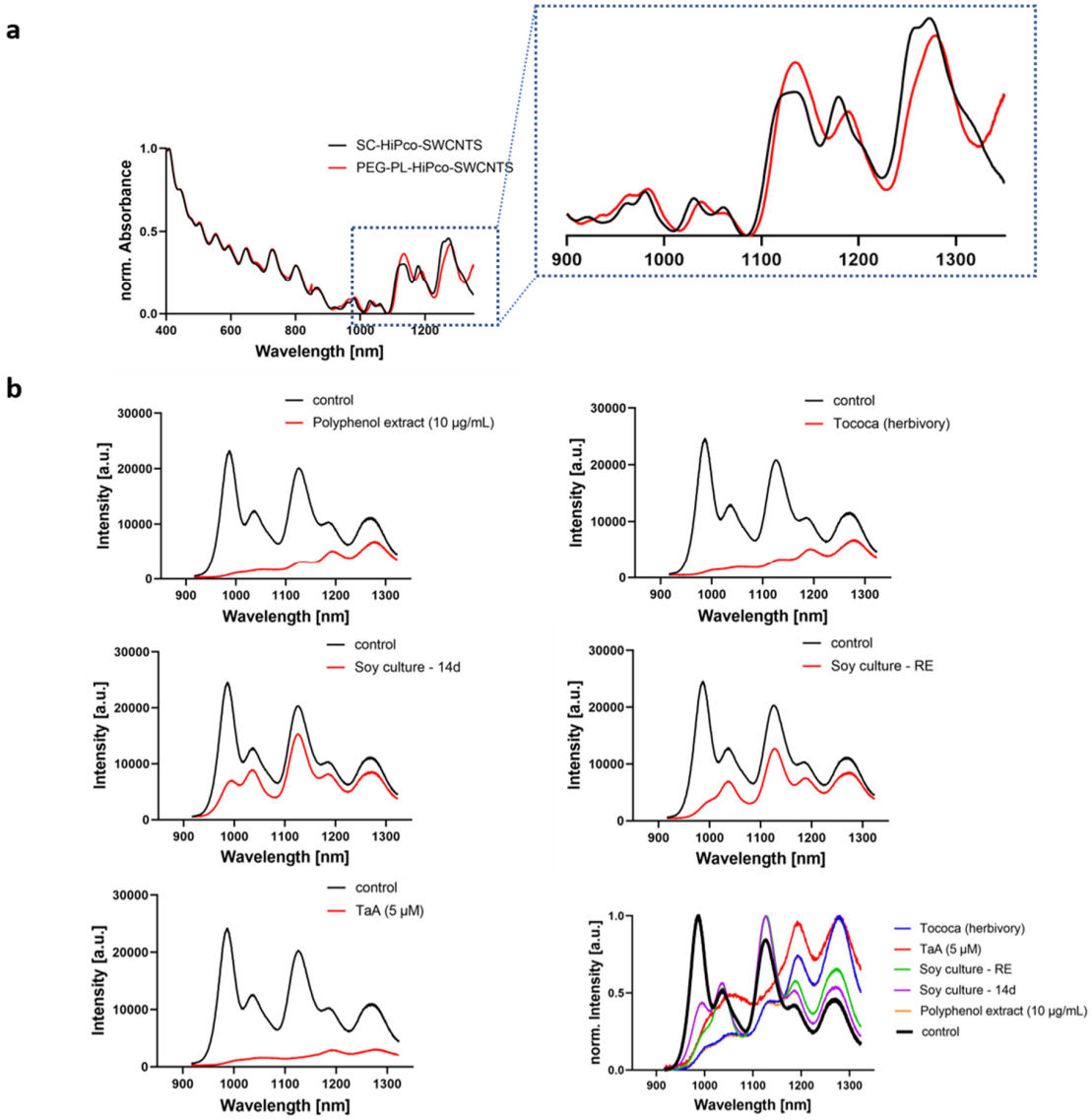

Figure S4: Polyphenol interaction with HiPco-SWCNTs.

a) Normalized absorbance spectra of SWCNTs dispersed in SC and after further surface exchange to PEG-PL. Additionally, a magnified E_{11} transition region is shown. b) NIR fluorescence spectra of PEG-PL-HiPco-SWCNTs before (black spectra) and after (red spectra) the addition of polyphenol containing plant extracts or TaA (*Tococa* polyphenol extract and MeOH extract from herbivory treated plants). Strong photoluminescence modulations are visible with certain differences between SWCNT chiralities, which could point towards a chirality dependent effect regarding the polyphenol composition (see last plot, compared as normalized fluorescence emissions).

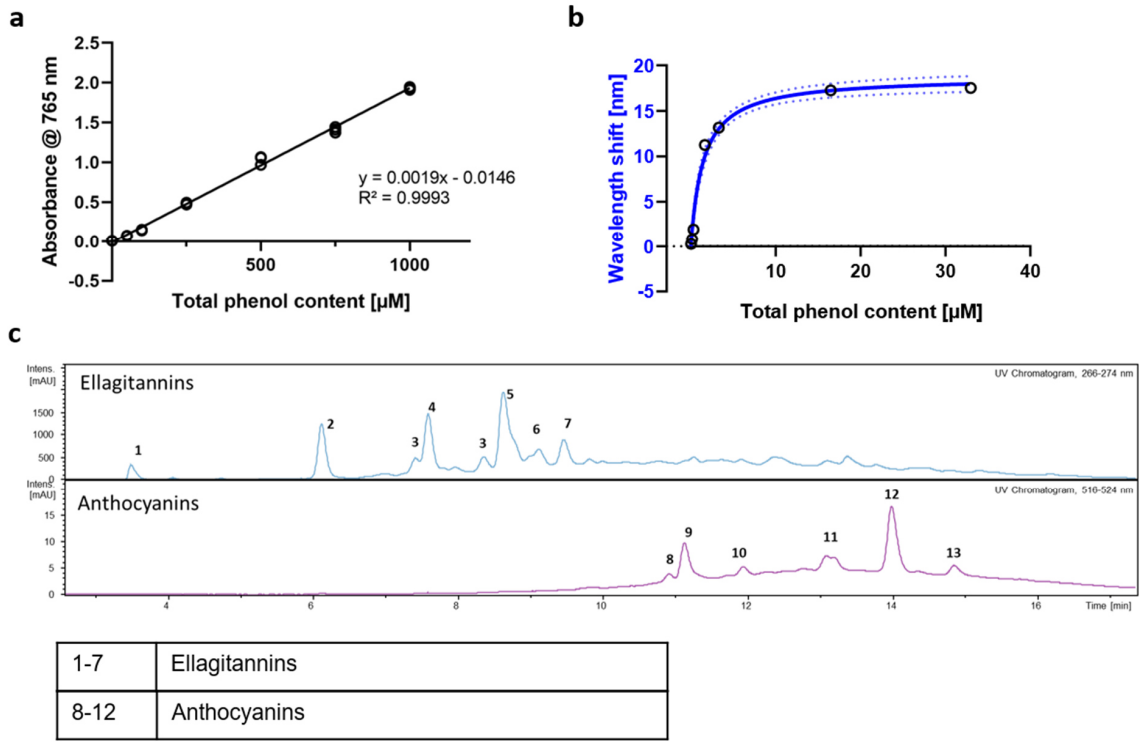

1-7	Ellagitannins
8-12	Anthocyanins

Figure S5: Total phenol content quantification and analysis of *Tococa spp.* polyphenol extract.

a) Calibration curve (linear regression) for the colorimetric assay[13] used to assess the total phenol content. Known concentrations of gallic acid are challenged with the Folin–Ciocalteu reagent, while quantifying the absorbance at 765 nm (n = 3). The resulting calibration, expressed as gallic acid equivalents, shows a linear trend in the µM regime. b) Corresponding plot similar to Figure 3c. It shows the PEG-PL-SWCNT response to purified polyphenol extract from *Tococa spp*., expressed as the total phenol content vs. wavelengths emission shifts (mean ± SD, n = 3, blue line = hyperbolic fit). Compared to the classical Folin–Ciocalteu assay, the sensors display a highly dynamic response in the low µM range with a K_d of 1.5 µM. c) HPLC-UV-Vis chromatogram of the used *Tococa spp.* sample, containing all extractable leaf polyphenols with a predominantly high ellagitannin content, as seen from the counts in the UV trace (266 -274 nm). Substance assignment as ellagitannins and anthocyanins were further confirmed by high resolution mass spectrometry and comparison of the LC-MS results to literature.[15–17] As the sensors probe the total phenol content and the response depends partwise on the polyphenol profile, it would be likely most accurate to create a sensor calibration curve for each plant species/genus of interest.

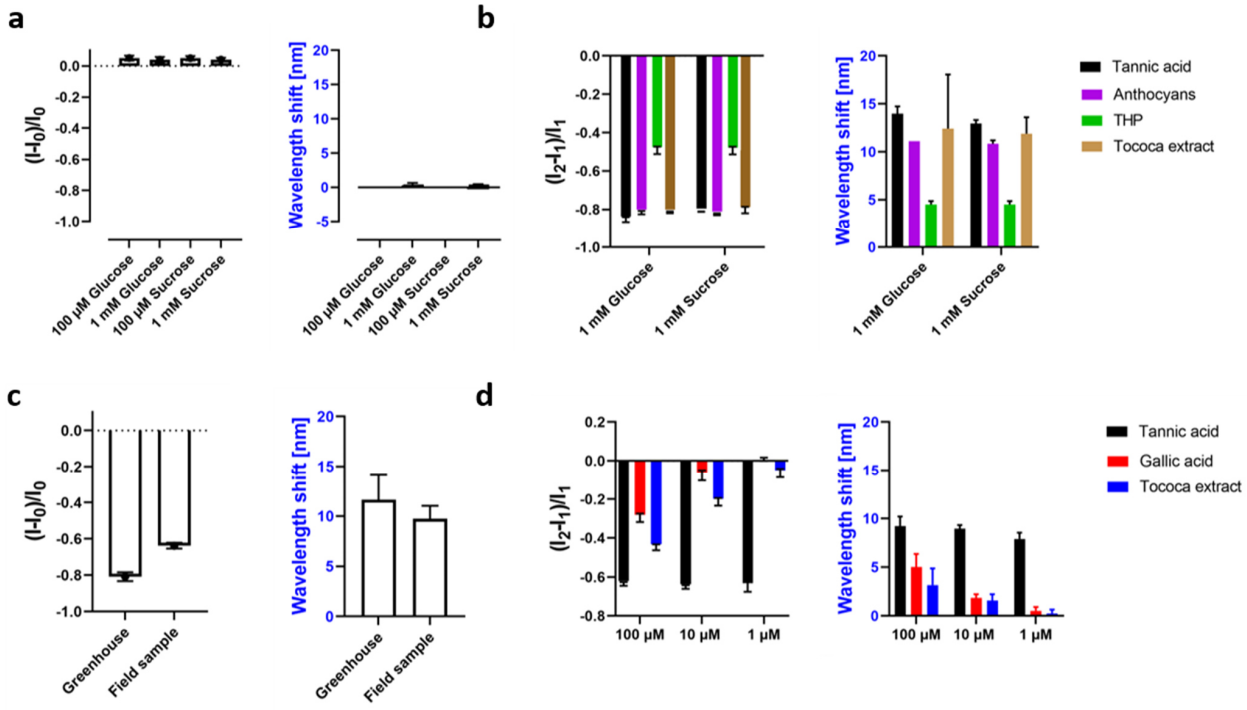

Figure S6: Polyphenol sensing with sugar and leaf extract background.

a) Polyphenol sensing with mono- and disaccharide background. Addition (I) of up to 1 mM glucose or sucrose is not changing the nanosensors responses. b) Further addition (I_2) of polyphenols leads to a similar sensor response, as seen in previous experiments in PBS (10 µM polyphenol concentration, 10 µg/ml extracted polyphenol fraction for the Tococa extract (similar to Figure 3c and S5), mean ± SD, n = 3). However, it should be mentioned, that the intensity changes of the sensors were unbiased, compared to similar experiments in the absence of saccharides, while the detected shift in emission wavelength was slightly reduced (e.g. Tococa extract shifted nanosensor emission by 17 nm w/o saccharides and ~12 nm with glucose/sucrose background). Since 2 µL leaf extract is added to 180 µL sensor solution, such unphysiological high background concentrations of sugars would not be expected in primary samples.
c) Polyphenol sensing with a Tococa leaf extract background. Addition (I) of 2 µL Tococa leaf extract, ether from a 'field' or 'greenhouse sample' (see materials and methods), leads to a strong sensor response. d) Further addition (I_2) of polyphenols to e.g. 'field sample' can still be sensed in a concentration dependent way, illustration the principle of a standard addition in a chlorophyll (and polyphenol) containing background (mean ± SD, n = 3). Similar results were obtained, when spiking the 'greenhouse sample', showing slightly smaller responses. Note that wavelengths shifts in (d) are compared to the addition (I) of totoca extracts, so overall shifts to the starting conditions (I_0) would be e.g. for tannic acid close to 20 nm.

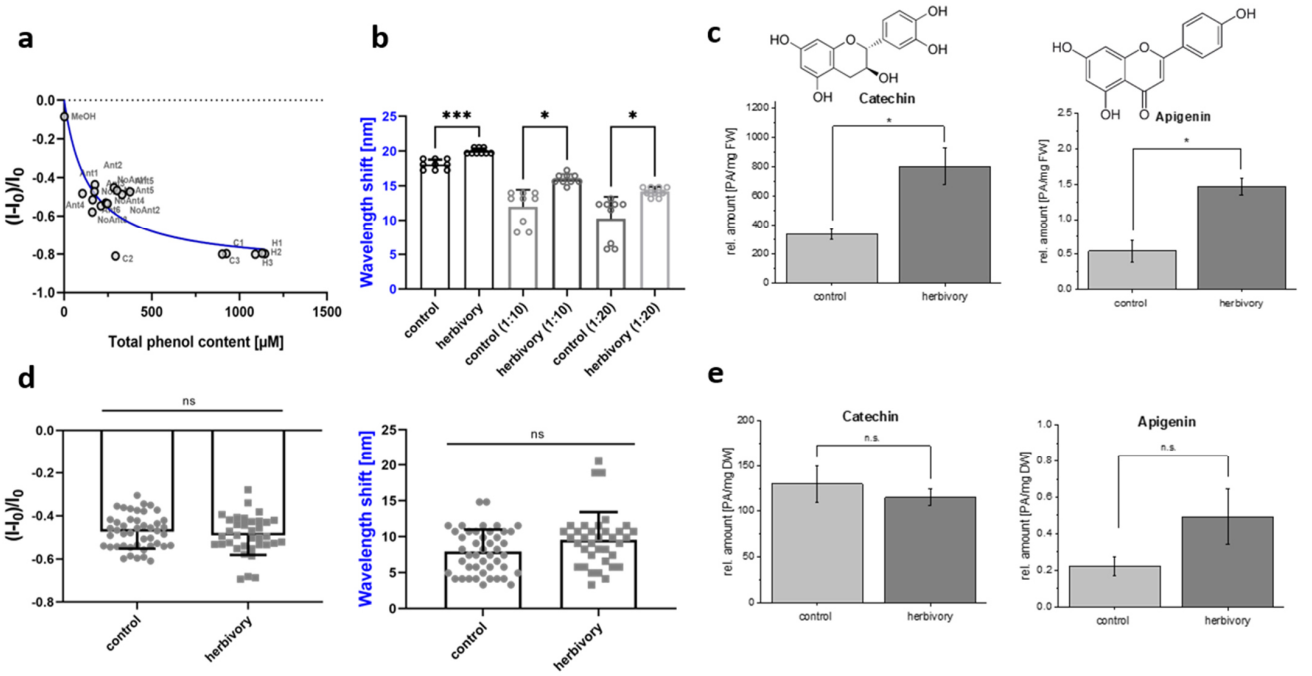

Figure S7: Analysis of crude *Tococa spp.* leaf extracts.

a) Correlation of the intensity changes against the total phenol content from multiple *Tococa* leaf MeOH-extracts (corresponding plot to Figure 3d, 2 µL undiluted MeOH extract was added to the nanosensors). It should be mentioned, that first unknown Tococa extracts were analyzed by the nanosensors and then correlated with the established Folin–Ciocalteu assay. For such a species-specific calibration fit, a dynamic response in the µM range of total phenols is observed (expressed as gallic acid equivalents) (mean ± SD, N =1, n = 3, blue line = hyperbolic fit). b) When diluting the plant extract from herbivore treated *Tococa* plants from the greenhouse, the phenol concentration is shifted to the dynamic response region of the nanosensors. This increases the mean difference in emission wavelength shift, which is hereafter still significantly different (complementary to Figure 3e, mean ± SD, N =3, n = 3). c) HPLC-MS quantification of catechin and apigenin as two prominent examples show as well a significant increase after herbivore treatment. d) Nanosensor responses of different extracts from wild *Tococa* plants show no significant difference in polyphenol levels after herbivore attack, which was carried out as described in the MM section. Hereby, a strong variation in the total phenol concentration is detected, pointing towards more complex interactions in the wild plants (e.g. previous pathogen / herbivore attack mediated a constant increase in polyphenol levels) (mean ± SD, N =6, n = 3). e) HPLC-MS quantification confirmed those results, by showing no significant differences in the most prominent flavonoid compounds (note that apigenin levels show a slight increase, not effecting the overall total phenol concentration, as seen from magnitudes higher, not varying catechin levels).
(nanosensor analysis: ***P<0.001; *P<0.03; ns = not significant; unpaired t-test; PA = peak area, FW = fresh weight, DW = dry weight)

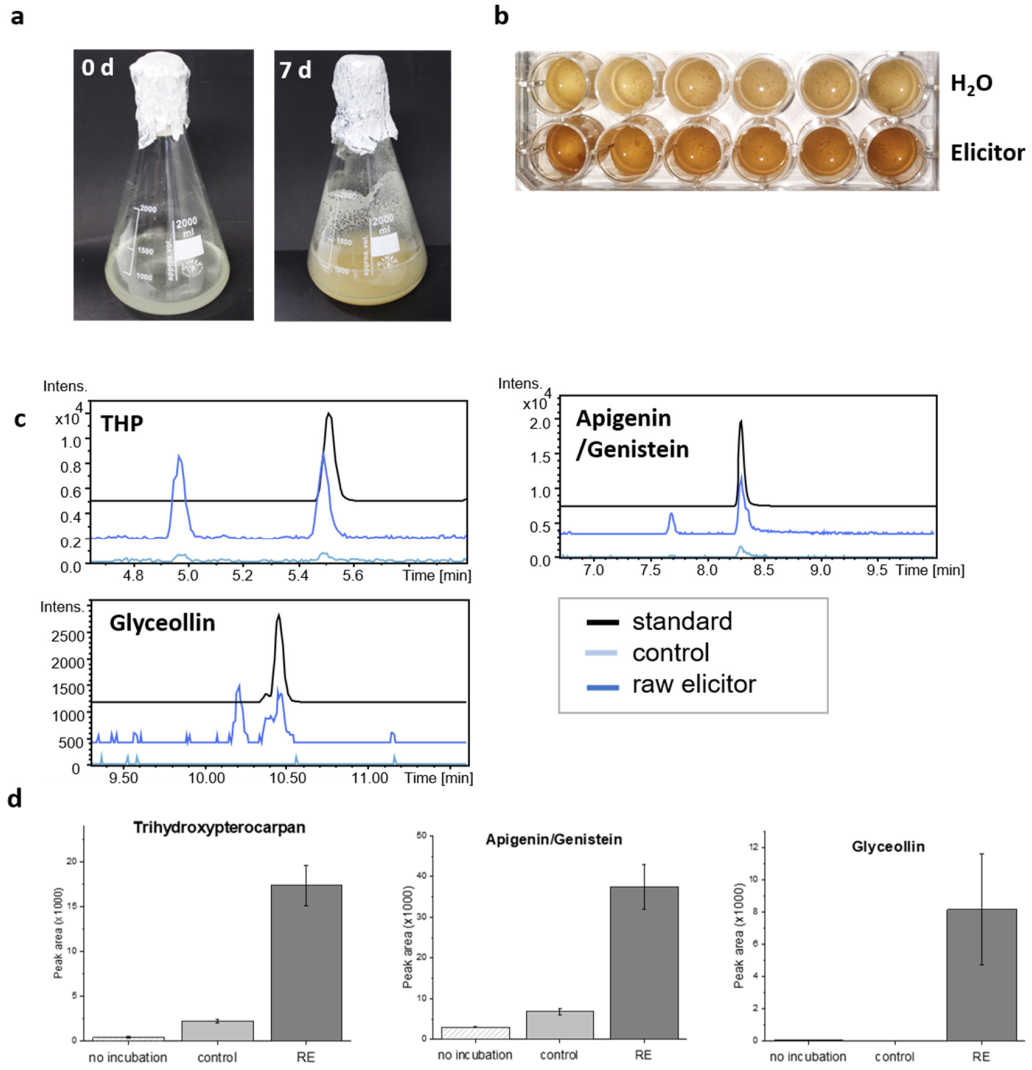

Figure S8: Characterization of polyphenols from soybean cell cultures.

a) Pictures of the soybean cultures show a clear browning after 7 days, indicating a release of polyphenols during growth and maturation. b) Six soybean culture replicates, stimulated with 0.5 mg/mL raw elicitor (lower row) or with H_2O (upper row) as a control. Again, a clear browning of the induced cultures is visible, which indicates accumulation of phenolic compounds.[18] c) Extracted ion chromatograms (EIC) of the most abundant *m/z* values of the respective standards are shown. Comparison of these signals in samples from raw elicitor (RE) treated and control cultures shows that these compounds are accumulating after stimulation with RE. d) Peak areas of these EIC signals were used for relative quantification of the compounds. A drastic increase in flavonoids after raw elicitor treatment was detected.

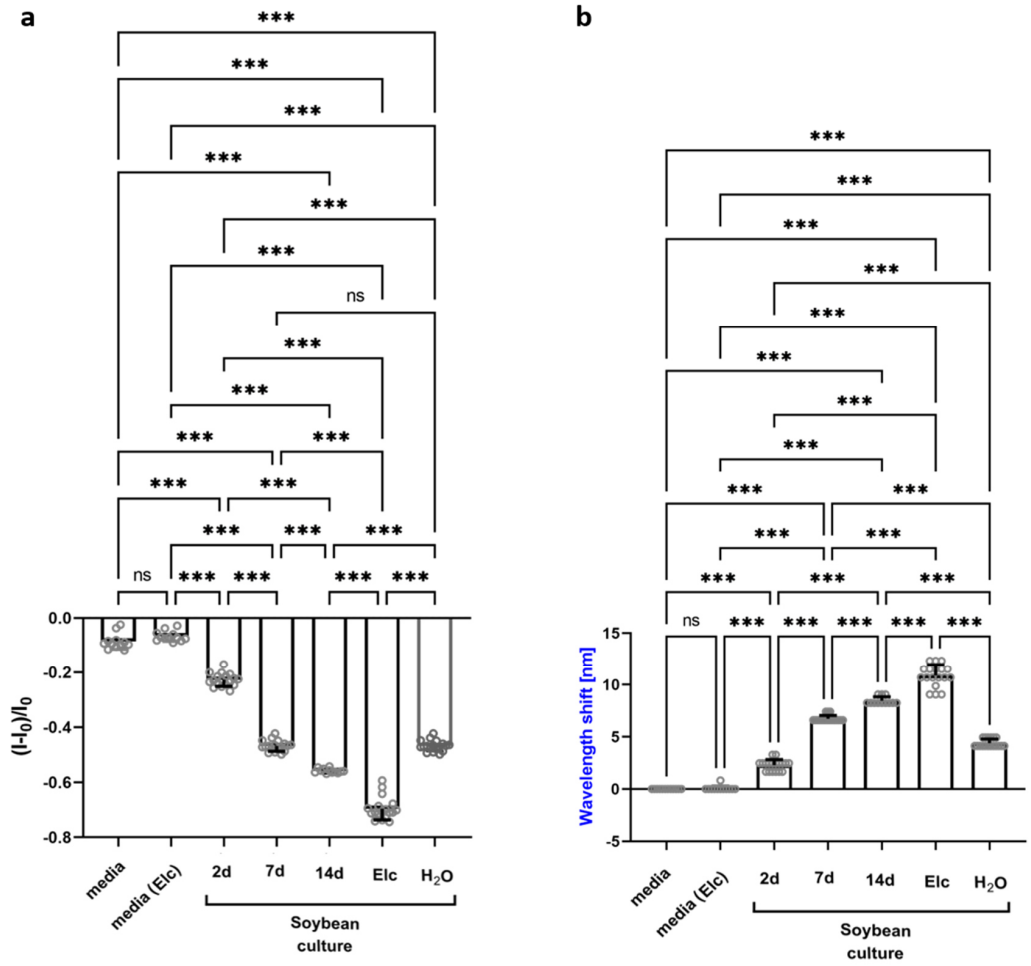

Figure S9: Sensor response to soybean cell cultures.

a) and b) Full statistical analysis (one-way ANOVA) for the shown sensor responses in Figure 3f and 3g. Here, soybean cell cultures (as cell-free supernatants) are added to the PEG-PL-SWCNT nanosensors, which react with a fluorescence decrease and emission wavelengths shift to the age and stimulus (elicitor, Elc) dependent polyphenol content (mean ± SD, N = 6, n =3; nanosensor analysis: ***P<0.001; ns = not significant).

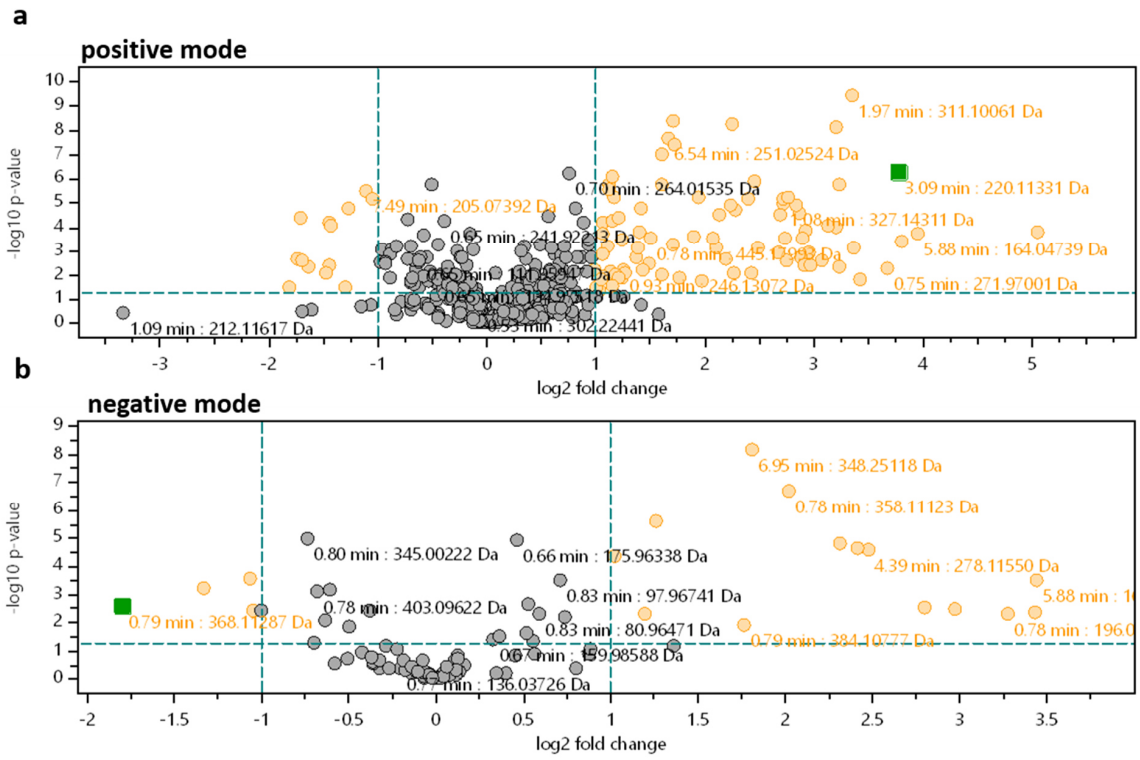

Figure S10: Volcano plot comparing feature abundance in control and elicitor induced soybean cell cultures.

LC-MS analysis of control and elicitor induced soybean cell cultures was conducted with the mass spectrometer operating in positive (a) and negative (b) ionization mode to compare the relative abundance of the extracted features. The volcano plot visualizes the metabolic differences (orange features, $p<0.05$, fold change > 2) and non-affected features (grey) upon raw elicitor treatment. Green color marks the selected feature, which is not relevant for this result.

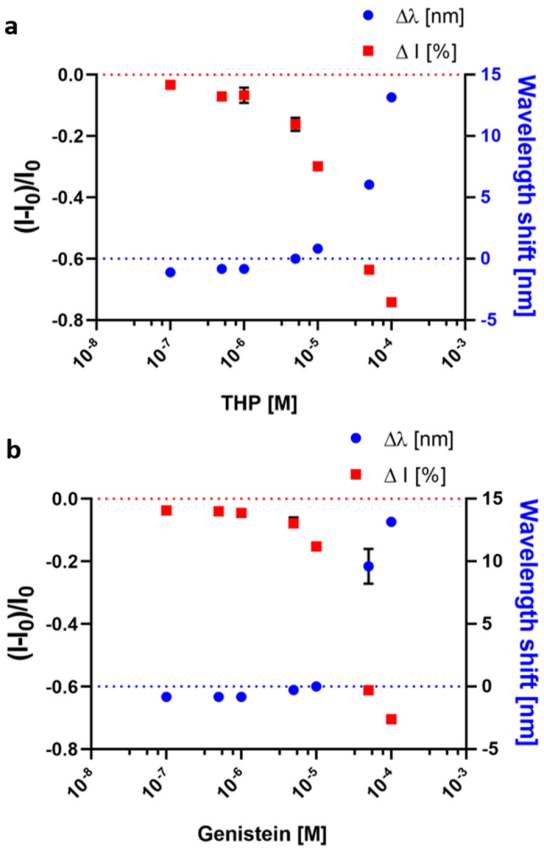

Figure S11: Sensor response to prominent soybean polyphenols.

a) Trihydroxypterocarpan (THP), an important compound released after pathogen (elicitor) stimulus and b) genistein, which is released during maturation, quench and shift the nanosensor fluorescence in a similar concentration dependent manner (mean ± SD, n =3).

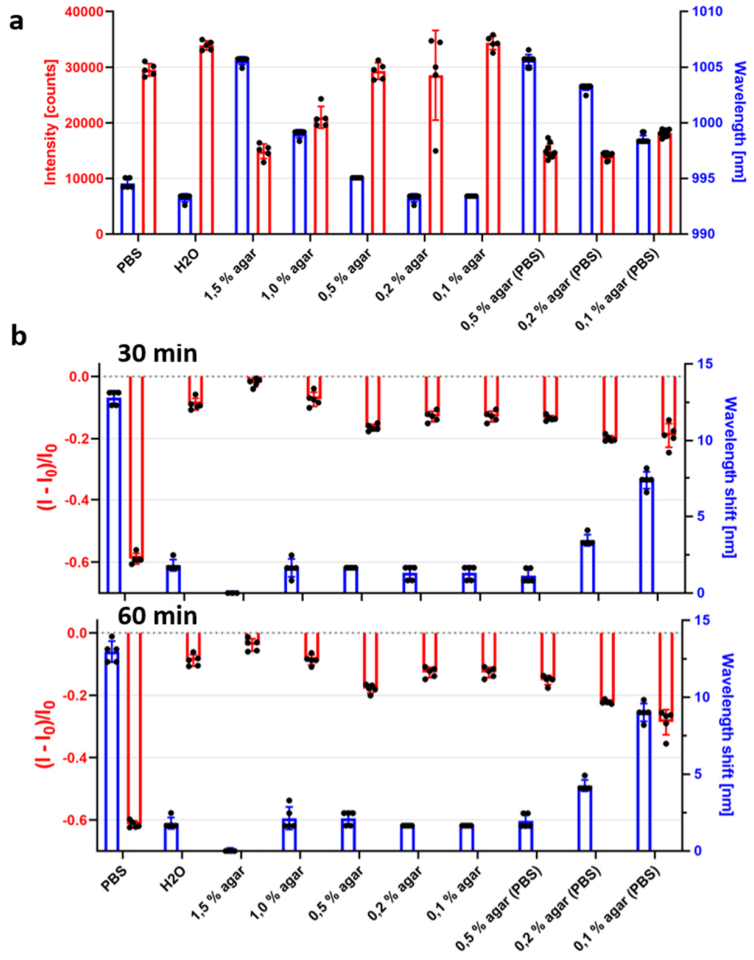

Figure S12: Tuning the nanosensor incorporation into functional agar medium.

a) Photoluminescence properties (intensity and emission wavelength) of PEG-PL-SWCNTs in different environments. 90 µL SWCNT solution was placed in a 96-well plate and analyzed. Increasing agar concentration decreases the emission intensity and redshifts the maxima (mean ± SD, n = 5). b) Sensing of polyphenols, here genistein with a final concentration of 100 µM, seems to be strongly affected by a higher agar concentration, as well as by the ion concentration (agar system in H_2O or in PBS) (mean ± SD, n = 5).

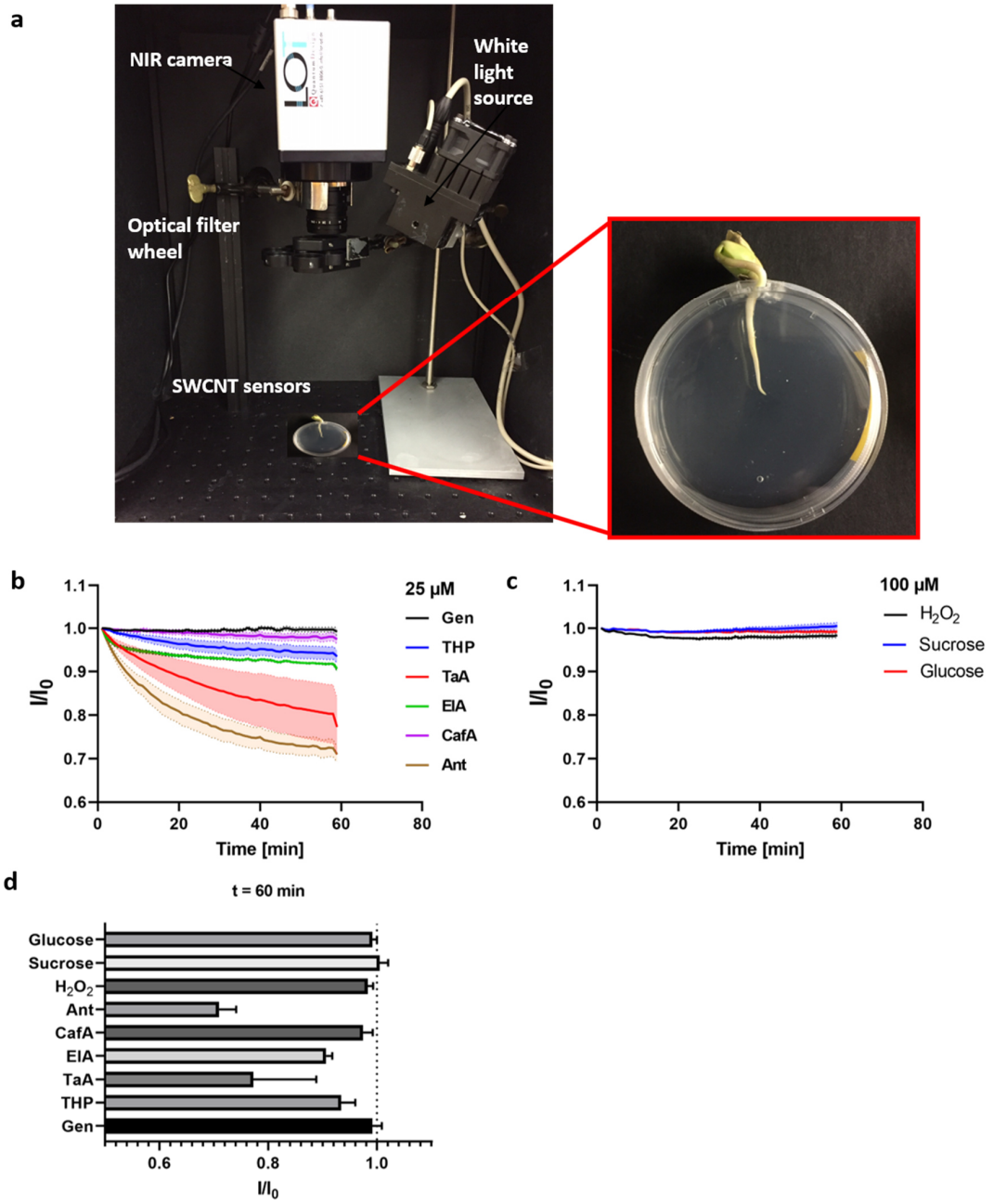

Figure S13: Imaging of sensor response during agar diffusion. a) Picture of the NIR stand-off imaging systems. A specialized InGaAs-Camera detects the fluorescence emission of the SWCNT sensors, incorporated into a agar medium (see close up image). b) PEG-PL-SWCNTs in 0.4 % culture medium agar (Murashige-Skoog-Medium) were challenged with different prominent polyphenols or possible interfering substances during NIR stand-off imaging. Nanosensor responses to 25 µM of different polyphenol compounds (line = mean, SD = pale boundaries, n = 3). c) Sensor response to potential interfering substances such as H_2O_2, mono- or disaccharides. Four times higher concentrations with 100 µM did not change the nanosensors (line = mean, SD = pale boundaries, n = 3). d) Plotted NIR-fluorescence changes of the PEG-PL-SWCNTs agar after 60 min (mean ± SD, n = 3). The sensors response to large (for rhizosphere conditions even unphysical high) H_2O_2 concentrations is within a range of ~3%, far less than the detected polyphenol secretion after elicitor stimulus. However, a small contribution of released H_2O_2 on a short timescale can not be excluded, but should not affect the overall sensing outcome (as seen in Figure 4 e,f).

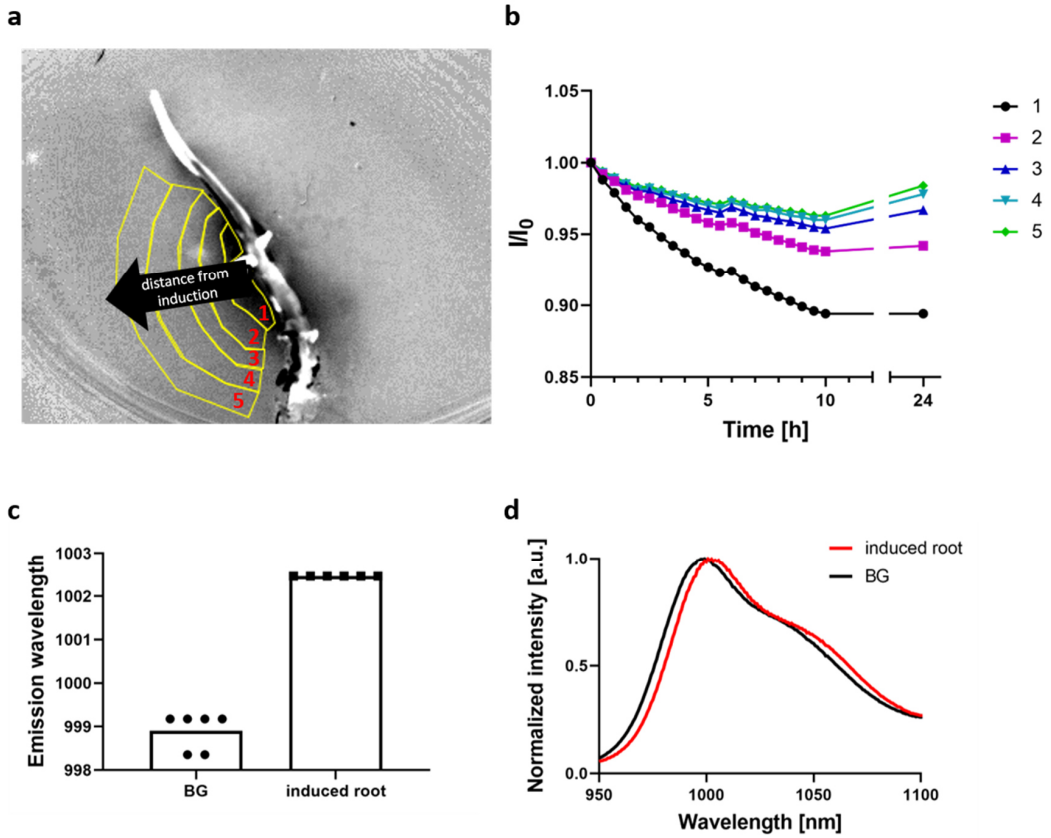

Figure S14: Elicitor induced polyphenol release from soybean seedlings. a) NIR fluorescence image of the *G. max* seedling shown in Figure 4d (10 h after induction). Different regions of interests (ROI) in the nanosensor-agar are marked, with an increasing distance from the induced root position. b) Mean intensity changes (I/I_0) of the associated ROI 1-5 are plotted over time, suggesting a constantly increasing release of polyphenols for 5-8 h after stimulus. c) Measuring the photoluminescence of the nanosensors at six random spots in the background (BG) and close to the induced region (ROI 1, labeled as 'induced root'), a clear redshift of the nanosensor emission becomes visible (mean, n = 6). d) Normalized mean fluorescence spectra of the described positions in (c) visualize the redshifted maxima. The fluorescence reduction during NIR stand-off imaging correlates therefore also with a shift in the emission spectra, as expected from polyphenol – nanosensor interaction. Moreover, with specialized optical systems also spectral-resolved imaging[19] would be possible, likely increasing sensitivity of the presented approach. However, implementation of this technique for scientific of agricultural research and crop production would be more straightforward with the simple NIR imaging system we presented. In general, Polyphenol concentrations in the soil depend on several abiotic and biotic factors. The amounts can change with the season[20], plant age[21] and nutrient supply[22]. These factors, however, are predictable and the changes are bound to occur slowly with an overall low fold change (≤ 2).[20] Induction after pathogen attack on the other hand leads to a drastic increase of defensive compounds within 4-72 h. So, soybean root cell cultures exposed to fungal pathogen (Fusarium) showed 30x increase in glyceollin concentration.[23] Overall, the sensor response from pathogen-mediated fast and drastic increase in polyphenol levels should not be biased by other factors. These findings and visualization of spatiotemporal polyphenol release are therefore in agreement with previous studies, which measured the bulk accumulation of glyceollin and THP over the course of 32 h[24] or *via* radioimmunoassay analysis.[18]

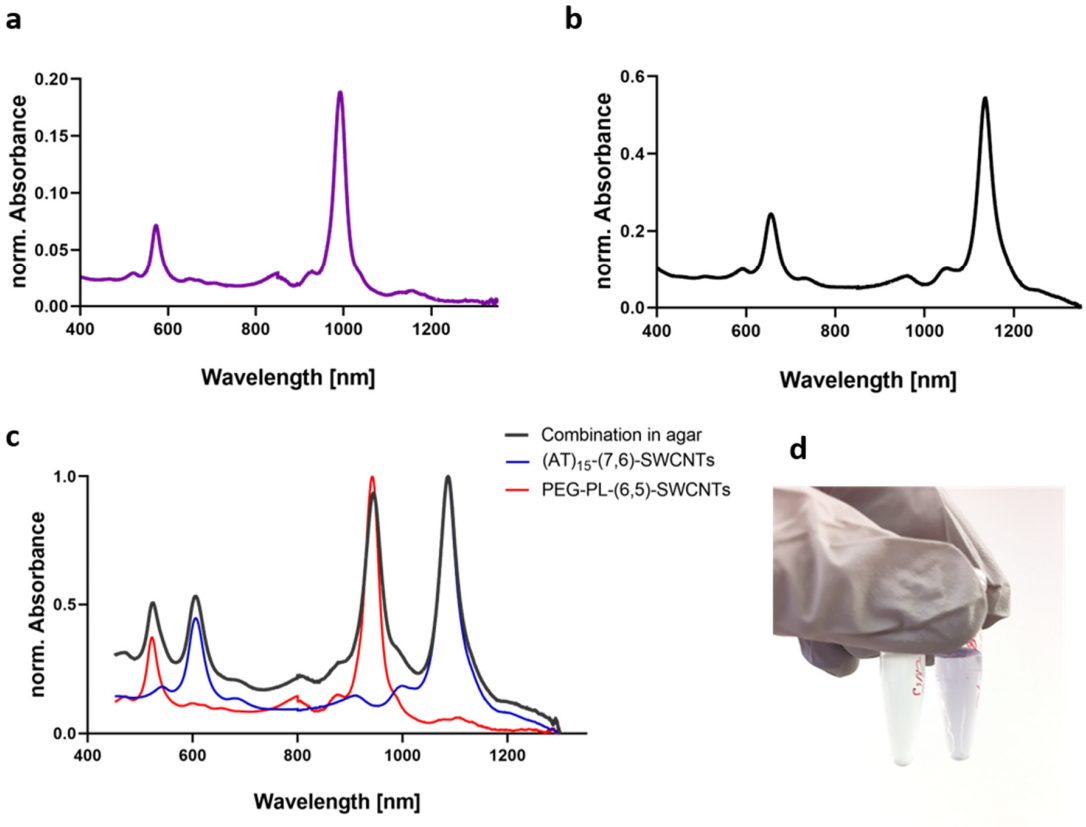

Figure S15: Separated SWCNT fractions for hyperspectral sensing. a) Absorbance spectra of PEG-PL-(6,5)-SWCNTs. b) Absorbance spectra of $(AT)_{15}$-(7,6)-SWCNTs. c) Normalized absorbance spectra of the purified and specifically modified SWCNT chiralities, measured independently and combined in agar. d) Photograph of Eppendorf tubes, containing $(AT)_{15}$-(7,6)-SWCNTs (left) and PEG-PL-(6,5)-SWCNTs (right).

References

[1] R. Nißler, F. A. Mann, P. Chaturvedi, J. Horlebein, D. Meyer, L. Vukovic, S. Kruss, *J. Phys. Chem. C* **2019**, *123*, 4837–4847.
[2] K. Welsher, Z. Liu, S. P. Sherlock, J. T. Robinson, Z. Chen, D. Daranciang, H. Dai, *Nat. Nanotechnol.* **2009**, *4*, 773–780.
[3] F. Schöppler, C. Mann, T. C. Hain, F. M. Neubauer, G. Privitera, F. Bonaccorso, D. Chu, A. C. Ferrari, T. Hertel, *J. Phys. Chem. C* **2011**, *115*, 14682–14686.
[4] H. Li, G. Gordeev, O. Garrity, S. Reich, B. S. Flavel, *ACS Nano* **2019**, *13*, 2567–2578.
[5] R. Nißler, L. Kurth, H. Li, A. Spreinat, I. Kuhlemann, B. S. Flavel, S. Kruss, *Anal. Chem.* **2021**, *93*, 6446–6455.
[6] R. Nißler, O. Bader, M. Dohmen, S. G. Walter, C. Noll, G. Selvaggio, U. Groß, S. Kruss, *Nat. Commun.* **2020**, *11*, 1–12.
[7] R. Bergomaz, M. Boppre, *J. Lepid. Soc.* **1986**, *40*, 131–137.
[8] J. Fliegmann, G. Schüler, W. Boland, J. Ebel, A. Mithöfer, *Biol. Chem.* **2003**, *384*, 437–446.
[9] C. Grajeda-Iglesias, M. C. Figueroa-Espinoza, N. Barouh, B. Baréa, A. Fernandes, V. De Freitas, E. Salas, *J. Nat. Prod.* **2016**, *79*, 1709–1718.
[10] A. Mithöfer, A. A. Bhagwat, M. Feger, J. Ebel, *Planta* **1996**, *199*, 270–275.
[11] A. Mithöfer, A. A. Bhagwat, D. L. Keister, J. Ebel, *Zeitschrift fur Naturforsch. - Sect. C J. Biosci.* **2001**, *56*, 581–584.
[12] N. D. Lackus, A. Müller, T. D. U. Kröber, M. Reichelt, A. Schmidt, Y. Nakamura, C. Paetz, K. Luck, R. L. Lindroth, C. P. Constabel, S. B. Unsicker, J. Gershenzon, T. G. Köllnera, *Plant Physiol.* **2020**, *183*, 137–151.
[13] E. A. Ainsworth, K. M. Gillespie, *Nat. Protoc.* **2007**, *2*, 875–877.
[14] D. P. Salem, X. Gong, A. T. Liu, V. B. Koman, J. Dong, M. S. Strano, *J. Am. Chem. Soc.* **2017**, *139*, 16791–16802.
[15] J. Moilanen, J. Sinkkonen, J. P. Salminen, *Chemoecology* **2013**, *23*, 165–179.
[16] D. M. O. Serna, J. H. I. Martínez, *Molecules* **2015**, *20*, 17818–17847.
[17] D. Fracassetti, C. Costa, L. Moulay, F. A. Tomás-Barberán, *Food Chem.* **2013**, *139*, 578–588.
[18] M. G. Hahn, A. Bonhoff, H. Grisebach, *Plant Physiol.* **1985**, *77*, 591–601.
[19] D. Roxbury, P. V. Jena, R. M. Williams, B. Enyedi, P. Niethammer, S. Marcet, M. Verhaegen, S. Blais-Ouellette, D. A. Heller, *Sci. Rep.* **2015**, *5*, 1–6.
[20] T. Sosa, C. Valares, J. C. Alías, N. C. Lobón, *Plant Soil* **2010**, *337*, 51–63.
[21] S. Cesco, T. Mimmo, G. Tonon, N. Tomasi, R. Pinton, R. Terzano, G. Neumann, L. Weisskopf, G. Renella, L. Landi, P. Nannipieri, *Biol. Fertil. Soils* **2012**, *48*, 123–149.
[22] S. Cesco, G. Neumann, N. Tomasi, R. Pinton, L. Weisskopf, *Plant Soil* **2010**, *329*, 1–25.
[23] V. V. Lozovaya, A. V. Lygin, O. V. Zernova, S. Li, G. L. Hartman, J. M. Widholm, *Plant Physiol. Biochem.* **2004**, *42*, 671–679.
[24] P. Moesta, H. Grisebach, *Nature* **1980**, *286*, 710–711.

8 References

(1) Ostwald, W., *The Scientific Foundations of Analytical Chemistry Treated in an Elementary Manner*; Leipzig, Wilhelm Engelmann: 1894.

(2) Kevadiya, B. D. et al. *Nature Materials* **2021**, *20*, 593–605.

(3) Adli, M. *Nature Communications* **2018**, *9*, 1–13.

(4) Pardi, N.; Hogan, M. J.; Porter, F. W.; Weissman, D. *Nature Reviews Drug Discovery* **2018**, *17*, 261–279.

(5) Pelaz, B. et al. *ACS Nano* **2017**, *11*, 2313–2381.

(6) Iijima, S. *Nature* **1991**, *354*, 56–58.

(7) Dresselhaus, M. S.; Dresselhaus, G.; Avouris, P., *Carbon nanotubes: synthesis, structure, properties, and applications*; Springer-Verlag Berlin Heidelberg: 2001; Vol. 80.

(8) Kruss, S.; Hilmer, A. J.; Zhang, J.; Reuel, N. F.; Mu, B.; Strano, M. S. *Advanced Drug Delivery Reviews* **2013**, *65*, 1933–1950.

(9) Hong, G.; Antaris, A. L.; Dai, H. *Nature Biomedical Engineering* **2017**, *1*, 10.

(10) Zhang, J. et al. *Nature Nanotechnology* **2013**, *8*, 959–968.

(11) Kruss, S.; Salem, D. P.; Vuković, L.; Lima, B.; Vander Ende, E.; Boyden, E. S.; Strano, M. S. *Proceedings of the National Academy of Sciences* **2017**, *114*, 1789–1794.

(12) Giraldo, J. P.; Wu, H.; Newkirk, G. M.; Kruss, S. *Nature Nanotechnology* **2019**, *14*, 541–553.

(13) Jeevanandam, J.; Barhoum, A.; Chan, Y. S.; Dufresne, A.; Danquah, M. K. *Beilstein Journal of Nanotechnology* **2018**, *9*, 1050–1074.

(14) Bati, A. S. R.; Yu, L.; Batmunkh, M. *Nanoscale* **2018**, *10*, 22087–22139.

(15) Liu, B.; Wu, F.; Gui, H.; Zheng, M.; Zhou, C. *ACS Nano* **2017**, *11*, 31–53.

(16) Yang, C.; Younis, M. R.; Zhang, J.; Qu, J.; Lin, J.; Huang, P. *Small* **2020**, *16*, 2001518.

(17) Zamolo, V. Z.; Vazquez, E.; Prato, M. *Topics in Current Chemistry* **2013**, *286*, 1–72.

(18) Odom, T. W.; Huang, J.-l. *Nature* **1998**, *391*, 1997–1999.

(19) Hong, G.; Diao, S.; Antaris, A. L.; Dai, H. *Chemical Reviews* **2015**, *115*, 10816–10906.

(20) Amori, A. R.; Hou, Z.; Krauss, T. D. *Annual Review of Physical Chemistry* **2018**, *69*, 81–99.

(21) Iijima, S.; Lchihashi, T. *Nature* **1993**, *363*, 603–605.

(22) Journet, C.; Maser, W. K.; Bernier, P.; Loiseau, A.; Lamyde la Chapelle, M.; Lefrant, S.; Deniard, P.; Lee, R.; Fischer, J. E. *Nature* **1997**, *388*, 20–22.

(23) Guo, T.; Nikolaev, P.; Rinzler, A. G.; Tomdnek, D.; Colbert, D. T.; Smalley, R. E. *Journal of Physical Chemistry* **1995**, *99*, 10694–10697.

(24) Hofmann, S. et al. *Nano Letters* **2007**, *7*, 602–608.

(25) Janas, D. *Mater. Chem. Front.* **2018**, *2*, 36–63.

(26) Li, M.; Liu, X.; Zhao, X.; Yang, F.; Wang, X.; Li, Y. *Topics in Current Chemistry* **2017**, *375*, 1–43.

(27) Zhang, M.; Wang, W.; Wu, F.; Yuan, P.; Chi, C.; Zhou, N. *Carbon* **2017**, *123*, 70–83.

(28) Liu, J.; Wang, C.; Tu, X.; Liu, B.; Chen, L.; Zheng, M.; Zhou, C. *Nature Communications* **2012**, *3*, 1–7.

(29) Sanchez-Valencia, J. R.; Dienel, T.; Gröning, O.; Shorubalko, I.; Mueller, A.; Jansen, M.; Amsharov, K.; Ruffieux, P.; Fasel, R. *Nature* **2014**, *512*, 61–64.

(30) Wang, J.-Q. et al. *Nature* **2014**, *510*, 522–524.

(31) Fouquet, M.; Bayer, B. C.; Esconjauregui, S.; Blume, R.; Warner, J. H.; Hofmann, S.; Schl, R. *Physical Review B* **2012**, *235411*, 1–7.

(32) You, A.; Be, M. A. Y.; In, I. *Applied Physics Letters* **2008**, *93*, 1–4.

(33) Saito, R.; Dresselhaus, G.; Dresselhaus, M. S., *Physical Properties of Carbon Nanotubes*; Imperial College Press, London: 1998.

(34) Weisman, R. B. In *Contemporary Concepts of Condensed Matter Science, Carbon Nanotubes: Quantum Cylinders of Graphene*; 08; Elsevier B.V.: 2008; Vol. 0934, pp 109–133.

(35) Weisman, R. B.; Bachilo, S. M. *Nano Letters* **2003**, *3*, 1235–1238.

(36) Tu, X.; Manohar, S.; Jagota, A.; Zheng, M. *Nature* **2009**, *460*, 250–253.

(37) Ao, G.; Streit, J. K.; Fagan, J. A.; Zheng, M. *Journal of the American Chemical Society* **2016**, *138*, 16677–16685.

(38) Ghosh, S.; Bachilo, S. M.; Simonette, R. A.; Beckingham, K. M.; Weisman, R. B. *Science* **2010**, *330*, 1656–1659.

(39) Sykes, M. E.; Kim, M.; Wu, X.; Wiederrecht, G. P.; Peng, L.; Wang, Y.; Gosztola, D. J.; Ma, X. *ACS Nano* **2019**, *13*, 13264–13270.

(40) Kim, M.; Adamska, L.; Hartmann, N. F.; Kwon, H.; Liu, J.; Velizhanin, K. A.; Piao, Y.; Powell, L. R.; Meany, B.; Doorn, S. K.; Tretiak, S.; Wang, Y. *The Journal of Physical Chemistry C* **2016**, *120*, 11268–11276.

(41) Wang, P.; Barnes, B.; Huang, Z.; Wang, Z.; Zheng, M.; Wang, Y. *Advanced Materials* **2021**, *2005890*, 1–30.

(42) Wei, N.; Tian, Y.; Liao, Y.; Komatsu, N.; Gao, W.; Lyuleeva-Husemann, A.; Zhang, Q.; Hussain, A.; Ding, E. X.; Yao, F.; Halme, J.; Liu, K.; Kono, J.; Jiang, H.; Kauppinen, E. I. *Advanced Materials* **2021**, *33*, 1–7.

(43) Brozena, A. H.; Kim, M.; Powell, L. R.; Wang, Y. *Nature Reviews Chemistry* **2019**, *3*, 375–392.

(44) He, S.; Song, J.; Qu, J.; Cheng, Z. *Chemical Society Reviews* **2018**, *47*, 4258–4278.

(45) Janas, D. *Materials Horizons* **2020**, *7*, 2860–2881.

(46) Kwon, H.; Powell, L. R.; Schatz, G. C.; Meany, B.; Valley, N.; Piao, Y.; Wang, Y. *Nature Chemistry* **2013**, *5*, 840–845.

(47) Settele, S.; Berger, F. J.; Lindenthal, S.; Zhao, S.; El Yumin, A. A.; Zorn, N. F.; Asyuda, A.; Zharnikov, M.; Högele, A.; Zaumseil, J. *Nature Communications* **2021**, *12*, 1–10.

(48) Kwon, H.; Furmanchuk, M.; Kim, M.; Meany, B.; Guo, Y.; Schatz, G. C.; Wang, Y. *Journal of the American Chemical Society* **2016**, *138*, 6878–6885.

(49) Berger, F. J.; Lüttgens, J.; Nowack, T.; Kutsch, T.; Lindenthal, S.; Kistner, L.; Müller, C. C.; Bongartz, L. M.; Lumsargis, V. A.; Zakharko, Y.; Zaumseil, J. *ACS Nano* **2019**, *13*, 9259-9269.

(50) Gillen, A. J.; Boghossian, A. A. *Frontiers in Chemistry* **2019**, *7*, 13713–13793.

(51) Kruss, S.; Hilmer, A. J.; Zhang, J.; Reuel, N. F.; Mu, B.; Strano, M. S. *Advanced Drug Delivery Reviews* **2013**, *65*, 1933–1950.

(52) Pan, J.; Li, F.; Choi, J. H. *Journal of Materials Chemistry B* **2017**, *5*, 6511–6522.

(53) Kupis-Rozmysłowicz, J.; Antonucci, A.; Boghossian, A. A. *ECS Journal of Solid State Science and Technology* **2016**, *5*, M3067–M3074.

(54) Singh, P.; Campidelli, S.; Giordani, S.; Bonifazi, D.; Bianco, A.; Prato, M. *Chemical Society Reviews* **2009**, *38*, 2214–2217.

(55) Moore, V. C.; Strano, M. S.; Haroz, E. H.; Hauge, R. H.; Smalley, R. E.; Schmidt, J.; Talmon, Y. *Nano Letters* **2003**, *3*, 1379–1382.

(56) Graf, A.; Zakharko, Y.; Schießl, S. P.; Backes, C.; Pfohl, M.; Flavel, S.; Zaumseil, J.; Flavel, B. S.; Zaumseil, J. *Carbon* **2016**, *105*, 593–599.

(57) Liang, L.; Xie, W.; Fang, S.; He, F.; Yin, B.; Tlili, C.; Wang, D.; Qiu, S.; Li, Q. *Journal of Materials Chemistry C* **2017**, *5*, 11339–11368.

(58) Rajter, R.; French, R. H. *International Journal of Materials Research* **2010**, *101*, 27–42.

(59) Angelikopoulos, P.; Bock, H. *Physical Chemistry Chemical Physics* **2012**, *14*, 9546–9557.

(60) Antonucci, A.; Kupis-Rozmysłowicz, J.; Boghossian, A. A. *ACS Applied Materials & Interfaces* **2017**, *9*, 11321–11331.

(61) Fujigaya, T.; Nakashima, N. *Science and technology of advanced materials* **2015**, *16*, 1–21.

(62) Hirano, A.; Kameda, T.; Yomogida, Y.; Wada, M.; Tanaka, T.; Kataura, H. *ChemNanoMat* **2016**, *2*, 911–920.

(63) Gomulya, W.; Gao, J.; Antonietta, M. *The European Physical Journal B* **2013**, *86*, 1–13.

(64) Zheng, M.; Jagota, A.; Strano, M. S.; Santos, A. P.; Barone, P.; Chou, S. G.; Diner, B. A.; Dresselhaus, M. S.; Mclean, R. S.; Onoa, G. B.; Samsonidze, G. G.; Semke, E. D. *Science* **2003**, *302*, 1545–1549.

(65) Johnson, R. R.; Johnson, A. T. C.; Klein, M. L. *Nano Letters* **2008**, *8*, 69–75.

(66) Connell, M. J. O. et al. *Science* **2002**, *297*, 593–597.

(67) Haggenmueller, R.; Rahatekar, S. S.; Fagan, J. A.; Chun, J.; Becker, M. L.; Naik, R. R.; Krauss, T.; Carlson, L.; Kadla, J. F.; Trulove, P. C.; Fox, D. F.; DeLong, H. C.; Fang, Z.; Kelley, S. O.; Gilrnan, J. W. *Langmuir* **2008**, *24*, 5070–5078.

(68) Wenseleers, W.; Vlasov, I. L.; Goovaerts, E.; Obraztsova, E. D.; Lobach, A. S.; Bouwen, A. *Advanced Functional Materials* **2004**, *14*, 1105–1112.

(69) Larsen, B. A.; Deria, P.; Holt, J. M.; Stanton, I. N.; Heben, M. J.; Therien, M. J.; Blackburn, J. L. *Journal of the American Chemical Society* **2012**, *134*, 12485–12491.

(70) Silvera-Batista, C. A.; Wang, R. K.; Weinberg, P.; Ziegler, K. J. *Physical Chemistry Chemical Physics* **2010**, *12*, 6990–6998.

(71) Ju, S.-y.; Kopcha, W. P.; Papadimitrakopoulos, F. *Science* **2009**, *323*, 1319–1323.

(72) Fagan, J. A.; Becker, M. L.; Chun, J.; Nie, P.; Bauer, B. J.; Simpson, J. R.; Hight-Walker, A.; Hobbie, E. K. *Langmuir* **2008**, *24*, 13880–13889.

(73) Hersam, M. C. *Nature Nanotechnology* **2008**, *3*, 387–394.

(74) Krupke, R.; Hennrich, F.; Löhneysen, H. v.; Kappes, M. M. *Science* **2003**, *301*, 344–347.

(75) Zheng, M. *Topics in Current Chemistry* **2017**, *375*, 1–36.

(76) Naumov, A. V.; Ghosh, S.; Tsyboulski, D. A.; Bachilo, S. M.; Weisman, R. B. *ACS Nano* **2011**, *5*, 1639–1648.

(77) Flavel, B. S.; Kappes, M. M.; Krupke, R.; Hennrich, F. *ACS Nano* **2013**, *7*, 3557–3564.

(78) Tanaka, T.; Jin, H.; Miyata, Y.; Fujii, S.; Suga, H.; Naitoh, Y.; Minari, T.; Miyadera, T.; Tsukagoshi, K.; Kataura, H. *Nano Letters* **2009**, *9*, 1497–1500.

(79) Liu, H.; Tanaka, T.; Urabe, Y.; Kataura, H. *Nano Letters* **2013**, *13*, 1996–2003.

(80) Yomogida, Y.; Tanaka, T.; Zhang, M.; Yudasaka, M.; Wei, X.; Kataura, H. *Nature Communications* **2016**, *7*, 1–8.

(81) Fagan, J. A. *Nanoscale Advances* **2019**, *1*, 3307–3324.

(82) Liu, G.; Hong, R.; Guo, L.; Li, Y.; Li, H. *Applied Surface Science* **2011**, *257*, 6711–6717.

(83) Hennrich, F.; Lebedkin, S.; Kappes, M. M. *Journal of Physical Chemistry C* **2009**, *113*, 14628–14632.

(84) Hwang, J. Y.; Nish, A.; Doig, J.; Douven, S.; Chen, C. W.; Chen, L. C.; Nicholas, R. J. *Journal of the American Chemical Society* **2008**, *130*, 3543–3553.

(85) Nish, A.; Hwang, J. Y.; Doig, J.; Nicholas, R. J. *Nature Nanotechnology* **2007**, *2*, 640–646.

(86) Ide, N.; Yasuro, N. *Chemistry Letters* **2011**, 239–241.

(87) Toshimitsu, F.; Nakashima, N. *Nature Communications* **2014**, *5*, 1–9.

(88) Xu, L.; Valášek, M.; Hennrich, F.; Sedghamiz, E.; Penaloza-Amion, M.; Häussinger, D.; Wenzel, W.; Kappes, M. M.; Mayor, M. *ACS Nano* **2021**, *15*, 4699–4709.

(89) Jakubka, F.; Schießl, S. P.; Martin, S.; Englert, J. M.; Hauke, F.; Hirsch, A.; Zaumseil, J. *ACS Macro Letters* **2012**, *1*, 815–819.

(90) Liang, S.; Li, H.; Flavel, B. S.; Adronov, A. *Chemistry - A European Journal* **2018**, *24*, 9799–9806.

(91) Joo, Y.; Brady, G. J.; Shea, M. J.; Oviedo, M. B.; Kanimozhi, C.; Schmitt, S. K.; Wong, B. M.; Arnold, M. S.; Gopalan, P. *ACS Nano* **2015**, *9*, 10203–10213.

(92) Kanimozhi, C.; Brady, G. J.; Shea, M. J.; Huang, P.; Joo, Y.; Arnold, M. S.; Gopalan, P. *ACS Applied Materials and Interfaces* **2017**, *9*, 40734–40742.

(93) Pochorovski, I.; Wang, H.; Feldblyum, J. I.; Zhang, X.; Antaris, A. L.; Bao, Z. *Journal of the American Chemical Society* **2015**, *137*, 4328–4331.

(94) Arnold, M. S.; Stupp, S. I.; Hersam, M. C. *Nano Letters* **2005**, *5*, 713–718.

(95) Arnold, M. S.; Green, A. A.; Hulvat, J. F.; Stupp, S. I.; Hersam, M. C. *Nature Nanotechnology* **2006**, *1*, 60–65.

(96) Simien, D.; Fagan, J. A.; Luo, W.; Douglas, J. F.; Migler, K.; Obrzut, J. *ACS Nano* **2008**, *2*, 1879–1884.

(97) Niyogi, S.; Densmore, C. G.; Doorn, S. K. *Journal of the American Chemical Society* **2009**, *131*, 1144–1153.

(98) Khripin, C. Y.; Fagan, J. A.; Zheng, M. *Journal of the American Chemical Society* **2013**, *135*, 6822–6825.

(99) Yang, S. S.; Yu, H. X.; Wang, Z. Z.; Liu, H. L.; Zhang, H.; Yu, X.; Shang, W.; Chen, G. Q.; Gu, Z. Y. *Chemistry - A European Journal* **2018**, *24*, 2024.

(100) Fagan, J. A.; Khripin, C. Y.; Silvera Batista, C. A.; Simpson, J. R.; Hároz, E. H.; Hight Walker, A. R.; Zheng, M. *Advanced Materials* **2014**, *26*, 2800–2804.

(101) Li, Z.; Askim, J. R.; Suslick, K. S. *Chemical Reviews* **2019**, *119*, 231–292.

(102) Subbaiyan, N. K.; Cambré, S.; Parra-Vasquez, A. N. G.; Hároz, E. H.; Doorn, S. K.; Duque, J. G. *ACS Nano* **2014**, *8*, 1619–1628.

(103) Ao, G.; Khripin, C. Y.; Zheng, M. *Journal of the American Chemical Society* **2014**, *136*, 10383–10392.

(104) Yang, Y.; Zheng, M.; Jagota, A. *npj Computational Materials* **2019**, *5*, 1–7.

(105) Lyu, M.; Meany, B.; Yang, J.; Li, Y.; Zheng, M. *Journal of the American Chemical Society* **2019**, *141*, 20177–20186.

(106) Howes, P. D.; Chandrawati, R.; Stevens, M. M. *Science* **2014**, *346*, 1247390.

(107) Tîlmaciu, C.-M.; Morris, M. C. *Frontiers in Chemistry* **2015**, *3*, 1–21.

(108) Jacobs, C. B.; Peairs, M. J.; Venton, B. J. *Analytica Chimica Acta* **2010**, *662*, 105–127.

(109) Vashist, S. K.; Zheng, D.; Al-Rubeaan, K.; Luong, J. H.; Sheu, F. S. *Biotechnology Advances* **2011**, *29*, 169–188.

(110) Barone, P. W.; Baik, S.; Heller, D. A.; Strano, M. S. *Nature Materials* **2005**, *4*, 86–92.

(111) Bisker, G.; Dong, J.; Park, H. D.; Iverson, N. M.; Ahn, J.; Nelson, J. T.; Landry, M. P.; Kruss, S.; Strano, M. S. *Nature Communications* **2016**, *7*, 1–14.

(112) Bisker, G.; Bakh, N. A.; Lee, M. A.; Ahn, J.; Park, M.; O'Connell, E. B.; Iverson, N. M.; Strano, M. S. *ACS Sensors* **2018**, *3*, 367–377.

(113) Kruss, S.; Landry, M. P.; Vander Ende, E.; Lima, B. M. A.; Reuel, N. F.; Zhang, J.; Nelson, J.; Mu, B.; Hilmer, A.; Strano, M. *Journal of the American Chemical Society* **2014**, *136*, 713–724.

(114) Harvey, J. D.; Jena, P. V.; Baker, H. A.; Zerze, G. H.; Williams, R. M.; Galassi, T. V.; Roxbury, D.; Mittal, J.; Heller, D. A. *Nature Biomedical Engineering* **2017**, *1*, 1–11.

(115) Galassi, T. V. et al. *Science Translational Medicine* **2018**, *10*, 1–11.

(116) Harvey, J. D.; Baker, H. A.; Ortiz, M. V.; Kentsis, A.; Heller, D. A. *ACS Sensors* **2019**, *4*, 1236–1244.

(117) Cognet, L.; Tsyboulski, D. A.; Rocha, J.-D. D. R.; Doyle, C. D.; Tour, J. M.; Weisman, R. B. *Science* **2007**, *316*, 1465–1468.

(118) Hendler-Neumark, A.; Bisker, G. *Sensors (Switzerland)* **2019**, *19*, 1–16.

(119) Kallmyer, N. E.; Musielewicz, J.; Sutter, J.; Reuel, N. F. *Analytical Chemistry* **2018**, *90*, 5209–5216.

(120) Shumeiko, V.; Paltiel, Y.; Bisker, G.; Hayouka, Z.; Shoseyov, O. *Sensors (Switzerland)* **2020**, *20*, 1–14.

(121) Beyene, A. G.; Delevich, K.; Del Bonis-O'Donnell, J. T.; Piekarski, D. J.; Lin, W. C.; Wren Thomas, A.; Yang, S. J.; Kosillo, P.; Yang, D.; Prounis, G. S.; Wilbrecht, L.; Landry, M. P. *Science Advances* **2019**, *5*, eaaw3108.

(122) Dinarvand, M.; Neubert, E.; Meyer, D.; Selvaggio, G.; Mann, F. A.; Erpenbeck, L.; Kruss, S. *Nano Letters* **2019**, *19*, 6604–6611.

(123) Yum, K.; Ahn, J. H.; McNicholas, T. P.; Barone, P. W.; Mu, B.; Kim, J. H.; Jain, R. M.; Strano, M. S. *ACS Nano* **2012**, *6*, 819–830.

(124) Lee, M. A.; Wang, S.; Jin, X.; Bakh, N. A.; Nguyen, F. T.; Dong, J.; Silmore, K. S.; Gong, X.; Pham, C.; Jones, K. K.; Muthupalani, S.; Bisker, G.; Son, M.; Strano, M. S. *Advanced Healthcare Materials* **2020**, *2000429*, 1–13.

(125) Jena, P. V.; Galassi, T. V.; Roxbury, D.; Heller, D. A. *ECS Journal of Solid State Science and Technology* **2017**, *6*, M3075–M3077.

(126) Yudasaka, M.; Yomogida, Y.; Zhang, M.; Tanaka, T.; Nakahara, M.; Kobayashi, N.; Okamatsu-Ogura, Y.; Machida, K.; Ishihara, K.; Saeki, K.; Kataura, H. *Scientific Reports* **2017**, *7*, 1–12.

(127) Shumeiko, V.; Paltiel, Y.; Bisker, G.; Hayouka, Z.; Shoseyov, O. *Biosensors and Bioelectronics* **2021**, *172*, 112763.

(128) Heller, D. A.; Jin, H.; Martinez, B. M.; Patel, D.; Miller, B. M.; Yeung, T. K.; Jena, P. V.; Höbartner, C.; Ha, T.; Silverman, S. K.; Strano, M. S. *Nature Nanotechnology* **2009**, *4*, 114–120.

(129) Kim, J. H.; Patra, C. R.; Arkalgud, J. R.; Boghossian, A. A.; Zhang, J.; Han, J. H.; Reuel, N. F.; Ahn, J. H.; Mukhopadhyay, D.; Strano, M. S. *ACS Nano* **2011**, *5*, 7848–7857.

(130) Kim, J. H.; Heller, D. A.; Jin, H.; Barone, P. W.; Song, C.; Zhang, J.; Trudel, L. J.; Wogan, G. N.; Tannenbaum, S. R.; Strano, M. S. *Nature Chemistry* **2009**, *1*, 473–481.

(131) Mann, F.; Herrmann, N.; Meyer, D.; Kruss, S. *Sensors* **2017**, *17*, 1521.

(132) Jeong, S.; Yang, D.; Beyene, A. G.; Del Bonis-O'Donnell, J. T.; Gest, A. M.; Navarro, N.; Sun, X.; Landry, M. P. *Science Advances* **2019**, *5*, 1–13.

(133) Polo, E.; Nitka, T.; Neubert, E.; Erpenbeck, L.; Vuković, L.; Kruss *ACS Applied Materials & Interfaces* **2018**, *10*, 17693-17703.

(134) Williams, R. M.; Lee, C.; Galassi, T. V.; Harvey, J. D.; Leicher, R.; Sirenko, M.; Dorso, M. A.; Shah, J.; Olvera, N.; Dao, F.; Levine, D. A.; Heller, D. A. *Science Advances* **2018**, *4*, 1–11.

(135) Mann, F. A.; Lv, Z.; Grosshans, J.; Opazo, F.; Kruss, S. *Angewandte Chemie International Edition* **2019**, *58*, 1469–11473.

(136) Landry, M. P.; Ando, H.; Chen, A. Y.; Cao, J.; Kottadiel, V. I.; Chio, L.; Yang, D.; Dong, J.; Lu, T. K.; Strano, M. S. *Nature Nanotechnology* **2017**, *12*, 368–377.

(137) Pan, J.; Zhang, H.; Cha, T.-G. G.; Chen, H.; Choi, J. H.; Cha, T.-G. G.; Zhang, H.; Pan, J.; Chen, H. *Analytical Chemistry* **2013**, *85*, 8391–8396.

(138) Dunn, M. R.; Jimenez, R. M.; Chaput, J. C. *Nature Reviews Chemistry* **2017**, *1*, 1–16.

(139) Keefe, A. D.; Pai, S.; Ellington, A. *Nature Reviews Drug Discovery* **2010**, *9*, 537–550.

(140) Benayas, A.; Hemmer, E.; Hong, G.; Jaque, D., *Near Infrared-Emitting Nanoparticles for Biomedical Applications*; Springer Nature Switzerland: 2020.

(141) Cao, J.; Zhu, B.; Zheng, K.; He, S.; Meng, L.; Song, J.; Yang, H. *Frontiers in Bioengineering and Biotechnology* **2020**, *7*, 1–21.

(142) Liu, P.; Mu, X.; Zhang, X. D.; Ming, D. *Bioconjugate Chemistry* **2020**, *31*, 260–275.

(143) Bardhan, N. M.; Ghosh, D.; Belcher, A. M. *Nature Communications* **2014**, *5*, 1–11.

(144) Ghosh, D.; Bagley, A. F.; Na, Y. J.; Birrer, M. J.; Bhatia, S. N.; Belcher, A. M. *Proceedings of the National Academy of Sciences* **2014**, *111*, 13948–13953.

(145) Welsher, K.; Liu, Z.; Sherlock, S. P.; Robinson, J. T.; Chen, Z.; Daranciang, D.; Dai, H. *Nature Nanotechnology* **2009**, *4*, 773–780.

(146) Zheng, M.; Jagota, A.; Semke, E. D.; Diner, B. A.; McLean, R. S.; Lustig, S. R.; Richardson, R. E.; Tassi, N. G. *Nature Materials* **2003**, *2*, 338–342.

(147) Gillen, A. J.; Kupis-rozmysłowicz, J.; Gigli, C.; Schuergers, N.; Boghossian, A. A. *The Journal of Physical Chemistry Letters* **2018**, *9*, 4336-4343.

(148) Schöppler, F.; Mann, C.; Hain, T. C.; Neubauer, F. M.; Privitera, G.; Bonaccorso, F.; Chu, D.; Ferrari, A. C.; Hertel, T. *Journal of Physical Chemistry C* **2011**, *115*, 14682–14686.

(149) Cathcart, H.; Nicolosi, V.; Hughes, J. M.; Blau, W. J.; Kelly, J. M.; Quinn, S. J.; Coleman, J. N. *Journal of the American Chemical Society* **2008**, *130*, 12734–12744.

(150) Brunecker, F. K.; Scho, F.; Hertel, T. *Journal of Physical Chemistry C* **2016**, *120*, 10094-10103.

(151) Campbell, J. F.; Tessmer, I.; Thorp, H. H.; Erie, D. A. *Journal of the American Chemical Society* **2008**, *130*, 10648–10655.

(152) Salem, D. P.; Gong, X.; Liu, A. T.; Koman, V. B.; Dong, J.; Strano, M. S. *Journal of the American Chemical Society* **2017**, 16791–16802.

(153) Albertorio, F.; Hughes, M. E.; Golovchenko, J. A.; Branton, D. *Nanotechnology* **2009**, *20*, 395101.

(154) Jang, D.; Na, W.; Kang, M.; Kim, N.; Shin, S. *Analytical Chemistry* **2016**, *88*, 968–973.

(155) Choi, J. H.; Strano, M. S. *Applied Physics Letters* **2007**, *90*, 223114 – 223114–3.

(156) Beyene, A. G.; Alizadehmojarad, A. A.; Dorlhiac, G.; Goh, N.; Streets, A. M.; Král, P.; Vuković, L.; Landry, M. P. *Nano Letters* **2018**, *18*, 6995–7003.

(157) Zhao, X.; Johnson, J. K.; Pennsyl, V. *Journal of the American Chemical Society* **2007**, 10438–10445.

(158) Roxbury, D.; Mittal, J.; Jagota, A. *Nano Letters* **2012**, *12*, 1464-1469.

(159) Roxbury, D.; Jagota, A.; Mittal, J. *Journal of Physical Chemistry B* **2013**, *117*, 132-140.

(160) Wu, H.; Nißler, R.; Morris, V.; Herrmann, N.; Hu, P.; Jeon, S.-J.; Kruss, S.; Giraldo, J. P. *Nano Letters* **2020**, *20*, 2432–2442.

(161) Nißler, R.; Bader, O.; Dohmen, M.; Walter, S. G.; Noll, C.; Selvaggio, G.; Groß, U.; Kruss, S. *Nature Communications* **2020**, *11*, 1–12.

(162) Pinals, R. L.; Yang, D.; Lui, A.; Cao, W.; Landry, M. P. *Journal of the American Chemical Society* **2020**, *142*, 1254–1264.

(163) Lew, T. T. S.; Sarojam, R.; Jang, I. C.; Park, B. S.; Naqvi, N. I.; Wong, M. H.; Singh, G. P.; Ram, R. J.; Shoseyov, O.; Saito, K.; Chua, N. H.; Strano, M. S. *Nature Plants* **2020**, *6*, 1408–1417.

(164) Tritsch, N. X.; Granger, A. J.; Sabatini, B. L. *Nature Reviews Neuroscience* **2016**, *17*, 139–145.

(165) Kaper, J. B.; Nataro, J. P.; Mobley, H. L. *Nature Reviews Microbiology* **2004**, *2*, 123–140.

(166) Ramachandran, G. *Virulence* **2014**, *5*, 213–218.

(167) Jakubka, F.; Grimm, S. B.; Zakharko, Y.; Gannott, F.; Zaumseil, J. *ACS Nano* **2014**, 8477–8486.

(168) Lei, T.; Chen, X.; Pitner, G.; Wong, H. S.; Bao, Z. *Journal of the American Chemical Society* **2016**, *138*, 802–805.

(169) Liang, S.; Zhao, Y.; Adronov, A. *Journal of the American Chemical Society* **2014**, *136*, 970–977.

(170) Wang, D.; Chen, L. *Nano Letters* **2007**, *7*, 1480–1484.

(171) Rajter, R. F.; French, R. H.; Ching, W. Y.; Podgornik, R.; Parsegian, V. A. *RSC Advances* **2013**, *3*, 823–842.

(172) Harris, J. M.; Huh, J. Y.; Semler, M. R.; Ihle, T.; Stafford, C. M.; Hudson, S. D.; Fagan, J. A.; Hobbie, E. K. *Soft Matter* **2013**, *9*, 11568–11575.

(173) Berger, F. J.; De Sousa, J. A.; Zhao, S.; Zorn, N. F.; El Yumin, A. A.; Quintana García, A.; Settele, S.; Högele, A.; Crivillers, N.; Zaumseil, J. *ACS Nano* **2021**, *15*, 5147–5157.

(174) Fagan, J. A.; Hároz, E. H.; Ihly, R.; Gui, H.; Blackburn, J. L.; Simpson, J. R.; Lam, S.; Hight Walker, A. R.; Doorn, S. K.; Zheng, M. *ACS Nano* **2015**, *9*, 5377–5390.

(175) Streit, J. K.; Fagan, A.; Zheng, M. *Analytical Chemistry* **2017**, *89*, 10496–10503.

(176) Giraldo, J. P.; Landry, M. P.; Kwak, S. Y.; Jain, R. M.; Wong, M. H.; Iverson, N. M.; Ben-Naim, M.; Strano, M. S. *Small* **2015**, *11*, 3973–3984.

(177) Salem, D. P. D.; Landry, M. P. M.; Bisker, G.; Ahn, J.; Kruss, S.; Strano, M. M. S. *Carbon* **2016**, *97*, 147–153.

(178) Landry, M. P.; Vukovic, L.; Kruss, S.; Bisker, G.; Landry, A. M.; Islam, S.; Jain, R.; Schulten, K.; Strano, M. S. *Journal of Physical Chemistry C* **2015**, 10048-10058.

(179) Xhyliu, F.; Ao, G. *Carbon* **2020**, *167*, 601–608.

(180) Spreinat, A.; Dohmen, M. M.; Herrmann, N.; Klepzig, L. F.; Nißler, R.; Weber, S.; Mann, F. A.; Lauth, J.; Kruss, S. *The Journal of Physical Chemistry C* **2021**, *125*, 18341–18351.

(181) Váradi, L.; Luo, J. L.; Hibbs, D. E.; Perry, J. D.; Anderson, R. J.; Orenga, S.; Groundwater, P. W. *Chemical Society Reviews* **2017**, *46*, 4818–4832.

(182) Carbonnelle, E.; Mesquita, C.; Bille, E.; Day, N.; Dauphin, B.; Beretti, J. L.; Ferroni, A.; Gutmann, L.; Nassif, X. *Clinical Biochemistry* **2011**, *44*, 104–109.

(183) Bertelli, C.; Greub, G. *Clinical Microbiology and Infection* **2013**, *19*, 803–813.

(184) Kumar, A.; Roberts, D.; Wood, K. E.; Light, B.; Parrillo, J. E.; Sharma, S.; Suppes, R.; Feinstein, D.; Zanotti, S.; Taiberg, L.; Gurka, D.; Kumar, A.; Cheang, M. *Critical Care Medicine* **2006**, *34*, 1589–1596.

(185) Lim, S. K.; Chen, P.; Lee, F. L.; Moochhala, S.; Liedberg, B. *Analytical Chemistry* **2015**, *87*, 9408–9412.

(186) Holden, V. I.; Bachman, M. A. *Metallomics* **2015**, *7*, 986–995.

(187) Wilson, H.; Ripp, S.; Prisbrey, L.; Brown, M. A.; Sharf, T.; Myles, D. J. T.; Blank, K. G.; Minot, E. D. *Journal of Physical Chemistry C* **2016**, *120*, 1971–1976.

(188) Petrik, M.; Zhai, C.; Haas, H.; Decristoforo, C. *Clinical and Translational Imaging* **2017**, *5*, 15–27.

(189) Cheung, W.; Patel, M.; Ma, Y.; Chen, Y.; Xie, Q.; Lockard, J. V.; Gao, Y.; He, H. *Chem. Sci.* **2016**, *7*, 5192–5199.

(190) Weizman, H.; Ardon, O.; Mester, B.; Libman, J.; Dwir, O.; Hadar, Y.; Chen, Y.; Shanzer, A. *Journal of the American Chemical Society* **1996**, *118*, 12368–12375.

(191) Li, Y.; Geyer, C. R.; Sen, D. *Biochemistry* **1996**, *35*, 6911–6922.

(192) Letoffe, S.; Heuck, G.; Delepelaire, P.; Lange, N.; Wandersman, C. *Proceedings of the National Academy of Sciences of the United States of America* **2009**, *106*, 11719–11724.

(193) Wu, S. J.; Schuergers, N.; Lin, K. H.; Gillen, A. J.; Corminboeuf, C.; Boghossian, A. A. *ACS Applied Materials and Interfaces* **2018**, *10*, 37386–37395.

(194) Wong, M. H.; Giraldo, J. P.; Kwak, S. Y.; Koman, V. B.; Sinclair, R.; Lew, T. T. S.; Bisker, G.; Liu, P.; Strano, M. S. *Nature Materials* **2017**, *16*, 264–272.

(195) Lee, M. A. et al. *ACS Sensors* **2019**, *4*, 32–43.

(196) Kozawa, D.; Cho, S. Y.; Gong, X.; Nguyen, F. T.; Jin, X.; Lee, M. A.; Lee, H.; Zeng, A.; Xue, G.; Schacherl, J.; Gibson, S.; Vega, L.; Strano, M. S. *ACS Nano* **2020**, *14*, 10141–10152.

(197) Dong, J.; Salem, D. P.; Sun, J. H.; Strano, M. S. *ACS Nano* **2018**, *12*, 3769–3779.

(198) Selvaggio, G. et al. *Nature Communications* **2020**, *11*, 1495.

(199) Doern, G. V.; Carroll, K. C.; Diekema, D. J.; Garey, K. W.; Rupp, M. E.; Weinstein, M. P.; Sextong, D. J. *Clinical Microbiology Reviews* **2020**, *33*, 1–21.

(200) Wilson, M. L. *Clinical Microbiology and Infection* **2020**, *26*, 319–324.

(201) Dodds, P. N.; Rathjen, J. P. *Nature Reviews Genetics* **2010**, *11*, 539–548.

(202) Li, C.; Yan, B. *Environmental Science: Nano* **2020**, *7*, 2863–2874.

(203) Chakraborty, S.; Newton, A. C. *Plant Pathology* **2011**, *60*, 2–14.

(204) Fisher, M. C.; Henk, D. A.; Briggs, C. J.; Brownstein, J. S.; Madoff, L. C.; McCraw, S. L.; Gurr, S. J. *Nature* **2012**, *484*, 186–194.

(205) Alexandratos, N.; Bruinsma, J. World agriculture towards 2030/2050: the 2012 revision. Food and Agriculture Organization ofthe United Nations: Rome, Italy, 2012.

(206) Lew, T. T. S.; Park, M.; Cui, J.; Strano, M. S. *Advanced Materials* **2021**, *33*, 1–11.

(207) Mur, L. A.; Kenton, P.; Lloyd, A. J.; Ougham, H.; Prats, E. *Journal of Experimental Botany* **2008**, *59*, 501–520.

(208) Balint-Kurti, P. *Molecular Plant Pathology* **2019**, *20*, 1163–1178.

(209) Jin, H.; Heller, D. A.; Kim, J.-h.; Strano, M. S. *Nano Letters* **2008**, *8*, 4299–4304.

(210) Jin, H.; Heller, D. A.; Kalbacova, M.; Kim, J. H.; Zhang, J.; Boghossian, A. A.; Maheshri, N.; Strano, M. S. *Nature Nanotechnology* **2010**, *5*, 302–309.

(211) Crochet, J. J.; Duque, J. G.; Werner, J. H.; Doorn, S. K. *Nature Nanotechnology* **2012**, *7*, 126–132.

(212) Ensing, B.; Buda, F.; Baerends, E. J. *Journal of Physical Chemistry A* **2003**, *107*, 5722–5731.

(213) Enami, S.; Sakamoto, Y.; Colussi, A. J. *Proceedings of the National Academy of Sciences of the United States of America* **2014**, *111*, 623–628.

(214) Atsumi, H.; Belcher, A. M. *ACS Nano* **2018**, *12*, 7986–7995.

(215) Traylor, T. G.; Xu, F. *Journal of the American Chemical Society* **1990**, *112*, 178–186.

(216) Safaee, M. M.; Gravely, M.; Roxbury, D. *Advanced Functional Materials* **2021**, *2006254*, 1–14.

(217) Albert, M. *Journal of Experimental Botany* **2013**, *64*, 5269–5279.

(218) Walia, A.; Waadt, R.; Jones, A. M. *Annual Review of Plant Biology* **2018**, *69*, 497–524.

(219) Wu, F. et al. *Nature* **2020**, *578*, 577–581.

(220) Giraldo, J. P.; Landry, M. P.; Faltermeier, S. M.; McNicholas, T. P.; Iverson, N. M.; Boghossian, A. A.; Reuel, N. F.; Hilmer, A. J.; Sen, F.; Brew, J. A.; Strano, M. S. *Nature Materials* **2014**, *13*, 400–408.

(221) Meyer, D.; Telele, S.; Zelená, A.; Gillen, A. J.; Antonucci, A.; Neubert, E.; Nißler, R.; Mann, F. A.; Erpenbeck, L.; Boghossian, A. A.; Köster, S.; Kruss, S. *Nanoscale* **2020**, *12*, 9104–9115.

(222) Neubert, E.; Meyer, D.; Rocca, F.; Günay, G.; Kwaczala-Tessmann, A.; Grandke, J.; Senger-Sander, S.; Geisler, C.; Egner, A.; Schön, M. P.; Erpenbeck, L.; Kruss, S. *Nature Communications* **2018**, *9*, 1–13.

(223) Zhou, J.; Lin, Z.; Ju, Y.; Rahim, M. A.; Richardson, J. J.; Caruso, F. *Accounts of Chemical Research* **2020**, *53*, 1269–1278.

(224) Jakobek, L. *Food Chemistry* **2015**, *175*, 556–567.

(225) Ishibashi, Y.; Ito, M.; Homma, Y.; Umemura, K. *Colloids and Surfaces B: Biointerfaces* **2018**, *161*, 139–146.

(226) Umemura, K.; Ishibashi, Y.; Ito, M.; Homma, Y. *ACS Omega* **2019**, *4*, 7750–7758.

(227) Yamazaki, Y.; Umemura, K. *Journal of Near Infrared Spectroscopy* **2020**, 1–3.

(228) Polo, E.; Kruss, S. *Journal of Physical Chemistry C* **2016**, *120*, 3061–3070.

(229) Khoddami, A.; Wilkes, M. A.; Roberts, T. H. *Molecules* **2013**, *18*, 2328–2375.

(230) Pelle, F. D.; Compagnone, D. *Sensors (Switzerland)* **2018**, *18*, 1–32.

(231) David, M.; Florescu, M.; Bala, C. *Biosensors* **2020**, *10*, 1–19.

(232) Salminen, J.-p.; Karonen, M. *Functional Ecology* **2011**, *25*, 325–338.

(233) Singh, S.; Kaur, I.; Kariyat, R. *International Journal of Molecular Sciences* **2021**, *22*, 1–19.

(234) Lanoue, A.; Burlat, V.; Schurr, U.; Röse, U. S. *Plant Signaling and Behavior* **2010**, *5*, 1037–1038.

(235) Baetz, U.; Martinoia, E. *Trends in Plant Science* **2014**, *19*, 90–98.

(236) Fisher, D. B.; Frame, J. M. *Planta* **1984**, *161*, 385–393.

(237) Lohaus, G.; Schwerdtfeger, M. *PLoS ONE* **2014**, *9*, 1–8.

9 | Abbreviations

A	Adenine
AFM	Atomic force microscopy
ANOVA	Analysis of variance
ATPE	Aqueous two-phase extraction
B-phase	Bottom-phase
BSA	Bovine serum albumin
C	Cytosine
CNTs	Carbon nanotubes
CoMoCAT	Cobalt-Molybdenum catalysis
CoPhMoRe	Corona phase molecular recognition
CPEP	Corona phase exchange purification
CT	Calf thymus (DNA)
CVD	Chemical vapor deposition
DGU	Density gradient ultracentrifugation
DNA	Desoxyribonucleic acid
DOC	Sodium deoxycholate
DOS	Density of states
EB-NS	Egyptian Blue-nanosheets
EtOH	Ethanol
Elc	Elicitor
flg22	Flgiella peptide (from *Pseudomonas* spp)
G	Guanine
GaA	Gallic acid
GC-MS	Gas chromatography mass spectrometry
HeApta	Hemin-aptamer
HG	Hydrogel
HiPco	High-pressure carbon monoxide (CNT synthesis)
HPLC	High-pressure liquid chromatography
HR	High-resolution
HR-STM	High-resolution scanning tunnelling microscopy

HR-TEM	High-resolution transmission electron microscopy
IEC	Ion exchange chromatography
InGaAs	Indium gallium arsenide (camera)
LDA	Linear discriminant analysis
LP	Long-pass filter
LPS	Lipopolysaccharide
MD	Molecular dynamic (simulations)
MeOH	Methanol
mRNA	Messenger-ribonucleic acid
MS	Mass spectrometry
m-SWCNT	Metallic single-walled carbon nanotube
MW	Molecular weight
MWCNTs	Multi-walled carbon nanotubes
MWCO	Molecular weight cut-off
NETosis	Neutrophil extracellular trap formation
NIR	Near-infrared
OD	Optical density
PBS	Phosphate-buffered saline
PCA	Principal component analysis
PCR	Polymerase chain reaction
PEG	Poly(ethylene glycol)
PEG-DA	Poly(ethylene glycol) – diacrylate
PEG-PL	Poly(ethylene glycol) – phospholipids
PET	Positron emission tomography
PFO	Polyfluorene(polymer)
PFO-BPy	Poly[(9,9-dioctylfluorenyl-2,7-diyl)-alt-co-(6,6'-2,2'-bipyridine)
PL	Photoluminescence
QY	Quantum yield
RNA	Ribonucleic acid
ROS	Reactive oxygen species
s-SWCNT	Semiconducting single-walled carbon nanotube
SC	Sodium cholate
SD	Standard deviation
SDBS	Sodium dodecylbenzenesulfonate
SDS	Sodium dodecyl sulfate
SEC	Size exclusion chromatography

SEM	Standard error of the mean
SMCC	Succinimidyl 4-(N-maleimidomethyl) cyclohexane-1-carboxylate
ssDNA	Single-stranded desoxyribonucleic acid
SWCNTs	Single-walled carbon nanotubes
T	Thymine
TaA	Tannic acid
THP	Trihydroxypterocarpan
T-phase	Top-phase
UV-Vis	Ultraviolet – visible

10 | List of Figures

List of Figures

A | Publications

First-author publications:

1. *Detection and imaging of the plant pathogen response by near infrared fluorescent polyphenol sensors*
   R. Nißler, A. T. Müller, F. Dohrman, L. Kurth, H. Li, E. G. Cosio, B. S. Flavel, J. P. Giraldo, A. Mithöfer, S. Kruss,
   Angewandte Chemie Int. Ed. **2021**. DOI: 10.1002/anie.202108373

2. *Sensing with Chirality-Pure Near-Infrared Fluorescent Carbon Nanotubes*
   R. Nißler, L. Kurth, H. Li, A. Spreinat, I. Kuhlemann, B. S. Flavel, S. Kruss,
   Analytical Chemistry **2021**. DOI: 10.1021/acs.analchem.1c00168

3. *Remote near infrared identification of pathogens with multiplexed nanosensors*
   R. Nißler, O. Bader, M. Dohmen, S. G. Walter, C. Noll, G. Selvaggio, U. Groß, S. Kruss, *Nature Communications* **2020**. DOI: 10.1038/s41467-020-19718-5

4. *Monitoring Plant Health with Near Infrared Fluorescent H_2O_2 Nanosensors*
   H. Wu, R. Nißler, V. H. Morris, N. Herrmann, P. Hu, S. J. Jeon, S. Kruss, J. P. Giraldo, *Nano Letters* **2020**. DOI: 10.1021/acs.nanolett.9b05159

5. *Chirality enriched carbon nanotubes with tunable wrapping via corona phase exchange purification (CPEP)*
   R. Nißler, F. A. Mann, F. A. Mann, H. Preiß, G.Selvaggio, N. Herrmann, S. Kruss, *Nanoscale* **2019**. DOI: 10.1039/C9NR03258D

6. *Quantification of the Number of Adsorbed DNA Molecules on Single-Walled Carbon Nanotubes*
   R. Nißler,F. A. Mann, P. Chaturvedi, J. Horlebein, D. Meyer, L. Vuković, S. Kruss, *The Journal of Physical Chemistry C* **2019**. DOI: 10.1021/acs.jpcc.8b11058

Co-authored publications:

1. *Quantum Defects in Fluorescent Carbon Nanotubes for Sensing and Mechanistic Studies* A. Spreinat, M. M. Dohmen, N. Herrmann, L. F. Klepzig, R. Nißler, S. Weber, F. A. Mann, J. Lauth and S. Kruss, *The Journal of Physical Chemistry C* **2021**. DOI: 10.1021/acs.jpcc.1c05432

2. *Exfoliation and Optical Properties of Near-Infrared Fluorescent Silicate Nanosheets* G. Selvaggio, M. Weitzel, N. Oleksiievets, T. A. Oswald, R. Nißler, I. Mey, V. Karius, J. Enderlein, R. Tsukanov, and S. Kruss, *Nanoscale Advances* **2021**. DOI: 10.1039/d1na00238d

3. *Transport and programmed release of nanoscale cargo from cells by using NETosis* D. Meyer, S. Telele, A. Zelena, A. J. Gillen, A. Antonucci, E. Neubert, R. Nißler, F. A. Mann, L. Erpenbeck, A. Boghossian, S. Köster, S. Kruss, *Nanoscale* **2020**. DOI: 10.1039/D0NR00864H

4. *Chemical Imaging with Fluorescent Nanosensors*
   S. Hamsici, R. Nißler, F. A. Mann, D. Meyer, S. Kruss, *21st Century Nanoscience* **2020**. ISBN: 9780815384731

5. *Exfoliated near infrared fluorescent silicate nanosheets for (bio)photonics*
   G. Selvaggio, A. Chizhik, R. Nißler, I. Kuhlemann, D. Meyer, L. Vuong, H. Preiss, N. Herrmann, F. A. Mann, Z. Lv, T. A. Oswald, A. Spreinat, L. Erpenbeck, J. Grosshans, V. Karius, A. Janshoff, J. P. Giraldo, S. Kruss, *Nature Communications* **2020**. DOI: 10.1038/s41467-020-15299-5

B | Oral talks

1. R. Nißler, A. T. Müller, F. Dohrman, L. Kurth, H. Li, E. G. Cosio, B. S. Flavel, J. P. Giraldo, A. Mithöfer, S. Kruss, NT21 - 21th International Conference on the Science and Application of Nanotubes and Low-Dimensional Materials **2021** (Digital meeting)
   Detection and imaging of plant pathogen response by NIR-fluorescent polyphenol sensors

2. R. Nißler, O. Bader, M. Dohmen, S. G. Walter, C. Noll, G. Selvaggio, U. Groß, S. Kruss, 239th ECS Meeting - B02 Carbon Nanostructures in Medicine and Biology **2021** (Digital meeting)
   Remote near infrared detection and identification of pathogens with multiplexed nanosensors

3. R. Nißler, L. Kurth, H. Li, A. Spreinat, I. Kuhlemann, B. S. Flavel, S. Kruss, 239th ECS Meeting - B03 Carbon Nanotubes - From Fundamentals to Devices **2021** (Digital meeting)
   Sensing with Chirality-Pure Near-Infrared Fluorescent Carbon Nanotubes

4. R. Nißler, S. Kruss, 18th International Meeting on Chemical Sensors (IMCS) **2021** (Digital meeting)
   Towards Tailored Carbon Nanotube-Based Fluorescent Sensors

5. R. Nißler, S. Kruss, REVOLV Spring Workshop **2021** (Digital meeting)
   Carbon nanotubes as highly sensitive and selective sensors for biomolecular interactions

6. R. Nißler, F. A. Mann, H. Preiß, G.Selvaggio, N. Herrmann, S. Kruss, NT19 - 20th International Conference on the Science and Application of Nanotubes and Low-Dimensional Materials **2019** (Würzburg)
   Chirality enriched carbon nanotubes with tunable wrapping via corona phase exchange purification (CPEP)

C | Posters

1. R. Nißler, O. Bader, M. Dohmen, S. G. Walter, C. Noll, G. Selvaggio, U. Groß, S. Kruss, NT21 - 21th International Conference on the Science and Application of Nanotubes and Low-Dimensional Materials **2021** (Digital meeting)
   Remote near infrared detection and identification of pathogens with multiplexed nanosensors

2. R. Nißler, O. Bader, M. Dohmen, S. G. Walter, C. Noll, G. Selvaggio, U. Groß, S. Kruss, Bunsentagung **2021** - Multi-Scale Modelling & Physical Chemistry of Colloids (Digital meeting)
   Remote near infrared detection and identification of pathogens with multiplexed nanosensors

3. R. Nißler, L. Kurth, H. Li, A. Spreinat, I. Kuhlemann, B. S. Flavel, S. Kruss, Bunsentagung **2021** - Multi-Scale Modelling & Physical Chemistry of Colloids (Digital meeting)
   Sensing with Chirality-Pure Near-Infrared Fluorescent Carbon Nanotubes

4. R. Nißler, S. Kruss, 3rd Infinity Conference **2020** (Göttingen)
   Towards tailored near infrared fluorescent nano sensors for detecting bacterial interactions

5. R. Nißler, F. A. Mann, P. Chaturvedi, J. Horlebein, D. Meyer, L. Vuković, S. Kruss, NT19 - 20th International Conference on the Science and Application of Nanotubes and Low-Dimensional Materials **2019** (Würzburg)
   Quantification of the Number of Adsorbed DNA Molecules on Single-Walled Carbon Nanotubes

6. R. Nißler, S. Hamsici, F. A. Mann, E. Polo and S. Kruss, Bunsentagung **2019** - Functional Materials, (Jena)
   Detection of bacterial motifs with near-infrared fluorescent single walled carbon nanotubes

7. R. Nißler, S. Hamsici, F. A. Mann, E. Polo and S. Kruss, 4th Statussymposium: Integration of Molecular Components in functional macroscopic Systems **2018** (Hannover)
   Tailored near infrared fluorescent carbon nanotubes to detect bacteria

8. R. Nißler, S. Hamsici, F. A. Mann, E. Polo and S. Kruss, Bunsentagung **2018** - Kinetics in the Real World, (Hannover)
   Quantification of DNA-oligonucleotide adsorption on near infrared fluorescent carbon nanotubes

D | Acknowledgements

I want to thank my supervisor Prof. Sebastian Kruss that he gave me the possibility to do my PhD in his research group. Thanks for your constant mentorship, for the fruitful working atmosphere and for supporting me, as well as enabling realization of own research ideas. Next, I want to thank the other members of the thesis advisory committee, Prof. Uwe Groß and Prof. Marina Bennati, for their helpful discussions during the TAC meetings, for their input and their time examining this thesis. Furthermore, I am truly grateful for all members of the disputation examination board, including the TAC members and Prof. Timo Betz, Prof. Frauke Alves and Dr. Tim Schäfer. Thank you for your interest and your time!

On the way towards the PhD, I came across a lot of people, who supported me and influenced my research interests. I learned so much from all of you, therefore I want to say thanks! Starting in a chronological way with Dr. Johanna Kirchhoff and Prof. Ute Neugebauer from the Leibniz-IPHT Jena, Dr. Rodolfo Piazza and Prof. Jafelicci Junior Miguel from São Paulo State University, PD. Dr. Axel Mithöfer and Dr. Christian Pätz from the MPI Chemical Ecology Jena, Prof. Eric Cosio from INTE-PUCP Lima, as well as Prof. Christian Hertweck and Prof. Georg Pohnert for establishing and guiding through the Chemical Biology master program.

Now to my truly great colleagues, without your help and support during the last nearly four years, it would have been by far not as funny and successful as it was! Big, big thanks to Gabriele (Gabi) Selvaggio, Florian (Flo) Mann, Meshkat Dinarvand, Daniel Meyer, Elsa Neubert, Alexander Spreinat and Niklas Herrmann. Also, thanks to my bachelor students Frederike (Rike) Dohrmann and Larissa Kurth for their support! It was a lot of fun to work with you! Also big thanks to the members of the groups from Prof. Janshoff and Prof. Steinem and the Abholungspartys we had together!

I want to thank all collaboration partners within the several projects presented in this thesis, with special thanks to Prof. Lela Vucovic (University of Texas), Prof. Hong Hong Wu and Prof. Juan Pablo Giraldo (UC Riverside), Dr. Oliver Bader (University Medical Center Göttingen) and Dr. Han Li and Dr. Ben Favel (Karlsruhe Institute of Technology) and PD Dr. Axel Mithöfer (MPI-CE Jena).

Furthermore, I want to thank the *Studienstiftung des deutschen Volkes* for financial support during my master studies! Moreover, many thanks to the graduate school *IMPRS Physics of Biological and Complex Systems* for the academic and financial support.

Special thanks also to those proof reading this thesis! Thanks to Martin Gebhardt, Gabriele Selvaggio, Andrea Müller, Lennard Scholz, Tanmaya Sethi, Sebastian Walter, Maximillian Dommke and Daniel Nißler!

Finally, yet importantly, I want to thank my parents, family members and friends for their support during my whole studies and for their help in good times as in bad! Thank you all so much and I hope we will see each other at the Gänseliesel for the PhD celebration!